The University Of Sheffield.

Department of Materials Science and Engineering

Study of intermetallic alloys for high temperature applications “beyond the Ni superalloys”

Ofelia Del Carmen Hernández-Negrete

Thesis submitted for the degree of Doctor of Philosophy

October 2016

Abstract

Future aero-engines must run hotter than current ones to meet performance and environmental targets. This makes it necessary to search for new ultra-high temperature alloys with capabilities beyond those of Ni based superalloys (NBS). This thesis is about the former materials.

Niobium silicide based alloys (NSBAs) have the potential to meet material property goals for future aero-engines. Significant improvements of their oxidation at low, intermediate and high temperatures have been achieved via alloying. In service, like the NBS, the NSBAs will need a coating system and should have acceptable oxidation resistance to "survive" in case of coating failure. The coating is envisaged to be thermal barrier (type) coating system (TBC) consisting of multi-alloy or compositionally gradient bond coat (BC), thermally grown oxide (TGO) and ceramic top coat (CTC).

This thesis is about the search of intermetallic based alloys without "exotic" alloying additions (i.e., no Ru, Re, Pt) suitable for application in BC (alloys OHC1=Si-23Fe-15Cr-15Ti-1Nb, OHC2=Si-22Fe-12Cr-12Al-10Ti-5Nb, OHC3=Al-25.5Nb-8Cr-0.5Hf, OHC5=Si-25Nb-5Al-5Cr-5Ti) and the microstructure and oxidation of a model substrate alloy (OHS1=Nb-24Ti-18Si-5Al-5Cr-5Ge-5Sn) all nominal compositions in at.%. The alloys were prepared using arc melting. Their cast, heat treated and oxidised microstructures and their oxidation were studied using DSC, XRD, SEM, EDS and TG.

The alloy OHS1 exhibited strong and weak macrosegregation respectively of Si and Ti and Al, Cr and Sn. The cast microstructure consisted of the A15-Nb_3Sn, $(\beta Nb_5Si_3)_{primary}$, Nb_{ss}, C14-$NbCr_2$ Laves phases and a ternary eutectic of the latter three. Of these only the Nb_{ss} was not stable after heat treatment at 1400 °C/100 h. The synergy of Sn and Ge with Al, Cr and Ti improved the oxidation at 800 and 1200 °C, there was no pest oxidation at 800 °C and no scale spallation at 1200 °C.

The microstructure of the alloy OHC1 was composed of the $[(TM)_6Si_5]_{primary}$ (T phase), τ_1 ($FeSi_2Ti$) and (Fe,Cr,Ti)Si phases and the eutectic of the latter two (T_{eu} = 1300 °C). The three phases were stable after heat treatment at 1200 °C/48 h and the latter two had coarsened. In the T phase the partition of Fe was opposite to that of Nb, Ti and Cr. A thin and compact oxide scale formed at 800 °C with linear kinetics. At 1200 °C the oxide scale formed with para-linear kinetics, consisted of a Cr_2O_3 outermost layer and SiO_2 at the metal/scale interface and some parts of it had experienced melting at ~ 1155 °C. There was internal oxidation of the alloy.

The microstructure of the alloy OHC2 was composed of the $[(TM)_6Si_5]_{primary}$, $(TM)_5Si_3$, $FeSi_2Ti$, $Fe_3Al_2Si_3$ and (Fe,Cr)(Si,Al) and an unidentified dark phase (DP). The latter two phases were not stable after heat treatment at 950 °C / 48 h. The Al solubility in the T phase was very low. The alloy suffered liquation at 1200 °C. The oxidation at 800 °C was sub-parabolic. Owing to formation of low melting point phases, liquation at temperatures of interest and melting in the scale, the alloys OHC1 and OHC2 were not considered suitable for application in a BC for NSBAs.

The alloy OHC5 was composed of the $[(Nb,Ti)(Si,Al)_2]_{primary}$, $(Cr,Ti,Nb)_6Si_5$, $(Cr,Ti,Nb)(Si,Al)_2$, and (Si) and (Al) solid solutions. The former two phases were stable after heat treatment at 1400 °C/100 h. At 800 °C there was no pesting, the oxidation was parabolic and a multiphase oxide scale was formed where the main oxides were Al_2O_3, SiO_2 and rutile type oxides. A critical Al content was required for external Al_2O_3 oxide formation on top of the $(Nb,Ti)(Si,Al)_2$ phase, this was ~ 3 at.% Al at 800 °C. At 1200 °C an external α-Al_2O_3 scale was formed and the oxidation was parabolic at t >21.5h.

The alloy OHC3 was composed of the $(Al_3Nb)_{primary}$, C14 - $(Al,Cr)_2(Nb,Hf)$ Laves, a Hf-rich phase and $(Cr,Al,Nb)_{ss}$. The former three phases were stable after heat treatment at 1400 °C. The alloy followed parabolic oxidation kinetics at 800, 1200 and 1300 °C. The oxide scale was composed of an outer layer of $(Al,Cr)NbO_4$ and an inner oxide layer of α-Al_2O_3 at all three temperatures. However, some internal oxidation occurred at 800 °C and it was deeper along phase boundaries. At 1200 and 1300 °C the layer of α-Al_2O_3 was thicker and C14-$(Al,Cr)_2(Nb,Hf)$ was formed at the metal/scale interface after oxidation of Al_3Nb. The presence of Hf in the alloy was beneficial for the adhesion of the α-Al_2O_3. At 1300 °C the $(Al,Cr)NbO_4$ top layer suffered partial spallation.

The alloys OHC3 and OHC5 are considered suitable candidates for applications in BC for NSBAs after some improvements. Areas where future alloy development research should concentrate were recommended.

Acknowledgements

This dissertation becomes true because during the course of my research project and its writing, I have received a lot of support from many people and organizations that I would like to recognise.

First and foremost, I would like to express my deep and sincere gratitude to professor Panos Tsakiropoulos who was always very supportive in everything. He is an expert in his field, an enthusiastic mentor who patiently guided me. The conclusion of this dissertation would not have been possible without his help and advice.

Thank you to the National Research and Technology Council from Mexico (CONACyT) and the Roberto Rocca Education Program for giving me the financial support to undertake my PhD studies. I also want to thank the founding received from Professor Panos Research Group which was also essential for the conclusion of these.

In the department of materials science and engineering, there are very valuable people who love their work and were always willing to help and I also appreciate very much. In special, I owe a deeply thank to Mrs. Ann Newbould who always gave me very kind and helpful guidance. I also want to show my sincere gratitude to all the staff from Sorby centre. Dr. Peter Korgul always gave me kind support and friendly advice, it was always a pleasure to talk with him and I really owe a deeply thank and my sincere appreciations.

I really want to give a heartily thank you to my husband who has been very patience and supportive all this time, to my children from which I missed valuable moments during the development of this dissertation. Deeply thanks to my family, friends, and colleagues that contributed in different ways and encouraged me up to the achievement of this dream.

Table of contents

Introduction

In the last 50 years a substantial effort in the aerospace industry has been to design more efficient power systems. One of the most viable ways is through the increase of the working temperature ranges in gas turbines. In the same context, environmental issues have been also addressed as the performance of turbine engines improves.

Ni-based superalloys have been used as structural materials for airfoils in the hottest parts of turbine engines. However, their melting temperature (~ 1350 ˚C for the most advanced) restricts their use. The aerospace industry has been operating these superalloy airfoils with turbine entry temperatures TET ≤ 1500 °C with the use of thermal barrier coatings (TBC) and internal cooling but even with these advances, the increase of the high temperature capabilities of the Ni-based superalloys has reached a limit [Subramanian et al. (1997), Bewlay et al. (2003), Pint et al. (2006)]. Further improvements of the engine's performance as the TET will increase beyond 1600 ˚C will require new high temperature materials.

Therefore, new materials capable of operating with higher TETs are required for the next generation of gas turbine engines. These materials should have some inherent resistance to high temperature corrosion and have good mechanical properties at room, intermediate and high temperatures.

Specifically, the properties required from the new high temperature materials are:

- High melting temperature
- Low density
- Good balance of mechanical properties at high, intermediate and room temperature
- Good oxidation resistance
- Good processability.

Niobium

Among the refractory metals Nb is considered as the base element for new structural materials for high temperature applications. Nb has density (ρ=8.57 g/cm^3) lower than Ni (ρ=8.9 g/cm^3), high solubility for transition and free electron metals (essential for solid solution strengthening), good processability, and very low ductile/brittle transition temperature (DBTT ≈ - 200 °C [Olson et al. (2006), Tsakiropoulos (2010)]. However, Nb has poor oxidation resistance and high solubility of atmospheric components (O, N and C) which cause embrittlement and deterioration of its mechanical properties [Geng et al. (2007b), Begley (1994)].

Niobium has the atomic number 41 and its atomic mass is 92.906. Its crystal lattice is body centered cubic (bcc) with the unit cell parameters a=b=c=0.33067 nm and space group Im3m. It has a five-valent metal behaviour in chemical compounds although the oxidation states 2, 3 and 4 have been found. The Nb does not exhibit allotropic transformations.

Niobium is the most abundant of the refractory metals in the earth crust, its concentration is about 0.001 %. Its high grade ore reserves are mainly found in Brazil. Nb has been used as structural material in the chemical and nuclear industries as well as in spacecraft industry owing to its high melting point (2470 ˚C) and its capacity of strength retention at high temperature.

Nb-silicide based in-situ composites

The Nb-silicides have been considered as suitable intermetallics for use in structural components at high temperature owing to their high melting points, strength and low density. Despite these properties, they do not provide adequate balance of mechanical properties for their practical application and their oxidation resistance can be modest or poor according to temperature. The Nb-silicide in situ composites (also known as Nb-silicide based alloys) consist of the Nb_3Si or Nb_5Si_3 silicides and the bcc Nb solid solution (Nb_{ss}) and are considered the most suitable candidate materials for the replacement of the Ni-based superalloys from the hottest parts of turbine engines as their chemistry can be adjusted for desirable properties.

As we shall see in the next chapter, the Nb-silicide in-situ composites originate from the Nb-Si binary system with the eutectic reaction L→ Nb_{ss} + Nb_3Si that occurs at 1915 °C and Si 17.5 at.% Si. However, the poor mechanical behaviour and the low oxidation resistance of the Nb_3Si, deteriorates the properties of the composites while the Nb_5Si_3 offers appropriate strength and better oxidation resistance at high temperature. Thus, the preferable Nb-silicide based in-situ composites contain Nb_{ss} and Nb_5Si_3. The latter would form via the eutectoid reaction Nb_3Si→ Nb_{ss} + αNb_5Si_3 at 1765 °C [Schlesinger et al. (1993)]. The latter reaction could produce Nb_{ss} + Nb_5Si_3 in-situ composites with densities ranging from 6.5 to 7.5 g/cm^3 compared with 8 to 9 g/cm^3 for Ni base alloys.

Main challenges

The Nb-silicide based alloys require tuning of their chemistry and processing to get suitable properties for practical applications. In this context, the Nb-silicide in-situ composites represent a big challenge in many different ways; first, their mechanical properties second, their environmental resistance third, their processability and fourth, finding a proper balance of all aforementioned. In the first instance, when one considers their promising mechanical properties with ductile phase strengthening and thoughening in mind, assuming that the metallic phase Nb_{ss} is the ductile phase and the silicide is the strengthening phase, complications arise given that the Nb_{ss} has low strength at high temperature whilst the strong Nb_5Si_3 has low fracture toughness at room temperature [Zinsser and Lewandowski (1998)]. Furthermore, balance of the mechanical properties at room and high temperatures is important, first because these materials must be able to show high creep resistance given that as high temperature structural materials they would be subjected to big loads for prolonged times at high temperatures, while at room temperature they must endure their final assemblage [Bewlay et al. (2002)]. On the other hand, a challenge for the improvement of the environmental resistance of the Nb-silicide based in-situ composites comes from the fact that their oxidation behaviour can change from catastrophic at medium temperatures to complex at high temperatures. Furthermore, their processing must ensure the feasibility of particular architecture for a component, allowing at the same time the control of their chemistry and

microstructure for the best mechanical behaviour of the in-situ composites [Bewlay et al. (1999), Tsakiropoulos (2010)]. Like the Ni based superalloys that are currently in use, the new alloys would require coatings.

Aim and Objectives of this research

The aim of this project is to design and develop oxidation resistant alloys that could be suitable for their use as bond coat (BC) alloys for Nb-silicide based in situ composite substrates. The project runs in parallel with two other projects in the ultra high temperature alloys group that are also developing alloys suitable for use as BCs. The objectives of this research are to design oxidation resistant silica or silica and alumina forming intermetallic alloys, to understand phase selection and stability in these alloys, to evaluate their oxidation resistance, and to propose a substrate/BC materials system. To achieve the above objectives the research will initially concentrate on Nb lean and Si (or Si and Al) rich Si-Cr-Al-TM alloys without exotic alloying additions (i.e., no Ru, Re, Pt) in order to study (i) alloy making and handling (ii) stability of microstructure and (iii) oxidation behaviour. The selection of TM elements will consider solutes that substitute for Nb and influence the stability of the $NbCr_2$ Laves phase, which is known to be beneficial for the oxidation resistance of Nb-silicide based in-situ composites.

Literature Review

1.1 Mechanical properties of Nb-silicide based in situ composites

Different Nb-Nb_5Si_3 microstructures can be produced owing to the wide two-phase region in the Nb-Si binary system, and several processing methods have been explored to find the best mechanical performance of the composites varying the Nb_{ss} and Nb_5Si_3 volume fractions [Bewlay et al. (1997b), (1999), Zinsser and Lewandowski (1998)]. It has been observed that the chemistry of the Nb-silicide in-situ composites plays a very important role concerning their mechanical behaviour, because their Si content is directly related to the volume fraction of metallic (Nb_{ss}) and the silicide phases. Initially, Dimiduk et al. (1995) suggested that Si contents ranging from 6 to 18.7 at. % Si would produce Nb/Nb_5Si_3 composites with good balance of mechanical properties. The studies of Bewlay et al. (2002) indicated that Si contents ranging from 12 to 20 at. % Si would provide composites with better balance of mechanical properties. According to Bewlay, the creep behaviour of Nb-silicide in situ composites with Si contents <12 at. % Si was controlled by the metallic phase and by the silicide phase for Si contents > 20 at. % Si. The best creep rates were observed for composites with Si contents in the range 18 - 20 at. % Si for which the Nb_{ss} volume fraction in the composites is in the range 0.35 to 0.30 in Nb-Si binary alloys. Research also showed the lowest creep rate is achieved for 18 at.% Si and that alloys can have fracture toughness above 20 MPa$\sqrt{m}$ for volume fraction of metallic phase above 30 % [Jackson et al. (2005)].

The ability of Nb-silicide based in situ composites to retain their strength at high temperature is one of their most attractive properties when this property is compared with the strength retention of Ni-based superalloys [Subramanian et al. (1997) and Bewlay et al. (2002)]. However, their strength at intermediate temperatures needs to be improved to meet the structural requirements of airfoils, otherwise a redesign of airfoils will be needed to reduce the level of stress [Bewlay et al. (2002)]. Solid-solution strengthening of Nb_{ss} has contributed to improving their retention of strength.

The fracture toughness of Nb-silicide based in-situ composites depends on the fracture toughness, volume fraction and geometry of the Nb_{ss} [Chan et al. (2002)]. The Nb_{ss} ductility and fracture toughness depend on the alloy composition. The microstructure of hypoeutectic in situ composites (Si < 18 at. %) usually contains a eutectic of Nb_{ss} and Nb_3Si. The microstructure of hypereutectic in situ composites (Si ≥ 18at. %) contains the Nb_{ss} and βNb_5Si_3. Alloying strategies can suppress Nb_3Si in hypoeutectic alloys and can also enhance the $\beta Nb_5Si_3 \rightarrow \alpha Nb_5Si_3$ transformation during solidification.

1.2 Oxidation resistance of Nb-silicide based in situ composites

The mechanical properties of Nb-silicide in situ composites have been advanced compared with the second and third generation of Ni based superalloys, and if they were to be applied in structural parts in high temperature applications a reduction of weight of ~ 25 % could be achieved compared with Ni single-crystal superalloys. However, the performance of these new alloys in oxidising environments has to be improved [Bewlay et al. (1997b) and ShiYu et al. (2009)]. The oxidation goal is metal loss less than 25 μm in 100 h at their likely operational temperature (~ 1315 °C) [Bewlay et al. (1997b)], which is achieved by the Ni base superalloys at 1150 °C, see figure 1.

The new Nb-silicide based in-situ composites are not alumina or chromia formers. This is because (i) their Al content is low (≤ 5 at%), owing to the effect of Al on the DBTT of $(Nb,Al)_{ss}$ (the DBTT of aerospace materials must not be higher than – 50 °C) and on the fracture toughness of the latter and (ii) their Cr content is also low (≤ 8 at%), owing to the strong effect of Cr (a) on the $T_{liquidus}$ (the $T_{solidus}$ must be at least 1700 °C) and (b) the stability of the C14 $NbCr_2$ Laves phase at high Cr contents (and its adverse effect on fracture toughness).

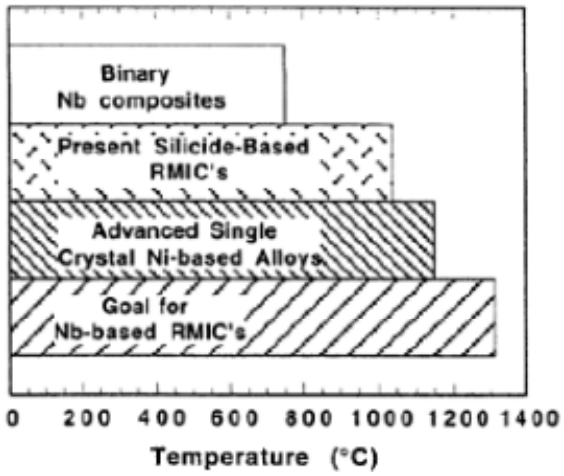

Figure 1. A comparison of the maximum temperature capability with less than 25 μm of loss of metal from Nb-silicide (metallic-intermetallic) systems against the advanced single-crystal Ni-based superalloys (Bewlay et al. (1997b)).

The new alloys are rich in Ti, which is a beneficial alloying addition for oxidation resistance and tend to form mixed $TiNb_xO_y$, and $AlNb_xO_y$ and $CrNb_xO_y$ type oxides of which the latter seems to be the most effective. Silica cannot form easily on these new alloys, but is the most likely of the high temperature oxides that can be exploited for oxidation resistance especially with metalloid alloying additions to form silica based glasses.

Oxidation resistance of Nb-silicide based in-situ composites at intermediate temperature

Refractory metals and alloys can suffer pest damage under oxidation at intermediate temperatures (≤ 850 °C) and Nb-silicide based in-situ composites are not immune to this phenomenon which consists of preferential oxygen attack in imperfections like microcracks, causing embrittlement, and defragmentation in the way of self-pulverization [Bewlay et al. (2002), Zhang et al. (2005)]. Alloy design has shown improvements in the control of the pest oxidation. The pesting phenomenon was reduced by additions of Hf and Al but was not completely suppressed. The addition of ≥1.5 at.% Sn proved to be more efficient for eliminating the pest damage [Bewlay et al. (2002)].

Oxidation resistance of Nb-silicide based in-situ composites at high temperature

The oxidation resistance of Nb-silicide based alloys must be strongly influenced by the solubility of oxygen in the Nb at intermediate and high temperatures [Hurlen (1961), Kofstad and Kjöllesdal (1961)]. Considering that Ti and Hf are two of the main alloying elements in Nb alloys and that they also show high affinity for oxygen at high temperature, one should consider that equilibrium at the metal/scale interface would not develop [Kosfstad (1966)]. The main feature of the oxidation of the composites is the lack of local equilibrium at the metal / scale interface and the detachment of the oxide scale (oxide spallation). To date the developmental Nb-silicide in situ composites do not form a protective oxide scale under oxidation at high temperature even though their oxidation behaviour has been dramatically improved in the last decade. According to Jackson et al. (1995), Subramanian et al. (1997) and Bewlay et al. (2003), these alloys would require coatings like the Ni based superalloys.

It would be unwise to rely on coatings for the environmental protection of the Nb-silicide in situ composites, because damage of the coating would expose these oxygen sensitive alloys to severe attack. Therefore, it is important to design Nb-silicide in-situ composites able to form protective oxide layers in case of environmental exposure. Such protection should be offered by improving the ability of the alloys to form protective and stable oxides in the surface under an oxidising environment. Research to develop suitable coatings for the Nb-silicide based in situ composites is under way as well as to provide self-protection capability to these alloys.

The most important high temperature alloys take advantage of the selective oxidation of alloying elements that can offer the formation of stable and protective oxide scales on their surface. The elemental additions of Ti, Al, Cr, Hf, Ge, Sn, B, and Mo [Bewlay et al. (1997a), Subramanian et al. (1997), Liang et al. (1999), Menon et al. (2001), Jackson et al. (2005), Zelenitsas and Tskiropoulos (2006a), Geng et al. (2006b), (2007a) and (2007b)] are being used to improve the oxidation resistance of the Nb-silicide in-situ composites.

1.3 A coating system

Despite of the great efforts to provide environmental protection to Nb-silicide base alloys with alloying additions, their oxidation behaviour is such that these alloys must be provided with an environmental protection system if they were to be considered for practical applications.

The new Nb-silicide based in situ composites will require, like the state of the art Ni based superalloys, oxidation coatings. It is expected that the next generation of gas turbine engines, in order to meet performance and environmental targets, will operate with turbine entry temperature (TET) around 2100 K (1827 °C) and thus substrate surface temperatures $T_{substrate\ surface}$ could be at least 1300 °C (i.e., at least 150 degrees higher compared with state of the art internally cooled and TBC coated single crystal Ni based superalloys). This will only be possible using a materials system approach where the materials system will comprise a substrate, which should have some inherent resistance, and a coating, which could comprise of bond coats and ceramic thermal barrier. In other words, an environmental protection system for Nb-silicide in situ composites would be required to have features seen in the conventional coating systems used for Ni-base superalloys [Bewlay (2004a), Olson et al. (2006)] that consist of the substrate alloy (SA), an oxidation resistant bond coat (BC), a thermally grown oxide (TGO), and a thermal barrier coating (TBC), see figure 2. The industry is “confident” about “handling” TBCs sitting on α-Al_2O_3, and thus the expectation is that the BC would be able to form alumina TGO.

With increasing temperature, alloys can offer oxidation protection via in situ formation of Cr, Si and Al oxides, with Al_2O_3 being the preferred oxide at high temperatures.

Given the susceptibility of Nb alloys to contamination by interstitial elements, in particular oxygen and nitrogen, and thus their sensitivity to environmental embrittlement, an extra requirement must be met by the new high temperature materials systems. The substrate must also have inherent resistance to environmental contamination and the environmental protection system must “stop” the diffusion of contaminants to the substrate.

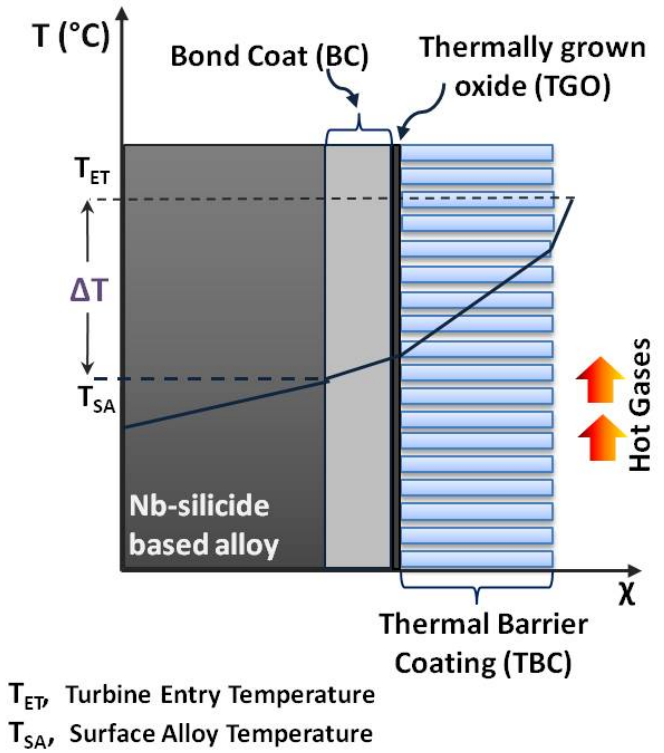

Figure 2. Environmental protection system for Nb-silicide based alloys.The bond coat could be multi-material or compositionally gradient material (s)

Essential requirements for the BC are its ability to form protective, dense and compact oxide scales like those mentioned above, have good mechanical behaviour, and adhere to the substrate alloy, which requires a coefficient of thermal expansion (CTE) close to that of the substrate alloy, have good thermal stability, and be able to supply its selective oxidation element after oxide spallation, and be mechanically stable.

Thermal and chemical stability are very important since the formation of other intermetallic phases, which could also include very hard intermetallics or low temperature phases, compromises the balance of mechanical properties, stability and the oxidation at high temperature. Besides, the very narrow composition ranges of most intermetallic phases compromise the long term stability of a protective oxide scale, since oxidation can lead to the formation of a lower compound right under the oxide scale. Sometimes, these lower compounds are unable to sustain the oxide scale growth complicating even more the oxidation behaviour. Oxide stabilities are also very important because oxides like Al_2O_3 and SiO_2 are very

close to the stabilities of Nb and Ti oxides, which encourage the formation of intermixed oxide scales which tend to be non protective.

Cr_2O_3 scales can offer protection up to 1100 °C owing to volatility at higher temperatures. SiO_2 is permeable to oxygen and nitrogen and its melting point (between 1405 and 1700 °C) depends on its structure. The best protection is offered by alpha Al_2O_3 scales due to the high melting point of α-Al_2O_3 (2050 °C) and low O and N diffusivities, which are lower than those of SiO_2. However, the Al_2O_3 does not function as a good oxygen barrier as the temperature increases, since it has high activation energy for diffusion. In this context SiO_2 could be a better oxidation barrier at high temperature than Al_2O_3 due to its low activation energy for diffusion [Perkins et al. (1989)]. Among the forms of SiO_2 the amorphous one is the most preferred since it presents a high protectiveness glassy microstructure derived from its flexibility to include elements of the environment and substrate at high temperatures [Mitra (2006)]. However, in order to exploit these properties it is necessary to design alloys that are able to form a continuous glassy SiO_2 oxide scale. This has not been observed in Nb-silicide base alloys.

Despite of the efforts to improve their oxidation, the Nb-silicide in-situ composites did not show equilibrium at the metal / scale interface even when they were aluminized and / or siliconized owing to the formation of detrimental phases that were found to decrease the coating efficiency. However, it has been claimed by Olson et al. (2006) that a protective oxide scale consisting of Al_2O_3, Y_2O_3 and their reaction product (YAG) could form upon oxidation at high temperatures ($T \geq 1100$ °C) of Nb alloys with additions of exotic elements like Pt, Pd and Y along with Al and some of the elements Hf, Si, Ti, Cr and W.

The need for bond coats with good adherence and chemical stability to promote the formation of the protective oxides mentioned above has lead to the development of different complex coating systems for Nb-silicide base alloys [Jackson et al. (2007)]. They proposed different configurations of coating systems for turbine blades made of Nb or Mo intermetallic base alloys. According to them, the oxidation resistance coatings could consists of different diffusion barrier layers and inert bond coats. The diffusion barrier layers developed by them may or may

not contain a layer consisting of silicide phases, a Cr_2Nb Laves layer, a ruthenium layer, a chromium layer. The inert bond coat layer could include elements like platinum, palladium and / or rhodium. On top of the inert bond coat layer, there would be a thermal barrier coating (TBC). The use of materials such as rhodium, palladium and platinum in the inert bond coat layer would increase the cost of this component considerably.

It has been claimed that a successful approach would be to develop bond coats based on traditional Si-Cr-Fe alloys that are known to be able to form oxidation resistant phases with limited oxygen penetration [Jackson et al. (1998)]. Silicides and Si-rich intermetallic alloys such as the R512E coating (Nb-Fe-Cr-Si) can develop SiO_2 rich oxidation resistant coatings with the potential to form a viscoelastic glass layer able to prevent oxidation, cracking and spallation. SiO_2 also prevents the increase of the temperature of the metallic surface and offers self-healing properties [Kirkwood et al. (1995)]. However, even though complex Si-rich intermetallics were found to provide optimum protection against oxidation to conventional Nb-rich alloys, poor mechanical behaviour has been reported for coating systems with high silicon contents that formed SiO_2 protective scales [Weber et al. (1973), Wahl (1983)].

Aluminium rich intermetallics that act as the reservouir of Al to form Al_2O_3 are desirable for the microstructures of alloys used in a coating system. Additions of Cr are also considered because Cr tends to reduce the Al required to form Al_2O_3 scales.

One approach in the design of an environmental protection system for a Nb-silicide alloy based high temperature materials system is to use a “composite” or functional gradient BC with decreasing Nb content and increased capability of forming Cr, Si and Al oxides as one moves away from the Nb-silicide based substrate towards the TBC, which would be deposited on a material that can form α-alumina (preferred) or silica.

1.4 High temperature oxidation of Fe-silicide coatings

Successful oxidation protection of “conventional” Nb-rich alloys has been claimed by the deposition of iron-modified silicide coatings. This was attributed to the selective oxidation of

silicon in coating with phases such as FeSi, $FeSi_2$, $FeSi_2Ti$, and $(TM)_7Si_6$ where TM= Fe, Ti, Cr, Nb [Tsirlin et al. (1981), Jackson et al. (1998) and L. Portebois et al. (2013)].

Due to its abundance on the Earth's core there is a special commercial interest on Fe based coatings such as Fe-silicide coatings. If the latter were proved to be suitable to protect Nb-Si base alloys they will also be non-high cost coatings. Studies of the oxidation resistance of Si-rich Fe-Si alloys at medium and high temperatures claim a reduction in the oxidation rate due to the formation of SiO_2 [Adachi and Meier (1987)]. Amorphous SiO_2 has been the desirable main oxidation product for these alloys since it has good adhesion to silicide phases, low oxygen diffusion rate and ability to resist plastic deformation at high temperatures.

However, there is limited information about the oxidation behaviour of modified iron silicides. Thus, it is of interest for this research to understand the effects of Ti, Cr, Nb and Al additions in Fe silicide base alloys that could be considered suitable for Nb-silicide based alloys coatings.

Additions of the above elements could alter the melting point of Fe silicides, and affect their oxidation and mechanical performance at high temperatures. Also it is important to know if formation of protective oxides such as Cr_2O_3, SiO_2, and Al_2O_3 could be possible with Al addition to the Fe based silicides. Thus, two alloys with modified Fe-silicides will be studied in this work.

1.5 High temperature oxidation of Nb Aluminides

The ability of different alloys to form alpha Al_2O_3 scale at high temperatures has high commercial interest owing to the superior corrosion resistant properties of this phase. While the 5 at.% Al addition in Ni-based superalloys is enough for the formation of continuous α-Al_2O_3 scale at high temperature, this has not been observed in Nb base aluminides, even with the considerable Al content of about 25 at. % Al. This is the case of the intermetallic Nb_3Al which does not form a protective Al_2O_3 scale upon oxidation.

In the Al-Nb binary system, the lightest aluminide with lowest oxidation rate is the Al_3Nb. The Al_3Nb suffers from pest oxidation in the intermediate temperatures range 700-900°C [Meier

(1989)]. Moreover, the Al content of the Al_3Nb influences its oxidation behaviour at temperatures above the pest regime [Meier and Pettit (1992)]. The Al-rich Al_3Nb forms a continuous Al_2O_3 scale at temperatures up to 1200 °C that breaks above this temperature. Apparently, the Al-rich Al_3Nb is able to sustain the Al_2O_3 scale growth without Al depletion at the metal / scale interface. On the other hand, Al-lean Al_3Nb does not form an exclusive Al_2O_3 layer under oxidation at high temperatures instead the scale consists of outer $AlNbO_4$ and inner Al_2O_3 oxide layers. In the later case, the depletion of Al at the metal/scale interface occurs with a solid phase transformation of Al_3Nb to $AlNb_2$ phase. The formation of the $AlNb_2$ phase does not have positive effects on the oxidation resistance because the Al has low activity in this phase.

Alloying additions of Cr have been used for several purposes, for example in Ni-based superalloys Cr is added to increase their resistance to hot corrosion in the temperatures range 650 -1000 °C, to solid solution strengthen the Ni_{ss}, to change the melting point of alloys and to promote the formation of an exclusive outer layer of Al_2O_3 at the minimum Al content required to sustain the scale growth [Meier and Pettit (1992)]. A reduction of oxidation rate at 1200 °C of the Al_3Nb has been achieved by additions of Cr and Y [Hebsur et al. (1989), Doychak and Hebsur (1991)].

1.6 Phase Equilibria

1.6.1 The Nb-Si binary phase diagram

The Nb-Si phase diagram has been assessed by Schlesinger et al. (1993), Fernandes et al. (2002) and Okamoto, (2005) (Figure 3). More recently, thermodynamic modelling has been used to describe this phase diagram [Liang et al. (1999), Fernandes et al. (2002), Yang et al. (2003) and David et al. (2006)]. There are three eutectics in the Nb-Si phase diagram. The first eutectic is between the Nb and Nb_3Si at 17.5 at.% of Si at 1933 ˚C although Bewlay et al., (2004b) found this eutectic at 18.2 at% Si. The second eutectic is between in the βNb_5Si_3 and $NbSi_2$ at 1878 ˚C and 57 at. % Si. Finally, liquid transforms to $NbSi_2$ and Si via a eutectic reaction at 1406 ˚C and

98 at. % Si. There is very small and almost negligible solubility of Si in the Nb solid solution at low temperature, and the solubility increases to 3.5 at.% Si at 1915 ˚C.

There are two polymorphs of the Nb_5Si_3 phase. The low temperature αNb_5Si_3 (LT) with composition range 36.7 to 39.8 at.% Si that is stable up to 1939 °C and the high temperature βNb_5Si_3 (HT) with composition range 37.5 to 40.5 at.% Si that is stable up to 2518 ˚C. The eutectoid decomposition of Nb_3Si at 1667 ˚C, gives Nb_{ss} and αNb_5Si_3. The βNb_5Si_3, melts at 2518 ˚C with a composition of 37.5 at. %Si and transforms to αNb_5Si_3 and $NbSi_2$ at 1645 ˚C in a eutectoid reaction.

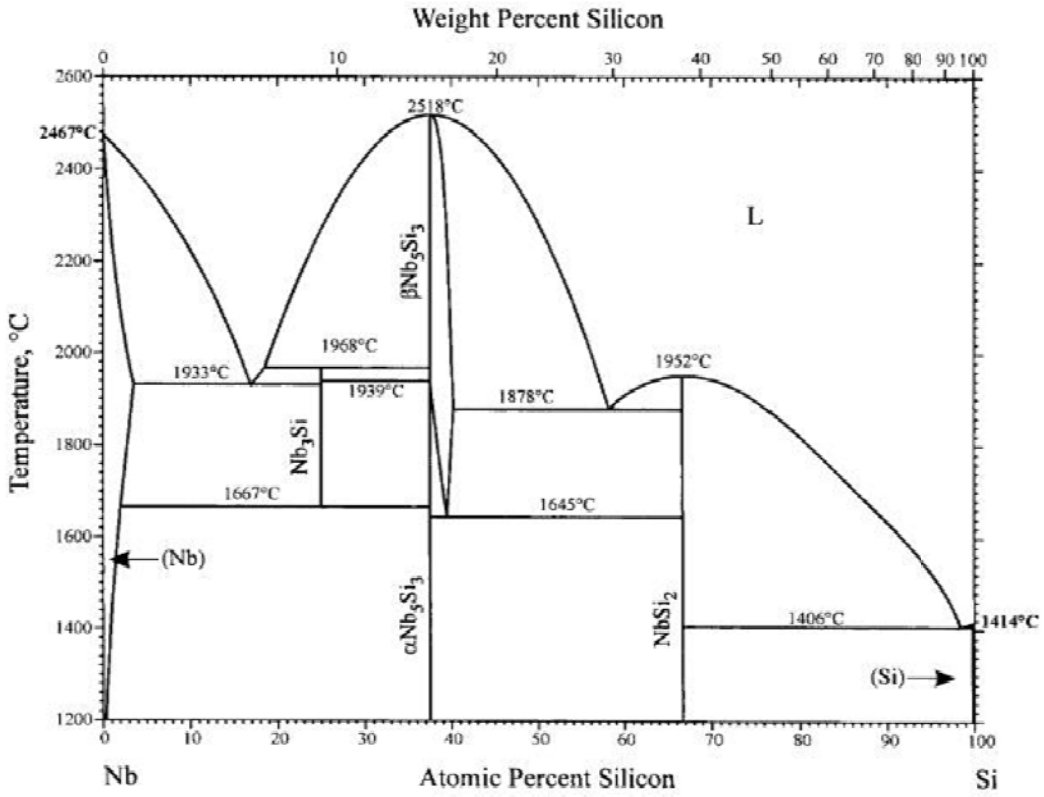

Figure 3. The binary Nb-Si phase diagram according to Schlesinger et al. (1993).

The Nb_3Si silicide forms via a peritectic reaction from L and βNb_5Si_3 (HT) at 25 at. % Si and is stable from 1667 to 1968 ˚C. The Nb_3Si decomposes via a eutectoid reaction to Nb and αNb_5Si_3 (LT) below 1667 ˚C. This eutectoid decomposition of Nb_3Si was reported by Henshall et al.,

(1997) to be very slow, even during heat treatment at 1500 ˚C for 100 h. In unidirectionally solidificated alloys this phase was present even after 500 h at 1500 ° C [Sekido et al. (2006)].

The congruent melting $NbSi_2$ disilicide is formed at 66.5 at% Si and 1952 ˚C. The crystal data of stable and metastable phases in the Nb-Si binary is given in Table 1.

Table 1 The crystal structure data of phases in the Nb-Si binary summarized by Schlesinger et al. (1993).

Phase	Pearson Symbol	Space Group	Strukturbericht designation	Prototype
(Nb)	cI2	Im-3m	A2	W
Nb_3Si	tP32	$P4_2/n$	-	Ti_3P
αNb_5Si_3	tI32	I4/mcm	$D8_1$	Cr_5B_3
βNb_5Si_3	tI32	I4/mcm	$D8_m$	W_5Si_3
$NbSi_2$	hP9	$P6_422$	C40	$CrSi_2$
(Si)	cF8	Fd-3m	A4	C(diamond)
Metastable phases				
Nb_7Si	c	-	-	-
Nb_4Si	h	-	-	εFe_2N
Nb_3Si_m	cP8	Pm-3n	-	Cr_3Si
$Nb_3Si_{m'}$	cF4	Fm-3m	-	Cu
$Nb_3Si_{m''}$	cF4	Pm-3m	-	$CuAu_3$
Nb_3SiI	c	-	-	-
Nb_3SiI	h	-	-	Mn_5Si_3
γNb_5Si_3	h	-	-	Ti_5Si_3

The metastable γNb_5Si_3 silicide is stabilised by interstitial elements, in particular C, Ti and Hf.

1.6.2 Additions of Cr in the Nb-Si system

Oxidation resistance is one of the weaknesses of the Nb-silicide based in situ composites that must be improved. Addition of Cr to other alloys (e.g steels, superalloys) has improved their oxidation and environmental resistance. In Nb alloys, Cr is beneficial to oxidation via the formation of the oxidation resistant Cr_2Nb Laves phase [Bewlay et al. (2003)]. However, Cr_2Nb could have an adverse effect on mechanical properties in particular fracture toughness. It is important to know how Cr affects phase selection in the Nb-Si-Cr system.

The Nb-Cr binary phase diagram

The Nb-Cr system (Figure 4) has two solid solutions and one intermetallic phase. The intermetallic phase is the Cr_2Nb Laves phase and has two polymorphs; the C14 βCr_2Nb Laves phase which forms congruently at 1730 °C and 66.5 at. % Nb and is stable down to 1625 °C. Its solubility range is 30.5 to 38.2 at. % Nb and its structure is hP12 with $MgZn_2$ as the prototype. The other polymorph is the C15 αCr_2Nb Laves phase that is stable below 1625 °C. Its Nb solubility increases with temperature from 31.5 to 39.5 at.% Nb at 1625 °C (its maximum temperature of stability), and has the cF24 structure with Cu_2Mg as the prototype.

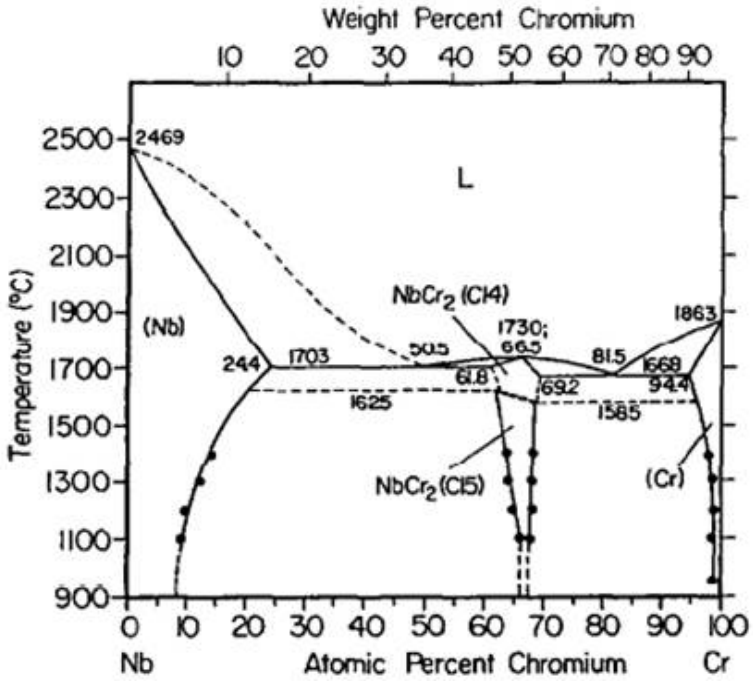

Figure 4. The Nb-Cr phase diagram proposed by Thoma and Perepezko (1992) [cited by Kumar and Liu (1997)].

The solid solutions in this system are the Nb_{ss} that melts at 2469 °C (A2, cI2 structure with W as prototype) and dissolves up to 24.4 at. % Cr at 1703 °C and the Cr_{ss} (A2, cI2 structure) which has low Nb solubility (5.6 % at 1668 °C). There are two eutectic reactions, one between Nb_{ss} and Cr_2Nb at 1703 ° C and 50.5 at. % Nb, and the other between Cr_{ss} and Cr_2Nb at 1668 °C and 81.5 at. % Nb.

The Cr-Si binary phase diagram

The Cr-Si system (Figure 5) has four intermetallic compounds and two solid solutions. The Cr_{ss} contains up to 13 at.% Si at 1701 °C and melts at 1907 °C. The intermetallic compound Cr_3Si (A15 structure) forms congruently at 1780 °C and has Si solubility in the range 22 to 27.5 at. % Si. The crystal structure data of the phases in this system is showed in Table 2. At 1701 °C a eutectic reaction occurs between the Cr_{ss} and Cr_3Si.

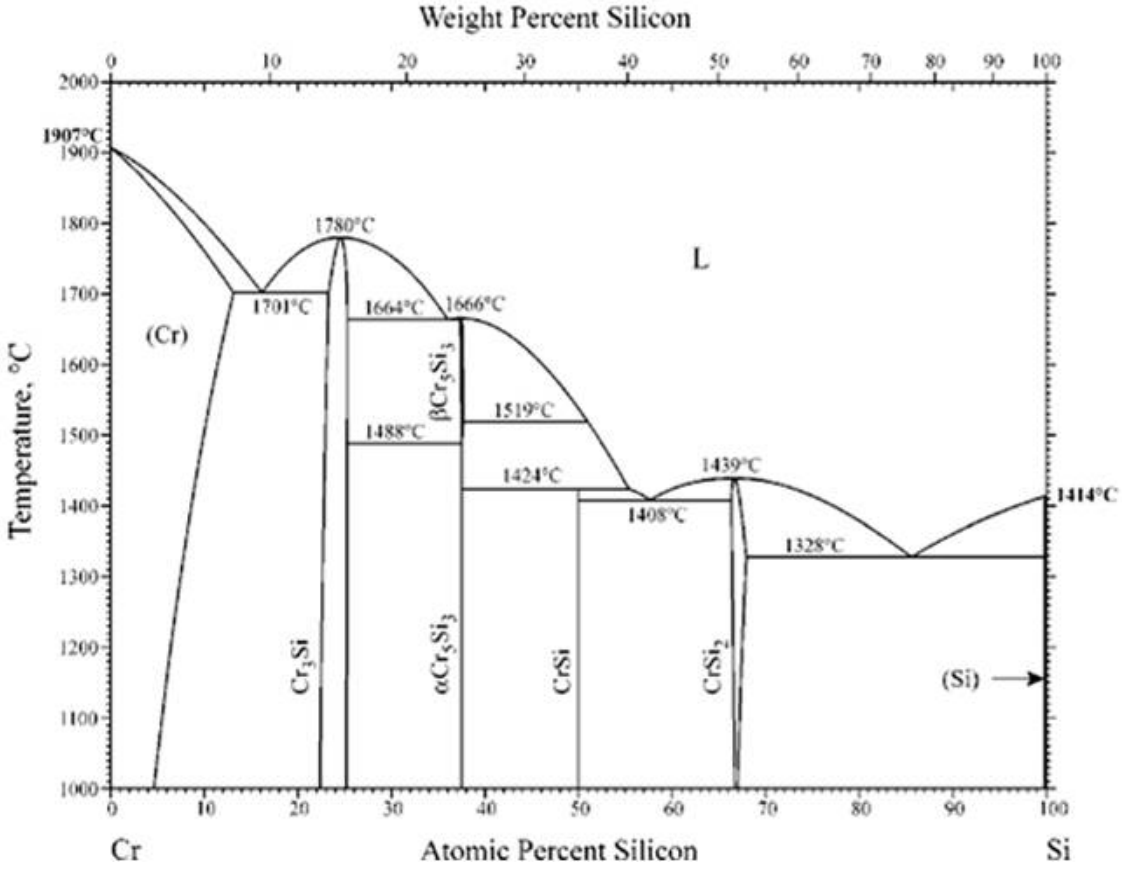

Figure 5. The Cr-Si phase diagram [Okamoto (2001)].

The Cr_5Si_3 line compound melts congruently at 1666 °C and earlier it was thought to have two polymorphic forms, namely βCr_5Si_3 and αCr_5Si_3, with the αCr_5Si_3 phase stable up to 1488 °C and the βCr_5Si_3 stable from 1488 to 1666 °C. Nowadays, it is accepted that only one form exists for Cr_5Si_3 with the prototype W_5Si_3. This form is referred to as βCr_5Si_3 and is isomorphous with βNb_5Si_3.

Table 2 Crystal structure data of the Cr-Si system reported by Okamoto (2001).

Phase	Pearson symbol	Space group	Strukturbericht designation	Prototype
(Cr)	cI2	$Im\bar{3}m$	A2	W
Cr_3Si	cP8	$Pm\bar{3}n$	A15	Cr_3Si
βCr_5Si_3	tI32	I4/mcm	$D8_m$	W_5Si_3
CrSi	cF8	$P2_13$	B20	FeSi
$CrSi_2$	hP9	$P6_222$	C40	$CrSi_2$
(Si)	cF8	$Fd\bar{3}m$	A4	C (diamond)

At 1424 °C and 50 at. % Si a peritectic reaction occurs in which the CrSi phase forms.The $CrSi_2$ phase melts congruently at 1439 °C and has a homogeneity range extending from 65.7 to 67.5 at. % Si. A eutectic reaction occurs between this phase and CrSi at 1408 °C and 57 at. % Si. There is also a eutectic at 1328 °C and 86 at. % Cr between Si and $CrSi_2$.

The Nb-Si-Cr ternary alloy system

In 1961, Goldschmidt and Brand made the first recorded attempt to determine the phase equilibria in the Nb-Si-Cr alloy system. They produced an isothermal section at 1000 °C (Figure 6), in which the stability of the C14 Laves phase (ρ) and its wide range of solubility should be noted. In other words, the solubility of Si in the $NbCr_2$ stabilises the C14-$NbCr_2$ to temperatures lower than 1625 °C. Besides, the C14 Laves phase appears in six different three phase equilibria, of which the most important to this work are the C14+αNb_5Si_3+βNb_5Si_3 and C14+αNb_5Si_3+Nb_{ss}. Phases like αNb_5Si_3 and β=Nb_4CrSi_3 (with the βNb_5Si_3 structure) appear with a wide range of solubility and the Θ=$(Cr,Nb)_6Si_5$ ternary phase has wider field than the τ=$(Cr,Nb)_{11}Si_8$.

Zhao et al. (2003b) used the diffusion multiples method and electron-probe micro-analysis (EPMA) to study phase equilibria in Nb-Si-Cr ternary claiming that the traditional method of equilibrating the alloy via heat treatment does not allow one to reach thermodynamic equilibrium owing to very slow kinetics in this system. They studied the local equilibrium in interfaces in diffusion multiple samples heated in argon at 1000 °C for 4000 h and 1150 °C for 2000 h and purposed isothermal sections for 1100 and 1150 °C (Figure 7). Data for the phases present is given in Table 3. The stabilization of the C14 Laves phase at lower temperature was also observed but it was suggested that the C14 Laves phase is not in equilibrium with the Nb_{ss}

and Nb_5Si_3, instead the Nb_{ss} + CrNbSi + αNb_5Si_3 three- phase field was proposed. The range of compositions of the ternary phases $(Cr,Nb)_6Si_5$ and $(Cr,Nb)_{11}Si_8$ was different compared with the study of Goldschmidt and Brand study. The Nb solubility increased with temperature in the $(Cr,Nb)_6Si_5$ silicide, and in the $(Cr,Nb)_{11}Si_8$ phase the Cr solubility increased from 76 to 83 at. %.

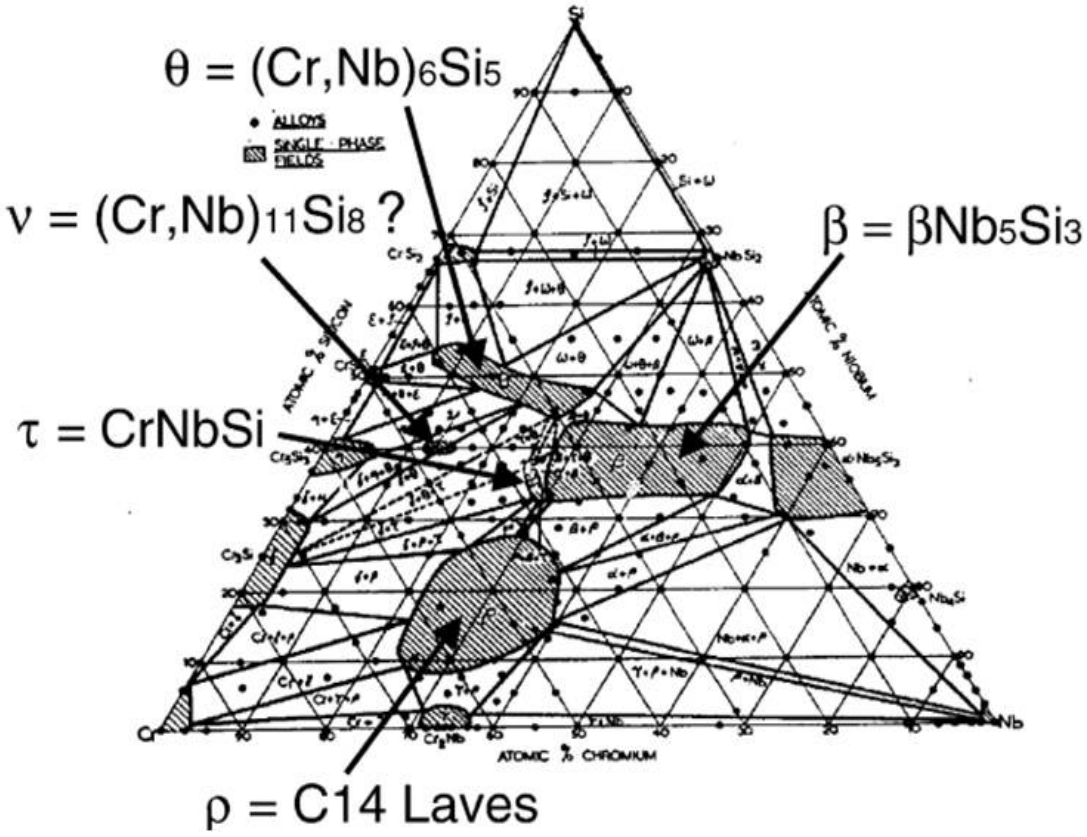

Figure 6. The Nb-Cr-Si isothermal section at 1000 °C proposed by Goldschmidt and Brand [diagram cited by Zhao et al. (2003b)].

Shao (2005) used experimental data available in the literature and calculated isothermal sections at 1000 °C, 1150 °C, 1500 °C (Figures 8 and 9) and a liquidus surface projection. His work was mostly in agreement with Zhao et al. (2003b). But the liquidus surface projection proposed by Shao was not validated against experimental work.

However, Shao (2005) found that the Nb_{ss} cannot be in direct equilibrium with the CrNbSi ternary phase, instead he confirmed the three-phase equilibria (Nb)+C14+αNb_5Si_3 (Figures 8 and 9) proposed by Goldschmidt and Brand. Geng et al. (2006a) confirmed via experimental

work the three-phase equilibria (Nb)+C14+αNb_5Si_3 in an alloy in the Nb rich corner of the Nb-Si-Cr system that was annealed at 1000 and 1500 °C for 100 h. The βNb_5Si_3 was present in the as cast alloy and transformed to αNb_5Si_3 after annealing at 1500 °C. The C14 Laves phase was present in the alloy and coarsened after annealing, confirming the stabilization of this phase to lower temperatures.

Table 3 Phases present in the Nb-Cr-Si system [Zhao et al. (2003b)].

Phase	Pearson symbol	Space group	Strukturbericht designation	Prototype
(Cr)	cI2	$Im\bar{3}m$	A2	W
Nb	cI2	$Im\bar{3}m$	A2	W
(Si)	cF8	$Fd\bar{3}m$	A4	C (diamond)
Cr_3Si	cP8	$Pm\bar{3}n$	A15	Cr_3Si
βCr_5Si_3	tI32	I4/mcm	$D8_m$	W_5Si_3
CrSi	cF8	$P2_13$	B20	FeSi
$CrSi_2$	hP9	$P6_222$	C40	$CrSi_2$
Nb_3Si	tP32	$P4_2/n$	-	PTi_3
βNb_5Si_3	tI32	I4/mcm	$D8_m$	W_5Si_3
αNb_5Si_3	tI32	I4/mcm	$D8_l$	Cr_5B_3
$NbSi_2$	hP9	$P6_222$	C40	$CrSi_2$
Cr_2Nb	hP12	$P6_3/mmc$	C14 Laves	$MgZn_2$
Cr_2Nb	cF24	$Fd\bar{3}m$	C15 Laves	$MgCu_2$
CrNbSi	hP9	$P\underline{6}2m$	-	-
$(Cr,Nb)_6Si_5$	oI44	Ibam	-	-
$(Cr,Nb)_{11}Si_8$	oP76	Pnma	-	-

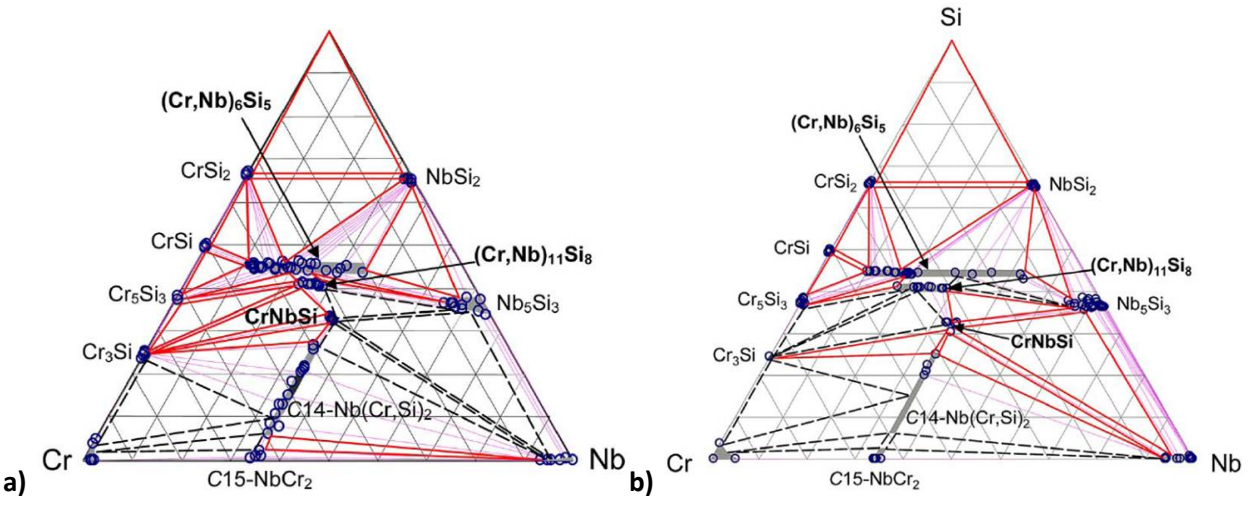

Figure 7. The isotermal sections at 1000 and 1150 °C obtained by Zhao et al. (2003b), The (Nb) is not in equilibriumm with the C14 Laves and αNb_5Si_3 phases.

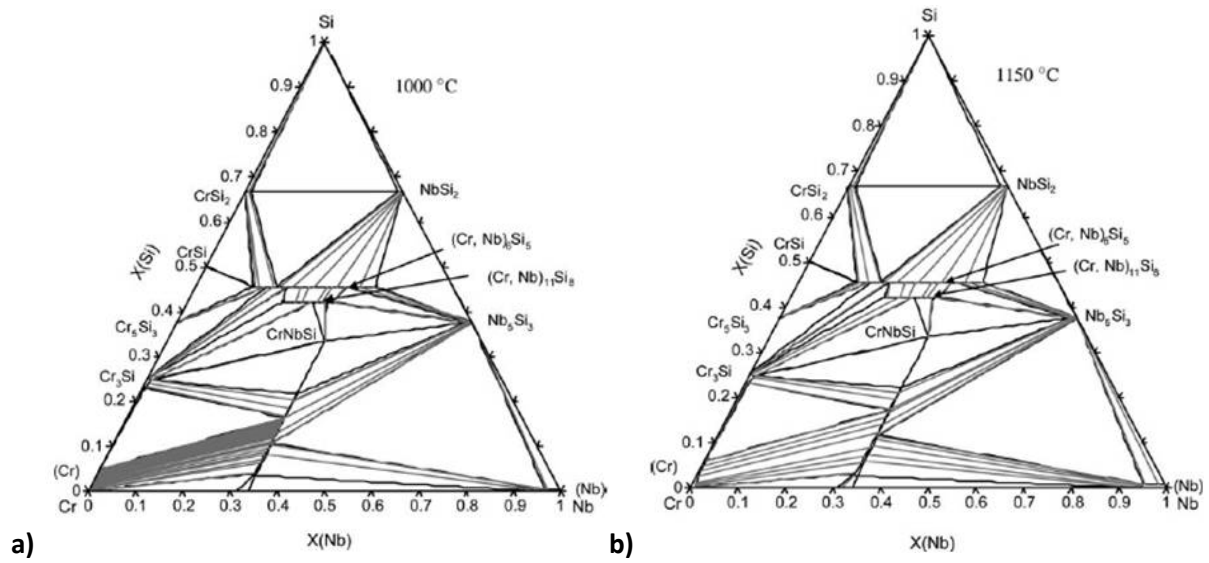

Figure 8. The isotermal sections at (a) 1000 °C and (b) 1150 °C obtained by Shao (2005). Both sections show the three-phase field equilibria (Nb)+C14+ αNb_5Si_3.

David et al., (2006) also calculated an isothermal section at 1200 °C for the Nb-Si-Cr system, which can be seen in figure 10. The solubility range of the $(Cr,Nb)_6Si_5$ was in agreement with Zhao et al., (2003b) and the three-phase equilibria (Nb)+αNb_5Si_3+C14 was also confirmed.

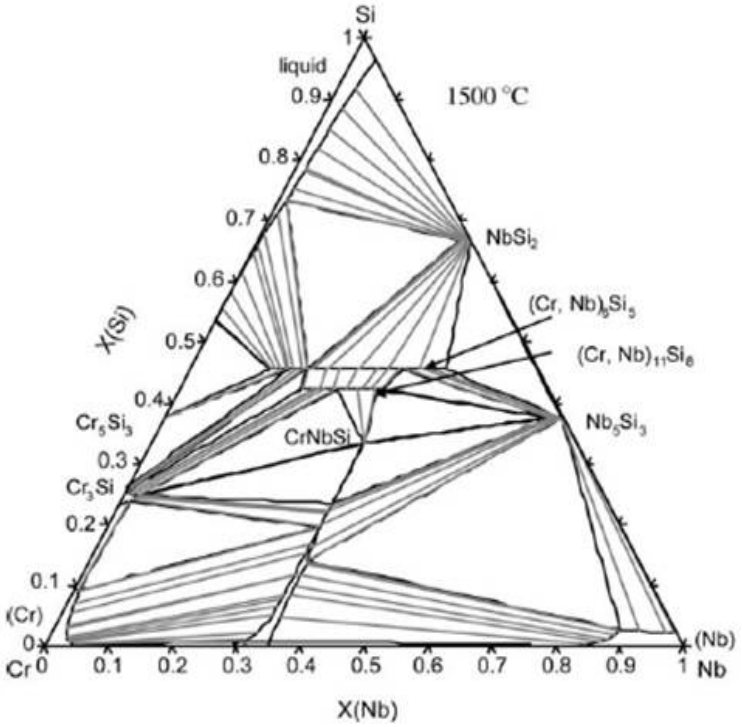

Figure 9. Isotermal section at 1500 ° C of the Nb-Cr-Si system calculated by Shao (2005).

Deal et al., (2007) proposed the new $Nb_9(Cr,Si)_5$ ternary phase in this system with the same structure as $Nb_9Co_3Ge_2$ (I4/mcm).

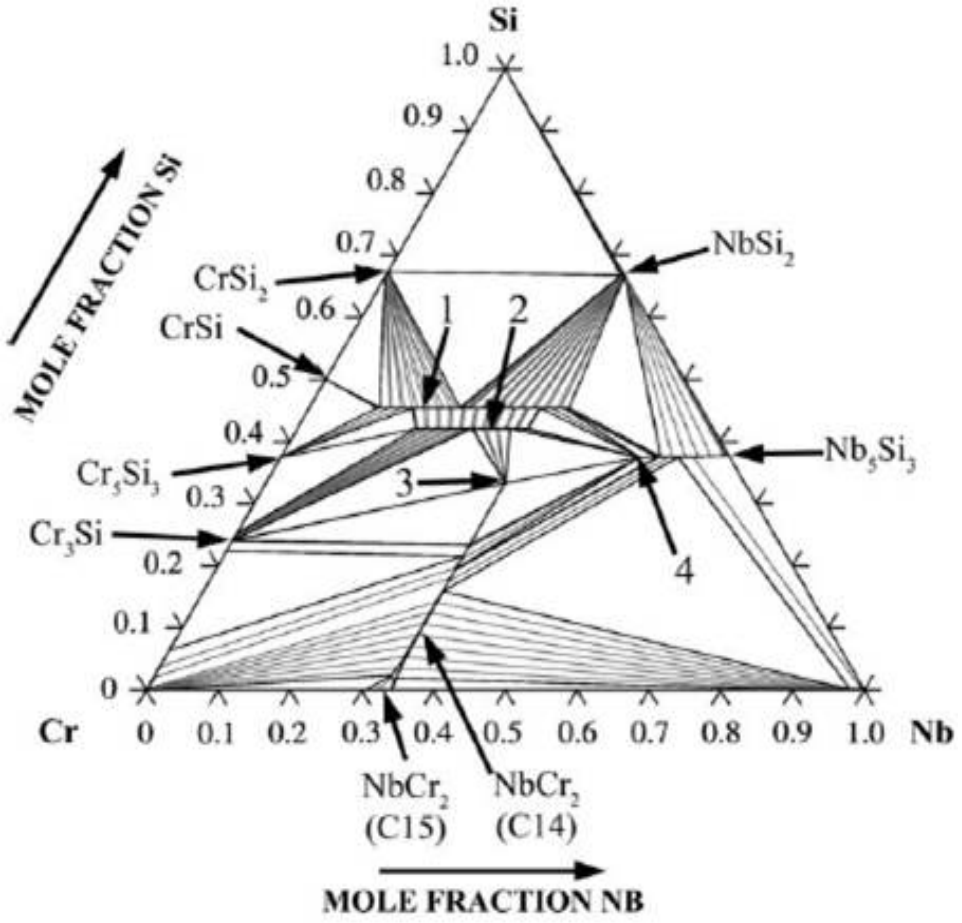

Figure 10. Isothermal section at 1200 °C of the Cr-Nb-Si system calculated by David et al. (2006).

Bewlay et al., (2009) performed an experimental study of Nb-Si-Cr alloys in the metal rich part of the system to gather information about the liquid-solid equilibrium. They used directionally solidificated alloys instead of the arc melted alloys of Geng et al. (2006a). In the DS alloys the ternary phase $Nb_9(Cr,Si)_5$ was observed. This phase was seen in the microstructure of the directionally solidificated (DS) Nb-18Si-15Cr alloy forming a eutectic with Cr_2Nb and (Nb) (Figure 11). Bewlay et al., (2009) proposed that this phase formed via the following reactions:

$$L+Nb_5Si_3 \rightarrow Nb_9(Cr,Si)_5+ (Nb)$$

$$L+ Nb_5Si_3 \rightarrow Nb_9(Cr,Si)_5+Cr_2Nb$$

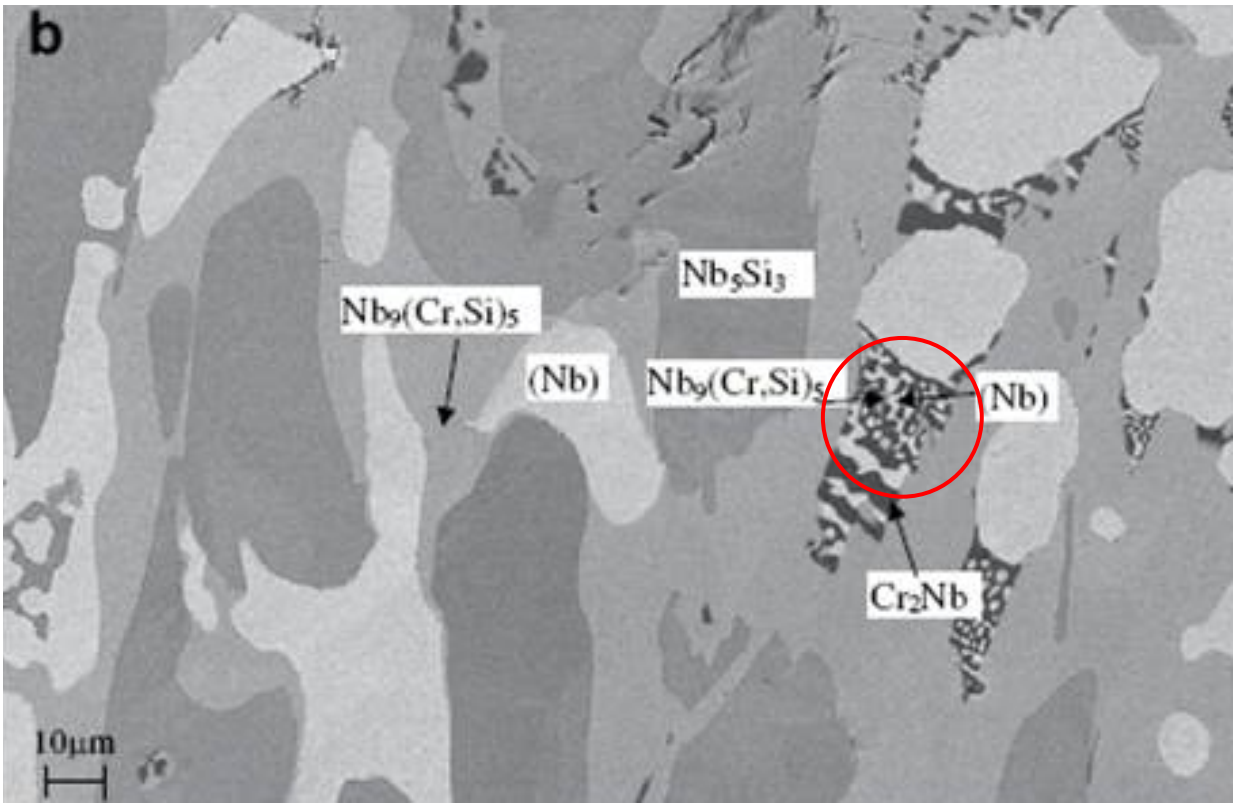

Figure 11. Image of the DS Nb-18Si-15Cr alloy typical microstructure. Nb is the light phase, Cr_2Nb isthe black phase, the gray phase is the Nb_5Si_3, and the light gray phase is the $Nb_9(Cr,Si)_5$ [Deal et al. (2007)].

The liquidus projection shown in figure 12b was proposed for the Cr-Nb-Si system up to 30 at. % Si by Bewlay et al. (2009), and includes the new ternary phase $Nb_9(Cr,Si)_5$. The liquidus projection, though similar to that calculated by Shao has some differences. Bewlay et al. (2009) found a higher solubility of Cr in the αNb_5Si_3 silicide, a larger range of stability of the βNb_5Si_3 silicide, and no range of stability for the CrNbSi phase, the range of stability for the phase Cr_5Si_3 in Shao's thermodynamic model was considered as the range for the $(Cr,Nb)_{11}Si_8$ phase and the solubility of Si in the Laves phase is appreciably less.

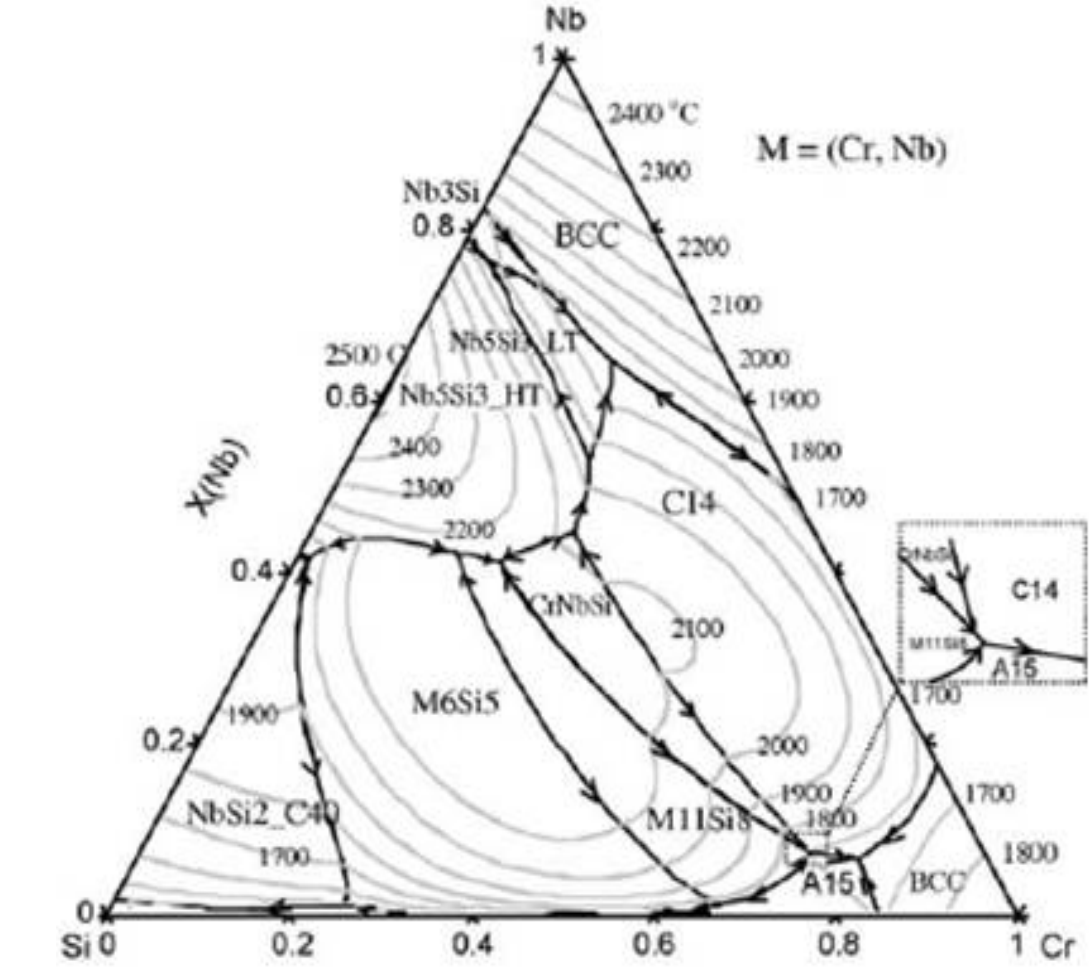

a)

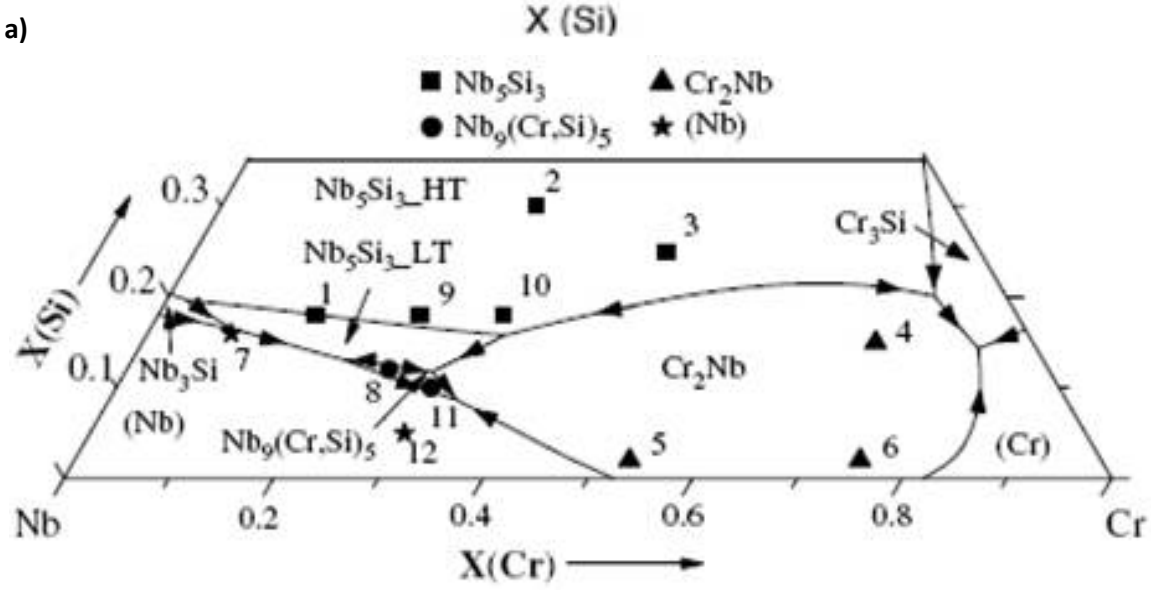

b)

Figure 12. Liquidus projections for the Nb-Cr-Si system: (a) calculated by Shao (2005) (b) experimentally obtained by Bewlay et al. (2009) in directionally solidified alloys up to 34 %Si.

1.6.3 The Nb-Al binary phase diagram

This system has two solid solutions and three intermetallic phases, and one eutectic and three peritectic reactions. The Al phase (A1-structure, Cu prototype), melts at 660 °C and has no Nb solubility at low temperature. The intermetallic phase Al_3Nb ($D0_{22}$-structure, Al_3Ti prototype) extends from 24.5 to 25.5 5 at. %Nb and decomposes congruently at 1680 °C. The $AlNb_2$ phase ($D8_b$-structure, σCrFe prototype) forms from a peritectic reaction at 1940 °C and extends from 58 to 70 at. %Nb. Between Al_3Nb and $AlNb_2$ a eutectic reaction occurs at 1590 °C and 45 % of Nb. The $AlNb_3$ phase (A15–structure, Cr_3Si prototype) is formed via a peritectic reaction at 2060 °C and extends from 75 to 81.4 at. % Nb. In the bcc (Nb) phase, which melts at 2469 °C and has W as prototype, the solubility of Al increases with temperature to a maximum 21.5 at. % Al at 2060 °C (Figure 13).

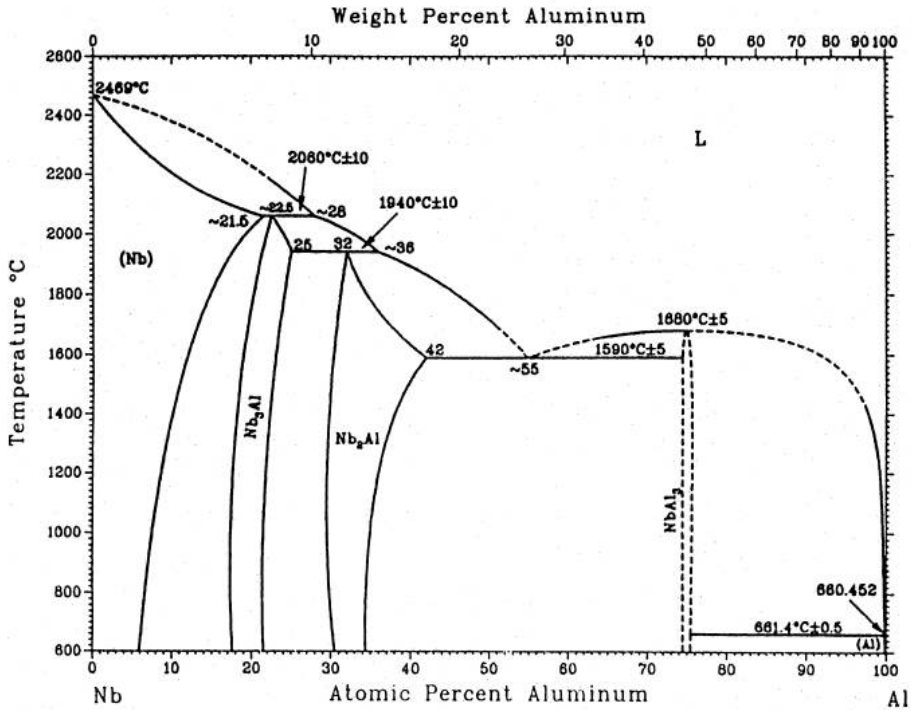

Figure 13. The Nb-Al phase diagram proposed by Massalski [cited by Mahdouk et al. (1998)].

In a later study Witusiewicz et al. (2009) reported a solubility range 25.1 to 25.7 5 at. %Nb in the Al_3Nb, decomposing congruently at 1714 °C, and a temperature of 1571 °C for the eutectic reaction L → Al_3Nb + $AlNb_2$.

The Nb-Si-Al ternary alloy system

The first studies of this system were performed by Brukl et al. (1961) who proposed the partial isothermal sections at 1400 °C and 500 °C shown in figure 14a. Two ternary phases were reported to form in this system. The $Nb_3Si_5Al_2$ phase with the C54 structure and the $Nb_{10}Si_3Al_3$ with the $D8_m$ structure, which were stable in the three-phase field equilibria with the $NbAl_3$ phase. The solubility of Si in Nb_3Al at 1400 °C was around 7 at. % Si and Nb_3Al was in equilibrium with Nb_5Si_3 and $Al_3Nb_{10}Si_3$. The range of homogeneity of the Nb_2Al phase extended from 60 to 70 at.% Nb with very low solubility of Si while the Nb_5Si_3 phase did not show Al solubility at all.

Pan et al. (1984) obtained a partial isothermal section of the Nb-rich corner at 1500 °C, see Figure 14b. According to Pan et al., the Nb_5Si_3 phase has Al solubility up to about 12 at. % Al and is in equilibrium with $NbAl_3$ and $Nb_{10}Si_3Al_3$ which is different from the $Nb_3Si_5Al_2$+$Nb_{10}Si_3Al_3$+Nb_3Al equilibria proposed by Brukl et al. Moreover, the phases Nb_5Si_3 and Nb_3Al with approximately 5 at.% content of Al and Si respectively were in equilibrium with $Nb_{10}Si_3Al_3$ and the Nb_{ss} was in equilibrium with Nb_5Si_3 and Nb_3Al.

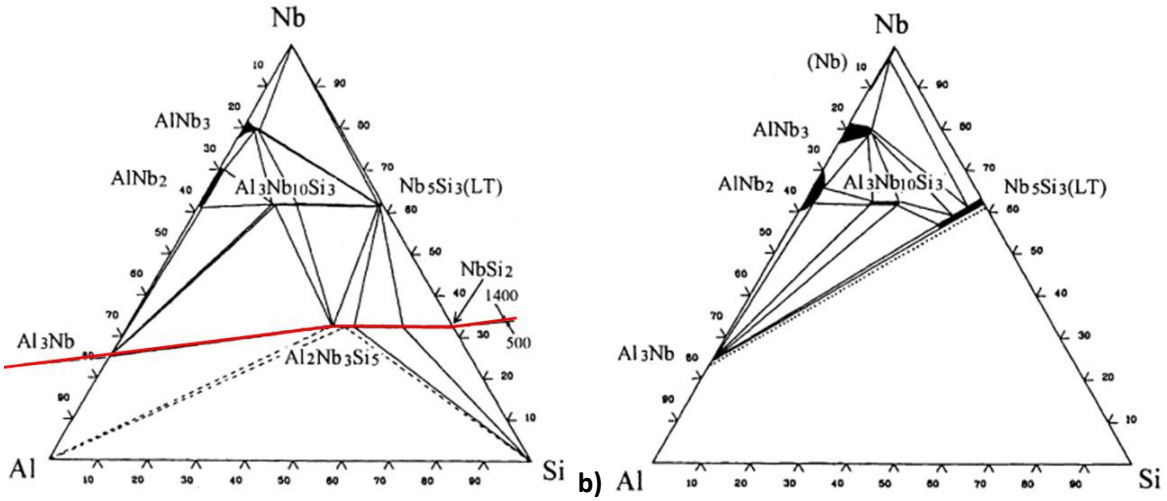

Figure 14. Partial isothermal sections obtained experimentally: (a) by Brukl et al. (1961), at 1400 °C (upper part) and 500 °C (lower part), and (b) by Pan et al. (1984) at 1500 °C (upper part).

Murakami et al. (2001a), carried out experiments in the Nb-Al-Si system with alloys prepared by spark plasma sintering (SPS) and purposed an isotherm section from 1200 to 1600 °C (Figure

15). They confirmed the three-phase field equilibria $NbAl_3$+ $Nb_{10}Si_3Al_3$ + αNb_5Si_3 proposed by Pan et al. However, in agreement with Brukl et al., they obtained very low solubility of Al in the Nb_5Si_3 phase.

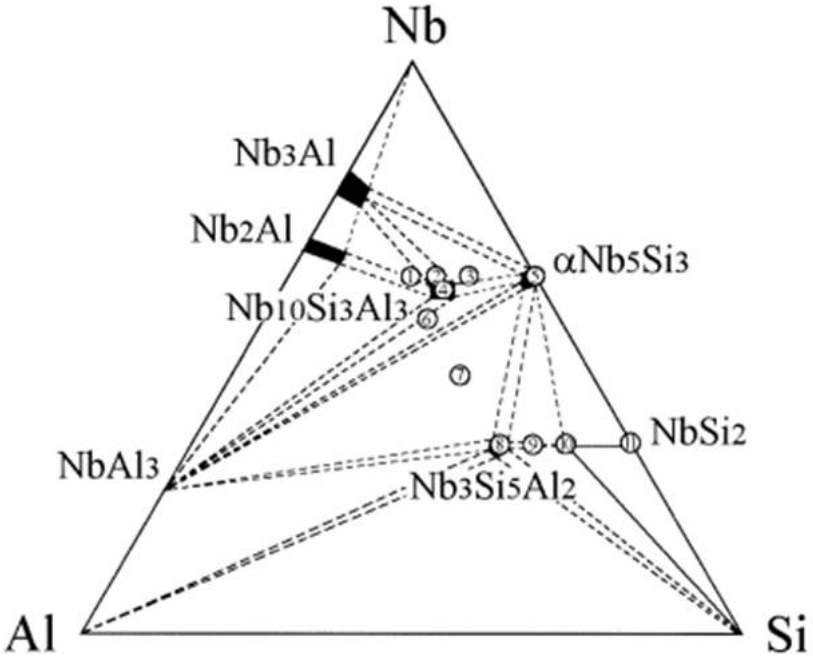

Figure 15. Estimated Isothermal section from 1200 to 1600 °C by Murakami et al. (2001a).

An isothermal section at 1000 °C was proposed by Zhao et al. (2003a) (Figure 16a) using data from diffusion multiples. They confirmed only the ternary phase $Nb_3Si_5Al_2$ and proposed that the ternary phase $Nb_{10}Si_3Al_3$ is the binary βNb_5Si_3 phase stabilized with Al at 1400 °C but not at 1000 °C. They also reported an 8 at.% Al solubility in the αNb_5Si_3 at 1000 °C. The latter, was supported by the results of ShiYu et al. (2009), suggesting a direct substitution of Si atoms by Al in βNb_5Si_3 .Crystal structure data for the phases in this system is given in table 4.

At 1000 °C, the Si solubility in Nb_3Al and Nb_2Al was very low and around 2 at.% in the $NbAl_3$. Si substitutes Al in $NbAl_3$ and Al substitutes Si in $NbSi_2$. When αNb_5Si_3 was in equilibrium with Nb_{ss}, the solubility of Al in the binary silicide decreased to 3 at. %. Al additions higher than 3 at.% lead to the formation of the Nb_3Al phase.

Table 4 Stable phases in the Nb-Al-Si system and their crystal structure, Zhao et al. (2003a).

Phase	Pearson symbol	Space group	Strukturbericht designation	Prototype
Al	cF4	$Fm\bar{3}m$	A1	Cu
Nb	cI2	$Im\bar{3}m$	A2	W
(Si)	cF8	$Fd\bar{3}m$	A4	C (diamond)
Nb_3Si	tP32	$P4_2/n$	-	PTi_3
βNb_5Si_3	tI32	I4/mcm	$D8_m$	W_5Si_3
αNb_5Si_3	tI32	I4/mcm	$D8_l$	Cr_5B_3
$NbSi_2$	hP9	$P6_222$	C40	$CrSi_2$
$Nb_2Al(\sigma)$	tP30	$P4_2/mnm$	$D8_b$	σCrFe
Nb_3Al	cP8	$Pm\bar{3}n$	A15	Cr_3Si
Al_3Nb	tI8	I4/mmm	$D0_{22}$	$TiAl_3$
$Al_2Nb_3Si_3$	oF24	Fddd	C54	$TiSi_2$
$Al_3Nb_{10}Si_3$	tI32	I4/mcm	$D8_m$	W_5Si_3

The equilibrium between the Nb_5Si_3 and $NbAl_3$ phases was also determined. This confirmed the results obtained by Pan et al. (1984) and Murakami et al. (2001a) and therefore, suggested incorrect data by Brukl et al. (1961).

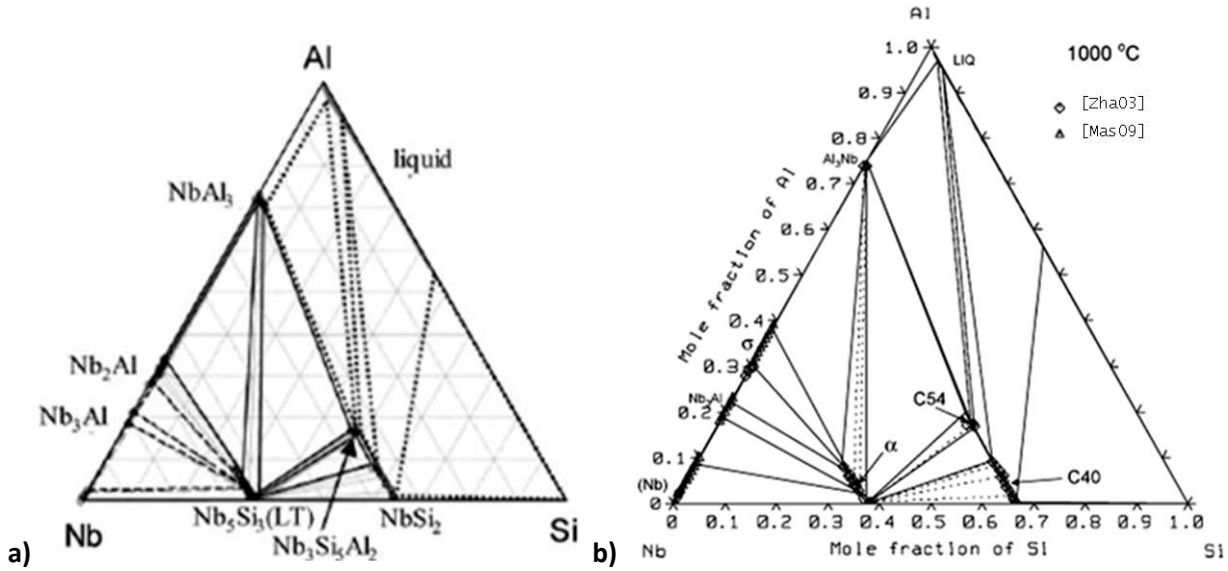

Figure 16. Isothermal sections at 1000 °C: (a) by Zhao et al. (2003a), (b) by Shao (2004).

Shao (2004) calculated isothermal sections at 1000 °C (Figure 16b) and 1400 °C and a liquidus projection for the Nb-Si-Al system, using experimental data from Zhao et al, Brukl et al., Pan et al., and Murakami et al., (see Figure 17b). The isothermal section in figure 16b, shows clearly similarities with figure 16a with slight changes in solubility ranges, for example at 1000 °C, the

Nb_{ss} shows a considerably higher Al solubility in the isothermal section calculated by Shao. It can also be seen in figure 17a, that the βNb_5Si_3 phase is stabilized to 1400 °C and has considerable Al solubility. The liquidus projection (Figure 12b) shows that both α-Nb_5Si_3 and β-Nb_5Si_3 will form from the liquid and that the β-Nb_5Si_3 presents a much larger range of stability though it is not clear in figure 17b.

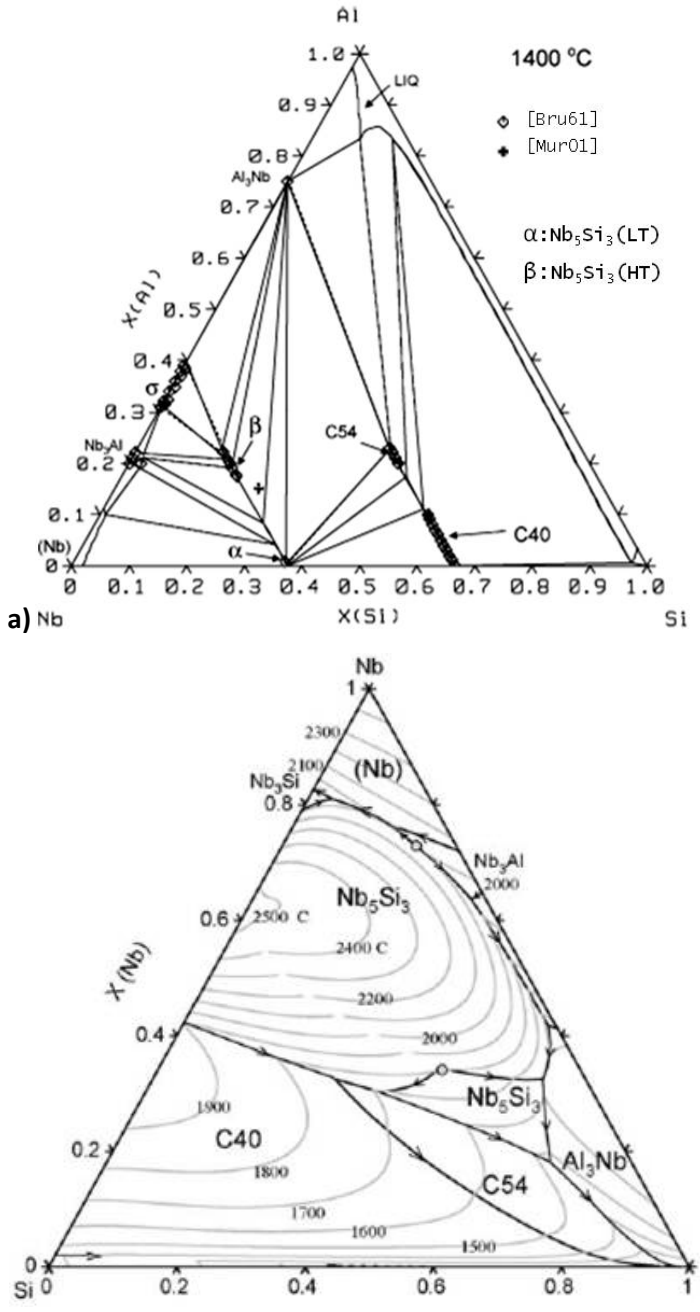

Figure 17. (a) Isothermal section at 1400 °C and (b) liquidus projection calculated by Shao (2004).

1.6.4 Ti addition in Nb-silicide based in situ composites

Additions of Ti in Nb–silicide based in-situ composites increase their fracture toughness at room temperature, reduce their density and increase the oxidation resistance of the composites [Bewlay et al. (1996) Chan. et al. (2001) and (2002)]. However, Ti reduces their melting temperature. Thus, it is necessary to find a balance of alloying additions to control the melting point that must be above 1700 °C. Also it is important to know how Ti affects phase selection and stability in the Nb-Ti-Si system as the latter forms the basis on which Nb-silicide based in-situ composites are developed.

The Ti-Si binary phase diagram

In the Ti-Si system (Figure 18), the α-Ti is stable up to 882°C and has the hP2 crystal structure and the β-Ti, which is stable from 882 to 1670 °C, has the cI2 crystal structure.

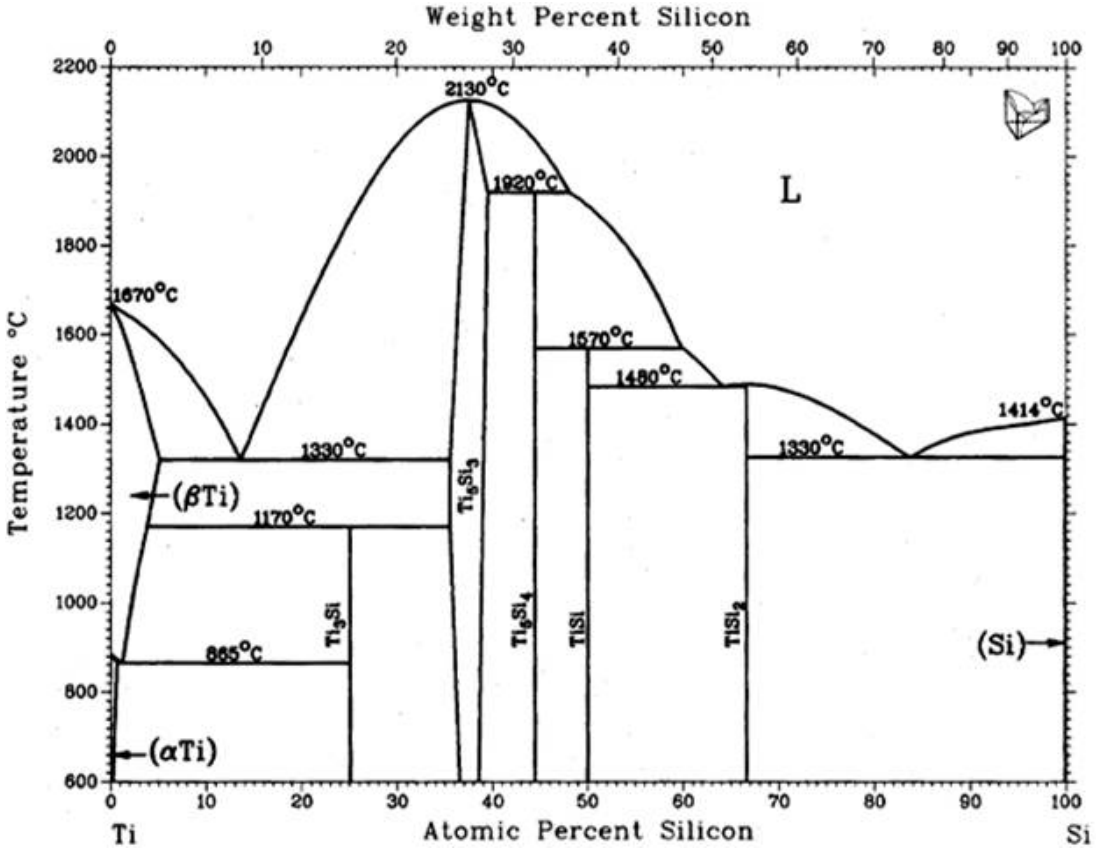

Figure 18. Ti-Si binary system from Alloys Phase Diagrams by ASM [cited by Da Silva Costa et al. (2010)]

The Ti_3Si has the tP32 crystal structure and forms pericteto idally at 1171°C at 25 at.% Si and is isomophous with Nb_3Si. The Ti_5Si_3 has homogeneity range 37.5-39 at.% Si, melts congruently at 2130 °C, has the hP16 crystal structure and is isomophous with the metastable γ-Nb_5Si_3. The Ti_5Si_4 silicide with the tP36 crystal structure forms peritectically at 1900 °C and 44.4 at.%Si. The TiSi silicide with the oP8 crystal structure forms peritectically at 1543 °C. Finally, the $TiSi_2$ silicide forms at 66.6 at.% Si, has the oF24 crystal structure and melts congruently at 1485°C.

This binary system has three eutectic reactions. The first $L \rightarrow \beta Ti + Ti_5Si_3$ is at 1330 °C and 17 at.% Si, the second $L \rightarrow TiSi + TiSi_2$ at 1480 °C and 63 at.% Si, and the third $L \rightarrow Si + TiSi_2$ is at 1330 °C and 85 at.% Si.

The Nb-Ti-Si ternary alloy system

In the Nb-Ti-Si system Nb and Ti form a continuous solid solution. In Table 5 the crystal structure data of the compounds in this system is listed. The first study was performed by Subramanian et al. (1994), with emphasis on ternary solubility at 1500 °C that can be seen in Figure 19. In the bcc-(Nb,Ti) phase there is solubility of Si from 0.5 to 1.5 at. % Si and for the Nb_5Si_3 and Ti_5Si_3 phases there is a ~ 10% solubility for their respective ternary component.

Table 5 Crystal structure of the phases in the Nb-Ti-Si system, Zhao et al. (2004a).

Phase	Pearson symbol	Space group	Strukturbericht designation	Prototype
α-Ti	hP2	$P6_3/mmc$	A3	Mg
β-Ti	cI2	$Im\bar{3}m$	A2	W
Nb	cI2	$Im\bar{3}m$	A2	W
(Si)	cF8	$Fd\bar{3}m$	A4	C (diamond)
Nb_3Si	tP32	$P4_2/n$	-	PTi_3
βNb_5Si_3	tI32	I4/mcm	$D8_m$	W_5Si_3
αNb_5Si_3	tI32	I4/mcm	$D8_l$	Cr_5B_3
$NbSi_2$	hP9	$P6_222$	C40	$CrSi_2$
TiSi	oP8	Pnma	-	FeB
Ti_3Si	tP32	$P4_2/n$	-	PTi_3
$TiSi_2$	oF24	Fddd	C54	$TiSi_2$
Ti_5Si_3	hP16	$P6_3/mcm$	-	Mn_5Si_3
Ti_5Si_4	tP36	$P4_12_12$	-	Zr_5Si_4

The phases Nb_3Si and Ti_3Si are isomorphous with the tP32 crystal structure but while the Nb_3Si is stable at higher temperatures (1667-1939 °C), figure 3, the Ti_3Si is stable below 1170°C. Thus, none of these tri-silicide appear at 1500 °C in their respective binaries but it is clear that the $(Nb,Ti)_3Si$ is stable at this temperature with Ti solubility up to 50% (Figure 19).

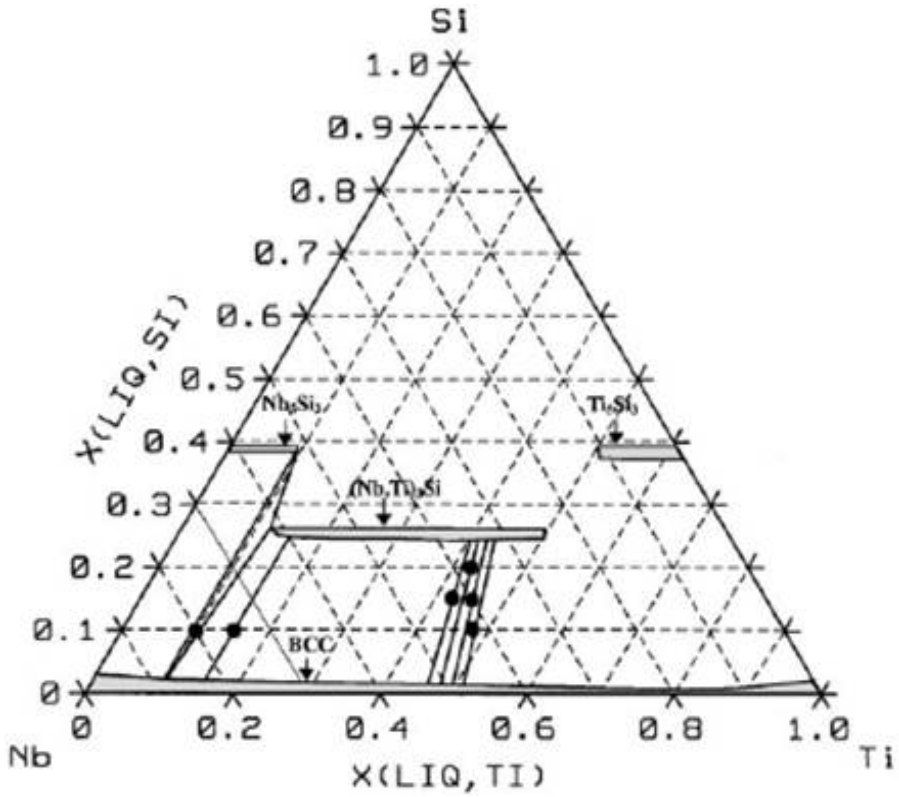

Figure 19. Isothermal section obtained at 1500 °C experimentally by Subramanian et al. [cited by Liang and Chang (1999)], showing the ranges of ternary solubility for the former binary phases in the Nb-Ti-Si system.

An experimental study with DS alloys was performed by Bewlay et al. (1997a). The Nb_5Si_3 was represented as $Nb(Ti)_5Si_3$ considering that Ti is in solid solution substituting Nb, the Ti_5Si_3 as $Ti(Nb)_5Si_3$, the Nb as (Nb,Ti) and the Nb_3Si as $(Nb,Ti)_3Si$. They suggested a partial ternary phase diagram up to 37.5 at. % Si, as shown in Figure 20.The eutectic reaction L → Nb + Nb_3Si was found at 18.2 at % Si and the eutectic microstructure consisted of Nb rods in Nb_3Si matrix. The Nb_3Si phase was stabilized at lower temperature as $(Nb,Ti)_3Si$ by the solubility of Ti, as was suggested by Subramanian et al. (1994), whereas the Ti_3Si phase was stabilized by Nb solubility at higher temperature forming a continuous solid solution with the Nb_3Si. The Nb_5Si_3 melting

point was decreasing with increasing Ti solubility and the Ti_5Si_3 phase changed from congruent melting to a peritectically formed $Ti(Nb)_5Si_3$.

Liang and Chang (1999) used existing experimental data to obtain isothermal sections at 1200, 1500 and 1800°C and a liquidus projection, see Figure 21. The isothermal section at 1200 °C would suggest that Ti dissolves up to 43 at.% Nb and about 5 at.% Si. The phases $NbSi_2$ and $TiSi_2$ are in equilibrium with Si, as well as with the TiSi. There is three-phase field equilibria $(Nb,Ti)_5Si_3$-$(Nb,Ti)_3Si$-Nb, which was also observed by Bewlay et al., and two phase equilibria Nb_5Si_3-$(Nb,Ti)_3Si$ and $(Nb,Ti)_3Si$-(Nb,Ti).

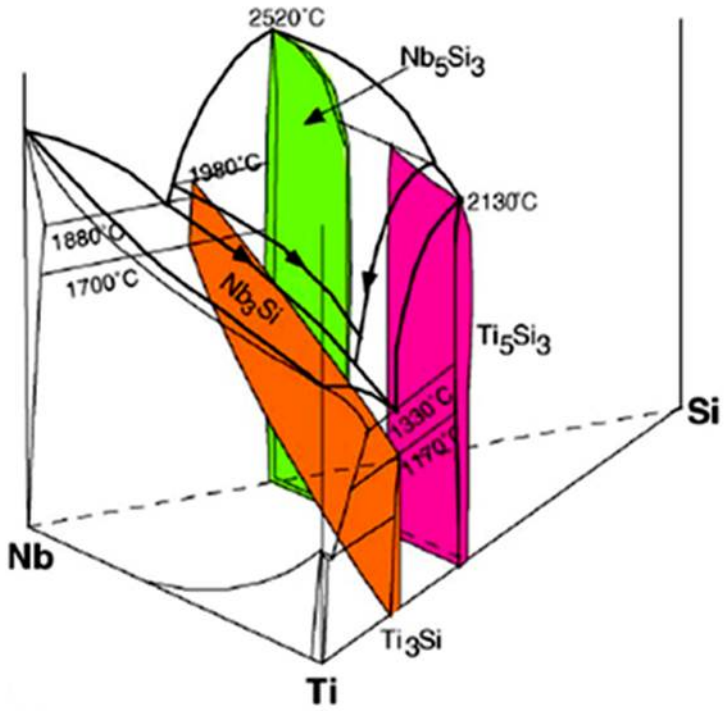

Figure 20. Proposed ternary phase diagram for the Nb-Ti-Si system by Bewlay et al. (1997a) [cited by Zhao et al. (2004a)].

According to Liang and Chang their isotherm calculated for 1500 °C agreed well with the isotherm at 1500 °C obtained with experimental data by Subramanian et al. (1994), see Figure 20. An important detail to notice is that at 1500 °C the solubility of Ti and Nb in the bcc-(Nb,Ti) increased up to 100% enhancing its Si solubility and that the three-phase field equilibria $(Nb,Ti)_5Si_3$-$(Nb,Ti)_3Si$-bcc(Nb) range was smaller than at 1200 °C.

An important characteristic to note in the isotherms calculated by Liang and Chang at 1500 °C and 1800 °C is the presence of liquid phase respectively near the Ti rich, the Si-rich and Ti-rich corners, confirming the strong effect of Ti on the liquidus temperature.

The liquidus projection in figure 21d does not indicate the structure type of Nb_5Si_3 forming from the liquid. It should be noted that the liquidus projection for the Nb-Si-Cr (Figure 12a) shows that both αNb_5Si_3 and βNb_5Si_3 can form from the melt.

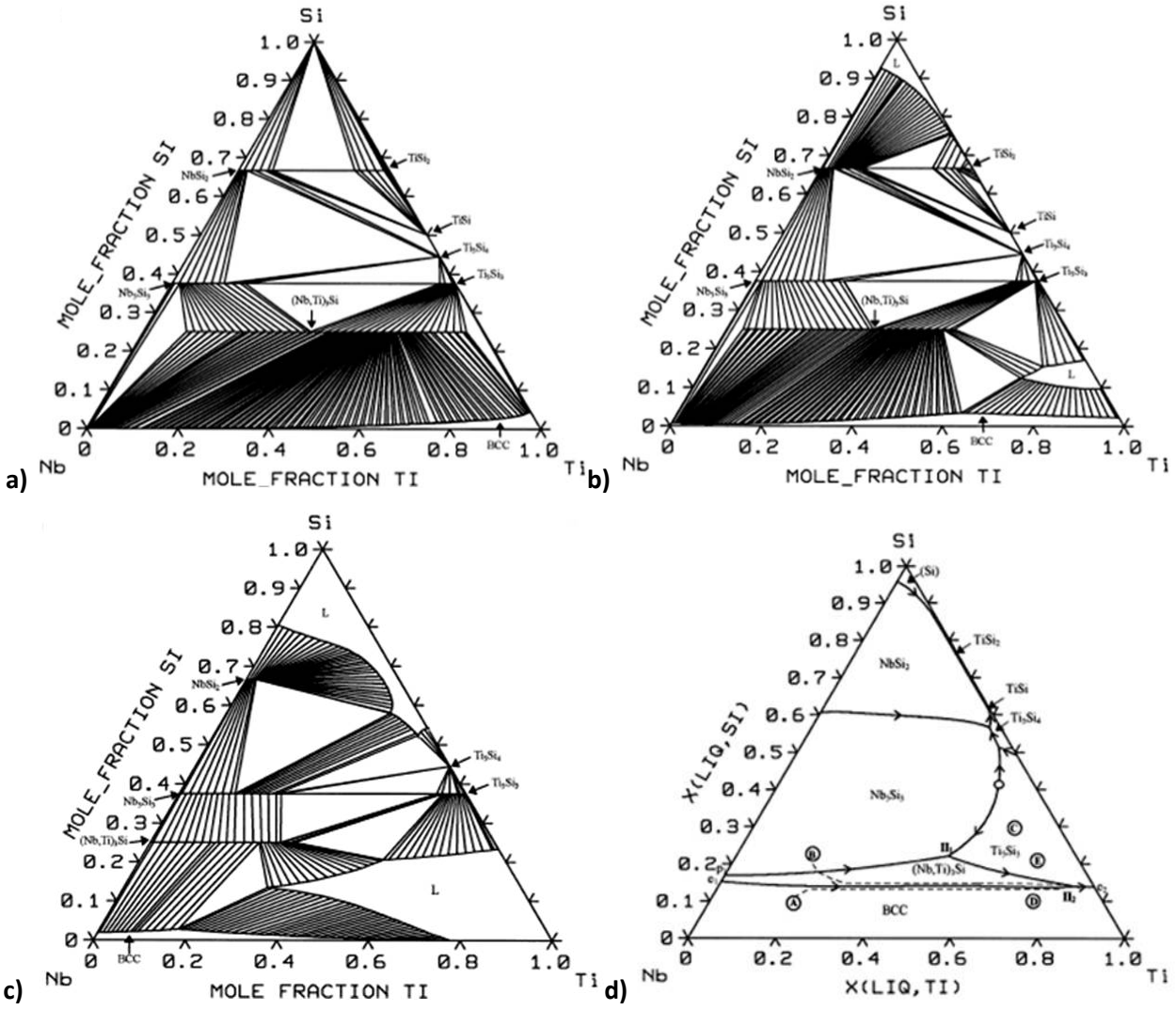

Figure 21. Isothermal sections at: (a) 1200 °C, (b) 1500 °C, (c) 1800 °C and (d) liquidus projection calculated by Liang and Chang (1999).

The diffusion-multiples approach was used by Zhao et al. (2004a) to get isothermal sections at 1000, 1150 and 1200 °C. The results suggested appreciable changes in solubility for the stable phases. The Ti solubility in Nb_5Si_3 increased from 18 to 26 and 28 at.% and the Nb solubility in Ti_5Si_4 increased from 36 to 45 and 47 at.% as the temperature increased from 1000 to 1150 and 1200 °C, respectively (see Figure 22).

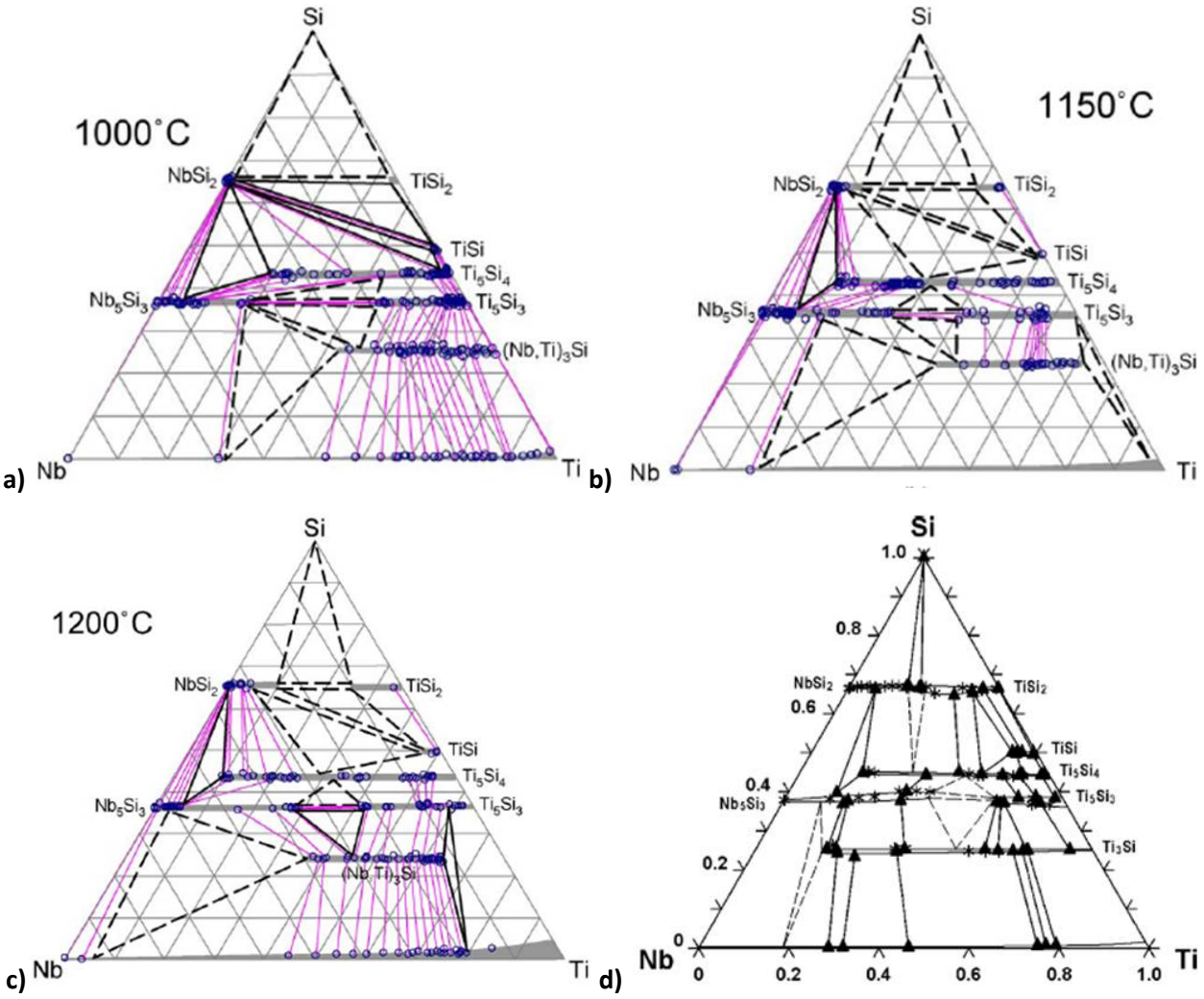

Figure 22. Isothermal sections at: (a) 1000 °C, (b) 1150 °C and (c) 1200 °C obtained by Zhao et al. (2004a) and (d) at 1000 °C obtained by Honghui Xu et al. (2005).

Since, the addition of Ti promotes the formation of Ti_5Si_3 above some critical concentration and reduces the liquidus temperature, its concentration in Nb-silicide based alloys should not exceed 25 at.% to retain a liquidus temperature higher than 1700 °C for good strength in the

range of 1200-1400 °C and to avoid the formation of the Ti_5Si_3 phase which is considered to be detrimental for the creep rupture strength of the composites.

Zhao et al. (2004a) also suggested that the Ti_3Si phase forms peritectoidly between 1100 and 1150 °C, since it was not observed in their experiment at 1150 °C but was present at 1100 °C.

Xu et al. (2005) also used diffusion couples to produce an isothermal section at 1000 °C, see Figure 22. The data showed that the $(NbTi)_3Si$ and Ti_3Si phases were stable. Different solubility ranges were observed and compared with the data obtained by Zhao et al. (2004a). The Nb solubility in their work was 60, 41 and 17.6 at. % Nb in Ti_3Si, Ti_5Si_4 and $Ti(Nb)Si_2$, respectively, and the solubility of Ti in Nb_5Si_3 and $NbSi_2$ was 31 and 13 at.% Ti, respectively. At 500 °C (Figure 23) the solubilities of Nb in $TiSi_2$, TiSi, Ti_3Si, Ti_5Si_4, and Ti_5Si_3 were 21.0, 8.0, 12.0, 12.0, and 23.0 at.% Nb, respectively, and the solubility of Ti in Nb_5Si_3 was 20 at.% Ti.

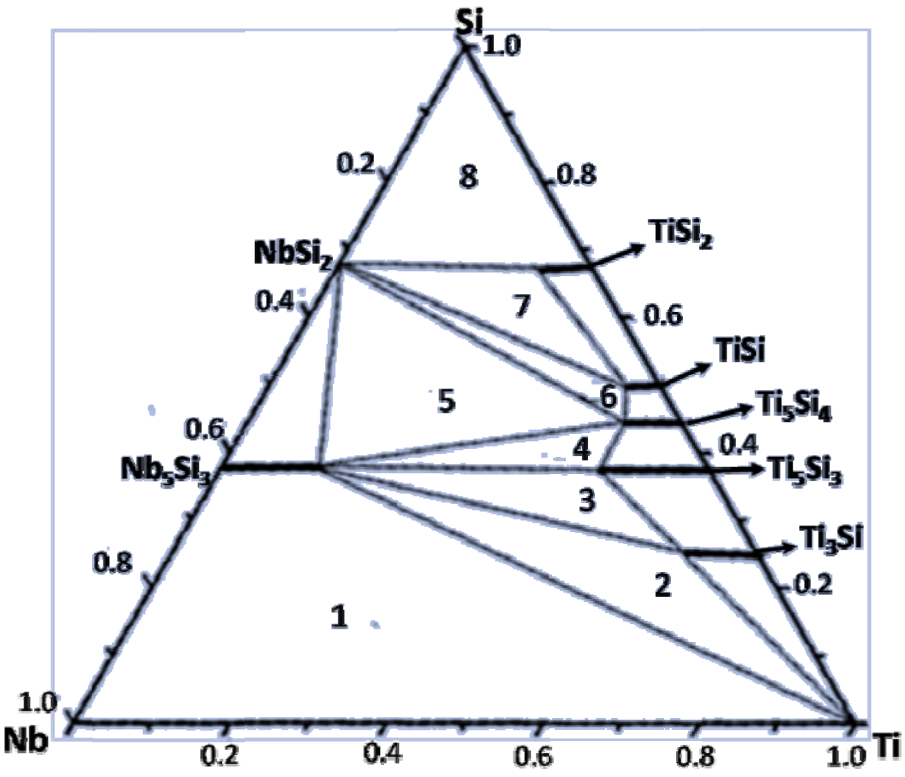

Figure 23. Isothermal section at 500 °C obtained by Xu et al. (2005).

1.6.5 Hf addition in Nb-silicide based in situ composites

The high melting point of Hf (2233 °C) makes it an attractive alloying addition to maintain a high liquidus temperature of Nb-silicide in situ composites particularly since Hf can improve the fracture toughness of Nb_{ss} without affecting the Nb_{ss} ductile brittle transition temperature [Chan (2002)] and Hf has high affinity for oxygen and thus can scavange oxygen to form HfO_2 which can be beneficial for high temperature oxidation. From an alloy design perspective it is important to control the concentration of Hf in Nb-silicide based in situ composites to avoid the formation of detrimental phases.

The Hf-Si binary phase diagram

The Hf-Si phase diagram is shown in Figure 24. Like Ti, Hf has two allotropes. The hexagonal α-Hf phase, which is stable up to 1743 °C , shows very small Si solubility that does not affect the allotropic transformation temperature. The bcc β(Hf) phase is stable from 1743 to 2233 °C.

The Hf-rich intermetallic Hf_2Si has tetragonal structure, forms peritectically at 2092 °C and 33 at. % Si via the reaction L +Hf_5Si_3 → Hf_2Si. The silicide transforms via the peritectoid decomposition β(Hf) + Hf_2Si → α(Hf) at 1743 °C.

The Hf_5Si_3 silicide has a hexagonal structure, forms peritectically at 2355 °C and 37 at. %Si and is stable to 1925 °C. This silicide is isomorphous with Ti_5Si_3 and the metastable γNb_5Si_3. The Hf_3Si_2 silice has a tetragonal structure and melts congruently at 2463 °C and 40 at. % Si. The Hf_5Si_4 silicide has a tetragonal structure and forms peritectically at 2321 °C and 44 at.% Si via the reaction L + Hf_3Si_2 → Hf_5Si_4. The HfSi silicide has an orthorhombic structure, forms peritectically at 2145 °C via the reaction L + H f_5Si_4 → HfSi. The orthorhombic base-centred $HfSi_2$ di-silicide forms peritectically at 1541 °C and 67 at.% Si via the reaction L + HfSi → $HfSi_2$.

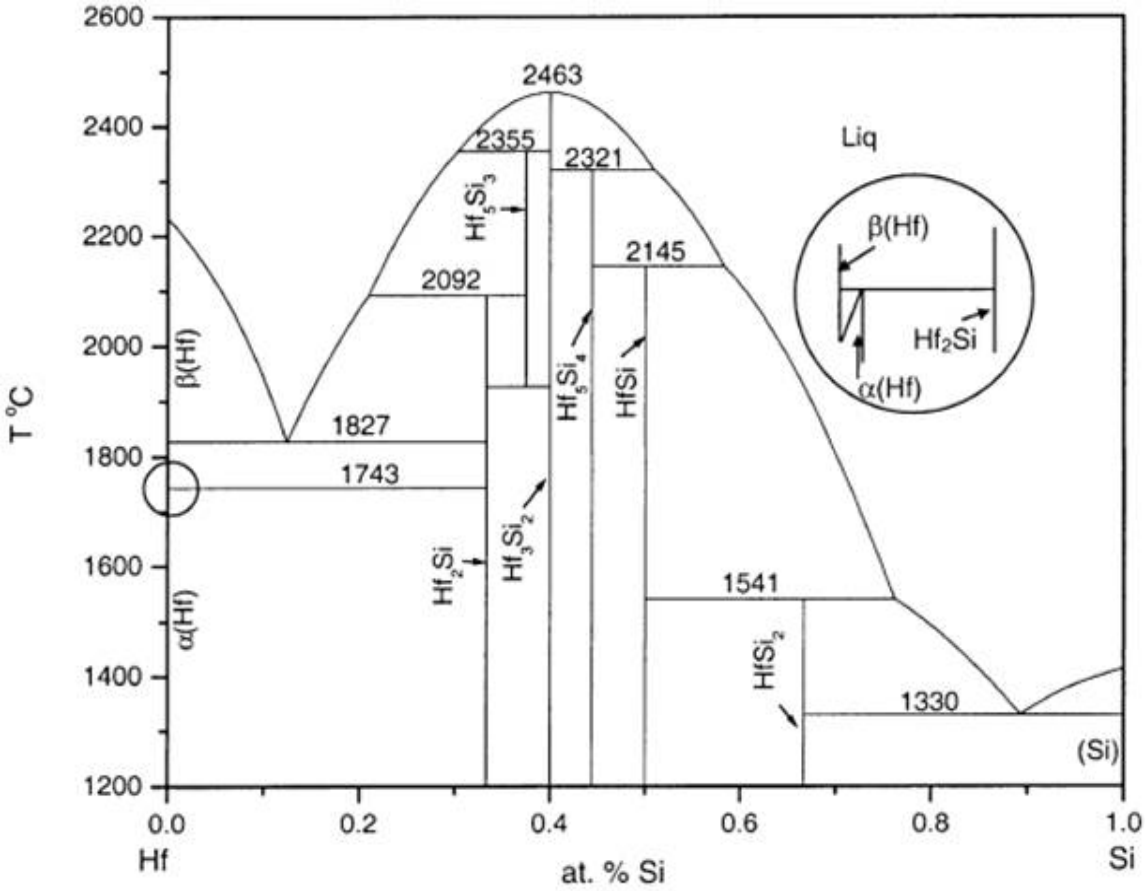

Figure 24. The Hf-Si phase diagram calculated by Yang et al. (2003).

Two eutectic reactions occur in this system; the eutectic reaction L→ bcc (Hf) + Hf_2Si at 1827 °C and 12.5 at. % Si and the eutectic reaction L→ Si + $HfSi_2$ at 1330 °C and 89.3 at.% Si. The crystal structure data of the phases of this system is given in Table 6.

Table 6 Crystal structure data of the phases in the Nb-Hf system [Cai et al. (2010)].

Phase	Pearson symbol	Space Group	Strukturbericht designation	Prototype
α-Hf	hP2	$P6_3/mmc$	A3	Mg
β-Hf	cI2	Im-3m	A2	W
HfSi	oP8	Pnma	-	FeB
Hf_2Si	tI12	I4/mcm	-	Al_2Cu
Hf_5Si_3	hP16	$P6_3/mcm$	-	Mn_5Si_3
Hf_3Si_2	tP16	P4/mbm	-	Si_2U_3
Hf_5Si_4	tP36	$P4_12_12$	-	Si_4Zr_5
$HfSi_2$	hP9	Cmcm	-	$ZrSi_2$
Si	cF8	Fd-3m	A4	C (diamond)

The Nb-Si-Hf ternary alloy system

The study of this system is important in order to understand the influence of Hf on the microstructure of Nb-silicide based in situ composites. An experimental assessment of this system was done by Zhao et al. (2001). They used experimental data from directional solidificated (DS) alloys that were given a heat treatment at 1500 °C for 100 h. They suggested that the binary eutectics L → bcc-Hf + Hf_2Si and L → bcc-Nb + Nb_3Si are linked (Figure 25). An isothermal section at 1500 °C was also obtained (Figure 26a).

Ternary solubilities for most of the ten phases were identified. In Table 7 the crystal structure data is given for binary and solid solution phases. The silicides Nb_3Si, Nb_5Si_3, and $NbSi_2$ with Hf in solid solution are shown as $Nb(Hf)_3Si$, $Nb(Hf)_5Si_3$ and $Nb(Hf)Si_2$, respectively, and the silicides such as HfSi, Hf_5Si_4, Hf_3Si_2, Hf_5Si_3 and Hf_2Si with Nb in solid solution are shown as Hf(Nb)Si, $Hf(Nb)_5Si_4$, $Hf(Nb)_3Si_2$, $Hf(Nb)_5Si_3$, and $Hf(Nb)_2Si$, respectively.

Significant differences resulted from the ternary solubilities. While the Hf_5Si_3 silicide was not stable below about 1900 °C in the binary (Figure 24), the $Hf(Nb)_5Si_3$ was stabilized at 1500 °C by the presence of Nb. At 1500 °C the two polymorphs α(Nb,Hf,Si)and β(Nb,Hf,Si) were also identified. The solubility of Hf in the $Nb(Hf)_5Si_3$ and $Nb(Hf)Si_2$ phases was approximately 16 and 9.4 at. %,respectively, whereas the solubilities of Nb in the $Hf(Nb)_2Si$, $Hf(Nb)_3Si_2$, $Hf(Nb)_5Si_4$ and Hf(Nb)Si silicides were 46, > 6.5, ≥ 22 and 5 at.%, respectively. Furthermore, they found that the $Nb(Hf)_3Si$ silicide was unstable at 1500 °C and decomposed through the eutectoid reaction $Nb(Hf)_3Si$ → β(Nb,Hf,Si) + $Nb(Hf)_5Si_3$. It is important to notice that Nb can be in equilibrium with $Nb(Hf)_5Si_3$ and that $Hf(Nb)_2Si$ can form in alloys with over 10 at. % Hf.

A thermodynamic modeling of this system was performed by Yang et al. (2003). The calculated isothermal at 1500 °C (shown in Figure 26b) is mostly in agreement with the experimentally diagram obtained by Zhao et al. (2001).

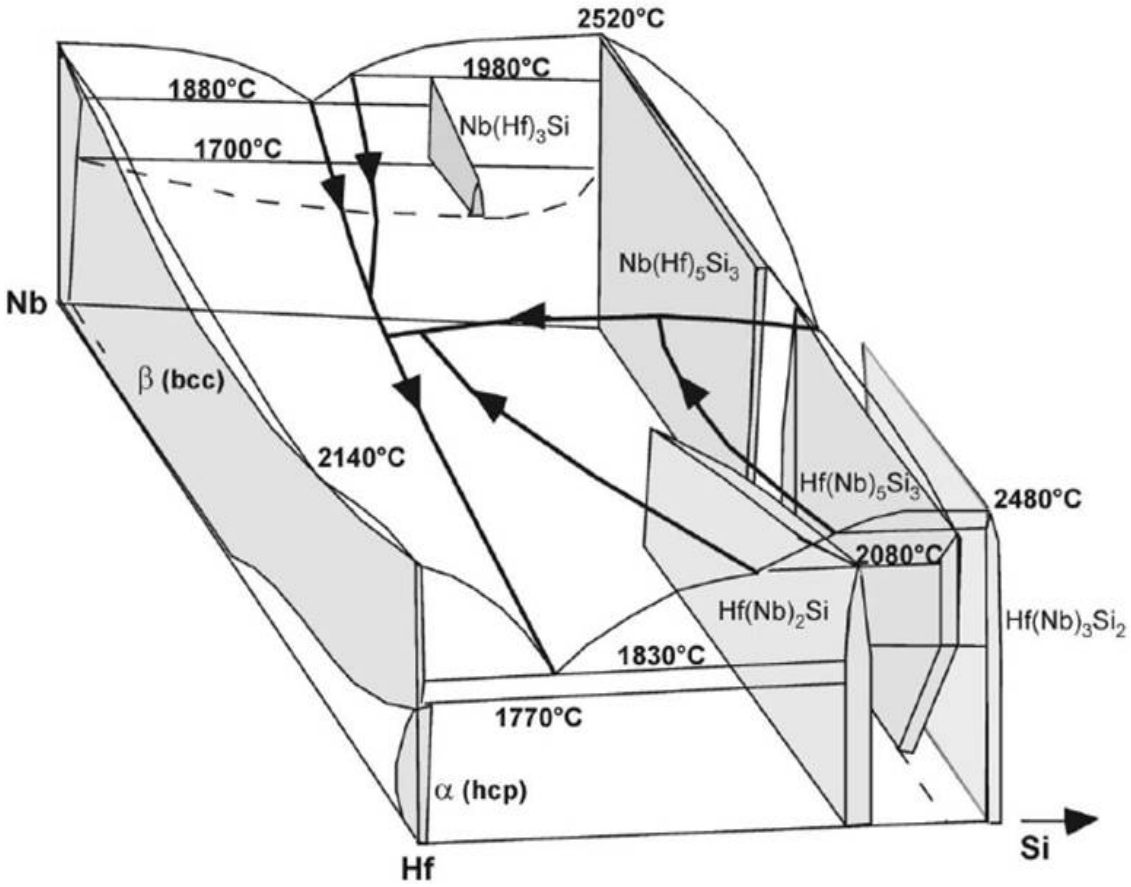

Figure 25. Suggested three-dimension projection of the Nb-Hf-Si system with 40 at.% Si by Zhao et al. (2001).

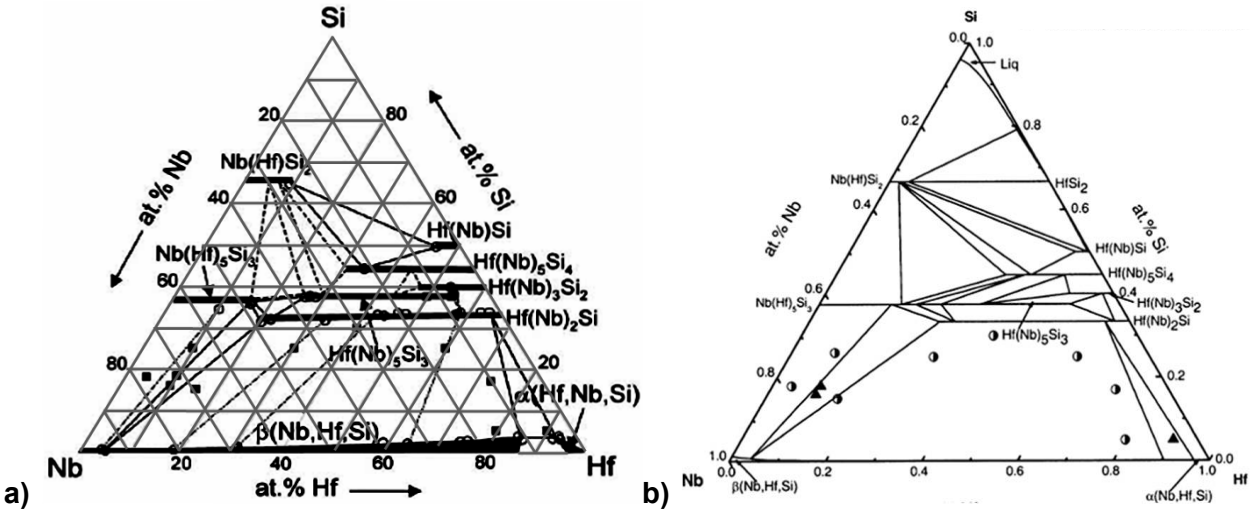

Figure 26. Isothermal sections at 1500 °C obtained by (a) Zhao et al. (2001) and (b) Yang et al. (2003).

Some ternary solubilities were calculated. The solubility of Hf in the Nb(Hf)$_5$Si$_3$ silicide was proposed to be 17.6 at.% and the Nb solubilities in Hf(Nb)$_5$Si$_3$ and Hf(Nb)Si$_2$ were 43.1 and 37.6

at.%, respectively. The Nb-rich corner of the liquidus projection calculated in this work shows that alloys with low content of Hf can solidify without formation of un-desirable phases (Figure 27). It should be noted that the data in table 7 and the liquidus projection in figure 27 show that the αNb_5Si_3 prototype Cr_5B_3 can form from the liquid

Table 7 Crystal structure data for phases in Nb-Hf-Si system Zhao et al. (2001) and Yang et al. (2003).

Phase	Pearson symbol	Space Group	Prototype
α(Hf,Nb,Si)	hP2	$P6_3/mmc$	Mg
β(Nb,Hf,Si)	cI2	Im-3m	W
Hf(Nb)Si	oP8	Pnma	FeB
$Hf(Nb)_2Si$	tI12	I4/mcm	Al_2Cu
$Nb(Hf)_5Si_3$	tI32	I4/mcm	Cr_5B_3
$Hf(Nb)_5Si_3$	hP16	$P6_3/mcm$	Mn_5Si_3
$Hf(Nb)_3Si_2$	tP10	P4/mbm	Si_2U_3
$Hf(Nb)_5Si_4$	tP36	$P4_12_12$	Si_4Zr_5
$Nb(Hf)Si_2$	hP9	$P6_422$	$CrSi_2$
$Nb(Hf)_3Si$	tP32	$P4_2/n$	PTi_3
Si	cF8	Fd-3m	C (diamond)

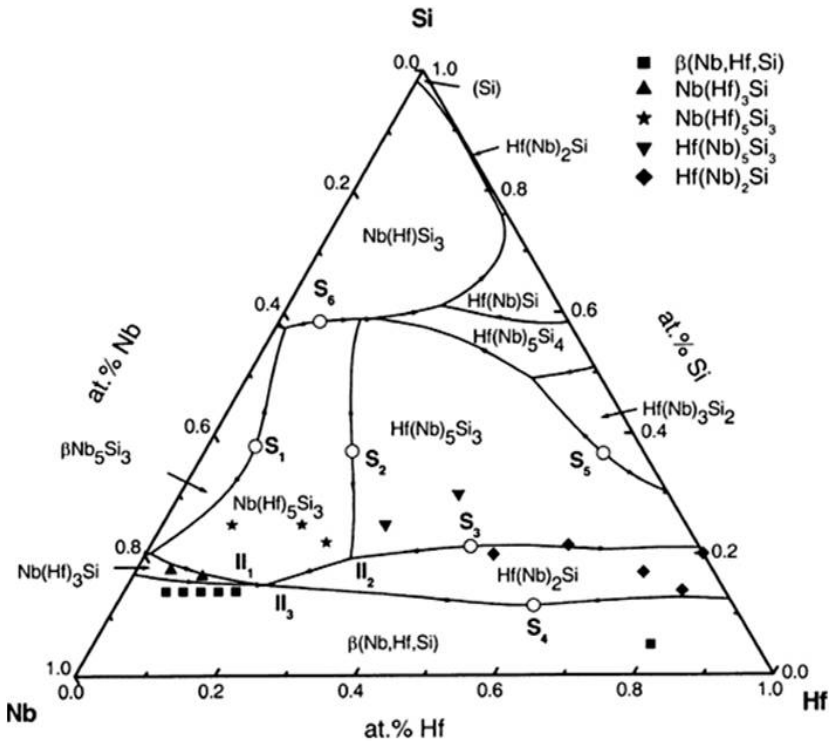

Figure 27. Liquidus projection of Nb-Hf-Si proposed by Yang et al. (2003).

1.6.6 The Nb-Cr-Al ternary alloy system

This system is useful for the design of alloys and coatings for high temperatures. Cr additions were found to improve the corrosion resistance of Nb-aluminides which have good strength and creep resistance at high temperatures including the Al rich Al_3Nb phase which has high melting point and low density [Zhao et al. (2004b)].

Hunt and Raman (1968) produced an isothermal section at 1000 °C (Figure 28a). No data about the Al corner was given in their study. The C14 Cr_2Nb Laves phase and the Cr_{ss} phase boundaries were defined, the former was stabilized at this temperature with up to 45 at.% Al solubility and the Al solubility in Cr_{ss} was 42 at.%. In their isothermal section the three-phase field equilibria and the boundaries of the other phases were not defined.

Mahdouk and Gachon (2001) used experimental data to determine an isothermal section at 1000 °C (Figure 28b). Seven three-phase field phase equilibria, binary phases and ternary solubilities were defined. The solubility of Cr in the Nb-aluminides was rather different to the previous work. No ternary compound was determined. The C14 $(Cr,Al)_2Nb$ Laves phase appears with a narrow homogeneity rather than the wide homogeneity range and the limits of its two forms were not clearly defined, because their compositions are very close. The C14-$(Cr,Al)_2Nb$ Laves phase appears to be in equilibrium firstly with $(Cr,Al)Nb_{ss}$ and $Al_3(Nb,Cr)$, secondly with $(Al,Cr)Nb_2$ and $Nb(Al,Cr)_{ss}$ and thirdly with $(Al,Cr)Nb_2$ and $Al_3(Nb,Cr)$. In figure 28b tie lines are represented with dashed lines. The Al_3Nb phase has up to 10.8 at. % Cr solubility.

To clarify the discrepancies between the work of Hunt and Raman (1968) and Mahdouk and Gachon (2001), a partial isothermal section was constructed by Zhao et al. (2004b) using diffusion multiples annealed at 1000 °C for 2000 h in which $NbAl_3$ was used instead of Al to avoid melting. Furthermore, they studied the gap between the two forms of the Laves phase, namely the C14 and C15 $(Cr,Al)_2Nb$ (Figure 29). Crystal structure data of the binary phases in the Nb-Cr-Al system is summarized in Table 8.

Two three-phase field equilibria were determined in the Laves phase gap, C14+C15+(Cr,Al)Nb_{bcc} and C14+C15+$(Cr)_{bcc}$. The C14-Laves phase with higher Al content was in equilibrium with (Al,Cr)Nb_2 and (Cr,Al)Nb_{ss}. Lower Cr solubility in Nb_3Al was determined. Zhao et al. suggested that like Si, Al promotes the formation of the C14-Laves phase.

Table 8 Crystal data of binary intermetallic compounds and solid solutions in Nb-Cr-Al [Zhao et al. (2004c)].

Phase	Pearson symbol	Space Group	Strukturbericht designation	Prototype
Al	cF4	Fd-3m	A1	Cu
Cr	cI2	Im-3m	A2	W
Nb	cI2	Im-3m	A2	W
Cr_2Al	tI6	I4/mmm	$C11_b$	$MoSi_2$
Cr_5Al_8	hR26	R-3m	-	Cr_5Al_8
Cr_4Al_9	cI52	I4-3m	-	-
$CrAl_4$	hP574	$P6_3/mmc$	-	$\mu MnAl_4$
Cr_2Al_{11}	oC16	Cmcm	-	-
$CrAl_7$	mC104	C2/m	-	V_7Al_{45}
Nb_2Al	tP30	$P4_2/mnm$	$D8_b$	σCrFe
Nb_3Al	cP8	Pm-3n	A15	Cr_3Si
$NbAl_3$	tI8	I4/mmm	$D0_{22}$	Al_3Ti
$NbCr_2$-Laves	hP12	$P6_3/mmc$	C14	$MgZn_2$
$NbCr_2$-Laves	cF24	Fd-3m	C15	$MgCu_2$

Eutectic alloys of this system with compositions Al-(37.6-43.5)Cr-(10.7-12.5)Nb (at.%) were studied by Souza et al. (2005). They observed the formation of Al_3(Nb,Cr) and Cr(Al,Nb) phases from the eutectic reaction L→ Al_3(Nb,Cr)+Cr(Al,Nb) at 1347.9 °C and noted that Cr(Al,Nb) undergoes a polymorphic transformation at ~ 892.3 °C to the Al(Nb,Cr) phase. The peritectic transformation L + $(Cr,Al)_2Nb$ → Al_3(NbCr) and the eutectoid decomposition Cr(Al,Nb) → Al(Nb)Cr_2 + Al_8Cr_5 were also observed (Figure 30). In 2006 Souza et al. obtained a partial isothermal section near the Al_3(Nb,Cr) and Cr(Al,Nb) phases, suggesting that the Al(Nb)Cr_2 phase forms from Cr(Al,Nb). The two monovariant eutectic were L →$(Cr,Al)_2Nb$+Al(Nb)Cr_2 and L→Al_3(Nb,Cr)+ Al(Nb)Cr_2 .

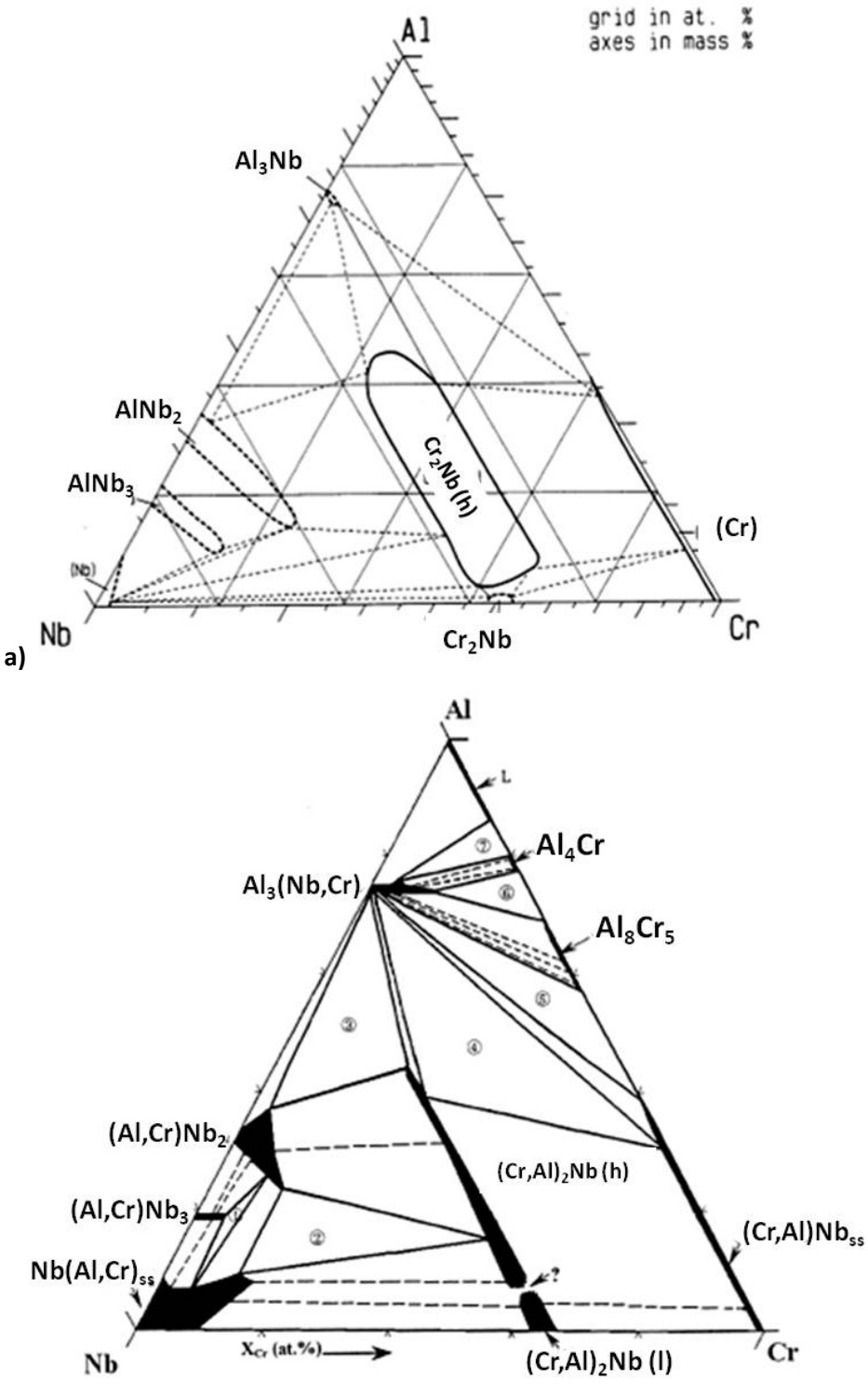

Figure 28. Nb-Cr-Al isothermal sections at 1000 °C obtained (a) by Hunt and Raman (1968) and (b) Mahdouk and Gachon (2001).

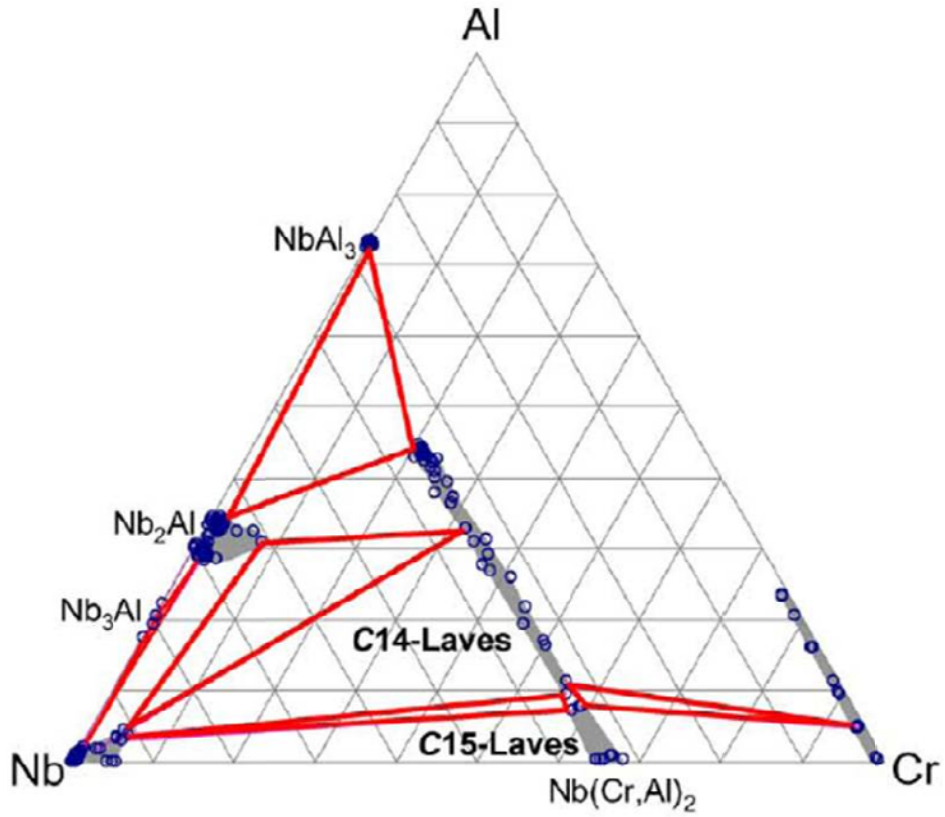

Figure 29. Partial isothermal section at 1000 °C obtained by Zhao et al. (2004b).

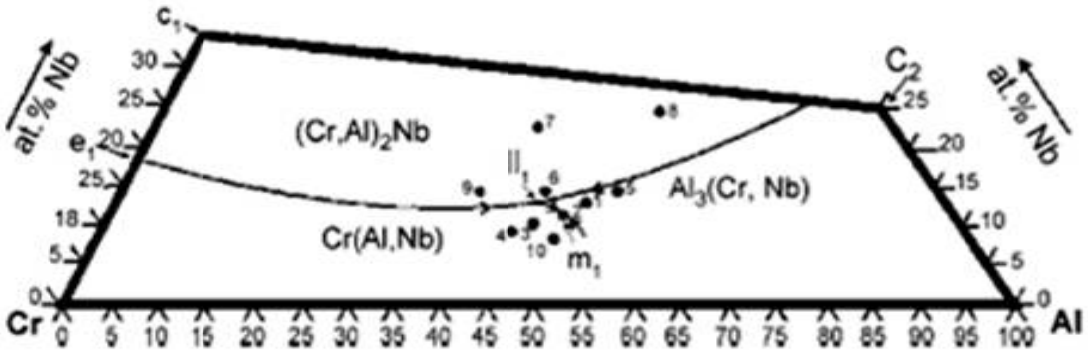

Figure 30. Liquidus projection obtained by Souza et al. (2006).

A detailed isothermal section for this system has been proposed by Raghavan (2008) based on the results obtained by Mahdouk and Gachon (2001) and Zhao et al. (2004c) (Figure 31). This section shows that the C14 Laves phase cannot be in equilibrium with Nb_3Al.

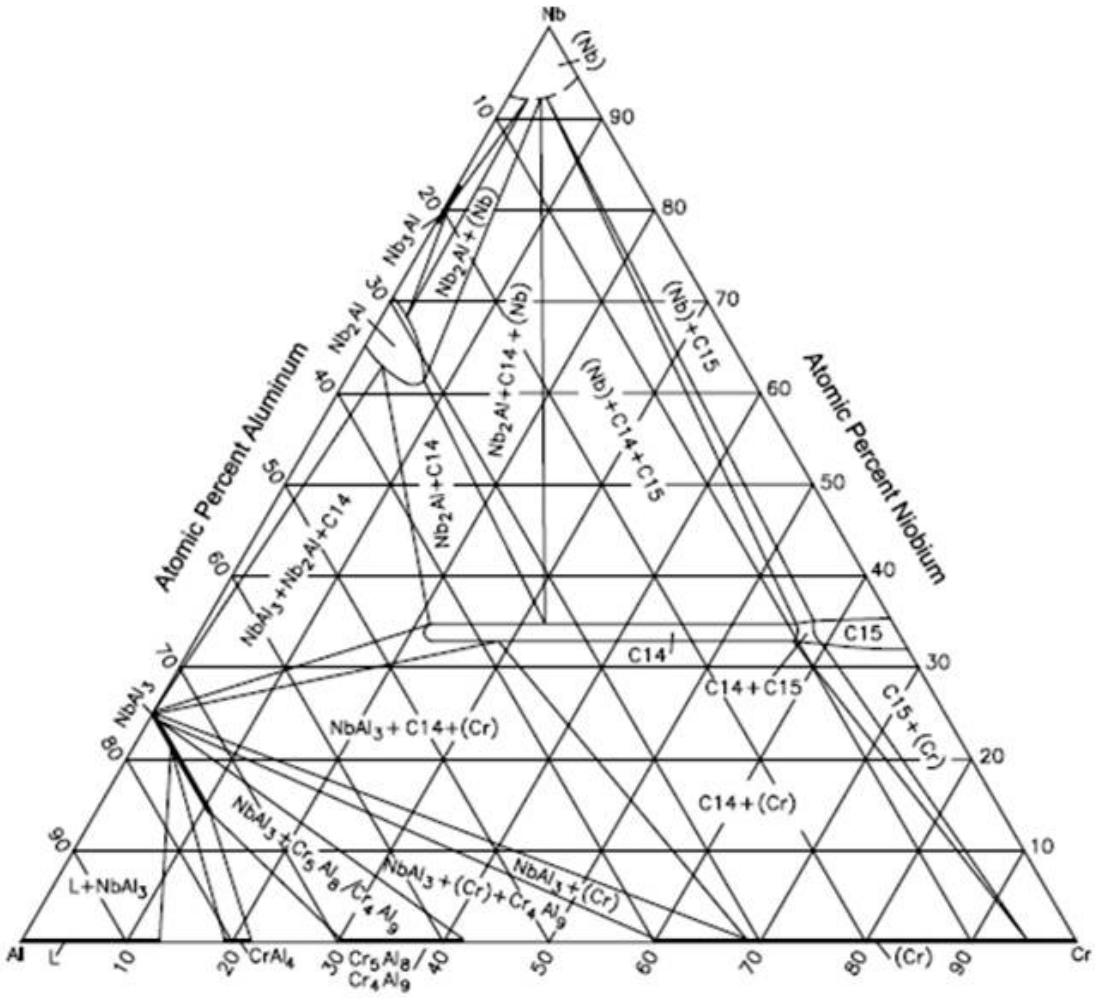

Figure 31. The isothermal section produced by Raghavan (2008) using data obtained at 1000 °C by Mahdouk and Gachon (2001) and Zhao et al. (2004b).

1.6.7 The Cr-Si-Ti ternary alloy system

Lysenko et al. (1971) proposed an isothermal section for this system at 1000 °C (Figure 32b). The ternary T phase $(Cr,Ti)_6Si_5$ with composition range 11 to 41 at.% Ti and structure type Ti_6Ge_5 (Ibam, oI44) observed by Hallais et al. (1968 and 1971) was confirmed by Lysenko with composition range 15 to 39 at.% Ti and 43 to 48 at.% Si. At 1300 °C the solubility between $TiSi_2$ and $CrSi_2$ found by Nowotny et al. (1953) was confirmed later by Du and Schuster (2002).

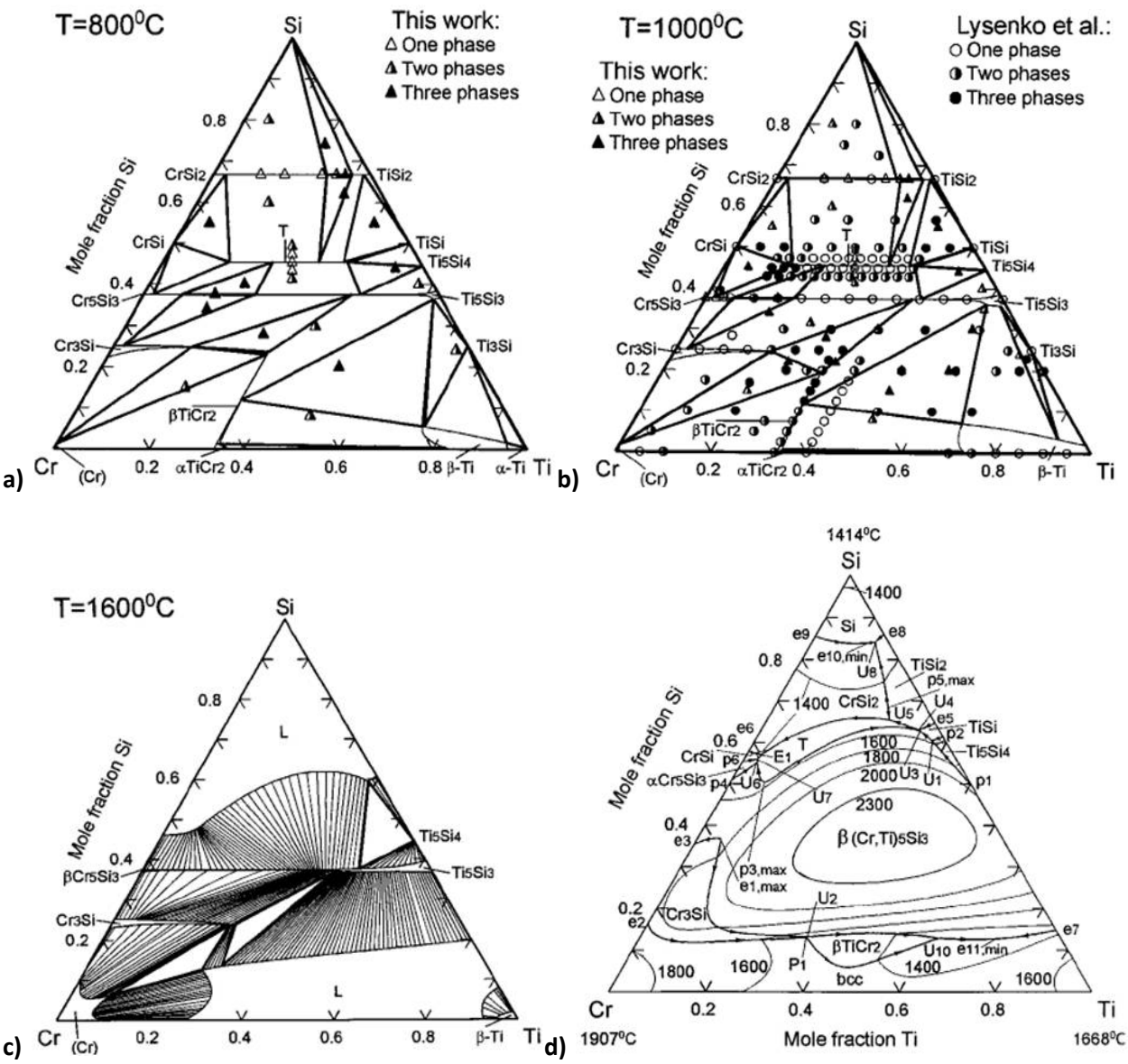

Figure 32. Isothermal sections of the Cr-Si-Ti system obtained by Du and Shuster (2002), (a) at 800 °C and compared with their experimental data, (b) at 1000 °C and compared with their data and that of Lysenko et al., (c) calculated at 1600 °C and (d) liquidus surface projection.

Du and Schuster (2002) used experimental data and calculated isothermal sections at 800 °C, 1000 °C, 1600 °C and liquidus surface projection for the Cr-Si-Ti system (Figure 32). Phases such as $TiSi_2$, Ti_5Si_3, $CrSi_2$, αCr_5Si_3, Cr_3Si, and $\beta TiCr_2$ were shown to have ternary solubilities whereas these were negligible for the (Si), TiSi and CrSi phases confirming previous work. The T (TM_6Si_5) phase changes according to its Cr and Ti contents being $Ti_2Cr_4Si_5$ when it is in equlibrium with CrSi and αCr_5Si_3 and $Ti_4Cr_2Si_5$ when it is in equilibrium with TiSi and $TiSi_2$. A continuous solid

solution between the binary phases Ti_5Si_3 and Cr_5Si_3 was observed in the isothermal sections at 800 °C and 1000 °C. At 1600 °C, the continuous solid solubility of Ti_5Si_3 is with βCr_5Si_3 instead.

1.6.8 The Fe-Si binary phase diagram

The Fe-Si phase diagram (Figure 33) has been assessed by Kubaschweski (1982) and Kubaschweski and Okamoto (1993). According to the latter assestment, there are ten stable solid phases in the binary Fe-Si system, the Fe-rich bcc solid solution which exists in three modifications, one disordered modification (A2, W-type) referred to as αFe phase and the two ordered modifications (B2, CsCl-type) and ($D0_3$, BiF_3-type) referred to as α_1 Feand α_2Fe respectively, the fcc Cu-type Fe-rich solid solution (γFe), the hexagonal Fe_2Si, the hexagonal Mn_5Si_3-type Fe_5Si_3 phase, isomorphous to γNb_5Si_3 (referred to as η), that is not stable above 1060 °C, the bcc FeSi phase, the $FeSi_2$ phase which forms in two allotropes, the high temperature tetragonal $\beta FeSi_2$ (referred to as ζ_β) and the low temperature orthorhombic $\alpha FeSi_2$ (referred to as ζ_α) and the terminal diamond-type Si-rich solid solution, (Si), which dissolves negligible concentrations of Fe. The crystal structure data for the Fe-Si system is given in the table 9.

Table 9 Fe-Si crystal structure data [Kubaschewski and Okamoto, (1993)].

Phase	Composition at. % Si	Pearson symbol	Space group	Strukturbericht designation	Prototype
(αFe)	0 to 19.5	cI2	Im3m	A2	W
(γFe)	0 to 3.19	cF4	Fm3m	A1	Cu
α_2	10 to 22	cP2	Pm3m	B2	CsCl
α_1	10 to 30	cF16	Fm3m	$D0_3$	BiF_3
Fe_2Si	~ 33.3	hP6	P3m1	-	-
Fe_5Si_3	37.5	hP16	$P6_3/mcm$	$D8_8$	Mn_5Si_3
FeSi	~ 50	cP8	$P2_13$	B20	FeSi
$\alpha FeSi_2$	~ 66.7	oC48	Cmca	-	-
$\beta FeSi_2$	69.5 to 73	tP3	P4/mmm	-	-
(Si)	~100	cF8	Fd3m	A4	C (diamond)

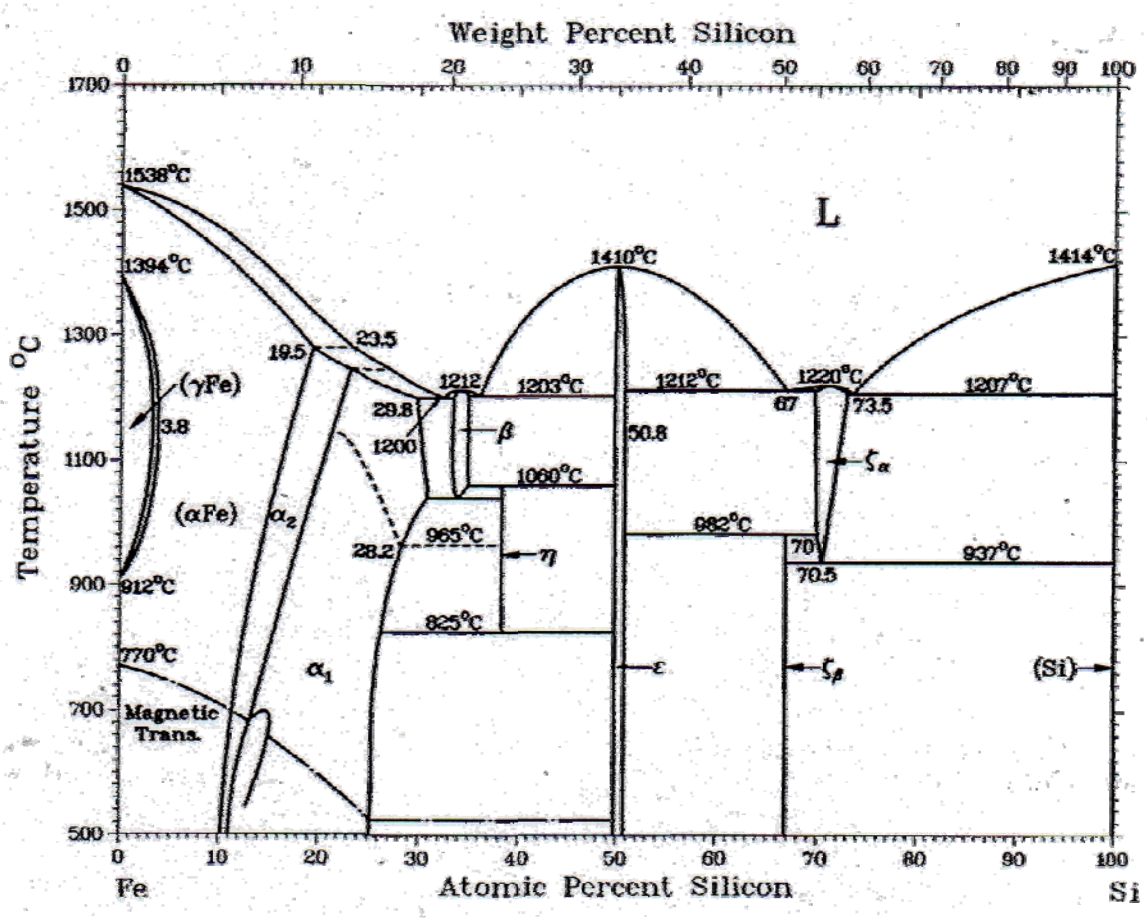

Figure 33. The Fe-Si phase diagram assesed by Kubaschweski and Okamoto (1993).

1.6.9 The Fe-Si -Cr ternary alloy system

Awais (1995) measured Cr and Si activities in the liquid phase and studied solid state phase equilibria. Lindholm (1997) calculated the most recent isothermal sections at 900 °C, 947 °C, 1047 °C and 1150 °C. The experimental data obtained by Awais was used by Lindholm to support the isothermal sections at 947 °C and 1047 °C shown in figure 34. The isomorphous FeSi and CrSi phases form a continuous solid solution at both temperatures. The phase field of the very hard and brittle σ phase, is enhanced by Si. Indeed, the FeCr(σ)phase with the $D8_b$ structure is not stable at high temperature in the binary Fe-Cr system but in the ternary it is stabilized at high temperature by the dissolution of up to 21 at.% Si and eventually becomes the only ternary phase in this system. Ternary solubilities were also determined; for the Cr_3Si phase with the A15 structure a solid solubility of 16 at.% Fe, for the Cr_5Si_3 with the $D8_m$

structure up to 4.5 at.% Fe, up to 17 at.% Cr for both the $Fe_3Si(\alpha_1)$ ($D0_3$) structure and $Fe_3Si(\alpha_2)$ (B2) structure and up to 23 at.% Cr for the Fe_5Si_3 phase with the $D8_8$ structure. Phases such as $CrSi_2$, Fe_2Si, and both polymorphs of the $FeSi_2$ phase (α) and (β) showed negligible ternary solubilities.

Yamamoto et al. (2004) obtained a partial isothermal section at 600 °C to provide data for the order disorder transition as function of the composition of Fe-rich alloys (Figure 35). At 10 at. % Cr phase boundaries of A2, B2 and $D0_3$ were established. A two-phase field of the α(A2) and $\alpha_1(D0_3)$ from 12 to 15 at. % Si and another of the α_2 (B2) and α_1 ($D0_3$) was found. The transition temperature α_2 to α_1 increased with the increase of Si content.

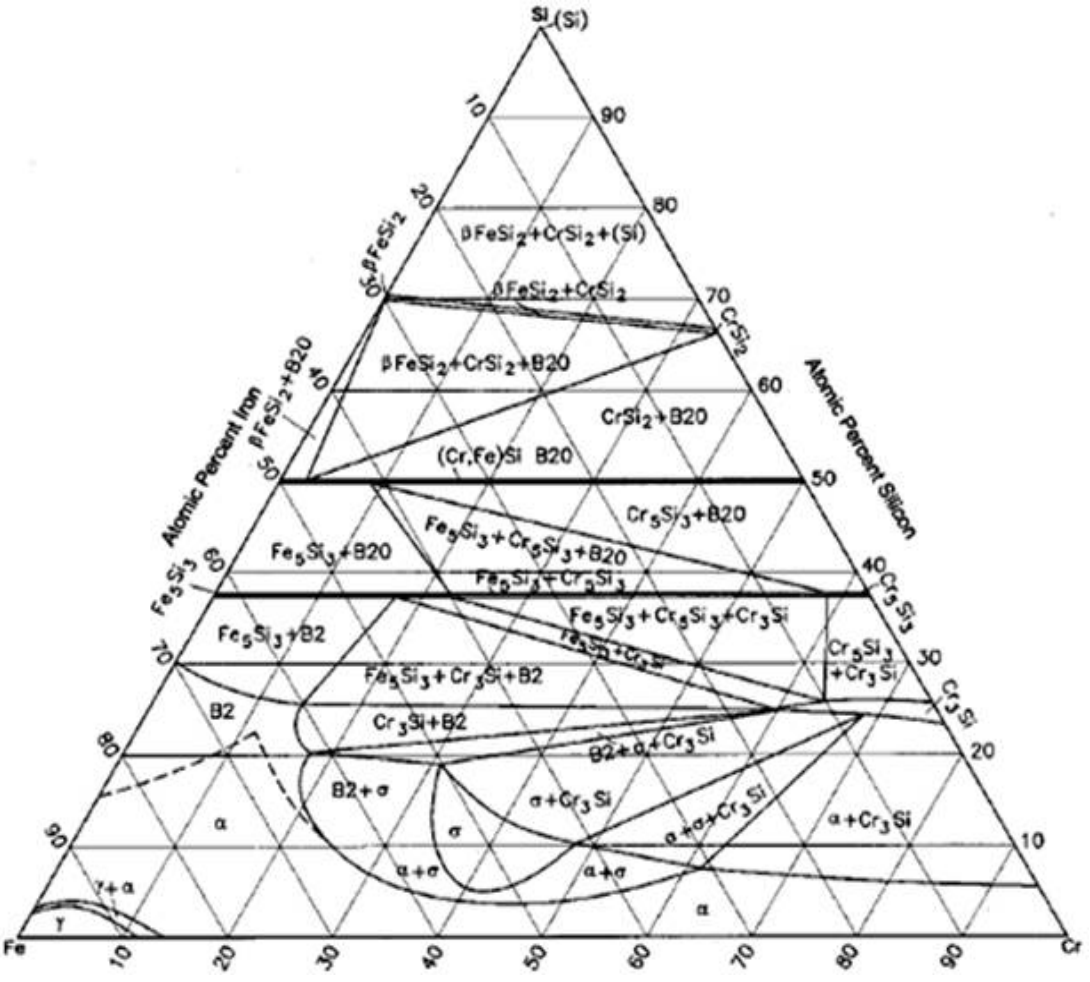

a)

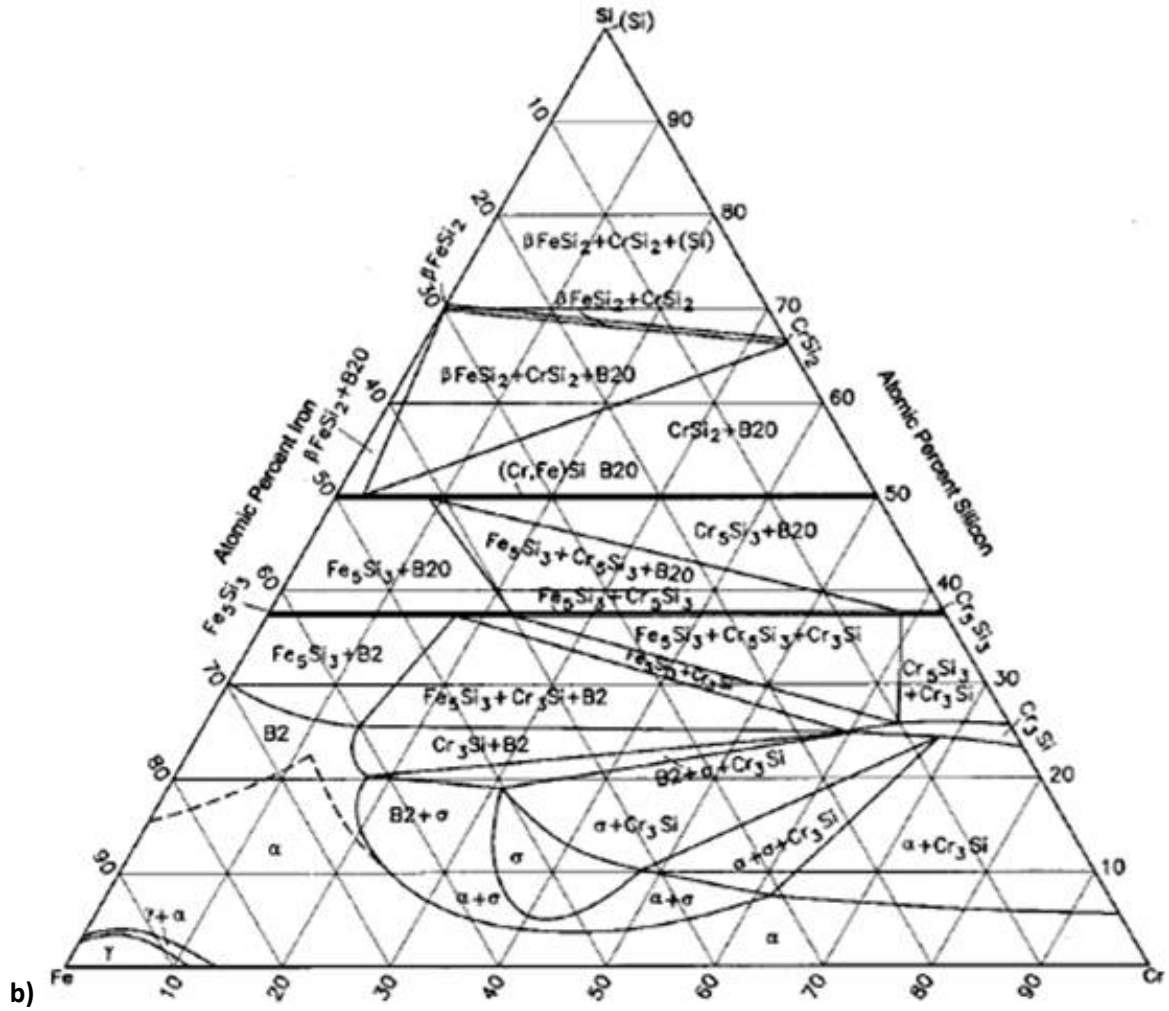

Figure 34. Fe-Si-Cr isothermal sections obtained by Lindholm (a) at 947 °C and (b) at 1047 °C [reported by Raghavan (2003)].

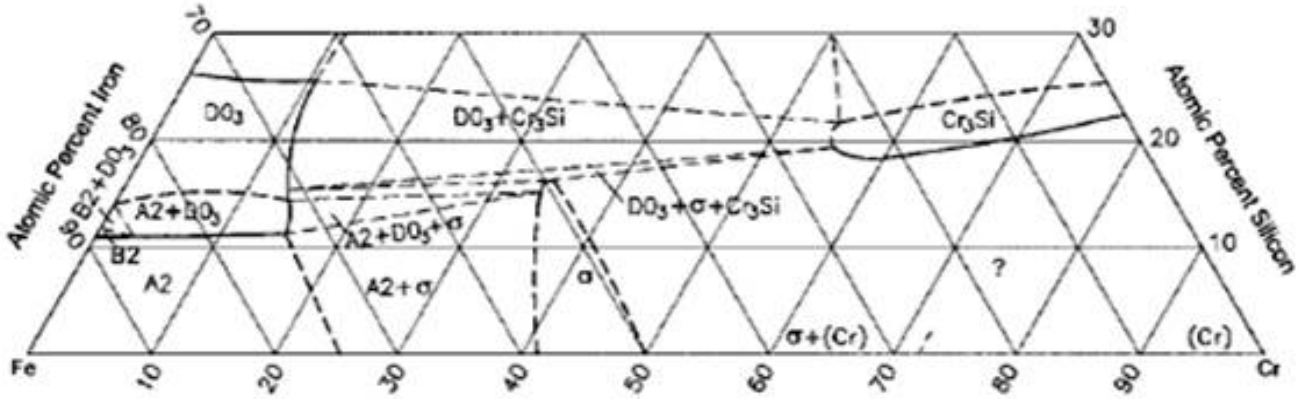

Figure 35. Partial Fe-Si-Cr isothermal section at 600 °C obtained by Yamamoto et al. (2004) [cited by Raghavan (2004)]

1.6.10 The Fe-Si-Ti ternary alloy system

The constituent phases of the Fe-Si-Ti ternary system are the Fe (fcc) phase, α phase (bcc as A2 and $D0_3$), Fe_2Si (h), Fe_5Si_3 ($D8_8$), FeSi(B20), $\alpha FeSi_2$ (o), $\beta FeSi_2$ (t),β-Ti, Fe_2Ti (C14) Laves phase, FeTi (B2), Ti_3Si , Ti_5Si_3 ($D8_8$), Ti_5Si_4 (o), Ti_5Si_4 (t), TiSi (B27), and $TiSi_2$ (C54), and eleven ternary phases were also found in this system.

At 800 °C five ternary phases where reported by Markiv et al. (1966), namely the τ_1-$FeSi_2Ti$, τ_2-FeSiTi, τ_3-($Fe_{52}Si_{36}Ti_{12}$ that corresponds to Fe_4Si_3Ti), X' (at $Fe_{10}Si_{44}Ti_{46}$), and X'' (at $Fe_{15}Si_{40}Ti_{45}$). They also observed a larger homogeneity field of Si in the Fe_2Ti Laves phase (Figure 36). Löffler (2002) studied alloys with < 40 at. % Si and presented isothermal sections at 800 °C, 1000 °C and 1150 °C. He found that the Fe_5Si_3 phase was stabilized by Ti solubility at high and at low temperature, the τ_2 phase was stable at all the aforementioned temperatures, the τ_3 and Fe_7Si_2Ti phases were found at 1000 °C and 1150 °C but not at 800 °C, as suggested by Markiv et al. (1966). Raghavan (2009c) redrew the isothermal sections in the Si-lean region at 800 °C and 1150 °C (Figure 36). Only the τ_2 ternary phase seems to be stable at 800 °C, while at 1150 °C the three ternary phases τ_2, τ_3 and Fe_7Si_2Ti were present.

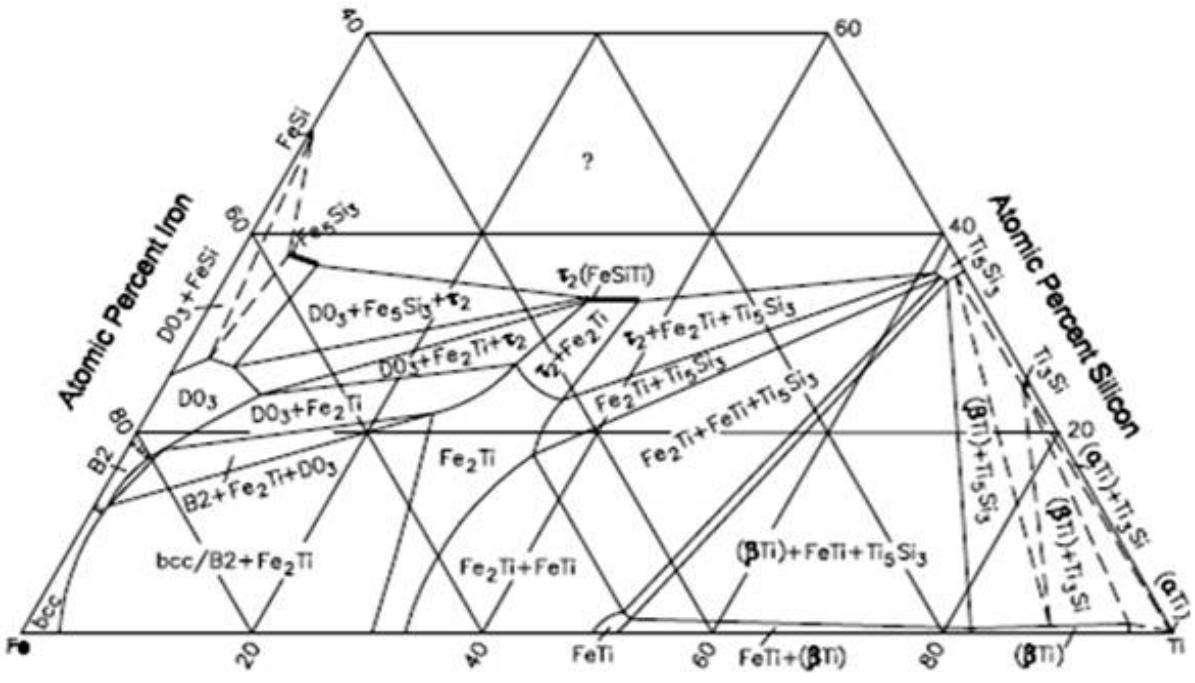

a)

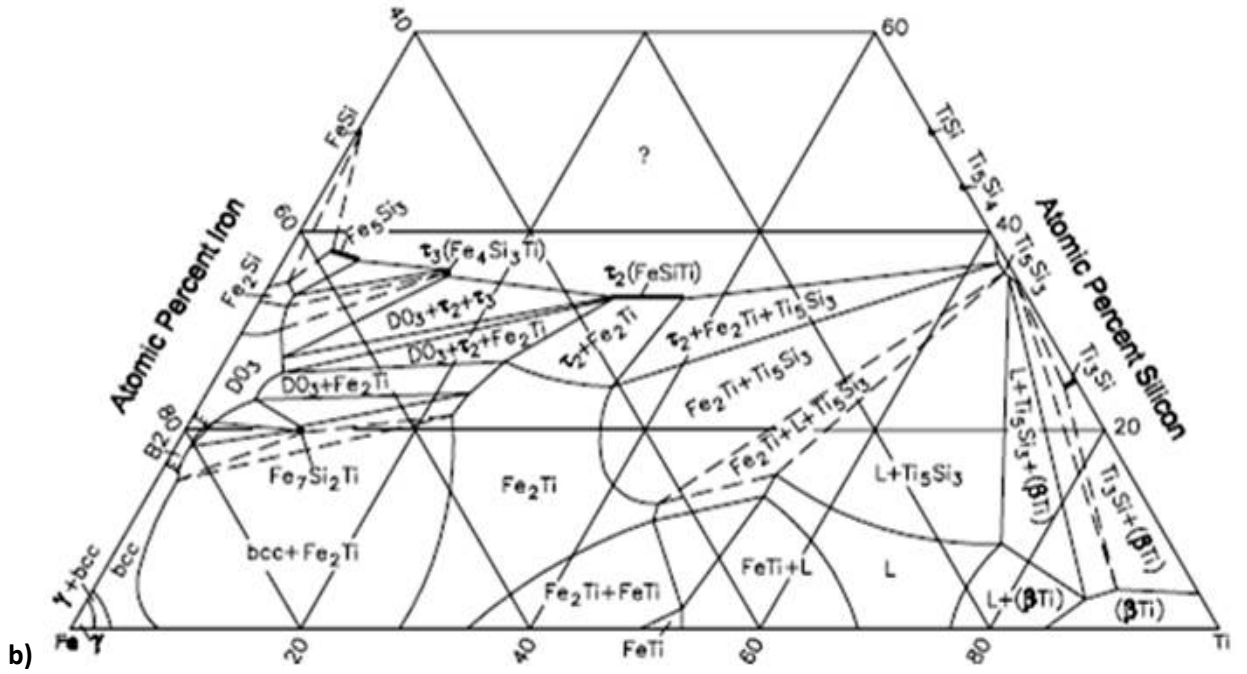

Figure 36. Isothermal sections obtained by Löffler (2002) and Stein et al. (2005) at (a) 800 °C and (b) 1150 °C. [cited by Raghavan (2009c)].

Crystal structure data and lattice parameters are available for the τ_1, τ_2, τ_3, Fe_7Si_2Ti and $Fe_{3-x}SiTi_x$ compounds as follows: τ_1 (Pbam space group and $MnSi_2Ti$ prototype), τ_2 (Ima2 space group and FeSiTi prototype), τ_3 (P6/mm space group and $Pd_{40}Sn_{31}Y_{13}$ prototype), Fe_7Si_2Ti (Fm3m space group and $MnCu_2Al$ prototype).

The Fe_3Si (α_1) phase dissolves up to x=0.7 Ti in the $Fe_{3-x}SiTi_x$. The Fe_2SiTi phase is based on Fe_3Si, a metastable $L2_I$-type superstructure. Weitzer et al. (2008) determined the composition of the phases τ_4, τ_5 , τ_6, τ_7, τ_8 and τ_9 and Weitzer (2008) found that the phase X' was a mixture of τ_9 and Ti_5Si_4 (o) and the X'' phase was a mixture of τ_7 and τ_8. The ternary phases τ_1, τ_2 , τ_3, τ_5, τ_7, τ_8 and τ_9 are present in the a tentative isothermal section at 900 °C proposed by Weitzer et al. (Figure 37).

Weitzer et al. proposed the liquidus projection shown in figure 38. The τ_1 and τ_2 phases have large areas of primary crystallization and form at temperatures C_3 (1328 °C) and C_1 (> 1662 °C). Four ternary eutectic reactions were determined E_1 (at 1254 °C), E_2 (at 1175 °C), E_3 (at 1151 °C) and E_4 (at 1034 °C). The Fe_2Ti and Fe_5Si_3 phases form in the ternary region through the

peritectic reactions P_3 (at 1591 °C) and P_8 (at 1201 °C), respectively. The formation of ternary phases from peritectic reactions; τ_3 phase (P_7 at 1241 °C), τ_4 (P_5 at 1414 °C), τ_5 (P_6 at 1263 °C), τ_6 (P_4 1450 < T < 1480 °C), τ_8 (P_1 at 1640 °C), and τ_9 (P_2 at 1201 °C) was also found.

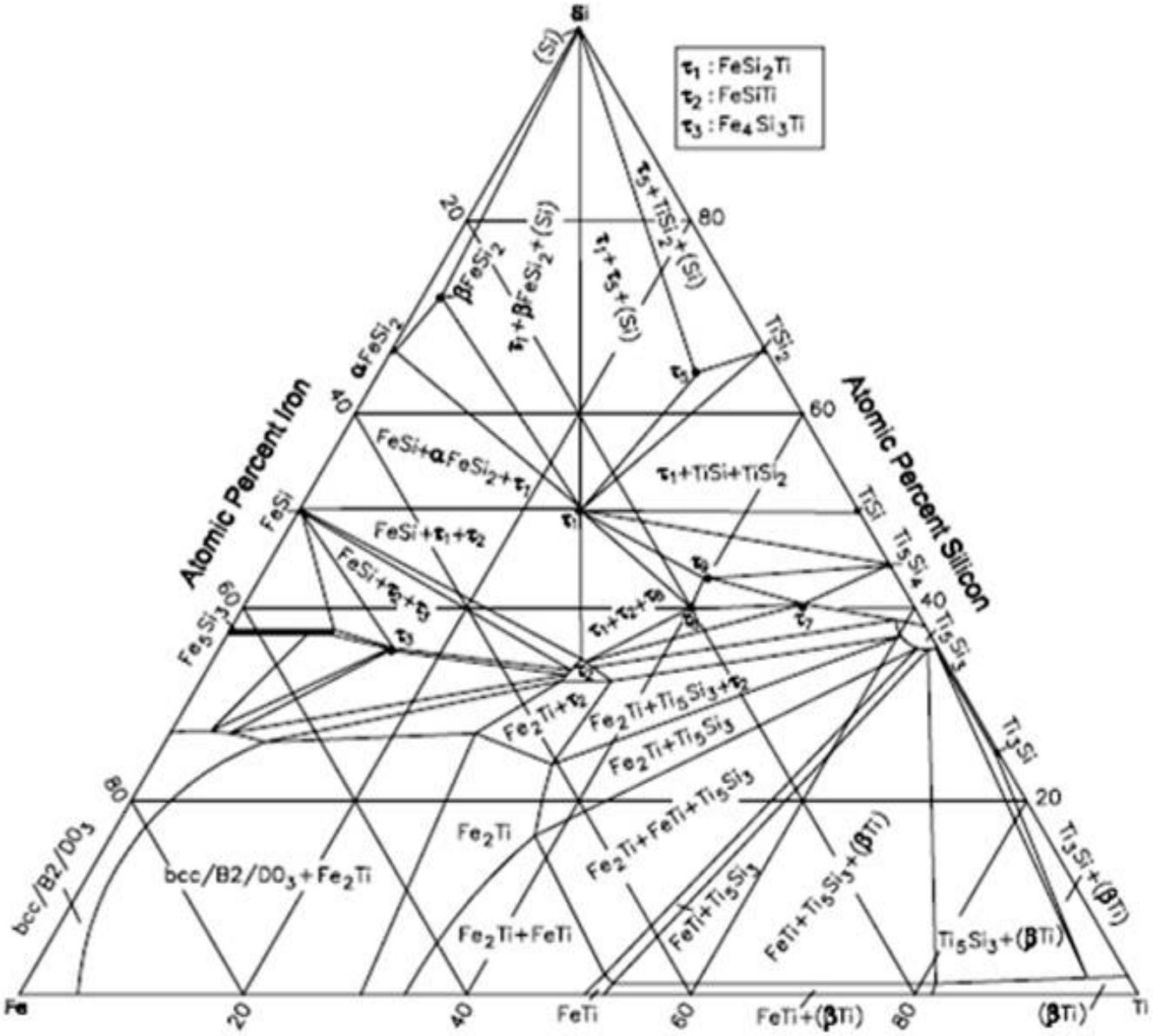

Figure 37. Tentative isothermal section of the Fe-Si-Ti system at 900 °C by Weitzer et al. (2008).

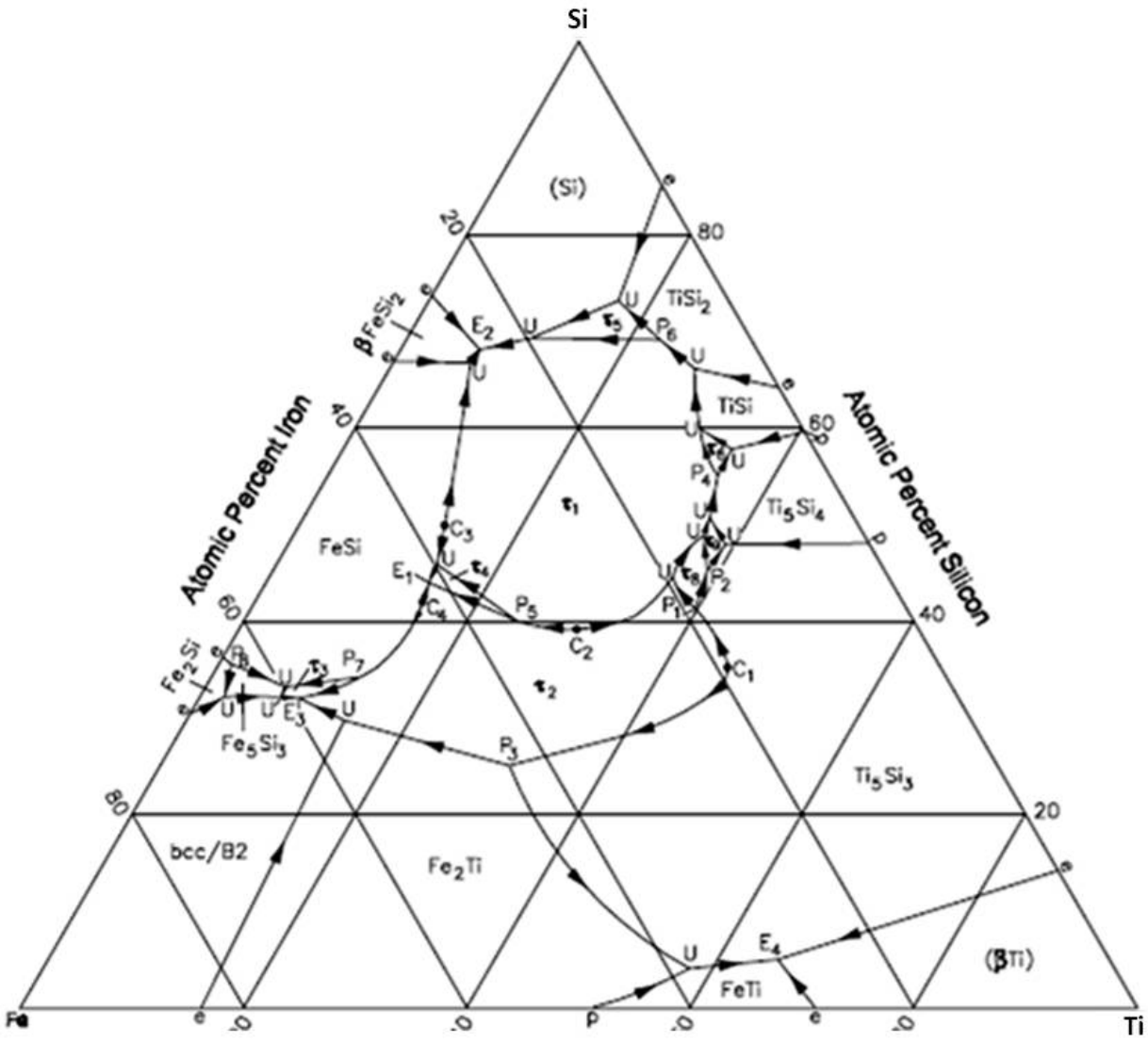

Figure 38. Liquidus projection of the Fe-Si-Ti system proposed by Weitzer et al. (2008) [cited by Raghavan (2009c)].

1.6.11 The Fe-Al-Si ternary alloy system

Attention has been drawn to this system because of the potential oxidation resistance of alloys of this system. Binary intermetallic phases such as Fe_2Si, Fe_5Si_3, FeSi, both polymorphs of $FeSi_2$ ($\alpha FeSi_2$ and $\beta FeSi_2$), $FeAl_2$, Fe_2Al_5 and $FeAl_3$ and many ternary compounds have been found to be stable in this system. Even though there are some discrepancies in the research of this system, an agreement has been reached. Six ternary compounds that were designated as τ_1-τ_6 by Raynor and Rivlin (1988) were first observed by Takeda and Mutuzaki (1940). Lui and Chang

(1999) suggested that the τ_2 and τ_3 were the same due to an identical Fe content and this compound was named τ_{23}. A compound designated as γ was found by Munson (1967) and was later designated as τ_7, Guenau et al. (1995) obtained the $Al_6Fe_4Si_6$ that was designated as τ_8. The ($Al_2Fe_3Si_4$) and ($Al_4Fe_{1.7}Si$) were found and designated as τ' and τ'' by Anglezio et al. (1994) and Yanson et al. (1996), respectively. Phases such as τ_1 ($Al_2Fe_3Si_3$), τ_{23} (Al_2FeSi), τ_4 ($Al_{2.7}FeSi$), τ_5 ($Al_{15}Fe_6Si_5$), τ_6 ($Al_{4.5}FeSi$), τ_7 ($Al_{63.5}Fe_{20.5}Si_{16}$), and τ_8 ($Al_6Fe_4Si_6$) were used in the thermodynamic study performed by Liu and Chang (1999). The composition of these phases was confirmed by many authors who also gave some structural details.

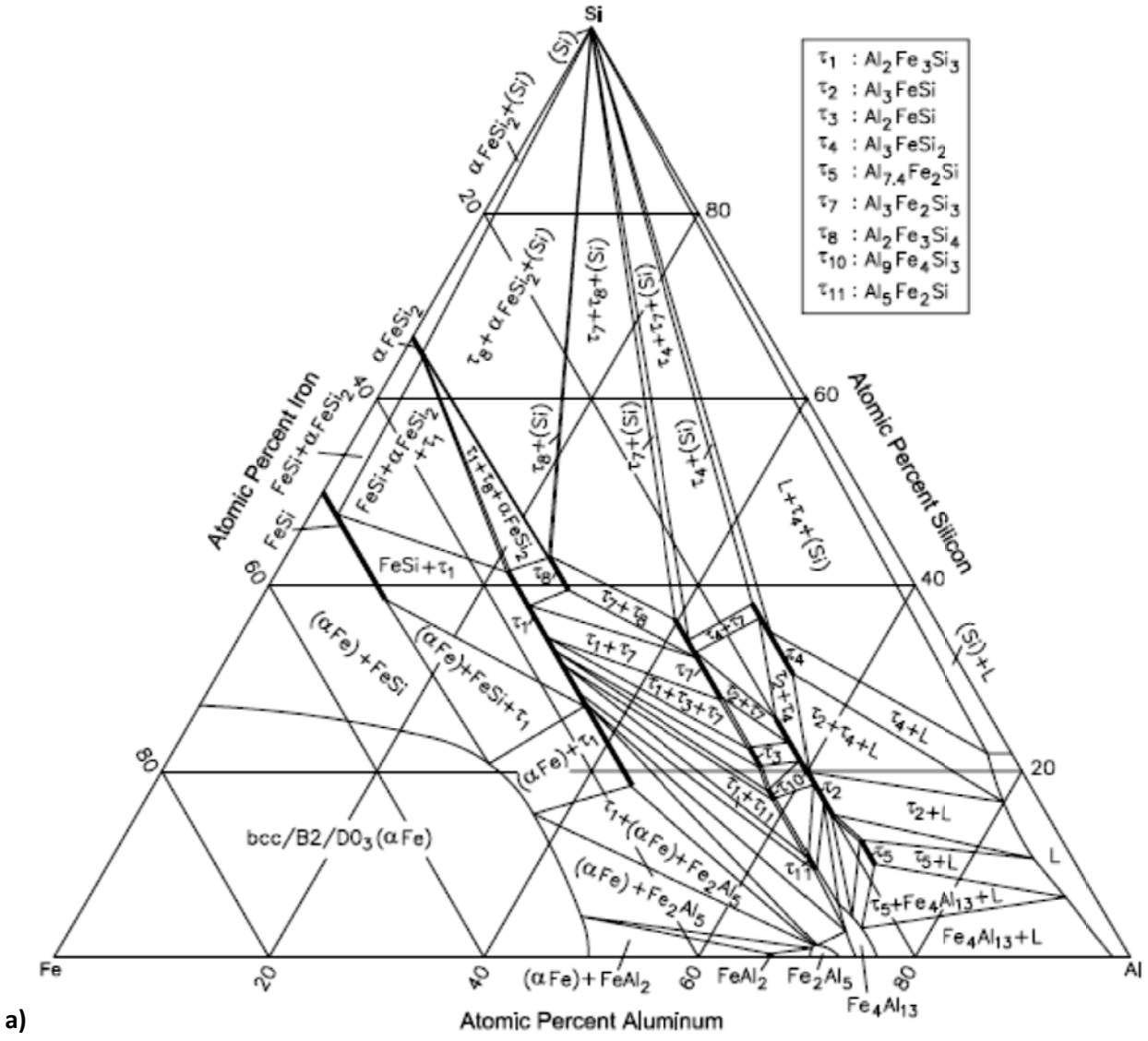

a)

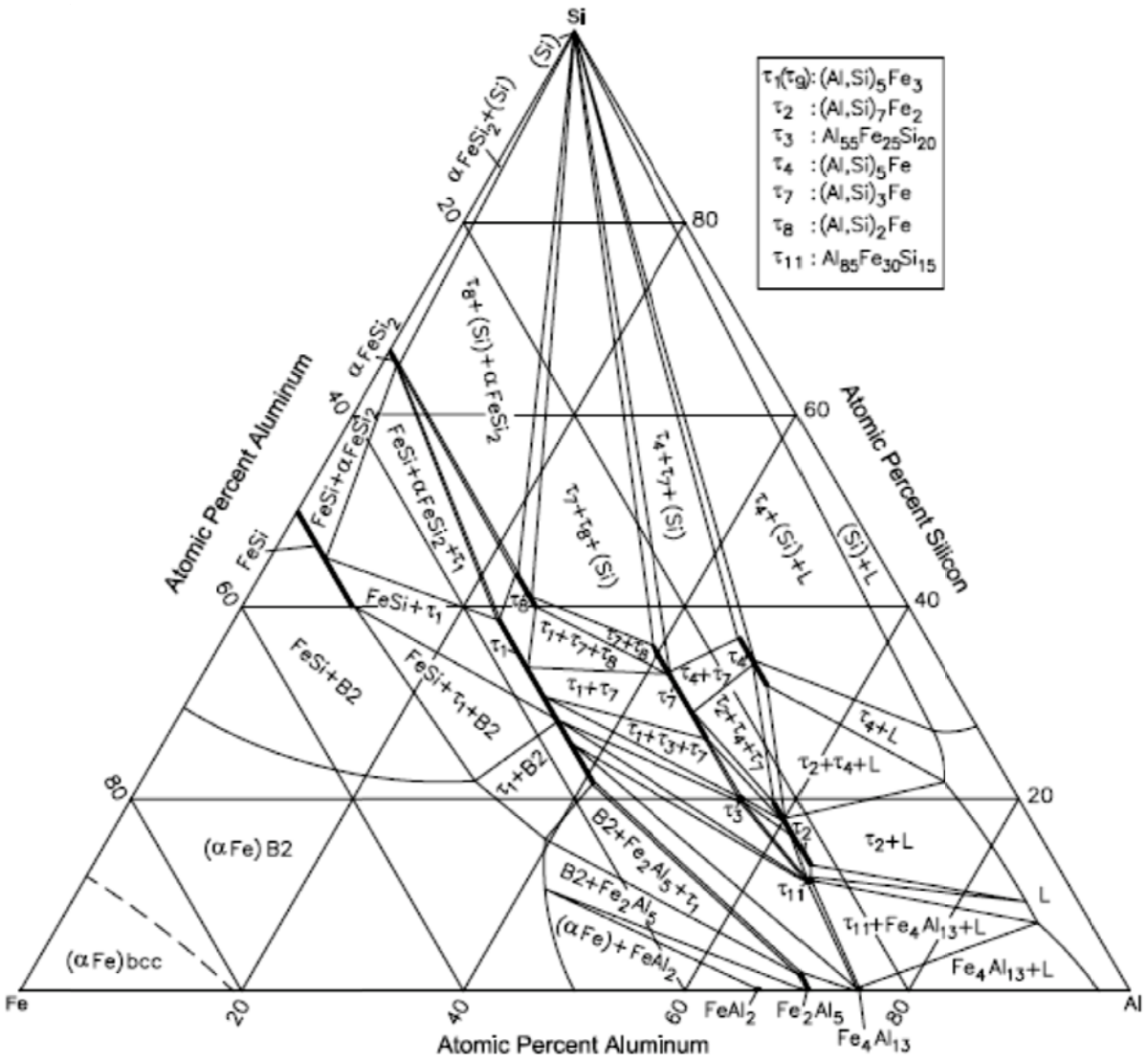

b)

Figure 39. Isothermal sections of the Al-Fe-Si system obtained (a) at 727 °C by Bosselet et al. (2004) and (b) at 800 °C and Du et al. 2008 [cited by Raghavan (2009b)].

To complicate matters, some authors changed the designations of some ternary compounds of this system. More recently Du et al. (2008) purposed three isothermal sections at 550 °C, 727 °C and 800 °C that were in good agreement with Krendelsberger et al. (2007) and Bosselet et al. (2004). They also calculated a liquidus projection. Ten stable ternary phases in the Al-Fe-Si system were determined: $Al_2Fe_3Si_3$ (τ_1 or τ_9), Al_3FeSi (τ_2 or γ), Al_2FeSi (τ_3), Al_3FeSi_2 (τ_4 or δ), $Al_{7.4}Fe_2Si$ (τ_5 or α), $Al_{4.5}FeSi$ (τ_6 or β), $Al_3Fe_2Si_3$ (τ_7), $Al_2Fe_3Si_4$ (τ_8), $Al_9Fe_4Si_3$ (τ_{10}) and Al_5Fe_2Si (τ_{11}).

At 727 °C all the ternary phases where stable except the τ_6 whereas at 800 °C only seven ternary phases appeared, as shown in figure 39. The FeSi phase dissolves up to 12 at. % Al at 727 °C but this solubility is reduced up to 10 at. % Al at 800 °C. The $FeAl_3$ phase dissolves up to 5 at. % Si.

The liquidus projection proposed by Krendelsberger et al. (2007) is shown in figure 40 and differs from the liquidus projection calculated by Liu and Chang (1999). Some ternary phases form through peritectic reactions, for example; (τ_1 or τ_9) phase (P_2 at 1052 °C), τ_2 (934 > T > 900 °C), τ_3 (P_4 at 940 °C), τ_4 (P_7 at 875 °C), τ_5 (P_8 at 766 °C), τ_6 (P_9 at 665 °C), τ_7 (P_5 at 934 °C), and τ_{11} (P_3 at 997 °C). The τ_8 ternary phase forms at (P_{max}) 1010 °C.

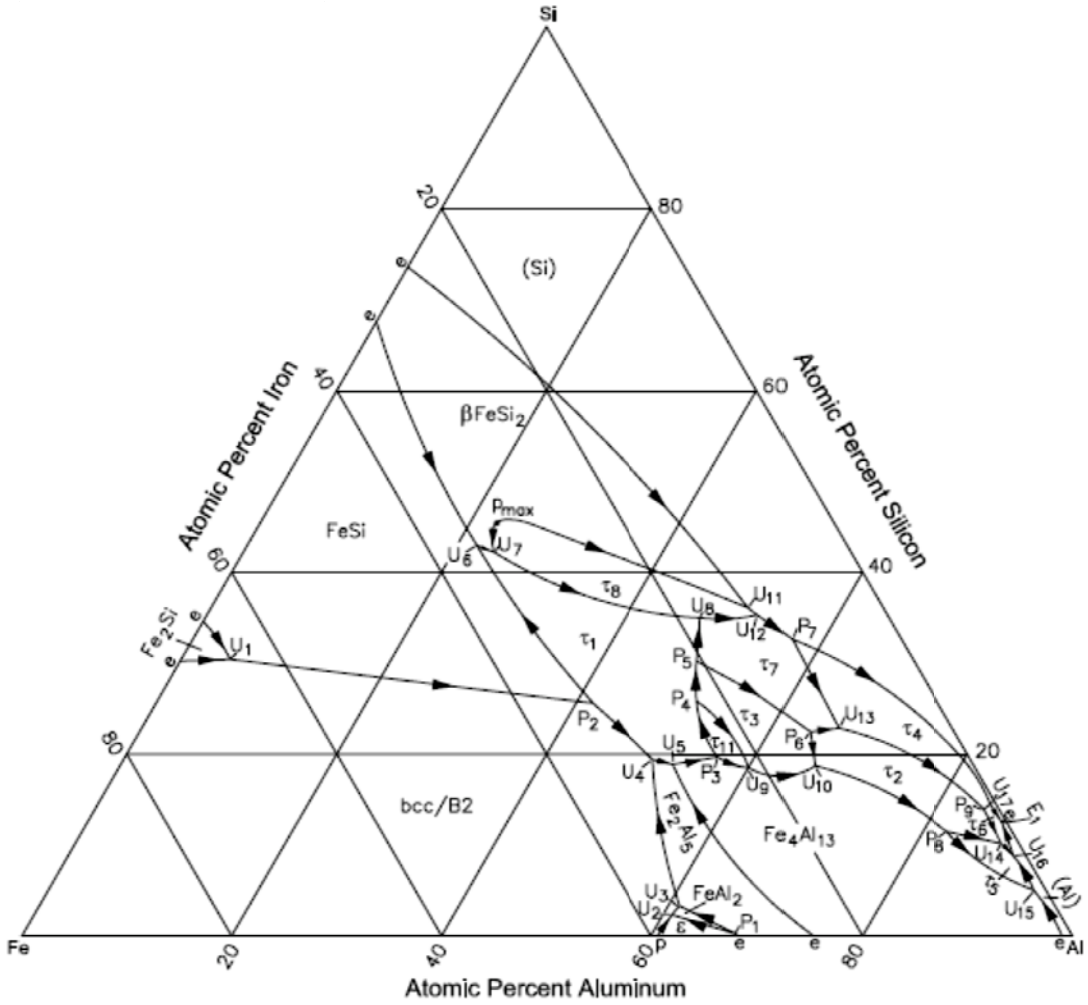

Figure 40. A liquidus projection of the Al-Fe-Si proposed by Krendelsberger et al. (2007) [cited by Raghavan (2009b)].

Marker et al. (2011) used experimental data to obtain two isothermal sections at 800 °C and 900 °C , and suggested different composition ranges of the ternary phases τ_1, τ_3, τ_7, τ_8 and τ_{11} and the new τ_{12} which was found to be stable from 720-1005 °C. Their study included an analysis of the crystal structure of τ_1 obtaining cell parameters according to composition; they also determined solid state reactions that involve both high and low temperature forms of the $FeSi_2$ that coexisted from 800 to 900 °C, while the HT-$FeSi_2$ was stabilized further down to 700 °C by Al solubility (Figure 41).

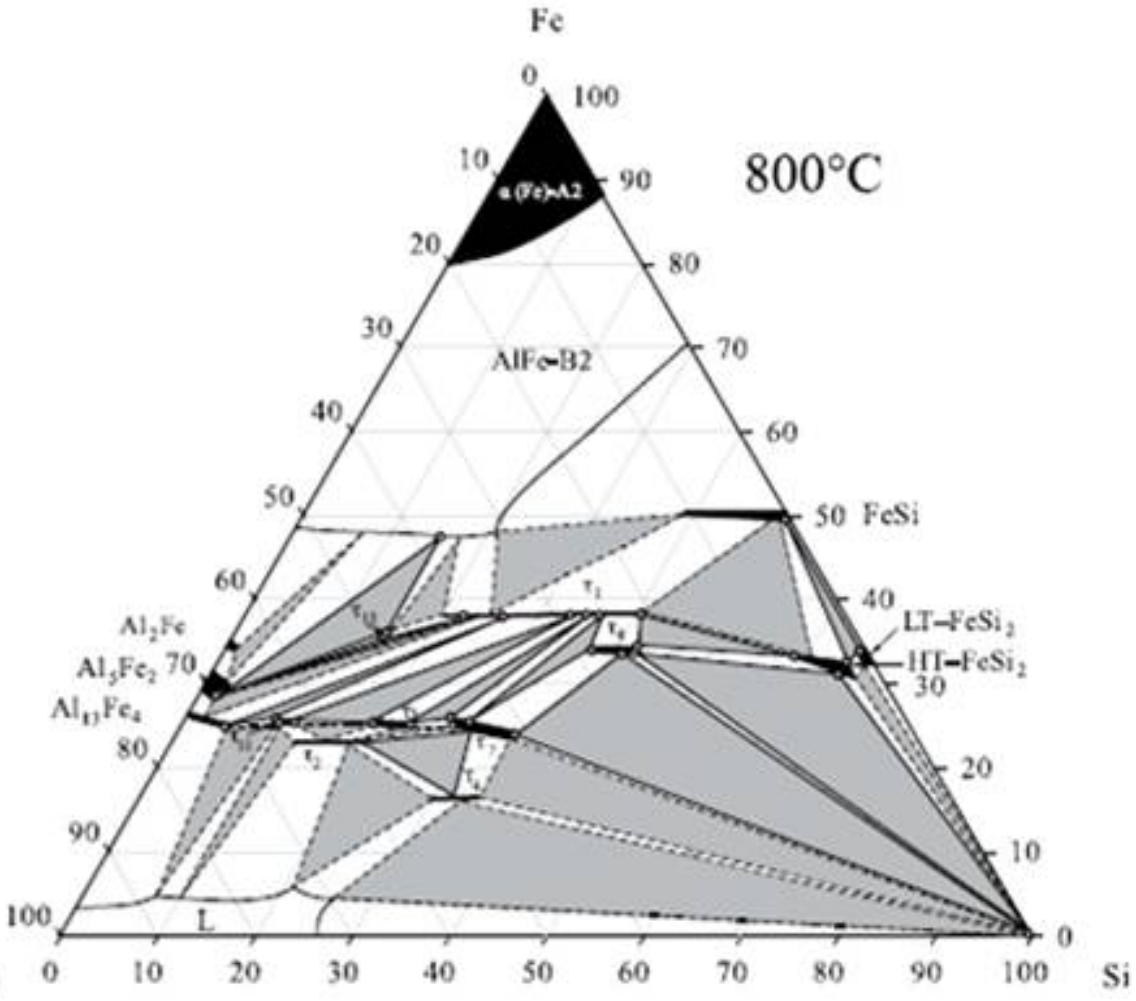

a)

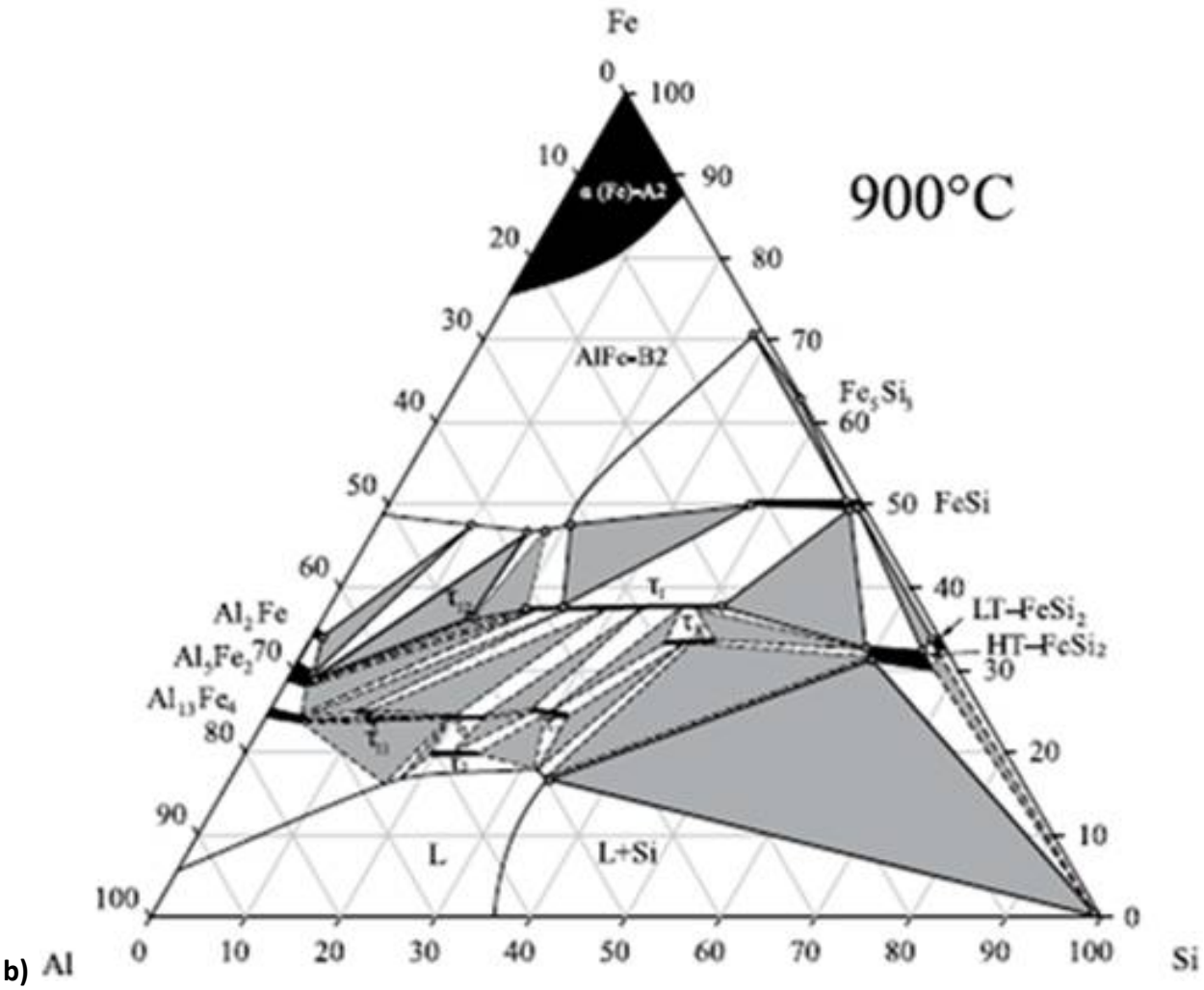

b)

Figure 41. Isothermal sections of the Al-Fe-Si system obtained (a) at 800 °C and (b) at 900 °C by Marker et al. 2011.

Chapter 2

Experimental procedures

2.1 Selection of alloys

As it was mentioned in the introduction, the ambition of this project was to develop alloys that could be considered for BC alloys for oxidation resistant coatings systems of Nb-silicide in-situ composites. The oxidation behaviour of model Nb-silicide in-situ composites have also been studied. The alloys were selected from different systems and with alloying elements that can be found in developmental Nb-silicide based alloys (Fe can substitute Cr, as both can form Laves phases that can improve oxidation). In the latter, the roles of Al, Cr, Fe, Hf and Ti have studied in our research group.

The first two alloys were Nb lean and were designated OHC1 and OCH2 with nominal compositions (all the compositions are given in at. %) Si-23Fe-15Ti-15Cr-1Nb and Si-22Fe-12Cr-12Al-10Ti-5Nb, respectively. According to the Fe-Si-Ti ternary system (see section 1.6.9) the alloy OHC1 could have in equilibrium the phases FeSi, $FeSi_2Ti$, FeSiTi and a phase named τ_4 for which the range of compositions is known, considering the Cr-Si-Ti system, phases that could also be present could be the T phase $(Cr,Ti)_6Si_5$, CrSi and Cr_5Si_3. Moreover, it was important to establish whether other alloys were able to form Al_2O_3 at high temperature and prevent the formation of Nb_2O_5 and for this reason Al was added in the alloy OHC2. In the alloy OHC2 the phases FeSi, $FeSi_2Ti$, FeSiTi, τ_4 , T $(Cr,Ti)_6Si_5$, CrSi and Cr_5Si_3 intermetallics could form as well as Ti aluminides or Al-rich Fe-silicides aluminides or Al-rich Fe-silicides, for example (Fe,Cr)(Si,Al) and $Fe(Si,Al)_2$. The alloy OHC1 was expected to form SiO_2 under oxidation conditions and the alloy OHC2 was expected to form Al_2O_3.

The Al-rich alloy OHC3 with nominal composition Al-25.5Nb-8Cr-0.5Hf was also selected. The nominal composition of this alloy is within the field of three phase equilibria Al_3Nb-Cr_2Nb-Cr_{ss} (figure 31) in the Al-Nb-Cr ternary system (see section 1.6.6). These phases can form Al_2O_3,

Cr_2O_3 under oxidation conditions at high temperature. The additions of Hf, was expected to improve the adhesion the Al_2O_3 scale.

A silicide based alloy without Fe was also included. This was designated alloy OHC5 and had nominal composition Si-25Nb-5Cr-5Ti-5Al. This alloy could also form SiO_2 and Al_2O_3 under oxidation conditions. Additions of Ti and Cr were set to 5 at. % each to study phase selection and its influence on pest oxidation of Si-rich Nb-silicide based alloys without the addition of Fe.

A substrate alloy, the Nb-silicide in situ composite designated alloy OHS1, was also selected. This had the nominal composition Nb-24Ti-18Si-5Al-5Cr-5Ge-5Sn. The selection of this composition was guided by the results of other research performed in our research group which discovered that Sn controls the pest oxidation of Nb-silicide in-situ composites and Ge enhances their oxidation resistance at high temperatures. In this particular alloy, microstructural development, phase selection and oxidation behaviour would be studied for the first time in the presence of Sn and Ge additions at 5 at. % each. The nominal alloy compositions are summarised in Table 10.

Table 10 Nominal compositions of the alloys of this study.

Alloy	Nominal Composiition (at.%)								
	Al	Cr	Fe	Ge	Hf	Nb	Si	Sn	Ti
OHC1	-	15	23	-	-	1	46	-	15
OHC2	12	12	22	-	-	5	39	-	10
OHC3	63	8	-	-	0.5	28.5	-	-	-
OHC5	5	5	-	-	-	25	60	-	5
OHS1	5	5	-	5	-	38	18	5	24

2.2 Alloy making

The alloys were prepared using pure elements (≥ 99.9 wt % purity) and clean melting with non-consumable tungsten electrode at a voltage of 50 V and a current of 650 A. The configuration of the electro-arc melter used is shown in figure 42a. Alloy buttons of 10 g weight were produced. Each was melted 5 times to homogenize its composition.

The raw materials were placed inside the water cooled crucible and on top of the crucible in a small grove pure Ti was placed (as oxygen getter). The melting process was performed under an Ar atmosphere. The arc melter chamber was first pumped down to high vaccum, then back filled wih Ar and pumped down again before it was filled again with Ar for the melting process. The pure Ti (oxygen getter) was melted first followed by the melting of the raw materials.

Figure 42. (a) Arc melter and (b) OHC1 alloy showing the typical shape of the alloys buttons prepared for this work.

2.3 Specimen preparation

Control of solidification in arc melting is very poor and macrosegregatiopn is highly likely to develop. The center of the ingot is expected to be the last area to solidify after melting. The specimens for the microstructural studies, and thermal analyses of the cast alloys were selected from the central area (bulk) of the alloy buttons (Figure 43). The bulk of the button had experienced the lowest cooling rates, the top area near the surface of the button higher cooling rates and the bottom of the alloy button the highest cooling rates since the latter area was in contact with the water cooled crucible.

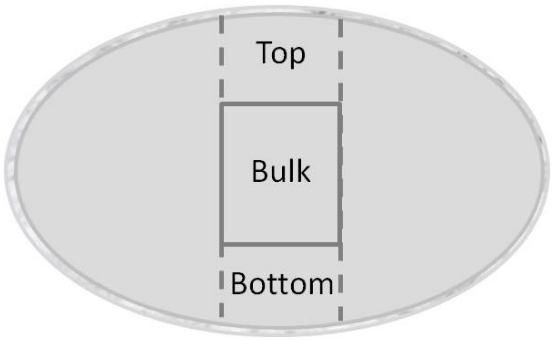

Figure 43. Schematic diagram of the cross section of arc melted buttons showing areas of study.

The button was cut and the selected area to be studied was sectioned in the ISOMET using diamond wheel at 2000 rpm. The brittleness of some of the alloys sometimes complicated this step. Conventional metallographic preparation of the specimens was performed. This involved mounting in conductive bakelite, grinding with graded SIC paper (from 120-1200 grit) and then to grade 4000 and cashmere cloth polishing with 1µm diamond suspension to obtain suitable surface for optical and electron microscopy studies.

From the oxidised specimens samples were prepared for the study of the oxide scale surface and of the cross section of the oxide scale. For the former study, the oxidised specimens were fixed with silver dag in an aluminium stub followed by the sputter deposition of a carbon film on top. The latter study was performed after the study of the oxide scale surface. This involved taking the specimen out of the aluminium stub, then the specimen was embedded in resin followed by the conventional grinding (from 800-4000) and cloth polishing to mirror finish. Then the specimen was carbon coated to prevent the accumulation of electron charge and improve image acquisition.

2.4 Heat treatment

During solidification macro and microsegregation can develop, and metastable phase can form. Heat treatments were carried out to produce an equilibrium microstructure and observe any change from the cast alloy. The heat treatment temperatures depended on the composition of the alloy, and where appropriate their selection was guided by DSC results.

The heat treatments were carried out in a tube furnace under inert atmosphere (argon) to avoid oxidation during the experiment. An alumina boat containing the specimens was placed inside the tube furnace between other two boats containing pure Ti sponge used as an oxygen getter. The alloy OHS1 was wrapped in Ta foil to minimize contamination by oxygen.

The alloys OHC1, OHC2 and OHC3 were air cooled by taking their specimens out of the furnace immediately after the heat treatment. The alloys OHC5 and OHS1 alloys were furnace cooled.

2.5 Scanning Electron Microscopy (SEM) and Energy Dispersive X-ray Spectroscopy (EDS) analysis

The microstructural study and analysis of the alloys was performed with the use of Scanning Electron Microscopes (SEM). These were the Phillips PSEM 500 SEM with 10 nm resolution, Jeol JSM 6400 with 3.5 nm resolution and Inspect F FEG SEM high resolution adjusted according to accelerating voltage and operating mode. The BSE mode was the main mode used for all the alloys to generate contrast among the phases for a particular alloy. EDS was used for qualitative and quantitative microanalysis of the phases. EDS standardization was performed using specimens of high purity Nb, Ti, Cr, Fe, Si, Ge, Al, Sn, Hf and Co elements that were polished to 1 μm finish. The EDS system in the PSEM 500 SEM and Jeol JSM 6400 was calibrated prior to EDS analysis with pure Co standard.

At least five large area analyses (area scans) were performed in the top, bulk and bottom of the ingot and at least ten measurements (spot analyses) were obtained from each phase with size ≥5 μm to determine actual composition. At least five EDS analyses were performed in oxidised specimens.

2.6 X-ray diffraction

2.6.1 Conventional X-ray diffraction

Phase identification was performed by the analysis of recorded XRD data. For some alloys the XRD experiments were performed on powders and for others bulk specimens were used. The

XRD experiments were carried out using a Siemens Bruker D500 XRD diffractometer with CuKα radiation source (λ = 1.540562 Å) 2θ from 20-120 and a step size of 0.02 deg. The alloys OHC1, OHC2 and OHC3 were studied in powder form, and the OHC5 and OHS1 in bulk form. The powders of brittle alloys were prepared by manually crushing the button with a hammer in a steel container followed by grinding using a pestle in an agate mortar to get fine particles.

2.6.2 Glancing angle X-ray diffraction

For GA-XRD experiments a Siemens D5000 (Cu, GA-XRD) diffractometer with Cu Kα1 and Kα2 radiation source (λ = 1.54178 Å), 2θ from 10-100 and a step size of 0.02 was used. The diffractometer was also used for bulk specimens. The scan type used for glancing angle was detector scan while for regular bulk specimens it was locked coupled. Prior to GA-XRD experiments glancing angle was selected with the aid of the AbsorbDX software which evaluates the X-ray penetration depth for particular glancing angle conditions.

2.7 Thermal analysis

2.7.1 Thermo-gravimetric analysis (TGA)

The isothermal oxidation tests were carried out in the thermogravimetric analyzer Netzsch STA F3 TG/DSC using a SiC furnace with air flow rate of 20 ml/min at 800, 1200 °C and for the alloy OHC3 up to 1300 °C for 100 h with heating and cooling rates of 3 °C/ min. Cubic specimens of size 3 mm x 3 mm x 3 mm and with 800 grit SIC finish were used for TGA.

2.7.2 Differential Scanning Calorimetry (DSC)

DSC analyses were performed on the Netzsch STA F3 TG/DSC using the Rh/Pt furnace with an Ar flow rate of 20 ml/min. Different heating and cooling rates were used to study phase stability in the alloys OHC1, OHC2, OHC3 and OHC5 up to 1600 °C. Heat treatment temperatures were chosen by finding the first melting temperature that corresponds to the onset of endothermic peak during heating in the plot of heat flow vs. sample temperature.

Chapter 3

The microstructure and oxidation of Fe-silicide based alloys

3.1 Introduction

Although Nb-silicide base alloys are Si rich, their oxidation behaviour is dominated by the selective oxidation of Nb. The Nb oxides are not protective at high temperatures and cannot protect these alloys from environmental attack at high temperatures. Alloying additions of Ti, Al, Cr, Hf, Ge, and Sn are among the most effective at improving their oxidation resistance. However, these alloys will require the use of oxidation resistant coatings (Jackson et al, (1995), Subramanian et al. (1997) and Bewlay et al. (2003)), to protect these alloys from oxidation and other environmental contaminants during service.

Oxidation resistant coatings must be capable of forming protective oxides at high temperatures but be thermally stable and have balance of mechanical properties and suitable CTE. Some of these requirements have been considered in the design of coatings for Nb-rich alloys. Some of the latter have been considered as suitable systems for Nb-Si based alloys.

Successful oxidation protection of Nb-rich alloys has been claimed by the deposition of iron-modified silicide coatings. This was attributed to the selective oxidation of silicon in phases such as FeSi, $FeSi_2$, $FeSi_2Ti$, and $(TM)_7Si_6$ where TM= Fe, Ti, Cr, Nb (M.S. Tsirlin et al. (1981), Jackson et al. (1998) and Portebois et al. (2013)).

3.2 Results

3.2.1 Microstructure characterization

3.2.1.1 Si-23Fe-15Cr-15Ti-1Nb (alloy OHC1)

As cast microstructure

The actual composition (at.%) of the cast alloy (OHC1-AC) was Si-23Fe-14.5Cr-15Ti-1Nb. This composition was obtained from the average of the analyses taken from the top, centre and near the bottom of the button (Table 11). The data revealed that there was chemical inhomogeneity of Ti, Cr and Fe in the cast alloy (macro-segregation) using the criterion $C_{max}^{i} - C_{min}^{i} \geq 2$ at. %, where C_{max}^{i} is the maximum concentration of element i and C_{min}^{i} is the minimum concentration of element i. The data in Table 11 show that the concentrations of Ti, Cr and Fe were respectively in the range 8.7-15.7, 8.1-15.6 and 22-35.5 at. % with the bottom of the ingot being rich in Fe and lean in Ti and Cr.

The compositions in the top and bulk of the alloy were practically the same as the nominal composition, however, near the bottom, where a chill zone was also observed, there was severe macrosegregation and the microstructure was leaner in Cr and Ti and richer in Fe. The actual chill zone was even richer in Fe and probably Si with average values of 34.0 at. % Fe and 47.2 at.%Si, and leaner in Cr, Ti and Nb with average values of 8.9, 9.6 and 0.4 at.%, respectively.

According to the SEM studies, and the EDS analysis data and the XRD data (figures 44, 46, 47 and 48 and Table 11), the alloy consisted of three phases, namely the $(TM)_6Si_5$, (Fe,Cr,Ti)Si and $FeSi_2Ti$ where TM = Nb, Ti, Fe, Cr. The figure 44 shows the typical microstructure found in the centre of this alloy. The primary $(TM)_6Si_5$ dendrites were severely cracked. In these faceted hexagonal dendrites of the $(TM)_6Si_5$ phase there was consistent increase of the Si concentration (see figures 67 and 68) from the centre to the grain boundaries from 45.4 to 46.4 at. % Si. Further, the (TM) content of this phase varied with location, in the centre the Nb, Ti and Cr contents were higher and the Fe content lower, but towards the edges the Fe content was higher and the Nb, Ti and Cr had lower values. All the analysis data for the (TM) elements was

considered in the chemical analysis data given in table 11 which explains the large standard deviations for Fe, Cr and Ti in the $(TM)_6Si_5$ silicide. This microsegregation confirmed that Fe was partitioning to the liquid during cooling. A chemical analysis performed over an hexagonal cross-section of a $(TM)_6Si_5$ grain showed the Fe partition from the centre towards the edge of the dendrite (Figure 45). Along the columnar dendrites of the $(TM)_6Si_5$ phase, the (Fe,Cr,Ti)Si phase exhibited an elongated faceted morphology and surrounded a thin dark grey layer of the $FeSi_2Ti$ phase.

The microstructure in the top of the button displayed the same characteristics as those described above for the centre.

Table 11 EDS data (at. %) of the as cast alloy OHC1.

Area/Phase	Nb (at%)	Ti (at%)	Cr (at%)	Fe (at%)	Si(at%)
Top	1. 1 ± 0.1 1.2 – 1.1	15.5 ± 0.1 15.6 – 15.4	15.0 ± 0.3 15.4 – 14.6	22.5 ± 0.5 23.1 – 22.0	45.9 ± 0.2 46.1 – 45.7
Centre	1. 2 ± 0.1 1.3 – 1.0	15.4 ± 0.3 15.7 – 15.0	14.8 ± 0.3 15.2 – 14.5	23.0 ± 0.6 23.7 – 22.2	45.7 ± 0.3 45.9 – 45.2
Near bottom	1. 0 ± 0.2 1.2 – 0.8	13.8 ± 0.2 13.9 – 13.6	12.8 ± 0.4 13.2 – 12.5	26.0 ± 0.5 26.3 – 25.5	46.4 ± 0.3 46.8 – 46.2
Bottom chill zone	0.4	9.6 ± 0.8 10.8 – 8.7	8.9 ± 0.7 10.1 – 8.1	34.0 ± 1.4 35.5 – 31.7	47.2 ± 0.3 47.6 – 46.9
(Fe,Cr,Ti)Si ^	0. 1	0.9 ± 0.4 2.0 – 0.5	5.9 ± 0.6 6.5 – 4.8	41.7 ± 0.6 42.8 – 40.8	51.4 ± 0.2 51.9 – 51.1
$FeSi_2Ti$ *	0.2	14.1 ± 1.1 15.6 – 12.1	7.0 ± 1.3 9.1 – 4.6	31.2 ± 1.0 32.3 – 29.5	47.0 ± 0.5 48.0 – 46.3
$(TM)_6Si_5$ +	0.8 ± 0.3 1.7 – 0.4	15.9 ± 1.4 19.1 – 14.5	13.8 ± 2.7 20.0 – 10.9	23.5 ± 4.3 28.7 – 13.7	45.9 ± 0.3 46.4 – 45.4
Eutectic (large area analysis)	0. 1	10.4 ± 0.4 11.2 – 9.9	3. 7 ± 0.2 4.0 – 3.4	35.6 ± 0.4 36.1 – 35.0	50.2 ± 0.2 50.5 – 50.0
(Fe,Cr,Ti)Si in eutectic	0. 1	8.2 ± 2.0 10.3 – 5.1	4.0 ± 0.5 4.7 – 3.4	36.9 ± 1.5 39.0 – 35.1	50.8 ± 0.4 51.2 – 50.2
$FeSi_2Ti$ in eutectic	0. 2	15.3 ± 1.3 17.0– 13.4	3.4 ± 0.3 3.9 – 3.1	31.0 ± 1.1 32.3 – 29.6	50.0 ± 0.2 50.3 – 49.8

+ From the Nb-Fe-Cr-Si and Cr-Si-Ti systems

* τ_1, from the Fe-Ti-Si system

^ Based on FeSi

In the lower part of the bulk (centre) towards the bottom of the button of the cast alloy a very fine (~ 1 µm) “lamellar” eutectic was found in the boundaries of the (Fe,Cr,Ti)Si phase (Figures

46 and 47). This eutectic consisted of the (Fe,Cr,Ti)Si (bright contrast) and $FeSi_2Ti$ (dark contrast). The chemical composition of the eutectic and the eutectic phases are given in Table 11.

In the chill zone in the bottom of the button a higher volume fraction of the (Fe,Cr,Ti)Si and $FeSi_2Ti$ phases with a coarser microstructure was observed (Figures 46 and 47). The aforementioned eutectic was also present. In contrast to the results obtained for the $(TM)_6Si_5$ silicide that was observed in the bulk of the alloy, the Fe microsegregation in the $(TM)_6Si_5$ phase was not detected and instead only Fe-rich $(TM)_6Si_5$ phase was observed which would suggest that under the high cooling rate in the area there was "no time" for the Fe to partition to the liquid.

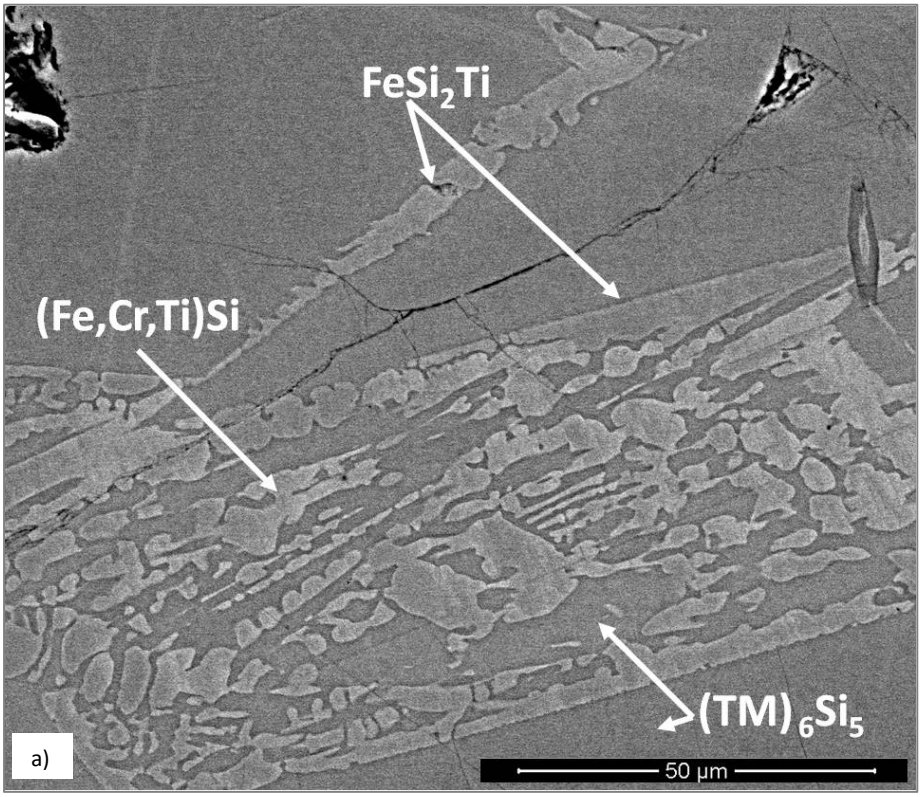

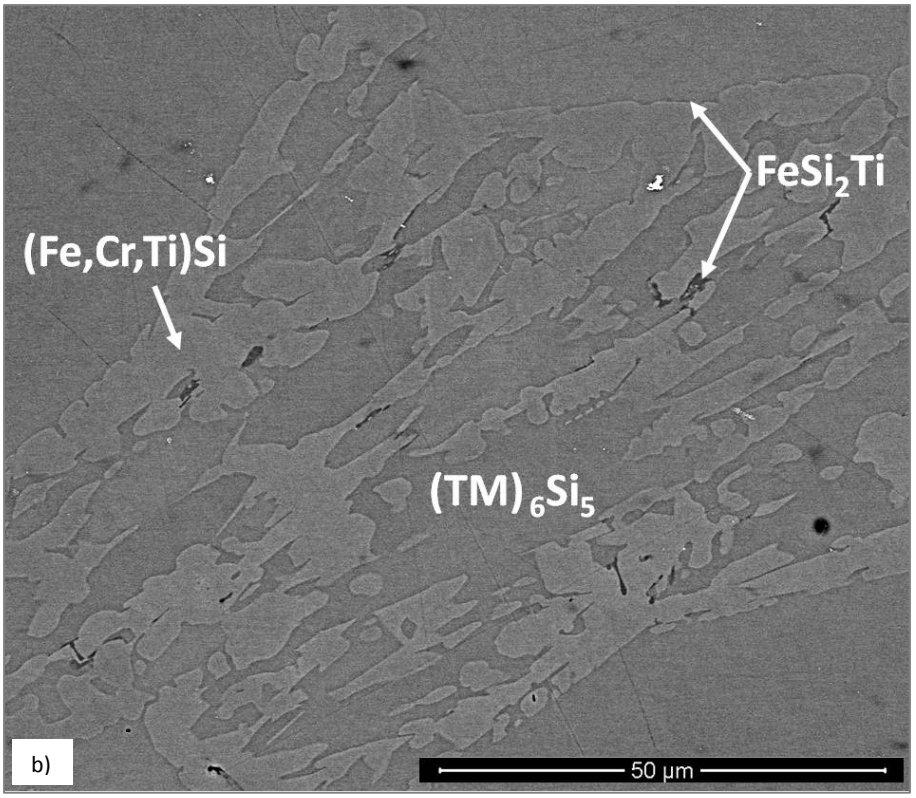

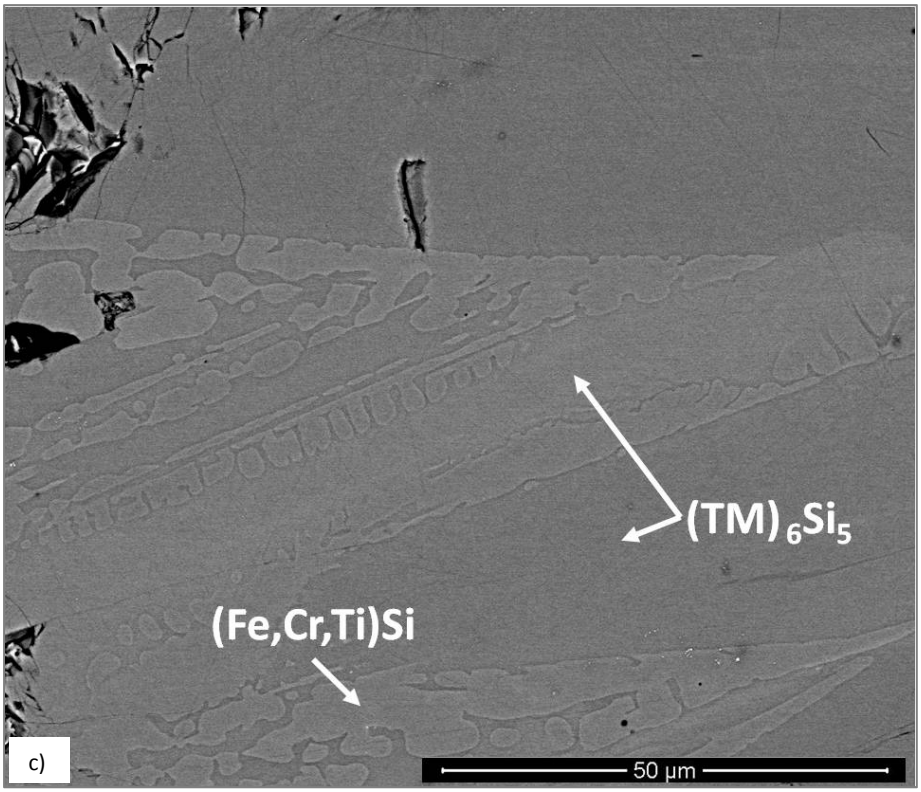

Figure 44. Typical microstructure of alloy OHC1, BSE images from a) the centre, at X2000, b) centre at X2500 and c) centre near top, at X2500.

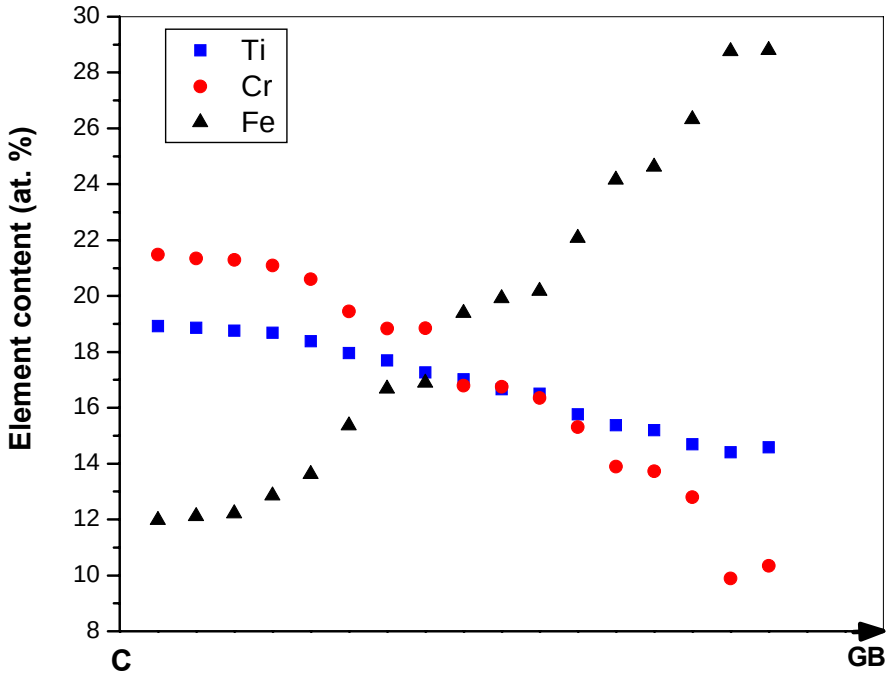

Figure 45. Average Fe, Cr and Ti concentrations from the centre (C) of a hexagonal $(TM)_6Si_5$ dendrite towards its grain boundaries (GB).

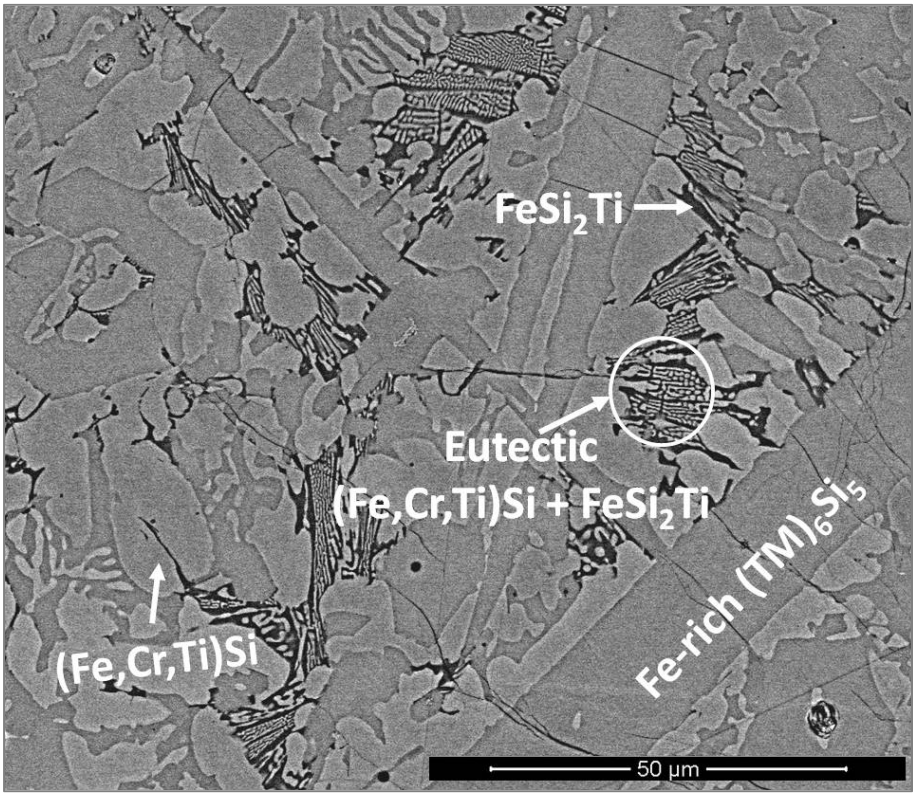

Figure 46. BSE image of the chill zone in the bottom of cast alloy OHC1, X2000.

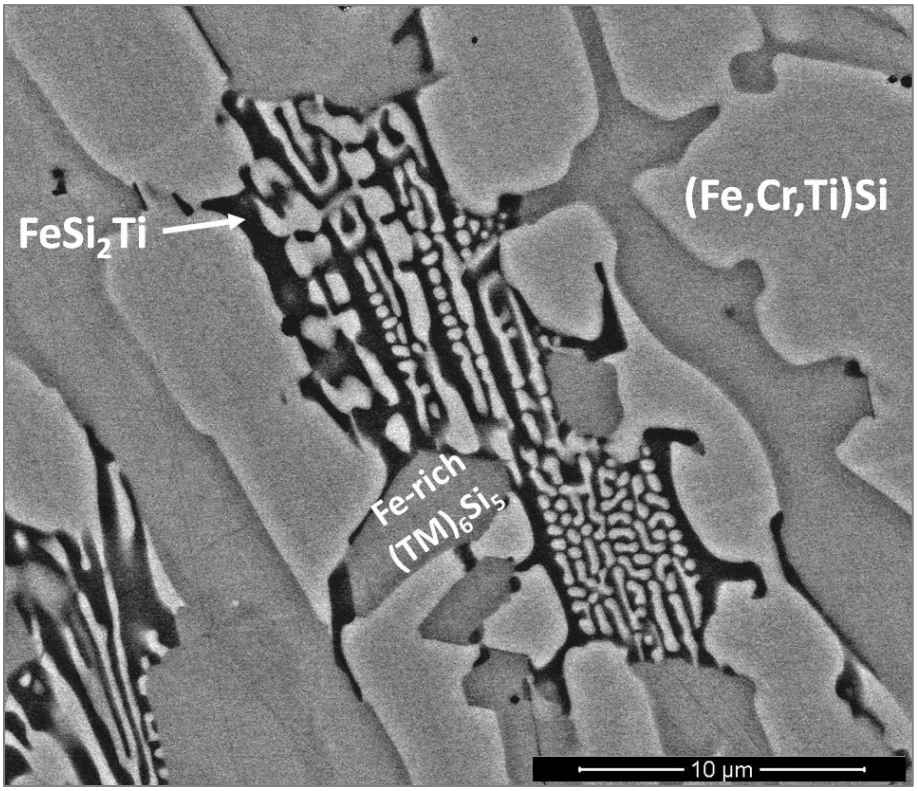

Figure 47. BSE image from the bottom of as cast alloy OHC1, X8000.

The analysis of the XRD data (Figure 48) and the phase compositions obtained by EDS allowed the identification of the phases in the alloy OHC1-AC. The results of these two complementary techniques confirmed the presence of the $(TM)_6Si_5$ phase, which is the T phase in the Ti-Cr-Si system [Lysenko et al. (1971) from ASM data base]. Indeed, the measured compositions were within the range of the T phase. The $(TM)_6Si_5$ phase crystallizes in the orthorhombic system with the V_6Si_5 as the proto-type and its space group is the Ibam according to the crystallographic information in the XRD PDF file 04-007-8927. The presence of the τ_1=$FeSi_2Ti$ phase from the Fe-Si-Ti system was also confirmed. This phase has the $MnSi_2Ti$ proto-type, and its crystalline system is orthorhombic with the Pbam space group according to the crystallographic information in the XRD PDF file 01-075-2180. Its composition (Table 11) matched with the composition of the τ_1 phase reported by Weitzer et al. (2008), particularly when the data for the alloy OHC1-HT was taken into account (see below). Finally, the FeSi phase with the B20 structure was identified. This phase crystallizes in the cubic system with the $P2_13$ space group according to the crystallographic information in the XRD PDF file 04-007-

1414. The composition of the (Fe,Cr,Ti)Si phase was in agreement with the composition and solubility range of the FeSi phase.

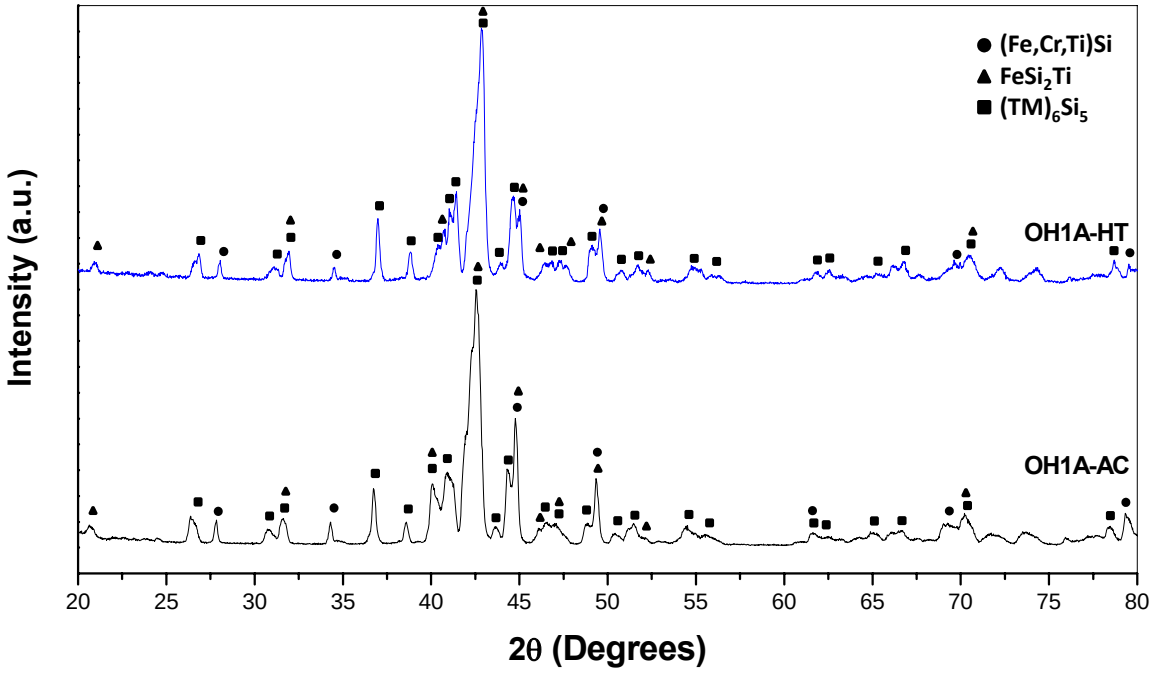

Figure 48. XRD diffractograms of the alloy OHC1 powder showing the phases present in the cast and heat treated conditions.

It is desirable for practical applications that alloys in the bond coat for refractory metal alloys have phases with high melting points. According to the Fe-Si binary system, the melting point of the FeSi phase is 1410 °C and in the case of alloy OHC1 it is expected that the Cr and Ti additions will increase the melting temperature of the (Fe,Cr,Ti)Si phase. Moreover, according to Du and Shuster (2002) and Weitzer et al. (2008), the melting points of the $(TM)_6Si_5$ and $FeSi_2Ti$ phases should be above 1500 °C.

The DSC trace of the alloy OHC1 (Figure 49) showed a thermal event on heating at ~ 1300 °C. This thermal event consisted of a double peak signal and on cooling there was a single signal at ~ 1298 °C that could correspond to the crystallization of the previous. The fact that the endotermic signal showed a double peak could be due to heterogeneities in the participating phases. These signals could correspond to the eutectic FeSi + $FeSi_2Ti$ clearly observed in the bottom of the alloy and the observed eutectic reaction by Weitzer et al. (2008) at 1328 °C (L →

FeSi + $FeSi_2Ti$). However, Weitzer et al. (2008) also assigned a signal at 1298 °C to the invariant reaction L + $FeSi_2Ti$ → FeSi + τ_4 where of τ_4= $Fe_{28.1}Ti_{26.3}Si_{45.6}$. The τ_4 was not observed in the microstructure of this alloy.

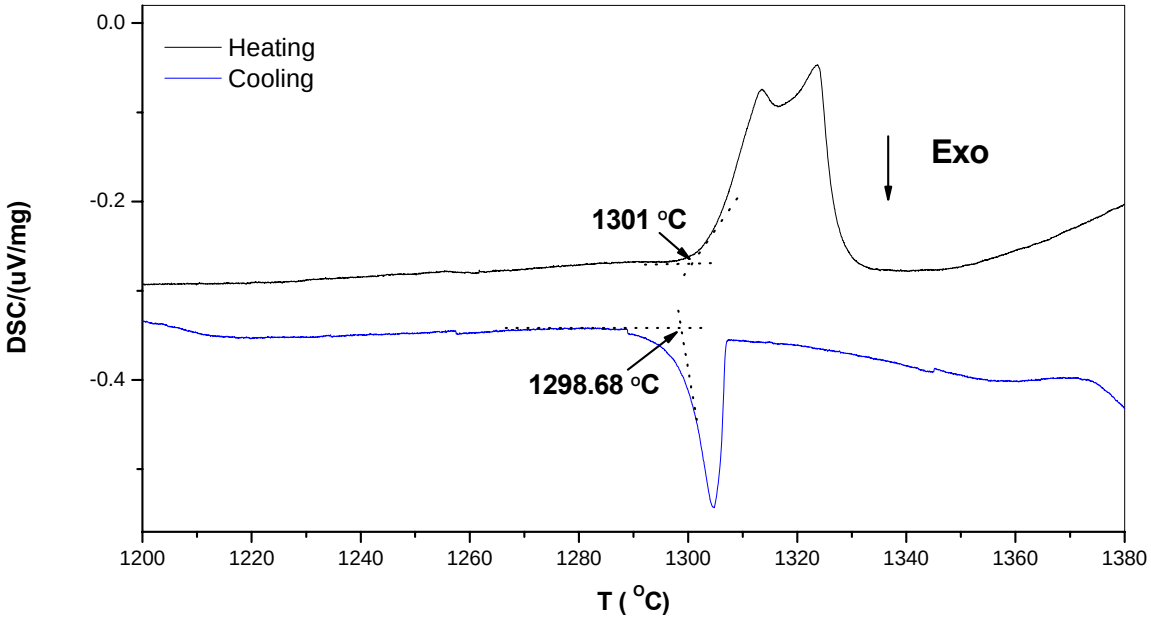

Figure 49. DSC trace of the alloy OHC1.

Heat treated microstructure

The heat treatment temperature was selected based on the DSC data. The actual composition of the heat treated alloy (OHC1-HT) (1200 °C / 48h) was Si-22.1Fe-15.1Cr-15.8Ti-1.1Nb. The EDS analysis data is given in Table 12. The data in table 12 is the average values of the large area and phases analyses taken from the top, centre and the bottom of the button after the heat treatment. The typical microstructure in the centre of the heat treated alloy is shown in figure 50a. As it was the case in the as cast alloy the microstructure of OHC1-HT consisted of the phases (Fe,Cr,Ti)Si, $(TM)_6Si_5$ and $FeSi_2Ti$, see also figure 48.

The microstructure of this alloy was very similar in the top and bulk (Figures 50a and 50c). The volume fraction of the (Fe,Cr,Ti)Si phase decreased while the volume fractions of the $FeSi_2Ti$ and $(TM)_6Si_5$ increased after the heat treatment. In the alloy OHC1-HT, it was more noticeable that the (Fe,Cr,Ti)Si phase enveloped a thin layer of the $FeSi_2Ti$. Two phase regions consisting of

the (Fe,Cr,Ti)Si + $FeSi_2Ti$ phases were found dispersed in the $(TM)_6Si_5$ matrix and in general the $FeSi_2Ti$ was coarser. The Si and Ti contents of the $FeSi_2Ti$ increased by 9% and 49 % respectively bringing its composition very close to that reported by Weitzer et al. (2008) and its volume fraction increased in the top and bulk compared with those observed in figures 44 from the as cast alloy. The $(TM)_6Si_5$ phase exhibited the same characteristics to those found in the as cast alloy. It had cracks and pores, and its Fe composition did not significantly change after the heat treatment having only a slight reduction in the values. Thus, chemical inhomogenity was still present in the $(TM)_6Si_5$ phase, probably because of its high melting point (Du and Shuster (2002)) and the heat treatment homologous temperature not being high enough to reach equilibrium.

Table 12 EDS data (at. %) for heat treated alloy OHC1 at 1200 °C for 48h.

Area/Phase	Nb (at%)	Ti (at%)	Cr (at%)	Fe (at%)	Si(at%)
Large area analysis	1. 1 ± 0.1 1.2 – 1.0	15.8 ± 0.6 16.8 – 15.1	15.1 ± 0.4 15.8 – 14.6	22.1 ± 0.8 22.8 – 20.4	45.9 ± 0.4 46.3 – 45.2
(Fe,Cr,Ti)Si ^	0. 1	1.0 ± 0.4 1.5 – 0.6	5.9 ± 0.5 7.0 – 5.4	41.7 ± 0.8 42.6 – 40.4	51.3 ± 0.2 51.6 – 51.0
$FeSi_2Ti$ *	0.6 ± 0.1 0.9 – 0.5	20.9 ± 1.1 22.9 – 19.6	3.3 ± 0.6 4.6 – 2.7	25.0 ± 0.6 25.7 – 24.1	50.2 ± 0.6 50.8 – 49.0
$(TM)_6Si_5$ +	0.9 ± 0.5 1.8 – 0.2	16.3 ± 1.1 18.6 – 14.6	14.4 ± 2.8 20.0 – 10.9	22.4 ± 4.1 27.4 – 14.3	46.0 ± 0.3 46.6 – 45.5

+ From the Nb-Fe-Cr-Si and Cr-Si-Ti systems

* τ_1, from the Fe-Ti-Si system

^ Based on FeSi

In the bottom of the alloy OHC1-HT, a higher volume fraction of coarsened (Fe,Cr,Ti)Si phase was found (Figure 51). The prior eutectic had coarsened too (Figure 52). The $FeSi_2Ti$ phase was found in the prior eutectic and was enveloping the (Fe,Cr,Ti)Si phase.

After the heat treatment, the XRD data did not show any significant changes (see figure 48). In other words, the XRD data confirmed that all the three phases that were observed in the as cast alloy were still present after the heat treatment.

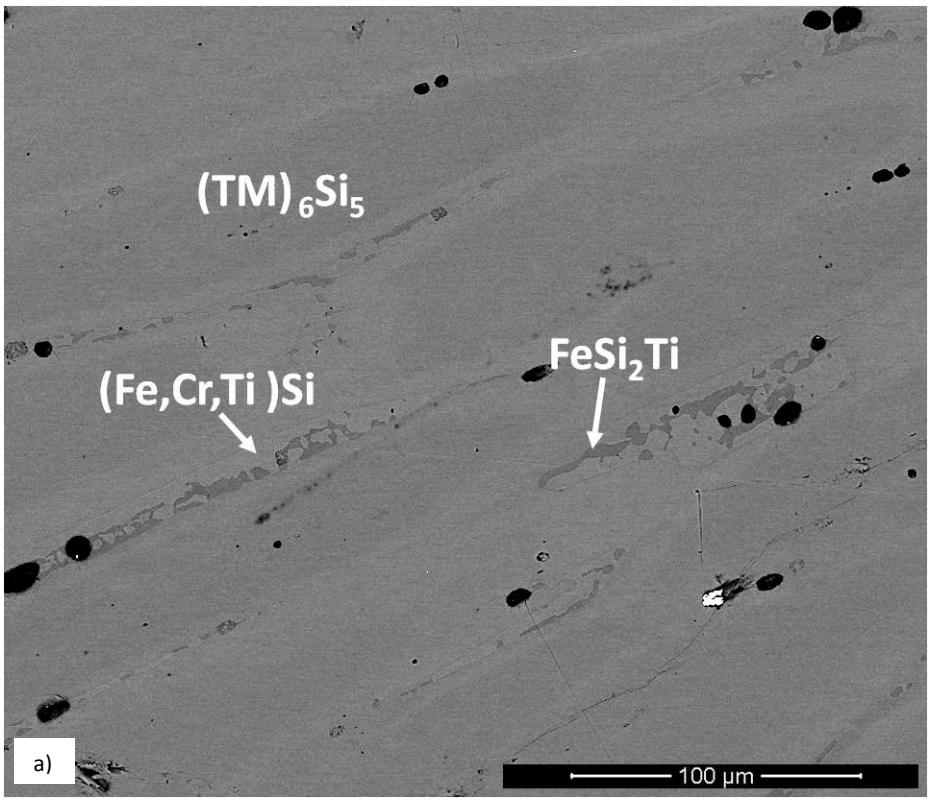
(TM)6Si5
(Fe,Cr,Ti)Si
FeSi2Ti
a)
100 µm

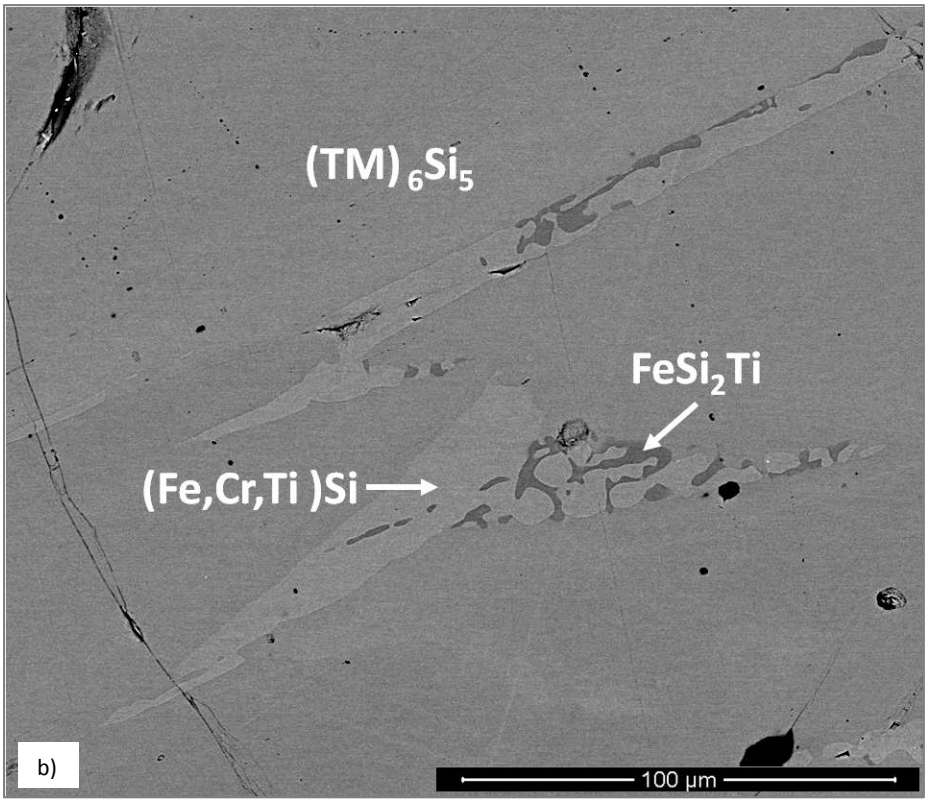
(TM)6Si5
FeSi2Ti
(Fe,Cr,Ti)Si
b)
100 µm

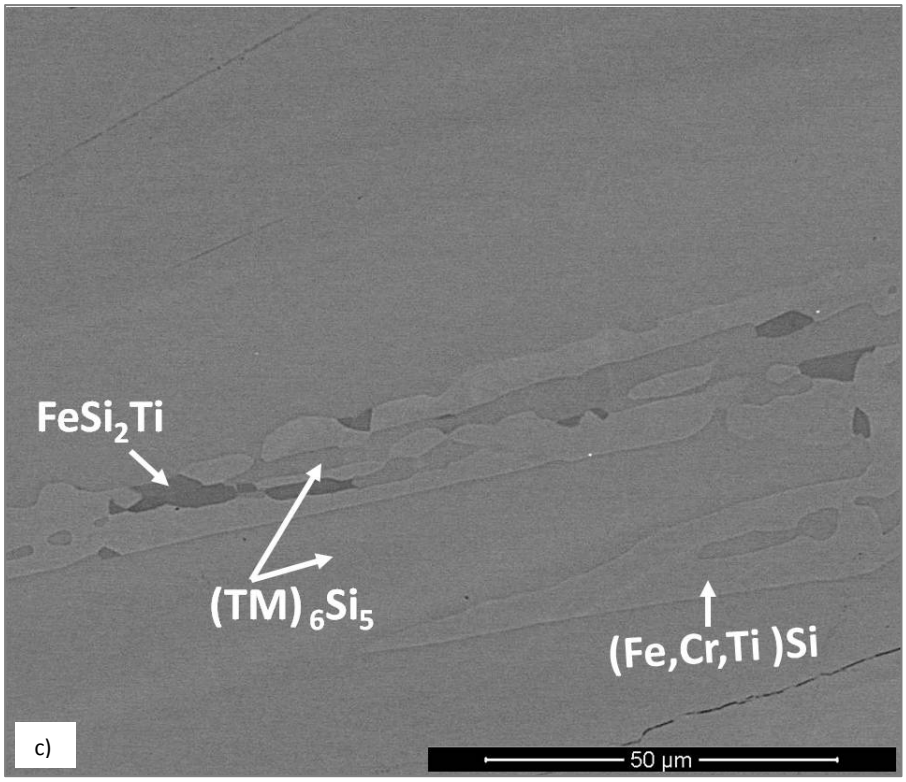

Figure 50. Typical microstructure of the alloy OHC1-HT, BSE image a) from the centre, X800, b) from the bottom, X1200 and c) from the top, X2000.

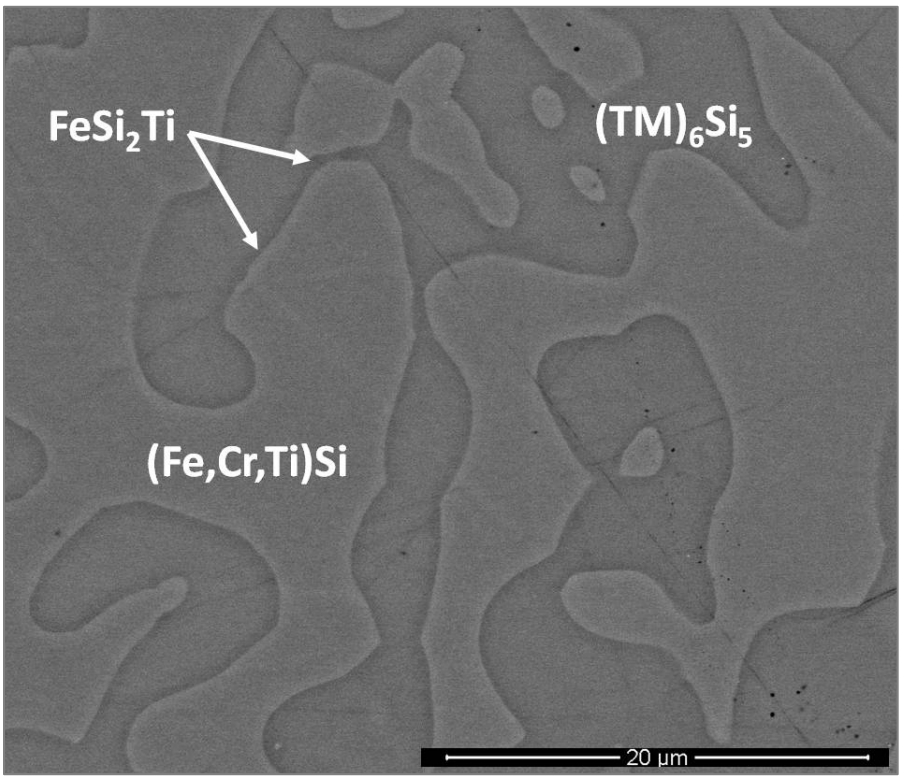

Figure 51. Typical microstructure of the alloy OHC1-HT, BSE image from the bottom, X6000.

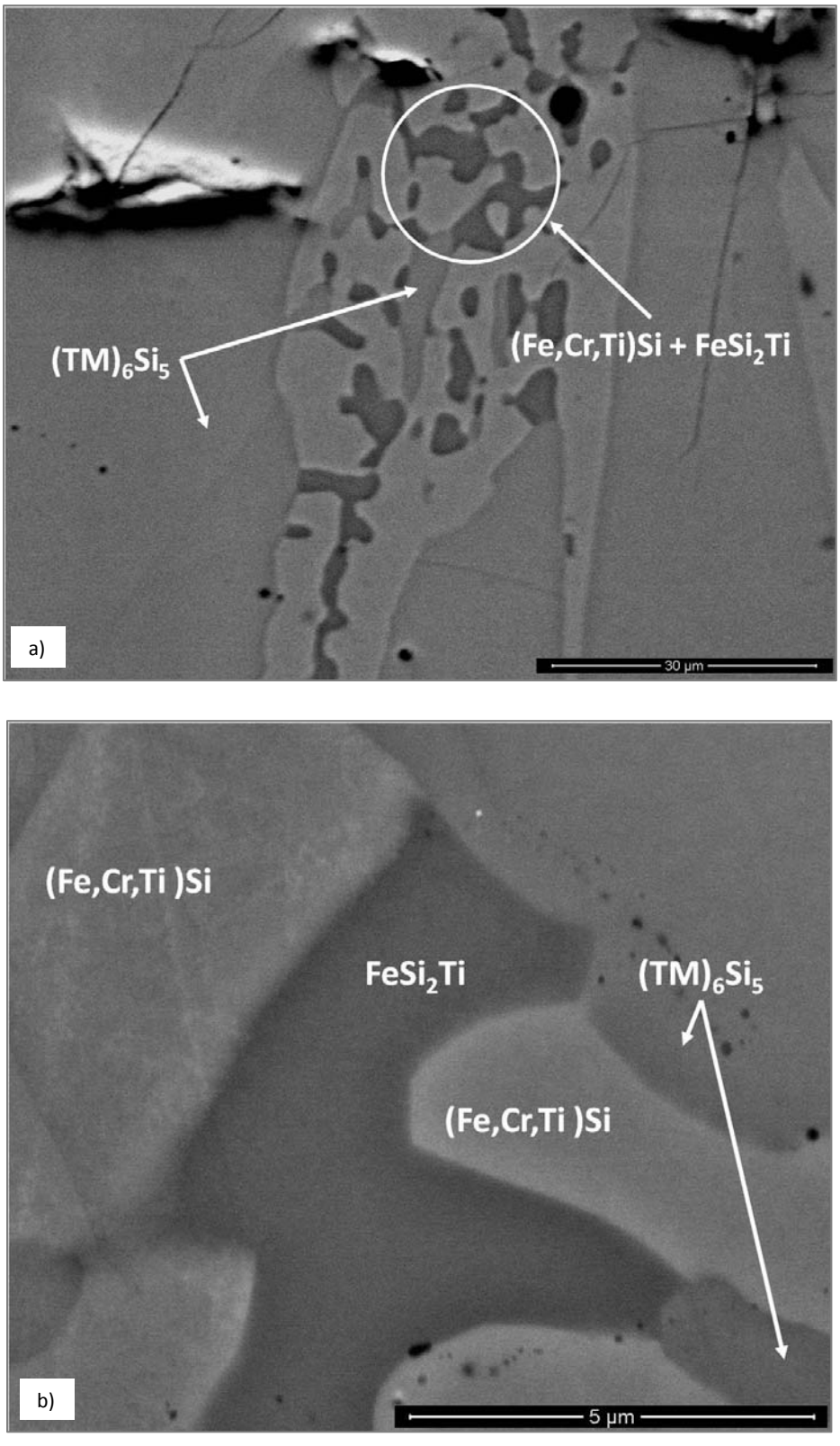

Figure 52. BSE images of the alloy OHC1-HT: (a) section near the bottom, X1250, and (b) section of the prior eutectic, X25000.

3.2.1.2 Si-22Fe-12Cr-12Al-10Ti-5Nb (alloy OHC2)

As cast microstructure

The actual composition (at.%) of the as cast alloy OHC2 (OHC2-AC) was Si-21.5Fe-13.7Al-11.2Cr-8.5Ti-4.9Nb. This was the average composition from the top, centre and bottom of the button. The analysis data is given in Table 13 and would suggest that there was macrosegregation of all the elements in the as cast alloy with the bottom of the button being leaner in Nb, Ti,Cr and Si and richer in Fe and Al compared with other parts of the ingot. The typical microstructure of the alloy OHC2-AC is shown in figures 53 and 56.

Table 13 EDS data (at. %) of the as cast alloy OHC2.

Area/Phase	Nb (at%)	Ti (at%)	Cr (at%)	Fe (at%)	Al(at%)	Si(at%)
Large area analysis	4.9 ± 0.3 5.9 - 4.6	8.5 ± 0.3 9.5 – 8.3	11.2 ± 0.3 12.1 – 10.8	21.5 ± 0.4 22.1 – 20.4	13.7 ± 0.6 14.6 – 12.0	40.1 ± 0.3 40.5 – 39.5
Bottom	1.1 ± 0.3 1.4 – 0.6	3.0 ± 0.7 3.8 – 1.7	7.1 ± 0.5 8.0 – 6.5	27.9 ± 0.6 29.0 – 26.8	25.5 ± 2.1 29.7 – 22.7	35.4 ± 1.0 37.0 – 33.4
$(TM)_5Si_3$ ^^	16.2 ± 1.1 17.9 – 14.3	21.4 ± 1.2 22.9 – 18.9	16.1 ± 0.7 17.3 – 15.0	6.7 ± 0.9 8.3 – 5.4	1.8 ± 0.7 3.3 – 1.1	37.7 ± 1.0 40.0 – 36.8
T=$(TM)_6Si_5$ or $Ti_2Cr_4Si_5$ +	7.9 ± 2.0 11.2 – 4.1	12.4 ± 0.8 13.8 – 10.9	18.5 ± 0.8 20.0 – 17.0	14.5 ± 2.8 20.0 – 10.2	2.0 ± 0.4 2.8 – 1.3	44.8 ± 0.4 46.4 – 44.1
$FeSi_2Ti$ *	4.3 ± 0.6 5.2 – 3.1	14.6 ± 0.8 15.9 –13.1	5.7 ± 0.3 6.3 – 5.3	23.3 ± 0.4 23.8 –22.7	12.5 ± 1.0 13.8 –10.4	39.6 ± 0.6 40.9 – 38.6
(Fe,Cr)(Si,Al) ^	0.1	0.4	9.2 ± 0.8 10.4 – 7.2	37.1 ± 0.7 38.8 – 36.0	8.5 ± 0.6 10.2 – 7.4	44.7 ± 0.4 45.4 – 43.7
$Fe_3Al_2Si_3$	0.1	0.3	4.6 ± 0.4 5.4 – 3.7	30.2 ± 0.6 31.1 – 28.6	32.2 ± 0.8 34.2 – 30.7	32.6 ± 0.6 34.4 – 31.5
Dark phase (DP)	0.1	0.3	3.5 ± 0.3 4.3 – 2.9	21.3 ± 0.5 22.7 – 20.6	57.5 ± 1.7 59.3 – 54.0	17.3 ± 1.2 19.5 – 16.0
Eutectic large area analysis	5.5 ± 0.6 6.3 – 4.2	11.8 ± 0.7 12.9 – 10.6	5.0 ± 0.6 6.1 – 4.4	22.5 ± 0.7 23.4 – 21.6	16.0 ± 2.2 20.8 – 12.6	39.3 ± 1.0 40.9 – 37.0
Nb-rich $FeSi_2Ti$ ^	7.1 ± 0.8 8.5 – 5.8	14.4 ± 0.4 15.5 – 14.0	5.2 ± 0.7 7.6 – 4.2	21.9 ± 0.6 23.0 – 21.0	9.7 ± 0.8 11.6 – 8.5	41.7 ± 0.6 42.5 – 40.0
$Fe_3Al_2Si_3$ (DGPEu)	0.9	2.4 ± 1.9 5.7 – 0.6	4.5 ± 0.4 5.3 – 4.0	28.5 ± 1.4 30.1 – 25.6	29.2 ± 2.1 31.6 – 26.4	34.5 ± 0.7 35.4 – 33.7
(DPEu)	2.5 ± 0.6 3.4 – 1.7	5.8 ± 1.0 7.4 – 4.6	3.9 ± 0.3 4.3 – 3.5	20.7 ± 0.3 21.1 – 20.3	39.8 ± 3.9 45.3 – 35.2	27.3 ± 2.4 30.3 – 23.9

+ From the Nb-Fe-Cr-Si and Cr-Si-Ti systems
* τ_1, from the Fe-Ti-Si system
^ Based on FeSi
^^ based on $(Ti,Cr)_5Si_3$

According to the SEM studies, and the EDS data and the XRD data (figures 53, 54, 56 and Table 13), the alloy consisted of six phases, namely the $(TM)_5Si_3$ silicide that exhibited white contrast, the $(TM)_6Si_5$ silicide with light graded contrast, the phases $FeSi_2Ti$ and (Fe,Cr)(Si,Al) with similar grey contrast but different morphology, the $Fe_3Al_2Si_3$ phase with the dark grey contrast, and a phase with a dark contrast named DP in the Table 13. In the phases TM = Nb, Ti, Fe, Cr.

A three phase eutectic was found near the bottom. This consisted of the $FeSi_2Ti$ phase (light contrast), the $Fe_3Al_2Si_3$ phase with dark grey contrast (DGPEu in the Table 13) and a dark contrast phase (DPEu in the Table 13).

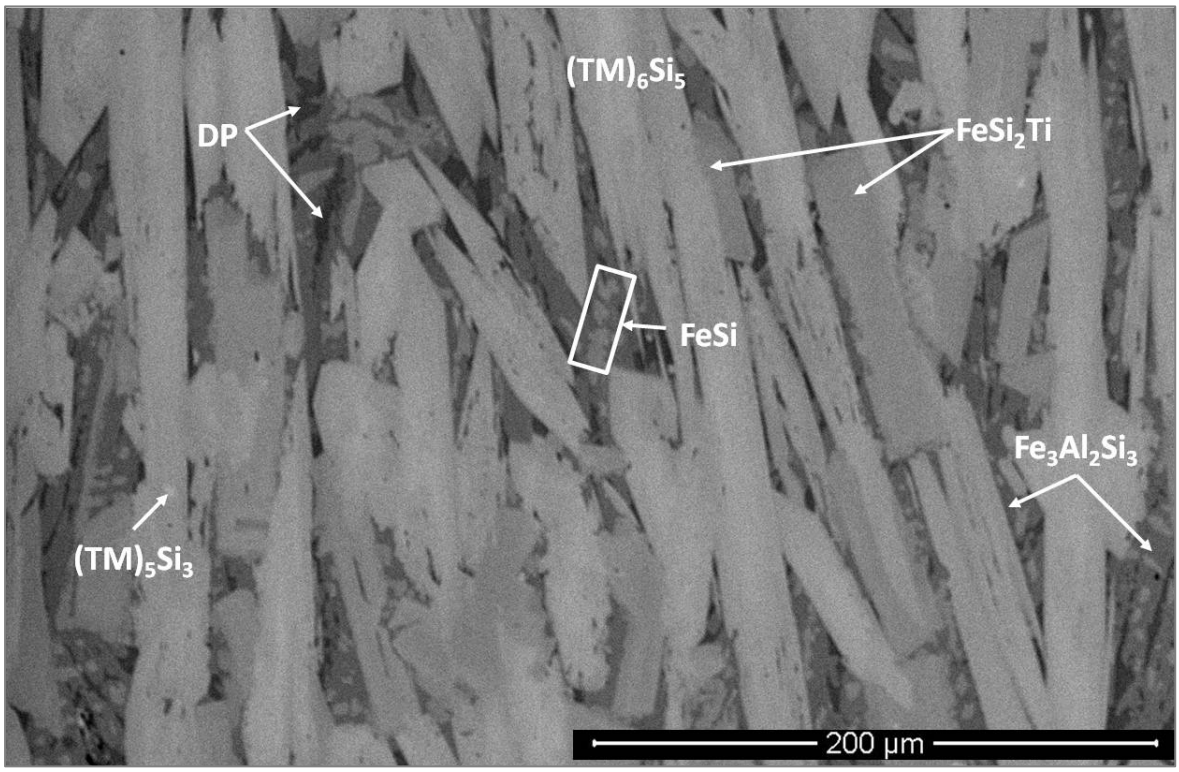

Figure 53. Typical microstructure of as cast allo OHC2, BSE image taken from the bulk, X270.

The XRD data (Figure 54) and the phase compositions obtained by EDS allowed the identification of the phases in the alloy OHC2-AC and OHC2-HTA and OHC2-HTB (see below). The results of these two complementary techniques confirmed the presence of the $(TM)_6Si_5$ silicide that was also found in the alloy OHC1. A criterion based on the (Si + Al) content was used to designate a particular phase to the compositions obtained. The $(TM)_6Si_5$ silicide crystallizes in the orthorhombic system with the V_6Si_5 as the proto-type and its space group is

the Ibam according to the crystallographic information in the JPCDS card 54-381. The τ_1=$FeSi_2Ti$ phase was also confirmed, it has the $MnSi_2Ti$ proto-type with the Pbam space group according to the information in the JPCDS card 75-2180. Its composition (Table 13) matched with the composition of the τ_1 phase when the Si+Al content was considered. The FeSi phase with the B20 structure was identified. This phase crystallizes in the cubic system with the $P2_13$ space group according to the crystallographic information in the JPCDS card 38-1397. The composition of the (Fe,Cr,Ti)Si phase was in agreement with the composition and solubility range of the FeSi phase. The $Fe_3Al_2Si_3$ phase crystallizes in the triclinic system within the P-1 space group according to the information in the JPCDS card 87-1920. The $(TM)_5Si_3$ silicide was found to be based on the $(Ti,Cr)_5Si_3$ hexagonal with the $P6_3$/mcm space group (Table 5) according to the information in the JPCDS card 89-3721 and had an extended solubility range.

The microstructure in the top of the cast button, was finer (Figure 56a). The $(TM)_6Si_5$ silicide had a faceted morphology and according to EDS chemical analysis presented microsegregation. The $FeSi_2Ti$ had an irregular shape and was mainly formed in the grain boundaries of the $(TM)_6Si_5$ while the $Fe_3Al_2Si_3$ displayed faceted plate type morphology. Very low volume fraction of small hexagonal grains of the $(TM)_5Si_3$ silicide were randomly distributed and formed only in areas of the top that were close to the bulk. The dark phase DP was formed at a very low volume fraction.

In the centre of the button, the microstructure comprised of a large volume fraction of faceted dendrites of the $(TM)_6Si_5$ phase. As in the alloy OHC1, this phase presented microsegregation observed by graded contrasts under BSE conditions (Figure 56b), showing a light contrast in the centre and dark grey contrast in the edges. EDS analysis indicated changes in the concentration of the Nb, Ti, Cr and Fe elements from the centre to the grain boundaries, with the center being richer in Nb, Ti and Cr and the grain boundaries rich in Fe (Figure 56). This would account for the large standard deviations for the concentration of the elements in the $(TM)_6Si_5$ phase (see Table 13).

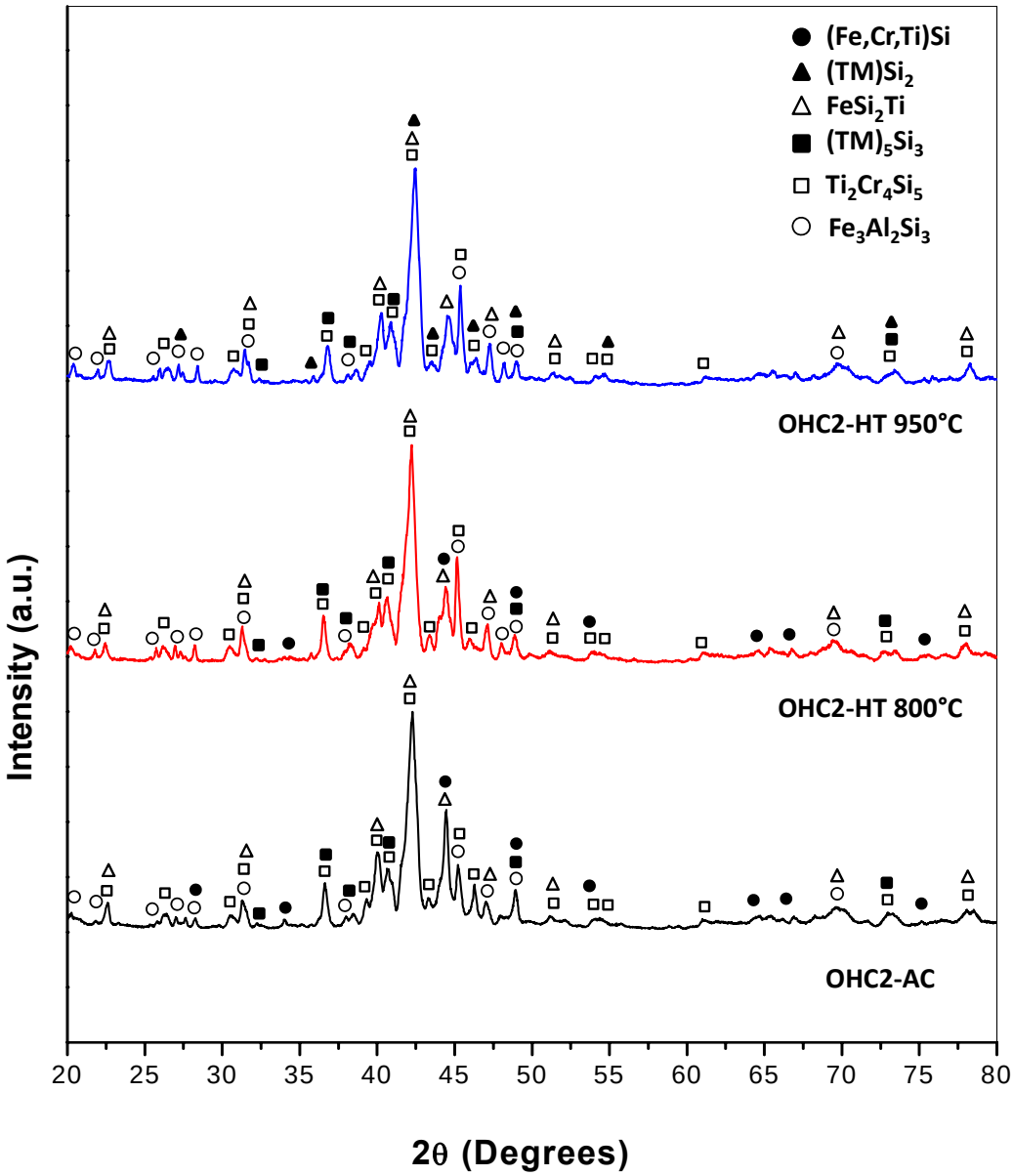

Figure 54. XRD diffractograms of the OHC2 alloy.

Likewise, in the centre of the button the phases $FeSi_2Ti$ and (Fe,Cr)(Si,Al) were present. They exhibited a very similar grey contrast but different morphology. The $FeSi_2Ti$ phase presented a faceted microstructure (like rectangles) and formed on the grain boundaries of the $(TM)_6Si_5$. The (Fe,Cr)(Si,Al) phase was generally found as isolated particles in the vicinity of $FeSi_2Ti$. Moreover, faceted plates of the $Fe_3Al_2Si_3$ phase exhibited considerable cracking. The dark phase DP was mainly found between the $(TM)_6Si_5$ and the $Fe_3Al_2Si_3$ at low volume fraction, and its Si

and Al concentrations varied significantly. Finally, small hexagonal faceted grains of the $(TM)_5Si_3$ silicide exhibited a darker contrast in the centre and were randomly distributed in this area.

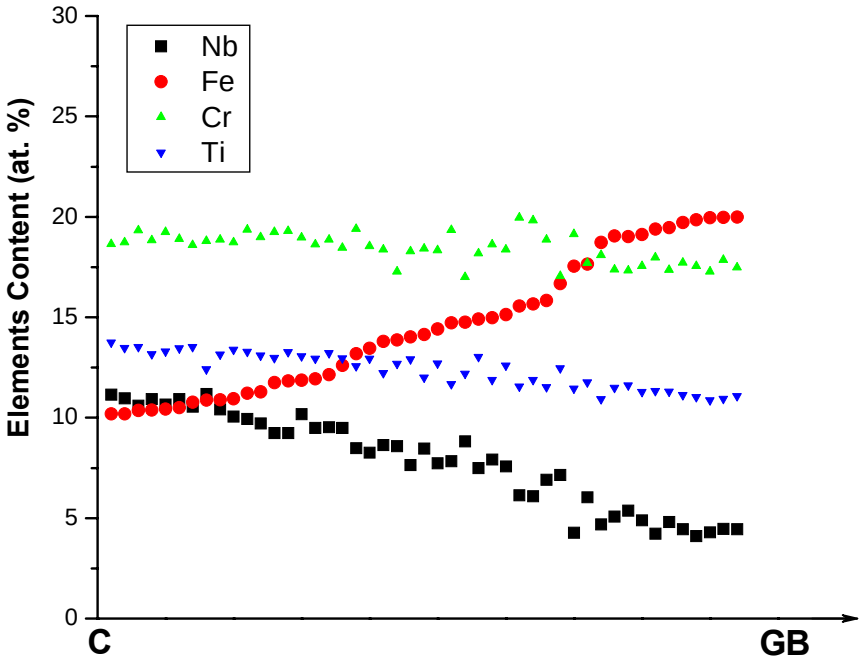

Figure 55. Nb, Fe, Cr and Ti concentrations from the centre (C) of $(TM)_6Si_5$ grains towards grain boundaries (GB).

Near the bottom of the button (Figure 56c), the microstructure presented different characteristics. The volume fraction of the faceted $(TM)_6Si_5$ was reduced. The phases $(TM)_5Si_3$, $Fe_3Al_2Si_3$, and DP were present with the same features as in the bulk of the button. However, in this area the $(TM)_6Si_5$ presented more voids, cracking and a ternary eutectic was formed in its vicinity. The eutectic consisted of Nb-rich $FeSi_2Ti$, $Fe_3Al_2Si_3$ and the dark phase (DPEu) (Figure 56d). Compositions of the phases are given in Table 13. The (Fe,Cr)(Si,Al) was in the form of isolated particles embedded in the $Fe_3Al_2Si_3$ phase. The eutectic had (Si+Al) 55.3 at. %. The data for $Fe_3Al_2Si_3$ and DPEu could be not very accurate because the analyses were performed in very small areas. However, it was clear that the $Fe_3Al_2Si_3$ was the phase with the dark grey contrast.

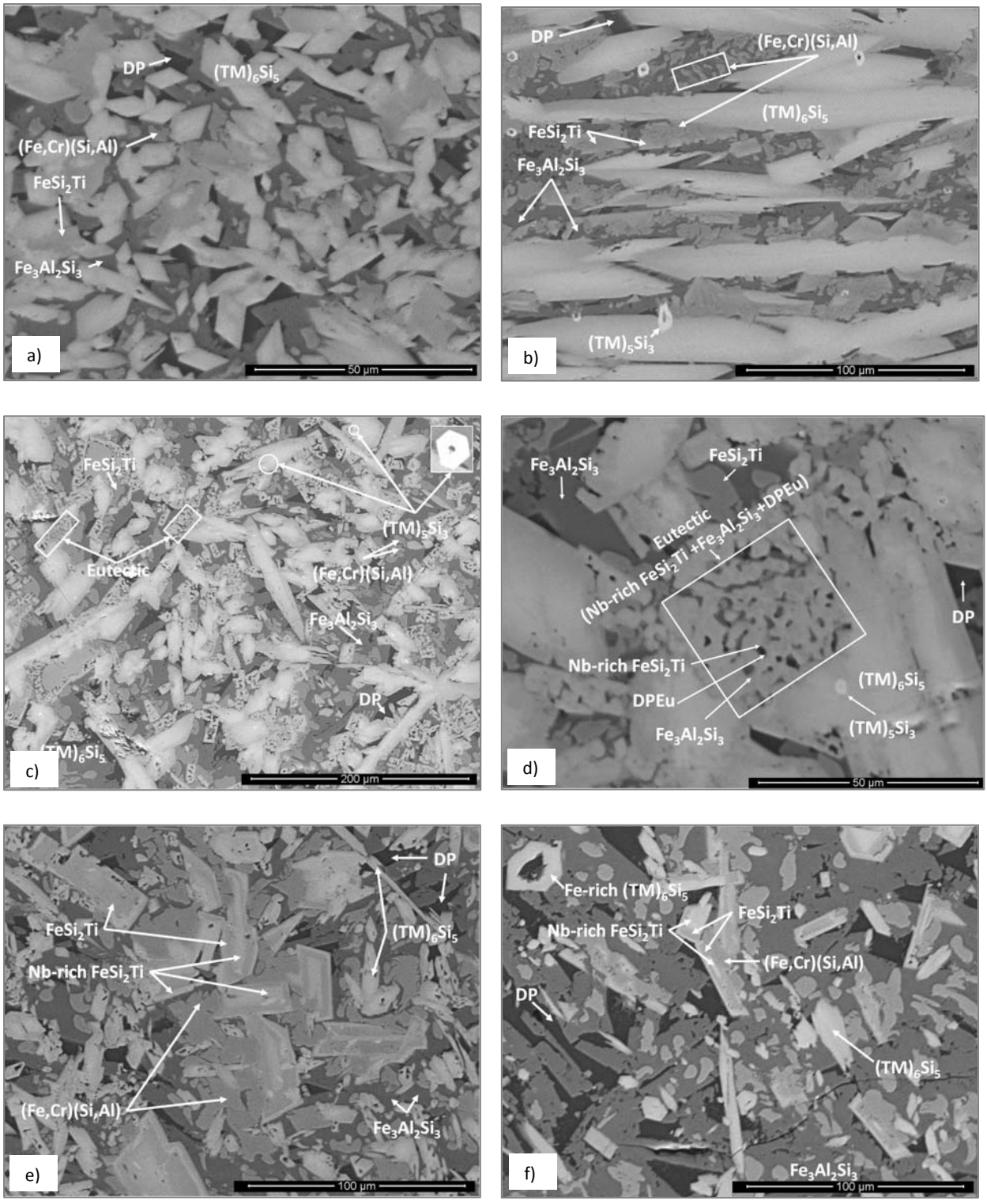

Figure 56. BSE images from cross section of as cast button alloy OHC2 (a) top, X1250, (b) bulk, X1250, (c) near the bottom, X640, (d) near the bottom showing the eutectic, X1250, (e) bottom, X640, (f) the bottom, X640.

In the bottom of the button (Figures 56e and 56f), there was a notable higher concentration (macrosegregation) of Fe and Al. The large area analysis of this zone is included in Table 13. SEM images indicated that the volume fraction of the dark phase (DP) was slightly higher than in the rest of the alloy. The phases $(TM)_6Si_5$, $FeSi_2Ti$ and (Fe,Cr)(Si,Al) were present at lower volume fraction while the volume fraction of the $Fe_3Al_2Si_3$ was almost the same as in the rest of the alloy. The $FeSi_2Ti$ phase was faceted (like trapezoids) and showed some segregation; a Nb-rich composition was present in the brighter contrast areas and a Nb-poor composition in the areas with the darker contrast. Moreover, the (Fe,Cr)(Si,Al) was found surrounding these faceted grains (Figure 56e). The Fe-rich $(TM)_6Si_5$ was either faceted or irregular (Figure 56f). No $(TM)_5Si_3$ phase was observed in the botttom.

Heat treated microstructures

Heat treated (800 °C / 48h)

The actual composition of the alloy OHC2 after the heat treatment at 800 °C for 48h (OHC2-HTA) was Si-21.5Fe-11.4Cr-12.9Al-8.6Ti-5Nb. According to the SEM studies, and the EDS analysis data and the XRD data (figures 54, 57, 58 and Table 14), the alloy consisted of the same six phases namely the $(TM)_5Si_3$, $(TM)_6Si_5$, $FeSi_2Ti$, (Fe,Cr)(Si,Al), $Fe_3Al_2Si_3$ and the dark phase (DP) where TM = Nb, Ti, Fe, Cr. According to the EDS data segregation was still present (Table 14). The typical microstructure of the OHC2-HTA alloy is shown in figures 57 and 58.

The microstructure in the top was coarser (Figure57a). The $(TM)_6Si_5$ silicide was cracked, had an elongated morphology and presented some degree of homogenization since the Fe-rich composition was completely suppressed in this part of the alloy. The $FeSi_2Ti$ appeared more faceted. Although the $FeSi_2Ti$ was mainly found in the boundaries of the $(TM)_6Si_5$, it was also found as faceted isolated plates. The $(TM)_5Si_3$ conserved its hexagonal morphology and distribution pattern. The (Fe,Cr)(Si,Al) was found as dispersed particles of grey contrast and irregular morphology. The $Fe_3Al_2Si_3$ was found everywhere, and presented some porosity. The dark phase (DP) was not found in the top of the button. The volume fraction of $Fe_3Al_2Si_3$ had increased while the volume fraction of the rest of the phases remained practically the same.

Table 14 EDS data (at. %) of the heat treated alloy OHC2 at 800 °C for 48 h.

Area/Phase	Nb (at%)	Ti (at%)	Cr (at%)	Fe (at%)	Al(at%)	Si(at%)
Large area analysis	5.0 ± 0.3 5.6 – 4.7	8.6 ± 0.4 9.4 – 8.2	11.4 ± 0.3 11.9 – 11.0	21.5 ± 0.5 22.2 – 20.8	12.9 ± 0.8 13.8 – 11.0	40.6 ± 0.5 41.6 – 40.0
Bottom	0.8	2.3 ± 0.3 2.8 – 1.9	6.6 ± 0.3 7.1 – 6.4	27.1 ± 0.4 27.7 – 26.4	29.3 ± 0.6 29.9 – 28.2	33.9 ± 0.4 34.6 – 33.5
$(TM)_5Si_3$ ^^	16.0 ± 0.6 17.1 – 15.1	21.5 ± 0.8 22.7 – 20.3	15.8 ± 0.6 16.5 – 14.7	7.5 ± 0.9 8.7 – 6.2	2.1 ± 0.8 3.6 – 1.2	37.1 ± 0.6 37.7 – 36.3
T=$(TM)_6Si_5$ or $Ti_2Cr_4Si_5$ +	8.3 ± 1.9 11.0 – 4.8	13.0 ± 0.6 13.9 – 11.2	18.6 ± 1.0 20.1 – 16.7	13.8 ± 2.4 17.7 – 10.3	2.0 ± 0.6 3.5 – 1.4	44.2 ± 0.3 44.7 – 43.6
$FeSi_2Ti$ *	3.6 ± 0.7 4.9 – 2.7	15.5 ± 0.8 16.6 – 14.1	5.4 ± 0.5 6.5 – 4.8	24.0 ± 0.5 25.2 – 23.0	12.2 ± 0.6 13.6 – 11.1	39.4 ± 0.4 40.1 – 38.8
(Fe,Cr,Ti) (Si,Al) ^	0. 1	0.9 ± 1.0 2.8 – 0.3	7.9 ± 0.3 8.3 – 7.4	38.1 ± 0.6 38.8 – 37.0	8.5 ± 0.7 10.1 – 7.9	44.4 ± 0.4 44.7 – 43.5
$Fe_3Al_2Si_3$	0.1	0.3	4.9 ± 0.7 6.6 – 4.1	30.6 ± 0.7 31.5 – 28.9	30.6 ± 0.7 31.6 – 28.9	33.6 ± 0.6 34.8 – 32.8
Dark phase (DP)	0.1	0.5	3.5 ± 0.7 5.3 – 2.3	22.6 ± 0.8 24.1 – 21.6	59.1 ± 2.3 62.0 – 54.9	14.3 ± 1.4 16.9 – 12.1
Prior eutectic large area analysis	5.6 ± 0.5 6.6 – 4.9	12.0 ± 1.0 13.6 – 10.5	5.7 ± 1.6 9.0 – 4.2	22.8 ± 1.1 24.8 – 21.3	14.9 ± 2.3 18.5 – 11.8	38.9 ± 1.2 40.3 – 37.1
Nb-rich $FeSi_2Ti$ *	7.0 ± 0.8 8.4 – 5.3	14.7 ± 1.0 15.9 – 12.9	5.3 ± 0.7 6.9 – 4.6	22.0 ± 0.7 23.5 – 20.8	10.1 ± 1.2 13.9 – 8.8	40.9 ± 0.8 41.9 – 38.9

+ From the Nb-Fe-Cr-Si and Cr-Si-Ti systems
* τ_1, from the Fe-Ti-Si system
^ Based on FeSi
^^based on $(Ti,Cr)_5Si_3$

The microstructure in the bulk of the alloy was very similar to the microstructure in the top. However, in the bulk, the $(TM)_6Si_5$ silicide grains were much more larger and the $FeSi_2Ti$ acquired a more faceted morphology (like rectangles) (Figure 57). The dark phase (DP) was not present in this area of the heat treated alloy. This suggested that it was dissolved its solutes redistributed in the microstructure.

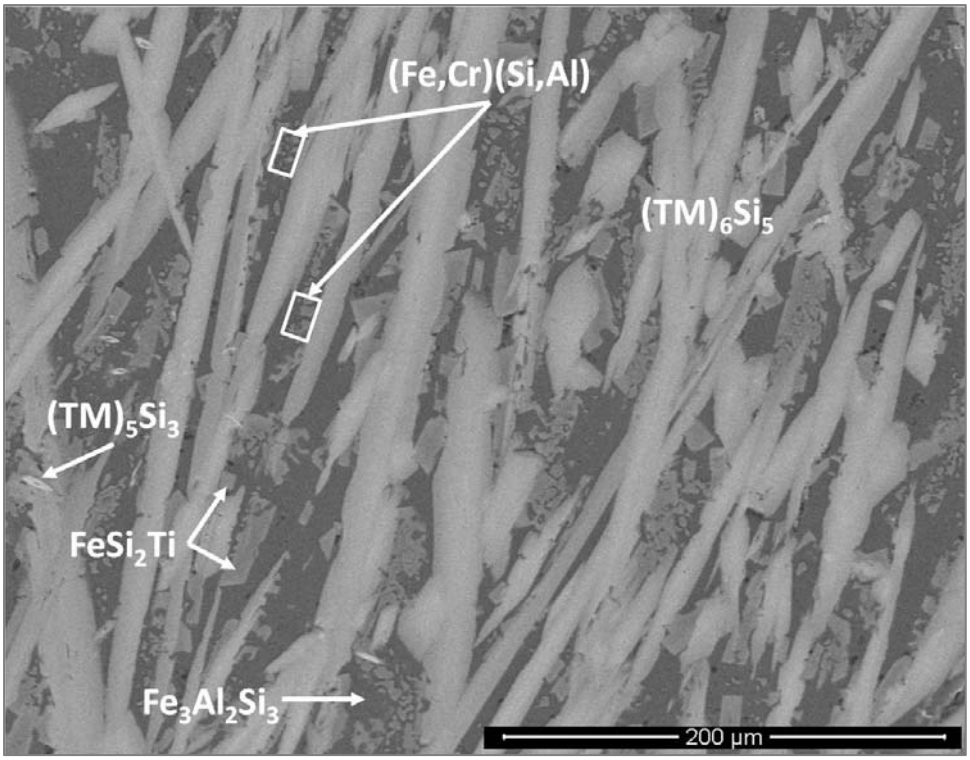

Figure 57. Typical microstructure of the alloy OHC2-HTA, BSE image from the bulk, X320.

Near the bottom, the retained prior eutectic consisted of the Nb-rich $FeSi_2Ti$, $Fe_3Al_2Si_3$ and the DPEu phases. As in the as cast microstructure, the prior eutectic was in the vicinity of the elongated grains of the $(TM)_6Si_5$ phase (Figure 57b). A considerable volume fraction of $Fe_3Al_2Si_3$ plates were observed and the dark phase (DP) phase was still present. Some faceted grains of $FeSi_2Ti$ with segregation in their boundaries were found. The hexagonal grains of the $(TM)_5Si_3$ silicide were also observed in this area.

The bottom was richer in Al, see Table 14. In this area the volume fraction of the $(TM)_6Si_5$ silicide was dramatically reduced and its morphology was finer but still as elongated grains (Figure 58c). The Fe-rich $(TM)_6Si_5$ was still stable in the bottom. The $FeSi_2Ti$ was of irregular morphology and dispersed in the $Fe_3Al_2Si_3$ similar to the (Fe,Cr)(Si,Al). Tiny hexagonal particles with the brightest contrast were assumed to be the $(TM)_5Si_3$ (but no chemical analysis was performed since their size was out of the spatial resolution limit of EDS technique). Finally, $Fe_3Al_2Si_3$ plates at considerable volume fraction with multiple voids filled by the dark phase (DP) were also observed.

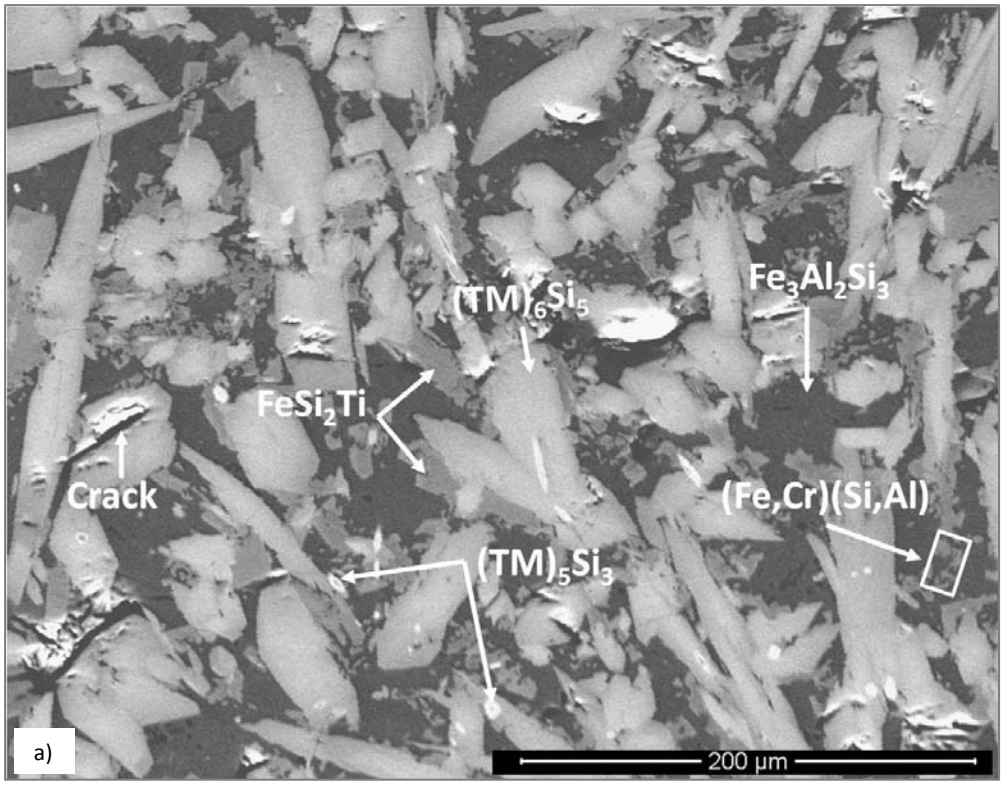
(TM)6Si5
Fe3Al2Si3
FeSi2Ti
Crack
(Fe,Cr)(Si,Al)
(TM)5Si3
a)
200 µm

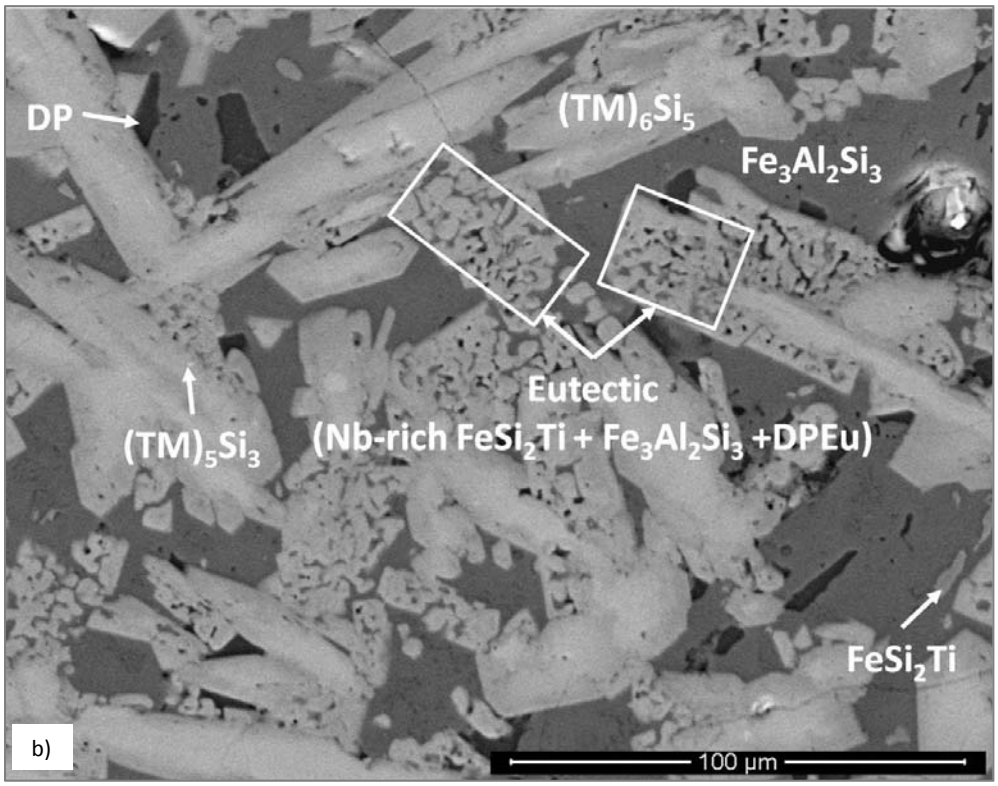
DP
(TM)6Si5
Fe3Al2Si3
Eutectic
(Nb-rich FeSi2Ti + Fe3Al2Si3 +DPEu)
(TM)5Si3
FeSi2Ti
b)
100 µm

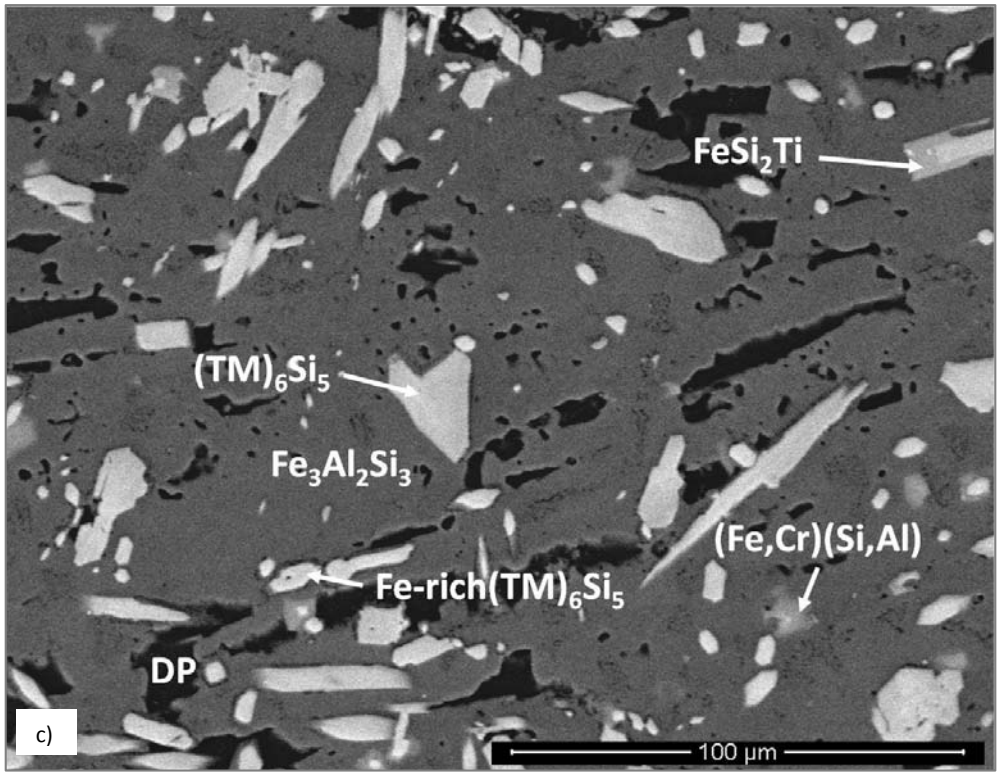

Figure 58. BSE images of the alloy OHC2-HTA after 800 °C/48 heat treatment, (a) top, X320, (c) near the bottom showing the eutectic, X640, (d) the bottom, X640.

Heat treated (950 °C / 48h)

The actual composition of the heat treated alloy at 950 °C for 48h (OHC2-HTB) was Si-21.5Fe-11.5Cr-13Al-9.9Ti-4.3Nb. The EDS analysis data is given in Table 15 and is the average composition of the large area and phases analyses taken from the top, bulk and bottom after this heat treatment. The typical microstructure in the centre of the heat treated alloy (OHC2-HTB) is shown in figure 59.

According to the SEM studies, the XRD data, and the EDS analysis data (figures 54, 59, 60 and Table 15) the microstructure of the OHC2-HTB consisted of the $(TM)_6Si_5$, $FeSi_2Ti$, $Fe_3Al_2Si_3$ and $(TM)_5Si_3$ phases.

The microstructure in the top of the alloy OHC2-HTB was similar to the microstructure in the bulk (Figures 59 and 60a). The $(TM)_6Si_5$ was faceted, elongated and less cracked. The microsegregation in this phase was still present and its Fe content was ≤ 15.2 at. % Fe. The

faceted $FeSi_2Ti$ was coarser and was observed at the grain boundaries of the $(TM)_6Si_5$ and sometimes was coarse enough to link $(TM)_6Si_5$ grains. The tiny hexagonal grains of $(TM)_5Si_3$ were found in this part of the alloy (Figure 60a) but their composition was not measured owing to their small size.

Table 15 EDS data (at. %) for the heat treated alloy OHC2 at 950 °C for 48h.

Area/Phase	Nb (at%)	Ti (at%)	Cr (at%)	Fe (at%)	Al(at%)	Si(at%)
Large area analysis	4.3 ± 0.2 4.6- 4.0	9.9 ± 0.4 10.6 – 9.3	11.5 ± 0.3 12.4 – 10.9	21.5 ± 0.4 22.1 – 20.7	13 ± 0.6 14.0 – 12.0	39.9 ± 0.5 41.0 – 39.2
$(TM)_5Si_3$ ^	16.0 ± 0.6 17.1 – 15.1	21.5 ± 0.8 22.7 – 20.3	15.8 ± 0.6 16.5 – 14.7	7.5 ± 0.9 8.7 – 6.2	2.1 ± 0.8 3.6 – 1.2	37.1 ± 0.6 37.7 – 36.3
T=$(TM)_6Si_5$ or $Ti_2Cr_4Si_5$ +	8.2 ± 1.1 10.0 – 6.1	14.7 ± 0.4 15.3 – 13.4	19.1 ± 0.7 21.5 – 17.8	11.9 ± 1.6 15.2 – 9.6	1.7 ± 0.3 2.6 – 1.3	44.4 ± 0.2 44.9 – 43.9
$FeSi_2Ti$ *	4.3 ± 0.3 4.9 – 3.8	17.0 ± 0.5 17.9 – 16.3	4.6 ± 0.3 5.0 – 3.9	23.1 ± 0.3 23.4 – 22.3	10.5 ± 0.6 12.3 – 10.0	40.5 ± 0.4 40.9 – 39.5
$Fe_3Al_2Si_3$	0.0	0.3	4.6 ± 0.4 5.5 – 4.0	30.9 ± 0.6 31.9 – 30.0	31.6 ± 0.7 32.2 – 29.9	32.6 ± 0.5 33.9 – 31.5
$(TM)Si_2$	1.1 ± 0.3 1.5 – 0.6	2.9 ± 1.7 5.1 – 1.3	22.9 ± 2.8 26.5 – 20.3	7.4 ± 2.2 10.3 – 5.2	18.6 ± 0.9 19.7 – 17.5	47.1 ±1.2 48.4 – 45.6
Prior eutectic large area analysis	5.9 ± 0.2 6.2 – 5.6	13.8 ± 0.5 14.6 – 13.0	5.6 ± 0.6 6.5 – 4.7	21.9 ± 0.4 22.5 – 21.3	12.4 ± 0.7 13.7– 11.6	40.3 ± 0.3 40.7 – 39.9
Nb-rich $FeSi_2Ti$ *	6.2 ± 0.8 7.9 – 5.4	16.7 ± 0.7 17.7 – 15.5	5.9 ± 1.5 9.3 – 4.4	20.8 ± 0.5 21.5 – 19.9	8.8 ± 0.5 9.7 – 7.9	41.8 ± 0.3 42.3 – 41.4

+ From the Nb-Fe-Cr-Si and Cr-Si-Ti systems
* τ_1, from the Fe-Ti-Si system
^based on $(Ti,Cr)_5Si_3$

Near the bottom the retained prior eutectic consisted of the Nb-rich $FeSi_2Ti$ and $Fe_3Al_2Si_3$ phases, the DPEu was absent (Figure 60b) and was surrounded by faceted grains of $FeSi_2Ti$ in the vicinity of the $(TM)_6Si_5$. Tiny hexagonal particles of the $(TM)_5Si_3$ silicide were also observed in this area.

Below the prior eutectic towards the bottom there were large faceted plates of $FeSi_2Ti$ with Nb-rich composition in the edges and a darker contrast in the centre. These $FeSi_2Ti$ grains were in the $Fe_3Al_2Si_3$ (Figure 60c). The faceted $(TM)_6Si_5$ was finer and was observed next to the large $FeSi_2Ti$ grains. Also some small dark grey “spots” (DGS) were visible and according to the EDS analysis this phase could be the $(TM)Si_2$ phase.

In the bottom the same microstructure was found as the one described above but this was at a finer scale.

The XRD data, microstructure and chemical analyses (Figures 54,59 and 60 and Table 15) would suggest that the (Fe,Cr)(Si,Al) was a metastable phase in this alloy since its diffraction peaks disappeared after the heat treatment at 950 °C and it was not observed in the microstructure.

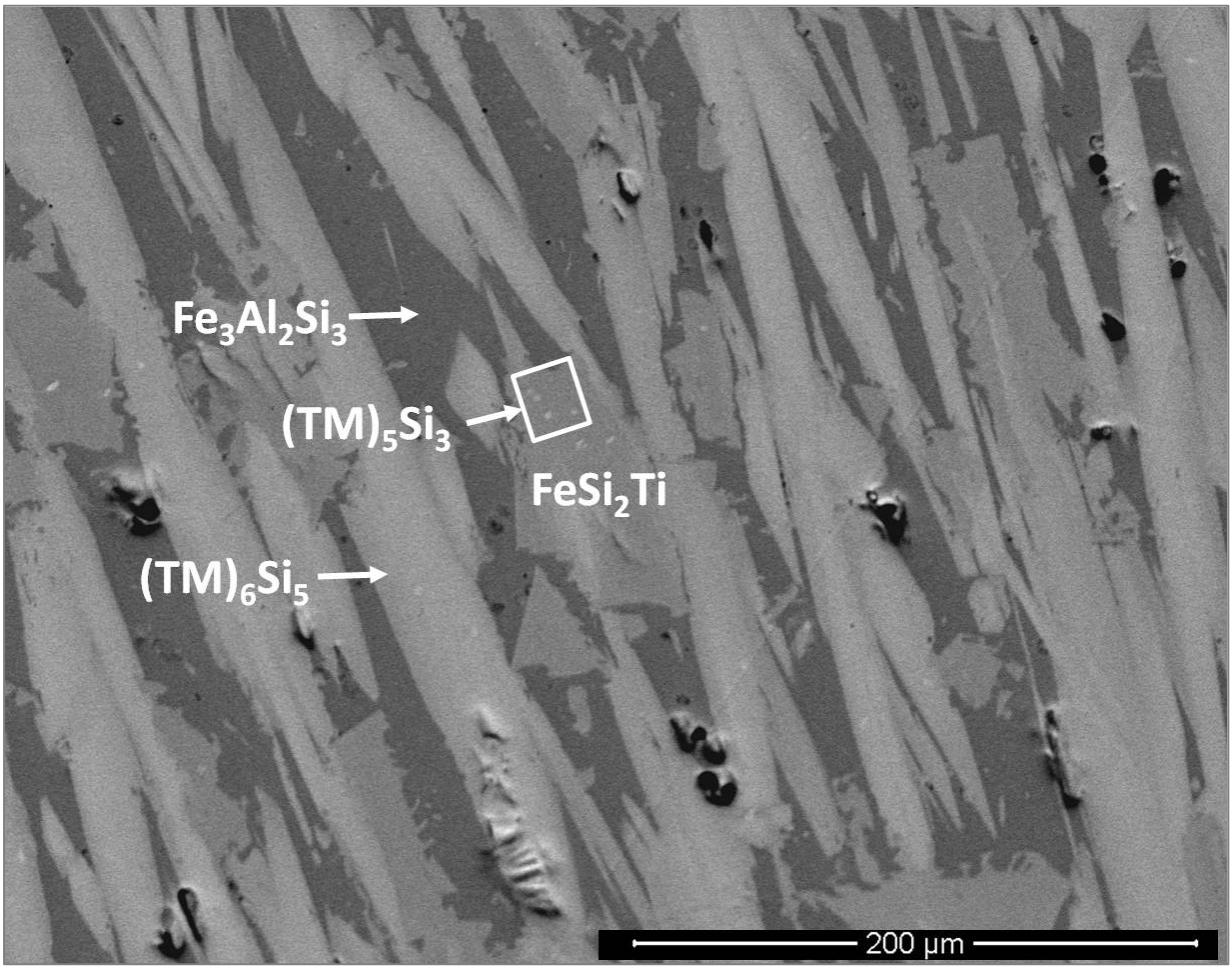

Figure 59. Typical microstructure of the alloy OHC2-HTB, BSE image from the centre, X320.

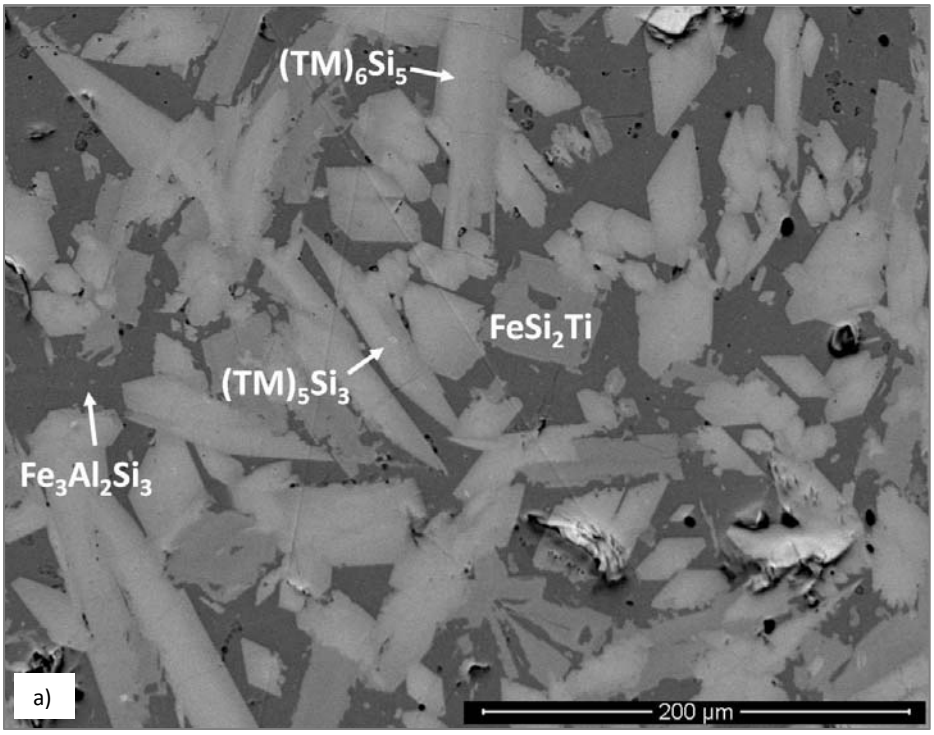
(TM)6Si5
FeSi2Ti
(TM)5Si3
Fe3Al2Si3
a)
200 µm

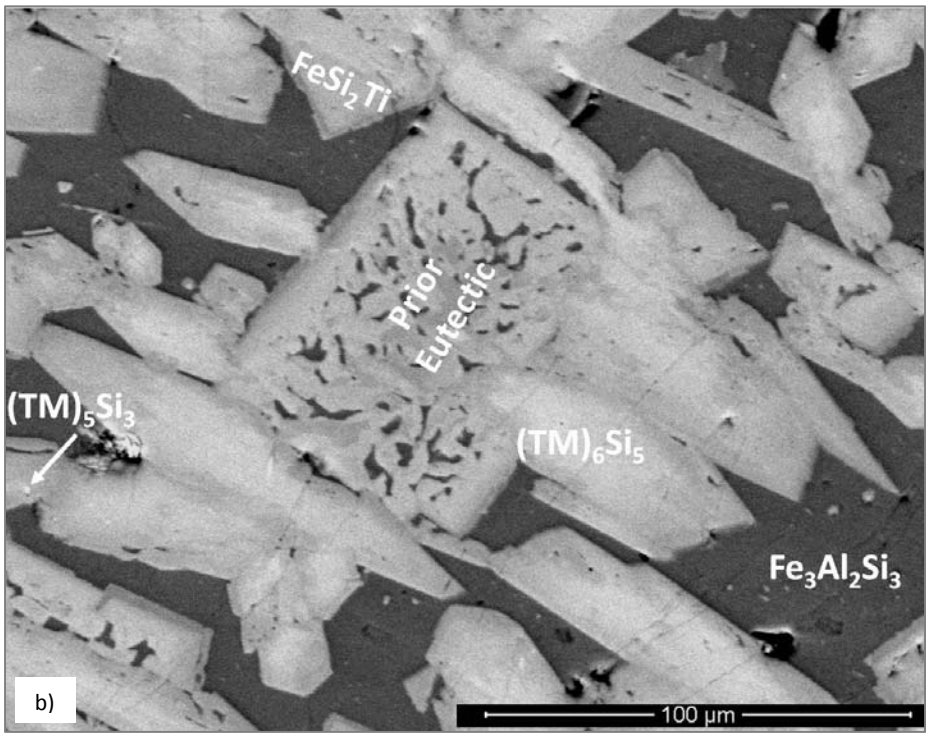
FeSi2Ti
Prior Eutectic
(TM)5Si3
(TM)6Si5
Fe3Al2Si3
b)
100 µm

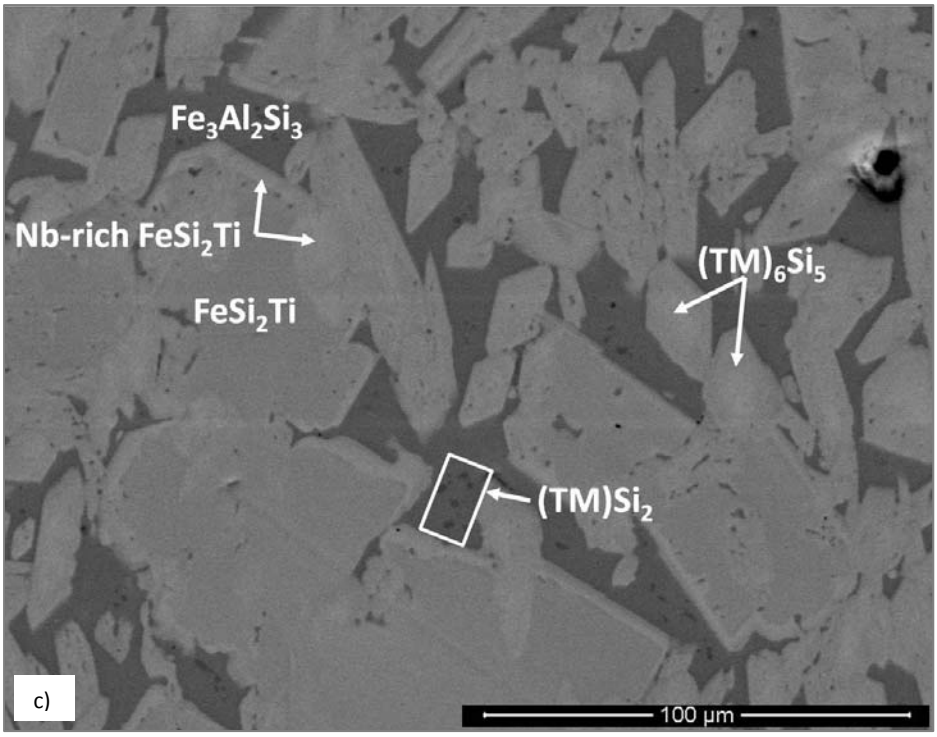

Figure 60. BSE images of the alloy OHC2-HTB, (a) top, X320, (b) near the bottom showing the prior eutectic, X640, (c) bottom, X640.

A further heat treatment at 1200 °C for 48h was carried out but the alloy exhibited liquation. The microstructure of this alloy was analyzed and it was found to be very similar to the as cast alloy.

In the DSC trace of the alloy OHC2 (figure 61) there was a small endothermic peak at 973.0 °C, with a corresponding strong peak in the cooling at 973.5 °C that could match with a crystallization event . The DTA results of Krendelsberger et al. (2007) showed T = 975 °C as the melting temperature of $Fe_3Al_2Si_3$. The DSC plot also showed a second stronger peak at 1014.0 °C on heating with a corresponding small peak at 1008.0 °C on cooling. These peaks could be attributed to metastable phases as they are very close to the first two peaks. The second peak on heating was very strong and could correspond to an invariant reaction. This peak could be related to the ternary eutectic ($L \rightarrow FeSi_2Ti + Fe_3Al_2Si_3 + DP$) observed in the as cast microstructure.

The above results showed that addition of Al had a strong effect on the thermal stability of this alloy. According to Du and Shuster (2002), the melting point of the $(Ti,Cr)_5Si_3$ phase should be above 1600 °C. The melting point of the $(TM)_6Si_5$ and τ_1=$FeSi_2Ti$ phases should be above 1500 °C according to DTA experiments carried out by Du and Shuster (2002) and Weitzer et al. (2008), respectively. The melting point of the FeSi phase is 1410 °C and it is expected that the addition of Cr would increase its melting temperature. However, the presence of 8.5 at %Al in this phase destabilised it at 950 °C. In the DSC trace of the alloy OHC2 alloy (Figure 61) there was a reaction involving liquid at 973 °C and liquation was confirmed after the heat treatment at 1200 °C. This data indicated that this alloy cannot be used for BC on Nb-silicide based alloys.

This data also indicated that caution would be required if the alloy OHC1 were to be used as BC, because diffusion of Al and Nb from the substrate could lead to phase equilibria linked with the phases observed in the alloy OHC2.

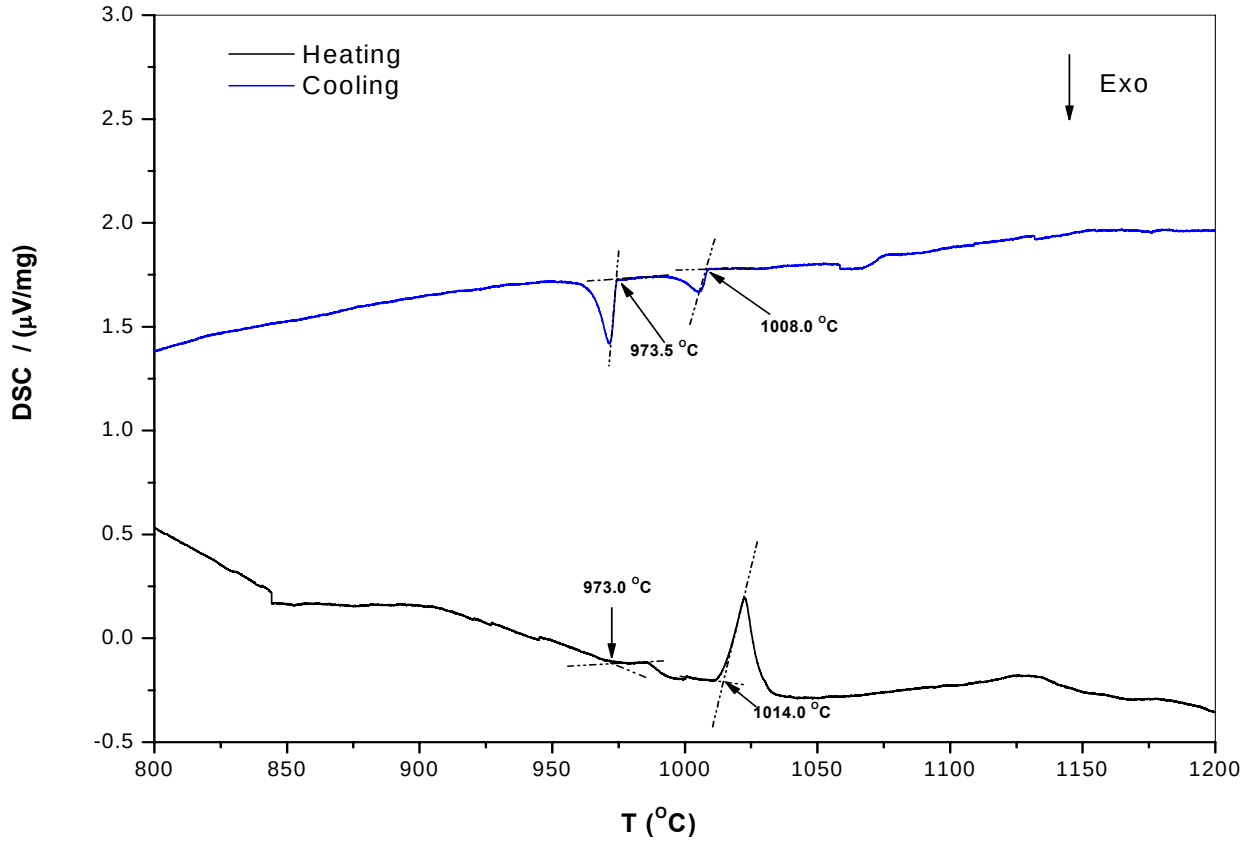

Figure 61 DSC trace of the alloy OHC2.

The exclusive formation of the eutectic near the bottom suggested it formed from Al and Fe rich melt solidification at higher cooling rates that the rest of the button. Besides, it was always found next to $(TM)_6Si_5$ which would suggest that its formation had a strong dependence on the local melt composition.

3.2.2 Thermo-gravimetric analysis

The oxidation behaviour of the alloys was studied using isothermal oxidation tests in air at 800 and 1200 °C. The weight change data was analysed using the equation,

$$\ln(\Delta w) = \ln K + n \ln t \quad \ldots\ldots\ldots\ldots \text{Eq. (1)}$$

where $\Delta w = \frac{\Delta m}{A}$ and

Δw = weight change per unit area
K = reaction rate constant that embodies the sum of reaction rates
Δm = weight change
A = surface area before exposure
t = exposure time

The equation 1 was used to determine the reaction mechanism that controlled the oxidation. According to the oxidation kinetics is regarded as linear (n = 1), parabolic (n = 0.5), subparabolic or cubic ($n \leq 0.3$). If there was more than one mechanism involved, the corresponding section was evaluated to determine the oxidation kinetics from the following equations,

Linear oxidation rate equation,

$$\Delta w = K_l.t \quad \ldots\ldots\ldots\ldots \text{Eq. (2)}$$

Parabolic oxidation rate equation,

$$(\Delta w)^2 = K_p.t \quad \ldots\ldots\ldots\ldots \text{Eq. (3)}$$

where

K_l= linear rate constant
K_p= parabolic rate constant

The obtained values of oxidation rate constants of the alloy OHC1 after isothermal oxidation at 800 and 1200 °C and in the case of alloy OHC2 at 800 °C are shown in Table 16. The oxidation behaviour of the alloy OHC1 at 800 and 1200 °C was paralinear which indicates that both parabolic and linear mechanisms occurred [Kofstad (1966)].

The evaluation of the oxidation data with equation (1) at 800 °C gave an n value of 0.89 (~ 1) and also suggested for linear oxidation rate for the predominant stage at this temperature. The oxidation in the first 10 h was parabolic and for the rest of the experiment linear. At 1200 °C the oxidation of the alloy OHC1 was paralinear, however, in the first 40 hours it was parabolic and then after this time it changed to a linear behaviour.

According to the n value, the oxidation behaviour of the alloy OHC2 alloy was subparabolic. This behaviour was related with a very short initial period of oxidation in which the alloy gained weight at a high oxidation rate and then stabilised into a very low parabolic oxidation rate. The K_l and K_p values are given in Table 16.

Table 16 Total weight gain, n values and oxidation rate constants of the alloys for isothermal oxidation at 800 and 1200 °C.

Alloy code and temperature	n	K_l ($g.cm^{-2}.s^{-1}$)	K_p ($g^2.cm^{-4}.s^{-1}$)	Weight gain (mg/cm^2)
OHC1-800 °C	0.89	3.9×10^{-9} >10h	5.47×10^{-13} (0-10h)	1.42
OHC1-1200 °C	0.68	3.74×10^{-9} >40 h	4.13×10^{-11} (0-40 h)	1.60
OHC2-800 °C	0.14	1.03×10^{-7} (0-1 h)	1.00×10^{-13} > 1h	0.27

Following the isothermal oxidation, the structures of the oxide scale and substrate were characterized using scanning electron microscopy (secondary electron image (SE) and back scattered electron imaging (BSE), EDS and glancing angle XRD (GAXRD).

3.2.2.1 Thermo-gravimetric analysis (TGA) at 800 °C

Figure 62 shows the mass gain per unit area versus time (Δm/A vs. t) during isothermal oxidation in air at 800 °C for the alloys OHC1 and OHC2. The two alloys clearly showed different oxidation kinetics. The alloy OHC1 gained more weight than OHC2 (Table 16). The addition of Al in the alloy OHC2 had a positive positive effect on the oxidation behaviour of the alloy OHC2.

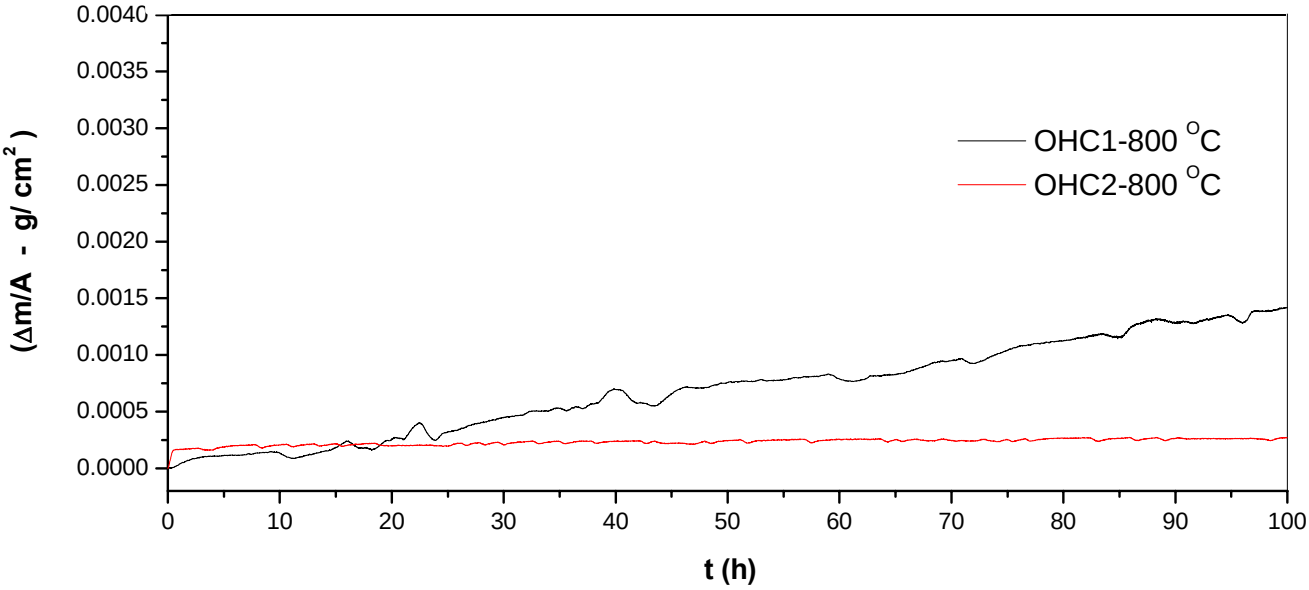

Figure 62. Isothermal oxidation TG plots of the alloys OHC1 and OHC2 in air at 800 °C for 100 h.

Thermo-gravimetric analysis of Si-23Fe-15Cr-15Ti-Nb (alloy OHC1) at 800 °C

According to the data in figure 62, the oxidation behaviour of the alloy OHC1 after isothermal oxidation in air at 800 °C was basically linear (Table 16). The data gave an n = 0.89 (Table 16) which confirmed that the linear oxidation behaviour was predominant. In the early stages of the experiment before the isothermal temperature was reached red rust like staining was found on top of the contact surface of the alumina crucible with the specimen and remained until the experiment was finished. This suggested that a chemical reaction of fast growing oxides with alumina occurred at the beginning of the experiment but did not continue during the isothermal oxidation.

Figure 62 shows repeated periods of weight loss after gain weight. The total time of weight loss was 19 h. The total time that the sample gained weight during the experiment, was 81 h of which 71 h was linear and 10 h parabolic oxidation. The gain weight of this alloy after 100 h at 800 °C was 1.42 mg/cm^2. The K_p and K_L values in Table 16 were obtained by plotting gain weight versus time using equations (2) and (3). The first 10 h did not present weight losses. After the first 10 h, the data was evaluated including the weight losses since the latter did not complicate the evaluation of the data, the trend of the plot or the K_l value given in Table 16.

The first 10 hours of isothermal oxidation were characterized by a parabolic rate which could be attributed to the formation of SiO_2 oxide which is the most protective oxide that this alloy could form. The oxide growth could develop some strains and leave unoxidised material exposed to further oxidation. There might have been some oxide evaporation. No oxide spallation was observed but some cracks on the surface of the scale were observed. These cracks could be caused by volume changes resulting from phase transformations due to the selective oxidation of the alloy's components.

Thermo-gravimetric analysis of Si-22Fe-12Cr-12Al-10Ti-5Nb (alloy OHC2) at 800 °C

The isothermal oxidation data gave n= 0.14 (Table 16) meaning that the oxidation behaviour of the alloy OHC2 was subparabolic. This behaviour suggests that initially there was a high rate oxide formation (lasting the first hour). This has been related to the exposure of grain boundaries at lower temperatures that initially oxidise rapidly, the growth of the oxide with time reduces the diffusion pathways and consequently the oxidation rate is slowed to the parabolic rate (the short-circuit mechanism) [Li et al. (2003)]. The TG data shows consecutive minute weight losses significantly smaller compared with the alloy OHC1. Continuous reaction with oxygen could also change the microstructural features of the oxide scale which implicates changes in volume ratio causing some cracking to the scale. The alloy showed evidence of its good capability to form a protective oxide since it was efficient self healing after weight loss.

Microstructure of oxide scale of Si-23Fe-15Cr-15Ti-Nb (alloy OHC1)

After isothermal oxidation in air at 800 °C for 100 h, the cubic specimen retained its shape with visibly sharp edges; its surface was slightly lustrous with some greenish and golden tones (Figure 63a). In figure 63 the SE images show two facets of the cubic specimen after oxidation, in both an adherent and continuous oxide scale on the surface of the alloy is observed. The scale consisted of a continuous glassy like oxide layer and regions with a dispersion of fine faceted particles. Numerous cavities can be also observed.

The oxide scale exhibited different characteristics in the two observed facets of the cubic specimen which were attributed to the anisotropy of the underlaying phases in the alloy. The

images in figure 63b and 63c suggest that the crystal orientation of the $(TM)_6Si_5$ phase may have influenced the oxide nucleation sites. This is because it was found that one side of the specimen presented higher volume fraction of fine granular particles in the continuous glassy oxide over this phase (Figure 63b) while, the (Fe,Cr,Ti)Si phase was covered by this continuous glassy oxide layer (Figure 63b). The other side of the specimen (Figure 63c) that shows the oxide surface formed perpendicular to the dendritic growth of the $(TM)_6Si_5$ phase, contained a lower volume fraction of the granular particles.

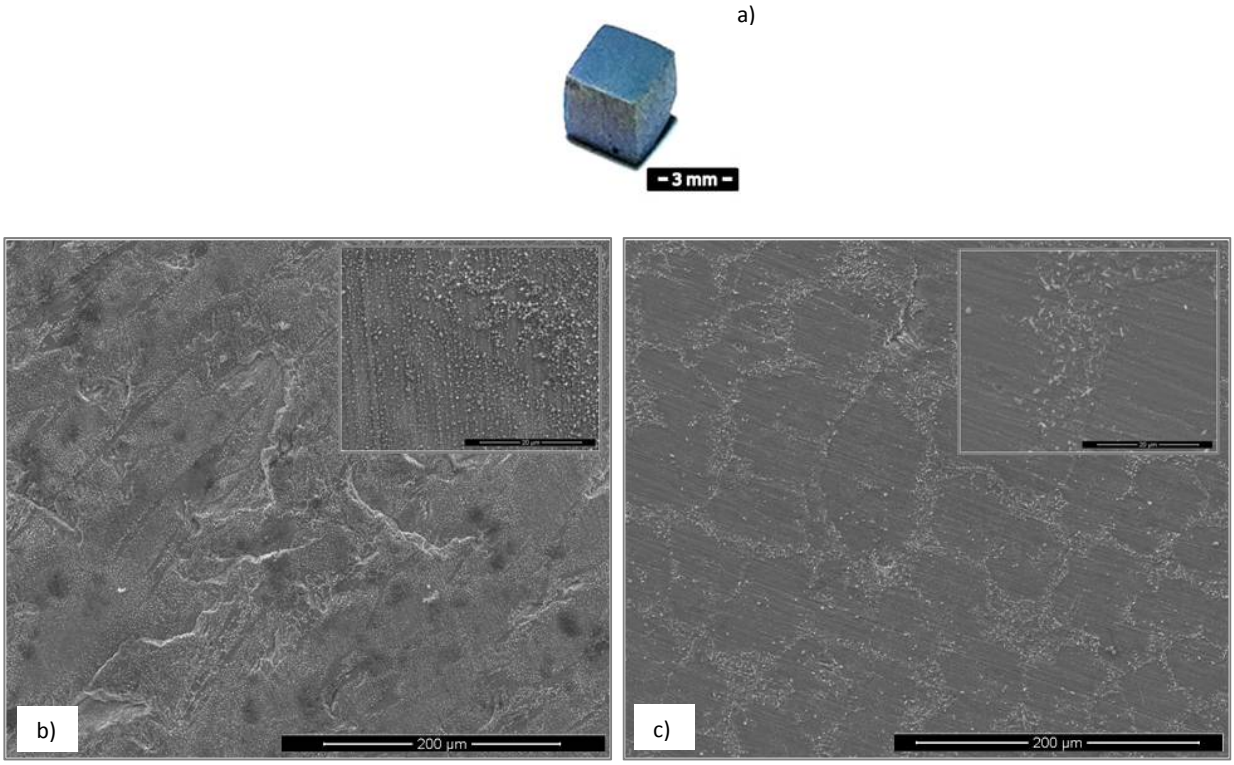

Figure 63. Images of alloy alloy OHC1 after isothermal oxidation in air at 800 °C for 100 h (a) Digital image from specimen, and SE images of oxide scale surface (b) oxide parallel to the dendritic growth of $(TM)_6Si_5$, X500 (c) oxide normal to the dendritic growth of the $(TM)_6Si_5$, X600.

The composition (stoichiometry) of the oxides developed over the $(TM)_6Si_5$ phase could be affected by the Fe segregation in this phase because it was observed that the granular oxides developed on this particular phase were coarser in the Fe rich areas (edges). In addition, some porosity was observed on the oxide scale in the centre of the $(TM)_6Si_5$ phase that could be

formed as a result of oxide evaporation; these areas were richer in Nb, Cr and Ti. Black areas in the figure 63c are excess of C deposition for sample preparation.

The EDS analysis performed in the diffusion zone revealed that there was Si depletion in all the phases which would indicate the growth of SiO_2. Near the metal/scale interface this Si depletion was more considerable leading to a phase transformation to phases gradually richer in transition metals.

The glancing angle XRD of the oxide scale was perfomed at different glancing angles. According to the GAXRD data (in figure 64), some peaks from the substrate alloy were still present with a glancing angle $\gamma = 1°$. These were mainly from the $FeSi_2Ti$ and $(TM)_6Si_5$ phases. Other peaks corresponding to the Fe_5Si_3 and Fe(α) were also detected. These phases were the result of phase transformation(s). The oxide peaks corresponded to SiO_2 in the form of cristobalite (JCPDS 39-14250), $(Cr,Fe)_2O_3$ (JCPDS 02-1357)and TiO_2 (rutile) (JCPDS 89-4920). According to EDS the oxide composition could be $(Ti,Cr)O_2$, $(Ti,Cr,Nb)O_2$ depending on the composition of the oxidised underlaying phase in the substrate.

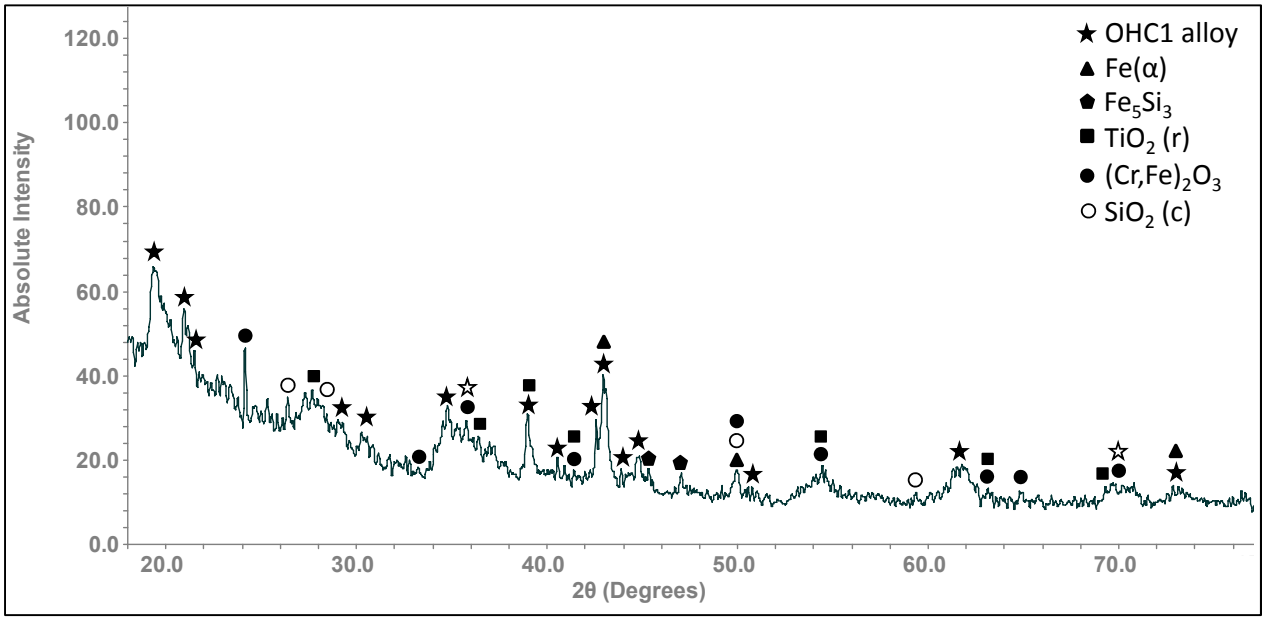

Figure 64. Glancing angle XRD data ($\gamma = 1°$) for the oxide scale formed on the alloy OHC1 in air at 800 °C.

The elemental X-ray maps from the surface of the oxide scale are shown in figure 65, and illustrate the elemental distribution of the oxides according to their location on the alloy surface. The maps reveal the development of different oxide compositions on the surface of the alloy OHC1. Considering the GAXRD data in figure 64 and figure 65, the SiO_2 and possibly some Fe_2O_3 formed over the (Fe,Cr,Ti)Si phase, coarse granular particles over the $FeSi_2Ti$ phase seem to be composed of a Ti-rich oxide enriched by Cr with a very weak Si signal, and over the $(TM)_6Si_5$ some SiO_2 was found together with Ti rich-oxide with some Cr and Nb enrichment and some oxides of the $(Cr,Fe)_2O_3$ type.

Qualitative chemical analysis was performed on the oxides (Figure 66). This confirmed that continuous SiO_2 was present all over the alloy but at different volume fraction depending on the oxidised phase and the dominant oxide. However, this analysis was not conclusive because some heavier elements could be detected from beneath the oxide scale.

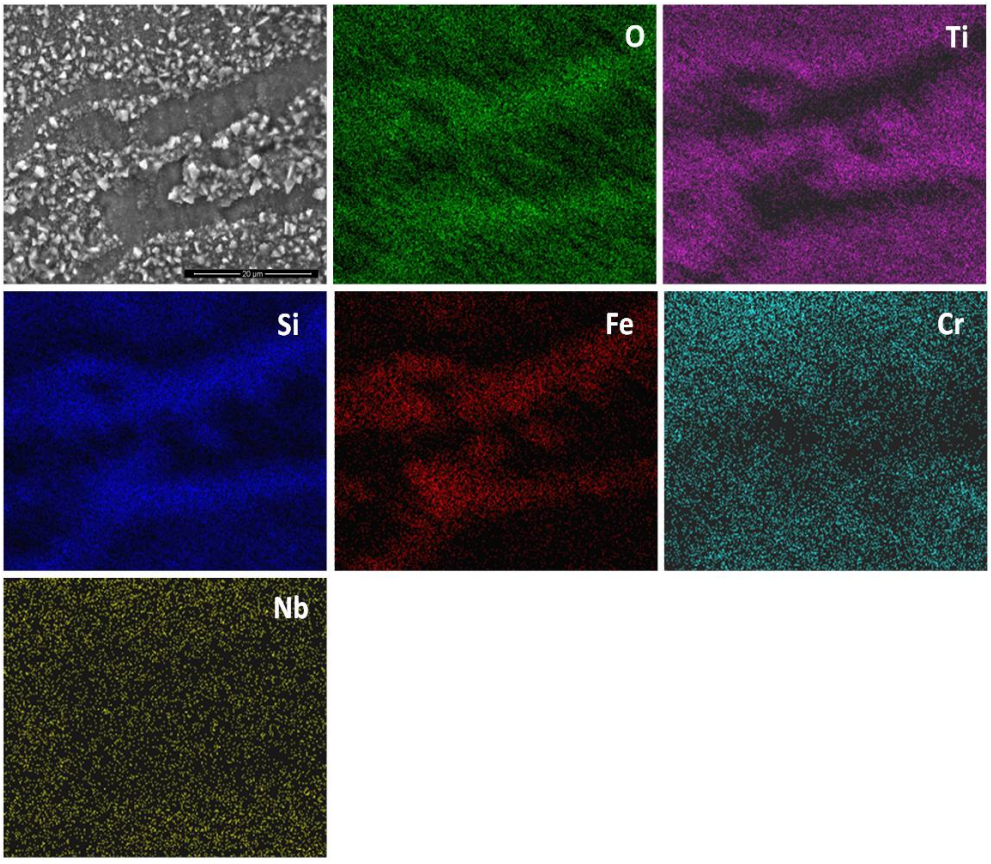

Figure 65. X-ray elemental maps from the oxide surface of the alloy OHC1 after isothermal oxidation in air at 800 °C for 100h, X4000.

The cross section of the alloy OHC1 after oxidation at 800 °C shown in figure 67a, depicts the thickness of the oxide scale and shows that there was a minimum metal recession. However, there were some areas in the metal/scale interface that showed cracks possibly due to embrittlement.

The thickness of the oxide scale formed on the alloy OHC1 was in the range 1-6 µm. This difference could be attributed to different oxidation rates of the phases that compose this alloy and their anisotropy, leading to an uneven scale thickness. Besides, the scale was composed by different oxides, all of them involving different oxygen and metal transport mechanisms.

The secondary image of the cross section of the specimen shown in figure 67b shows the scale integrity. While some areas were covered by a continuous oxide that enveloped granular particles, some other areas presented cavities in the metal/scale interface. Minimum metal recession in the metal/scale interface is also observed. In the figure 67c, cavities and porosity can also be seen across the oxide scale.

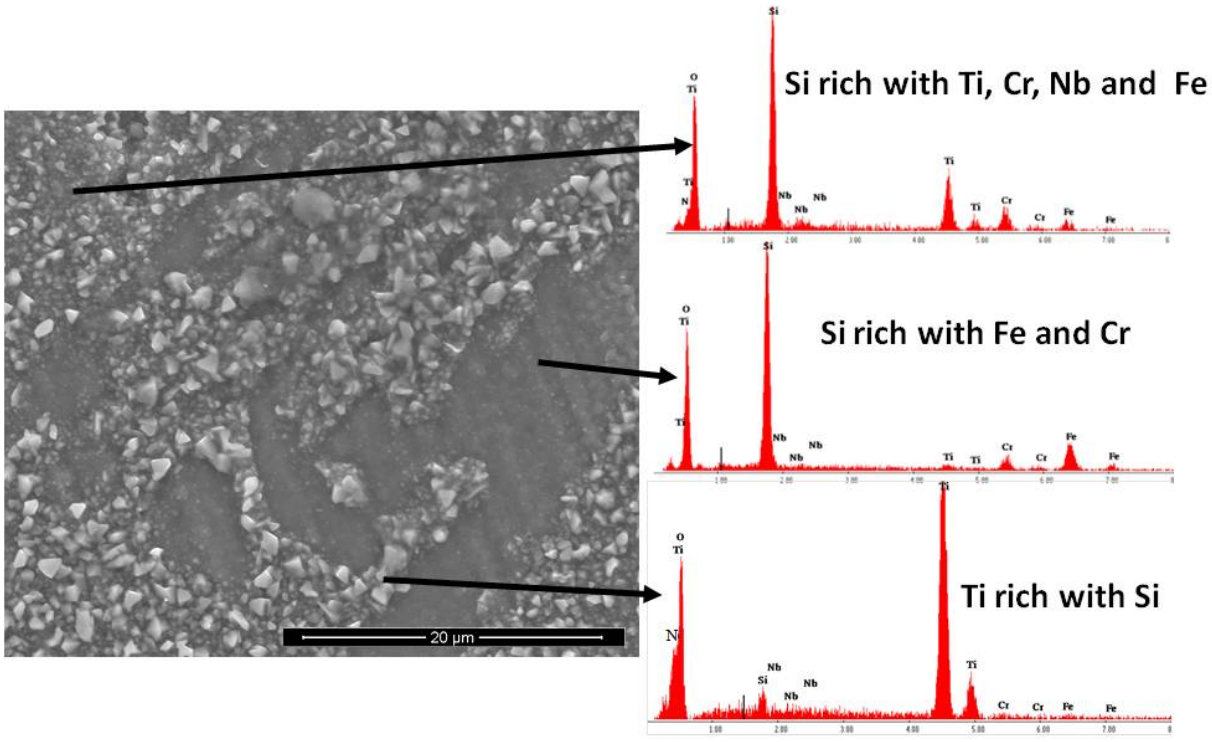

Figure 66. EDS analyses of three different regions from the oxide surface of alloy OHC1 al after isothermal oxidation in air at 800 °C for 100 h, X6000.

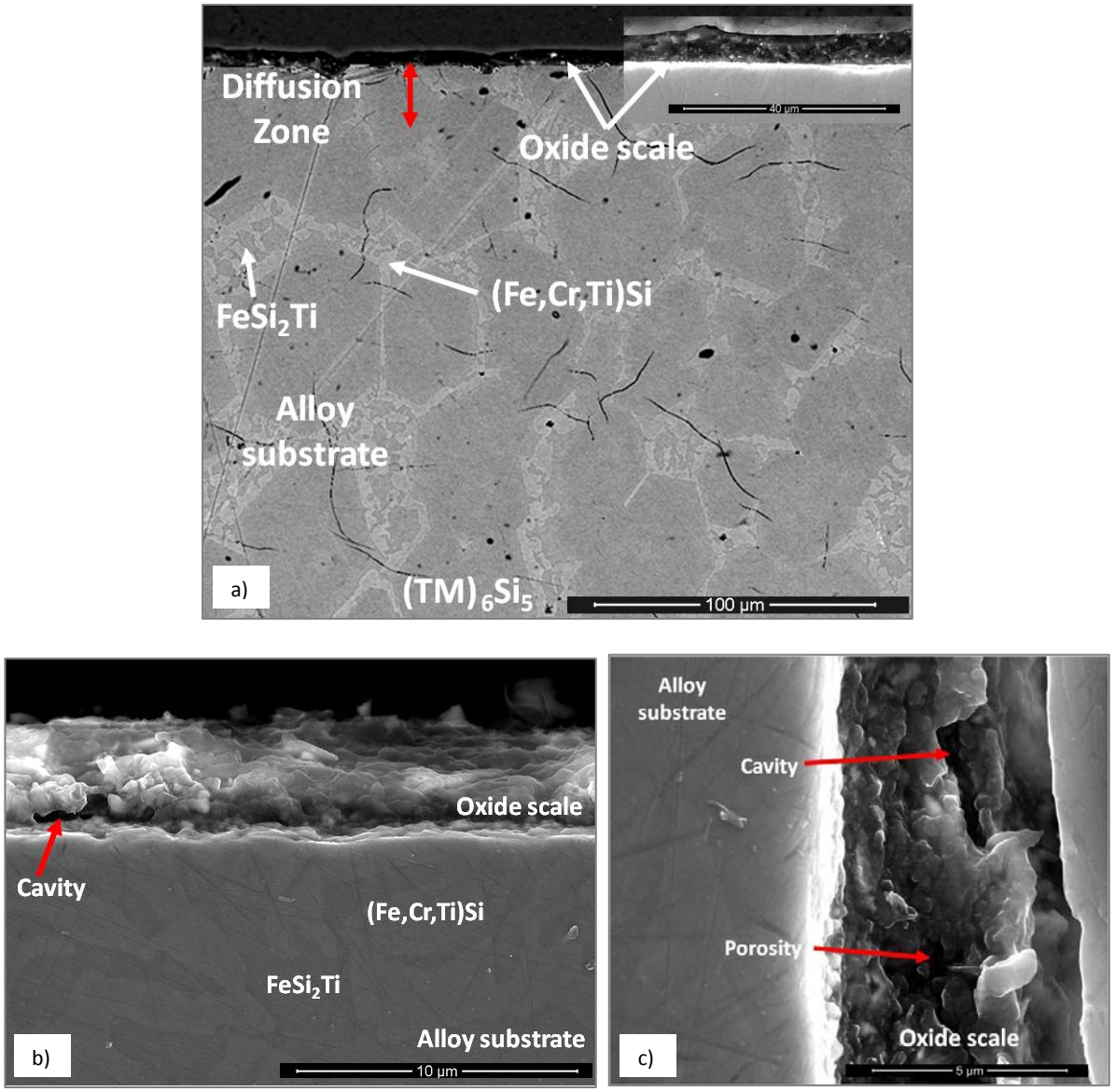

Figure 67. Images of the cross section of the alloy OHC1 after isothermal oxidation in air at 800 °C for 100 h, (a) BSE image, X1000, (b) SE image of the scale/metal interface, X12000 (c) SE image showing cavity and porosity in the oxide scale, X20000.

The X-ray elemental maps in figure 68 show the elemental distribution in the cross section of the specimen. This figure would suggest that there was no internal oxidation in the alloy. In addition, some important microstructural characteristics of the alloy OHC1 alloy can be also observed, the faceted hexagonal cross section of the $(TM)_6Si_5$ dendrites with its edges defined by the (Fe,Cr,Ti)Si phase, with the latter surrounding the $FeSi_2Ti$ phase. The oxide contains Si

that is also found in the oxide scale surface (the contrast from the Si pixels is not strong in the Si map). Moreover, in the oxide scale Ti, Fe and Cr were also observed.

The oxide growth by the further diffusion of oxygen and metal through the oxide scale, could develop compressive stresses and possibly some buckling and cracking.

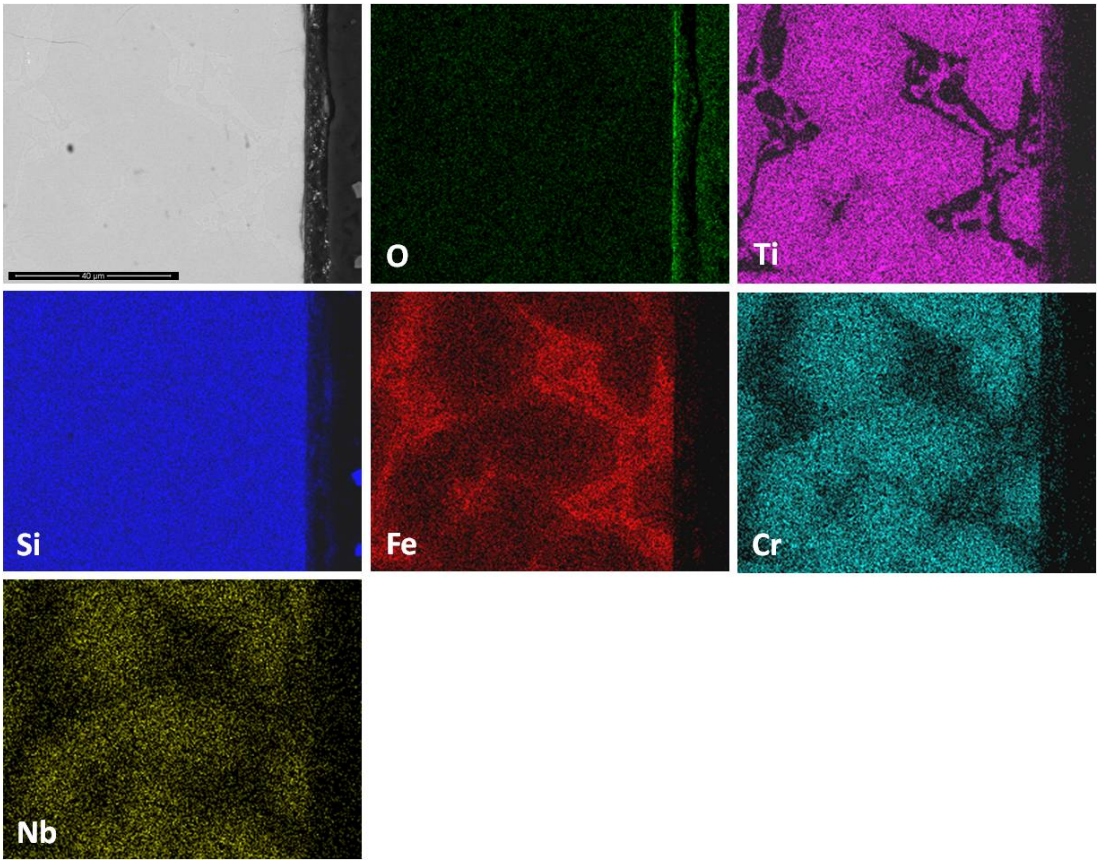

Figure 68. X-ray elemental maps from a cross section of the alloy OHC1 after isothermal oxidation in air at 800 °C for 100 h, X3500.

The contrast of the phases under BSE imaging did not change significantly near the metal/ scale interface, and the elemental X-ray map did not detect changes in Si concentration. The EDS chemical analysis performed along the diffusion zone of the oxidized specimen revealed that there was some Si depletion in all the phases as a result of selective oxidation. Furthermore, it was detected that some phases had decomposed after this Si depletion. The phases mostly affected by this phenomenon were the (Fe,Cr,Ti)Si and $FeSi_2Ti$ that were found to be gradually enriched with Fe. The Si depletion of the (Fe,Cr,Ti)Si lead to the formation of Fe_5Si_3 and Fe(α) at

the metal/scale interface, while in the case of the $FeSi_2Ti$ phase lead to the formation of τ_3 (from the Ti-Fe-Si system see section 1.6.9) and Fe(α). There was Si depletion from the $(TM)_6Si_5$, but not enough to decompose this phase. The Si depletion at the metal/scale interface and the mechanical damage to the SiO_2 layer as a result of the development of strains due to changes in volume (due to phase transformations), could lead to further oxidation by fast growing mixed oxides. Considering the scale composition and the above discussion it is possible that within the scale some strains could arise as different oxides formed, all with different volumes and yet more variations in chemistry affecting their volume during their growth.

Microstructure of oxide scale of Si-22Fe-12Cr-12Al-10Ti-Nb (alloy OHC2)

After isothermal oxidation in air at 800 °C for 100 h, the cubic specimen retained its shape with visibly well defined edges; it had a black colour with some blue and reddish tones (Figure 69). The oxide scale remained attached and did not present oxide spallation, which is in accordance to the oxidation behaviour observed in figure 62.

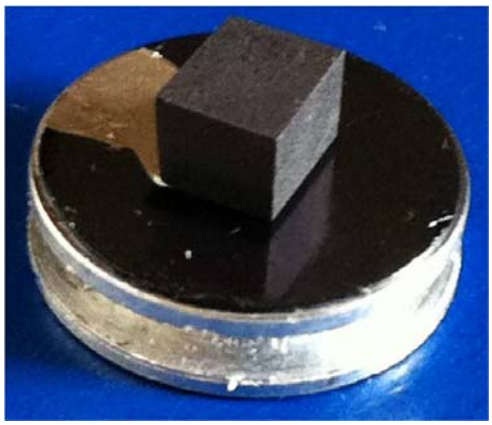

Figure 69. OHC2 specimen after isothermal oxidation at 800 °C for 100h.

The SE image in figure 70a shows the morphology of the surface of the oxide scale. After oxidation it was still possible to observe some microstructural characteristics of the alloy OHC2 and the scale was composed of different oxides. A continuous and adherent bright oxide with darker contrast near the Fe-rich interdendritic areas was formed over the elongated $(TM)_6Si_5$ grains (Figure 70b) and similar surface characteristics were observed for the oxide formed over

the $FeSi_2Ti$ phase. In figure 70a it is possible to observe the blade like whiskers grown over the $Fe_3Al_2Si_3$ phase and in the insert in figure 70b their contrast under BSE conditions.

The thickness of the oxide scale was not constant, in view of the fact that the phases in the alloy formed different oxides, with different oxidation rates and different microstructures.

The glancing angle XRD data (γ= 5°) in figure 71 had peaks that corresponded to the cubic γ-Al_2O_3 (JCPDS 29-63), and monoclinic θ-Al_2O_3 (JCPDS 35-121), monoclinic Al_2SiO_5 (JCPDS 44-27) and anorthic Al_2SiO_5 (JCPDS 11-46), SiO_2 (JCPDS 82-1556) trydimite, $FeTi_{3-x}O_x$ (JCPDS 09-320) and tetragonal TiO_2 (JCPDS 82-514).

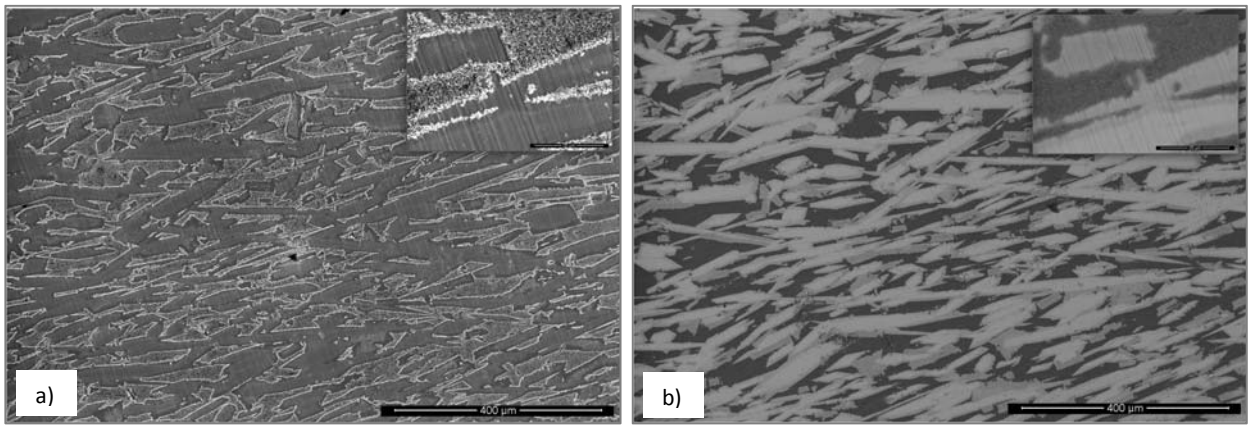

Figure 70. Oxide surface of the alloy OHC2 after isothermal oxidation in air at 800 °C for 100 h (a) SE image, X100, (b) BSE image, X100.

The X- ray elemental maps from the oxide surface in figure 72 show elemental distributions on the oxide scale. The whiskers developed over $Fe_3Al_2Si_3$ were Al_2O_3, over the $FeSi_2Ti$ phase formed the Al_2SiO_5, and $Ti_xFe_{(3-x)}O_x$, while over the scarcely oxidized $(TM)_6Si_5$ phase formed some SiO_2, Al_2O_3 and some $(Ti,Cr,Nb)O_2$ rutile type oxide.

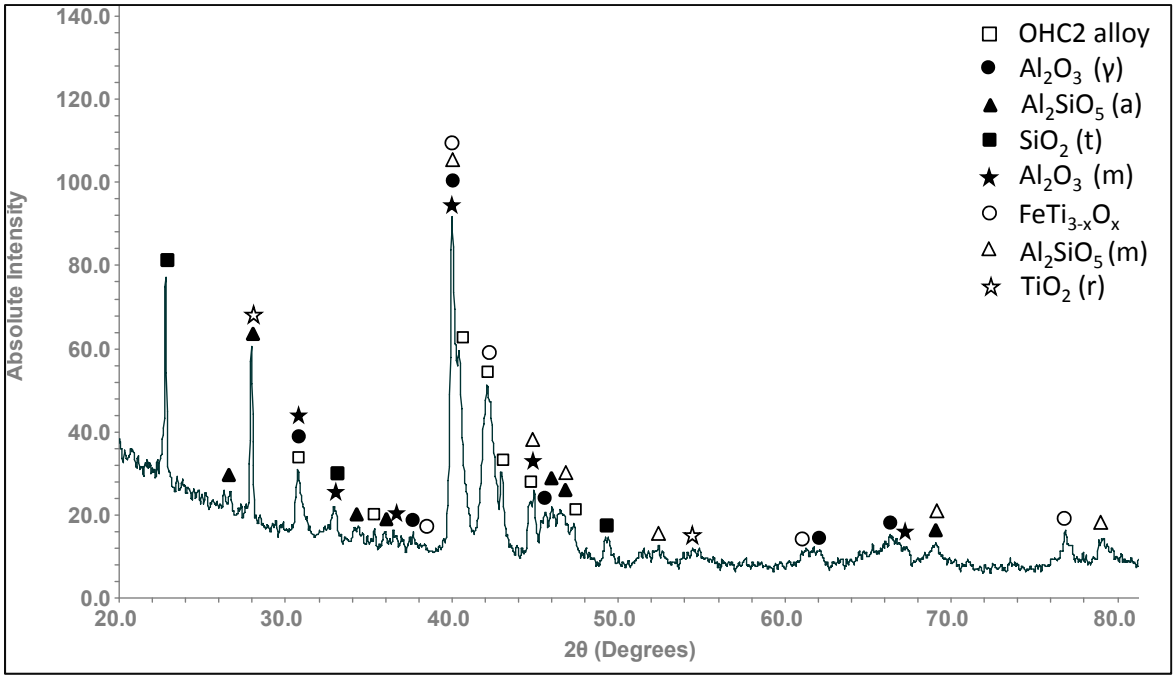

Figure 71. Glancing angle XRD data (γ= 5°) for the oxide scale formed on the alloy OHC2 in air at 800 °C for 100 h.

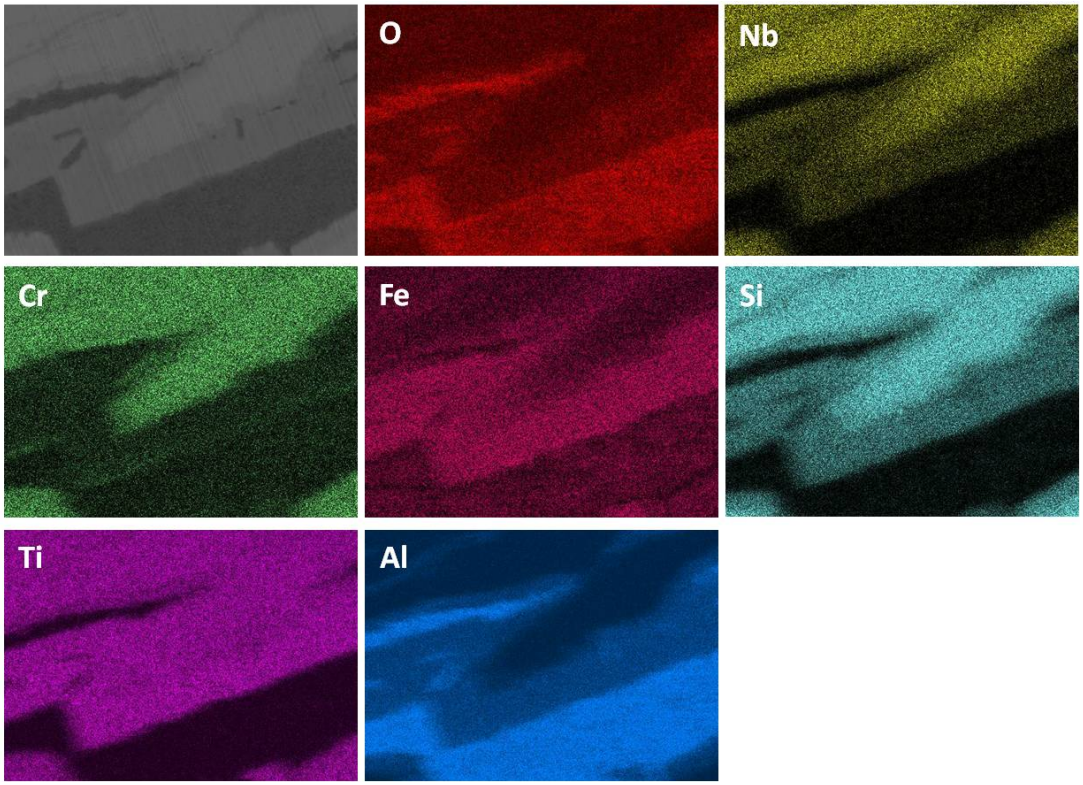

Figure 72. X-ray elemental maps from oxide surface of the alloy OHC2 after isothermal oxidation in air at 800 °C for 100h, X1500.

Cross section images from the oxide scale formed on the alloy OHC2 are shown in figure 73. The scale looks continous and adherent all over the alloy, and the profile of the oxide over the $(TM)_6Si_5$ phase shows a smaller thickness. The Al_2O_3 blade-like whiskers developed on the oxide surface over the $Fe_3Al_2Si_3$ phase can not be seen, because they could be easily removed during the sample preparation (Figure 73a). According to Kofstad (1988), these types of oxides grow from thick films or scales and they have been found not to be in direct contact with the metal.

The BSE image of the cross section (figure 73b) shows the oxide scale within the dark contrast area, a small change in the contrast of the $FeSi_2Ti$ phase, perhaps as a result of Al and Cr depletion. At the metal/scale interface this phase presented some areas that suggested that oxygen penetrated and preferentially oxidised Al without the formation of oxide internal precipitates in the matrix.

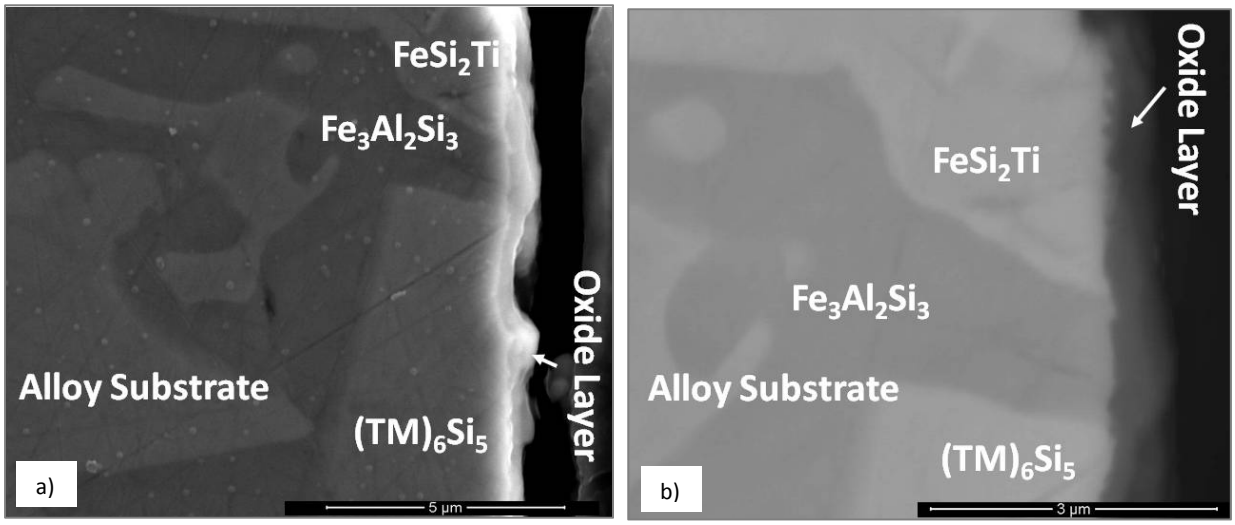

Figure 73. Images from a cross section of the alloy OHC2 after isothermal oxidation in air at 800 °C for 100h, a) SE image, X2000, (b) BSE image, X40000.

The elemental distribution in the cross section of the oxide scale is shown in figure 74. Apparently, Al_2O_3 was the main component of the oxide scale. Fe enrichment can be observed at the metal/scale interface (below the Al_2O_3 oxide layer) on the $Fe_3Al_2Si_3$ phase. Also observed were Cr concentrations in the metal/scale interface, some oxygen dissolution into the alloy, and Cr enrichment at the grain boundaries of the $FeSi_2Ti$ phase.

The elemental X-ray maps of the cross section showed a continuous Al_2O_3 layer between the $FeSi_2Ti$, $Fe_3Al_2Si_3$ and $(TM)_6Si_5$ phases. In figure 74 it is not evident that Al_2O_3 forms from the oxidation of the $(TM)_6Si_5$, it is possible that the strong contribution from the heavier elements of this phase makes it look as if it made a minimum contribution. The low Al content of this phase should be enough for it to contribute to form Al_2O_3 under these conditions.

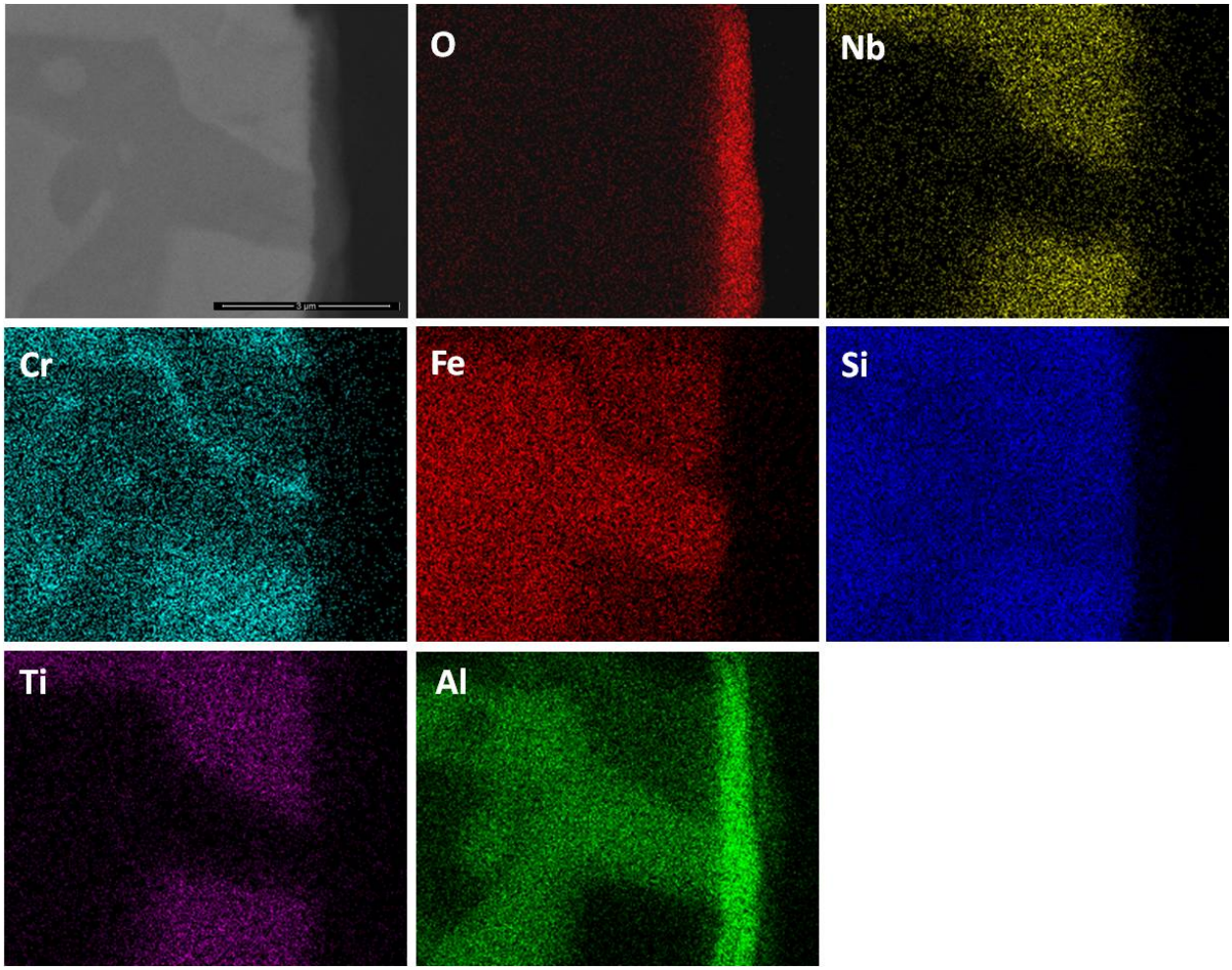

Figure 74. X-ray elemental maps from across section of the alloy OHC2 after isothermal oxidation in air at 800 °C for 100h, X20000.

3.2.2.2 Thermo-gravimetric analysis (TGA) at 1200 °C

Thermo-gravimetric analysis of Nb-15Ti-15Cr-23Fe-46S1 (alloy OHC1) at 1200 °C

The weight gain per unit area versus time data is plotted in figure 75. The data gives paralinear behaviour of the alloy OHC1 after oxidation at 1200 °C for 100 h, see Table 16. Indeed, the data analysis using equation (1), gave n = 0.68 (Table 16). Even though the n value is more close to parabolic, the analysis of the data suggests that the controlling mechanism was paralinear. During the experiment, the first 40 h registered a parabolic weight gain and in the following 60 hours the weight gain was linear. The mass gain of this alloy was 1.60 mg/cm^2. The protective character of the oxide scale was lost after the first 40 h. The nature of the oxides and some oxide volatilization could be responsible for the consecutive rise of the oxidation rate.

The K_p and K_l values in Table 16 were obtained by plotting gain weight versus time using equation (2) and (3), respectively.

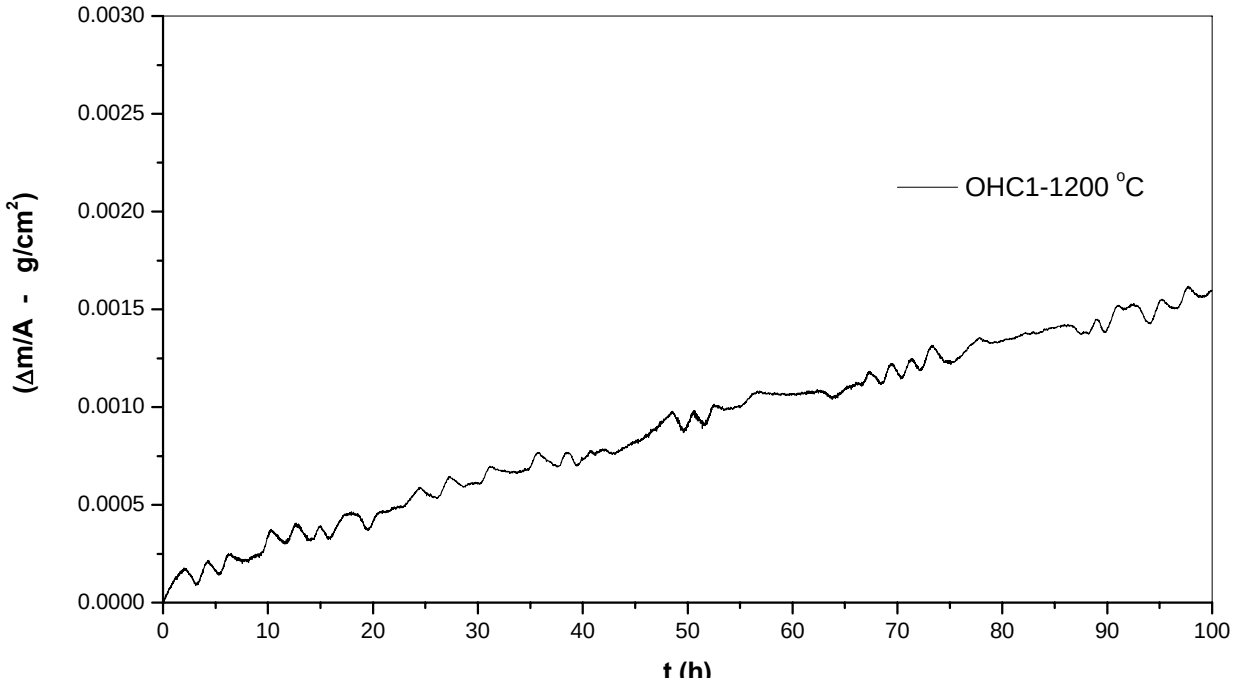

Figure 75. Isothermal oxidation behaviour of the alloy OHC2 in air at 1200 °C for 100 h.

Microstructure of the scale oxide of Si-23Fe-15Cr-15Ti-Nb (alloy OHC1)

After isothermal oxidation in air at 1200 °C, the oxidised specimen had retained its shape and had visibly well defined sharp edges and the scale had good adherence (figure 76a). The SEM images obtained from the oxide surface showed that in the oxide scale formed on the specimen there were visible layering, voids and discontinuities (Figure 76b).

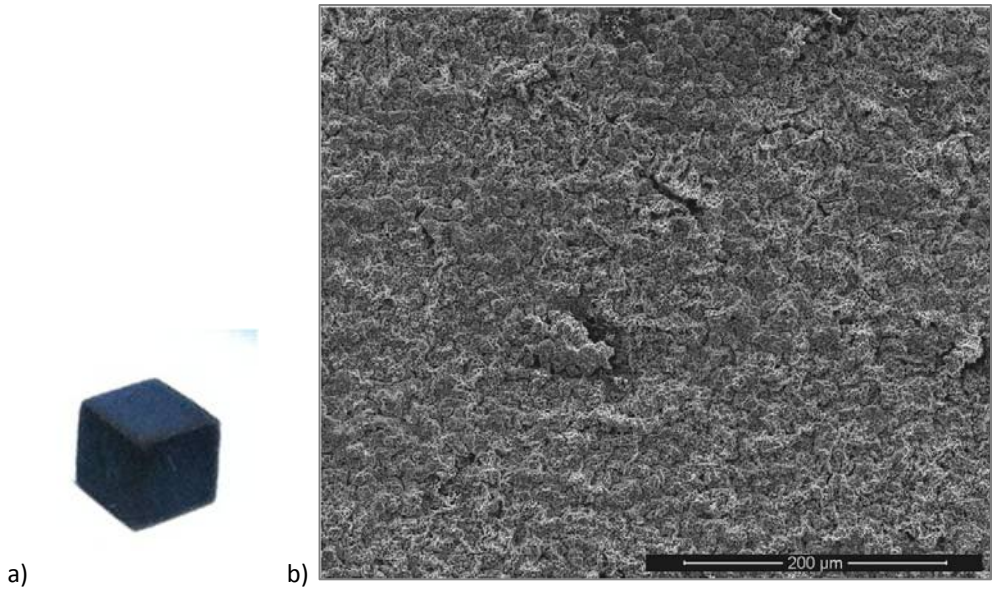

a) b)

Figure 76. Alloy OHC1 after isothermal oxidation in air at 1200 °C for 100 h, (a) oxidized specimen and, (b) SE image of the oxide surface, X500.

The XRD glancing angle data in figure 77, confirmed the presence of Cr_2O_3 (JCPDS 38-1479), at least two crystalline forms of SiO_2 (cristobalite JCPDS 39-1425, and quartz JCPDS 70-2537), TiO_2 (JCPDS 84-1284) and FeO (JCPDS 06-0615). The oxides were observed in the scale according to their microstructure, chemical analysis and the elemental distribution in the elemental X-ray maps.

Figure 78, shows the three typical morphologies of the oxides that composed the scale formed on the surface of the alloy. The insert image 1 shows the regions composed by granular oxide particles with different sizes formed on the surface of the $(TM)_6Si_5$ phase that were of the higher volume fraction. In the insert image 2 we observe that these regions were found in contact with areas covered by finer particles of an oxide with a glassy appearance on the top. In

insert image 3 there were some areas in which the microstructure looked more like a network formed by the melting of some oxide, this was particularly observed on the surface of the (Fe,Cr,Ti)Si phase .

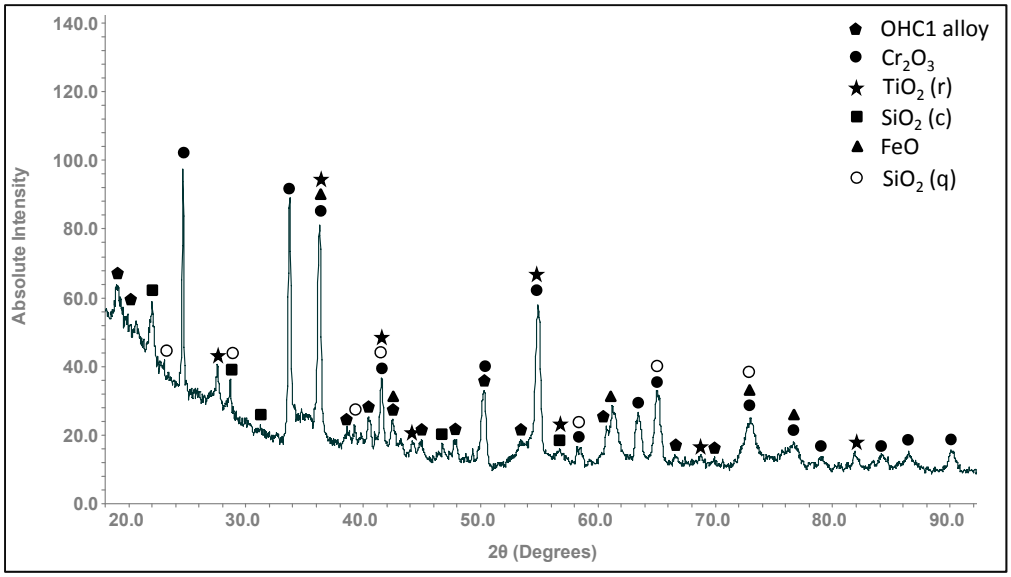

Figure 77. Glancing angle XRD data (γ= 10°) for the oxide scale formed on the alloy OHC1 at 1200 °C in air.

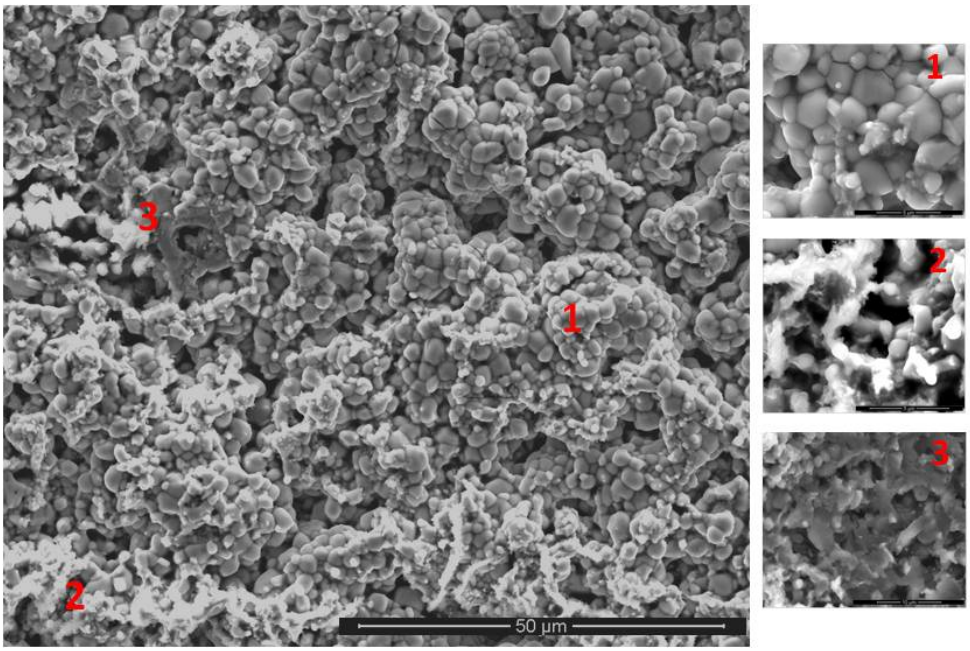

Figure 78. SE images of the oxide surface of the alloy OHC1 after isothermal oxidation in air at 1200 °C for 100 h, X1500, on the right the microstructures from different zones in the oxide (1) X8000, (2) X16000 and (3) X20000.

The images of the surface of the oxide scale illustrated that the oxide scale was mainly composed by agglomerated particles of Cr_2O_3 with different sizes that did not form a continuous oxide scale, showing clear discontinuities, possibly as a result of oxide evaporation, porosity and cracking resulting by the formation of oxides with different chemistry.

The areas in which SiO_2 was formed with a glassy like appearance on the oxide surface were mostly found at the grain boundaries between the (Fe,Cr,Ti)Si and $FeSi_2Ti$ phases.

According to the cross section images in Figure 79, the oxide scale was mainly composed of two oxide layers, where the Cr_2O_3 was mostly found in the outer part of the scale and the SiO_2 in the inner part. $(Cr,Ti)_2O_3$ was also found at the metal base interface in contact with the scale, these areas left some voids behind possibly as a result of metal transport through the oxide scale. In addition, the base metal at the metal/scale interface was composed of the $FeSi_2Ti$ and (Fe,Cr,Ti)Si phases suggesting that the $(TM)_6Si_5$ phase had transformed to $FeSi_2Ti$ phase when the Cr was preferentially oxidized and the (Fe,Cr,Ti)Si phase was oxidized and formed Si and Fe oxides.

There was also evidence of internal oxidation (Figure 79) with the oxide particles distributed not randomly. Chemical analysis revealed that these particles were mainly composed of a Si rich oxide.

The elemental distribution in a cross section of the alloy OHC1 after the isothermal oxidation at 1200 °C is shown in figure 80. The maps show that the outer part of the oxide scale was composed of Cr_2O_3 and the inner part of SiO_2. The presence of Ti, Fe and Nb (if any) in the oxide scale was weak, suggesting that Ti and Fe could be in solution in Cr_2O_3 considering that Fe_2O_3, and Cr_2O_3 have the same crystal structure. The Nb could be in solution in the TiO_2 phase.

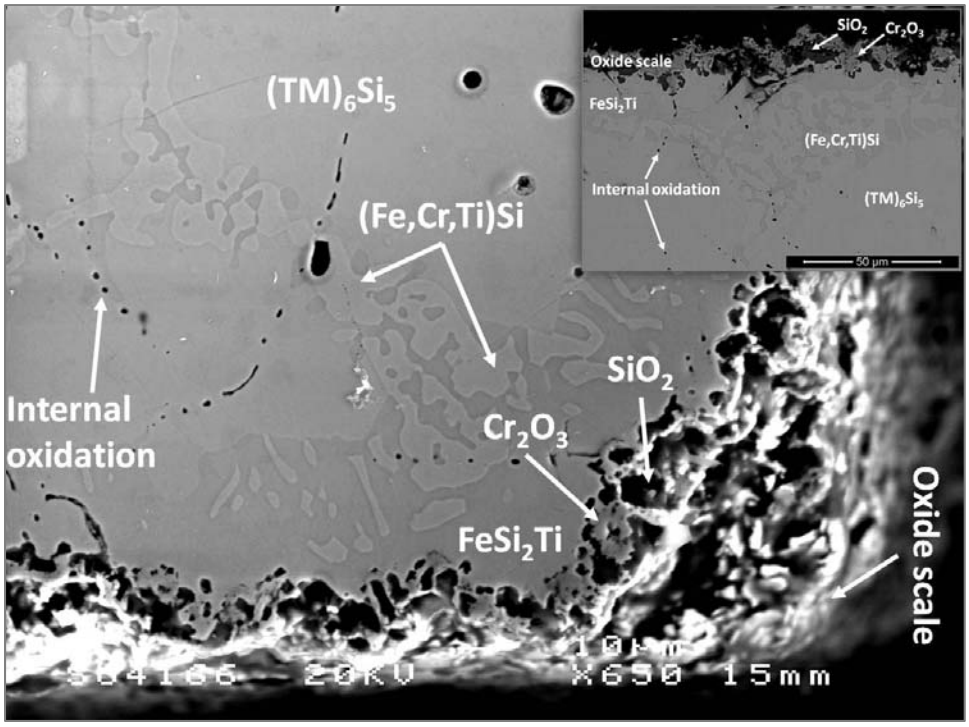

Figure 79. SEM images of the cross section of the alloy OHC1 after isothermal oxidation in air at 1200 °C for 100 h, the insert is from the corner (BSE image, X1500) at X650.

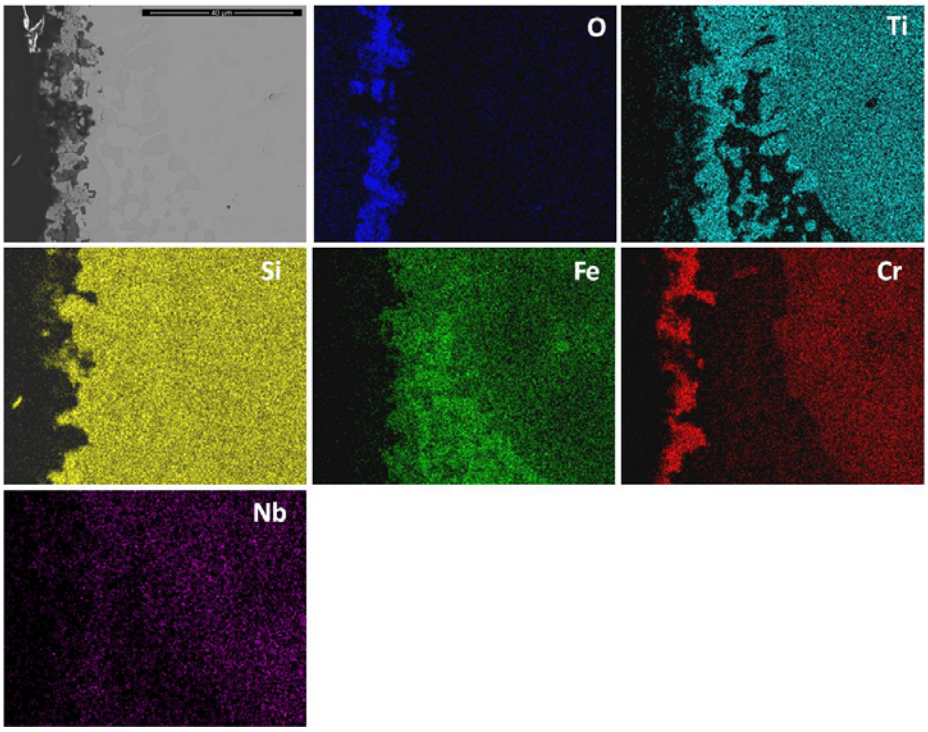

Figure 80. X-ray elemental maps from a cross section of the alloy OHC1 after isothermal oxidation in air at 1200 °C for 100h, X3500.

3.3 Discussion

3.3.1 Microstructures

Alloy OHC1

The existence of macrosegregation of Cr, Fe, and Ti in the alloy OHC1-AC makes it highly likely that different solidification paths were followed in different parts of the cast alloy. The large area analyses showed that the top and centre (bulk) areas of the button ingot had similar composition and that the near the bottom and chill zone areas of the ingot were richer in Fe, in particular the latter area. The microstructure studies also showed that in the near the bottom and chill zone areas of the ingot a lamellar eutectic was formed.

The phases present in the microstructure of the alloy OHC1 exhibited solubility for TM elements. The compositions of the T and (Fe,Cr,Ti)Si phases changed little after the heat treatment compared with the τ_1 phase. The identification of phases, as given in Table 11, was done using the XRD data, which confirmed the presence of FeSi, T and τ_1, and the EDS analysis data. The phase for which the EDS gave Si ≈ 50 at% with high solubility for Fe and TM/Si ratio of ~ 1 was designated as the (Fe,Cr,Ti)Si. The composition of the latter regarding Ti is also in agreement with Weitzer et al. (2008) who reported that the solubility of Ti in FeSi is about 1 at%. Given the high solubility of Cr in FeSi, the present data would suggest that the addition of Ti restricted significantly the solubility of Cr in this phase. The phase for which the EDS gave Si ≈ 50 at% and TM/Si ~ 1 but with high solubility for Ti and Fe, which after the heat treatment moved closer to the values given for the τ_1 (considering Ti and Cr together) by Weitzer et al (2008), was designated as the τ_1 ($FeSi_2Ti$). The phase with about 46 at% Si and TM/Si=6/5 was designated as the T phase that exists in the Cr-Ti-Si system (Lysenko et al, 1971, Du and Schuster, 2002) where it has a large solubility range (Figure 81).

The microstructure studies pointed to the T phase being the primary phase to form from the melt in all parts of the ingot. This is consistent with the temperatures where the types of phases observed in the alloy OHC1-AC can be in equilibrium with the melt in the Cr-Ti-Si system studied

by Du and Schuster (2002), and the Fe-Ti-Si system studied by Weitzer et al. (2008). In the former system the T phase is stable below 1565 °C and in the latter the τ_1 ($FeSi_2Ti$) is stable below 1532 °C and the FeSi below 1328 °C. Alloying the latter intermetallic with Cr would be expected to increase only slightly the above temperature (the FeSi and CrSi have the B20 structure and similar melting temperatures) but the effect of alloying with Ti could be more significant but would not raise the melting temperature of (Fe,Cr,Ti)Si above 1532 °C (in the Si rich region of the Fe-Ti-Si system the TiSi is stable below 1450 °C). This deduction is also consistent with the peritectic reaction L + τ_1 ($FeSi_2Ti$) $\rightarrow$ FeSi + τ_4 ($Fe_{28.1}Ti_{26.3}Si_{45.6}$) suggested by Weitzer et al. (2008). Thus, on the basis of the above discussion, the formation sequence, in terms of decreasing temperature, of the intermetallics in the alloy OHC1-AC should be T, then τ_1 ($FeSi_2Ti$) and finally (Fe,Cr,Ti)Si.

The formation of the T phase in the top and centre (bulk) of the ingot was accompanied by the partitioning of Fe and Cr, Nb and Ti. Iron was rejected into the melt, while the other elements partitioned in the solid, see figure 45. Thus, as the T phase was formed the surrounding melt became richer in Fe and leaner in Cr, Nb and Ti. It should be noted that the τ_1 ($FeSi_2Ti$) + (Fe,Cr,Ti)Si eutectic that was formed in OHC1-AC in-between T phase dendrites was richer in Fe and lean in Nb, Ti and Cr compared with the alloy composition. Furthermore, partitioning of solutes was not observed in the T phase in the near the bottom and chill zone areas of the ingot, owing to the high cooling rates prevailing in these areas. However, in these areas the melt was richer in Fe and leaner in Cr, Nb and Ti compared with the top and bulk of the ingot and the alloy composition.

In the top and bulk of the alloy OHC1-AC the T, τ_1 ($FeSi_2Ti$) and (Fe,Cr,Ti)Si phases were observed. The latter two phases were formed in-between the T phase dendrites, but it was not clear from the observed microstructure whether the τ_1 ($FeSi_2Ti$) was surrounded by the (Fe,Cr,Ti)Si, which would be consistent with a peritectic reaction or formed lamellae next to the (Fe,Cr,Ti)Si, which would be consistent with the eutectic L $\rightarrow$ τ_1 ($FeSi_2Ti$) + (Fe,Cr,Ti)Si, which was observed in the bottom and chill zone of the ingot.

A peritectic reaction would explain some of the microstructures shown in the figure 44 but is not in agreement with the peritectic reaction suggested by Weitzer et al. (2008) (see above) because the presence of the τ_4 ($Fe_{28.1}Ti_{26.3}Si_{45.6}$) was not confirmed by XRD (see also below). Some of the analyses designated as the T phase in Table 11, correspond to the latter composition (i.e., of the τ_4 phase) thus it could be argued that, owing to the partitioning of solutes, some τ_4 was actually present near the (Fe,Cr,Ti)Si. However, if the aforementioned peritectic reaction had occurred one would expect it to move towards completion upon heat treatment, which means that the size and volume fraction of the τ_1 ($FeSi_2Ti$) would decrease and the size and volume fraction of (Fe,Cr,Ti)Si would increase after the heat treatment. Exactly the opposite was observed, figure 48.

Thus, it is suggested that the solidification path in the top and centre (bulk) parts of the ingot was $L \rightarrow L + T$ with the Fe rich and Cr, Nb and Ti lean interdendritic melt (formed because of the solute partitioning) undergoing the eutectic reaction $L \rightarrow \tau_1$ ($FeSi_2Ti$) + (Fe,Cr,Ti)Si, locally resulting in a microstructure consisting of the two phases and an overall microstructure consisting of the T, τ_1 ($FeSi_2Ti$) and (Fe,Cr,Ti)Si phases but with a very small volume fraction of τ_1, owing to the composition of the interdendritic melt relative to the eutectic composition. According to the data in Weitzer et al. (2008), the solubility (composition) range of the τ_1 ($FeSi_2Ti$) phase is very tight, which could be another reason for its difficulty to form in the top and bulk of OHC1-AC. Indeed, the composition of this phase moved closer to the one reported by Weitzer et al. (2008) after the heat treatment, owing to the partitioning of solutes in the microstructure.

In the near the bottom and chill zone areas of the ingot, the solidification path was essentially the same as described above but because the melt was already richer in Fe and leaner in Cr, Nb and Ti (owing to the macrosegregation of elements in OHC1) the interdendritic melt was closer to the eutectic composition and thus the volume fraction of the eutectic was higher in these areas of the ingot. Formation of the $L \rightarrow \tau_1$ ($FeSi_2Ti$) + (Fe,Cr,Ti)Si eutectic in OHC1-AC is also consistent with the coarsening of the eutectic phases and the changes in their volume fractions are attributed to the microstructure moving towards equilibrium. Furthermore, the

composition of the above eutectic (see Table 11) is very close to the eutectic between the τ_1 ($FeSi_2Ti$) and FeSi phases in the Fe-Ti-Si system [Weitzer et al. (2008)], when the latter is considered as (Ti,Nb)-(Fe,Cr)-Si. The DSC data provided further support for the above eutectic reaction, when compared with the data in Weitzer et al. (2008).

In the T phase the partitioning behaviour of Nb, Ti and Cr was opposite to that of Fe, as the concentration of the former elements was higher in the core of the T dendrites than at their edges and the opposite was the case for Fe. Thus, for the former elements the partitioning coefficient k_o^{TM} (TM=Cr, Nb, Ti) was greater than one and for Fe it was less than one. The Fe concentration along the length of a T dendrite, shown in figure 45, can be described by the solute distribution given by the Scheil equation, which gives the composition of the solid phase $C_s^{Fe} = k_o^{Fe} C_o(1-f_s)^{(koFe-1)}$ where k_o^{Fe} is the partitioning coefficient for Fe, C_o is the Fe content (=23 at%) and f_s is the fraction solidified. For the centre of the dendrite (f_s=0) taking C_s^{Fe} = 12 at% gives k_o^{Fe} = 0.522. The C_s^{Fe} = 28.7 at% (value measured near the boundary of T dendrites) corresponds to $f_s \approx 0.84$. Application of the above equation for Cr and Ti using the data for these elements in figure 45 with C_o for Cr=14.5 at% and Ti=15 at% gives k_o^{Cr} = 1.482 and k_o^{Ti} = 1.267. For these elements, at $f_s \approx 0.84$ the $C_s^{Cr} \approx 9$ at% and $C_s^{Ti} \approx 11.7$ at%, which is in good agreement with the data in figure 45, particularly for Cr.

As discussed above, the composition of the τ_1 ($FeSi_2Ti$) + (Fe,Cr,Ti)Si eutectic was very close to the eutectic between the τ_1 ($FeSi_2Ti$) and FeSi phases in the Fe-Ti-Si system (Weitzer et al. (2008)). If we were to consider the composition of the alloy OHC1 as 16(Ti,Nb)-37.5(Fe,Cr)-46.5Si (at%) then the alloy falls in the FeSi, τ_1, τ_2 (FeSiTi) three phase field in the 900 °C isothermal section of the Fe-Si-Ti system. Given that the τ_2 phase was not observed in OHC1 it is suggested that Cr suppresses the formation of this phase.

Weitzer et al. (2008) also reported that the τ_4=$Fe_{28.1}Ti_{26.3}Si_{45.6}$ phase was present at extremely low volume fraction as a fourth phase in some of their alloys with compositions within the FeSi-τ_1-τ_2 field. This phase was formed in their as cast alloys, decomposed after annealing at 1000 °C and was present after prolonged annealing at 900 °C. Weitzer et al. (2008) did not provide XDR

data for this phase that was always found in traces in their analyzed miscrostructures. In the present work the composition of the Fe-rich $(TM)_6Si_5$ phase (Table 11) is close to the composition of the τ_4 but it is clear that Fe-rich $(TM)_6Si_5$ is not the τ_4 since this phase was formed at considerable volume fraction and was confirmed by XRD.

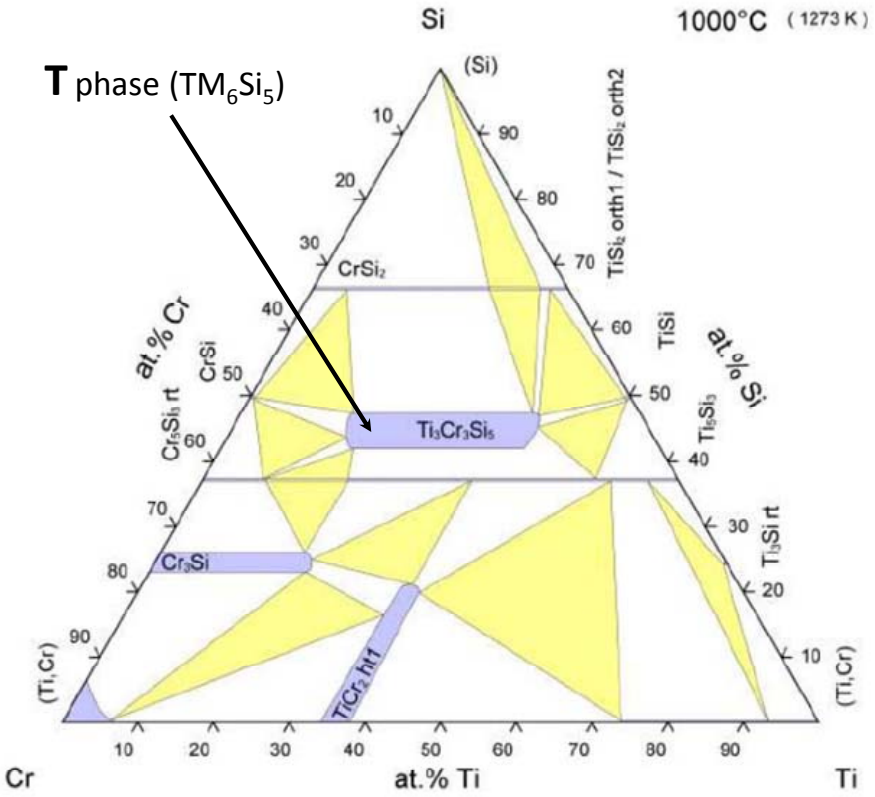

Figure 81. Ti-Cr-Si Isothermal section obtained by Lysenko et al. (1971).

Alloy OHC2

In the alloy OHC2-AC there was macrosegregation of all the elements (Table 13). The compositions of the top and bulk areas were close to the nominal. In the bottom a chill zone was formed, in which the Fe and Al concentrations were the highest and the Nb, Ti and Si were the lowest. Moreover, near the chill zone a eutectic and some porosity were found. Different microstructures were observed from the top to the bottom, which would suggest that different solidification paths were followed in different parts of the button ingot.

The phases present in the microstructure of OHC2-AC exhibited solubility for the TM elements. The compositions of all the phases changed little after the heat treatments except the (Fe,Cr)(Si,Al) phase that was not stable after the heat treatment at 950 °C. The identification of phases, as given in Table 13, was done using the XRD and EDS data. The indexed XRD data of the alloy OHC2 as cast and the after heat treatments is shown in figure 54. The identification of the phases was done based on data in the literature about the Fe-Ti-Si, Cr-Fe-Si, Ti-Cr-Si, Al-Cr-Si, Al-Fe-Si and Nb-Cr-Si systems.The phases in the alloy OHC2-AC were as follows: $(TM)_5Si_3$, $(TM)_6Si_5$, $FeSi_2Ti$, (Fe,Cr)(Si,Al), $Fe_3Al_2Si_3$ and the dark phase DP. The dark phase could belong to the Fe-Si-Al system. Its composition ranges were between those of the proposed τ_{10} and τ_{11} phases, see section 1.6.10 [Marker et al. (2011) and Krendelsberger et al. (2007)], namely τ_{10}=$Al_9Fe_4Si_3$ ($Al_{57\text{-}59}Fe_{24\text{-}25}Si_{17\text{-}18}$) or the τ_{11}=$Al_4Fe_{1.7}Si$ ($Al_{64\text{-}66.5}Fe_{24\text{-}25}Si_{9.5\text{-}11}$). According to the crystallographic data for τ_{11}, this phase was not present in the alloy OHC2. No crystallographic data is available for the τ_{10}. To characterize the DP a further study using TEM is required. All these phases were stable after the heat treatment at 800 °C for 48 h (Table 14). Only the $(TM)_5Si_3$, $(TM)_6Si_5$, $FeSi_2Ti$, $Fe_3Al_2Si_3$ and $(TM)Si_2$ phases were stable after the heat treatment at 950 °C for 48 h (Table 15).

The microstructural studies would suggest that the $(TM)_6Si_5$ was the primary phase to form from the melt in all parts of the ingot. The T phase exists in the Cr-Ti-Si and Cr-Nb-Si systems if we consider the alloy OHC2 as (Cr,Fe)-(Nb,Ti)-(Si,Al) or as (Cr,Fe,Ti)-Nb-(Si,Al) it falls in the $(Cr,Nb)_6Si_5$ field in the liquidus projection, meaning the 6-5 silicide is the primary phase to solidify. In the Cr-Nb-Si system the $(Cr,Nb)_6Si_5$ can be in equilibrium with the 5-3 silicide Nb_5Si_3 and Cr_5Si_3 as well as with the CrSi and $CrSi_2$. In the Cr-Ti-Si system, the $(Cr,Ti)_6Si_5$ can be in equilibrium with Cr_5Si_3 and CrSi and with TiSi and $TiSi_2$. The above justify the coexistence of $(TM)_6Si_5$ with (Fe,Cr)(Si,Al) and $(TM)_5Si_3$ in the cast alloy at 800 °C and with $TMSi_2$ at 950 °C. The τ_1- $FeSi_2Ti$ can be in equilibrium with TiSi and $TiSi_2$ in the Fe-Si-Ti system. In the Nb-Si-Fe system, the $FeSi_2Nb$ can form and this can be in equilibrium with $NbSi_2$ and Fe-Si but also with the $Nb_4Fe_4Si_7$, the latter with $(Nb_2Fe_2Cr_2)Si_5$, ie, $(TM)_6Si_5$ and given the crystal structure of $Nb_3Fe_3CrSi_6$, ie, $(TM)_7Si_6$ that vilasi and co-workers have reported to form in Nb-Si-Fe-Cr coatings (Vilasi et al. (1998a)). The above discussion justifies the coexistence of τ_1 with

(Fe,Cr)(Si,Al) and $TMSi_2$ but also with $(TM)_6Si_5$ as well as the existence of the Nb rich τ_1 (ie., τ "coming" from the Fe-Nb-Si phase equilibria) in the eutectic. As it was discussed in section 3.3.1.1, the $(TM)_6Si_5$ and $FeSi_2Ti$ phases are stable below temperatures that are close but higher for the former. Considering the melting temperature of the FeSi, the Al additions would decrease its melting temperature although Cr would be expected to slightly increase it and its Ti content would not be expected to raise the melting temperature of (Fe,Cr,Ti)(Si,Al) above 1532 °C given that in the Si rich region of the Fe-Ti-Si system the TiSi is stable below 1450 °C. The Al-rich phases $Fe_3Al_2Si_3$ and DP would be expected to have a lower melting point. Considering the $(TM)_5Si_3$, the melting temperatures of Nb_5Si_3, Ti_5Si_3 and Cr_5Si_3 are 2518, 2130 and 1780 °C, respectively and the Fe_5Si_3 forms via a peritectoid reaction at 1060 °C in the binary and in a peritectic reaction in the Fe-Ti-Si at 1201 °C and the solution of Al in the Nb_5Si_3 decrease the melting temperature. The above indicate that Fe has a strong effect on the stability of the $(TM)_5Si_3$ which it is suggested, would be stable at temperature at least lower that the $FeSi_2Ti$.

Thus, on the basis of the above discussion, the formation sequence, in terms of decreasing temperature, of the intermetallics in the alloy OHC2-AC should be $(TM)_6Si_5$, then $FeSi_2Ti$, $(TM)_5Si_3$ or (Fe,Cr,Ti)Si, $Fe_3Al_2Si_3$ and the dark phase DP. The heat treatment at 950 °C confirmed that the (Fe,Cr,Ti)(Si,Al) and DP phases were metastable.

In the top and bulk of the alloy OHC2-AC the $(TM)_6Si_5$, $FeSi_2Ti$, (Fe,Cr)(Si,Al), $(TM)_5Si_3$, $Fe_3Al_2Si_3$ and DP phases were observed. The formation of the $(TM)_6Si_5$ phase in the top and centre (bulk) of the ingot was accompanied by the partitioning of Fe and Cr, Nb and Ti. As the primary $(TM)_6Si_5$ silicide formed Fe and Al were rejected into the melt, while the other elements partitioned to the solid, see figure 55. Thus, the interdendritic melt became richer in Fe and Al and leaner in Cr, Nb and Ti and from this melt the $FeSi_2Ti$ phase formed via the peritectic reaction L + $(TM)_6Si_5 \rightarrow FeSi_2Ti$. As this reaction did not proceed to completion, the liquid became rich in Cr and Fe and the (Fe,Cr)(Si,Al) formed and the liquid became rich in Al, Cr, Nb and Ti and poorer in Si and Fe. From this formed the $(TM)_5Si_3$ making the melt poor in Nb, Cr and Ti and rich in Al and Fe and thus the $Fe_3Al_2Si_3$ and DP phases formed.

Near the bottom of the ingot, the volume fraction of the $(TM)_6Si_5$ was lower thus the melt was richer in Nb, Cr, Ti, Si, Al and Fe and it is suggested that its composition shifted closer to the ternary eutectic $L \rightarrow$ Nb- rich $FeSi_2Ti + Fe_3Al_2Si_3$ + DPEu that was formed in this part of the alloy OHC2-AC.

In the very bottom of the button (chill zone) the melt was richer in Fe, Al, and leaner in Cr, Nb, Ti and Si compared with the composition of the rest of the alloy. If the alloy were considered as (Nb,Ti)-(Cr,Fe)-(Si,Al) or as Nb-(Cr,Fe,Ti)-(Si,Al) in the Cr-Nb-Si phase equilibria, it falls in the $(TM)_6Si_5$ phase field, meaning the primary phase was $(TM)_6Si_5$. The solidification path was essentially the same as in the top and bulk. The absence of $(TM)_5Si_3$ in this part of the button is attributed to the consumption of Nb to form the Nb rich $FeSi_2Ti$ phase.

The partitioning behaviour of Nb, Ti and Cr was opposite of that of Fe in the $(TM)_6Si_5$ as was in the case in OHC1-AC. The former elements had partitioning coefficient k_o^{TM} (TM=Cr, Nb, Ti) greater than one and for Fe it was less than one. The Fe concentration along the length of the $(TM)_6Si_5$ dendrite, shown in figure 55, could be described by the solute distribution given by the Scheil equation, which gives the composition of the solid phase $C_s^{Fe} = k_o^{Fe} C_o(1-f_s)^{(koFe-1)}$ where k_o^{Fe} is the partitioning coefficient for Fe, C_o is the Fe content (=21.5 at %) and f_s is the fraction solidified. For the centre of the dendrite (f_s=0) taking C_s^{Fe} = 10 at% gives k_o^{Fe} = 0.47 compared with k_o^{Fe} = 0.52 for the alloy OHC1. The C_s^{Fe} = 20 at.% (value measured near the boundary of $(TM)_6Si_5$ dendrites) corresponds to $f_s \approx 0.72$ slightly small than $f_s \approx 0.84$ for OHC1.

The Ti_5Si_3, $CrSi_2$ and Cr_5Si_3 silicides exhibit solubilities for third elements [Du and Shuster (2002)]. Likewise, research has reported the solubility of Nb in Ti_5Si_3 and Cr_5Si_3 [Bewlay et al. (1997a), Zhan et al. (2009), Zhao et al. (2003b), Shao (2005)]. Solubility of 23 at. % Nb in the Ti_5Si_3 was reported in the temperatures range 500 to 1200 °C and no Nb solubility in the Cr_5Si_3. According to Weitzer et al. (2008) the solubility of Fe in Ti_5Si_3 was 4 at.% Fe and according to Lindholm (1997) the solubility of Fe in Cr_5Si_3 was 4.5 at.% Fe. The Al solubility in Cr_5Si_3 was ~ 2.0 at.% Al at 800 °C according to Chen et al. (2007) and in Ti_5Si_3 was ~ 12 at.% Al at 1000 °C according to Raghavan (2009a). Vilasi et al. (1998b) reported that the solubilities of Fe and Cr in

the Nb_5Si_3 silicide were negligible. The concentrations of Al and Nb in $(TM)_5Si_3$ were in agreement with reported solubilities, but the Fe content was above the reported values. Which would suggest that in the presence of Al and Nb the solubility of Fe in $(TM)_5Si_3$ was increased up to 8.7 at. % Fe).

In OHC2-AC, the $Fe_3Al_2Si_3$ had (Si+Al) in the range 64.2 to 64.8 at.% that is close to 66.66% of the $(TM)Si_2$. The reported XRD data for $CrSi_2$ (PDF file 00-035-0781) did not match with the experimental diffraction data. Furthermore, XRD data for OHC2-HTA in which the $Fe_3Al_2Si_3$ was at high volume fraction in the microstructure did not correspond to the $(TM)Si_2$. According to Chen (2007), the $CrSi_2$ phase can have in solution up to 25 at.% Al in the range 800 to 1100 °C. Marker et al. (2011) found no Al solubility in the $\alpha FeSi_2$ (low temperature) between 800 and 900 °C, and reported a maximum solubility of 8.5 at.% Al in $\beta FeSi_2$ (high temperature) at 750 °C and Lindholm (1997) reported negligible Cr solubility. In the $Fe_3Al_2Si_3$ phase in the alloy OHC2 the Al content was in the range 28.6 to 34.2 at.% Al. Considering, the Al and Si contents in the $Fe_3Al_2Si_3$ phase separately and Cr with Fe, the composition of $Fe_3Al_2Si_3$ was within the composition range of τ_1=$Fe_3Al_2Si_3$ ($Al_{21.5\text{-}45}Fe_{36.5\text{-}37.5}Si_{8.5\text{-}41.5}$) reported for the Al-Fe-Si system by Krendelsberger et al. (2007).

The XRD data confirmed the presence of this phase and its contribution in the diffractogram was also consistent with its volume fraction in the alloy. Therefore, it was concluded that the $Fe_3Al_2Si_3$ has a limited solubility for Cr that substitutes Fe, and negligible solubility for Nb and Ti. Marker et al. (2011) pointed to the homogeneity range of this phase noting the unusual combination of the broad homogeneity range of $Fe_3Al_2Si_3$ with its very low symmetry crystal structure (triclinic). Marker et al. (2011) suggested that this phase should be described as $Fe_3Al_{2+x}Si_{3-x}$ with $-0.3 < x < 1.3$ instead of $Fe_3Al_2Si_3$.

XRD data suggested that an hexagonal $(TM)Si_2$ phase with the space group $P6_222$ was present in the alloy OHC2-HTB. The $(TM)Si_2$ was found in the OHC2-HTB with (Si+Al) content = 65.7 at.% (Table 15). According to Chen et al. (2007), the solubility of Al in $CrSi_2$ is up to 25 at. % Al, which

is consistent with the Al content of $(TM)Si_2$. It is suggested that Al enhanced the solubility of Fe and Ti in this phase, because according to Lindholm (1997) the $CrSi_2$ phase does not dissolve Fe.

The $FeSi_2Ti$ phase had (Si+Al) ≈ 50 at% and exhibited high solubility for Ti and Fe. After heat treatment, its composition moved closer to the values given by Weitzer et al (2008) for the τ_1 ($FeSi_2Ti$) phase (considering Nb, Ti and Cr together). The XRD data supported the presence of this phase in the as cast and heat treated alloy (Figure 54). The compositions (at.%) of $FeSi_2Ti$ in the OHC2-AC, OHC2-HTA and OHC2HTB (see Tables, 13, 14 and 15), considering it as $(Al+Si)_{50-52}Fe_{23-25}(Ti+Nb+Cr)_{24-26}$ were consistent with the τ_1=$FeSi_2Ti$ ($Si_{49-50}Fe_{24-25}Ti_{25-26}$) in the Ti-Fe-Si system reported by Weitzer et al. (2008). Unlike the alloy OHC1-AC, the $FeSi_2Ti$ phase in OHC2 has up to 5.2 at. % Nb solubility and about 13.8 at. %Al which would suggest that the presence of Al enhanced the Nb solubility in τ_1. According to the data in the Tables 13, 14 and 15, the Al and Cr solubilities in the τ_1 decrease at higher temperature, this was also observed for Cr in the alloy OHC1-AC.

The phase designated as (Fe,Cr)(Si,Al) had (Si+ Al) ≈ 50 at% and high Fe solubility (see Tables, 13 and 14). The CrSi and FeSi are isostructural and have complete solubility [Lindholm (1997)], but do not show ternary solubilities for Ti and Nb. A limited Ti solubility of 1 at.% Ti in FeSi was confirmed by Marker et al. (2013) while Du and Shuster (2002) reported negligible ternary solubilities in TiSi and CrSi. Moreover, only ~ 2 at.% Al can be in solution in the CrSi phase according to the isothermal sections at 800 and 1100 °C of the Al-Cr-Si system [Gupta (2004) and Chen et al. (2007)]. Comparison with the composition of the (Fe,Cr,Ti)Si phase in the alloy OHC1, the Ti content in the (Fe,Cr)(Si,Al) in OHC2 was even lower. The latter phase showed Cr in the solubility range 7.9 to 9.2 at.% Cr and up to 8.5 at. %Al. The Al content in (Fe,Cr)(Si,Al) is in good agreement with the Al solubility in FeSi (~ 12 at.%Al) at 800 and 900 °C reported by Marker et al. (2011) and (2013). The microstructural and XRD data after heat treatment at 950 °C for 48 h confirmed that the (Fe,Cr)(Si,Al) phase was not stable in the alloy OHC2-HTB. No heat effects were observed in the DSC trace for a solid phase transformation at 950 °C or below.

3.3.2 Oxidation

Oxidation of the alloy OHC1 at 800 °C

The alloy OHC1 formed a very thin oxide scale after isothermal oxidation at 800 °C. The oxide scale was very brittle and easy to remove during sample preparation, complicating the characterization of cross sections. The microstructure of the alloy was comprised of the $(TM)_6Si_5$, (Fe,Cr,Ti)Si and $FeSi_2Ti$ phases (Table 11) on which different oxidation products were formed. The EDS and glancing angle XRD data suggested that the oxide scale was composed of SiO_2, TiO_2 and $(Cr,Fe)_2O_3$ oxides and also confirmed α-Fe, τ_3 ($Fe_{40}Si_{31}Ti_{13}$) and Fe_5Si_3 phases in the metal base below the scale as a result of the depletion of the reactant species.

The location of the aforementioned oxides in the scale can be seen in figures 65 and 66. There was variation in composition of the $(TM)_6Si_5$ phase across its grains (see figure 45), with the concentration of Fe increasing from the centre to the edges of the grains. The microsegregation in the $(TM)_6Si_5$ affected its oxidation at 800 °C. On top of the $(TM)_6Si_5$ grains the oxide scale was composed of refined granular particles of TiO_2 engulfed by SiO_2 oxide. According to the elemental distribution shown in the X-ray maps (see figure 65), the TiO_2 contained other elements that were in solubility in the $(TM)_6Si_5$; Cr and Nb concentrations were higher in the centre of the grains giving different compositions for the rutile type structure $(Ti,Cr,Nb)O_2$ while over the Fe-rich edges of the $(TM)_6Si_5$ Fe was not found in the oxide owing to the low solubility of Fe in the TiO_2. The low Fe and Cr solubility in TiO_2 ~ 1 and 4 at. % Fe and Cr, respectively, [Wittke (1967) and Koohpayeh et al. (2010)], and the fact that Fe can be transported through SiO_2 towards the surface of the scale [Adachi and Meier (1987)] suggested that some $(Fe,Cr)_2O_3$ + TiO_2 could have formed in the Fe-rich areas of the $(TM)_6Si_5$ phase.

The same behaviour was also observed along $(TM)_6Si_5$ dendrites but the TiO_2 particles formed on the top showed a coarser microstructure. The EDS analysis of the cross section of the interface of $(TM)_6Si_5$ with the scale showed a depletion of about 3.5 at. %Si and 2.5 at. %Ti at the metal/scale interface. Considering the above, and the fact that the volume fraction of

$(TM)_6Si_5$ was the higher in the alloy, glancing angle XRD data was performed at different angles to search for other phase in the scale, however none was found.

The X-ray maps in figure 65 showed Si, Fe and O over the (Fe,Cr,Ti)Si phase. Fe-Si alloys form a sequence of oxide layers according to their Si content. At low Si contents FeO forms next to the bare metal, this oxide engulfs a dispersion of Fe_2SiO_4 particles, then follows a layer of Fe_3O_4, and finally a layer of Fe_2O_3 is formed as the outermost layer. Some internal oxidation of Si has been found in these alloys [Birks et al. (2006)]. A reduction in the volume of Fe oxides was found in Fe-Si alloys with high Si content in which an inner layer of SiO_2 and an outer layer of Fe_2O_3 were observed [Adachi and Meier (1987)].

Considering the high Si content of the (Fe,Cr,Ti)Si phase the latter would be expected to form an inner SiO_2 layer and Fe_2O_3 as the top oxide at 800 °C. Thus, it is suggested that these two oxides were formed over the (Fe,Cr,Ti)Si phase since they were detected by glancing angle and Fe, Si and O on the X-ray map over the (Fe,Cr,Ti)Si phase (Figure 65). The EDS analysis revealed that there was mainly Si depletion from the (Fe,Cr,Ti)Si phase leading to the formation of consecutive layers of Fe_5Si_3 and α-Fe underneath the oxide scale. The Si depletion was the result of the formation of the SiO_2 layer. The α-Fe was found at the metal/scale interface with Si and Cr contents 17.3 at. %Si and 3.7 at. %Cr, respectively. According to Adachi and Meier (1987) this Si content is enough to form a continuous SiO_2 film over this phase. However, they also found some Fe_2O_3 at the scale/gas interface that was attributed to Fe transportation through the SiO_2 layer to form Fe_2O_3. Thus, it is also likely that a thin film of $(Fe,Cr)_2O_3$ formed on the top of the SiO_2 formed on the (Fe,Cr,Ti)Si phase.

The X-ray maps (Figure 65) showed that on the $FeSi_2Ti$ phase mainly formed coarse grains of TiO_2 (compare the Ti, Si and O maps). This is in agreement with the depletion of Ti and Si near the metal/scale interface and the formation of the τ_3 ($Fe_{40}Si_{31}Ti_{13}$) phase and α-Fe below the scale. The τ_3 phase was not detected on the XRD glancing angle data at any of the studied angles since the volume fraction of the $FeSi_2Ti$ phase in the alloy OHC1 was the lowest. A comparison of the current data with the oxidation of Si-rich Ti-silicides is reasonable since on

the $FeSi_2Ti$ phase TiO_2 and SiO_2 only were detected. According to Kofstad (1966) the Ti oxidizes more rapidly than Si, so it is possible that at this temperature the mobility of metal ions to the surface of this phase was higher that the mobility of Si thus resulting to the formation of coarse granular particles of TiO_2 engulfed by a glassy-like SiO_2 network, as it was observed in figure 66. The bottom spectrum on the right of the image shows Ti, Si, O and N. In the glancing angle XRD no nitride peaks were found. However, it is possible that in the earliest stage of oxidation Ti nitride formed and TiO_2 formed, and the N was then released and reacted again with the silicide or trapped under the oxide scale [Strydom and Lombaard (1985) and Chirkin et al. (2009)]. This could also explain the formation of pores and cavities beneath and across the oxide scale, see figure 67.

The figure 66 would also suggest that the high Fe content of the complex silicides could have increased the mobility of Ti to the surface because coarse grains of TiO_2 were observed on top of the $FeSi_2Ti$ phase and the same was observed near the grain boundaries of the $(TM)_6Si_5$ phase, where the Fe content was the highest.

There was some oxidation of the sample before the 800 °C (isothermal oxidation temperature) was reached. Some uneven reddish mark was observed on the crucible. It is likely that Fe oxides had reacted in contact with the alumina crucible. The Fe_2O_3 has a red colour and the XRD data confirmed the presence of this oxide in the oxide scale. It is unlikely that the reaction with the alumina crucible contributed to the isothermal oxidation behaviour because the initial staining on the crucible did not change with time.

The isothermal oxidation data at 800 °C (Figure 62) showed an initial parabolic weight gain in the first ten hours (Table 16). This may be attributed to the formation of SiO_2 as the most protective oxide which has been reported to have oxidation rates ~ 10^{-13} $g^2.cm^{-4}.s^{-1}$ at 800 °C and ~ 10^{-12} $g^2.cm^{-4}.$ s^{-1} at 950 °C. However, the predominant oxidation behaviour was linear after the first 10 h. It is not clear why the latter was the case for this alloy after the first 10 h, as no oxide spallation was observed, and the evaporation of CrO_3 (in dry conditions) at this

temperature is not expected. No considerable Cr depletion at the metal/scale interface was found and there was no considerable Cr_2O_3 formation in the oxide scale.

It is possible however that in the oxide scale time-dependent structural changes occurred that resulted in a linear rate even though diffusion controlled the oxidation. The oxidation of Ti above 700 °C has an initial parabolic oxidation rate (due to oxygen dissolution in the base metal) then changes to linear (after TiO0.35 forms as an outer layer where O diffusion is faster) due to the change in the diffusion controlling oxidation mechanism [Kofstad, (1961)]. Moreover, in the temperature range 800-1000 °C, the growth of TiO_2 scales is characterised by the diffiusion of Ti in the inner layer and by the diffusion of oxygen in the outher layer which creates stress and craks. TiO_2 formed at a high volume fraction in the oxide scale formed on the alloy OHC1 at 800 °C, thus it is suggested those changes in the oxidation behaviour of Ti could have had strong influence in the overall oxidation of the alloy.

Grain coarsening (i.e. growth) in the oxide scale could also be a microstructural factor that affected the oxidation behaviour of this alloy. If different oxide volume ratios were present as a result of the formation of different oxides, their consecutive growth would give rise to internal stresses and strains in the oxide layer. Then, the strain was released by cracking the oxide, thus exposing the metal surface to further oxidation. Besides, the depletion of some elements in the alloy near the scale/metal interface by means of oxidation, could lead to a phase transformation in these regions, increasing the mismatch at the interphase interfaces (with increasing mismatch, the nature of the interphase interface changes for coherent to semicoherent to incoherent with strains developing at the interface that are accommodated by the introduction of dislocations at the interphase), and resulting to strains that affected the adhesion of the oxide scale at the scale/metal interface.

Oxidation of the alloy OHC2 at 800 °C

This alloy formed a very thin oxide scale after isothermal oxidation at 800 °C. Its oxidation behaviour was better compared with the oxidation of the alloy OHC1. This was attributed to the Al content in the alloy OHC2 in the microstructure of which the main phases were the $(TM)_6Si_5$,

$FeSi_2Ti$ and the $Al_2Fe_3Si_3$ which clearly formed different oxidation products resulting to nonuniformity of oxidation and different oxide thicknesses. Overall, the oxide scale thickness was in the range 1 to 2 μm at the thickest areas. The aforementioned phases were stable after the isothermal oxidation at 800 °C. The studies did not show any considerable elemental depletion at the metal scale interface in these phases.

The oxidation behaviour was subparabolic (Table 16) with very high oxidation rate in the first hour followed by parabolic oxidation at a very low rate. This behaviour has been found in alumina forming superalloys [Li et al. (2003), Gonzalez-Carrasco et al. (2001), Garcıa-Alonso (2000)]. The subparabolic time dependence of growth rate is related to lower temperatures, and the result of the grain boundary linked mechanisms (short-circuit) where an initial fast oxygen penetration occurs giving a very high oxidation rate and then as the oxide grain growth occurs, the easy oxygen paths are blocked and the oxidation kinetics slows down.

As was the case in the alumina forming superalloys, the metastable γ and θ aluminas were formed in the alloy OHC2. In the case of the superalloys the α-Al_2O_3 was formed after an extended oxidation period (above 100 h). The transformation of γ-Al_2O_3 to θ-Al_2O_3 has been observed in the temperature range 800 to 1000 °C in Ni-Al alloys [Brumm and Grabke (1992)].

According to the glancing angle XRD data, the main components in the oxide scale were the γ-Al_2O_3 and θ-Al_2O_3, SiO_2, Al_2SiO_5, $FeTi_{3-x}O_x$ and TiO_2 (Figure 71). The main contribution in the XRD data was from the γ-Al_2O_3. The X-ray elemental maps (Figure 74) confirmed the presence of Al_2O_3 in the oxide scale of OHC2. When γ-Al_2O_3 was found to be the main phase upon oxidation of Ni-Al at 800 °C, the diffusion mechanism was linked with its modification (Brumm and. Grabke (1992)). The alloy OHC2 formed other oxides which could have also contributed to the $\gamma \rightarrow \theta$-$Al_2O_3$ change.

There is no information available about the oxidation of the $(TM)_6Si_5$ phase with Al additions. However, according to the current results, the low Al content in the $(TM)_6Si_5$ seemed to be enough to stabilise an Al_2O_3 layer, on the scale. Figure 72 shows low O content with this phase in figure 70 and it is also likely that the Al_2O_3 formed over this phase could have developed

different thicknesses depending on the Al availability in the microstructure. The latter would be affected by the Fe and Al segregation in the $(TM)_6Si_5$ phase, being more rich in Al in the edges. This could also lead to the gradual growth of aluminium silicates like Al_2SiO_5 and of SiO_2 in the centre of the dendrites (Figure 71). Moreover, it is also likely that in the centre of the dendrites other oxides like TiO_2 could grow with different compositions as a result of the Al being scarce allowing Si mobility towards the surface as it was discussed in the previous section for the oxidation of the $(TM)_6Si_5$ phase in the alloy OHC1, where the main oxidation products were TiO_2, SiO_2 and Fe_2O_3.

Al_2O_3 whiskers developed on the top surface of the oxide scale formed on the $Fe_3Al_2Si_3$. Kofstad (1966) suggested that whiskers do not grow on the top of the metal but develop on top of another thick oxide. Blade–like whiskers were formed on the alloy OHC2 (Figure 70a), but were not seen in figure 73 because the whiskers were removed during the preparation of the sample. Growth of whiskers on the top of the oxide scale on Ni-Al was attributed to the $\gamma \rightarrow \theta$-$Al_2O_3$ transformation by Brumm and Grabke (1992).

Novák et al. (2011) suggested that Fe-Si-Al alloys mainly form δ-Al_2O_3 under oxidation at 800 °C with some Fe_2O_3, and that the Fe_2O_3 content in the oxide scale decreases when the Si content in the Fe-Si-Al alloys is above 20 at.% Si. The δ-Al_2O_3 was not confirmed by the glancing angle XRD in the alloy OHC2. The Si content in the $Fe_3Al_2Si_3$ phase was above 30 at. % Si and there was some Fe enrichment at the metal/scale interface, which would suggest the possible formation of Fe oxides right below the Al_2O_3 scale. The glancing angle XRD did not detect them. It is suggested that under isothermal oxidation in air at 800 °C, the $Fe_3Al_2Si_3$ phase formed an Fe-oxide followed by γ-Al_2O_3 and then θ-Al_2O_3 whiskers formed at the oxide/gas interface.

As it was discussed in the previous section, the $FeSi_2Ti$ phase in the alloy OHC1 formed TiO_2 and SiO_2. This phase could be expected to form at least one of those oxides at 800 °C on the alloy OHC2. This phase would form the Al_2O_3, Al_2SiO_5 and $FeTi_{3-x}O_x$ that could correspond to the oxygen shown in the X-ray elemental maps (Figure 74). However, the X-ray elemental maps of the cross section (Figure 74) showed that Al_2O_3 was the main oxidation product and according

to the cross section image (Figure 73) the oxidation of the areas where Al_2O_3 was the main oxidation product was characterized by oxygen penetration. Thus, it is likely that the higher diffusion rate of oxygen in the Al_2O_3 scale allowed the oxidation of Fe, Ti and Si beneath the Al_2O_3 scale. According to Pownceby et al. (2003) there is a miscibility gap between Fe_2O_3 and Al_2O_3 but they found some solubility of Fe in Al_2O_3 at low temperatures, thus it is likely that some Fe was in solubility with the Al_2O_3, this could be the reason for having a very strong Fe signal on the X-ray maps and for not detecting Fe oxide by the glancing angle XRD (Figure 71).

Oxidation of the alloy OHC1 at 1200 °C

The alloy OHC1 showed paralinear oxidation kinetics after isothermal oxidation at 1200 °C for 100 h (Table 16). According to the EDS and glancing angle XRD data, the oxide scale was composed of the Cr_2O_3, SiO_2 and TiO_2 oxides. The thickness of the oxide scale was in the range 10 to 30 μm approximately. The Cr_2O_3 was mostly found in the outermost layer, and the SiO_2 in the inner part of the scale. The distribution of these oxides in the scale was irregular and was the reason for having thickness range for the oxide scale. The oxide scale was adherent, but its microstructure would not allow it to be considered as protective. This alloy presented paralinear oxidation since the main oxide in the scale was Cr_2O_3 and the latter has been linked with this oxidation behaviour at high temperatures [Birks et al. (2006)].

The insert number 1 in the figure 78 shows coarse and fine grains of Cr_2O_3 in the top of the oxide scale where the oxygen partial pressure was higher than at the oxide / metal interface. The paralinear behaviour of Cr_2O_3 is attributed to the fact that Cr_2O_3 can be further oxidised at high oxygen pressures and high temperatures to form CrO_3, which is volatile at 1200 °C. It is likely that the mixture of coarse and fine grained Cr_2O_3 in the oxide scale was the result of the following reaction:

$$Cr_2O_3\ (s) + 3/2\ O_2\ (g) = 2\ CrO_3\ (g)$$

This reaction could be responsible for the change in the oxidation behaviour of this alloy from parabolic to linear after 40 h at 1200 °C. According to Kofstad (1966), the oxidation of Cr_2O_3 into

CrO_3 is enhanced as the thickness of Cr_2O_3 increases. The EDS analyses performed on Cr_2O_3 at different distances from the scale / metal interface showed some Ti and Fe in solution in this oxide.

The insert number 2 in figure 78 also shows an oxide with glassy-like appearance. Qualitative EDS showed that this was SiO_2. These areas were mostly observed where the $FeSi_2Ti$ phase was in the microstructure. As was the case for the oxidation of this phase at 800 °C, TiO_2 and SiO_2 oxides were the oxidation products formed on this phase at 1200 °C. The EDS analysis also showed some Ti dissolved in the SiO_2. The glancing angle XRD also showed peaks that corresponded to TiO_2. Becker et al. (1992) suggested that the solubility of TiO_2 in SiO_2 is increased with temperature this would be the reason why it was possible to find TiO_2 dissolved in SiO_2 instead of coarse particles of TiO_2 dispersed in a SiO_2 network.

Despite of the high Fe content of the $FeSi_2Ti$ phase (Table 11), no Fe oxides were detected in the oxidation of this phase. This was attributed to the preferential oxidation of Si and Ti, and is in agreement with Tsirlin et al. (1981). One of the possible reasons for this behaviour is the low Fe solubility in TiO_2 allowed a mixture of TiO_2 and SiO_2 to be stabilised at 1200 °C. Indeed, according to Wittke (1967) the solid solubility of Fe in TiO_2 is about 1 at. % Fe in the range 800 to 1200 °C.

Oxide melting could be responsible for the network-like oxide microstructure observed on the insert number 3 in (Figure 78). This feature was observed on the oxide formed on top of the (Fe,Cr,Ti)Si phase. It is suggested that this melting could be the result of the eutectic reaction $L \rightarrow FeO+Cr_2O_3+SiO_2$ at 1155 °C reported by Kainarskii and Degtyareva (1977). EDS analysis from this area confirmed the prescence of Si, Cr and some Fe and thus is possible that some FeO formed. Its volume fraction could be low to be detected by the glancing angle XRD but enough to react with the SiO_2 and Cr_2O_3 which were the dominant oxides in the alloy.

In the cross sections of the metal/scale interface there were voids in the (Fe,Cr,Ti)Si phase and some Cr depletion in the metal underneath the scale. The solid solutions formed by Fe_2O_3-Cr_2O_3 are converted at high temperatures to the ternary FeO–Fe_2O_3-Cr_2O_3 by the dissociation of Fe_2O_3

[Kainarskii and Degtyareva (1977)]. According to the Fe-Cr-O system at 1200 °C the FeO dissolves Cr before some spinels are stabilized. Thus, if FeO oxide was formed this also could suggest that this phase could also transport some Cr towards the oxide surface.

The EDS detected some Cr in the SiO_2 formed on the top of the (Fe,Cr,Ti)Si phase which would suggest that there was some Cr transportation from the metal / scale interface towards the oxide / scale surface through the SiO_2 network.

The diffusion zone beneath the oxide scale was 30-40 μm thick. The Cr_2O_3 was the predominant oxide in the scale. The composition of this oxide was affected by the composition of the $(TM)_6Si_5$ phase and its different Ti, Fe and Cr contents (Table 11). The Fe_2O_3 and Cr_2O_3 oxides with rhombohedral crystal structure show a continuous series of solid solutions in the Fe-Cr-O ternary system. The Fe_2O_3, Cr_2O_3 and Ti_2O_3 are isostructural, thus it is not surprising to find different ranges of solubility according to the availability of Fe, Cr and Ti in the $(TM)_6Si_5$. The isothermal oxidation of the complex silicide $(TiFeCr)_7Si_6$ was reported by Portebois et al. (2013). Its oxidation products were similar to those formed on the $(TM)_6Si_5$ in OHC1 at 1200 °C except the formation of Cr_2TiO_5 which seems not to be in equilibrium with Cr_2O_3 below 1660 °C according to Kamiya et al.(1979).

According to Kosftad (1988), during the growth of Cr_2O_3 internal strains arise in the scale as a result of oxygen and Cr transportation through the oxide scale (counter–current) with the Cr diffusion being much faster than that of the O. The Cr_2O_3 layer presented a granular morphology. It is likely that grain boundaries allowed the transport of oxygen further in the alloy to oxidize the $FeSi_2Ti$ and form SiO_2 and some TiO_2 precipitates at this temperature. This would explain why the SiO_2 was mainly found underneath the Cr_2O_3.

Internal oxidation was observed at 1200 °C and did not show a particular pattern. However, it is important to remember that there were cracks in the cast alloy.

Considering all the above, it is likely that the oxidation behaviour of this alloy in the first 40 hours at 1200 °C involved the formation of Cr_2O_3 layer along with SiO_2 layer underneath and

some evaporation of CrO_3. When the Cr_2O_3 reached a certain thickness the CrO_3 evaporation became more important leading to a change in oxidation behaviour from parabolic to linear. There should have also been some contribution to the oxidation kinetics from the other minor oxides that were formed on the oxide scale at this temperature. The overall oxidation could be considered as paralinear even though n=0.68 (see Table 16).

According to Kosftad (1988) the paralinear oxidation occurs when a compact and protective oxide scale that forms at the scale / gas interface and becomes a non-protective surface owing to the formation of pores caused by oxide evaporation. Along this deterioration the oxidation kinetics transforms from parabolic to linear.

It was also observed that some areas of the oxide scale were still in contact to the Cr_2O_3 layer. The protectiveness of the oxide scale formed on the alloy OHC1 would rely on the establishment of a more continuous SiO_2 layer underneath the Cr_2O_3 that could act as a barrier for further metal and oxygen transport.

3.4 Conclusions

Alloy OHC1

The microstructural study of the as cast and heat treated alloy OHC1 allowed the following conclusions to be made:

In the alloy OHC1 the $(TM)_6Si_5$, $FeSi_2Ti$ and the FeSi phases were in equilibrium at 1200 °C. The $(TM)_6Si_5$ phase was the primary phase and presented partitioning with coefficients for Fe, Cr and Ti $k_o^{Fe} = 0.522$, $k_o^{Cr} = 1.482$ and $k_o^{Ti} = 1.267$, respectively.

The eutectic reaction $L \rightarrow FeSi + \tau_1$ ($FeSi_2Ti$) occurred and the composition of the eutectic was Si-35.6Fe-3.7Cr-10.4Ti-0.1Nb

The addition of Cr promoted the formation of the T phase and suppressed the formation of the τ_2 (FeSiTi) phase. The partitioning behaviour of Nb, Ti and Cr was opposite to that of Fe.

The FeSi presented a very low Ti solubility of ~ 1 at. % Ti, the Cr solubility was 5.9 at.% Cr and there was no Nb solubility.

The Cr solubility in the τ_1 ($FeSi_2Ti$) decreased after the heat treatment at 1200 °C and the Nb solubility slightly increased after this heat treatment but was still < 1 at. % Nb.

The thermogravimetric study at 800 °C of the alloy OHC1 allowed the following conclusions to be made:

No pesting was observed and the alloy exhibited initial parabolic oxidation behaviour during the first 10 h, followed by linear oxidation h and gained 1.42 mg/cm^2 after 100 h.

The oxide scale was composed of SiO_2, TiO_2 and $(Cr,Fe)_2O_3$ and these oxides formed in different proportion according to the location of a particular phase in the substrate alloy. The $FeSi_2Ti$ formed SiO_2 and TiO_2 and the (Fe,Cr)Si phase formed SiO_2 with a thin layer of $(Fe,Cr)_2O_3$ on top owing to Cr and Fe transport through the SiO_2.

The oxide scale formed on top of the $(TM)_6Si_5$ phase was affected by its microsegregation since the centre of the dendrites formed SiO_2 and TiO_2 and the Fe-rich edges formed SiO_2, TiO_2 and $(Cr,Fe)_2O_3$.

The thermogravimetric study at 1200 °C allowed the following conclusions to be made:

The alloy exhibited paralinear oxidation behaviour. An initial parabolic oxidation during the first 40 h followed by linear oxidation and gained 1.60 mg/cm^2 after 100 h.

The oxide scale was composed of a double oxide layer with a SiO_2 inner layer at the metal/ scale interface and an outer layer of Cr_2O_3 at the metal/gas interface, and TiO_2. The oxide surface suggested that the eutectic reaction L → FeO+ Cr_2O_3 + SiO_2 had ocurred.

There was internal oxidation which was attributed to prevailing cracks in the alloy. The oxide scale also presented CrO_3 evaporation which was attributed to change from parabolic to linear behaviour as the reaction became more predominant.

The relatively good oxidation resistance at 800 and 1200 °C of the alloy OHC1 is insufficient to suggest the use of this alloy in a coating system for temperatures above 1100 °C since it presented a eutectic reaction at ~ 1300 °C, a eutectic reaction in the oxide scale at ~ 1155 °C and the evaporation of CrO_3 from the Cr_2O_3 layer at 1200 °C even though SiO_2 sublayer could function as an excellent barrier.

Alloy OHC2

The microstructural study of the as cast and heat treated alloy OHC2 allowed the following conclusions to be made:

The phases in the as cast alloy were $(TM)_5Si_3$, $(TM)_6Si_5$, $FeSi_2Ti$, (Fe,Cr)(Si,Al), $Fe_3Al_2Si_3$ and the dark phase DP. These phases were also stable after the heat treatment at 800 °C. Only the $(TM)_5Si_3$, $(TM)_6Si_5$, $FeSi_2Ti$, $Fe_3Al_2Si_3$ and $(TM)Si_2$ phases were stable after the heat treatment at 950 °C.

The $(TM)_6Si_5$ was the primary phase with maximum Fe solubility of 21.5 at. % Fe near the boundaries of the T dendrites. This phase also showed very limited Al solubility and the partition of Al to the melt allowed the formation of low temperature phases ($Fe_3Al_2Si_3$, the dark phase DP and the (Fe,Cr)(Si,Al)).

A ternary eutectic L→ Nb-rich $FeSi_2Ti$ + $Fe_3Al_2Si_3$ + DPeu was formed.

The Al and Nb synergy enhanced the solubility of Fe in the $(TM)_5Si_3$ to 8.7 at. % Fe. The $Fe_3Al_2Si_3$ phase showed negligible Nb and Ti solubility while its Cr solubility was limited to 4.6 at. %Cr. The Al enhanced the Fe and Ti solubility in the $(TM)Si_2$ with space group $P6_222$. The $FeSi_2Ti$ phase had solubility for Al up to 13.8 at % and the Nb solubility up to 5.2 at. % Nb. Its Cr and Al solubilities decreased at higher temperature. With 8.5 at. % Al solubility the (Fe,Cr)(Si,Al) was destabilized upon heat treatment at 950 °C.

The thermogravimetric study at 800 °C of the alloy OHC2 allowed the following conclusions to be made:

The alloy OHC2 exhibited a subparabolic oxidation behaviour which indicated that the addition of Al was benefitial. No pesting was observed in the alloy, though it presented an initial linear behaviour during 1 h, followed by parabolic oxidation and gained 0.27 mg/cm^2 after 100 h.

The oxide scale was composed of γ-Al_2O_3, θ-Al_2O_3, SiO_2, Al_2SiO_5, $FeTi_{3-x}O_x$ and TiO_2 with γ-Al_2O_3 being the main oxide.

The addition of Al decreased the activity of (TM) elements in the $(TM)_6Si_5$ phase which formed Al_2O_3 at the edges (where the Al content was higher) and Al_2SiO_5 and SiO_2 in the centre of the dendrites.

The $Fe_3Al_2Si_3$ phase developed Al_2O_3 whiskers on top of Fe-oxide and γ-Al_2O_3. The $FeSi_2Ti$ phase formed Al_2O_3 with some Fe in solution.

The Al addition affected positively the oxidation resistance of the OHC2 alloy at 800 °C compared with the oxidation resistance of OHC1 at the same temperature, mainly because it controlled the activities of the TM reducing their motion towards the surface during oxidation. Thus Al_2O_3 , SiO_2 and Al_2SiO_5 oxides were among the main oxides in the oxide scale.

However, there was a strong effect of Al on the thermal stability of the alloy. The Al segregation from the $(TM)_6Si_5$ phase lead to the formation of low temperature phases, a eutectic reaction close to 1000 °C and liquation of the alloy at 1200 °C. Thus, this alloy can not be recommended for use in the BC of a coating system for Nb-silicide based alloys.

As it was indicated above, the use of the alloy OHC1 in a BC of a coating system for Nb-silicide based alloys must be considered with caution since the diffusion of Al and Nb from the substrate could lead to phase equilibria with the phases observed in the alloy OHC2.

Chapter 4

The microstructure and oxidation of the alloy Si-25Nb-5Al-5Cr-5Ti (OHC5)

4.1 Introduction

The thermal stability and compatibility of a coating with the base metal are very important characteristics to be considered in the design of coating systems. The idea of coating Nb-Si base alloys using high silicon Nb-silicide based alloys has been mentioned in the literature. The $NbSi_2$ disilicide has been the most popular proposition because it has a high melting point, close coefficient of thermal expansion with the base alloy and could form a glassy-like SiO_2 layer on its surface during oxidation. The $MoSi_2$ disilicide has been shown to have an excellent oxidation resistance at high temperatures (above 1200 °C) because it can form thin vitreous SiO_2 scale that has the capability of self-healing [Stergiou and Tsakiropoulos (1997a) and (1997b), Nakano et al. (2002) and Kurokawa et al. (2005)].

However, like most intermetallics the $NbSi_2$ disilicide suffers from pest oxidation in the pest regime of 600-900 °C where it forms α-Nb_2O_5 and SiO_2 [Pitman and Tsakiropoulos (1995), Murakami et al. (2001a) and (2001b)]. The pest oxidation was eliminated in $NbSi_2$ single crystals since this phenomenon has been linked with the presence of grain boundaries in the microstructure of $NbSi_2$ [Zhang et al. (2005) and (2006)], but even these single crystals oxidized following linear kinetics at 750 °C. Considering that this type of material would be working under load, the exposure of these "defect-free" alloys to a load would make them susceptible to the development of flaws which finally will lead them to pest.

Additions of key alloying elements to eliminate the pest oxidation in Nb-silicides could be a more feasible way to tackle this problem and would also create opportunities to improve their mechanical behaviour. Stergiou et al. (1997a) showed that alloying $MoSi_2$ with Al eliminated pest oxidation. Pitman and Tsakiropoulos (1995) added 8 and 20 at. % Cr to $NbSi_2$ to improve oxidation by the stabilization of the β-Nb_2O_5 instead of α-Nb_2O_5. They discovered that Cr additions in $NbSi_2$ suppressed the Nb_5Si_3 silicide and stabilized the $Nb_2Si_6Cr_3$ intermetallic. The

pest oxidation was suppressed at 750 °C with 20 at.% Cr but still partial pest oxidation occurred with 8 at.% Cr. At 1350 °C the oxidation behaviour was improved for both compositions and the alloys formed a duplex oxide scale composed by an inner SiO_2 layer and an outer layer of Cr_2O_3. These oxidation products were also observed by Murakami et al. (2001b) in Nb-66.7Si-X alloys (where X= 10, 20, 33.3 at.% Cr) after oxidation in static air at 1300 °C. It was also reported that their oxidation was extremely good in flowing air at 750 °C owing to the formation of a thin SiO_2 layer.

Aluminium additions in $NbSi_2$ improved not just the ductility of the disilicide [Nakano et al. (2000)] but also its oxidation resistance, making these alloys potential candidates as coatings for Nb-Si base alloys [Majumdar et al.(2006)]. However, it seems that at low temperature the addition of Al was not enough to optimize the oxidation resistance of $NbSi_2$. Murakami et al. (2003) studied the oxidation of the Nb-56Si-11Al (at. %) alloy that did not show pest oxidation but suffered from oxide spallation when it was exposed to dry air at 750 °C.

Despite of the latter results, some Nb-Si-Al alloys have shown outstanding oxidation resistance, which has been mainly attributed to the good oxidation resistance of the $Nb_3Si_5Al_2$ phase at 1300 °C even though, on this phase formed a very thick oxide scale composed of a mixture of Nb, Si and Al oxides after oxidation at 750 °C [Murakami et al. (2001b) and (2003), Zhao et al. (2003a)].

The beneficial effects of Cr and Al on oxidation have been widely demonstrated in Ni-Cr-Al and Fe-Cr-Al alloys where additions of Cr reduce the Al content necessary to grow and sustain an alumina scale. Furthermore, the reduction of the Al content also improved the ductility in alloys of these systems [Prescott et al. (1992)]. The substitution of Nb by Ti improves the oxidation resistance of Nb-silicides, their ductility and thoughness, but reduces their melting point [Bewlay et al. (1996)].

Additions of Cr and Al in $NbSi_2$ have also been studied. Murakami et al. (2003) reported excellent oxidation behaviour in the temperature range 500-1440 °C for the Nb-56Si-11Al-3Cr (at. %) alloy. The alloy consisted of the $Nb(Si,Al)_2$ phase and traces of Al_2O_3 confirmed by EDS

and XRD. The alloy formed a scale consisting of mixed oxides at 750 °C, and at higher temperatures a very adherent Al_2O_3 oxide scale was developed.

Considering the latter work and the improvement of the oxidation resistance of $NbSi_2$ by Cr and Al additions, it was decided to study the synergy of Cr, Al and Ti additions in the microstructure and oxidation behaviour of the alloy OHC5 with nominal composition Si-25Nb-5Cr-5Ti-5Al (at.%).

4.2 Results

4.2.1 Microstructure characterization

As cast microstructure

The actual composition (at.%) of the as cast alloy OHC5 was Si-25.6Nb-4.6Cr-5.2Ti-5.1Al. This composition was the average of the analyses taken from the top to the bottom of the button (Table 17). The data revealed that there was strong macrosegregation of all the elements. The highest Nb and Si and lowest Al, Cr and Ti concentrations were observed in the bulk of the button. The average compositions in the top, transition from bulk to bottom (TFBTB) and bottom areas were close to the nominal composition (Table 17).

According to the SEM study, and the EDS and XRD data (Table 17, figures 82, 83 and 84), there were five phases in the microstructure, namely $(Nb,Ti)(Si,Al)_2$, $(Cr,Ti,Nb)_6Si_5$, $(Cr,Ti,Nb)(Si,Al)_2$, and Si and Al solid solutions. Their chemical compositions are given in Table 17, and are the averages of the compositions of these phases in different areas in the button. Figure 82 shows the typical microstructures of the top, bulk, TFBTB and bottom of the button. In general the microstructure was characterized by enlongated faceted dendrites and there was porosity. The $(Si)_{ss}$ was not detected by XRD owing to its low volume fraction in the alloy.

Table 17 EDS data (at. %) of the as cast alloy OHC5.

Area/Phase	Nb (at%)	Ti (at%)	Cr (at%)	Al (at%)	Si (at%)
Top	24.0 ± 0.6 24.7 – 22.9	5.6 ± 0.5 6.4 – 5.1	5.8 ± 0.4 6.4 – 5.4	6.2 ± 0.4 6.9 – 5.6	58.4 ± 0.4 59.1 – 57.8
Bulk	28.9 ± 1.0 29.9 – 26.7	3.1 ± 0.5 3.9 – 2.6	2.3 ± 0.7 3.9 – 1.8	3.1 ± 0.7 4.4 – 2.4	62.5 ± 0.8 63.4 – 61.1
TFBTB*	24.6 ± 0.9 26.1 – 23.2	5.4 ± 0.3 5.8 – 4.9	5.2 ± 0.9 6.5 – 4.0	5.5 ± 0.7 6.5 – 4.8	59.2 ± 0.9 60.5 – 58.0
Bottom	24.8 ± 0.7 25.6 – 23.4	6.6 ± 0.5 7.6 – 6.0	5.2 ± 0.3 5.6 – 4.7	5.5 ± 0.7 6.7 – 4.8	57.9 ± 0.5 58.6 – 57.1
$(Nb,Ti)(Si,Al)_2$	31.6 ± 0.6 32.3 – 29.5	2.0 ± 0.5 3.7 – 1.4	0.4 ± 0.1 0.7 – 0.2	2.0 ± 0.6 3.5 – 1.1	64.2 ± 0.5 65.0 – 63.4
$(Cr,Ti,Nb)(Si,Al)_2$	3.8 ± 1.0 6.0 – 2.1	10.4 ± 1.0 12.3 – 8.4	19.3 ± 1.5 21.7 – 15.1	8.0 ± 1.5 10.0 – 5.0	58.6 ± 1.6 61.8 – 55.6
$(Cr,Ti,Nb)_6Si_5$	14.6 ± 5.7 25.4 – 5.0	18.0 ± 1.2 20.5 – 16.1	20.8 ± 4.8 27.7 – 11.5	1.2 ± 0.5 2.6 – 0.6	45.3 ± 0.4 46.2– 44.3
$(Al)_{ss}$	0.1 ± 0.1 0.2 – 0.0	0.2 ± 0.1 0.4 – 0.1	0.3 ± 0.3 0.7 – 0.1	97.0 ± 0.8 98.1 – 95.7	2.4 ± 0.7 3.3 – 1.4
$(Si)_{ss}$	2.5 ± 1.4 3.6 – 0.4	2.4 ± 1.2 3.5 – 1.3	3.6 ± 2.3 5.5 – 0.7	2.8 ± 0.8 7.4 – 0.8	88.7 ± 5.5 93.5 – 81.1

*TFBTB transition from bulk to bottom

The typical microstructure in the centre of the alloy is shown in the figures 82 and 83a. It consisted of primary faceted $(Nb,Ti)(Si,Al)_2$ dendrites.The interdendritic regions were small compared with the size and volume fraction of the $(Nb,Ti)(Si,Al)_2$ phase. These areas were composed of the $(Cr,Ti,Nb)_6Si_5$, and $(Cr,Ti,Nb)(Si,Al)_2$ phases and very low volume fraction of $(Si)_{ss}$ (observed in very narrow areas and exhibited black contrast). The $(Cr,Ti,Nb)_6Si_5$ was mostly formed in contact with the columnar $(Nb,Ti)(Si,Al)_2$ dendrites, then the $(Cr,Ti,Nb)(Si,Al)_2$ phase was formed and lastly the $(Si)_{ss}$.

The microstructures in the top, TFBTB and bottom were similar (Figure 82). The microstructure in the bottom is shown in the figure 83b. The $(Nb,Ti)(Si,Al)_2$, $(Cr,Ti,Nb)_6Si_5$, $(Cr,Ti,Nb)(Si,Al)_2$ were still present but in this area the $(Si)_{ss}$ was not found, instead the $(Al)_{ss}$ was detected. The $(Nb,Ti)(Si,Al)_2$ dendrites were thinner and the interdendritic regions larger than in the bulk. Some areas of the interdendritic regions presented a mixture of contrasts as a result of

microsegregation in the $(Cr,Ti,Nb)_6Si_5$ phase which had a higher concentration of heavier elements in the centre and higher concentration of lighter elements in the edges. This microsegregation was observed along the $(Nb,Ti)(Si,Al)_2$ dendrites in the top and bottom of the button but was not observed in those in the bulk.

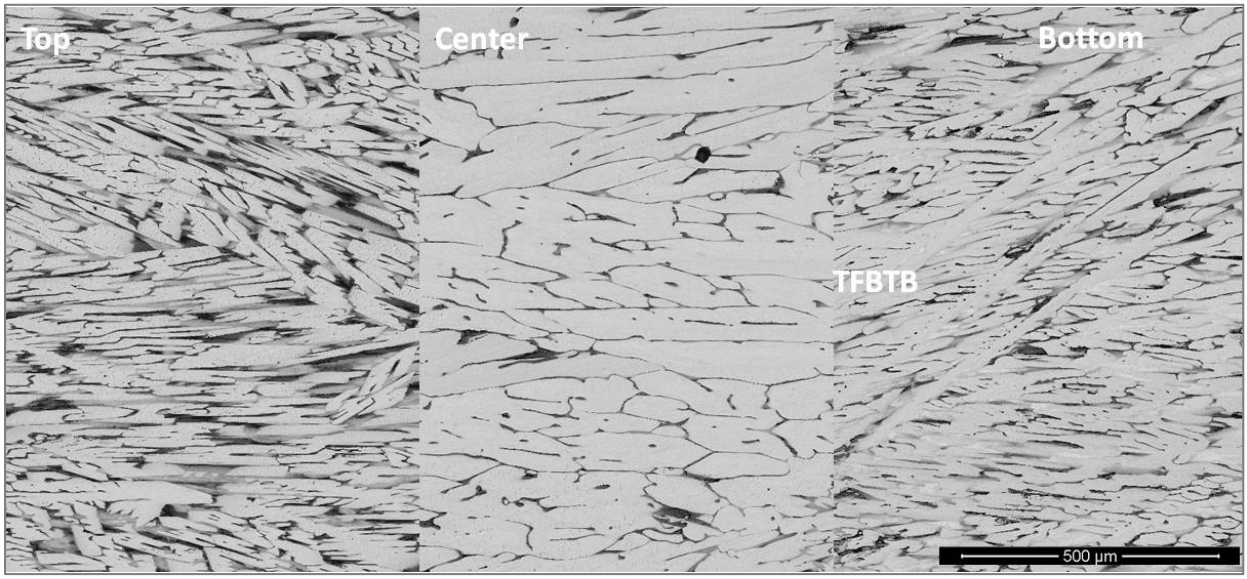

Figure 82. BSE images of typical microstructures of the alloy OHC5, in the top, bulk and bottom of the button, X200.

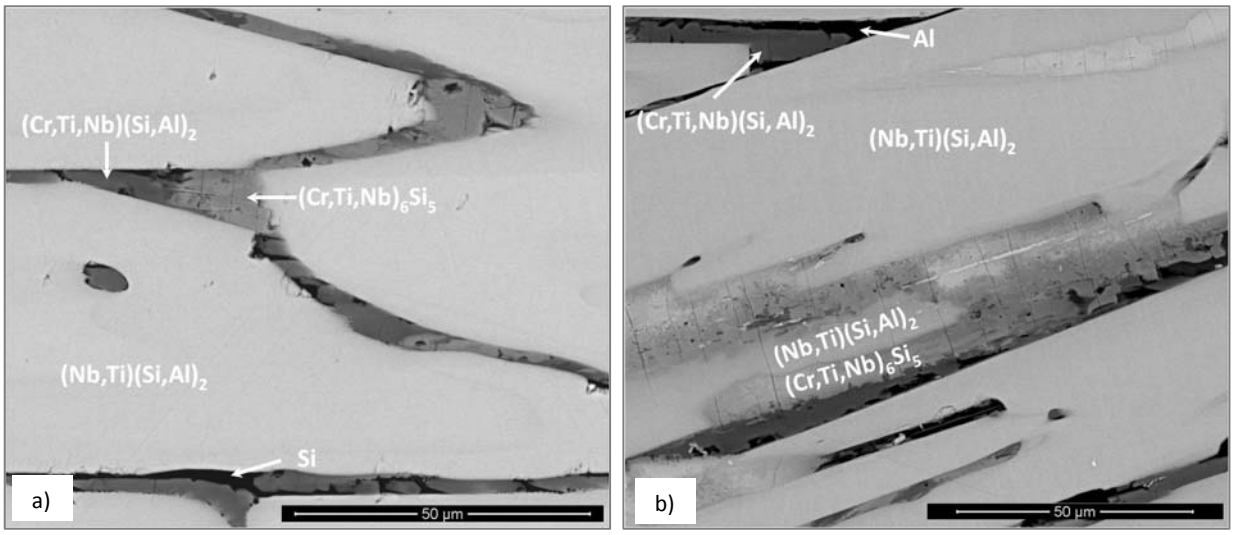

Figure 83. Higher magnification BSE images of the microstructure of the alloy OHC5: (a) bulk, X2500, and (b) bottom, X2000.

The XRD data from the as cast and heat treated alloys is shown in figure 84. These sets of data were obtained from bulk samples and therefore the intensities may not completely correspond to the phase volume fraction. The data suggested that the microstructures in the OHC5-AC contained the hexagonal phases $NbSi_2$ (JCPDS card 8-450) and $CrSi_2$ (PDF card 01-079-3529), the orthorhombic $(Cr,Ti,Nb)_6Si_5$ phase (JCPDS card 89-4813), and possibly the cubic Al_{ss} (JCPDS card 4-787). After heat treatment only the $NbSi_2$ and the $(TM)_6Si_5$ phases were present.

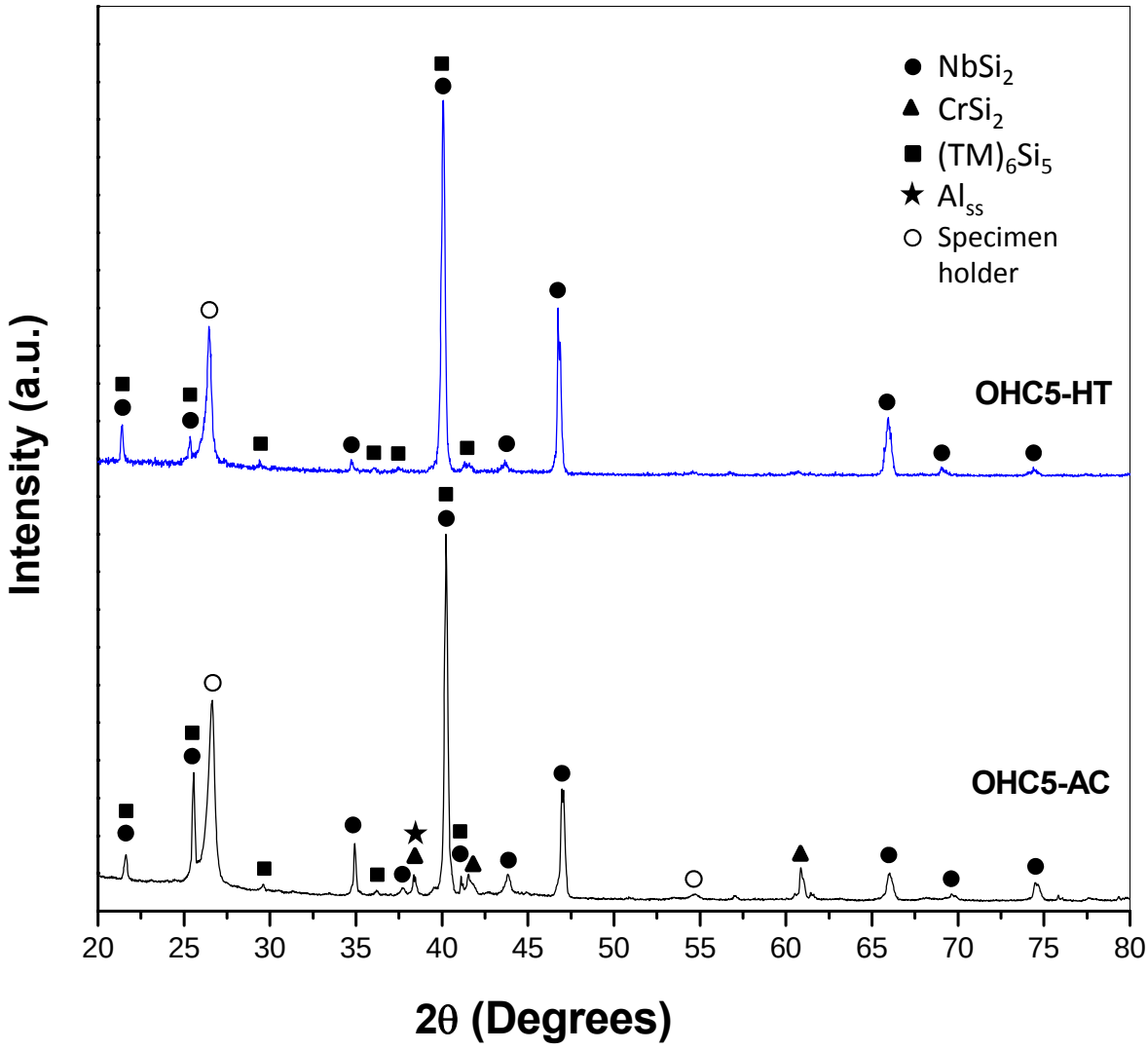

Figure 84. XRD diffractograms of the alloy OHC5 in the as cast and heat treated conditions.

Heat treated microstructure

After the heat treatment at 1400 °C for 100h in Ar atmosphere, the actual composition of the heat treated specimen was Si-26.2Nb-4.9Cr-5.2Ti-3.8Al. The EDS analysis data is given in Table 18. These data are the averages of the analyses values taken from the top to the bottom of the button after the heat treatment. The range of values would suggest that chemical inhomogeneity was still present in the heat treated alloy. In particular, the Al content in the alloy was lower by 25 % than the initial content in the as cast alloy. Liquation in the specimen or staining of the crucible after the heat treatment were not observed (by liquation it is meant that there was no noticeable distortion of the shape of the heat treated cube). The $(Al)_{ss}$ would be expected to melt at this temperature.

Table 18 EDS data (at. %) of the heat treated alloy OHC5 at 1400 °C for 100 h.

Area/Phase	Nb (at%)	Ti (at%)	Cr (at%)	Al (at%)	Si (at%)
Top	24.9 ± 0.8 26.3 – 24.2	5.7 ± 0.6 6.5 – 4.9	5.7 ± 0.7 7.4 – 4.8	3.7 ± 0.6 4.5– 2.6	60.0 ± 0.8 61.2 – 58.5
Bulk	29.4 ± 0.8 30.7 – 28.2	2.9 ± 0.4 3.6 – 2.4	2.2 ± 0.8 3.6 – 2.4	3.2 ± 0.3 3.7 – 2.9	62.3 ± 0.7 63.2 – 61.4
TFBTB*	25.7 ± 0.8 27.1 – 24.8	5.6 ± 0.6 6.3 – 5.0	5.9 ± 1.3 7.9 – 4.6	3.3 ± 0.6 3.8 – 2.5	59.5 ± 0.9 60.7 – 58.3
Bottom	24.9 ± 0.9 26.2 – 23.6	6.4 ± 0.7 7.3 – 5.5	5.8 ± 0.9 7.1 – 4.7	3.8 ± 0.5 4.7 – 3.0	59.1 ± 0.6 60.0 – 58.3
$(Nb,Ti)(Si,Al)_2$	31.1 ± 0.9 32.9 – 28.7	2.1 ± 0.6 3.6 – 0.9	0.9 ± 0.3 1.6 – 0.3	3.9 ± 0.5 4.8 – 2.8	62.1 ± 0.5 63.2 – 61.6
$(Nb,Ti,Cr)(Si,Al)_2$	26.0 ± 1.1 29.0 – 24.3	5.6 ± 0.8 6.9 – 4.2	2.3 ± 0.4 3.3 – 1.7	4.1 ± 0.5 4.8 – 3.0	62.0 ± 0.5 63.0 – 61.1
$(Cr,Ti,Nb)_6Si_5$	10.7 ± 1.3 12.8 – 8.4	15.1 ± 1.0 17.0 – 13.0	28.3 ± 1.7 30.9 – 26.1	0.7 ± 0.1 0.9 – 0.4	45.3 ± 0.2 45.8 – 44.7

*TFBTB = transition from bulk to bottom

The microstructures in the top, centre and bottom of OHC5-HT are shown in figure 85. The alloy consisted only of two phases namely the $(Cr,Ti,Nb)_6Si_5$ embedded in a matrix of $NbSi_2$ confirmed by the EDS analysis and XRD data (Table 18 and Figure 84). The $(Cr,Ti,Nb)(Si,Al)_2$ was not found in the microstructure and the XRD (Figure 84) confirmed this. In the Table 18 the two compositions for the $NbSi_2$ resulted from the disolution of the $(Cr,Ti,Nb)(Si,Al)_2$. In the

$(Cr,Ti,Nb)_6Si_5$ cracks were observed, its Cr content had increased to 28 at.% Cr and its Al content was practically negligible at this temperature.

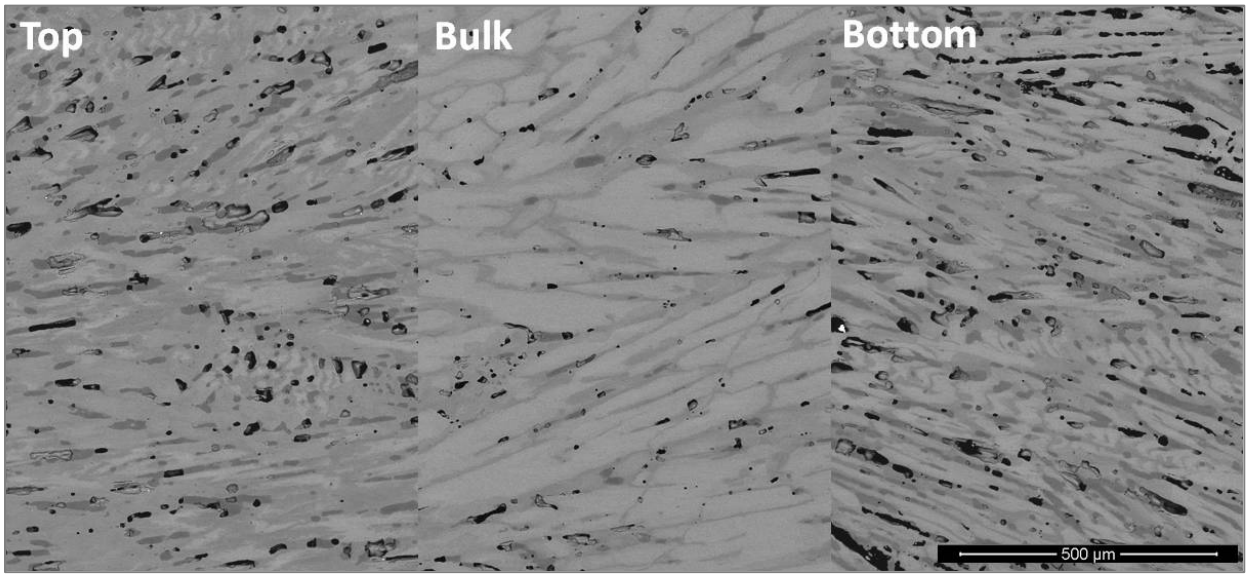

Figure 85. BSE images of the typical microstructures of OHC5-HT, from top, bulk and bottom, X200.

Details of the microstructure in the top and bottom are shown in Figure 86a. The $NbSi_2$ and the $(Cr,Ti,Nb)_6Si_5$ phases were present. The $NbSi_2$ presented two compositions, identified as the $(Nb,Ti)(Si,Al)_2$, and the $(Nb,Ti,Cr)(Si,Al)_2$ in Table 18 . The microsegregation in the $(Nb,Ti)(Si,Al)_2$ was more evident in the top and bottom than in the bulk, darker contrast areas were Cr-rich and there was an increase of the $(Nb,Ti,Cr)(Si,Al)_2$ volume fraction. The volume fraction of the $(Cr,Ti,Nb)_6Si_5$ phase had also increased and had similar morphology to that in the bulk . Its transition metals content was slightly changed. In the top of the alloy the Ti content in $(Cr,Ti,Nb)_6Si_5$ was practically fixed at 14 at. % Ti, but in the bottom it was in the range 15.31 to 17 at.% Ti.

The typical microstructure in the bulk of the heat treated button is shown in figure 86b. This microstructure also consisted of $NbSi_2$ matrix with coarsened $(Cr,Ti,Nb)_6Si_5$. There was a very low volume fraction of $(Nb,Ti,Cr)(Si,Al)_2$ along the $(Nb,Ti)(Si,Al)_2$ grain boundaries.

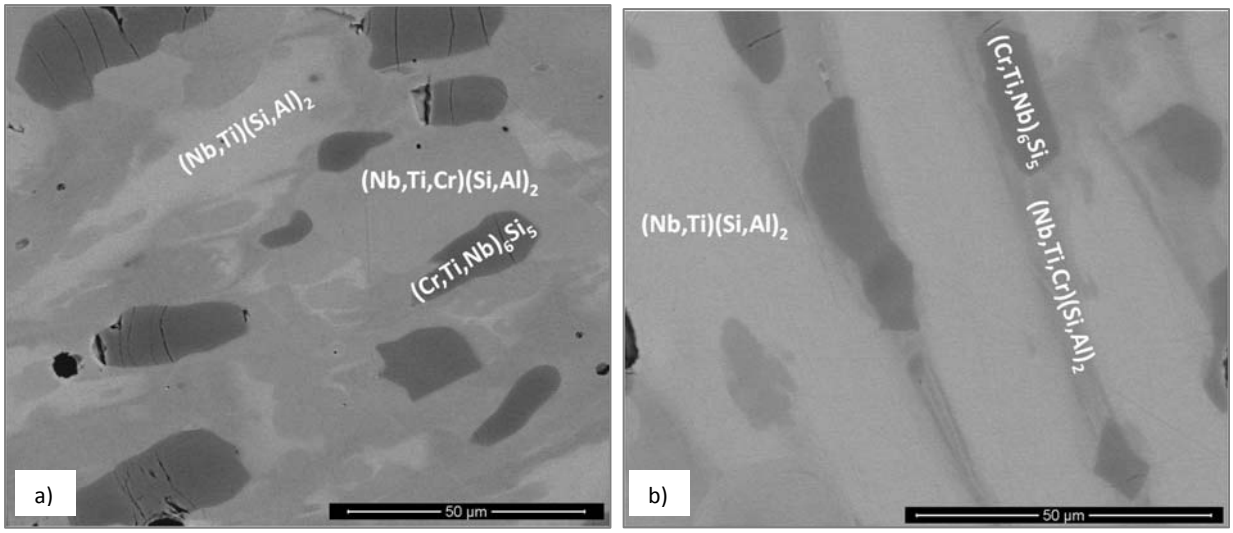

Figure 86. BSE images of the microstructure of OHC5-HT: a) top, X2000(b) bulk, X2500.

4.2.2 Thermo-gravimetric analysis

The oxidation rate constants of the alloy OHC5 after isothermal oxidation at 800 and 1200 °C are shown in table 19. According to the evaluation of the isothermal oxidation data with equation (1) at 800 °C, the n value was 0.54. Thus, the oxidation behaviour was parabolic and was composed of slightly different parabolic oxidation rates. That could be attributed to the nature of the grown oxides and any phase transitions that could had occurred during oxidation.

It was not possible to analyse the isothermal oxidation data at 1200 °C with equation (1). However, it was possible to evaluate the data with eqs. (2) and (3), thus rate constants were obtained for different periods during the isothermal oxidation time (see Table 19).

Table 19 Total weight gain n values and oxidation rate constants of the alloy OHC5 for isothermal oxidation at 800 and 1200 °C.

Alloy code at tested T	n	K_l ($g.cm^{-2} . s^{-1}$)	K_p ($g^2.cm^{-4}. s^{-1}$)	Weight gain (mg/cm^2)
OHC5 - 800 °C	0.54	-	3.4×10^{-13} (0-1.3)h 3.8×10^{-14} (1.3-24)h 1.5×10^{-13}(>24)h	0.22
OHC5 -1200 °C	-	4.4×10^{-8} (0-4.5)h 2.1×10^{-8} (17-21.5)h	1.41×10^{-12} (>21.5)h	0.85

4.2.2.1 Thermo-gravimetric analysis (TGA) at 800 °C

Figure 87, gives the isothermal oxidation data and shows three oxidation stages, the first lasted only 1.3h, the second lasted 22.7 and the third that lasted to the end of the experiment. This behaviour could be some type of transient oxidation in the first 24 h giving a slow growth oxide scale that possibly cracked and spallaled before a more protective oxide scale was stablished. Phase transitions and chemical reactions have been linked with changes of oxidation rate [Brumm and Grabke (1992)]. The weight gain after 100 h of the oxidation test at 800 °C was 0.22 mg/cm^2, see Table 19.

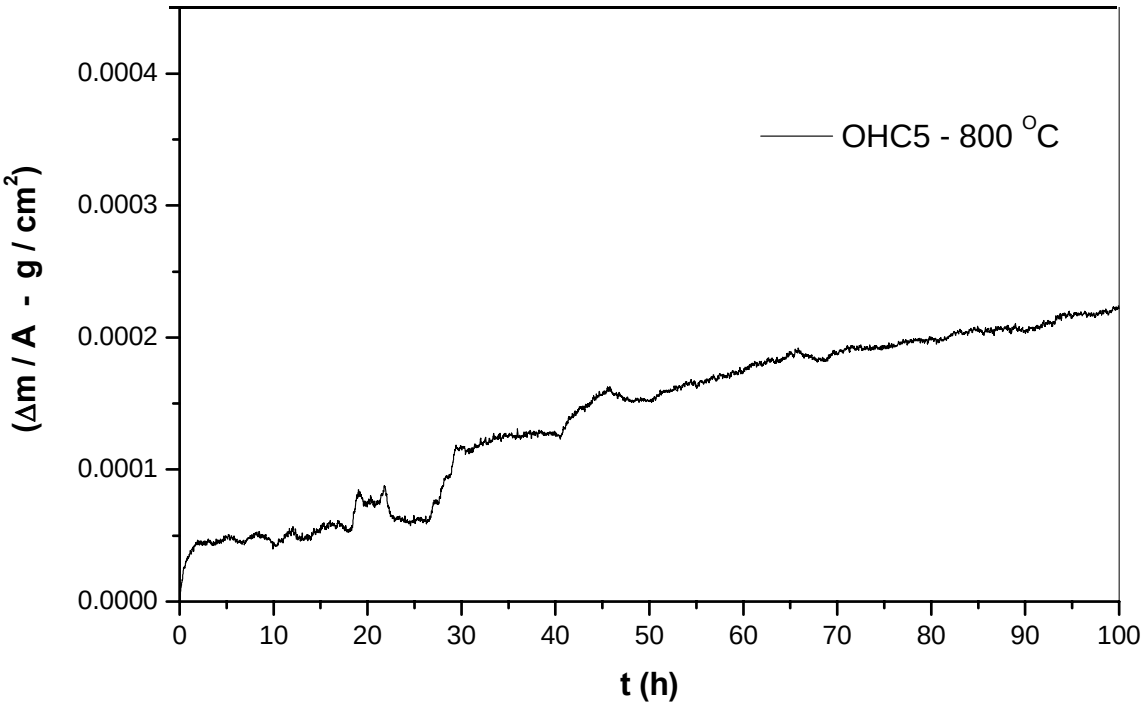

Figure 87. Isothermal oxidation TG plot of the alloy OHC5 in air at 800 °C for 100 h.

Microstructure of oxide scale at 800 °C

After isothermal oxidation in air at 800 °C for 100h, the cubic specimen remained intact with defined edges; its surface was covered by a black oxide layer. The images in figure 88 illustrate the surface after oxidation. The oxide was observed using secondary electron imaging (Figure 88a) and backscattered electron imaging (Figure 88b). Both images illustrate that an adherent oxide scale formed on the surface of the alloy and that the microstructure of the scale was not

the same over the surface. These different microstructures had resulted from the oxidation of the different phases in the alloy. The lumpy areas composed of clusters of angular oxide particles and ridge network like areas were formed over the Al rich areas in the alloy, the thin, flat and continuous oxide was observed over the rest of the alloy giving bright contrast over the $(Nb,Ti)(Si,Al)_2$ and grey contrast over the $(Cr,Ti,Nb)_6Si_5$ phase.

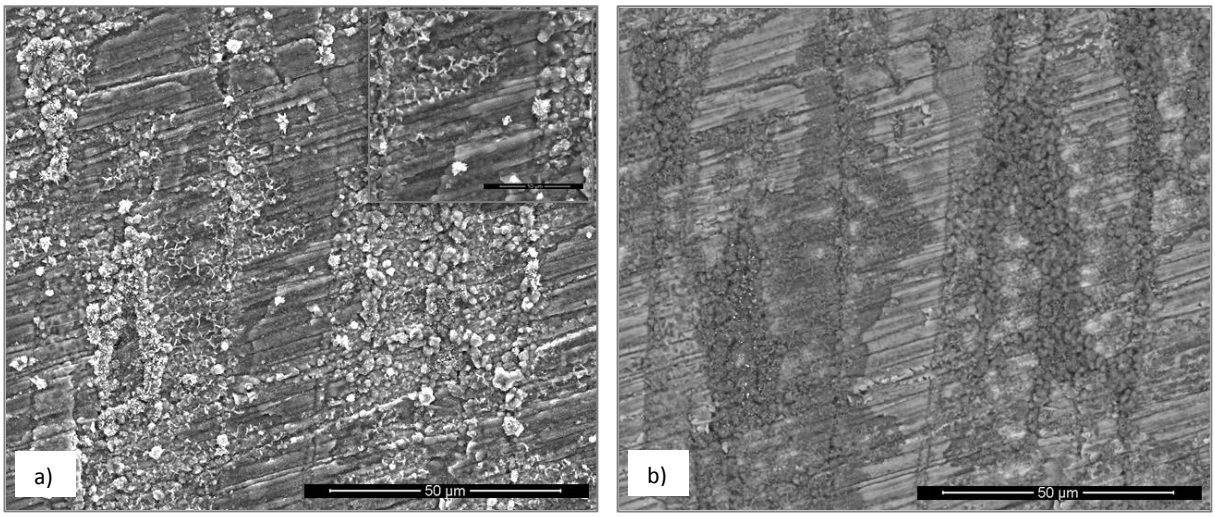

Figure 88. Images of the alloy OHC5 after isothermal oxidation in air at 800 °C for 100 h (a) SE image, oxide scale surface X2000 with insert, X8000 (b) BSE image, X2000.

The glancing angle XRD data in figure 89 suggested that the oxide scale formed during the isothermal oxidation at 800 °C consisted of α- Al_2O_3 (JCPDS No. 10-173), θ-Al_2O_3 (JCPDS No. 50-1496), quartz SiO_2 (JCPDS No. 47-1144), and rutile type TiO_2 (JCPDS No. 21-1276). It also suggested that the rutile type TiO_2 could have different compositions derived from its non stoichiometry and its solubility for Nb and Cr. Rutile type complex oxides like $(Ti_{(1-x-y)},Cr_x, Nb_y)O_2$ could be present in the oxide scale.

The X-ray elemental distribution maps (Figure 90) assisted the comparison of the oxides with the location of their chemical components. Although the oxide scale was mainly composed of Al and O some strong signals from the transition metals are also visible. These images also show the morphologies of Al_2O_3 in different regions and the regions where the Cr, Nb and Ti were the main components suggesting the formation of a complex oxide, Al_2O_3 and some SiO_2.

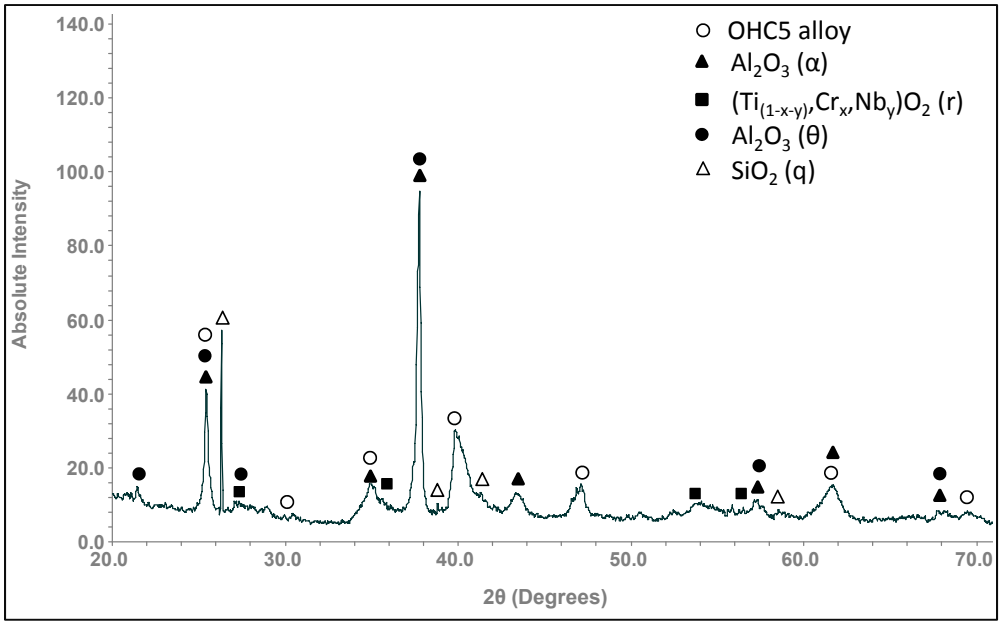

Figure 89. Glancing angle XRD data (γ= 5°) for the oxide scale formed on the alloy OHC5 at 800 °C in air.

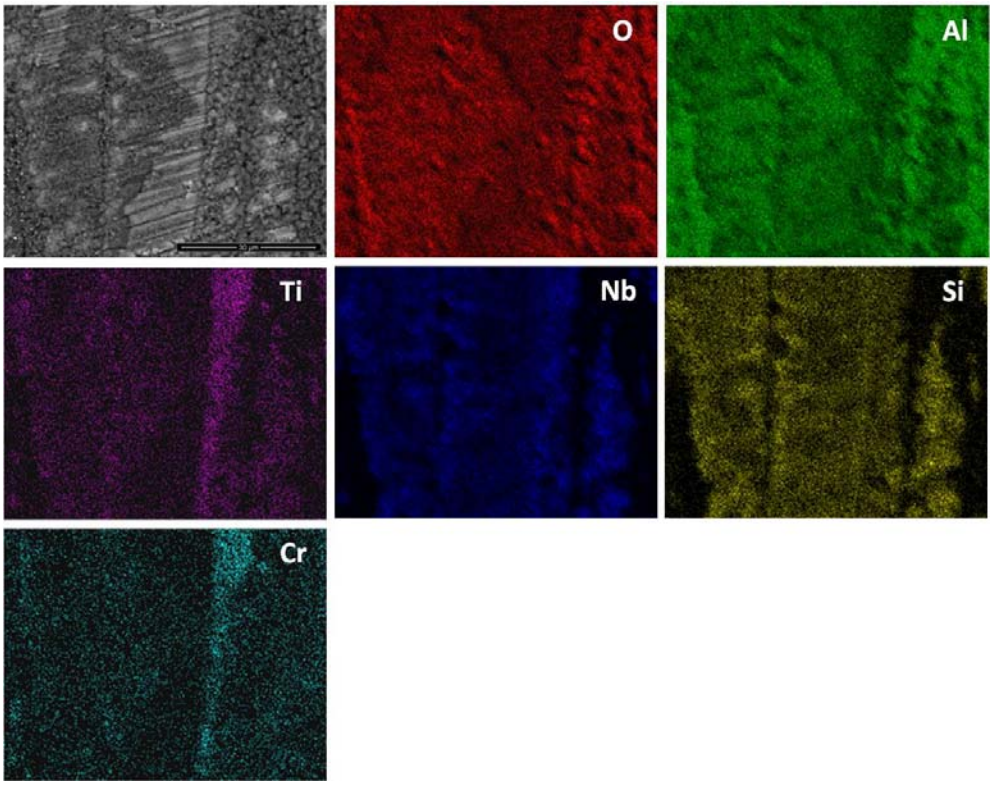

Figure 90. X-ray elemental maps from the oxide surface of the alloy OHC5 after isothermal oxidation in air at 800 °C for 100 h, X4000.

Images of the cross section of the oxide scale in figure 91 illustrate that the oxide scale had uneven thickness, in the range 1 to 4 μm. The oxide scale was adherent and continuous and its thickness depended on the oxidized phase. The oxide scale formed on top of the $(Nb,Ti)(Si,Al)_2$ was characterised by two different microstructures, both presented a transition oxide (TO) at the oxide/ gas interface, which, according to chemical analyses, was composed of all the phase components, then one presented an internal oxidation zone (IOZ) composed of Al_2O_3 particles dispersed in the $(Nb,Ti)(Si,Al)_2$ followed by a thin and continuous layer of Al_2O_3 at the scale/ metal interface, and the second one did not present an IOZ but a continuous Al_2O_3 layer up to the metal/ scale interface. The latter was also slightly enriched in Al at the metal/ scale interface and at grain boundaries which is consistent with the microsegregation in the $(Nb,Ti)(Si,Al)_2$ phase, the latter being richer in Ti, Al and Cr at the grain boundaries and leaner of these elements in the middle of the grains. The internal oxidation zone in the $(Nb,Ti)(Si,Al)_2$ phase was formed in the areas where the Al content at the metal / scale interface was below 3 at. % Al. The $(Cr,Ti,Nb)(Si,Al)_2$ was detected in the ridges at the metal/ scale interface. The oxide scale formed on top of these areas was found to be thinner with high Al and Si content on the top of this phase. The $(Nb,Cr,Ti)_6Si_5$ phase formed a very thin oxide and the chemical analysis performed in the cross section did not provide discernible data (Figure 91).

The X-ray elemental maps showed the elemental distribution in the cross section (Figure 92) and confirmed that Al and O were the main components of the oxide scale. A minor content of Nb, Ti Cr and Si was also found at the gas/oxide interface. Considering the images 90 and 92, it is possible to locate the rutile type oxides which are mostly found at the scale/gas interface with a significant Al_2O_3 content. In particular, the figure 92 shows that the Al_2O_3 was the main oxide formed on top of the $(Nb,Ti)(Si,Al)_2$ phase and that considerable signals for Nb and Si were also detected.

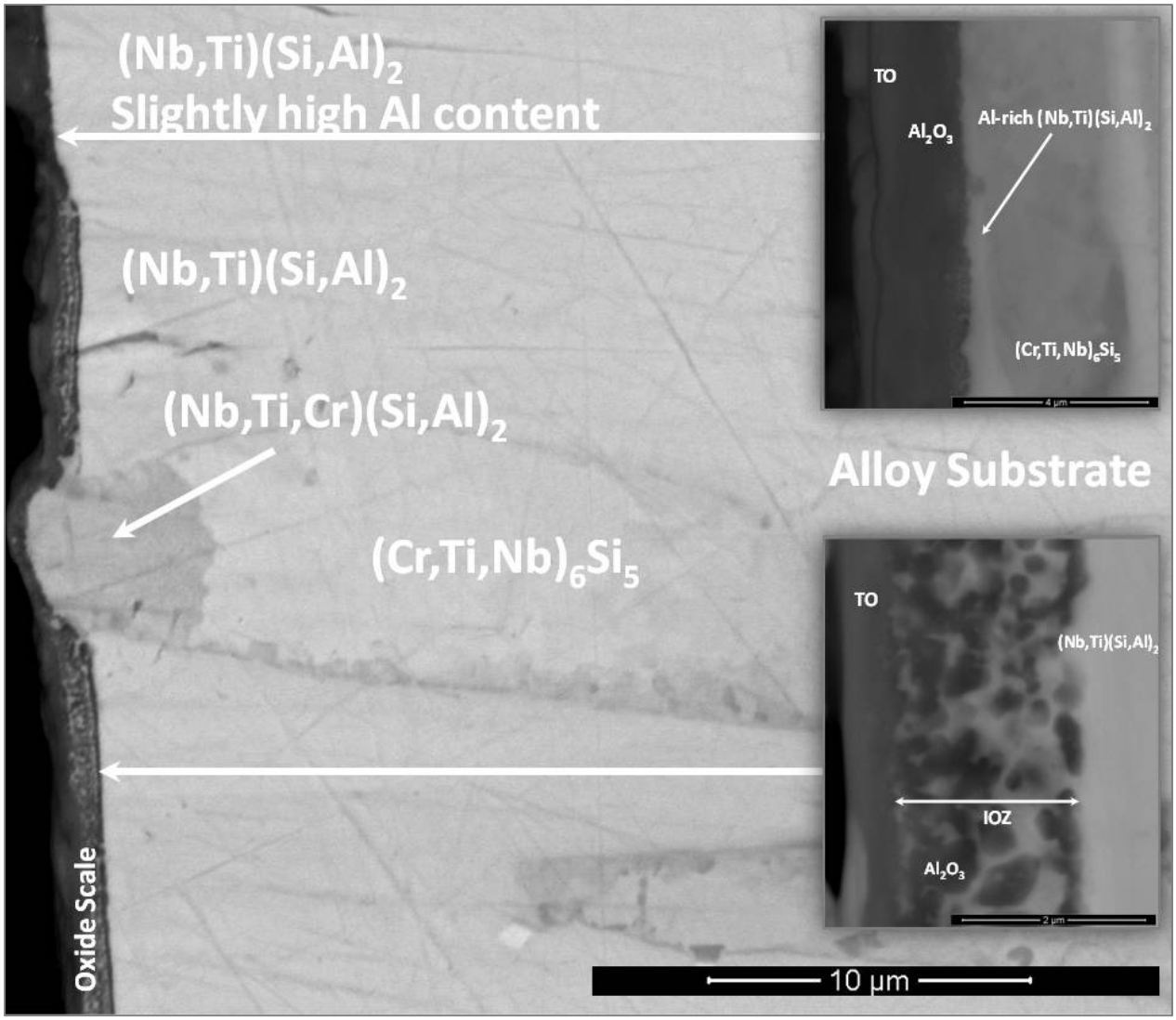

Figure 91. BSE images of a cross section of the alloy OHC5 after isothermal oxidation in air at 800 °C for 100 h. Main image, X7000, top insert, X30000 and bottom insert, X60000.

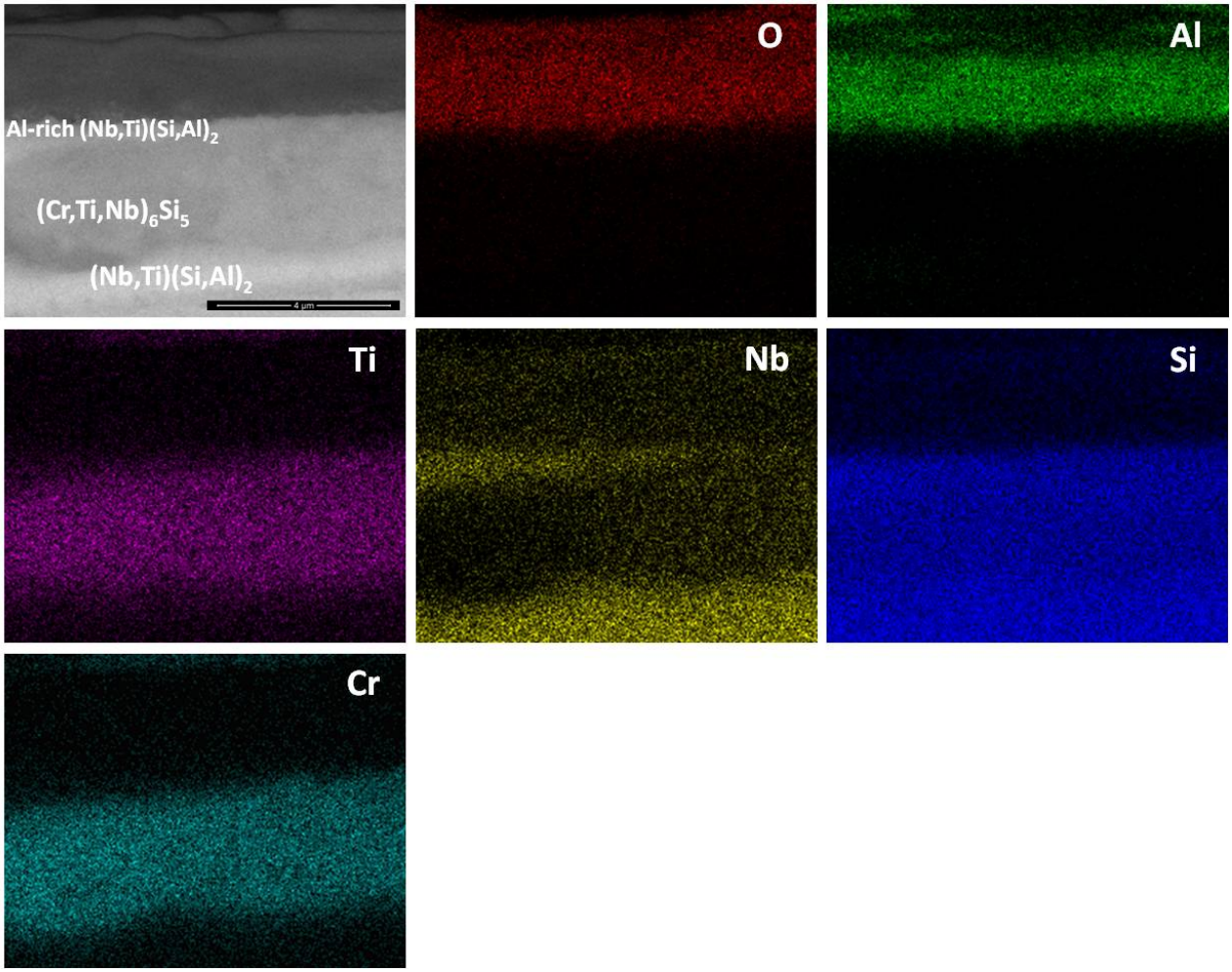

Figure 92. X-ray elemental maps from across section of the alloy OHC5 after isothermal oxidation in air at 800 °C for 100 h, X30000.

4.2.2.2 Thermo-gravimetric analysis (TGA) at 1200 °C

In figure 93 the isothermal oxidation data obtained at 1200 °C is illustrated. The data shows four different stages of oxidation. In the first three hours the alloy gained weight linearly and then up to 14 hours there was a period of weight loss. After this period, the specimen gained weight linearly for 4.5 h and then the alloy oxidised parabolically from 21.5 h until the end of the experiment. The weight gain after 100 h at 1200 °C was 0.85 mg/cm^2, see Table 19.

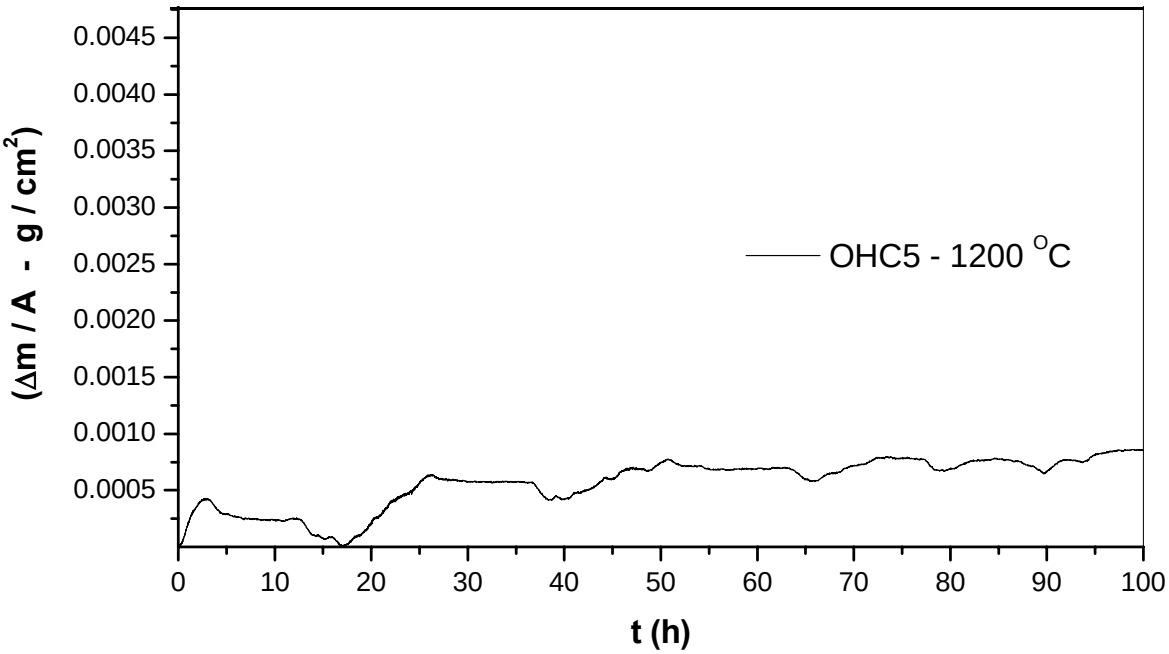

Figure 93. Isothermal oxidation TG plot of the alloy OHC5 in air at 1200 °C for 100 h.

Microstructure of oxide scale at 1200 °C

After isothermal oxidation in air at 1200 °C for 100 h, the cubic specimen remained intact with well defined and visible edges; its surface was covered by a light green colour oxide layer. The images in figure 94 illustrate the surface of the oxide scale formed on the specimen after oxidation. The SE image in figure 94a shows porosity and partial oxide spallation that did not expose the substrate. There were also ridges on the oxide surface. The oxide spallation was mostly found next to the oxide lumps.

The BSE image in Figure 94b would suggest that the oxide scale consisted of only one oxide phase, since an even contrast was observed under BSE conditions. The SE images in figure 94c and 94d illustrate an adherent oxide scale that was composed by a mixture of different particles whose morphology, size and shape were needle-like particles and faceted granular particles. Under BSE conditions these oxide particles did not show different contrasts. The glancing angle XRD data in figure 95 suggested that the oxide scale formed during the isothermal oxidation at 1200 °C consisted of Al_2O_3 corundum type with (JCPDS 10 -173). The different morphologies of the alumina particles observed on the oxide scale surface could be the result of a sluggish

transformation from some of its typical metastable forms. It is well known that the corundum type of Al_2O_3 is the stable form of Al_2O_3 above 1100 °C. However, it is possible that some trace amounts of transition aluminas could be retained. The peaks from the alloy corresponded to the $(Cr,Nb,Ti)_6Si_5$ phase with (JCPDS 54-0381).

As was the case for the specimen oxidized at 800 °C, the oxide lumps were located where the transformation from $(Cr,Ti,Nb)(Si,Al)_2$ to $(Nb,Ti,Cr)(Si,Al)_2$ could have occurred. It is possible that this transformation influenced the size of the oxide particles giving a finer grain size in these areas compared with the rest of the alloy. Furthermore, slight scale spallation occured mainly over the areas with segregation (in the interdendritic areas). As it was observed in the oxidised specimen at 800 °C, the excess of Al and Cr in such areas could promote a faster scale growth increasing the strain in the scale.

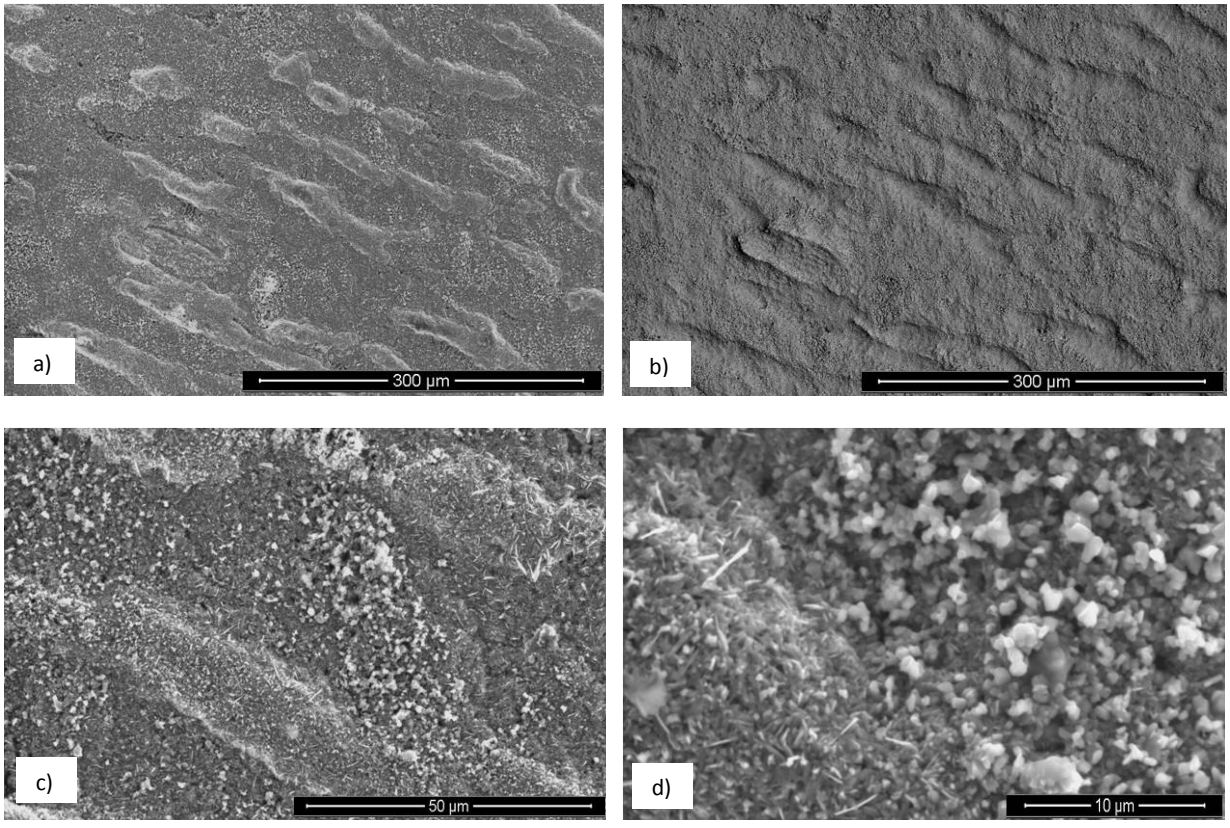

Figure 94. Images of the surface of the oxide scale of the alloy OHC5 after isothermal oxidation in air at 1200 °C for 100h (a) SE image, X200, (b) BSE image, X200, (c) SE image, X1000 and (d) SE image, X3500.

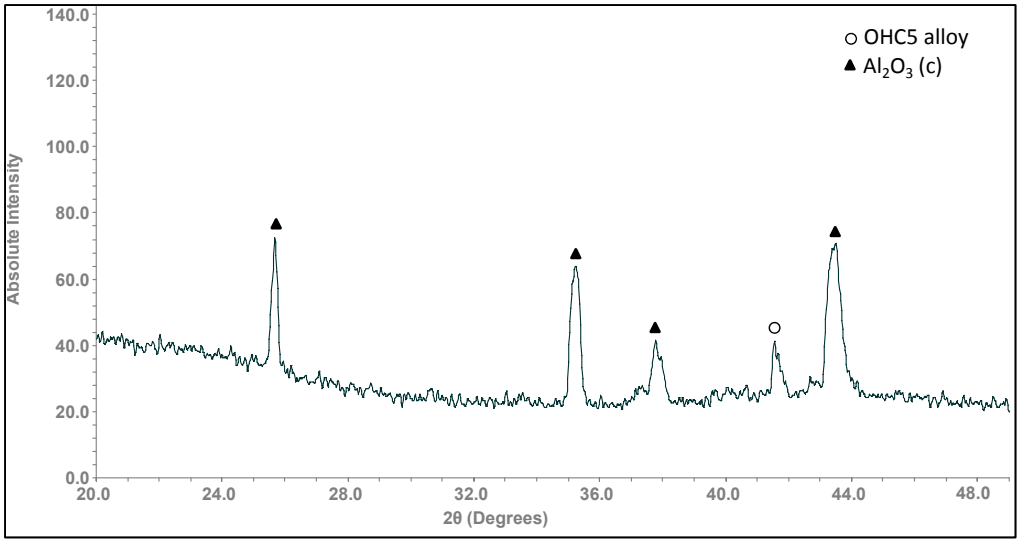

Figure 95. Glancing angle XRD data (γ= 5°) for the oxide scale formed on the alloy OHC5 at 1200 °C in air.

The oxide scale in the cross section images in figure 96 was seen to be continuous and compact with different thickness (5-10 µm) depending to the oxidised phase.

At 1200 °C only the $(Nb,Ti)(Si,Al)_2$, $(Nb,Ti,Cr)(Si,Al)_2$, $(Nb,Cr,Ti)_6Si_5$, and $(Cr,Nb,Ti)_6Si_5$ phases were stable and the $(Cr,Ti,Nb)(Si,Al)_2$ phase and the Al and Si solid solutions were not found. The EDS qualitative analyses presented in figure 97 give the composition of the phases in the metal scale interface. An increase of the scale thickness at the grain boundaries, where the transformation of $(Cr,Ti,Nb)(Si,Al)_2$ to $(Nb,Ti,Cr)(Si,Al)_2$ could occur at the metal/ scale interface was observed, which would suggest that the grain boundaries played an important role in the oxidation of the alloy OHC5 at this temperature.

According to the elemental distribution in the X-ray maps in figure 97, the oxide scale was composed of Al and O over all the component phases in the alloy. Even the $(Cr,Nb)_6Si_5$ phase with its low Al content was able to form some Al_2O_3 on its surface. After oxidation, EDS chemical analyses revealed that there was not significant Al depletion in the $(Nb,Ti)(Si,Al)_2$ silicide instead this phase was found to be richer in Al and Cr at the metal/ scale interface possibly as a result of the dissolution of the $(Cr,Ti,Nb)(Si,Al)_2$. The grain boundary areas were richer in Al and Cr in the places where the $(Cr,Ti,Nb)(Si,Al)_2$ phase could have dissolved into the

$(Nb,Ti,Cr)(Si,Al)_2$ and in these areas the $(Nb,Cr,Ti)_6Si_5$ phase was found to be richer in Cr by 63 %. A thicker Al_2O_3 oxide scale was also observed in these areas.

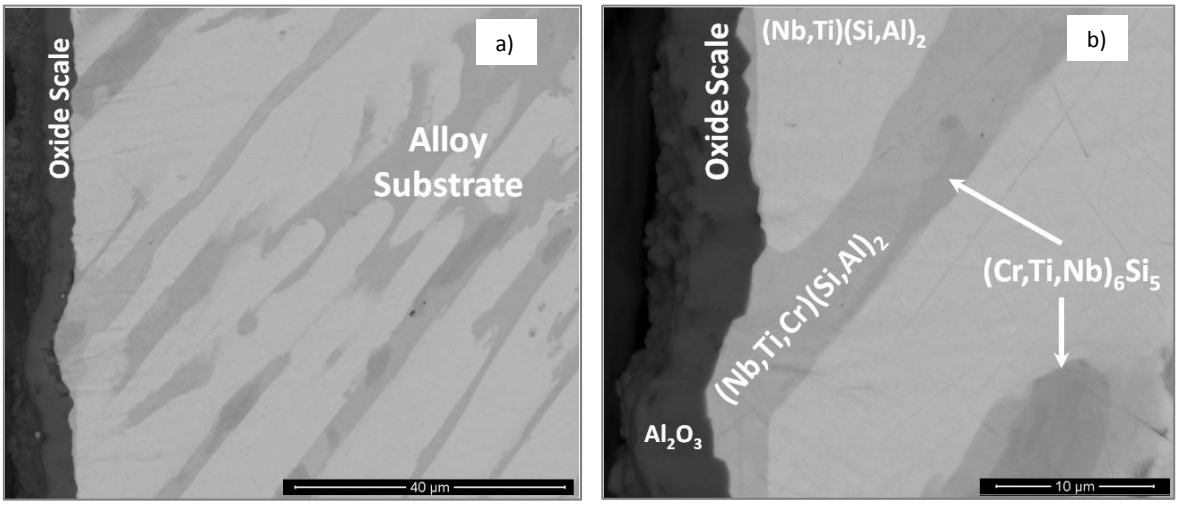

Figure 96. BSE cross section images of the alloy OHC5 after isothermal oxidation in air at 1200 °C for 100 h, (a) X3000, (b) X7000.

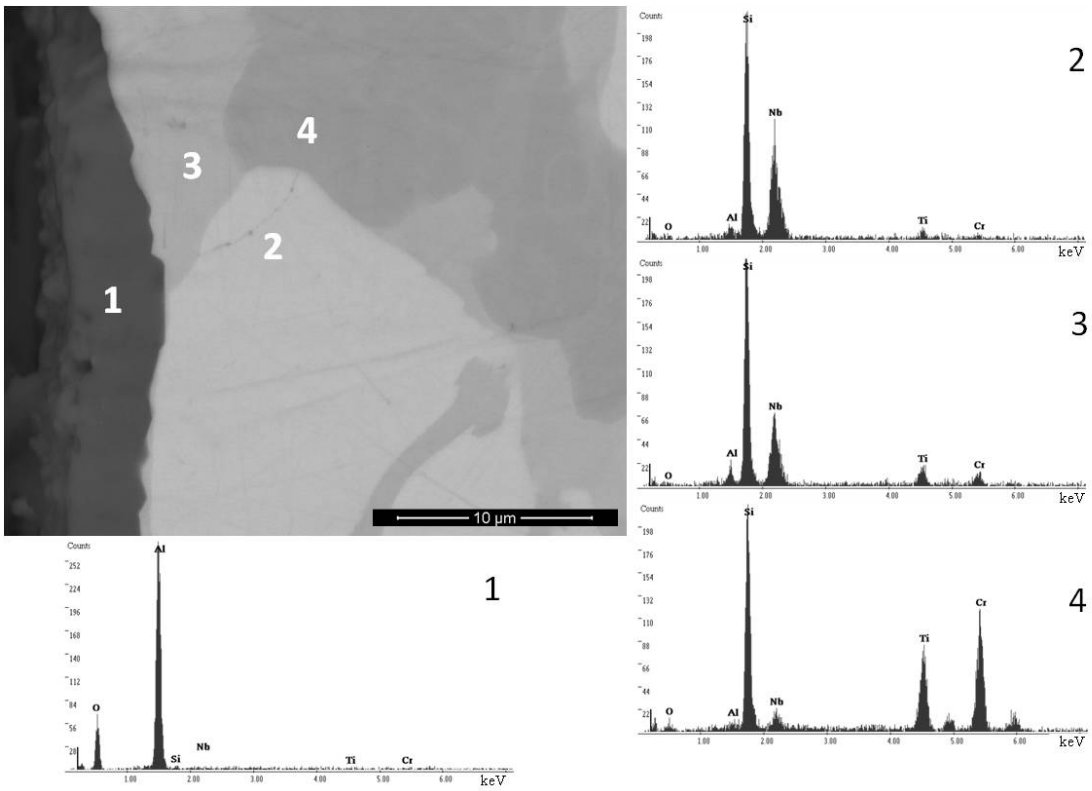

Figure 97. BSE cross section image (X8000) of the alloy OHC5 after isothermal oxidation in air at 1200 °C for 100 h with EDS spectra(1) Al_2O3, (2) $(Nb,Ti)(Si,Al)_2$, (3) $(Nb,Ti,Cr)(Si,Al)_2$ and (4) $(Nb,Cr,Ti)_6Si_5$.

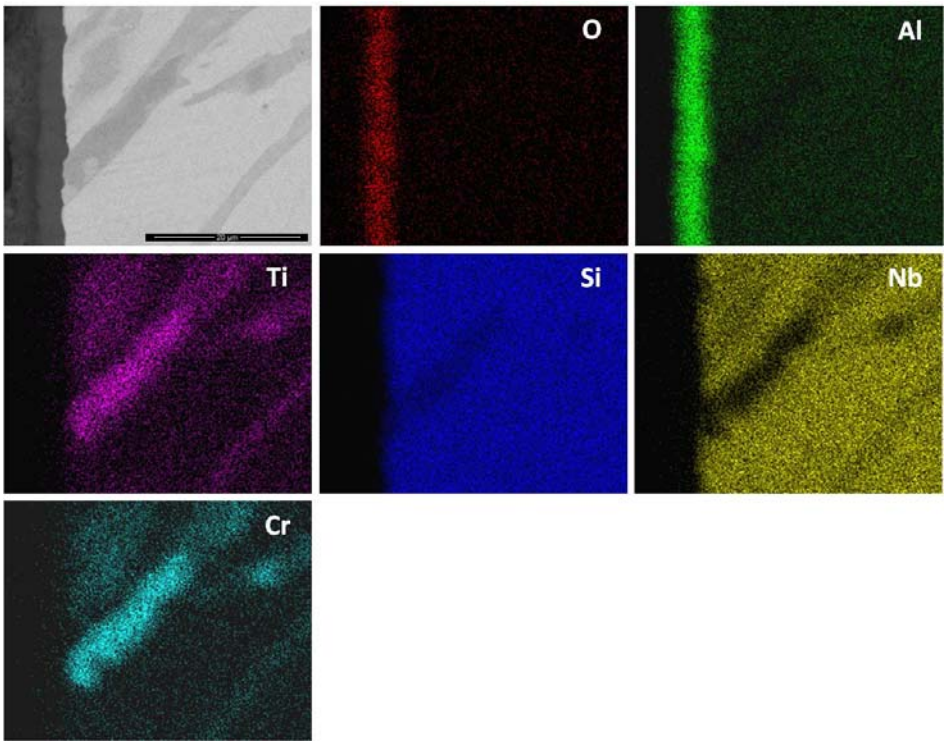

Figure 98. BSE image (X6000) and X-ray elemental maps from a cross section of the alloy OHC5 after isothermal oxidation in air at 1200 °C for 100 h.

4.3 Discussion

4.3.1 Microstructure

The alloy OHC5-AC exhibited macrosegregation of all its elements. Using the criterion $C_{max} - C_{min} \geq 2$ at.%, the macrosegregation of Nb was the most severe. Furthermore, the concentration of Nb and Si were the highest in the bulk of the button where the concentrations of Al, Cr and Ti were the lowest, meaning different macrosegregation profiles for the aforementioned elements (the data in the Table 17 for bottom, transition zone, bulk and top demonstrates this opposite trends in the concentrations of the above elements).

Macrosegregation is not uncommon in arc melted alloys using water cooled copper crucibles and is attributed to a variety of parameters and linked with microsegregation, as discussed by Tsakiropoulos (2014a). Chemical inhomogeneities (i.e., microsegregation) in the phases observed in the microstructure of OHC5-AC (Table 17) were suggested by the minimum and

maximum analyses values and/or large standard deviations for most elements, particularly for the $(Cr,Ti,Nb)(Si,Al)_2$ and $(Cr,Ti,Nb)_6Si_5$ phases.

In the microstructure of OHC5-AC the $(Nb,Ti)(Si,Al)_2$ was formed at the highest volume fraction with the other intermetallic and solid solution phases forming from the liquid between the $(Nb,Ti)(Si,Al)_2$ grains. Considering the binary disilicides $NbSi_2$, $CrSi_2$ and $TiSi_2$ and their crystal structures, the former two are isomorphous (C40) and could form a continuous solution phase while the latter is orthorhombic (C54). Nakano et al. (2000) suggested that very small substitutions of Nb and Si by Ti and Al in the $NbSi_2$ phase (with up to 1.7 at. %Ti substituting Nb and up to 2 at. % Al substituting Si) would stabilize the C54 crystal structure which was not confirmed by their results which could suggest that the content of these elements has to be higher to stabilize the C54 crystal structure.

The $TiSi_2$ phase was not detected in OHC5-AC and OHC5-HT by EDS and XRD, the $CrSi_2$ phase was detected by XRD and according to EDS its Nb, Ti and Al contents were up to 6.0 at. % Nb, 12.3 at.%Ti and 10.0 at.% Al. The solubility of these elements in the $CrSi_2$ based $(Cr,Ti,Nb)(Si,Al)_2$ was in agreement with the range of solubilities reported in the Ti-Cr-Si and Cr-Si-Al ternary systems [Du and Shuster (2002), and Chen et al. (2007)]. In the Cr-Ti-Si system there is solid solubility between the $CrSi_2$ and $TiSi_2$ phases [Du and Shuster (2002)]. The $CrSi_2$ solidifies with the C40 crystal structure and Al in solution does not change this.

Regarding the melting temperatures of the unalloyed disilicides, their ranking is T_m^{NbSi2} = 1935 °C, T_m^{TiSi2} = 1480 °C and T_m^{CrSi2} = 1450 °C, and as we discussed in the previous chapter the melting temperature of $(TM)_6Si_5$ is believed to be higher than 1500 °C. Thus, it would be expected that the primary phase to form from the melt was the intermetallic based on $NbSi_2$, namely the $(Nb,Ti)(Si,Al)_2$ phase followed by the $(TM)_6Si_5$ and then the $(Cr,Ti,Nb)(Si,Al)_2$ given the ternary solubilities of $TiSi_2$ and $CrSi_2$ and finally the solid solutions of Si and Al. The primary $(Nb,Ti)(Si,Al)_2$ phase formation is supported by the observed microstructures and the Nb-Cr-Si liquidus projection (Figure 12a) when the alloy is considered as Cr-(Nb,Ti)-(Si,Al). The formation of the $(TM)_6Si_5$ after the aforementioned primary phase is also in agreement with the liquidus

projection. Thus, the solidification path of the alloy OHC5-AC was L $\rightarrow$L + $(Nb,Ti)(Si,Al)_2$ $\rightarrow$L + $(Nb,Ti)(Si,Al)_2$ + $(TM)_6Si_5$ $\rightarrow$ L + $(Nb,Ti)(Si,Al)_2$ + $(TM)_6Si_5$ + $(Cr,Ti,Nb)(Si,Al)_2$ $\rightarrow$ $(Nb,Ti)(Si,Al)_2$ + $(TM)_6Si_5$ + $(Cr,Ti,Nb)(Si,Al)_2$ + $(Si)_{ss}$ or $(Al)_{ss}$ (depending on solidification conditions and the composition of the last to solidify melt).

After the heat treatment at 1400 °C for 100 h the $(Cr,Ti,Nb)(Si,Al)_2$ was not stable as well as the $(Al)_{ss}$ and $(Si)_{ss}$ and the Cr concentration in the 6-5 silicide increased significantly. The former is in agreement with the 1500 °C isothermal section of Cr-Nb-Si (Figure 9) when the heat treated alloy (Table 18) is considered as Cr-(Nb,Ti)-(Si,Al) and the latter is attributed to the dissolution of the $(Cr,Ti,Nb)(Si,Al)_2$. The smaller standard deviation values and differences between maximum and minimum analysis values are also indicative of the move of the microstructure towards equilibrium.

4.3.2 Oxidation

Oxidation at 800 °C

The alloy OHC5 did not pest at 800 °C, instead it followed parabolic oxidation kinetics with n = 0.54 and formed a very thin adherent oxide scale that mainly consisted of Al_2O_3. The EDS and glancing angle XRD data suggested that SiO_2 and rutile type oxides $(Ti_{(1-x-y),}Cr_x,Nb_y)O_2$ were also present in the scale. These did not appear to be detrimental to the oxidation resistance of the alloy. The TGA data gave different parabolic rate constants (Table 19). Oxides with different morphology and composition (Figures 88 and 90) formed in the oxide scale which would suggest that it is likely that the oxidation behaviour of a particular phase depended on its chemical inhomogeneity.

The phases in the alloy microstructure oxidised differently forming a scale of uneven thickness (1-4 μm), see figure 91. The thinner oxide scale was formed on the $(Nb,Cr,Ti)_6Si_5$. The thickness of the oxide scale formed on the $(Nb,Ti)(Si,Al)_2$ phase depended on its Al content, being thinner in those areas where the Al content was above 3 at. % Al while in the areas with a low Al content (less than 3 at. %) was formed the IOZ (Table 17). In this context not only the oxide scale thickness was affected by the Al content in the $(Nb,Ti)(Si,Al)_2$ phase but also the oxidation

mechanism since the development of a different microstructure in the oxide scale was seen (Figure 91). Thus, it is highly likely that the local composition of this phase dramatically affected its oxidation behaviour. Chemical analysis showed that in areas of the Al lean $(Nb,Ti)(Si,Al)_2$ phase, the oxide scale consisted of an external layer of transient complex oxides which might not be protective. Thus, Al was possibly internally oxidised until a continuous Al_2O_3 layer formed below the IOZ hindering further oxidation. According to Meier and Petit (1992) alloys with low solute contents oxidise by inner diffusion of oxygen. On the other hand, near the $(Nb,Ti)(Si,Al)_2$ grain boundaries (Al-rich areas) the activity of Al and Si was higher and an oxide scale formed that consisted of an outer layer (transient oxides) mainly composed of Al and Si and an inner layer very rich in Al (as it was observed in the cross section images). The ridges (lumps) at the metal/ scale interface were related to the $(Cr,Ti,Nb)(Si,Al)_2$ phase but it is not clear if they had formed as a result of the metal recession presented by the $(Nb,Ti)(Si,Al)_2$ phase (internally oxidised), or by coarsening caused by the ejection of Al and Cr from the $(Nb,Ti)(Si,Al)_2$ phase or by both phenomena.

Thus, considering the microstructure of the oxide scale, it is suggested that the oxidation mechanism of the $(Nb,Ti)(Si,Al)_2$ phase would depend on the availability of Al with about 3 at. % Al possibly being the critical content (in the presence of Ti and Cr). Aluminium contents below the critical would promote a faster inward diffusion of oxygen oxidising Al preferentially inside the phase (the solute effect). This mechanism is consistent with a parabolic behaviour. Above 3 at. % Al, the $(Nb,Ti)(Si,Al)_2$ phase would form an external oxide. The X-ray elemental maps showed Al, O_2, Nb and Si as the main components of the scale.

It was expected to find Nb and Si oxides from the oxidation of the $(Nb,Ti)(Si,Al)_2$ phase, as it was observed by Zhang et al. (2006) and Murakami et al. (2003). The data from our work suggests that the oxide scale formed on this phase was mainly composed of Al_2O_3 and that Si and Nb presented a minor contribution but with the same 1:2 ratio as in the $NbSi_2$ phase (according to EDS spectra), which suggests that their oxidation in those areas is unlikely to have occurred. Thus, it is suggested that the internal oxidation mechanism started from an initial oxidation of all the components where complex rutile oxides with different compositions formed along with

SiO_2 and Al_2O_3, the rutile type oxides could have served as a pathway allowing the inward diffusion of oxygen that reacted with Al (not being sufficient to establish a continuous Al_2O_3 layer). However, the scale/ metal interface receded up to an Al_2O_3 compact layer below the IOZ was established. The increase of the oxidation rate could also be related to a rapid Al transport through the oxide scale. According to Prescott and Graham (1992) θ-Al_2O_3 presents a faster Al transport. However, preferential orientation could also influence the Al diffusion towards the metal /scale interface.

Above it was discussed that the variation of the thickness of the oxide scale formed on top of the $(Nb,Ti)(Si,Al)_2$ disilicide was also dependent on the Cr concentration, as the latter affects the Al activity. It is already known that the addition of Cr reduces the concentration of Al required to grow and sustain an alumina scale in Ni-Cr-Al and Fe-Cr-Al alloys during oxidation. Previous studies have shown that a mixed oxide composed by SiO_2 and Nb_2O_5 formed at 750 °C when 8 at. % Cr was added to $NbSi_2$, while the addition of 20 at. % Cr improved the oxidation behaviour via the formation of an oxide scale composed by an inner layer of SiO_2 and an outer layer of Cr_2O_3. However, the underlying substrate alloy was depleted in Cr [Pitman and Tsakiropoulos (1995)]. According to Murakami et al. (2001b), a thin SiO_2 oxide layer was formed after oxidation in flowing air at 750 °C on Nb-66.7Si alloys with 10, 20, 33.3 at.% Cr additions. Al additions may not have a beneficial effect on the oxidation of $NbSi_2$ at low temperature. According to Murakami et al. (2003), an alloy with composition Nb-56Si-11Al (at. %) showed oxide spallation when it was exposed to dry air at 750 °C. Furthermore, alloys with compositions Nb-56Si-11Al-3Cr (Cr-doped alloy) and Nb-48Si-19Al-29Cr (Cr-rich alloy) showed very good oxidation resistance at low temperature but while the Cr doped alloy presented a very good oxidation resistance in the temperature range 500-1400 °C, the Cr-rich alloy presented a very poor oxidation resistance at high temperatures.

According to the microstructure observed in the scale/ metal interface it is suggested that the $(Cr,Ti,Nb)(Si,Al)_2$ phase presented higher Al and Si activities, allowing the formation of an outer SiO_2 +Al_2O_3 scale, and an inner layer of Al_2O_3.

The chemical analyses performed on the oxidation products of the $(Nb,Cr,Ti)_6Si_5$ phase were very limited owing to the very small thickness of the oxide scale formed on top of this phase. Images of the oxide surface suggested that the oxidation products were complex rutile type oxides, SiO_2 and some Al_2O_3 that could have formed from the lateral Al_2O_3 growth.

Chemical analyses of the $(Nb,Ti)(Si,Al)_2$ at the metal / scale interface did not reveal elemental depletion especially of Al which was actually slighly enriched at the metal/scale interface. Murakami et al. (2001b) observed a similar behaviour in their Nb-47Si-20Al alloys (with the $Nb_3Si_5Al_2$ phase as the matrix). However, the $(Cr,Ti,Nb)(Si,Al)_2$ phase presented some Al depletion of about 50 % less of the initial Al content. There is no data to compare with the $(Nb,Cr,Ti)_6Si_5$ phase.

It is not expected to form α-Al_2O_3 during oxidation at 800 °C. However, the glancing angle XRD data provided strong evidence of its presence. Furthermore, the EDS studies of the oxide surface showed that there were two microstructures in the areas with predominant Al and O signals, one consisting of spherical clusters of angular particles which were mostly allocated in the Al rich areas of the alloy, and ridge networks that spread over the Al-rich areas of the $(Nb,Ti)(Si,Al)_2$ phase. According to Brumm and Grabke (1992), the ridge network microstructure is related to the transformation of θ-Al_2O_3 to α-Al_2O_3. If this transformation had occurred, the oxidation rate should have decreased. Instead it increased which suggests that another contribution to the formation of less protective oxides influenced the slight increase of the oxidation rate. Thus, the above could suggest that Cr promoted a faster stabilization of α-Al_2O_3 at the scale/metal interface, while at the scale/ gas interface θ-Al_2O_3 whiskers were formed. According to Brumm and Grabke (1992) Cr promotes the transformation of θ-Al_2O_3 to α-Al_2O_3. The oxide surface formed over some Al-rich areas in the alloy presented a network-like structure Al_2O_3 that extended over the oxide scale of $(Nb,Ti)(Si,Al)_2$ which suggests a lateral growth that had resulted from the transformation of θ-Al_2O_3 to α-Al_2O_3.

The oxidation behaviour of the alloy OHC5 was different from those of Nb-Si-Al based alloys reported in the literature. Although the Nb-Al-Si-Cr alloys studied by Murakami et al. (2003) did

not suffer from pest oxidation at 750 °C and followed a parabolic oxidation rate, they did not form Al_2O_3 at low temperature instead mixed oxides of all the components were formed. This would suggest that the addition of Ti in OHC5 was beneficial for the establishment of an Al_2O_3 oxide scale on top of the $(Nb,Ti)(Si,Al)_2$ and $(Cr,Ti,Nb)(Si,Al)_2$ phases, and that the rutile type oxides were not detrimental for oxidation at 800 °C.

Oxidation at 1200 °C

According to the recorded data the isothermal oxidation of the alloy OHC5 at 1200 °C presented four stages. For the first 4.5 h the alloy followed linear kinetics, for the next 14 h the alloy lost weight, then in the third stage there was a linear gain of weight for 3 h, and finally from 21.5 h to the end of the experiment (the fourth stage), the alloy followed parabolic oxidation kinetics.

The EDS and glancing angle XRD data would indicate that the oxide scale was composed of α-Al_2O_3, see also figure 94b that shows the oxide scale under BSE imaging conditions where only one contrast is observed, and the spectrum number (1) in figure 97 and the X- ray maps of Al and O in figure 98. Thus, all the phases in the alloy must had contributed to α-Al_2O_3 formation at 1200 °C including the $(Nb,Cr,Ti)_6Si_5$ phase that had very low Al solubility. The data in figure 93 would suggest that initially some transient oxides might had also formed.

As it is often observed in alumina scales, the Al_2O_3 scale formed on the alloy OHC5 had uneven thickness, oxide lumps and lace-like ridges [Prescott et al. (1994)]. The growth of Al_2O_3 ridges is the result of the transformation of transient Al_2O_3 to α-Al_2O_3. According to Prescott et al. (1994) the transient Al_2O_3 to α-Al_2O_3 transformation starts and grows laterally until grain boundaries are reached. The last areas to convert in α-Al_2O_3 are the grain boundaries where ridges form as a result of the outward diffusion of Al ions thickening the oxide formed at the grain boundaries. On the oxide surface there were particles with same composition but different morphologies suggesting that some deformation that resulted from the build up of compressive stress from the oxide growth had affected the supply of Al and O for the continuous growth of the Al_2O_3 grains. Grain orientation and composition of the oxidised phase may have also contributed to the different morphology presented by the Al_2O_3 particles. The images of the cross section

showed that the scale was continuous and adherent and presented the classical morphology of a α-Al_2O_3 scale with coarsened grains at the metal/ scale interface.

4.4 Conclusions

The microstructural study of the as cast and heat treated alloy OHC5 allowed the following conclusions to be made:

The phases in the as cast alloy were the $(Nb,Ti)(Si,Al)_2$, $(Nb,Cr,Ti)_6Si_5$, $(Cr,Ti,Nb)(Si,Al)_2$ $(Si)_{ss}$ and $(Al)_{ss}$ with the $(Nb,Ti)(Si,Al)_2$ being the primary phase. After heat treatment only the $(Nb,Ti)(Si,Al)_2$ and $(Nb,Cr,Ti)_6Si_5$ phases were in equilibrium.

The $(Nb,Cr,Ti)_6Si_5$ phase exhibited microsegregation as was the case with the T phase in the alloys OHC1 and OHC2. The Al solubility in the $(Nb,Cr,Ti)_6Si_5$ phase was < 2 at . % Al, while the Nb solubility was up to 14.6 at. % Nb, above the Nb content in the homologous $(TM)_6Si_5$ phase in the alloys OHC1 and OHC2. After heat treatment the Cr solubility in the $(Nb,Cr,Ti)_6Si_5$ phase increased to 28.3 at.% Cr and the Al solubility decreased to below 1 at. % Al.

The thermogravimetric study at 800 °C of the alloy OHC5 allowed the following conclusions to be made:

No pest oxidation was observed in the alloy on which formed a very thin and adherent oxide scale composed of Al_2O_3 with SiO_2 and $(Ti_{(1-x-y),}Cr_x,Nb_y)O_2$ oxides. The alloy OHC5 followed parabolic oxidation kinetics and gained 0.22 mg/cm^2 after 100 h.

In the presence of Ti and Cr, the critical Al content in the $(Nb,Ti)(Si,Al)_2$ phase is 3 at. % Al to allow the formation of a continous and adherent Al_2O_3 scale. Below 3 at. % Al content in this phase an internal oxidation zone was formed under the scale / metal interface.

The oxidation of the $(Cr,Ti,Nb)(Si,Al)_2$ phase produced a two layer oxide scale where the outer layer was composed of SiO_2 and Al_2O_3 oxides and the inner layer of Al_2O_3.

The oxidation of the $(Nb,Cr,Ti)_6Si_5$ phase produced a thinner oxide scale where the $(Ti_{(1-x-y)},Cr_x,Nb_y)O_2$ oxides and SiO_2 were among the main oxides and some Al_2O_3 near the edges of the phase.

The addition of Ti in the $(Nb,Ti)(Si,Al)_2$ and $(Cr,Ti,Nb)(Si,Al)_2$ phases improved their oxidation behaviour by allowing the formation of Al_2O_3 scale on their top.

The thermogravimetric study at 1200 °C of the alloy OHC5 allowed the following conclusions to be made:

The oxide scale formed on the alloy was composed of α-Al_2O_3 and presented the classic microstructure with coarsened grains at the metal scale interface which suggest that this alloy is suitable for the use as a BC for Nb-silicide based alloys.

However, it is possible that in the first hours of oxidation it was not easy for the alloy to stablish such a scale. The oxidation occurred in four stages and the weight gain was 0.85 mg/cm^2 after 100 h.

The synergy of Cr and Ti allowed the formation of an α-Al_2O_3 oxide layer on top of the OHC5 alloy at 1200 °C.

Chapter 5

The microstructure and oxidation of the alloy Al-25.5Nb-8Cr-0.5Hf (OHC3)

5.1 Introduction

Nb-silicide base alloy will require coatings systems like the Ni base superalloys. Most likely these will be of the BC/TGO/Top coat type. In such a materials system it is desirable that the TGO is α-Al_2O_3, and is also desirable that the substrate alloy has some inherent oxidation resistance. In the case of Ni based superalloys additions of about 5-6 wt % Al and 6.7 wt. % Cr are good enough to promote inherent oxidation resistance via the formation of Al_2O_3 and Cr_2O_3 scales. The BC alloys are richer in Al (MCrAlY type BCs have about 16-20 at. % Al) and can form α-Al_2O_3 TGO. In the case of Nb-silicide based alloys high Al concentration is not possible because of the adverse effect of Al (and Cr) on the DBTT of the $(Nb,Al,Cr)_{ss}$. Furthermore, high Al content would promote the stability of Nb_3Al, which is an intermetallic that can pest in the range 700 - 900°C and can not form protective Al_2O_3 scales at high temperatures.

In the Al-Nb binary system, the lightest aluminide with lowest oxidation rate is the Al_3Nb. However, even the Al_3Nb pests in the temperature range 700-900°C [Meier (1989)]. According to Meier and Pettit (1992) the Al content of the Al_3Nb also influences its oxidation behaviour at temperatures higher than the pest regime. The Al-rich Al_3Nb forms a continuous Al_2O_3 scale at temperatures up to 1200 °C that breaks above this temperature. Apparently, the Al-rich Al_3Nb is able to sustain the Al_2O_3 scale growth without Al depletion at the metal/ scale interface. On the other hand, the Al-lean Al_3Nb does not form an exclusive Al_2O_3 layer at high temperatures instead a double oxide layer of outer $AlNbO_4$ and inner Al_2O_3 is formed. In the latter case, there is depletion of Al at the metal/scale interface with a consecutive solid state transformation of Al_3Nb to $AlNb_2$. The formation of the $AlNb_2$ does not have a positive effect on the oxidation behaviour because the Al has low activity in this phase despite its relatively high solid solubility.

Additions of Cr in alloys have been used for several purposes, among them is their use in superalloys to increase their resistance to hot corrosion, to change the liquidus temperature of

alloys and to promote the formation of an exclusive external layer of α-Al_2O_3 at the minimum Al content required to sustain the scale growth [Meier and Pettit (1992)]. A reduction of the oxidation rate of the Al_3Nb at 1200 °C has been achieved with additions of Cr and Y [Hebsur et al. (1989), Doychak and Hebsur (1991)].

Cr_2Nb has excellent oxidation resistance at high temperatures due to the formation of Cr_2O_3. According to Brady and Tortorelli (2004) the Cr_2O_3 scales formed on Cr_2Nb were protective up to 1000-1100 °C, and therefore the use of the Laves phase at high temperatures is limited by the CrO_3 volatilization which occurs above these temperatures. The C14 Laves phase can have high Al content (≈ 45 at. % Al) and Al stabilizes it to lower temperatures. However, Stein et al. (2014) reported a decrease in the melting point of the C14 Laves phase with increasing Al content in the compound. According to Zheng et al. (2009) Al additions increased the adhesion of the oxide scale formed on the Cr_2Nb. The best effect was observed in alloys with 12 % at. Al at 1100 °C but at 1200 °C this Al content was not enough to sustain the growth of Al_2O_3 scale because there was formation of Nb_2O_5 and Cr_2O_3 which increased the internal stress in the oxide scale [Zheng et al. (2009)].

In the Al-Nb-Cr ternary system there is a three field phase-equilibria between the Al_3Nb-Cr_2Nb-Cr_{ss} phases. The composition of the alloy OHC3 was chosen to fall within the three phase equilibria to include these phases in the alloy. Small additions of Hf significantly enhance the adhesion of Al_2O_3 scales in alumina forming alloys [Pint (2003) and Aerospace Materials Handbook (2010)]. According to Perkins et al. (1989) and Hebsur et al. (1989) Hf additions could act as oxygen trap and decrease the oxygen diffusivity. Thus, in the alloy OHC3 the addition of Hf was made to improve the adhesion of the Al_2O_3 scale on the alloy.

5.2 Results

5.2.1 Microstructure characterization

As cast microstructure

The actual composition (at.%) of the as cast alloy (OHC3-AC) was Al-26.6Nb-6.3Cr-0.5Hf. This composition was the average of the analyses taken from the top to the bottom of the button (Table 20). There was some weak chemical inhomogeneity (macro-segregation) of Al and Cr in the cast alloy.

Table 20 EDS data (at. %) of the as cast alloy OHC3.

Area/Phase	Hf (at%)	Cr (at%)	Nb (at%)	Al (at%)
Large area analysis	0.5 ± 0.2 1.0 – 0.1	6.3 ± 0.9 8.0 – 5.1	26.7 ± 0.4 27.6 – 25.9	66.6 ± 1.2 67.9 – 64.2
Top	0.3 ± 0.2 0.6 – 0.1	5.7 ± 0.4 5.9 – 5.1	26.7 ± 0.2 26.8 – 26.4	67.4 ± 0.1 67.5 – 67.3
Bulk	0.5 ± 0.2 0.8 – 0.3	6.6 ± 1.2 8.0 – 5.4	26.8 ± 0.3 27.1 – 26.2	66.1 ± 1.3 67.5 – 64.2
Bottom	0.3 ± 0.3 0.6 – (-0.1)	6.5 ± 0.5 7.2 – 6.1	26.5 ± 0.7 27.5 – 25.9	66.6 ± 1.2 67.9 – 64.2
Al_3Nb	0.2 ± 0.1 0.4 – 0.0	0.9 ± 0.2 1.2 – 0.7	25.7 ± 0.4 26.5 – 25.3	73.2 ± 0.5 73.8 – 72.2
$(Al,Cr)_2(Nb,Hf)$	1.1 ± 0.2 1.5 – 0.9	20.6 ± 0.9 22.1 – 19.3	32.1 ± 0.6 33.1 – 31.1	46.1 ± 0.8 47.6 – 45.0
$(Cr,Al,Nb)_{ss}$	0.6 ± 0.3 0.8 – 0.3	46.7 ± 1.6 47.5 – 44.4	7.3 ± 1.0 8.8 – 6.8	45.4 ± 0.8 46.5 – 44.9
Eutectic (large area analysis)	0.9 ± 0.4 1.3 – 0.7	15.7 ± 0.7 16.5 – 15.1	30.3 ± 0.3 30.5 – 29.9	53.1 ± 0.5 53.6 – 52.7
$Al_3(Nb,Cr)$ in eutectic	0.3 ± 0.2 0.5 – 0.1	3.5 ± 1.1 4.9 – 2.2	25.5 ± 0.4 25.8 – 24.6	70.7 ± 1.0 71.9 – 69.3
$(Al,Cr)_2(Nb,Hf)$ in eutectic	1.6 ± 0.1 1.8 – 1.5	21.3 ± 0.9 22.0 – 20.0	31.6 ± 0.3 32.1 – 31.3	45.5 ± 0.7 46.3 – 44.7

According to the SEM studies, and the EDS and XRD data (figures 99 to 101 and Table 20), the microstructure of the alloy consisted of four phases, namely the Al_3Nb, the C14 Laves

$(Al,Cr)_2(Nb,Hf)$, the $(Cr,Al,Nb)_{ss}$ and a Hf-rich phase. Typical images of the microstructure of the alloy OHC3-AC are shown in the figure 99.

The microstructure in the top and the bulk of the button was essentially the same regarding the phases present but finer in the top. The microstructure consisted of primary $NbAl_3$ with grey contrast surrounded by a halo of the $(Al,Cr)_2(Nb,Hf)$ Laves phase and a eutectic (Figure 99a). The eutectic microstructure consisted of the $(Al,Cr)_2(Nb,Hf)$ Laves and the $NbAl_3$ phases. Its composition is given in Table 20.

Near the interface of the Al_3Nb and $(Al,Cr)_2(Nb,Hf)$ phases two more phases were observed, both at very low volume fractions: The $(Cr,Al,Nb)_{ss}$ with dark grey contrast, and fine white contrast Hf-rich particles, the latter exhibitig a random distribution. These particles looked like tiny rods and/or spheres (< 3µm wide) and are indicated as Hf-rich phase in the insert in figure 99a).

The microstructure in the bottom consisted of the primary Al_3Nb phase, a higher volume fraction of the $(Al,Cr)_2(Nb,Hf)$ Laves phase with some uneven distribution of the $(Cr,Al,Nb)_{ss}$ solid solution between these phases (Figure 99b). The Hf-rich particles were also observed and these were always found near the $(Al,Cr)_2(Nb,Hf)$ Laves phase.

The XRD and EDS data (Figure 100 and Table 20) allowed the identification of the phases in OHC3-AC. The results of these two complementary techniques confirmed the presence of the Al_3Nb phase, the compositions studied were within the solubility range of this phase in the Al-Cr-Nb system. The Al_3Nb phase crystallizes in the tetragonal system with the Al_3Ti as the prototype and its space group is the I4/mmm (PDF 04-002-9616). The presence of the C14 Cr_2Nb Laves phase was also confirmed. This phase has the $MgZn_2$ prototype, and its crystalline system is hexagonal with the $P6_3/mmc$ space group (PDF 04-003-9845). In the $(Al,Cr)_2(Nb,Hf)$ Laves phase the Al content was 46.1 at.% Al (Table 20) which is in agreement with the composition of the C14 Laves phase reported by Zhao (2004c) and Prymak and Stein (2012) in the Al-Cr-Nb system.

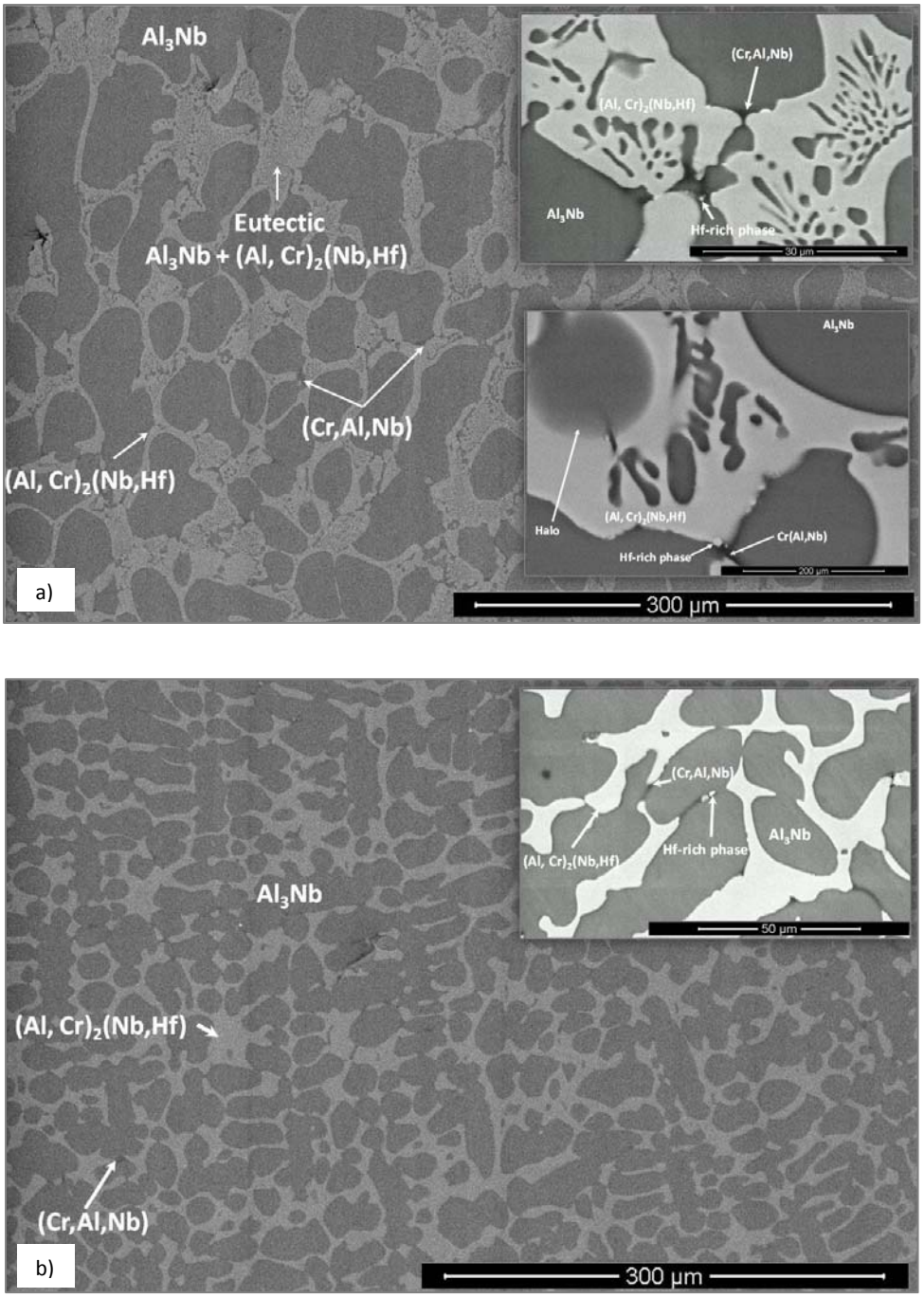

Figure 99. BSE images of the microstructure of the alloy OHC3-AC, (a) bulk, X190, (b) bottom, X200.

The $(Cr,Al,Nb)_{ss}$ phase was not detected by XRD because of its very low volume fraction. Furthermore its strongest (110) peak would overlap with the peaks of other phases. The substitution of Cr by Al and Nb could affect not just the peak intensities but could shift their positions. According to the PDF 01-089-4055 this phase crystallizes in the cubic system with the

Im-3m space group with W prototype. The composition of the $(Cr,Al,Nb)_{ss}$ phase was in agreement with the composition and solubility range of the Cr_{ss} in the Cr-Al-Nb system. The composition of the eutectic Al_3Nb + $(Cr,Al)_2(Nb,Hf)$ in Table 20 agrees well with the composition of the C14 $NbCr_2$ + $NbAl_3$ eutectic observed by Stein et al. (2014).

The very low volume fraction Hf-rich phase was also not detected by the XRD. The X-ray maps (Figure 101) revealed that these particles were also rich in Cr. Their composition could not be obtained because of their size and location in the microstructure. Their shape is similar to those of HfO_2 particles formed in Nb-silicide base alloys owing to the scavenging of oxygen by Hf, in other words it is possible that the Hf rich phase particles might be HfO_2 particles. In figure 101, it is possible to observe some Cr enrichment in the $(Cr,Al,Nb)_{ss}$ areas.

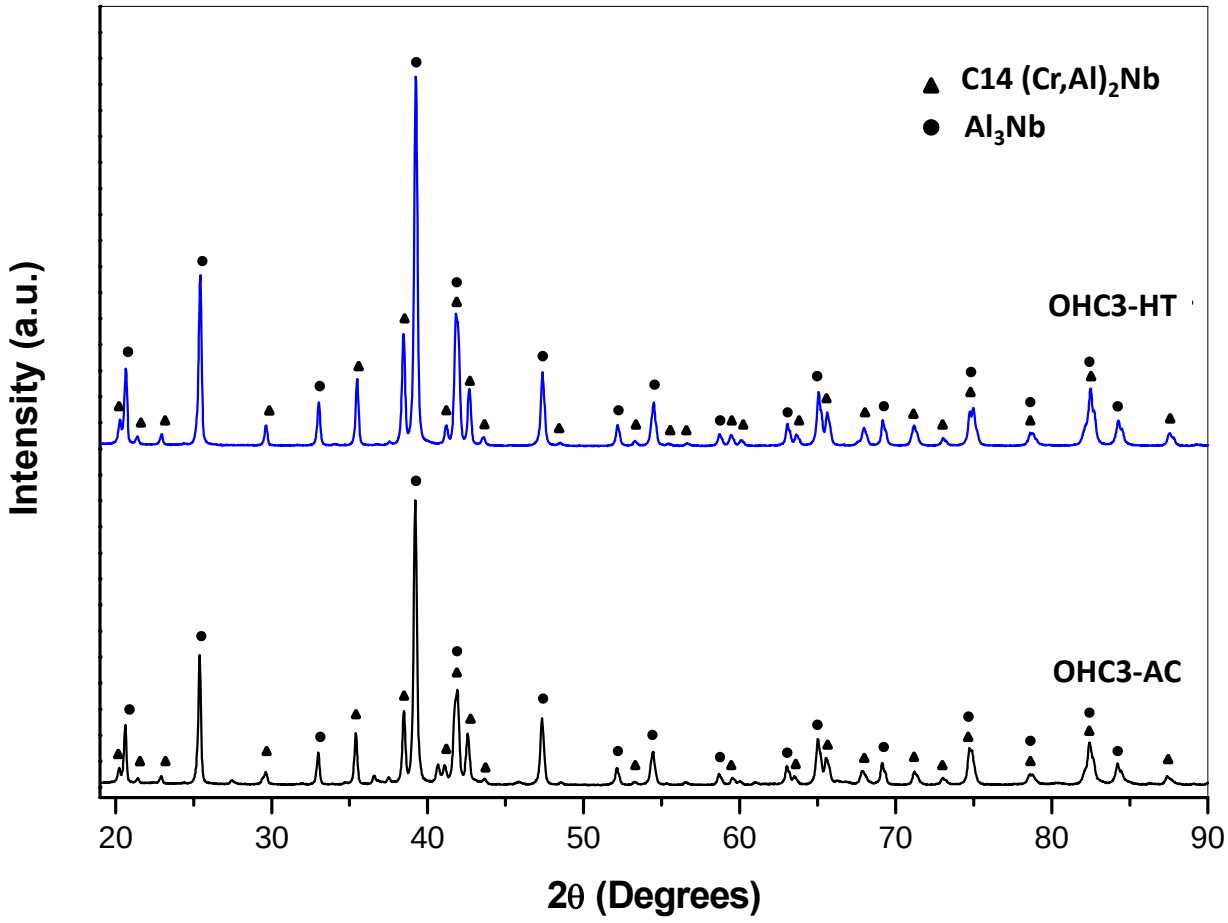

Figure 100. XRD diffractograms of the alloy OHC3 alloy powder showing the phases present in the cast and heat treated conditions.

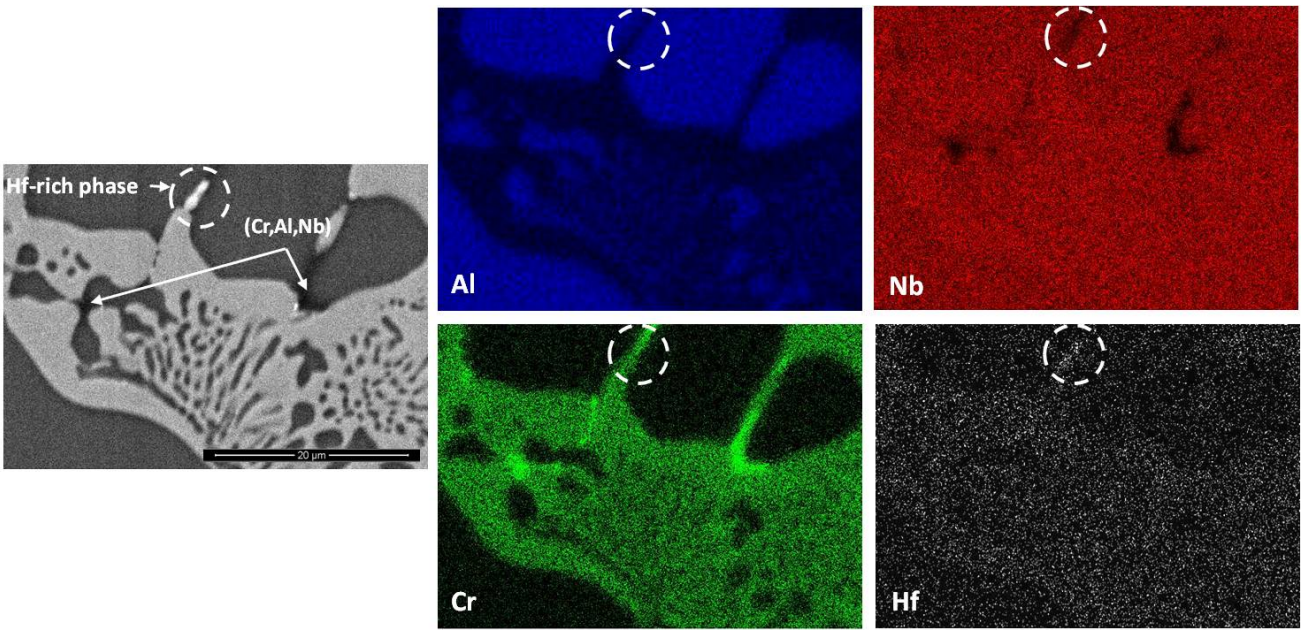

Figure 101. BSE image, X2000 and X-ray maps of the alloy OHC3-AC. The encircled areas in the elemental maps show the element content in the Hf-rich particle.

Stein et al. (2014) and Souza et al. (2006) studied Cr-Al-Nb alloys and reported a solid state phase transformation involving (Cr,Al,Nb) and Al(Nb)Cr_2 phases in the temperature range 700 to 900 °C depending on the Al content of the Cr_{ss}. In the DSC trace of the alloy OHC3 there was an endotermic signal at 845 °C (Figure 102) that might correspond to the same thermal event. However, a corresponding signal was not observed on cooling.

There was also a thermal event on heating with peak temperature ~1517 °C (Figure 102) and a thermal event on cooling at 1461 °C that could correspond to the crystallization of the previous. The thermal event could correspond to the eutectic Al_3Nb + Cr_2Nb observed in the top and bulk of the alloy and the eutectic reaction L → Al_3Nb + Cr_2Nb observed by Stein et al. (2014) at 1520 °C.

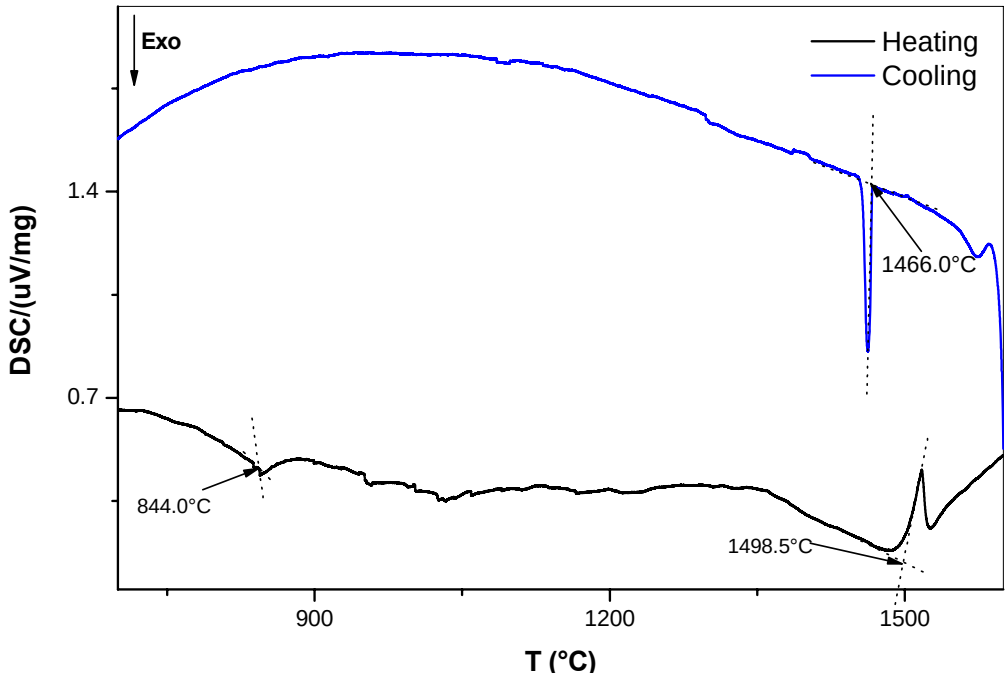

Figure 102. DSC traces showing thermal events on heating and cooling of the alloy OHC3-AC.

Heat treated microstructure

The actual composition of the heat treated alloy (OHC3-HT) (1400 °C / 100h) was Al-26.7Nb-7.0Cr-0.5Hf. The EDS analysis data is given in Table 21 and is the average values of the large area and phase analyses taken from the top, centre and the bottom of the button after the heat treatment. Figure 103 shows typical images of the microstructures in the alloy OHC3-AC.

Table 21 EDS data (at. %) for the heat treated alloy OHC3 at 1400 °C for 100 h.

Area/Phase	Hf (at%)	Cr (at%)	Nb (at%)	Al (at%)
Large area analysis	0.5 ± 0.1 0.8 – 0.3	7.0 ± 0.7 8.3 – 5.9	26.7 ± 0.3 27.4 – 26.4	65.7 ± 0.9 67.1 – 63.7
$Al_3(Nb,Cr)$	0.1	0.8 ± 0.1 0.9 – 0.6	25.6 ± 0.1 25.8 – 25.4	73.5 ± 0.2 73.8 – 73.3
$(Cr,Al)_2(Nb,Hf)$	1.5 ± 0.2 1.8 – 1.2	23.3 ± 0.8 24.2 – 22.0	32.1 ± 0.4 32.7 – 31.6	43.2 ± 0.5 43.9 – 42.4

As it was observed in the cast alloy, the microstructures in the top and bulk of OHC3-HT were essentially the same and comprised of three phases, namely the $Al_3(Nb,Cr)$, and $(Cr,Al)_2(Nb,Hf)$ phases and Hf-rich particles . The XRD confirmed the presence of the $Al_3(Nb,Cr)$ and C14 Laves

$(Cr,Al)_2(Nb,Hf)$ phases, see figure 103. The volume fraction and size of the Hf-rich particles had increased, but not enough to enable the measurement of their composition. The two intermetallics had formed a co-continnous microstructure in which the $(Cr,Al)_2(Nb,Hf)$ phase was coarsened.

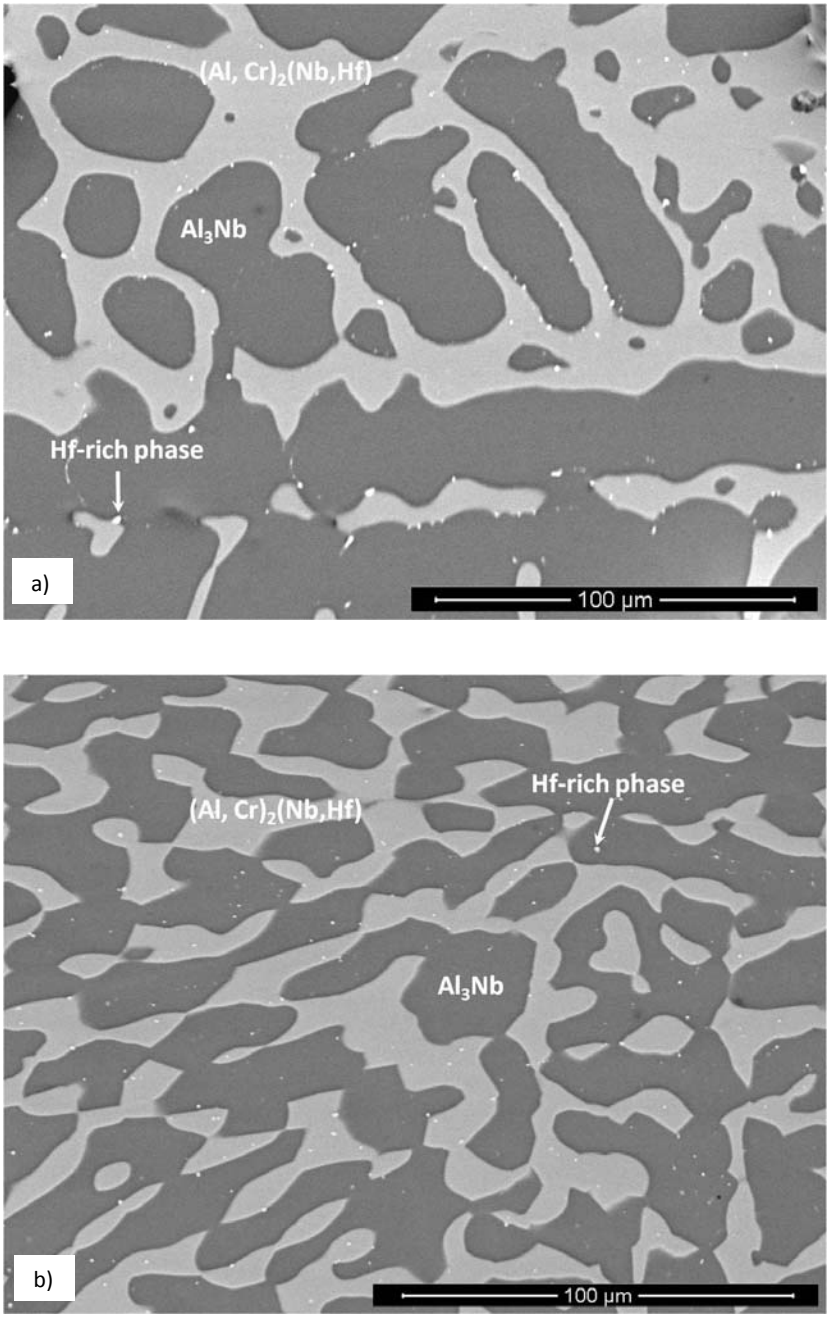

Figure 103. BSE images from cross section of OHC3-HT, (a) section from the Top, at X640, (b) section from the bottom, at X640.

5.2.2 Thermo-gravimetric analysis

The isothermal oxidation of the alloy OHC3 was studied in air at 800, 1200 and 1300 °C. The weight change data was analysed using the double logarithm equation (1) (see chapter 3) to obtain the n value for the reaction mechanism that controlled the oxidation. When the data suggested change of the oxidation mechanism, the data was segmented to determine the oxidation kinetics constants from the equations (2) and (3).

The n values and oxidation rate constant of the alloy OHC3 after isothermal oxidation at 800, 1200 and 1300 °C are shown in Table 22. The oxidation behaviour at 800 and 1200 °C was parabolic and at 1300 °C subparabolic. The n value at 800 °C was 0.68 and suggested a parabolic oxidation at this temperature, which was confirmed by the evaluation of the data with equations (2) and (3). At 1200 °C the oxidation of the alloy was also parabolic. However, there was a change in parabolic rate which slightly increased after the first 43 hours (Table 22). The n value at 1300 °C (0.41) suggested that the oxidation was subparabolic. As it was discussed in chapter 3, this behaviour is related to a very short initial period in which the alloy gains weight at very high oxidation rate and then stabilises into a very low parabolic oxidation rate. The K_p value at 1300 °C is given in Table 22.

Table 22. Total weight gain, n values and oxidation rate constants of the alloy OHC3 for isothermal oxidation at 800, 1200 and 1300 °C.

T	n	K_p ($g^2.cm^{-4}.s^{-1}$)	Weight gain (mg/cm^2)
800 °C	0.68	6.72×10^{-12}	1.54
1200 °C	0.56	1.78×10^{-11} (0-43 h) 5.7×10^{-11}(43-80 h)	4.47
1300 °C	0.41	1.88×10^{-10}	8.5

5.2.2.1 Thermo-gravimetric analysis (TGA) at 800 °C

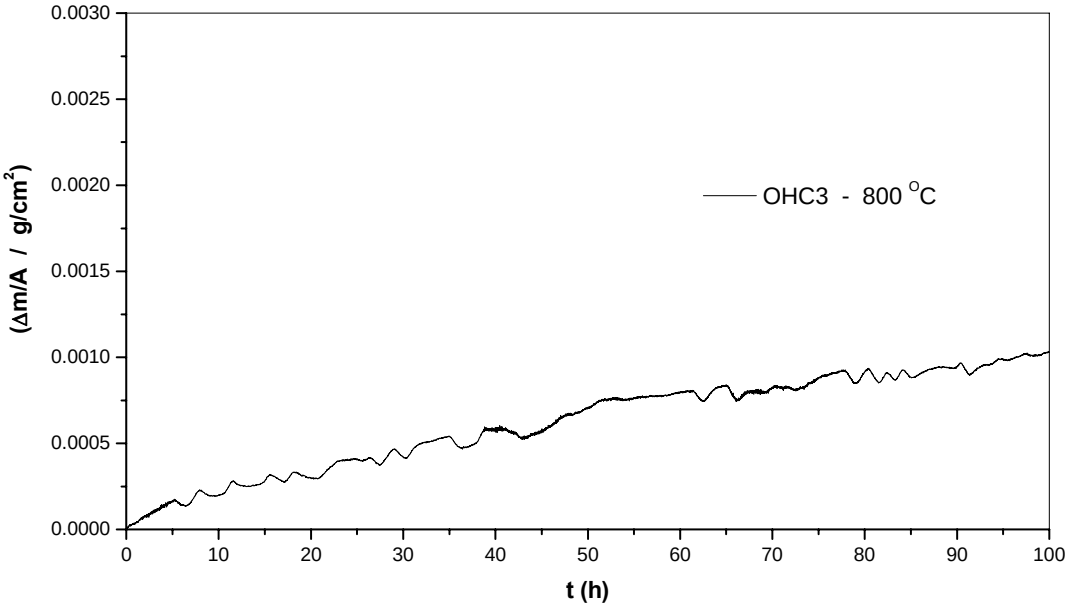

Figure 104. Isothermal oxidation behaviour of the alloy OHC3 in air at 800 °C for 100 h.

The plot in figure 104 depicts the mass gain per unit area versus time plot for the isothermal oxidation in air at 800 °C of the alloy OHC3. The alloy oxidation followed parabolic kinetics. The data would suggest that after an initial rapid oxidation some cracking and/or spallation "constantly" occured during the oxidation of the specimen. The weight gain recorded at the end of the isothermal oxidation experiment is given in Table 22 and was 1.54 mg/ cm^2, lower than the reported 4.17 mg/ cm^2 for the Nb-39.7Cr-49.3Al alloy after 48 h of oxidation in air by Souza et al. (2008).

Microstructure of oxide scale at 800 °C

The specimen did not pest, retained its sharp edges and exhibited no visible deformation after the isothermal oxidation in air at 800 °C for 100 h. The oxide scale was adherent and composed of a black continuous thin film. Grooves from sample preparation were still clearly visible (Figure 105a). The SE images showed a continuous and adherent oxide layer covering the specimen. This oxide scale was composed of different oxides formed over a particular phase. The insert in figure 105a shows a lumped oxide on top of the Al_3Nb phase that was composed

of a dark glassy-like oxide with some embedded bright particles. The oxide grown on the top of the $(Al,Cr)_2(Nb,Hf)$ phase was more flat and compact and its contrast under BSE imaging conditions was brighter. Over the $Al_3Nb/(Al,Cr)_2(Nb,Hf)$ phase boundaries the microstructure of the oxide was different from that formed over each individual phase. Despite of the micro-cracks observed in the oxide surface (Figure 105b and c) and the oxidation temperature (800 °C) being within the pest oxidation regime for the Al_3Nb phase [Tolpygo and Grabke (1993)], no pest oxidation occurred.

According to the cross section shown in figure 105d, the external oxide on top of the Al_3Nb was coarser than the one on top of the $(Al,Cr)_2(Nb,Hf)$ that was more compact. There was also internal oxidation, this was found in both phases and in the phase boundaries near the metal/scale interface. The insert in Figure 105d shows that at the phase boundaries near the metal/scale interface internal attack was deeper.

In the glancing angle XRD data ($\gamma = 2°$) shown in figure 106, some peaks from the substrate alloy were still visible due to the small scale thickness.These peaks were mainly from the Al_3Nb phase (JCPDS 65-7073) and the C14 $NbCr_2$ Laves phase (JCPDS 47-1638). The oxide peaks were for α-Al_2O_3 (JCPDS 10-0173), $CrNbO_4$ (JCPDS 30-0366), and $AlNbO_4$ (JCPDS 41-0347).

EDS analyses revealed that the scale formed over the Al_3Nb phase was composed of an outer layer of $(Al,Cr)NbO_4$ and an inner oxide layer of α-Al_2O3 (probably stabilized by Cr) and the scale formed on top of the $(Cr,Al)_2(Nb,Hf)$ phase was composed of an outer layer of $(Cr,Al)NbO_4$ with an inner layer of $(Cr,Al)_2O_3$.

The BSE image of a cross section in figure 107 shows the metal/scale interface of the alloy OHC3 after isothermal oxidation. The $(Cr,Al,Nb)_{ss}$ is not present in this image but it was observed in the bulk where it was coarser and it was surrounded the Al_3Nb phase. The Hf-rich particles were also observed at the phase boundaries between Al_3Nb and $(Cr,Al)_2(Nb,Hf)$. The image also shows internal oxidation (black contrast) along grain boundaries indicating that they served as a fast path for the inward diffusion of oxygen to about 12µm depth. This value was considered to be the deepest length of internal oxidation of the alloy after the TG experiment.

In the internal oxidation zone (IOZ) the Al in the Al_3Nb and $(Al,Cr)_2(Nb,Hf)$ phases was the "reactive" element. The internal oxidation zone (IOZ) in the Al_3Nb exhibited bright contrast under BSE imaging and dark grey contrast from oxide particles. The thin bright contour observed in the IOZ could be the Nb_2Al that was formed due to the selective oxidation of Al. The change of contrast in some areas of $(Al,Cr)_2(Nb,Hf)$ suggests that this phase suffered a remarkable change in composition. Qualitative EDS analyses revealed that there was Al enrichment and a decrease in Cr content near the grain boundaries. In this region the Al_3Nb showed a decrease in Al content and Cr enrichment.

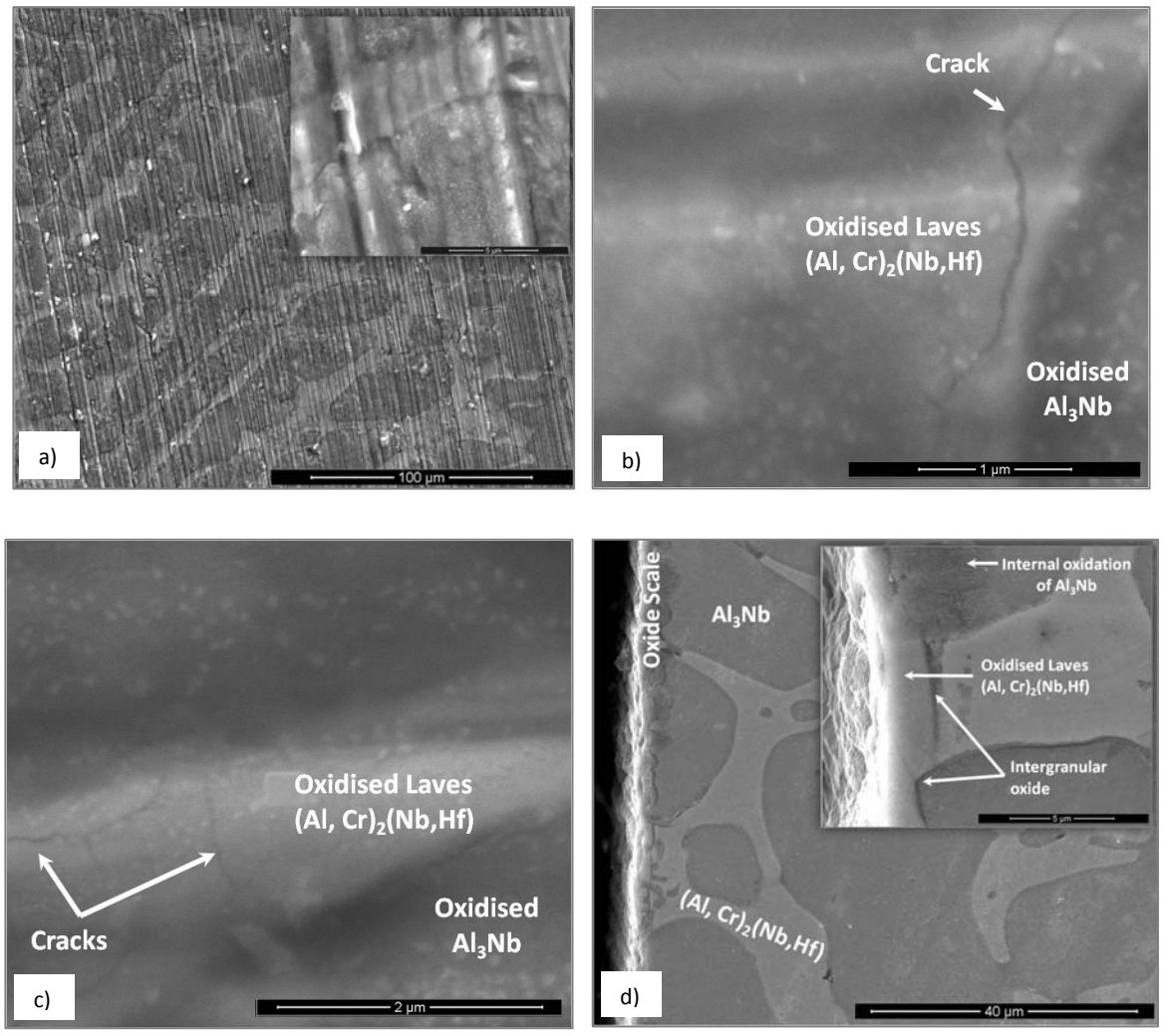

Figure 105. SE images of the oxide scale formed on the alloy OHC3 after isothermal oxidation at 800 °C for 100h, (a) to (c) taken for the oxide surface, (a) X1000, b) X70000, c) X 60000 and d) cross section image, X3000.

The oxide particles formed in the internal oxidation of the Al_3Nb were Al_2O_3 and presented different morphologies. Rod-like oxide particles formed in the $(Cr,Al)_2(Nb,Hf)$ as a result of its internal oxidation.

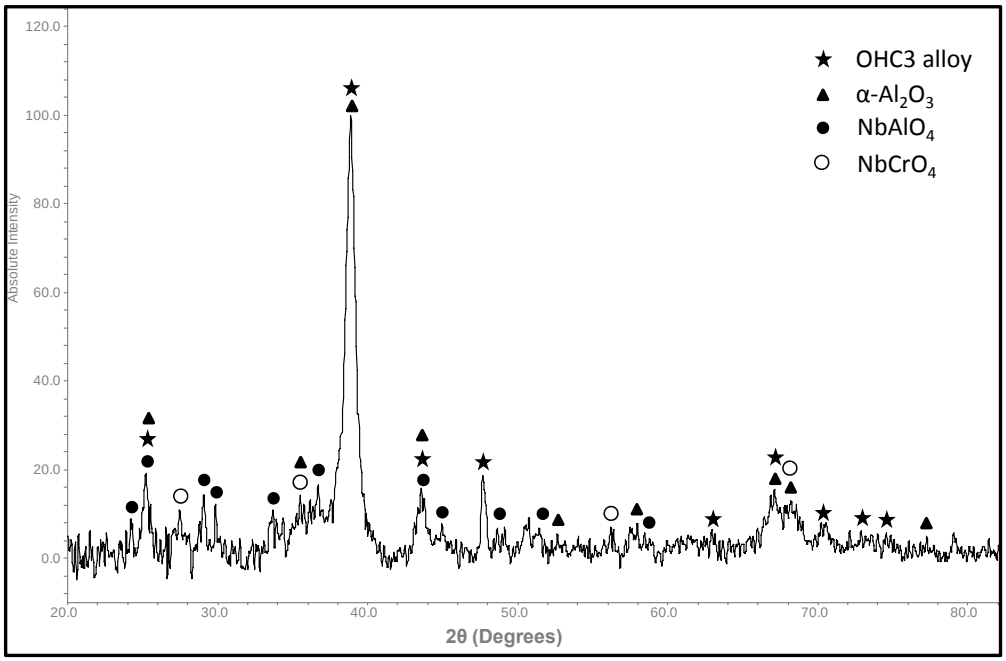

Figure 106. Glancing angle XRD data (γ= 2°) for the oxide scale formed on the alloy OHC3 at 800 C in air.

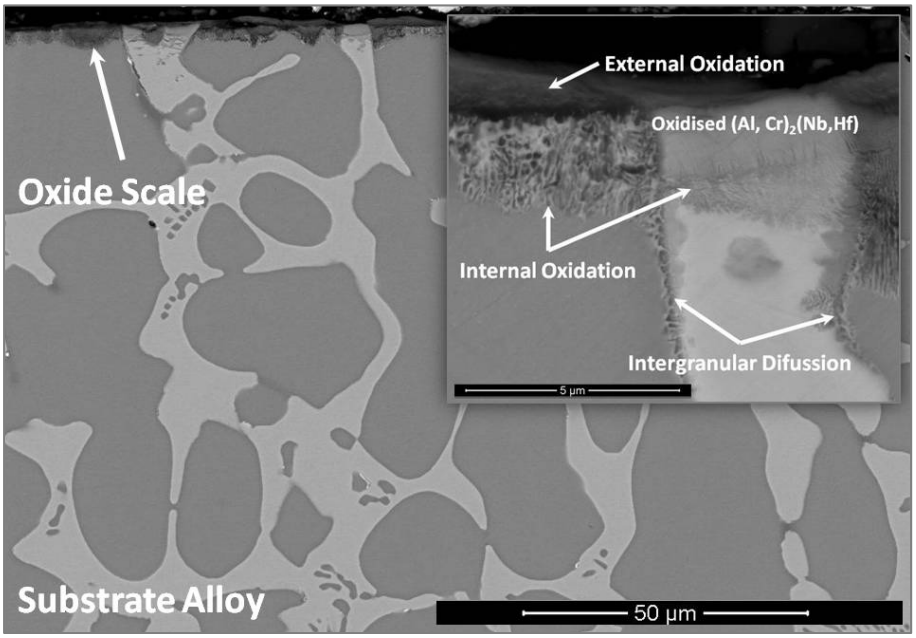

Figure 107. BSE cross section images of the alloy OHC5 after isothermal oxidation in air at 800 °C for 100 h, main image X1600, insert, X24000.

The elemental line scans shown in figure 108 show the elemental distribution along two lines of analyses from the metal/scale interface. The BSE image shows the oxides that were detected using the glancing angle XRD. Considering the XRD data, and the analysis along the line number 1 in figure 108, from the top of the oxide scale to the Al_3Nb phase, there was an external layer of $Al(Nb,Cr)O_4$ with Al enrichment at the metal/scale interface and an inner Al_2O_3 layer. The alloy was depleted in Al near the metal/scale interface where the Al was preferentially oxidised. Below the IOZ the Al content did not fall. The quantitative EDS analysis gave a 70 at. %Al content in the Al_3Nb below the IOZ. It was not possible to analize the bright contrast phase within the IOZ.

The line scan number 2 (over the $(Cr,Al)_2(Nb,Hf)$) starts with the $(Cr,Al)NbO_4$ at the surface of the oxide scale and shows Al_2O_3 as an internal oxide. The bright areas were Cr-rich and the areas with a dark grey contrast were Al-rich.

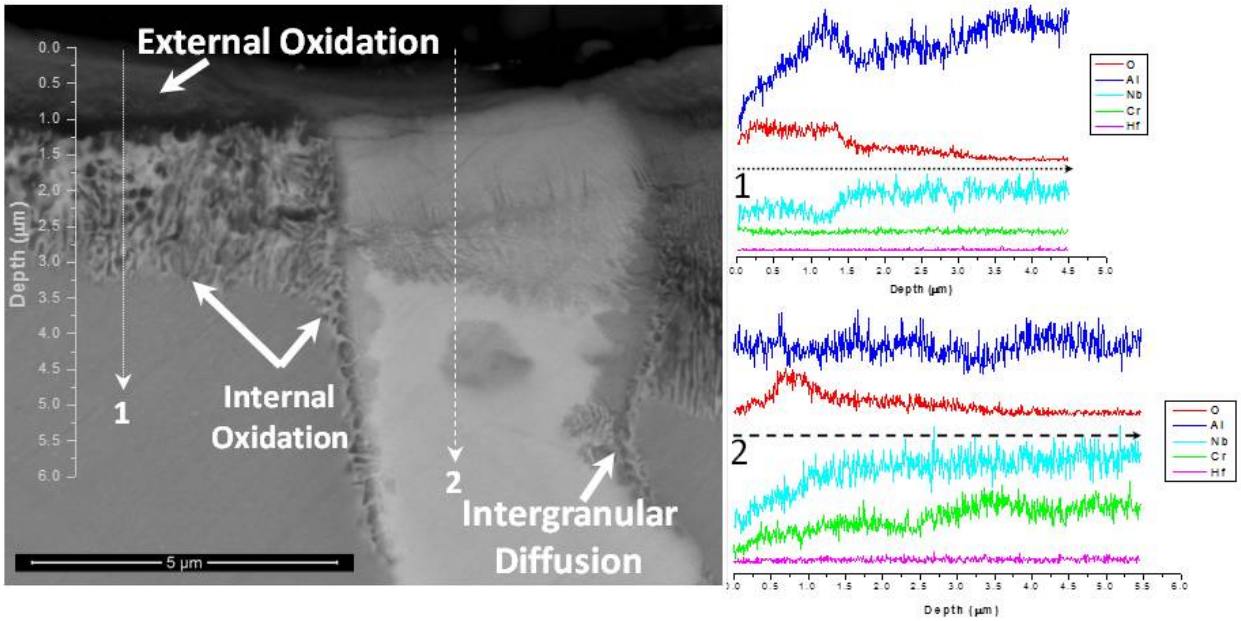

Figure 108. Elemental line scans of a cross section of the alloy OHC3 after isothermal oxidation at 800 °C for 100h, X24000.

The Al_3Nb has a narrow solubility range (in some Nb-Al phase diagrams it is shown as a line compound) and can transform to the $AlNb_2$ phase after Al depletion due to its selective oxidation. The EDS analyses performed below the IOZ revealed that the Al_3Nb was 3 at.% Al

leaner in Al than that in the initial cast alloy. The qualitative analyses also revealed that its grain boundaries were rich in Cr. The Cr content in the Al_3Nb could have increased the Al activity in the compound, thus promoting the formation of Al_2O_3. The (Cr,Al,Nb) was not found at the metal/scale interface.

5.2.2.2 Thermo-gravimetric analysis (TGA) at 1200 °C

The weight gain per unit area versus time data is plotted in figure 109.

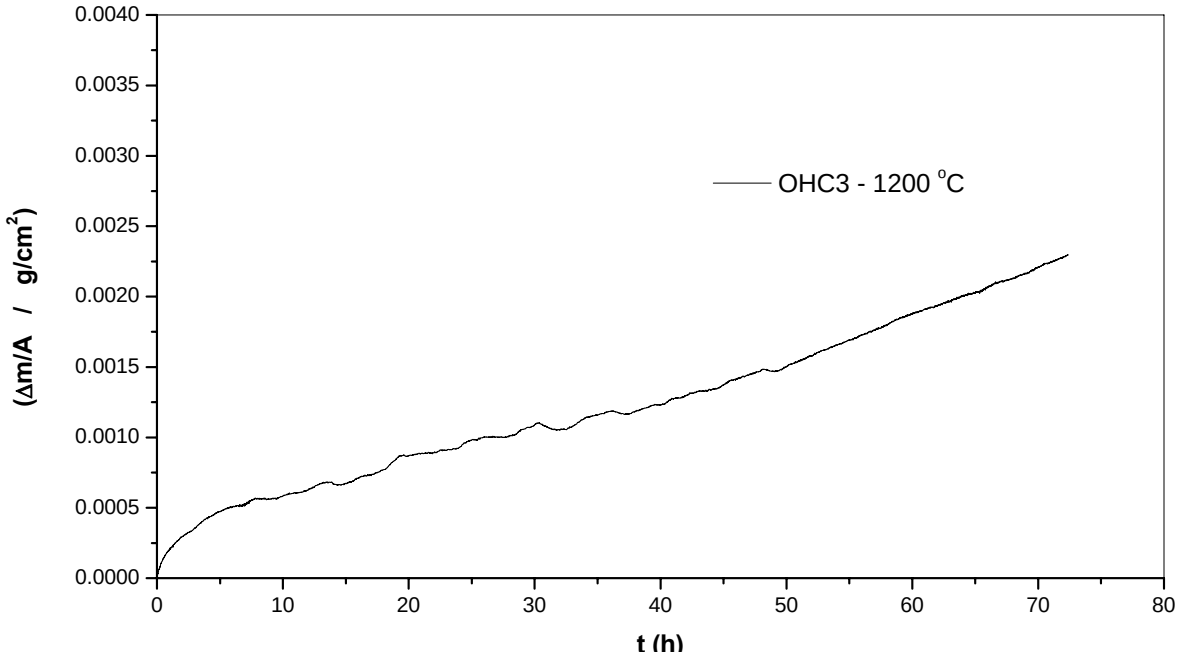

Figure 109. Isothermal oxidation behaviour of the alloy OHC3 in air at 1200 °C for 80 h.

The analysis of the data with equation (Eq. (1)), gave n = 0.56 (Table 22) meaning parabolic oxidation with the K_p values given in Table 22. The mass gain in this alloy was 4.47 mg/cm^2. The protective character of the oxide scale was slightly reduced after the first 43 h. Some external scale spallation occurred during the handling of the specimen after the oxidation experiment.

Microstructure of the oxide scale at 1200 °C

After isothermal oxidation in air at 1200 °C the scale showed good adherence. The SEM images (Figure 110 and 112) obtained from the oxide surface and cross section showed that the scale was composed of a continuous oxide that formed on top of the Al_3Nb phase and was different

from that formed over interface boundaries and over the eutectic and the $(Cr,Al)_2(Nb,Hf)$ phase where mixed oxides were formed. The combined effect of these features was to lessen the protective character of the oxide scale in the alloy and to promote the formation of a thicker oxide scale mainly in those areas at 1200 °C. Hf-rich oxide particles were more visible over the oxidized $(Cr,Al)_2(Nb,Hf)$ phase as they were always found within and at the grain boundaries of this phase in the cast alloy.

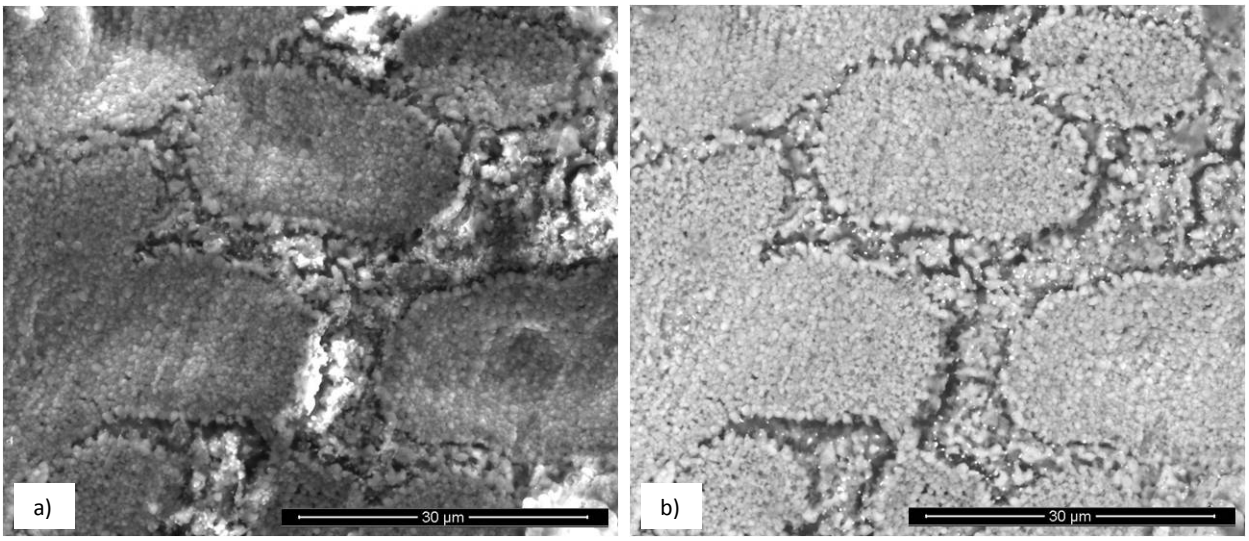

Figure 110. Images of the surface of the oxide formed on the alloy OHC3 after isothermal oxidation at 1200 °C for 80h, a) SE, X4000, b) BSE, X4000.

The XRD glancing angle data in figure 111, confirmed the presence of α-Al_2O_3 (JCPDS 10-0173) and $AlNbO_4$ (JCPDS 41-0347) as the main species of the oxide scale.

The scale thickness was in the range 7 to 32 µm, suggesting that the phases in the alloy presented different oxidation rates giving an uneven scale thickness (Figure 112a). In the areas where the eutectic was absent, even scale thickness was observed over the Al_3Nb and the $(Cr,Al)_2(Nb,Hf)$ Laves phase. Over the eutectic areas, the scale was thicker owing to the large number of phase boundaries that allowed a faster inward diffusion of oxygen. The oxide growth over the grain and phase boundaries would have increased the internal strains causing deformation of the scale and some splits in the Al_2O_3 layer. Cavities were observed over the $(Cr,Al)_2(Nb,Hf)$ phase at the metal/scale interface but no scale buckling.

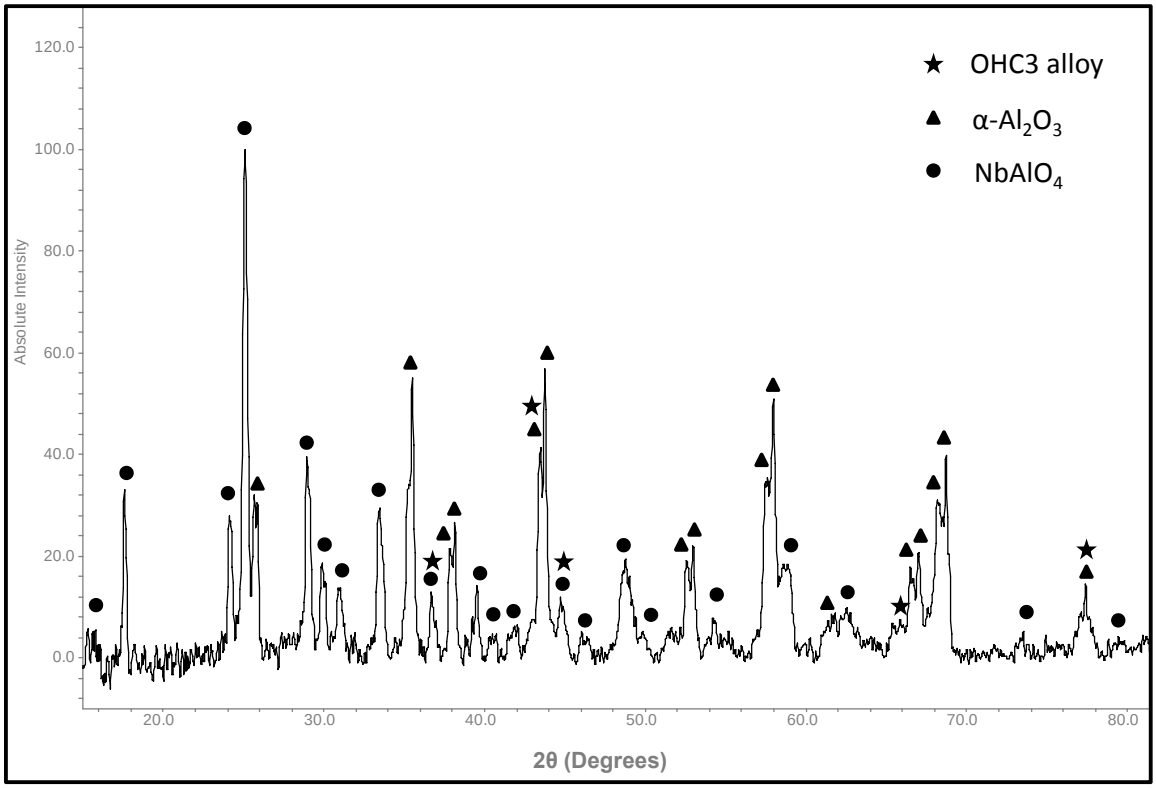

Figure 111. Glancing angle XRD data (γ= 2°) for the oxide scale formed on the alloy OHC3 at 1200 °C in air.

The image of the substrate (Figure 112a) also shows that some prior eutectic was still visible but the (Cr,Al,Nb) was not found. The Al_3Nb phase showed some internal precipitation (Figure 112b), EDS (analysis 1) showed that the precipitates were Cr-rich when compared with analysis 2 in the Al_3Nb phase.

The figure 113 shows that the oxide scale covering the alloy was mainly composed of two oxide layers, the outer layer (bright grey contrast) was (Al,Cr)NbO_4 mixed with Al_2O_3 particles (dark grey contrast) and the inner part of the oxide scale consisted of Al_2O_3 (analysis 1). The inner Al_2O_3 layer beneath the $AlNbO_4$ + Al_2O_3 mixture was adherent and formed continuously all over the substrate. The oxide scale had lumps over the grain or phase boundaries and the inner Al_2O_3 layer was adherent meaning that it was able to withstand the internal stresses (without buckling) that resulted from the oxidation of the eutectic.

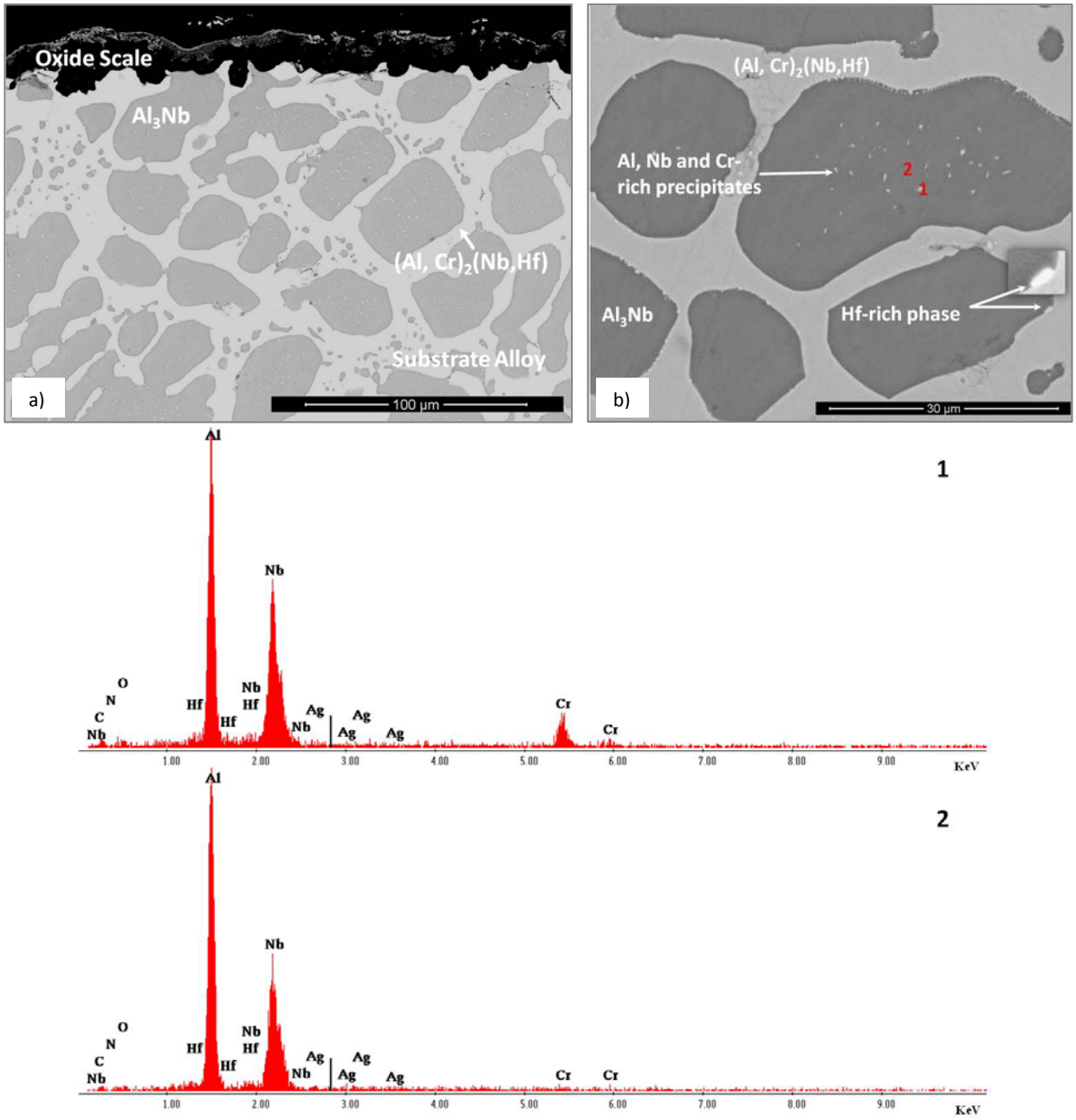

Figure 112. BSE image of the alloy OHC3 after isothermal oxidation at 1200 °C in air for 80h, (a) shows the oxide scale composed by two oxide species, X1000, (b) the microstructure of the substrate alloy, X4000 with EDS spectra (1) Nb, Al and Cr- rich precipitates and (2) Al_3Nb.

Some Al_2O_3 observed on top of the oxide surface presumably could have grown from the oxidation of the $Al_3Nb/(Cr,Al)_2(Nb,Hf)$ interface or from the dissolved (Cr,Al,Nb) (Figures 110 and 112). Some $(Cr,Al)_2(Nb,Hf)$ remained unoxidised near the scale surface, confirming its

superior oxidation resistance compared with the Al_3Nb phase. The EDS analyses show Ag signals from the silver dug used to stick the specimens.

Hf-rich oxide particles were observed in the oxidized $(Cr,Al)_2(Nb,Hf)$ areas and in the grain boundaries of the $(Cr,Al)_2(Nb,Hf)$ phase (analysis 3 in figure 113).

The cross section images (Figure 113) and EDS chemical analyses suggested that the oxide scale grew via simultaneous oxidation of the components in the substrate alloy since all the elemental components were found at the surface of the oxide scale in the $(Al,Cr)NbO_4$ (analysis 4). Comparing analysis 2 and 4 in figure 113 shows that the Cr content increased towards the surface of the scale, thus Cr_2O_3 could have also be formed and then CrO_3 evaporated at 1200 °C.

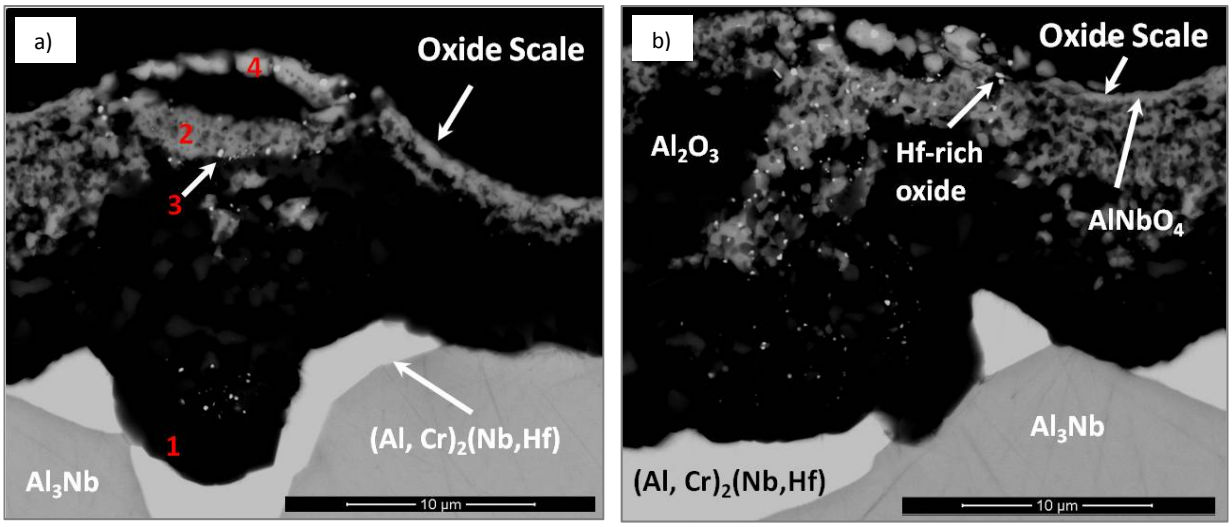

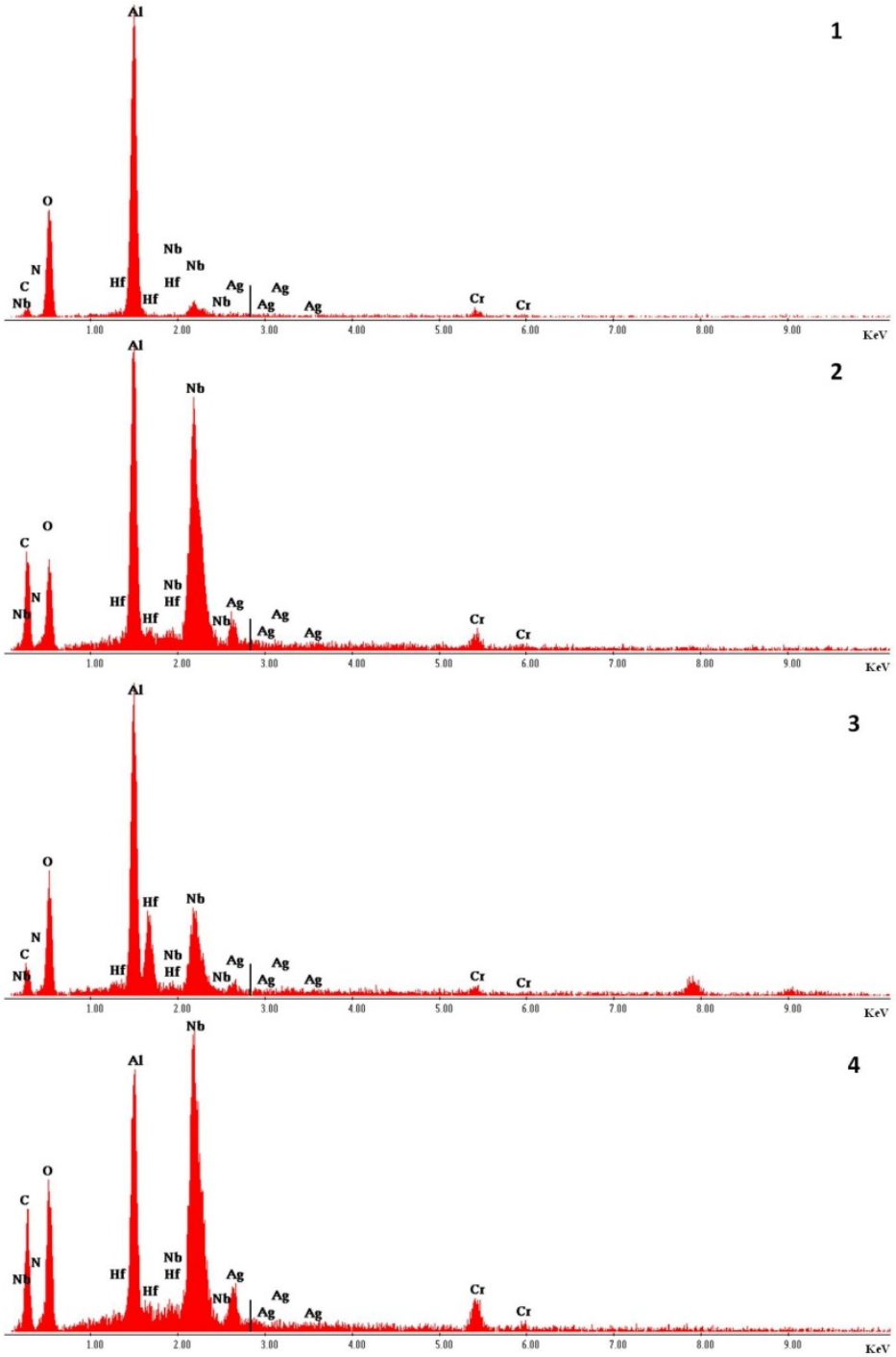

Figure 113. BSE images of the cross section of the alloy OHC3 after isothermal oxidation at 1200 °C, X8000 a) numbered areas correspond to the spectrums shown below, and b) Hf-rich particles in the oxide scale.

5.2.2.3 Thermo-gravimetric analysis (TGA) at 1300 °C

The weight gain per unit area versus time data is plotted in figure 114. The analysis of the data using equation (Eq. (1)), gave n = 0.41 (Table 22) which would suggests that the controlling mechanism was parabolic oxidation. Figure 114 shows an initial high oxidation rate followed by lower oxidation rate.The parabolic rate constant K_p is given in Table 22 and it was obtained by plotting gain weight versus time using equation (3). The mass gain was 8.5 mg/cm^2, see Table 22.

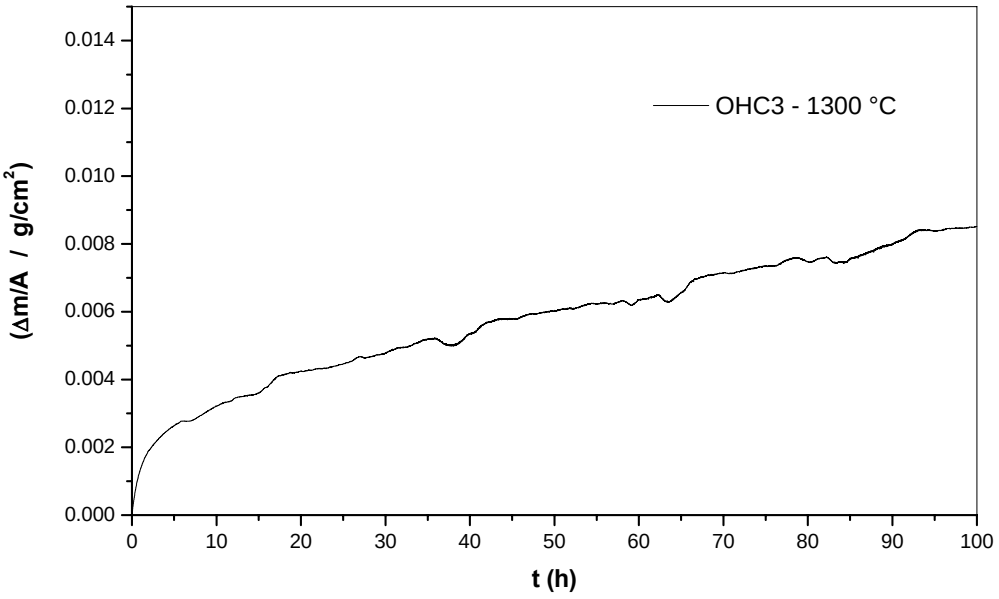

Figure 114. Isothermal oxidation behaviour of the alloy OHC3 in air at 1300 °C for 100 h.

Microstructure of the oxide scale at 1300 °C

After isothermal oxidation in air at 1300 °C, the oxidised specimen presented sharp edges, lumped corners and some oxide spallation that did not expose the metallic substrate but an inner oxide layer. The SEM images (Figure 115) obtained from the oxide surface showed that it was composed of a continuous oxide with some bulging over the interdendritic areas of the primary Al_3Nb where mixed oxides were formed. Some porosity in these areas was also observed instead of cracking, as it could be expected due to the scale bulging.

The BSE image (Figure 115b) shows areas with different contrast in the oxide surface, which clearly indicates that the oxide scale was composed of more than one oxide. The morphology of these oxides is shown in Figure 115 c and d. The latter two images were taken near the interdendritic areas where all the oxide particles could be captured in one image. Qualitative chemical analyses performed on the particles showed their main chemical components, (Al,Nb,Cr,O) in number 1, (Al,Cr,O) in number 2 and (Hf,Al,Nb,O) in number 3. The particles number 1 and 2 presented low Cr content, but the Hf-rich oxide particles (number 3) presented strong signals for Hf than the other components. The images show porosity in the oxide scale over the interdendritic areas. These areas were formed over the phases with high Cr content in the alloy but the oxide scale did not have a high concentration of Cr, which could be an indication that Cr_2O_3 evaporation occurred causing the porosity in the scale.

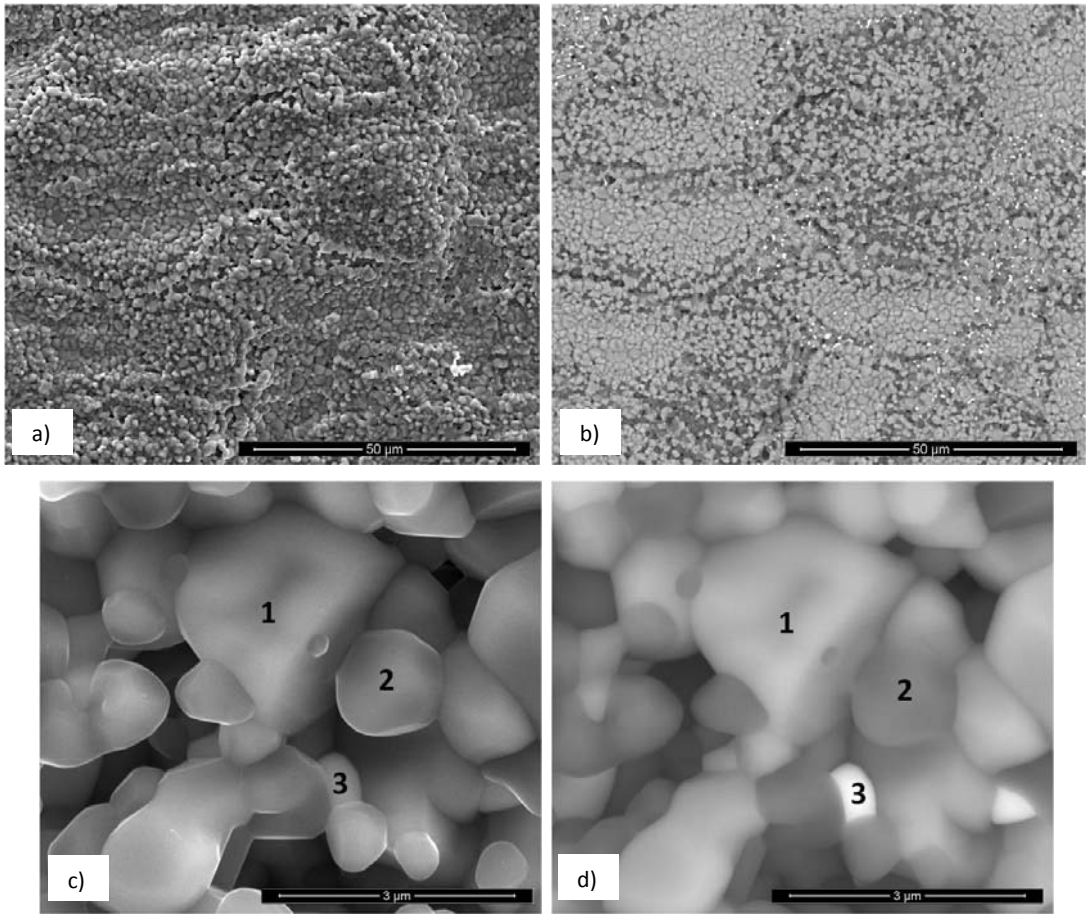

Figure 115. Images of the morphology of the oxide surface formed on the alloy OHC3 after isothermal oxidation at 1300 °C for 100 h, a) SE image, X2500, b) BSE image, X2500. Areas used for qualitative EDS analysis, c) SE, X40000, and d) BSE, X40000.

According to the glancing angle XRD data (Figure 116), the scale consisted of Al_2O_3 corundum (JCPDS 10-0173) and Al_2O_3 ruby (JCPDS 70-3321) and $AlNbO_4$ (JCPDS 41-0347). Different Cr contents in the Al_2O_3 could be responsible for some small peaks displacements.

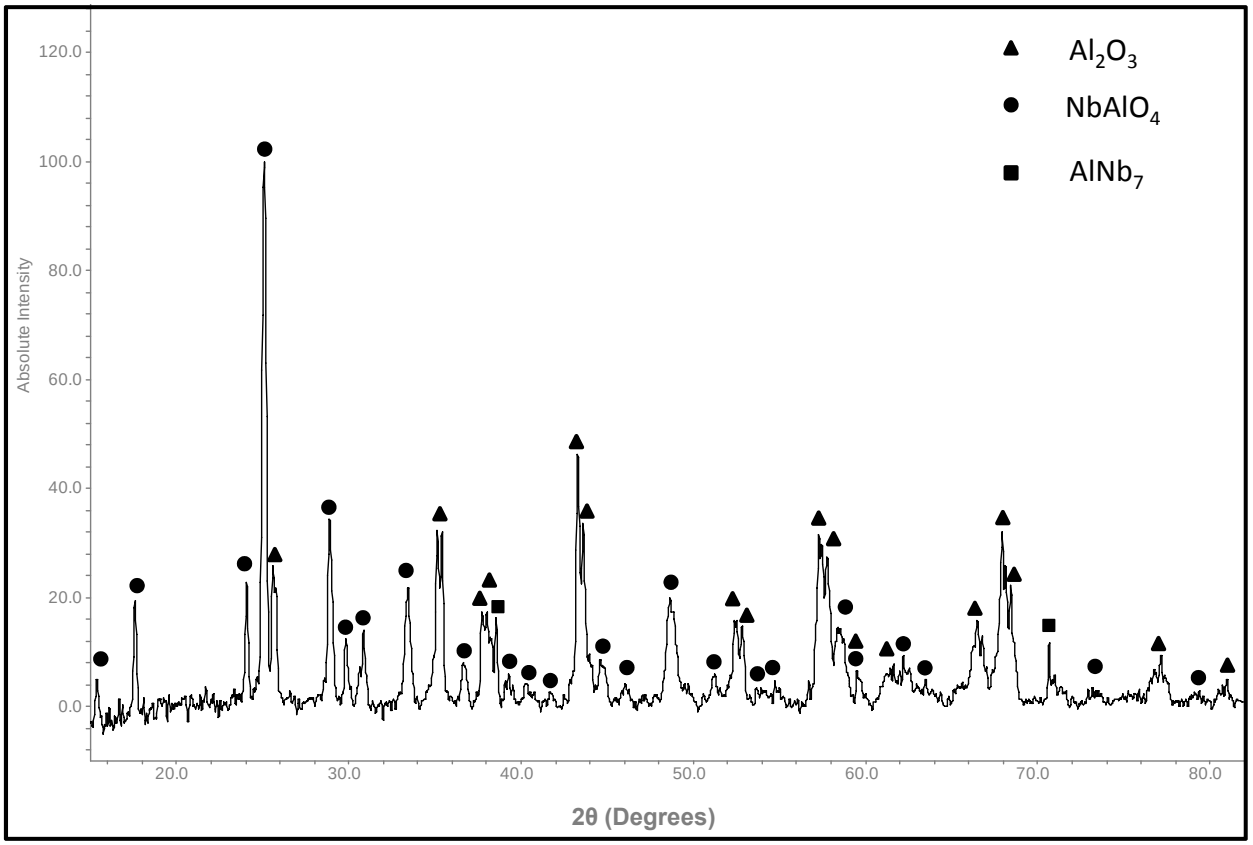

Figure 116. Glancing angle XRD data for the oxide scale formed on the alloy OHC3 at 1300 °C in air.

The images of a cross section of the oxide scale (Figure 117) showed a continuous two phase oxide scale composed of a thin outer oxide (bright contrast) and a thick inner oxide (dark contrast) with some gaps in the coarser areas, with thickness in the range 20 to 50 µm. The outer oxide layer thickness was in the range 3 to 15 µm and it was a mixture of $AlNbO_4$, Al_2O_3 and Hf-rich oxide particles. At the metal/scale interface the Al_2O_3 (dark contrast) was continuous, compact and adherent and with some Hf-rich oxide particles.

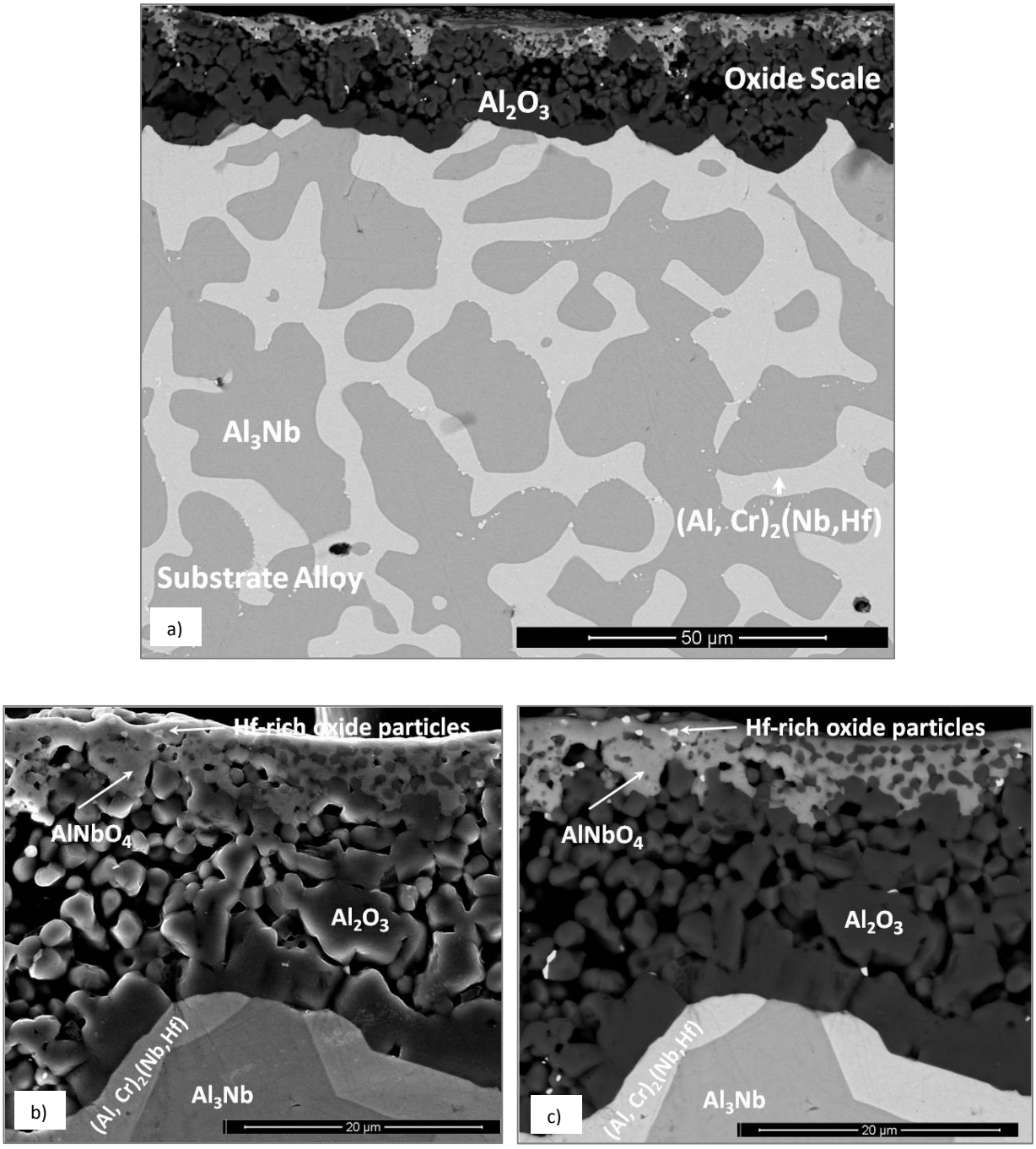

Figure 117. Cross section images of the alloy OHC3 after isothermal oxidation at 1300 °C for 100h, a) BSE, X1000, b) SE, X6000, and c) BSE, X6000.

EDS analyses revealed a small Al depletion in the Al_3Nb near the metal/scale interface from 73 to 69 at. % Al. The $(Cr,Al)_2(Nb,Hf)$ presented a larger decrease in Al content from 46 to 38

at.%Al. The Al depletion detectected in the Al_3Nb was not enough to cause transformation to $AlNb_2$.

The Al difussion was affected by surface orientation since it was found that the oxide scale was thicker in some faces of the cubic specimen, where both phases presented their highest values of Al depletion in these thick scale areas. The change in Al content in areas where the scale was thinner was different. In these areas the Al content in the Al_3Nb increased from 73 to 75 at.%Al while in the $(Cr,Al)_2(Nb,Hf)$ phase the Al content decreased from 46 to about 42 at.%. It is possible that the (Cr,Al,Nb) served as an effective Al reservoir but not large enough for the thicker areas (the (Cr,Al,Nb) was not observed in the microstructure after the oxidation at 1300 °C).

Overall the inner part of the oxide scale showed a good adherence to the substrate which would indicate that it was able to sustain the Al_2O_3 scale growth.

5.3 Discussion

5.3.1 Microstructures

Considering the ranking of the phases observed in the alloy OHC3 in terms of their melting temperatures, the data from the phase diagrams is T_m^{Al3Nb} = 1714 °C, $T_m^{C14\text{-}NbCr2}$ = 1730 °C, and T_m^{Cr} = 1863 °C respectively for the un-alloyed two intermetallics and pure Cr.

Table 20 shows that the concentrations of Cr and Hf in Al_3Nb were extremely low, meaning the above temperature should not be expected to be affected significantly by these elements. Indeed, using the data for Al_3Nb in Table 20 and figure 118, the liquidus of this intermetallic is slightly above 1700 °C.

The figure 118 shows that Al has a strong effect on the melting temperature of the C14-$NbCr_2$ Laves phase, which according to Stein et al (2014) decreases significantly with Al in solution and as shown in the figure 118 is about 1550 °C for the composition of the Laves phase in Table 20.

The solution of Al and Nb in (Cr) also reduces its liquidus to below 1500 °C, as shown in the figure 118. From the binaries the liquidus temperatures of $(Cr\text{-}7.3Nb)_{ss}$ and $(Cr\text{-}45Al)_{ss}$ respectively are about 1820 °C and 1580 °C. The liquidus temperature of $(Cr\text{-}45Al)_{ss}$ is also below 1580 °C in the revised Cr rich part of the Al-Cr binary by Stein et al. (2014).

Thus, for the alloyed phases their ranking in terms of decreasing temperature is T_m^{Al3Nb} (~ 1700 °C) > $T_m^{(Cr,Al,Nb)}$ (~ 1580 °C) > $T_m^{C14\text{-}(Nb,Hf)(Cr,Al)2}$ (~ 1550 °C). The microstructures shown in figure 99 would suggest that the Al_3Nb was the primary phase in OHC3-AC and that the Laves phase formed the eutectic with the Al_3Nb. The solid solution phase was formed at a very low volume fraction close to the eutectic.

The primary Al_3Nb is in agreement with the above ranking of the three phases in terms of their melting temperatures, the liquidus projection by Souza et al. (2006) shown in figure 30 and the liquidus projection proposed by Stein et al. (2014) which is shown below in the figure 118.

Thus, the solidification path of the alloy OHC3-AC was $L \rightarrow L + Al_3Nb \rightarrow Al_3Nb + (Al_3Nb + C14\text{-}(Nb,Hf)(Cr,Al)_2)_{eutectic} + (Cr,Al,Nb)_{ss}$ with the Al_3Nb + C14-$(Nb,Hf)(Cr,Al)_2$ eutectic forming between the Al_3Nb dendrites as shown in figure 99 (and the green line in figure 118). The Al and Nb concentrations in the eutectic given in Table 20 are in excellent agreement with the values (54.2 at% Al and 31.6 at% Nb) reported for the C14 + Al_3Nb eutectic formed in the alloy 35 (= Al-29.1Nb-9.5Cr) in Stein et al. (2104). The DSC study showed a reaction at 1498 °C which is attributed to the binary eutectic Al_3Nb + $(Cr,Al)_2(Nb,Hf)$. Stein et al. (2014) attributed a similar temperature ~ 1501 °C to the ternary eutectic Al_3Nb+ Cr_2Nb (C14)+ Nb_2Al. For this reason the alloy was studied extensively in search for the $AlNb_2$. This phase was not detected in the alloy OHC3.

Thus, it is also suggested that the $(Al_3Nb + C14\text{-}(Nb,Hf)(Cr,Al)_2)_{eutectic}$ formed about 1498 °C. The eutectic was observed in the top and bulk of the alloy OHC3 and was formed next to the Al_3Nb dendrites. The eutectic was absent in the bottom of the alloy. Considering that there were no significant differences in the composition of the alloy in the bottom and bulk and top (see Table 20) the absence of the eutectic in the bottom must be linked with solidification conditions at

high cooling rate leading to finer microstructure (Figure 99b) and back diffusion in the Al_3Nb dendrites affecting the composition of the melt between the Al_3Nb dendrites and altering the path the alloy took down the liquidus surface.

The solubility of Cr in Al_3Nb in the cast and heat treated conditions was in the range 0.7 to 1.2 at.% Cr and in the Al_3Nb phase in the eutectic respectively in the ranges 2.2-4.9 at. % Cr, 0.6-0.9 at.% Cr in the cast, and after the heat treatment. These values were consistent with the solubility values reported by Doychak and Hebsur (1991), and Prymak and Stein (2012) which were in the ranges 1.5-2.8, and 0.4-1.6 at.% Cr, respectively. Mahdouk and Gachon (2001) registered up to 10.8 at.% Cr solubility in Al_3Nb at 1000 °C, a value considerable higher than the above.

According to the XRD data the $(Al, Cr)_2(Nb,Hf)$ Laves phase was not the cubic C15 type. It has been suggested that in the Nb-Cr binary, the C14-$NbCr_2$ is a metastable phase (Stein et al. (2014)). The addition of Al is known to stabilize the C14-$NbCr_2$, see figures 28, 29 and 31. Zhao (2004c), and Prymark and Stein (2012) found that the C14-$NbCr_2$ Laves phase can dissolve up to 45 at.% Al and that is stabilized to low temperatures. The Al content in the $(Al,Cr)_2(Nb,Hf)$ phase was in the range 43 to 46 at.% Al, essentially in agreement with the published data. Doychak and Hebsur (1991) also reported similar values in the composition of a ternary compound named AlNbCr contained in their $NbAl_3$ + xCr (x= 1.2, 2.4, 4.8, 6.8 at. %) alloys, the compositions obtained of this compound were consistent with the compositions of the $(Al, Cr)_2(Nb,Hf)$ and the compositions reported for the $NbCr_2$ C14 Laves phase by Prymak and Stein (2012). Doychak and Hebsur (1991) gave the space group of AlCrNb as $P6_3/mmm$ while the space group of C14-$NbCr_2$ is $P6_3/mmc$ (Table 8). The solubility range of Nb in the $(Al,Cr)_2(Nb,Hf)$ was narrow being 31.1 to 33.1 at. %Nb in the as cast condition and 31.6 to 32.7 at. %Nb after the heat treatment.

The Cr_{ss} shows up to 45.5 at.% Al solubility at ~ 1320 °C in the Al-Cr binary system according to Okamoto (2008) and Stein et al. (2014) and up to 5.6 at.% Nb solubility at ~1668 °C in the Cr-Nb system according to Thoma and Perepezko (1992) and Liu et al. (1996). Prymak and Stein (2012) found that the solubility of Nb in the Cr_{ss} remained low even at high Al contents in Nb-Cr-Al

alloys and high temperatures. Besides, in the Cr-Hf binary system there is a negligible Hf solubility in the Cr_{ss}. The Hf content in the (Cr,Al,Nb) is consistent with the latter. The (Cr,Al,Nb) was not observed in the XRD because of its low volume fraction.

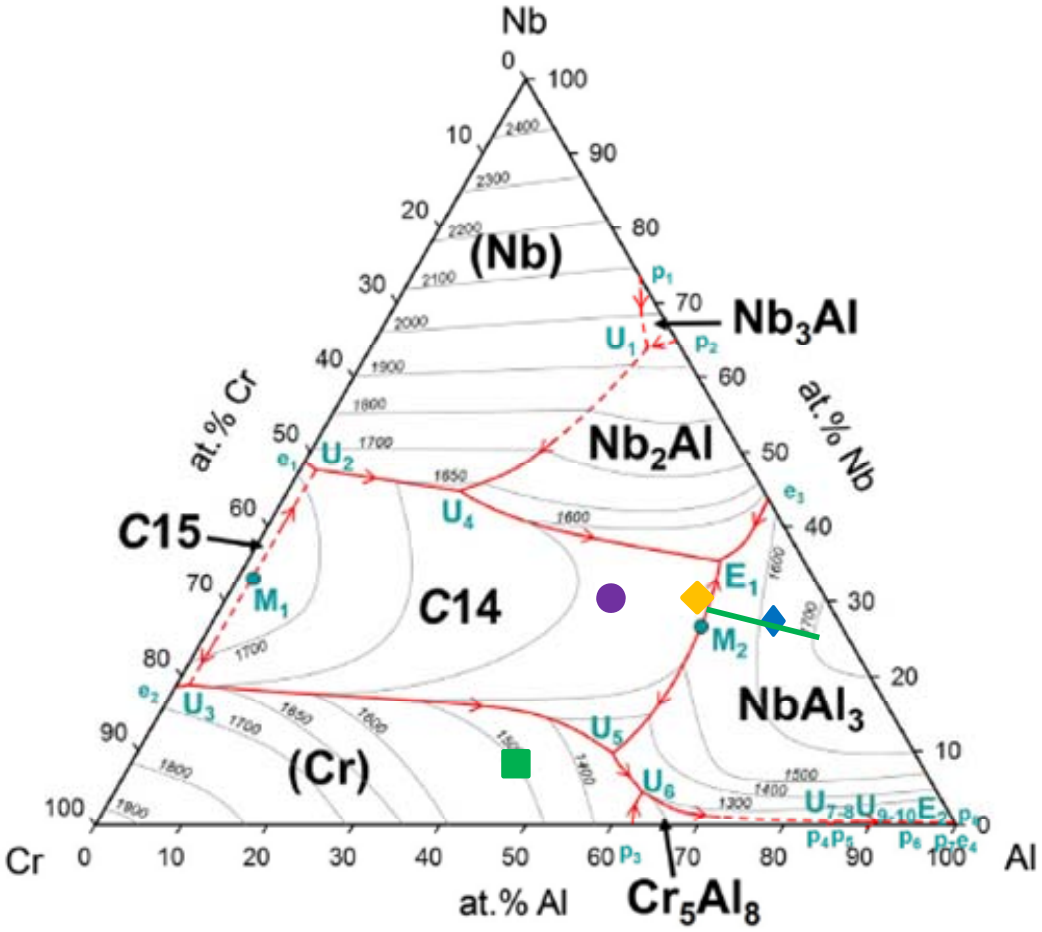

Figure 118. Liquidus projection of the Nb–Cr–Al system (Stein et al. (2014)), ♦ indicates the alloy OHC3, ● the liquidus of the C14 Laves, ■ the liquidus of $(Cr,Al,Nb)_{ss}$ and ♦ the composition of the eutectic. The green line joins the compositions of the Al_3Nb and the alloy and its extension shows the direction of cooling on the liquidus projection.

Following the heat treatment at 1400 °C for 100 h only the Al_3Nb and C14-$(Nb,Hf)(Cr,Al)_2$ phases were stable (Table 20). This is in agreement with the 1300 °C and 1450 °C Nb-Al-Cr isothermal sections proposed by Prymak and Stein (2012) in which the alloy OHC3-HT falls in the two phase Al_3Nb-C14 $NbCr_2$ field (see figure 119 for the tie line). In the 1300 °C isothermal section the alloy is very close to the Al_3Nb - $(Cr,Al,Nb)_{ss}$ - C14-$NbCr_2$ three phase field.

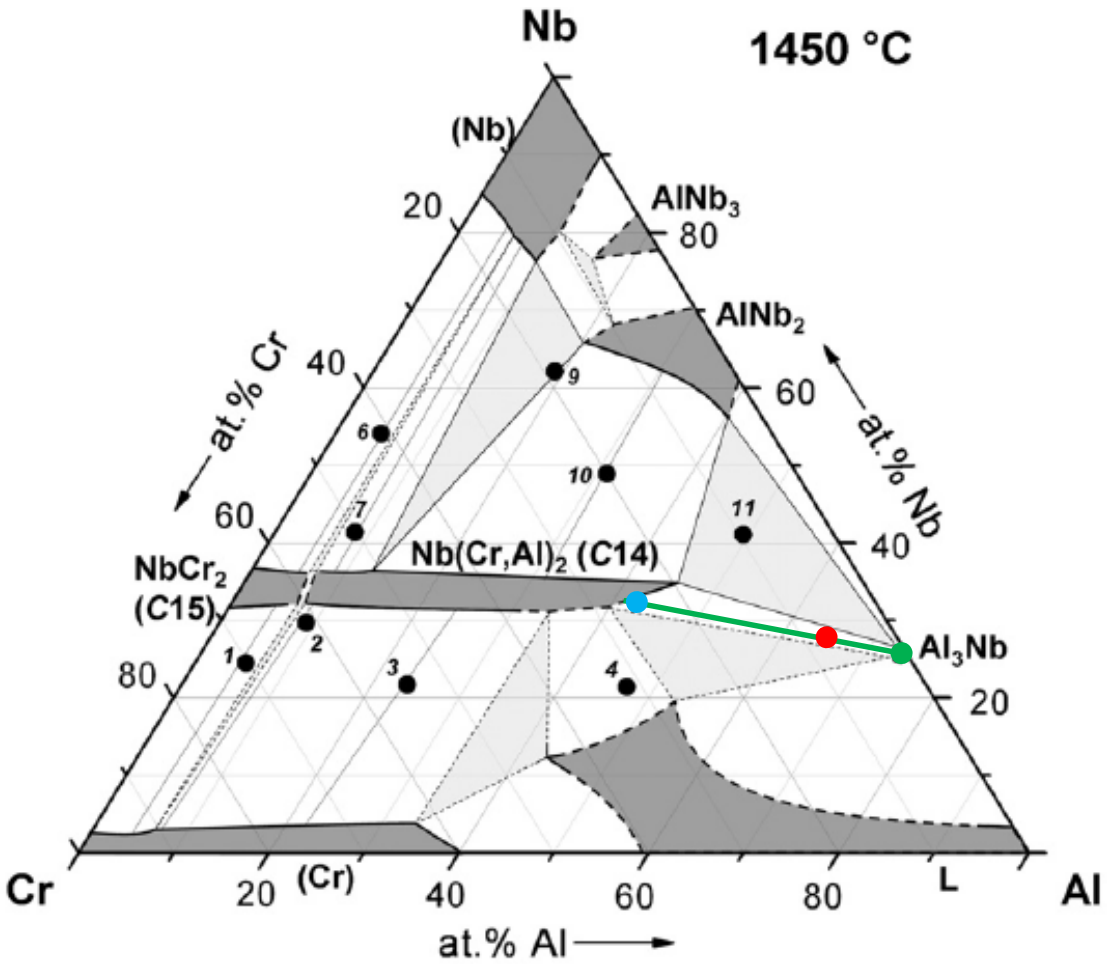

Figure 119 Isothermal section of the Cr-Al-Nb system at 1450 °C (Prymak and Stein (2012)). The green line is the tie line for the alloy OHC3-HT.

In the 1000 °C isothermal section from Ivanchenko (2004), the alloy is close to the two phase Al_3Nb-C14 $NbCr_2$ field, which is narrow and next to the Al_3Nb-$(Cr,Al,Nb)_{ss}$-C14-$NbCr_2$ three phase field. In the 1150 °C isothermal from Prymak and Stein (2012) it is just in the Al_3Nb-$(Cr,Al,Nb)_{ss}$-C14-$NbCr_2$ three phase field and close to the two phase Al_3Nb-C14 $NbCr_2$ field. The above data for 1000, 1150 and 1300 °C would suggest marginal and reducing stability for the $(Cr,Nb,Al)_{ss}$ in the oxidation at 1200 and 1300 °C, which together with the consumption of Al in the formation of the alumina scale contributed to the solid solution not being observed in the microstructure, particularly below the scale.

5.3.2 Oxidation

Oxidation at 800 °C

The isothermal oxidation of the alloy OHC3 at 800 °C was parabolic with scale formation and internal oxidation. The scale was composed by outer and an inner part with different oxides according to location. In the outer part the oxides $AlNbO_4$, $CrNbO_4$ and α-Al_2O_3 were detected, in the inner part of the scale only the α-Al_2O_3 was found. The Al_3Nb formed the $AlNbO_4$ at the top with an inner Al_2O_3 layer in contact with the metal. The $(Cr,Al)_2(Nb,Hf)$ formed the $CrNbO_4$ with an inner Al_2O_3 layer however, in some areas of the metal/scale interface the inner continuous Al_2O_3 layer was not formed instead an internal alumina oxide was observed. However, the internal oxidation was common in the alloy and deeper along the grain and phase boundaries. The internal oxidation is known to cause embrittlement of the substrate and contribute towards the occurrence of oxide spallation. However, at 800 °C the integrity of oxide scale was practically intact. The few microcracks observed were mostly found near the grain boundaries healed by an oxide.

According to Steinhorst and Grabke (1989), Meier (1989) and Grabke et al. (1991), Topylgo and Grabke (1993), the Al_3Nb suffers from pest oxidation at 800 °C, which was attributed to the selective oxidation of Al to form Al_2O_3 on the grain boundaries and cracking the latter resulting from its lack of plasticity to relieve the strain caused by the volume change from the oxide growth at this temperature. The depletion of Al in the grain boundaries also lead to the formation of the Nb_2Al phase which also affected the physical integrity of the microstructure due to the volume contraction generating microcracks that subsequently allowed further oxidation leading to the alloy disintegration i.e, pesting.

The primary phase in the alloy OHC3 was the Al_3Nb but the oxidised specimen did not suffer pest oxidation at 800 °C which would suggest that Cr played a very important role suppressing the pest oxidation probably via the segregation of Cr at the grain boundaries stabilising some Cr-rich ductile phase in the grain boundaries which was able to absorb the strain caused by the

oxide growth in these areas. According to Souza et al. (2008), the $(Cr,Al,Nb)_{ss}$ in Al_3Nb + Cr_{ss} eutectic alloys showed to be able to sustain Al_2O_3 growth at 900 °C acting as an Al reservoir.

The capability of alloys to form a continuous and protective alumina layer decreases with temperature, thus to promote the formation of an external alumina scale, the Al activity should be increased by adding Al in excess and/or adding elements that increase the Al activity and reduce the oxygen solubility at any Al content. Considering the classical theory for the transition from internal to external oxidation developed by Wagner (1959) the decrease of Al concentration in the alloy to critical values could promote its internal oxidation due to the reduction of the Al activity and the promotion of the rapid inward flux of oxygen into the alloy.

In the case of the alloy OHC3 the Al concentration in the Al_3Nb was below the stoichiometric concentration and the additions of Cr could have enhanced the Al activity and promoted the formation of α-Al_2O_3 after the development of the transient $AlNbO_4$ at the top surface. This effect could be sustained up to an Al critical content and when the latter was insufficient to produce a steady supply of Al to the oxide scale (because a substantial decrease in Al activity) the internal oxidation was promoted.

Internal oxidation was deeper at the grain boundaries near the metal/scale (insert image in figure 105d and figure 107), which is not surprising given that the grain boundaries are considered regions of high energy in which diffusion is more rapid. Tolpygo and Grabke (1993) suggested that the diffusion of Al and O is faster in the grain boundaries of pure Al_3Nb, due to the fact that this intermetallic has narrow solubility range and is brittle (high volume fraction of dislocations and low angle grain boundaries act as short-circuit leading to a maximum contribution to the mobility of species through grain boundaries).

According to the results of Doychak and Hebsur (1991) the CrAlNb phase formed in their Nb-Cr-Al alloys. The composition of this phase corresponded to that of the $Nb(Cr,Al)_2$ even though their TEM studies suggested different space group. This phase not just formed α-Al_2O_3 but was able to sustain a steady supply of Al to the oxide scale in their oxidation experiments at 1200 °C. Zheng et al. (2009) observed that oxidised Cr_2Nb alloys with 12 at. % Al content formed an Al_2O_3

scale at 1100 °C but could not sustain the Al_2O_3 scale growth. The Al content in the $(Cr,Al)_2(Nb,Hf)$ Laves phase in the alloy OHC3 was 46.1 at.% Al (higher compared with the AlCrNb in Doychak and Hebsur work) and formed a flat and compact oxide scale at 800 °C that consisted of external $(Cr,Al)NbO_4$ with inner α-Al_2O_3 at the metal/scale interface. However, some areas clearly showed internal oxidation and according to the EDS analysis the oxide was Al_2O_3. Thus, it is likely that the Al depletion in the $(Cr,Al)_2(Nb,Hf)$ at the metal/scale interface had an effect on the Al activity but was not enough to trigger a phase transformation presumably because the C14 Cr_2Nb has a wide Al solubility range. The $NbCr_2$ is a chromia former and it was expected to find Cr_2O_3 in the scale. This phase was not detected in the scale. Probably the supply of Cr by the $(Cr,Al)_2(Nb,Hf)$ was insufficient. However, Cr was detected in regions where Al_2O_3 was formed. What's more notable was to find only α-Al_2O_3 at a temperature where only the transient aluminas are regularly found. It should be noted that α-Al_2O_3 was also identified as one of the oxidation products formed on the Al_3Nb by Steinhorst and Grabke (1989). It is also possible that the Cr promoted the formation of the α-Al_2O_3 by forming Cr_2O_3 that acted as the nucleus for the growth of α-Al_2O_3 and remained in solution in the oxide. A similar mechanism was given by Brumm and Grabke (1992) for the oxidation of NiAl-Cr alloys. They observed that Cr promoted an accelerated transformation of transient aluminas into α-Al_2O_3 in which Cr_2O_3 nuclei served as nucleation site for α-Al_2O_3. This would also suggest that a higher nuclei density would lead to a faster formation of α-Al_2O_3. The finer grain size for the polycrystalline oxide would present more grain boundaries which served as diffusion paths enabling faster oxide growth. The formation of θ-Al_2O_3 can not be discarded since the internal rod-like oxides observed in the $(Cr,Al)_2(Nb,Hf)$ are similar to those observed by Doychack and Hebsur (1991) in the AlNbCr phase which were identified as the θ-Al_2O_3. However, this was not confirmed by the XRD data, see figure 106.

As the $(Cr,Al,Nb)_{ss}$ was no longer observed, it is suggested that it was dissolved as a result of the selective oxidation of Al and the growth of Al_3Nb and $(Cr,Al)_2(Nb,Hf)$ phases.

Hf additions have been shown to enhance the scale adhesion in alumina forming alloys, for example see Wang et al. (2014), Pint etal. (2006), Prescott and Graham (1992), Grabke et al.

(1991), Doychak and Hebsur (1991), and Perkins et al. (1990) and (1989). In the alloy OHC3, the addition of Hf promoted the formation of a Hf-rich phase(s). The alloy benefited from them regarding the oxide scale adhesion, since these particles were mostly found at the oxide grain boundaries and in these areas there was no oxide buckling.

The $AlNb_2$ phase was not detected in the microstructure according to the XRD and EDS data. This phase was expected to form following the consumption of the Al_3Nb phase and the fact that at low (<1000 °C) temperatures the alloy OHC3 seems to be in the three Al_3Nb+ C14 $(Cr,Al)_2Nb$ + $AlNb_2$ phase field, according to available phase equilibria. Considering its possible existence within the alloy, its volume fraction and size must have been too small for the resolution ranges of the experimental techniques used. It should also be remembered that in the available phase equilibria, the alloy, even though it falls in the three phase field at low temperatures (see above) it is very close to the two phase Al_3Nb + C14-$Nb(Al,Cr)_2$ phase field.

Doychak and Hebsur (1991) reported the transformation of Al_3Nb to $(Cr,Al)_2Nb$ owing to the Al depletion at the metal/ scale interface. The EDS analyses in the IOZ of the alloy OHC3 confirmed the formation of $(Cr,Al)_2(Nb,Hf)$ with composition of 43Al-24Cr-32Nb-1Hf near the Al_3Nb.

According to Doychak and Hebsur (1991), the Cr content in Nb-Cr-Al alloys enhances the oxidation resistance of the Al_3Nb by reducing its oxygen solubility and by increasing the Al activity. It was expected that the Cr addition in the alloy OHC3 would reduce the oxygen solubility in the alloy. This was not confirmed after oxidation at 800 °C because the alloy presented internal oxidation. However, the synergy of Cr and Al stabilized the $(Cr,Al)_2(Nb,Hf)$ and also promoted the formation of the (Cr,Al,Nb) phase and contributed to the suppression of pest oxidation at 800 °C.

Oxidation at 1200 °C

The isothermal oxidation of the alloy OHC3 at 1200 °C was parabolic. The oxidation kinetics was described by the two parabolic rates given in Table 21. The n value was 0.56 which clearly indicates that the overall kinetics was parabolic. Considering the K_p values for alumina forming

alloys reported by Pint et al. (2006), the values in Table 21 for the alloy OHC3 were in good agreement. The K_p value obtained for the alloy OHC3 was also in agreement with the value reported by Hebsur et al. (1989) for the Al-24Nb-6Cr alloy, but higher than those for the alloys with additions of Y and Zr below 5 at. %.

The oxide scale consisted of two oxides, an external layer of $Al(Nb,Cr)O_4$, a region of $Al(Nb,Cr)O_4$ + Al_2O_3, and the thicker Al_2O_3 layer at the metal/scale interface. The two main phases in the alloy were able to sustain the Al_2O_3 scale growth at the metal/scale interface where the scale was thinner over the Al_3Nb, suggesting that this phase had lower Al activity than the $(Cr,Al)_2(Nb,Hf)$ phase.

The oxide scale thickness over the eutectic areas indicated that the phase boundaries played a very important role in the oxidation. These areas were characterised by the retention of the eutectic microstructure at the metal/ scale interface, which presented a deeper oxide growth in the alloy as well as lumped areas at the scale/ gas interface. The Al_2O_3 layer showed cavities, forming as a result of the fast oxide growth in multiple directions in these regions causing strain owing to rapid volume change. However, the alumina was able to deform avoiding cracking and scale failure. Reactive element additions in alloys (like Hf and Y) have been associated with the improvement of alumina scale adherence and ductility [Prescott and Graham (1992)]. In the alloy OHC3 the areas of good scale adhesion presented a higher content of Hf-rich particles.

The eutectic areas presented more phase boundaries and on top of them formed a thicker oxide scale, an indication that they had served as easy paths for O and metal transport allowing the rapid growth of oxides (and raising the internal stress in the oxide scale due to the rapid change in volume in those areas). The local scale thickening featuring the extended oxide protrusions and ridges at the scale-gas interface would indicate that outward Al diffusion through short circuit paths had occurred. Counter-current diffusion of oxygen and aluminium are associated with ridges of the same oxide that extend inward and outward [Prescott and Graham (1992)].

It is likely that oxide spallation could occur at prolonged times considering the features observed in the eutectic regions where oxide lumps developed, raising the strain in such areas, but at the same time this also could indicate that a prior microstructural control (heat treatment for eutectic dissolution) could improve the oxidation kinetics.

Considering the thickness of the Al_2O_3 layer formed at the metal/scale interface and the solubility range of the Al_3Nb, it is suggested that this phase transformed into the $(Cr,Al)_2(Nb,Hf)$ phase after a considerable Al depletion. It is clear in figure 112a that the Al_3Nb and $(Cr,Al)_2(Nb,Hf)$ phases were effective at sustaining the Al_2O_3 scale at the metal/scale interface without the formation of Nb_2Al phase beneath the oxide scale as it could be expected after the decrease of the Al content in the Al_3Nb (the Nb_2Al is the next phase in the Nb-Al system as the Al concentration decreases see figure 13). The capability to form and sustain a continuous Al_2O_3 oxide scale was clearly improved. Above 1000 °C the Al_3Nb phase presents quasi-linear oxidation behaviour according to Steinhorst and Grabke (1989), and Meier (1989) because the parabolic growth is persistently interrupted by the constant cracking and spallation of its oxide scale. On the other hand, the oxidation of Nb-Al-Cr alloys at this temperature by Doychak and Hebsur (1991) produced a layer of AlNbCr (a phase having the chemical composition of the Laves) that not just formed Al_2O_3 but it was also able to sustain a steady supply of Al to the oxide scale at 1200 °C. The results of this work showed that there is a beneficial effect of Cr addition in the alloy OHC3 which is consistent with the results of Doychak and Hebsur (1991). However, in the particular case of the alloy OHC3, the $(Cr,Al)_2(Nb,Hf)$ did not form as a complete layer beneath the Al_2O_3 oxide at the metal/ scale interface.

As it was mentioned before, Souza et al. (2008) suggested that the dissolution of the $(Cr,Al,Nb)_{ss}$ functioned as Al reservoir for scale formation. In the alloy OHC3, the $(Cr,Al,Nb)_{ss}$ was no longer detected after isothermal oxidation at 1200 °C. The available phase equilibria would also suggest that the $(Cr,Al,Nb)_{ss}$ is not stable at 1200 °C.

The $(Cr,Al)_2(Nb,Hf)$ phase produced an outer layer of $(Al,Cr)NbO_4$ and an inner layer of Al_2O_3 at the metal/scale interface. Comparing with the results of the oxidation of Cr_2Nb at 1200 °C that

forms a different duplex oxide scale composed of an outer layer of Cr_2O_3 and an inner layer of $CrNbO_4$ [Tortorelli and Pint (1996), and Zheng et al. (2008)] it is suggested that the Al addition changed completely the oxidation behavior of the Cr_2Nb Laves phase and that this effect could be beneficial at high Al contents considering the results obtained by Zheng et al. (2009) who reported that the oxidation resistance increased with Al concentration in $NbCr_2$ alloys with 2 , 4 and 12 at.% Al additions. The oxide scale on top of the $(Cr,Al)_2(Nb,Hf)$ also showed ridges of Al_2O_3 grown by counter–current diffusion of Al and O [Prescott and Graham (1992)]. It is likely that oxygen found an easy path for its inward diffusion through the $AlNbO_4$ oxide layer and regions of intermixed $AlNbO_4$ + Al_2O_3 oxide.

There were some cavities beneath the Al_2O_3 on top of the $(Cr,Al)_2(Nb,Hf)$ at the metal/scale interface. The cavities were produced by the concentration of vacancies owing to faster diffusion of one of the species. This could suggest a high diffusivity rate for Cr along the phase boundaries of Al_3Nb, $(Cr,Al)_2(Nb,Hf)$ and grain boundaries of the Al_2O_3 scale, but in some way the losses by Cr evaporation could have been controlled as the Al_2O_3 layer coarsened (eliminating grain boundaries) avoiding a high Cr supply and an extensive formation of a Cr_2O_3 oxide with instantaneous evaporation. It was noticed that the alumina layer presented continuous microstructure at the metal/scale interface while the central regions presented some intergranular gaps that could have formed from the evaporation of CrO_3. Some Cr could also have been retained in the alloy by segregating at grain boundaries. The transport of Cr and Al through grain boundaries promoted the coarsening and growth of the $(Cr,Al)_2(Nb,Hf)$ layer beneath the Al_2O_3. The figures 112a and 113 show that beneath the Al_2O_3 layer there was a discontinuous layer of $(Cr,Al)_2(Nb,Hf)$.

It is likely that Hf (reactive element effect) enhanced the adherence of the oxide scale and its strongest effect could be observed above the grain boundaries of the alloy substrate where the oxide scale was thicker but not mixed. Thus, it is likely that in these regions the growth of the Al_2O_3 layer and the $(Al,Cr)NbO_4$ oxide was influenced by Hf that also improved the mechanical behaviour of Al_2O_3 layer. However, the oxidation rate was not favourably affected since it was

higher compared with the oxidation rates reported by Hebsur et al. (1989) in alloys doped with Y and Zr.

Oxidation at 1300 °C

The isothermal oxidation behaviour of the alloy OHC3 at 1300 °C was parabolic despite the partial oxide spallation. The oxidation rate was one order higher than that at 1200 °C (Table 22). The n value was 0.41 which indicates that the alloy followed parabolic kinetics in the experiment overall.

The oxide scale was very similar to that formed at 1200 °C and consisted of an external layer of $Al(Nb,Cr)O_4$ + Al_2O_3, and the thicker Al_2O_3 layer at the metal/scale interface. The oxide at the top of the scale suggested that initially there was a simultaneous oxidation of the elemental components in the alloy and some spallation of the scale. The Al_2O_3 oxide could start growing simultaneously because of the higher oxidation temperature. The two main phases in the alloy coarsened and were able to sustain a continuous and adherent Al_2O_3 scale at the metal/scale interface. The even thickness of the scale indicated that at 1300 °C the Al activity in Al_3Nb and $(Cr,Al)_2(Nb,Hf)$ could be similar.

The prior eutectic microstructure was no longer observed in the alloy and consequently lumped areas at the scale/gas interface were also absent. As was the case at 1200 °C, the Al_2O_3 layer showed cavities that could result from the fast oxide growth in multiple directions in these regions causing strain as a result of rapid volume change. The alumina was able to deform avoiding cracking and scale failure. As it was already mentioned, reactive elements have been associated with the improvement of alumina scale adherence and ductility [Prescott and Graham (1992)]. In the alloy OHC3 these areas presented a higher content of Hf-rich particles that could contributed to this phenomenon.

The Al_2O_3 layer formed at 1300 °C was thicker than that formed at 1200 °C. As it was observed at 1200 °C there was formation of the $(Cr,Al)_2(Nb,Hf)$ phase after a considerable Al depletion from the Al_3Nb without the formation of Nb_2Al beneath the oxide scale. The layer of

$(Cr,Al)_2(Nb,Hf)$ formed beneath the Al_2O_3 was more continuous but still did not entirely cover the metal/scale interface suggesting that Hf might have retarded the transformation. The Al_3Nb and $(Cr,Al)_2(Nb,Hf)$ phases showed their capability to form and sustain a continuous Al_2O_3 scale below an outer layer of $(Cr,Al)NbO_4$, see figure 117. At 1300 °C it was also observed that the alumina layer presented continuous microstructure at the metal/scale interface while the central regions presented some intergranular gaps that could indicate the evaporation of Cr_2O_3 oxide. The (Cr,Al,Nb) and precipitates of another phase in the Al_3Nb grains were no longer observed.

Despite the partial spallation of the $Al(Nb,Cr)O_4$ + Al_2O_3 layer, the inner Al_2O_3 layer did not fail since there was not metallic surface exposed. After the spallation of the outer oxide layer, the Al_2O_3 beneath presented Hf-rich particles dispersed over its surface, indicating that Hf had positively influence the Al_2O_3 scale but not the $(Al,Cr)NbO_4$ layer adherence.

Two possible mechanisms could be responsible for the increase of the oxidation rate at this temperature. First, the grain boundaries provided easy paths for faster outward and inward diffusion of reactants at this higher temperature being eventually blocked by the Al_2O_3 grain growth Li et al. (2003). Second, Cr was not effective owing to the evaporation of CrO_3. Slight Cr depletion was detected in the $(Cr,Al)_2(Nb,Hf)$ phase near the metal/ scale interface, but the $(Cr,Al,Nb)_{ss}$ was no stable. This suggests the some Cr was indeed transported through the oxide scale and formed Cr_2O_3 that was not stable at this temperature.

5.4 Conclusions

The microstructural study of the as cast and heat treated alloy OHC3 allowed the following conclusions to be made:

The phases in the as cast alloy were the Al_3Nb, $(Cr,Al)_2(Nb,Hf)$ and $(Cr,Al,Nb)_{ss}$ with the Al_3Nb being the primary phase. The eutectic reaction L → Al_3Nb + $(Cr,Al)_2(Nb,Hf)$ was confirmed in the DSC experiment at 1498 °C, and high cooling rates prevented formation of the eutectic in the bottom of the button ingot.

After heat treatment at 1400 °C for 100 h the $(Cr,Al,Nb)_{ss}$ was destabilised and only the Al_3Nb and $(Cr,Al)_2(Nb,Hf)$ phases were present together with Hf rich particles.

The Cr solubility in the Al_3Nb was low, showing a higher range 2.2-4.9 at. % Cr after the heat treatment. The Al solubility in the $(Cr,Al)_2(Nb,Hf)$ C14 Laves phase was 46 at. % Al and the Hf solubility was 1.1 at. % Hf. The Laves phase had the higher Hf content in the alloy. The solubility of Al and Nb in the $(Cr,Al,Nb)_{ss}$ was 45.4 and 7.3 at.% respectively. There was no Hf solubility in the solid solution.

The thermogravimetric study at 800 °C of the alloy OHC3 allowed the following conclusions to be made:

No pesting was observed in the alloy that presented a very thin and adherent oxide scale with no oxide spalltion. The alloy exhibited parabolic oxidation behaviour and gained 1.54 mg/cm^2 after 100 h.

The oxide scale was composed of $AlNbO_4$, $CrNbO_4$ and α-Al_2O_3. There was internal oxidation with a deeper attack along phase and grain boundaries. There was also Cr enrichment near the grain boundaries of the Al_3Nb. The addition of Hf was beneficial for scale adhesion.

The addition of Cr in the Al_3Nb phase was beneficial because it promoted the preferential oxidation of Al by increasing the Al activity and formed nucleation sites for the growth of an external α-Al_2O_3 layer whose growth was sustained up to a critical Al content in the Al_3Nb below which Al started to be internally oxidised.

The $(Cr,Al,Nb)_{ss}$ was dissolved as a result of the selective oxidation of Al and served as Al supply for the stablishment of an Al_2O_3 oxide scale.

The thermogravimetric study at 1200 °C of the alloy OHC3 led to the following conclusions:

The oxide scale was composed of external $Al(Nb,Cr)O_4$ layer, regions of mixed $Al(Nb,Cr)O_4$ + α-Al_2O and a thick inner layer of α-Al_2O_3 at the metal / scale interface.

The specimen presented an adherent oxide scale with no oxide spalltion. The alloy exhibited parabolic oxidation behaviour and gained 4.47 mg/cm^2 after 80 h.

Phase boundaries played a very important role in the oxidation rate by allowing a faster transport of O_2 and metal.

The $(Cr,Al)_2(Nb,Hf)$ phase formed after a considerable Al depletion in the Al_3Nb preventing the formation of the Nb_2Al phase.

The $(Cr,Al)_2(Nb,Hf)$ phase was able to sustain a steady supply of Al for the α-Al_2O_3 scale growth.

The synergy of Cr and Al promoted the formation of a continuous and coarse α-Al_2O_3 while the addition of Hf was beneficial for scale adhesion although there was no effect in the oxidation rate.

The thermogravimetric study at 1300 °C of the alloy OHC3 allowed the following conclusions to be made:

The oxide scale was composed of and external $Al(Nb,Cr)O_4$ layer with some spallation, regions of mixed $Al(Nb,Cr)O_4$ + α-Al_2O and a thicker and adherent inner layer of α-Al_2O_3 at the metal / scale interface. The alloy exhibited parabolic oxidation behaviour and gained 8.5 mg/cm^2 after 100 h.

The $(Cr,Al)_2(Nb,Hf)$ that formed below the α-Al_2O_3 layer was more continous. This phase was able to sustain a steady supply of Al for the α-Al_2O_3 scale growth. However, it was slightly depleted in Cr which could have been lost by evaporation of its oxide and thus, increasing the oxidation rate.

Hf was beneficial for the α-Al_2O_3 scale adhesion although there was no effect in the oxidation rate.

Chapter 6

Microstructure and oxidation of the alloy Nb-24Ti-18Si-5Al-5Cr-5Ge-5Sn (OHS1)

6.1 Introduction

Even the most superior coating systems are prone to fail under hostile environmental conditions, therefore it is necessary for the Nb-silicide based in-situ composites to be able to resist corrosive conditions in the meantime [Bewlay et al. (2001)]. These materials can offer oustanding balance of mechanical properties at temperatures between 1000 and 1600 °C [Dimiduk et al. (1995), Bewlay et al. (1995a), Jackson et al. (2005)], but their oxidation at medium and high temperatures must be improved [Bewlay et al. (2003)]. Thus, in order to be considered for practical applications an optimum balance of their mechanical and oxidation properties is necessary.

As it has been discussed earlier in this thesis, in these in situ composites the most common phases can be some or all of the Nb_{ss} (cI2-W), Nb_3Si (tP32-Ti_3P), αNb_5Si_3 (tI32, Cr_5B_3), βNb_5Si_3 (tI32,W_5Si_3) phases, depending on the alloy chemistry and processing [Subramanian et al. (1995)].

Like the Ni based superalloys, the addition of key elements could enable Nb-silicide in-situ composites to operate in aggressive environments. However, the control of the chemistry of the Nb-silicide based alloys represents a great challenge to metallurgists because the synergy of elemental additions could promote undesirable effects [Zelenitzas (2006b), Vellios (2007a) and (2007b)]. Thus, the key challenge is to design alloys with optimum balance of mechanical properties and oxidation resistance.

Mechanical properties and oxidation resistance have been evaluated in Nb-silicided base in-situ composites with elemental additions that include Ti, Cr, Hf, Al, Mo, Ge, B, Sn, W and Fe.

The alloys that were used as the basis to select the composition of the alloy OHS1 were the alloys KZ5 (Nb-24Ti-18Si-5Al-5Cr), JG6 (Nb-24Ti-18Si-5Al-5Cr-2Mo-5Hf-5Sn), NV6 (Nb-24Ti-18Si-5Sn) and ZF6 (Nb-24Ti-18Si-5Al-5Cr-5Ge) that had been studied in the research group previously. The base nominal composition of these alloys contained 18 at. % Si, 24 at.% Ti, and in some of them 5 at. % Cr and 5 At.% Al were also added. The addition of Si was expected to improve the oxidation resistance of the alloys by forming SiO_2. However, the fast oxidation of Nb does not allow SiO_2 to form a compact oxide scale. The 18 at. % Si content was selected to achieve low creep rates in alloys according to the data reported by Bewlay et al. (2002). The addition of Ti improves the fracture toughness by improving the ductility of the Nb_{ss} [Bewlay et al. (1995b) and (1996)] and increases the oxidation resistance of the in-situ composites. The Ti content was limited to 24 at. % because high Ti concentrations decrease the melting temperature of the composites and also stabilize the hexagonal Ti_5Si_3 phase that has inferior creep properties compared with the tetragonal Nb_5Si_3. The addition of Cr was made to improve oxidation resistance and the formation of Cr_2Nb Laves phase. However, high Cr contents would also decrease the melting point of the alloys. The addition of Al improves the oxidation resistance of the Nb-silicide in-situ composites reducing the pest oxidation [Bewlay et al. (2003) and Zelenitsas et al. (2006a)] and contributing to its suppression when in synergy with other simple metals. Al also stabilises the Cr_2Nb Laves phase. The Al content must be kept at $\leq$ 5 at. % Al to avoid the increase of the ductile-brittle transition temperature (DBTT) of the Nb_{ss} to above -50 °C.

Alloying additions of Sn, Ge and B can contribute to suppresing pesting [Bewlay et al. (2003) and Mitra (2006)] and their effectiveness depends on their concentration in the alloy. The preliminary results of Vellios and Tsakiropoulos (2007a) showed that 5 at. % Sn controlled the pest oxidation of a Nb-silicide base alloy at 800 °C . However according to Bewlay et al. (2003), Sn can be similarly effective at concentrations up to 2 at. %.

According to Jackson et al. (2005) the oxidation resistance of the composites is enhanced by the partial substitution of Si by Ge. Alloying additions of Ge can control the CTE of SiO_2, and the viscosity of SiO_2-GeO_2 at lower temperatures which would imply better scale self healing

properties [Mitra (2006)]. The addition of 5 at. % Ge suppressed the pesting of the alloy ZF6 (Nb-24Ti-18Si-5Cr-5Al-5Ge) but not the oxide scale spallation at high temperature.

The oxidation of the alloys KZ5 and ZF6 was considered in the design of the alloy (Nb-24Ti-18Si-5Cr-5Al-5Ge-5Sn) (OHS1). The aim of this part of the research was to study the synergetic effects of Ge and Sn additions on phase stability and oxidation behaviour at 800 °C and 1200 °C.

6.2 Results

6.2.1 Microstructure characterization

As cast microstructure

The actual composition (at.%) of the cast alloy (OHS1-AC) was Nb-23Ti-18.5Si-4.4Cr-4.7Al-5Ge-4Sn and was obtained from all the analyses taken from the top, centre and bottom of the alloy button. Using the criterion $C_{max}^{i} - C_{min}^{i} \geq 2$ at. %, for macrosegregation of element i, the data (Table 23) revealed macrosegregation of Ti and Si and weak macrosegregation of Al, Cr and Sn. Typical microstructures of OHS1-AC are shown in figure 121.

In the bottom of the button the microstructure was more homogeneous compared with the bulk and top. The average Sn concentration was lower than the nominal composition owing to loss of Sn by evaporation during melting.

According to the SEM studies, the EDS and XRD data (Figures 120 and 121 and Table 23), the following phases were present in the microstructure: the Nb_{ss}, $NbCr_2$, Nb_3Sn, βNb_5Si_3, γNb_5Si_3. The microstructure in the top was finer than that in the bulk and consisted of primary grains of Nb_5Si_3 with Ti segregation at its boundaries (Ti-rich Nb_5Si_3), the Nb_3Sn (bright contrast) that was observed in the interdendritic areas and had Ti-rich regions (dark grey contrast), the $(Nb,Ti,Cr)_{ss}$ and the $(Nb,Ti)(Cr,Si,Al)_2$ Laves phase with the darkest contrast.

The XRD data was matched with the data from the following JCPDS cards (34-370) for Nb_{ss}, (30-0875) for βNb_5Si_3, (65-4327) for Ti-rich Nbi_5Si_3, (19-875) for the Nb_3Sn and (47-1637) for the $NbCr_2$ Laves phase.

Table 23 EDS data (at. %) of OHS1 as cast.

Area/Phase	Nb (at%)	Ti (at%)	Si(at%)	Cr (at%)	Al (at%)	Ge (at%)	Sn (at%)
Top	40.0 ± 1.1 42.5 – 38.5	23.2 ± 1.4 25.0 – 20.4	18.8 ± 1.6 22.3 – 15.9	4.3 ± 0.6 5.1 – 3.3	4.6 ± 0.4 5.3 – 3.9	5.2 ± 0.4 5.6 – 4.5	3.9 ± 0.5 4.8 – 3.1
Centre	41.5 ± 1.7 43.6 – 38.0	22.1 ± 1.7 25.4– 20.1	18.7 ± 1.6 21.2 – 15.5	4.1 ± 0.5 5.3 – 3.2	4.7 ± 0.5 5.6 – 3.4	4.7 ± 0.5 5.7 – 3.7	4.1 ± 0.4 5.1– 3.2
Bottom	39.3 ± 0.6 40.7 – 38.0	24.2 ± 0.8 25.8 – 22.8	17.9 ± 0.8 19.1 – 16.7	4.8 ± 0.4 5.4 – 4.2	4.8 ± 0.4 5.6 – 4.0	5.2 ± 0.3 5.6 – 4.7	3.9 ± 0.4 4.5 – 3.4
(Nb,Ti,Cr)ss	23.3 ± 0.7 24.3 – 22.2	30.7 ± 1.0 32.1 – 29.5	5.3 ± 1.0 6.8 – 3.9	29.4 ± 1.6 31.9 – 27.4	7.2 ± 0.7 8.4 – 6.3	1.5 ± 0.5 2.2 – 0.7	2.7 ± 0.2 3.1 – 2.4
$(Nb,Ti)(Cr,Si,Al)_2$	23.1 ± 1.1 24.9 – 21.7	17.6 ± 1.2 19.6 – 16.2	7.3 ± 0.4 8.0 – 7.0	45.3 ± 2.6 48.2 – 42.0	5.1 ± 0.4 5.8 – 4.5	0.9 ± 0.1 1.1 – 0.9	0.7 ± 0.4 1.4 – 0.3
Nb_3Sn	49.0 ± 0.9 50.3 – 47.8	24.9 ± 0.5 25.7 – 24.3	2.9 ± 0.1 3.1 – 2.7	4.4 ± 0.3 4.6 – 3.8	5.8 ± 0.3 6.2 – 5.3	1.6 ± 0.2 1.9 – 1.4	11.4 ± 0.4 12.1 – 11.0
Ti rich Nb_3Sn	41.9 ± 0.9 43.2 – 40.4	29.4 ± 1.0 31.2 – 27.7	2.8 ± 0.2 3.2 – 2.4	7.4 ± 0.7 8.2 – 6.4	7.3 ± 0.3 7.8 – 6.8	1.5 ± 0.1 1.7 – 1.3	9.7 ± 0.5 10.5 – 8.8
Nb_5Si_3	43.4 ± 0.3 43.8 – 43.1	18.6 ± 0.3 19.1– 18.5	27.3 ± 0.5 27.7 – 26.7	1.2 ± 0.1 1.3 – 1.1	2.0 ± 0.2 2.2 – 1.8	6.2 ± 0.1 6.3 – 6.1	1.1 ± 0.2 1.4 – 1.0
Ti rich Nb_5Si_3	38.8 ± 2.0 40.5 – 36.1	23.0 ± 1.9 25.3 – 21.1	20.6 ± 0.6 21.3– 19.6	1.9 ± 0.4 2.5 – 1.6	5.2 ± 0.4 5.8 – 4.8	6.7 ± 0.2 7.1 – 6.4	3.8 ± 0.2 4.1 – 3.5

The BSE images confirmed microsegregation of Ti in the Nb_3Sn and the Nb_5Si_3. The Ti content in Nb_3Sn was 24.9 at.% Ti and the Si+Al+Ge+Sn concentration was 21.7 at.% but in the Ti-rich Nb_3Sn the Ti content was 29.4 at.% Ti with Si+Al+Ge+Sn = 21.3 at.%. The Ti-rich Nb_3Sn was also richer in Cr and Al than the Nb_3Sn (Table 23).

The Ti concentration in the Nb_5Si_3 was 18.6 at.% and the Si+Al+Ge+Sn concentration was 36.6 at.% while the Ti-rich Nb_5Si_3 had a 23 at.% Ti and Si+Al+Ge+Sn = 36.3 at.% (Table 23). The $(Nb,Ti,Cr)_{ss}$ and the $(Nb,Ti)(Cr,Si,Al)_2$ phases were observed in the areas of dark contrast and were present at lower volume fraction in the alloy. It was not possible to observe grain or phase boundaries in the regions with dark contrast as they were narrow and presented an irregular microstructure. The chemical compositions obtained confirmed the Nb_{ss} and Cr_2Nb Laves phases in agreement with the XRD data (Figure 120). However, it is likely that the analyses for the solid solution and the Laves phase in Table 23 might have error arising from collection of data from a neighbouring phase. The data for the Laves phase is in better agreement with that

from other researchers. The data for the solid solution is less trustable owing to the unusually high Cr content which is even higher than the maximum solid solubility of Cr in Nb (~24 at.%). The higher than usual Si concentration in the Nb_{ss} is in agreement with the higher solubility of Si in Ti in the Ti-Si binary compared with the Nb-Si binary. The solubility for Ge and Sn in the $(Nb,Ti)(Cr,Si,Al)_2$ Laves phase was very low.

The same phases were in the microstructure in the bottom (Fig 121b) but with different volume fractions. A higher volume fraction of the dark regions was observed compared with the top and bulk of the cast alloy button. In addition, a eutectic was observed in the microstructure in the bottom in areas of black contrast. The composition of the eutectic was Nb-33.5Ti-5.2Si-25.1Cr-7.7Al-1.8Ge-3.2Sn where (Si+Al+Ge+Sn = 17.9 at.%) a value close to the 17.5 at. % Si of the Nb + $NbSi_3$ eutectic in the Nb-Si binary.

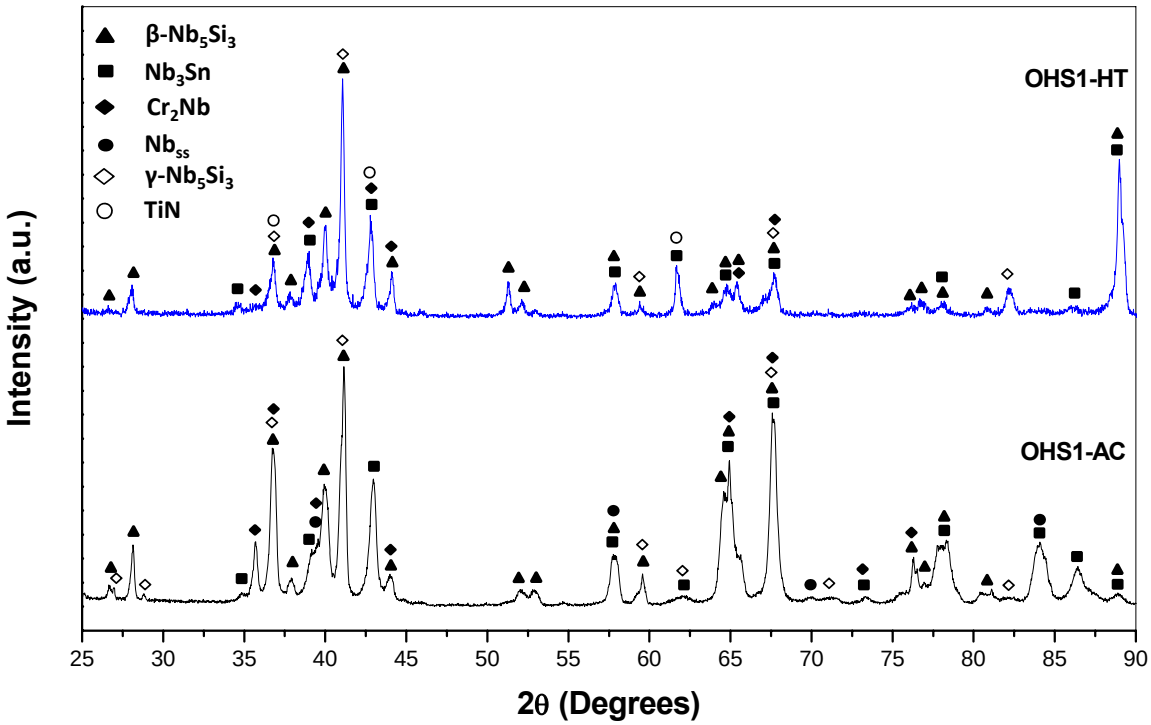

Figure 120. XRD diffractograms of the alloy OHS1 showing the phases present in the cast and heat treated conditions.

The observation of the eutectic was not easy owing to its fine structure. Thus, it is not possible to exclude the presence of the eutectic in the dark contrast areas in the top and bulk where the

average composition was Nb-27.5Ti-6.8Si-32Cr-6.7Al-1.3Ge-2.5Sn considerably richer and poorer in Cr and Ti compared with the eutectic in the bottom but with Al+Si+Ge+Sn=17.3 at.% which is close to the Nb+Nb_3Si eutectic in the binary and in the range of eutectic compositions for the binary Nb+Nb_3Si reported in the literature. In the bottom the range of eutectic compositions was (22.7-24.0)Nb-(30.6-35.9)Ti-(4.6-5.8)Si-(22.3-26.9)Cr-(7.2-8.3)Al-(1.5-2.0)Ge-(2.7-3.5)Sn with the highest values giving Al+Si+Ge+Sn ≈ 20 at. %.

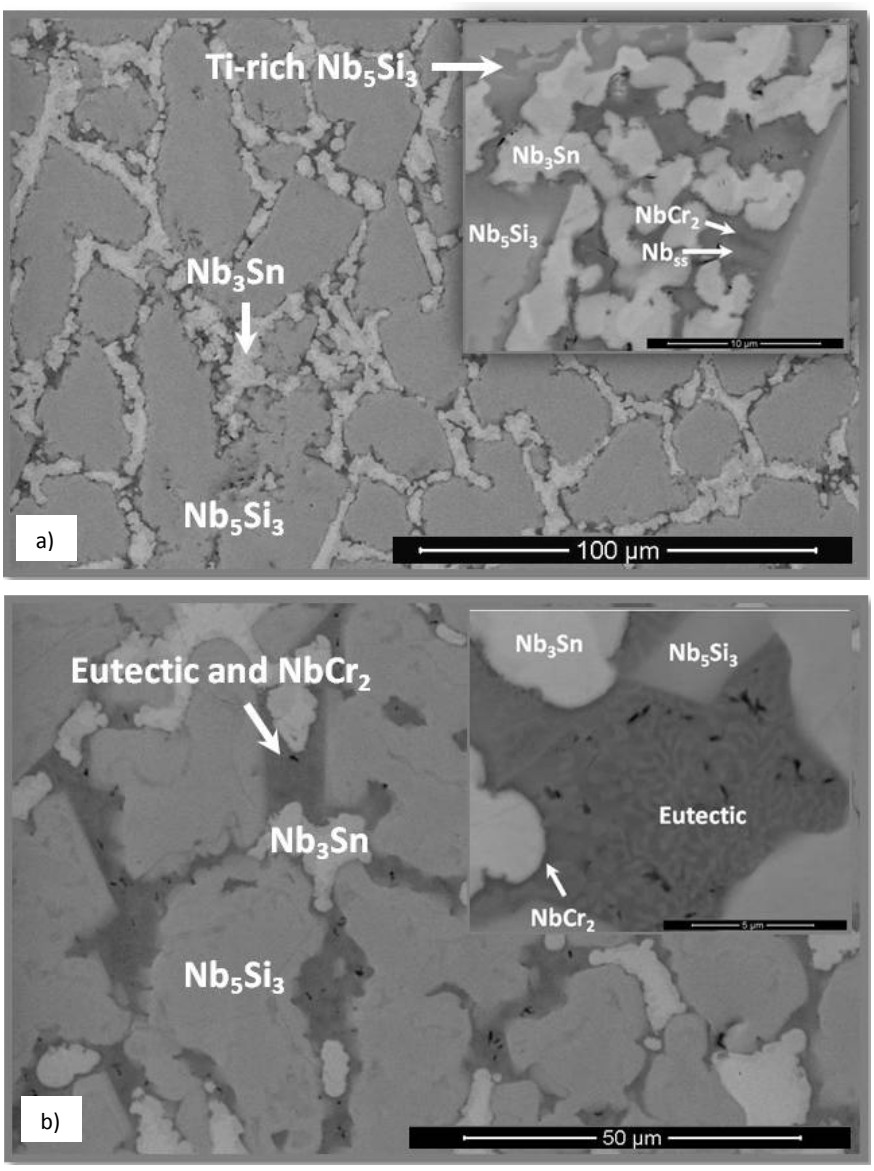

Figure 121. BSE images from cross section of OHS1-AC, (a) bulk, X500 (insert image X10000), (b) bottom, X1000, (insert image X16000).

Heat treated microstructure

The actual composition of the heat treated alloy (OHS1-HT) (1400 °C / 100h) was Nb -24Ti-18Si-4.4Cr-4.7Al-5.1Ge-4.2Sn. The EDS analysis data is given in Table 24. The data in Table 24 is the average values of the large area and phase analyses taken from the top, centre and the bottom of the button after the heat treatment. It is noticeable that weak chemical inhomogeneity of Si in the OHS1-HT alloy was still present. Figure 122 shows typical images of the microstructure in OHS1-HT.

Table 24 EDS data (at.%) of OHS1 heat treated at 1400 °C for 100h.

Area/Phase	Nb (at%)	Ti (at%)	Si(at%)	Cr (at%)	Al (at%)	Ge (at%)	Sn (at%)
Top	39.7 ± 0.4	24.1 ± 0.5	18.2 ± 0.8	4.2 ± 0.3	4.6 ± 0.3	5.1 ± 0.2	4.2 ± 0.3
	39.9 – 39.1	24.6 – 23.6	19.2 – 17.4	4.5 – 3.9	5.0 – 4.2	5.3 – 4.8	4.7 – 4.0
Bulk	39.9 ± 1.0	23.7 ± 0.6	17.8 ± 1.0	4.6 ± 0.4	4.7 ± 0.2	5.0 ± 0.2	4.2 ± 0.5
	41.1 – 38.4	24.6 – 23.2	19.1 – 16.3	5.0 – 4.0	5.0 – 4.5	5.3 – 4.6	5.2– 3.8
Bottom	39.4 ± 0.6	24.4 ± 0.4	18.0 ± 0.7	4.4 ± 0.5	4.5 ± 0.2	5.2 ± 0.2	4.1 ± 0.2
	40.3 – 38.8	24.9 – 24.0	18.6 – 17.1	4.9 – 3.8	4.7 – 4.3	5.4 – 5.0	4.3 – 3.8
$NbCr_2$	26.0 ± 0.6	10.1 ± 0.7	8.8 ± 0.2	50.4 ± 1.0	3.5 ± 0.4	0.7 ± 0.0	0.4 ± 0.3
	26.6 – 25.3	10.5 – 9.1	9.1 – 8.6	51.7 – 49.3	3.9 – 3.1	0.8 – 0.7	0.7 – 0.1
Nb_3Sn	47.1 ± 0.4	23.8 ± 0.4	2.6 ± 0.2	5.8 ± 0.2	5.0 ± 0.6	1.3 ± 0.1	14.5 ± 0.8
	47.5 – 46.7	24.1 – 23.1	2.8 – 2.4	6.1 – 5.5	5.5 – 4.0	1.3 – 1.2	15.8 – 14.0
Nb_5Si_3	37.0 ± 0.4	24.2 ± 0.8	22.0 ± 1.3	3.2 ± 0.3	4.8 ± 0.3	5.8 ± 0.7	2.9 ± 0.4
	37.6 – 36.5	25.0 – 23.5	23.5 – 20.9	3.5 – 3.0	5.0 – 4.5	6.4 – 5.0	3.2 – 2.5
Ti rich Nb_5Si_3	33.9 ± 0.2	28.1 ± 1.3	25.1 ± 0.7	2.2 ± 0.4	4.3 ± 0.5	5.6 ± 0.7	3.8 ± 0.2
	34.8 – 32.6	29.5 – 26.6	25.6– 24.1	2.7 – 1.7	4.9 – 3.7	6.7 – 5.1	4.1 – 3.5

The microstructure consisted of the β-Nb_5Si_3 matrix, with coarsened and elongated grains of the Nb_3Sn phase that in some areas were connected with the Cr_2Nb Laves phase. The Nb_{ss} was not present in the alloy (consistent with the XRD data in Figure 120). Black contrast areas with high N content were observed (TiN according to JCPDS 38-1420). The Ti content in the Nb_3Sn was essencially unchanged but the Si+Al+Ge+Sn concentration had increased to 23.4 at.%.

The Ti concentration in the Nb_5Si_3 had increased and the Si+Al+Ge+Sn concentration had decreased slightly compared with the cast alloy. No evidence of the prior eutectic microstructure was found in the OHS1-HT.

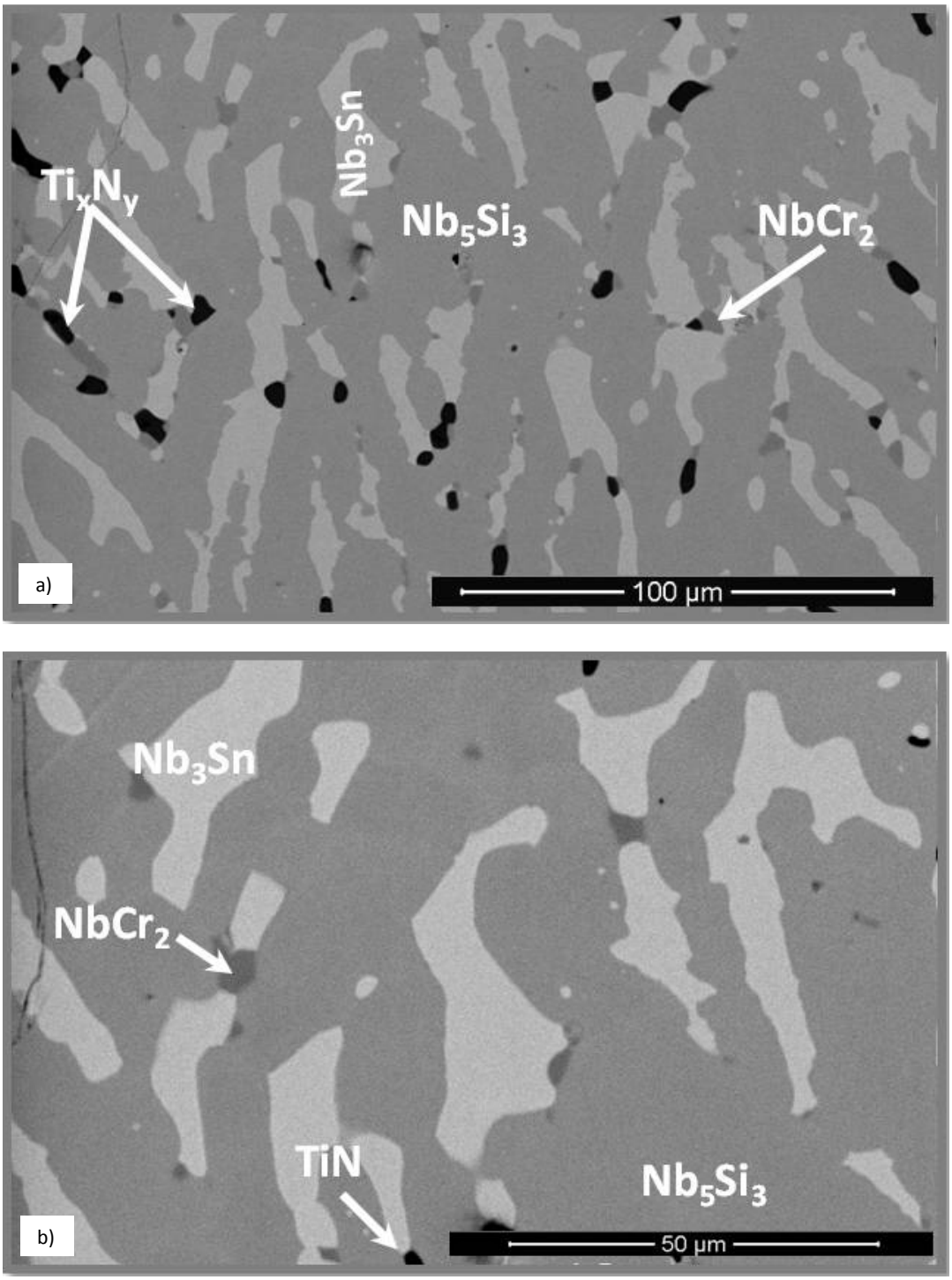

Figure 122. Typical microstructure of OHS1-HT alloy, BSE image a) from the centre, X500 and b) from the bottom, X1000.

6.2.2 Thermo-gravimetric analysis

The rate constant values of the alloy OHS1 after isothermal oxidation at 800 and 1200 °C are shown in Table 25. For the isothermal oxidation at 800 °C the n value was 0.46, meaning that the oxidation was parabolic. The alloy OHS1 showed improved oxidation at 800 °C compared with linear oxidation of the alloy KZ5 which gained 30 mg/cm^3 in weight after 85 h at 800 °C [Zelenitsas and Tsakiropoulos (2006a)].

The oxidation at 1200 °C was described by a transient parabolic mechanism during the first 3.1h following a linear mechanism until the 76.7 h when the experiment stopped, see Table 25. The n= 0.83 value suggested that the oxidation was linear.

Table 25. Total weight gain and oxidation rate constants of the alloy OHS1 at 800 and 1200 °C.

Alloy code at tested T	n	K_l (g.cm^{-2} . s^{-1})	K_p (g^2.cm^{-4}. s^{-1})	Weight gain (mg/cm^2)
OHS1 - 800 °C	0.46	-	2.4 x 10^{-11} (0-100)h	3.19
OHS1 - 1200 °C	0.83	1.1 x 10^{-7} (>3.1)h	4.9 x 10^{-10} (0-3.1)h	31.28

6.2.2.1. Thermo-gravimetric analysis (TGA) at 800 °C

Figure 123 shows the isothermal oxidation from which n=0.46 and K_p= 2.4 x 10^{-11} g^2.cm^{-4}. s^{-1} were calculated. Both values confirmed parabolic oxidation. The weight gain after 100 h of oxidation was 3.19 mg/cm^2. The Nb_{ss} volume fraction in the alloy was very low compared with the 30% average in Nb in-situ composites which must have had a strong effect on the oxidation behaviour. The decrease and increase in weight shown by the data in figure 123 suggest that the scale formed at 800 °C was no protective even though the oxidation was parabolic.

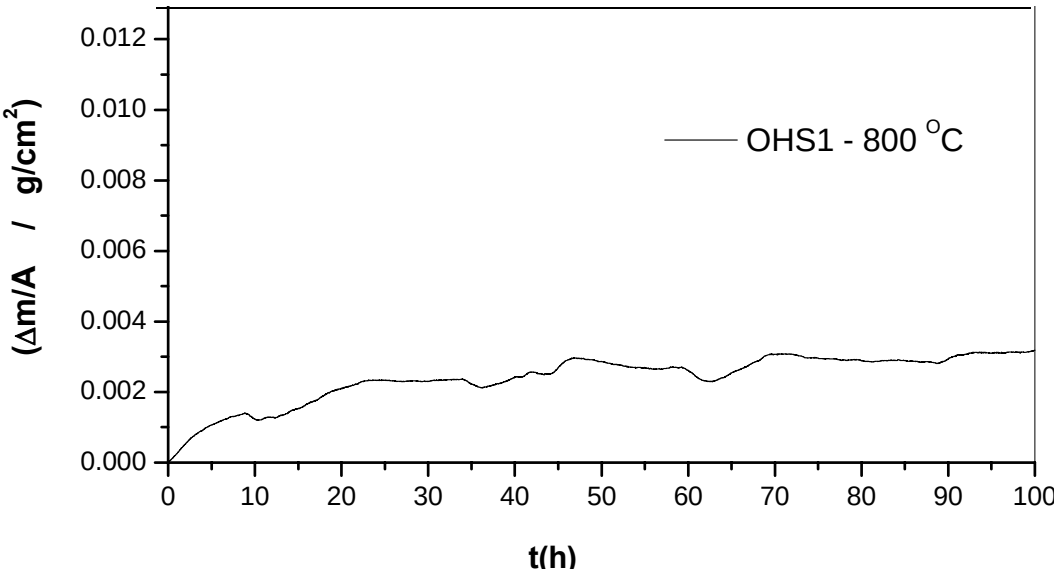

Figure 123. Isothermal oxidation TG plot of the alloy OHS1 in air at 800 °C for 100 h.

Microstructure of oxide scale

The specimen did no suffer from pest oxidation. Three main features were observed in the scale surface. A flat oxide with small round oxide particles mostly formed in the thick polishing marks, oxide whiskers, and bright lumps developed around the oxide whiskers (Figure 124). Figures 124a and b show the scale surface under SE and BSE imaging conditions, respectively. The oxide scale on top of the Nb_5Si_3 silicide was thin. However, the apparently adherent scale presented some buckling near the grain or phase boundaries (Figure 124b). The length of the oxide whiskers was ~ 10 µm.

The glancing angle XRD data indicated that the scale was composed of TiO_2 (JCPDS 21-1276), $TiNbO_4$ (JCPDS 81-911), $Nb_2O_5.GeO_2$ (JCPDS 19-0908), SiO_2 (JCPDS 39-1425), $CrNbO_4$ (JCPDS 81-909), $SnGeO_3$ (32-0413), $Ti_2Nb_{10}O_{29}$ (JCPDS 73-0242) and $TiNb_2O_7$ (JCPDS 77-1374) (Figure 125). The glancing angle XRD data included peaks that could be attributed to the substrate alloy, these were from the Nb_3Sn, and βNb_5Si_3 phases. The data also indicated that there were different titanium niobates formed as a result of the reaction of TiO_2 (rutile) with niobium oxides depending on their availability in different regions.

The X-ray elemental maps (figure 126), confirmed that the flat oxide had grown on top of the Nb_5Si_3 phase while the whiskers and the bright oxide lumps were formed over the area in-between the Nb_5Si_3 grains, which, as was discussed in section 6.2.1, consisted of the Nb_3Sn, $NbCr_2$ and the Nb_{ss}. The oxide grown on top of the Nb_5Si_3 phase presented Ge and Sn enrichment.

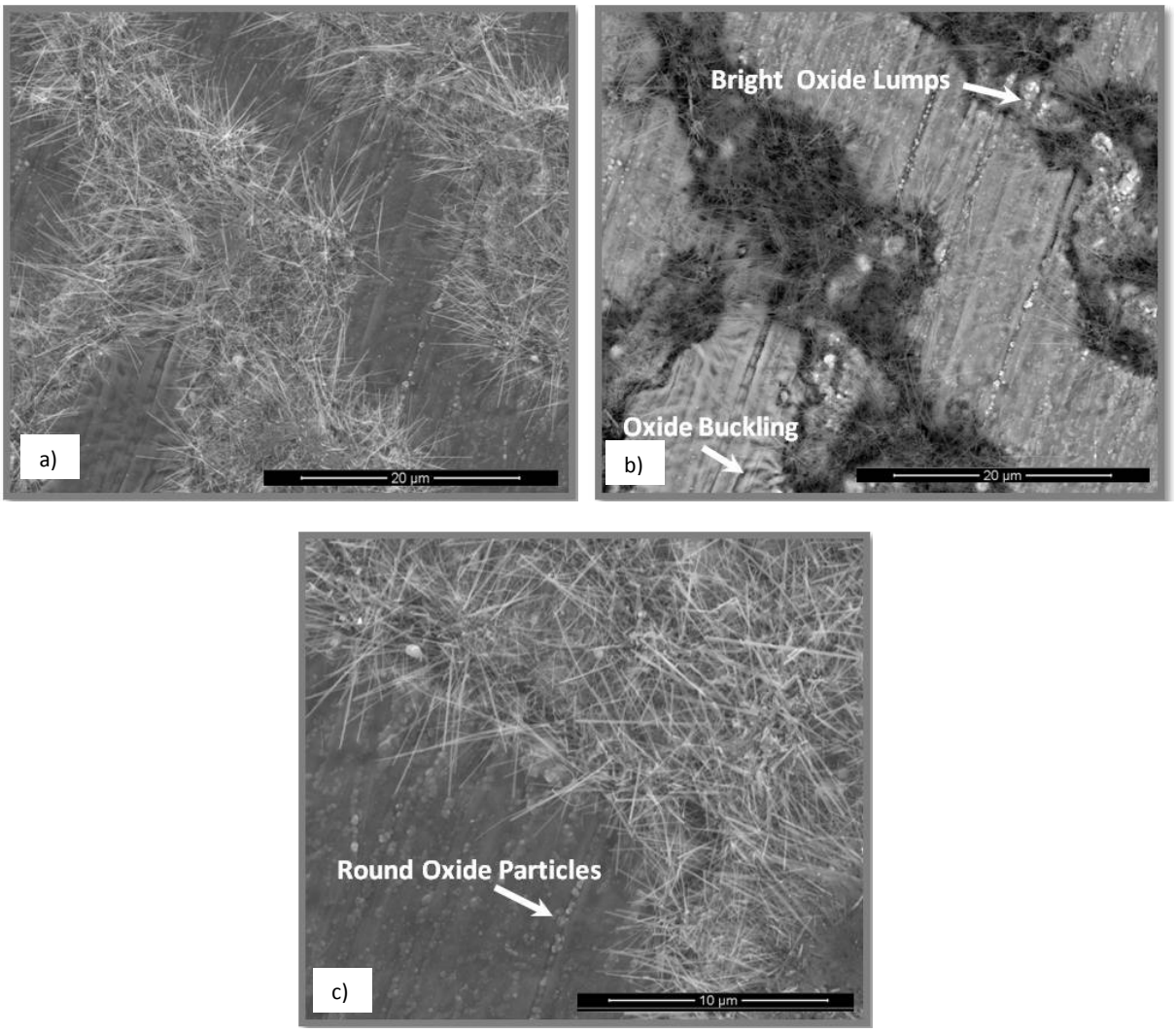

Figure 124. Images of OHS1 alloy after isothermal oxidation in air at 800 °C/100h images of oxide scale surface(a) SE image at X5000 (b) same region under BSE image at X5000 and (c) SE image at X10000.

The cross section images in figure 127 show a non homogeneous oxide scale, about 2-5 µm thick and an internal oxidation zone (IOZ) up to 3 µm deep. Some areas of the edge of the specimen presented large cracks parallel to the oxide surface suggesting embrittlement;

however this was rare in the specimen. The images also show that the scale had different microstructure depending on the oxidised phase.

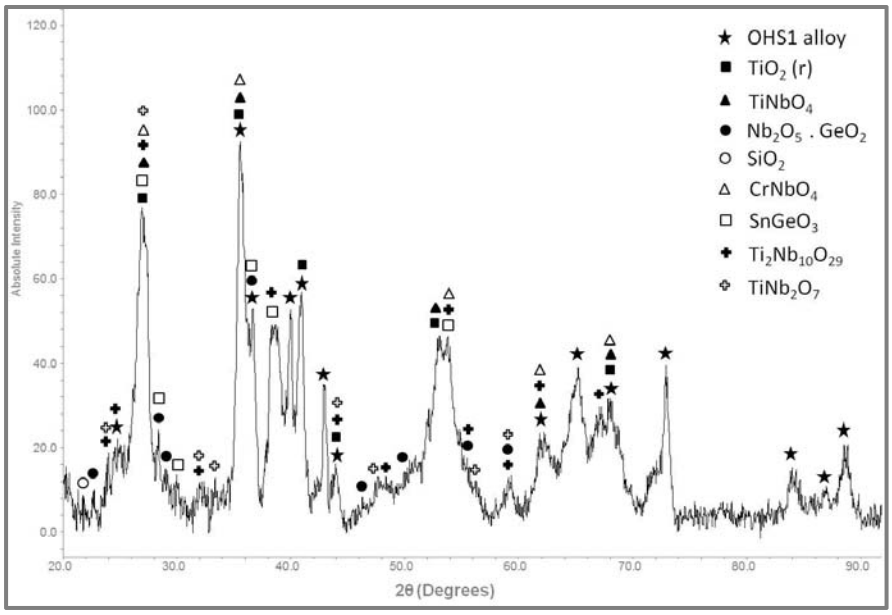

Figure 125. Glancing angle XRD data (γ= 2°) for the oxide scale formed on the alloy OHS1 at 800 C in air.

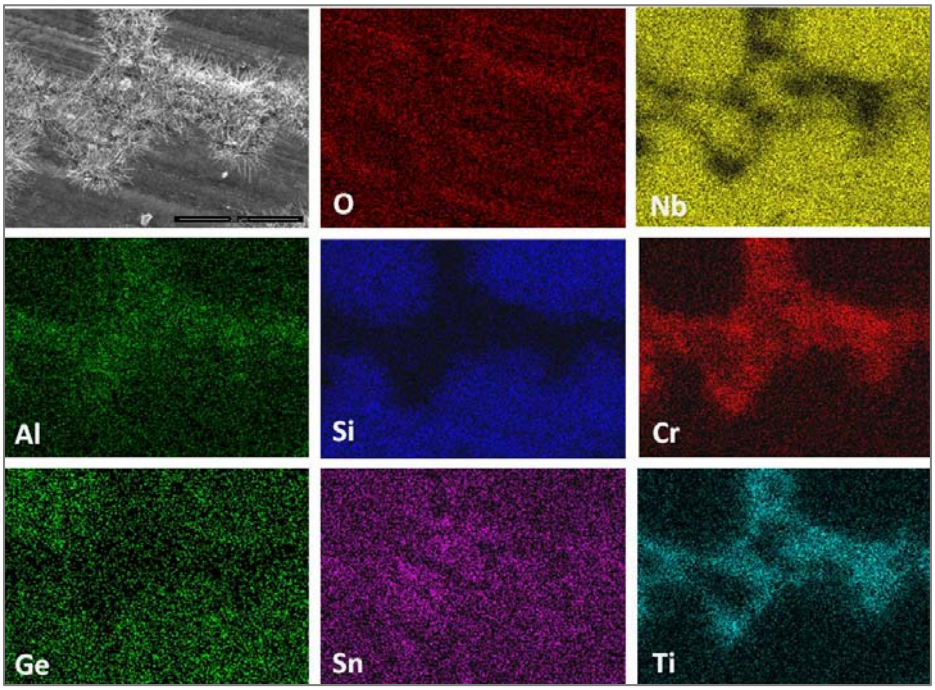

Figure 126. X-ray elemental maps from the oxide surface of the alloy OHS1 after isothermal oxidation in air at 800 °C, X6000.

The EDS analysis of the oxidised Ti-rich areas (composed of $(Nb,Ti)(Cr,Si,Al)_2$ and $(Nb,Ti,Cr)_{ss}$) was strongly affected by the oxidation of the Nb_3Sn, which was located in the same regions with higher volume fraction. Apparently, the crisscrossed oxide whiskers were grown from the Ti rich areas covering some oxide lumps. In the oxide scale, the intergranular areas also presented very particular microstructures. The Nb_5Si_3 presented a very compact oxide layer in the outermost part of its oxide scale (Figures 127 and 128). According to the chemical analysis it was rich in Ge and Sn suggesting that it could be the $GeSnO_3$ oxide whose presence was suggested by the XRD data, the inner part of the oxide scale in these areas was composed of SiO_2 and different $Ti_xNb_yO_z$ compounds, the Nb_2TiO_7 being the mostly detected. The XRD data and qualitative chemical analyses suggested the presence of the $Ti_2Nb_{10}O_{29}$ compound and the Nb content decreased towards the scale surface.

The EDS analyses confirmed that the Nb_3Sn had formed a complex oxide multilayer that consisted at least of three oxide layers; the outermost part contained TiO_2 whiskers and $(Ti,Sn)O_2$ lumps, then underneath there was a Ti, Cr and Al rich oxide layer, and just below another oxide layer that was mainly composed of $TiNbO_4$ oxide although some areas of this layer also contained some $CrNbO_4$, SiO_2 and perhaps some $AlNbO_4$ resulting from the oxidation of the Al containing Laves phase that was present in the vicinity (Figure 127b). The metal / scale interface was characterised by the internal oxidation of the Nb_3Sn and the formation of $(Sn,Ti)O_2$ precipitates. The average composition of these areas was 45O-27Nb-9Ti-10Sn-2Si-1Cr-4Al-2Ge. Just below the IOZ the composition of the Nb_3Sn was 44.6Nb-27.2Ti-9.7Sn-3Si-6.9Cr-6.6Al-2Ge.

The scale formed over the areas consisting of the Nb_{ss}, Laves phase and Nb_3Sn was mixed and composed of convoluted oxide, with a very irregular microstructure and dark contrast grain boundaries which would suggest that these areas served as the path for the diffusion of oxygen (Figure 127a and c). Around the darkened intergranular areas multiple microcracks were formed on the Nb_5Si_3 that were parallel to the oxide surface (Figure 127a and c).

In the IOZ the Nb_5Si_3 presented very small cracks parallel to the specimen surface. These cracked regions extended up to about 3 µm depth and the silicide was the Ti-rich Nb_5Si_3. The Nb_3Sn was depleted in Nb and Ti and presented some oxidation in the form of dark oxide particles dispersed within the phase indicating that its oxidation depended on a critical Ti concentration since the Ti–rich Nb_3Sn did not present oxygen penetration (Figure 127c). Oxygen could have diffused faster through the Nb_{ss} that was in the interdendritic areas since dark contrast particles were observed at different depths. The oxygen penetration depth was mostly associated to the extension of the cracked Nb_5Si_3 regions, the latter by the stresses generated by the oxide formation within the Nb_{ss}. The Cr_2Nb Laves phase in the IOZ seemed not to be oxidised.

The X-ray elemental maps in figure 128, show that the oxygen was mostly found in the scale, and that there was a small oxygen content in the areas of internal oxidation. The surface of the scale formed on top of the Nb_5Si_3 phase was enriched in Ge and Sn in the outermost part which is consistent with the high Ge and Sn contents observed in the elemental maps in figure 126. Towards the inner part of the scale the main components were the O, Nb and Ti from titanium niobates. The oxide scale formed on top of the Nb_5Si_3 was rich in Si.

The maps also show that the oxide formed on top of the three phase region was rich in Ti and O. In these areas the whiskers formed. The oxide below the oxide whiskers was rich in Cr, Al and Ti, following an oxide layer rich in O, Nb and Ti with minimal contribution of Ge (Figure 128). The Nb_3Sn phase at the metal / scale interface was richer in Sn compared with the rest of the alloy.

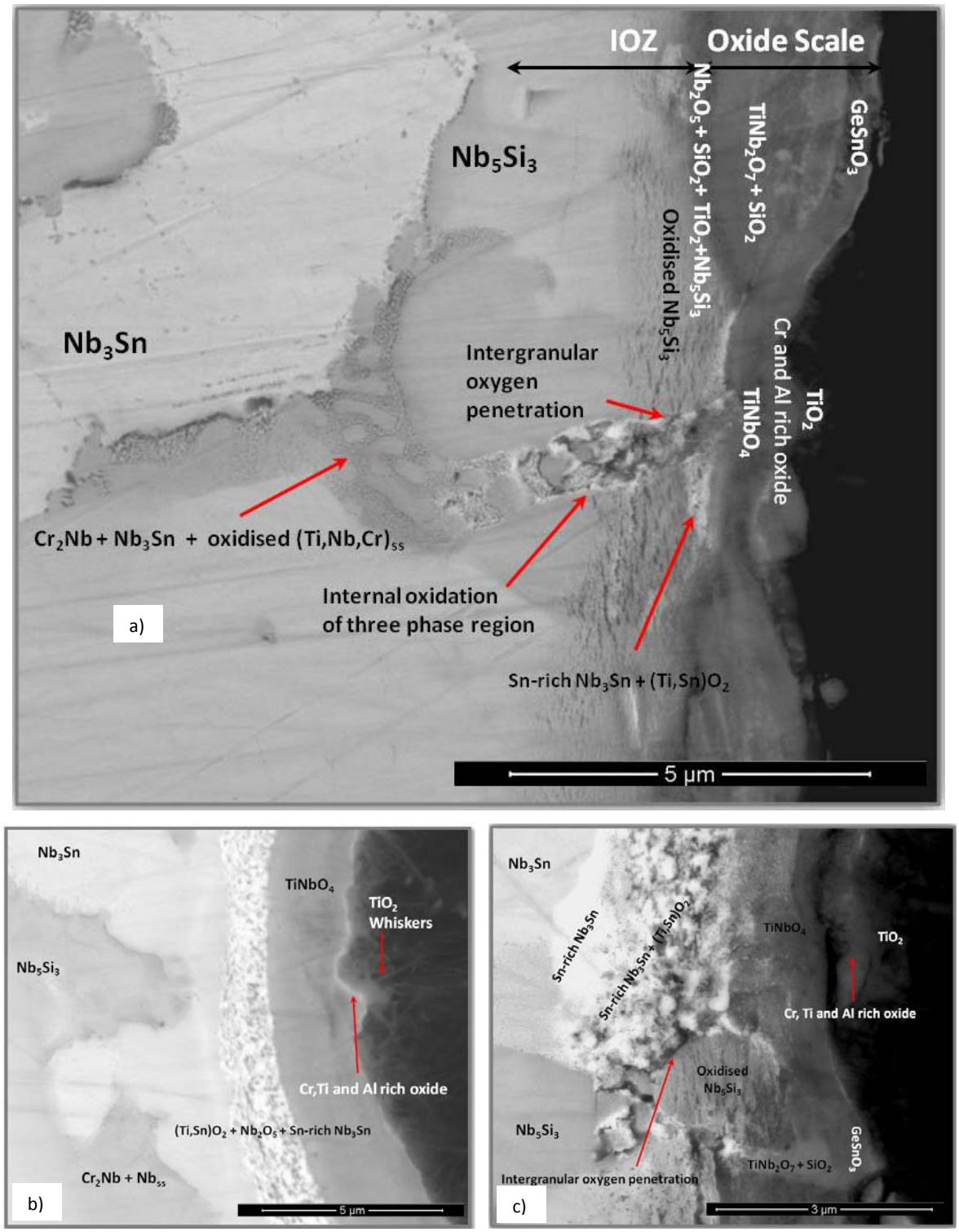

Figure 127. BSE images of a cross section of the alloy OHS1 after isothermal oxidation at 800 °C a) , the microstructure of the substrate alloy and oxide scale, X20000, b) microstructure of the scale formed on top of the Nb_3Sn phase, X20000 and c) microstructure of the three phase region after oxidation, X40000.

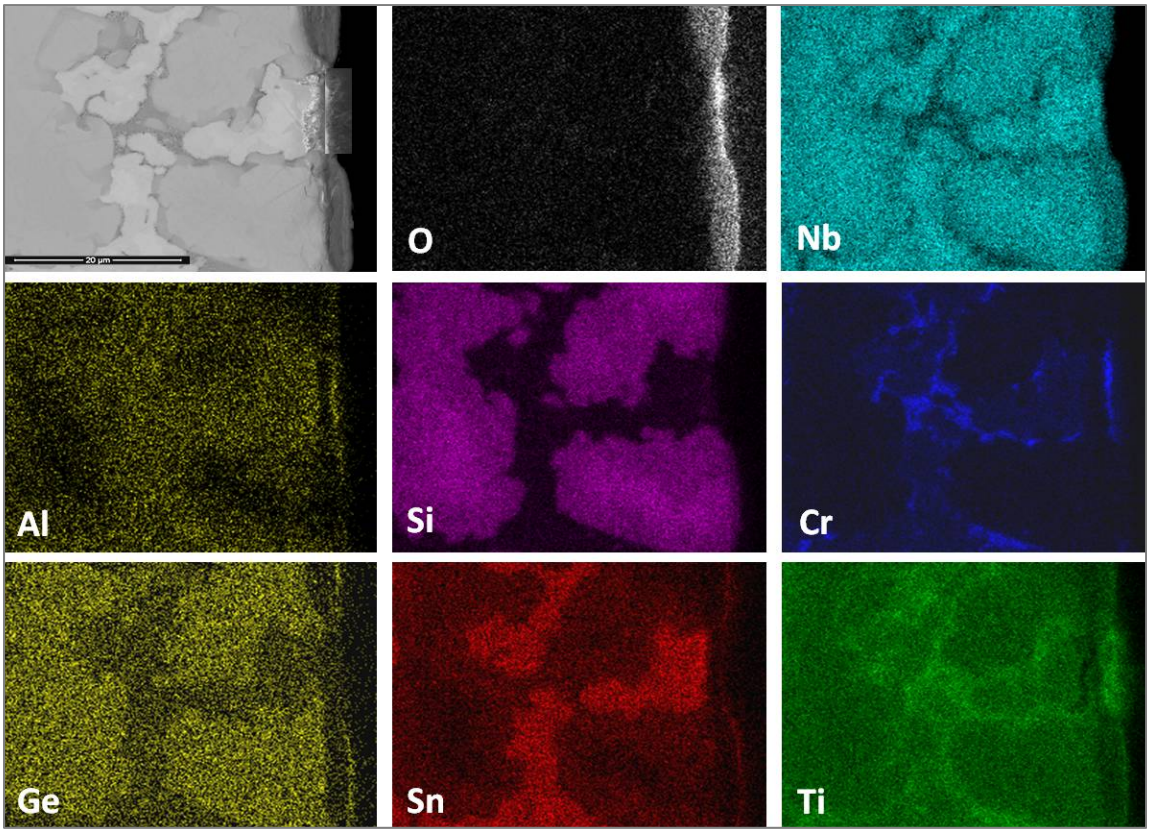

Figure 128. X-ray elemental maps and BSE image from a cross section of the alloy OHS1 after isothermal oxidation in air at 800 °C, X6000.

6.2.2.3 Thermo-gravimetric analysis (TGA) at 1200 °C

Figure 129 shows the isothermal oxidation data and clearly demonstrates that the oxidation was linear. However, there were two stages of oxidation, an initial parabolic stage that lasted 3.1 h followed by a linear stage to the end of the experiment. The weight gain after 76.7 h was 31.28 mg/cm^2.

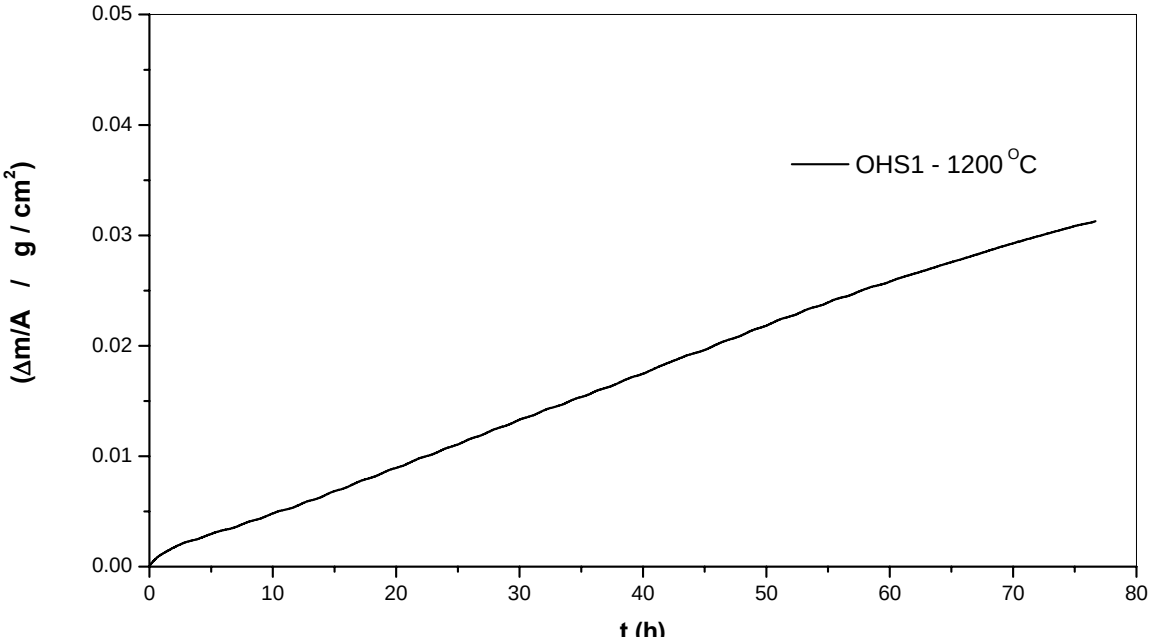

Figure 129. Isothermal oxidation TG plot of the alloy OHS1 in air at 1200 °C for 76.7 h.

Microstructure of the oxide scale

After the isothermal oxidation in air at 1200 °C, the cubic specimen did not present scale spallation instead it was covered by a light brown oxide scale with well defined edges and some long cracks in the scale. Typical images of the surface of the scale are shown in figure 130. The SE image (Figure 130a) shows a continuous and bulged scale with some small cracks. The images in figures 130b and c, show the surface at higher magnification and it is possible to observe particles with different morphology and some porosity. Different oxides had formed the scale as shown by the BSE imaging (Figure 130c). Based on their contrast, these were coarse and bright oxide particles, small and dense grey oxide particles and grey rods that protruded.

The glancing angle XRD data in figure 131 indicated that the oxide scale formed at 1200 °C was complex and consisted of binary and ternary oxides, among these TiO_2 (JCPDS 21-1276), SiO_2 (JCPDS 39-1425),$Ti_2Nb_{10}O_{29}$ (JCPDS 73-0242), $TiNb_2O_7$ (JCPDS 77-1374), rutile type $TiNbO_4$ (JCPDS 81-911) and $AlNbO_4$ (JCPDS 41-0347), Nb_2O_5 (JCPDS 28-0317), Al_2O_3 (JCPDS 70-3319). The XRD data was compared with EDS data taken from the oxidised specimen and the agreement was good. It is likely that some phases at the metal scale interface and in the IOZ

were undetected because of the thick scale. The highest selected glancing angle was sufficient to detect phases to 200 µm depth.

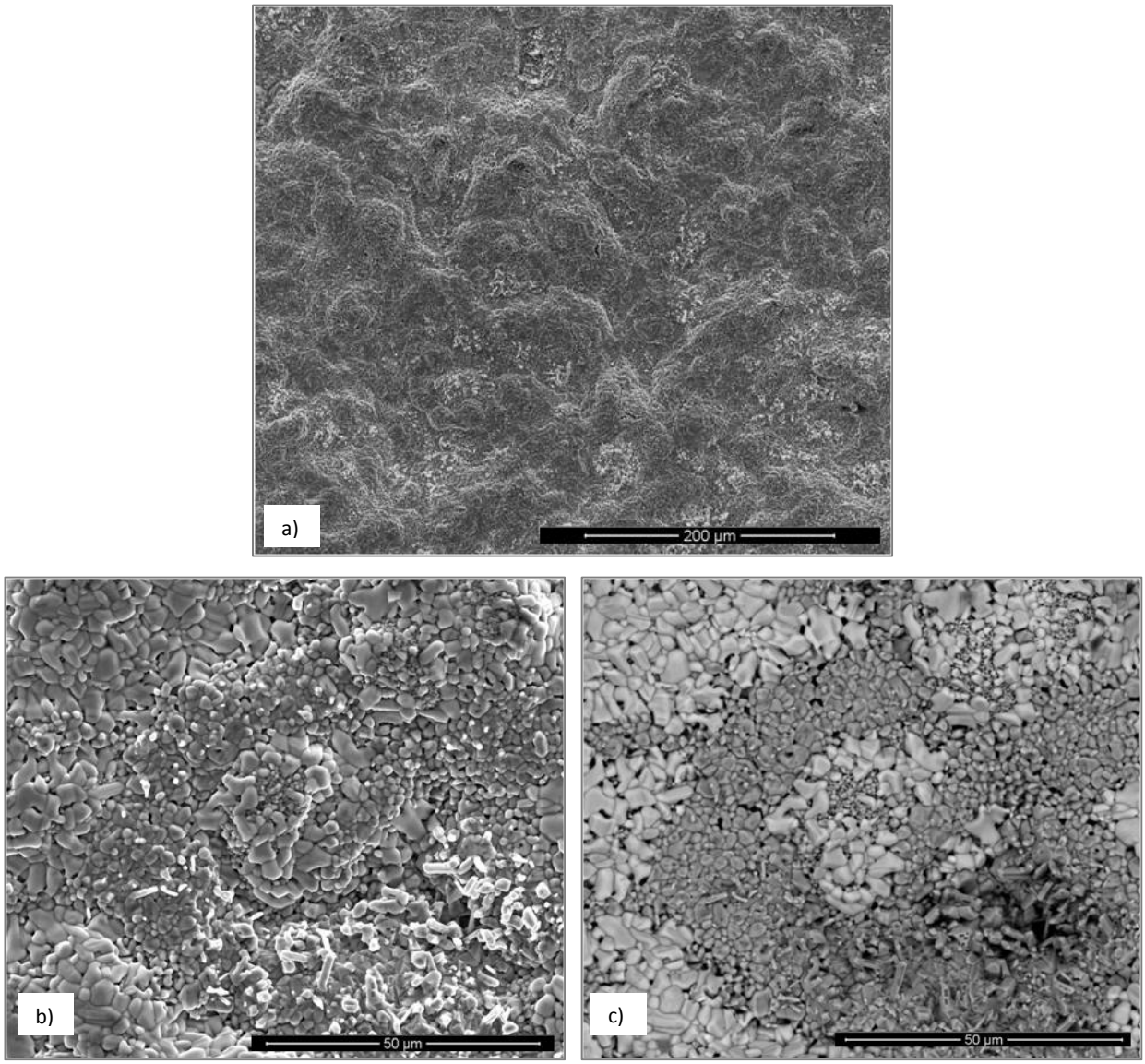

Figure 130. Images of the surface of the scale formed on the alloy OHS1 after isothermal oxidation in air at 1200 °C(a) SE, X500, (b) SE, X2500 and (c) BSE, X2500.

The X-ray elemental maps in figure 132, show an uneven elemental distribution on the oxide surface that would by expected for a multiphase scale determined by GAXRD. There was no Ge in the scale surface even though the alloy was expected to form GeO_2. It is also observed that the oxidation of the three phase areas (Cr_2Nb, Nb_{ss} and Nb_3Sn) showed a high presence of Cr, Ti, Al and Sn. The figure 132 also shows TiO_2 in the form of coarse whiskers or rods observed on

top of the three phase region where we can also observe Nb, Cr, Al and Sn. However, the latter could be from oxides formed right below the oxide rods, as it was observed in the scale formed at 800 °C.

There were Nb oxides formed on top of the Nb_5Si_3 with low Si on the surface of the oxide. There was high Nb content in all the oxides observed in the surface but the Nb concentration decreased when the oxides were rich in Ti, Cr, Al and Sn.

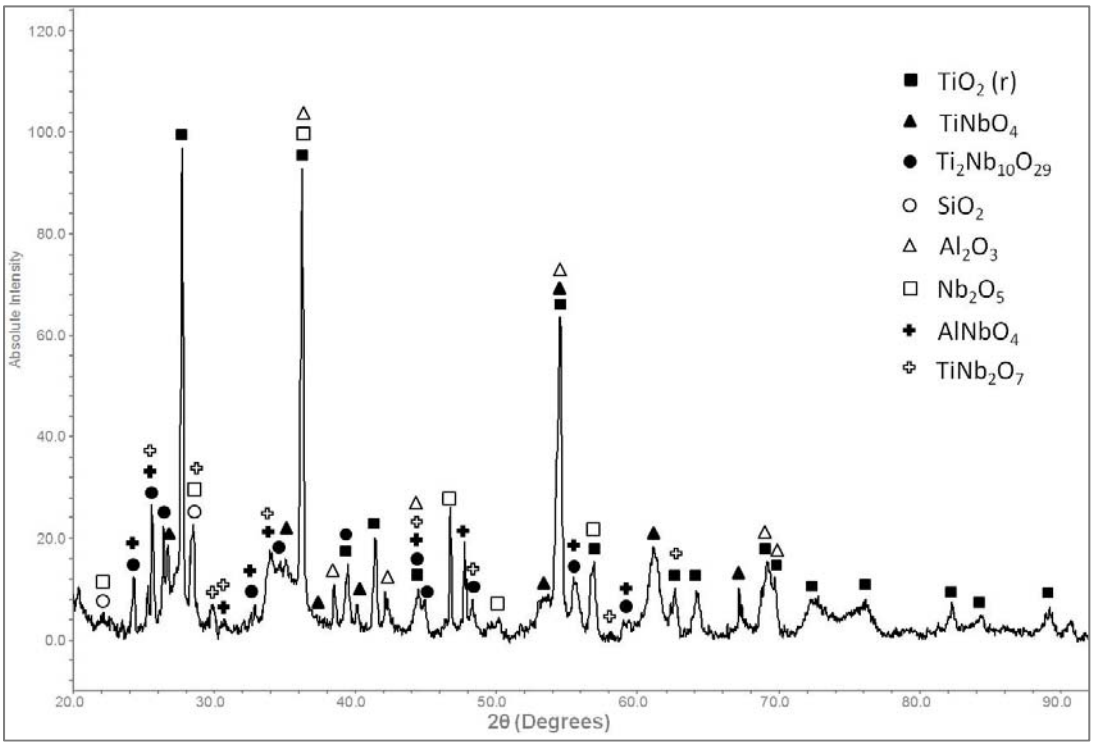

Figure 131. Glancing angle XRD data ($\gamma = 10°$) for the oxide scale formed on the alloy OHS1 at 1200 °C in air.

The X- ray elemental maps from a cross section of the specimen are shown in figure 133 and show the elemental distribution in the oxide scale, the diffusion zone (DZ) and the substrate after isothermal oxidation at 1200 °C. The diffusion zone (DZ) includes the internal oxidation zone (IOZ). We shall refer to IOZ only when talking about regions where the oxygen or nitrogen were present below the oxide scale otherwise the term DZ will be used.

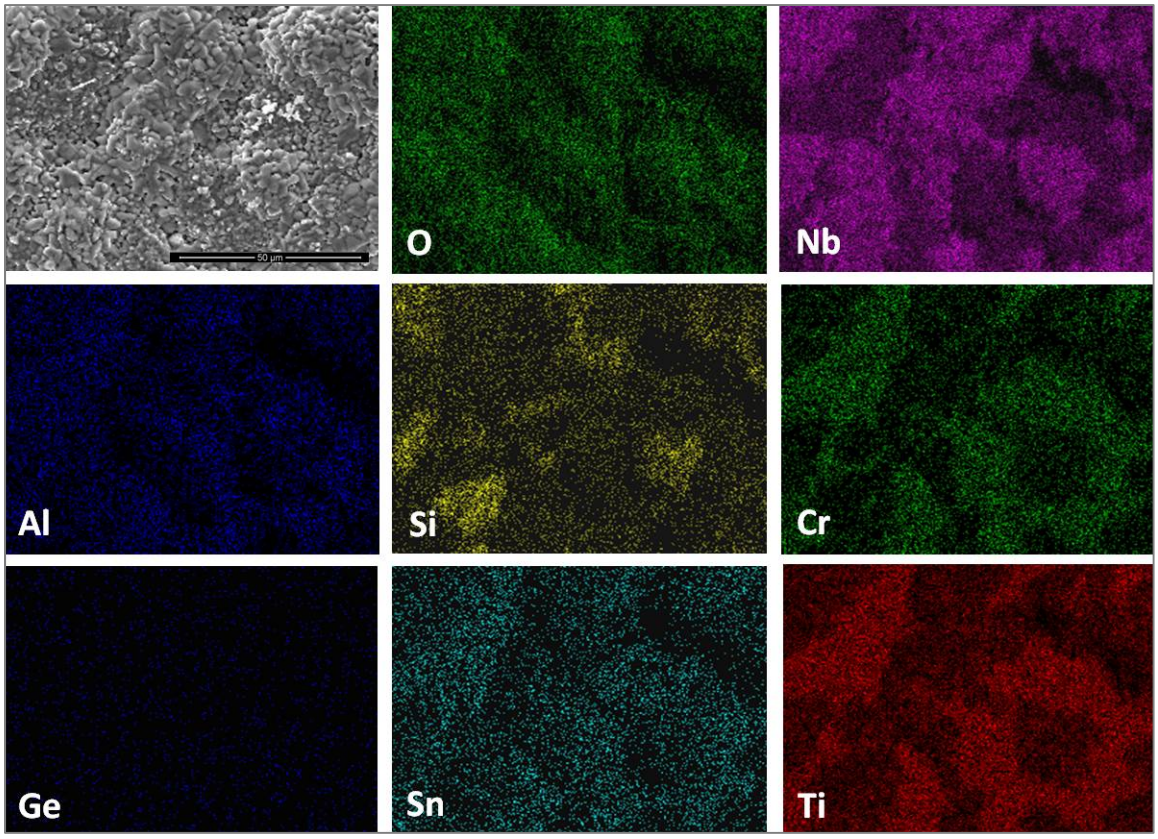

Figure 132. X-ray elemental maps from the oxide surface of the alloy OHS1 after isothermal oxidation in air at 1200 °C, X2500.

From the GAXRD data the oxide scale was expected to be complex. The figure 133 shows a high Nb, Si and Ti presence in the oxide scale. The Nb was mostly found in the $Ti_2Nb_{10}O_{29}$ and $(Cr,Ti)NbO_4$ phases, in agreement with the GAXRD data. Low Nb content regions near the scale / metal interface were rich in TiO_2 or SiO_2 oxides. Cr was found mostly dissolved in the $TiNbO_4$ phase with higher content at the oxide scale surface. The IOZ was depleted in Cr. There was Si present all over the oxide scale, in a glassy structure as SiO_2 and dissolved in the rutile type $(Ti,Cr)NbO_4$ oxide. The Al content was practically the same in most of the oxide scale and in the substrate, but in some parts of the scale the $AlNbO_4$, $(Ti,Cr,Al)NbO_4$ and Al_2O_3 around Ti-rich oxides presented a higher Al content. The oxide scale did not contain Ge but had some Sn in it and the IOZ presented a considerable enrichment of these two elements particularly Sn with a considerable reduction of Cr and Ti contents in these areas.

EDS analyses revealed that the Ge and Sn rich regions at the IOZ were the Nb_5Ge_3, Nb_6Sn_5 and Nb_5Si_2Sn phases although these were not recorded in the GAXRD experiments. These intermetallics were found in areas with strong segregation of Si and Sn. The composition of the Nb_6Si_5 was Nb-33.0Ti-0.3Si-2.5Cr-3.1Al-1.8Ge-41.5Sn. The Nb_5Si_2Sn had fixed values for Nb and Ti and its composition was Nb-20Ti-(11.6-17.9)Si-(2.6-3.4)Cr-(1.5-3.3)Al-(5.4-6.3)Ge-(11.8-18.1)Sn. The Nb_5Ge_3 presented a wide solubility range for Ti Si, Ge and Al. When its Ge content was 24.3 at. % Ge the Ti, Si and Al contents decreased to 11.3,13.4 and 0.2at. %, respectively and the Nb concentration was 45.8 at. % Nb. When the Ge content was 13.5 at. % Ge, the Ti, Si and Al concentrations were 34.1, 16.0 and 2.2 at. %, respectively and the Nb content was 29.1 at. %Nb.

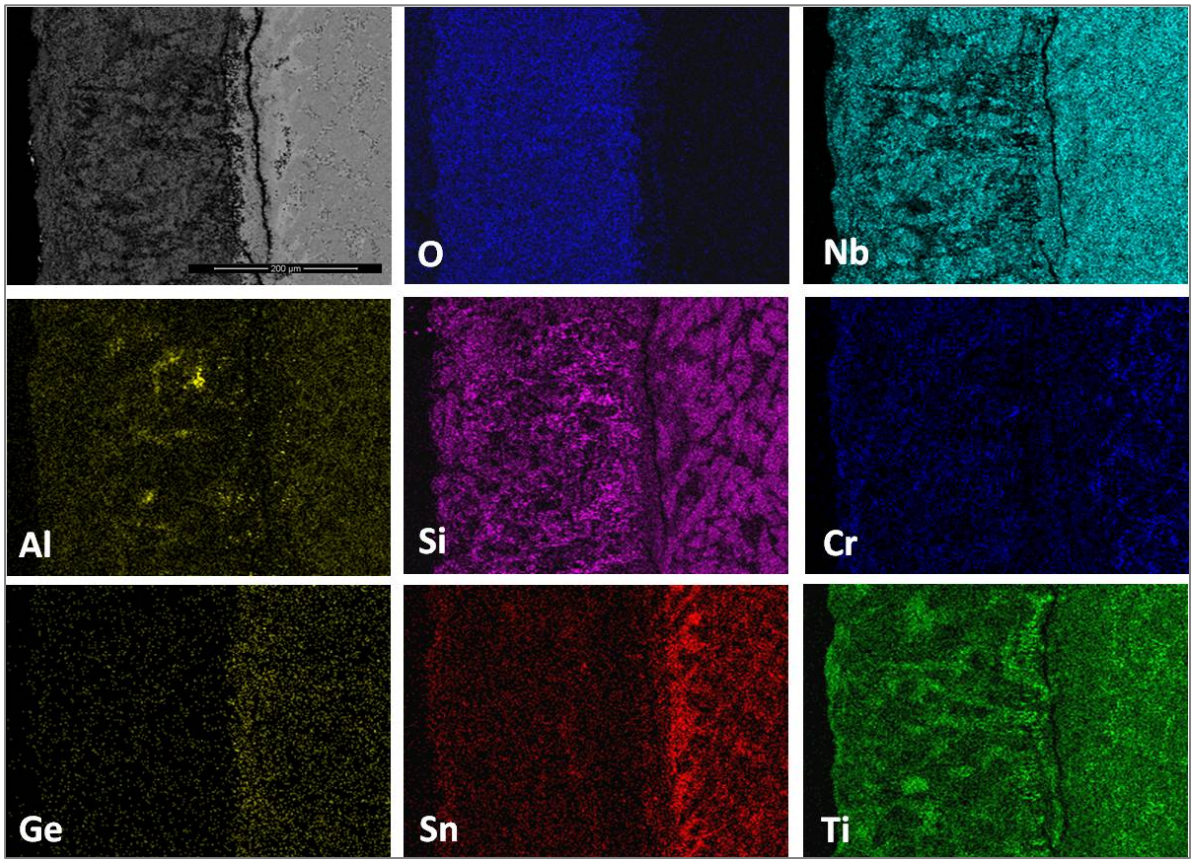

Figure 133. X-ray elemental maps and BSE image from a cross section of the alloy OHS1 after isothermal oxidation in air at 1200 °C, X400.

The cross section images in figure 134 show a very complex oxide scale formed after the isothermal oxidation at 1200 °C. The oxide scale thickness was ~ 300 µm, with ~150 µm of diffusion zone (DZ) in which the IOZ was ~ 100 µm.

According to the SE image (Figure 134a) the oxide scale had porosity, voids and cracks. The cracks were perpendicular to the surface and extended from the top of the scale up to about 100 µm deep into the scale. There were also extended cracks parallel to the oxide scale surface but these were mostly found at the metal/scale interface affecting the scale adherence. In the corners and regions near the corners of the specimen the oxide scale presented better adherence with no cracks. When the image in figure 134a is compared with the same area under BSE imaging conditions in figure 134b the data is consistent with the GAXRD data. There were at least three main contrasts related to the oxidation of the Nb_5Si_3 phase in the oxide scale and according to the EDS chemical analyses SiO_2 (black contrast), $Ti_2Nb_{10}O_{29}$ (bright contrast) and $TiNbO_4$ oxide (dark grey contrast). Particularly, the $TiNbO_4$ showed solubility for other elements; it contained Cr from 2.1 to 5.05 at.% Cr and Al from 1.85 to 4.58 at.%Al, while the $Ti_2Nb_{10}O_{29}$ showed some Si solubility, however this could have been from its close proximity to SiO_2. The oxidation of the Ti rich areas presented Ti-rich oxides, and oxides with the rutile type crystal structure. The Al_2O_3, SiO_2 and TiO_2 oxides were also detected. They were dispersed in some regions within the oxide scale and did not form a continuous scale. The internal oxidation of the alloy was observed along the grain boundaries of the Ti-rich areas.

The numbered BSE images in figure 134 show the scale microstructure in more detail. The phases were identified with EDS chemical analysis and were labelled accordingly. Images numbered from 1 to 6 correspond only to the oxide scale while images from 7 to 11 correspond to the DZ. The image 12 is from an area in the bulk of the alloy and shows that the core of the alloy was not oxidised.

The compositions of the phases in the bulk of the alloy after oxidation at 1200 °C were: Nb-22.8Ti-21.8Si-1.7Cr-4.4Al-6.9Ge-3.3Sn for the Nb_5Si_3, Nb-20Ti-21.8Si-2Cr-5.5Al-7.8Ge-3.2Sn for the Ti-rich Nb_5Si_3, Nb-21.3Ti-1.8Si-4.4Cr-8.4Al-1.9Ge-10.8Sn for the Nb_3Sn, Nb-58.7Ti-7.8Si-

12.1Cr-5.6Al-4.1Ge-1.6Sn for the solid solution, and the Laves phase was Nb-11.6Ti-8.1Si-47.5Cr-4.0Al-1.8Ge.

The figure 135 shows the elemental distribution in the selected area in figure 134b (within the yellow rectangle). The maps revealed that Ti_xN_y and TiO_2 formed close to each other at the metal/scale interface. Apparently, Al_2O_3, SiO_2 and TiO_2 were around the Ti_xN_y compound.

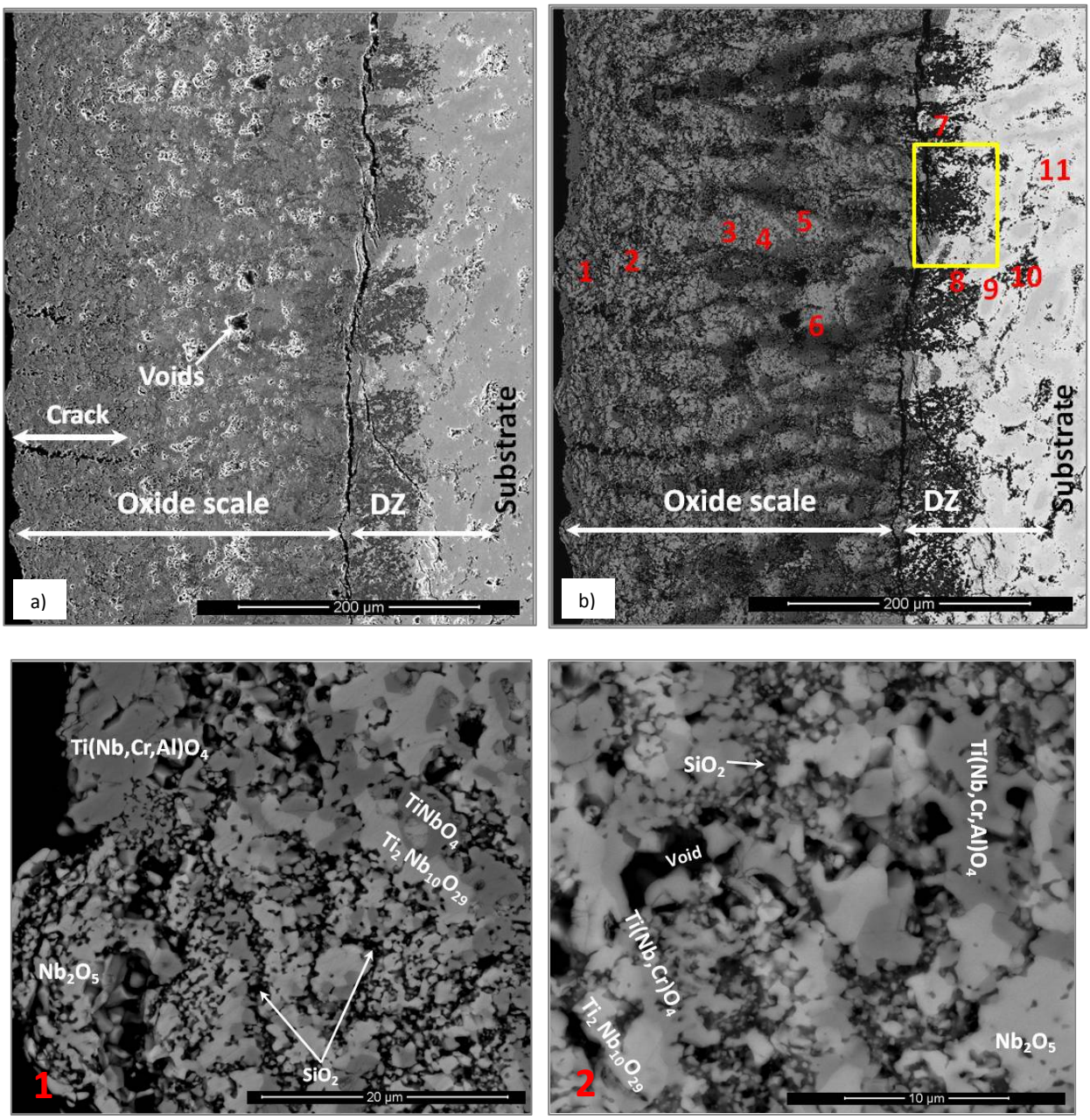

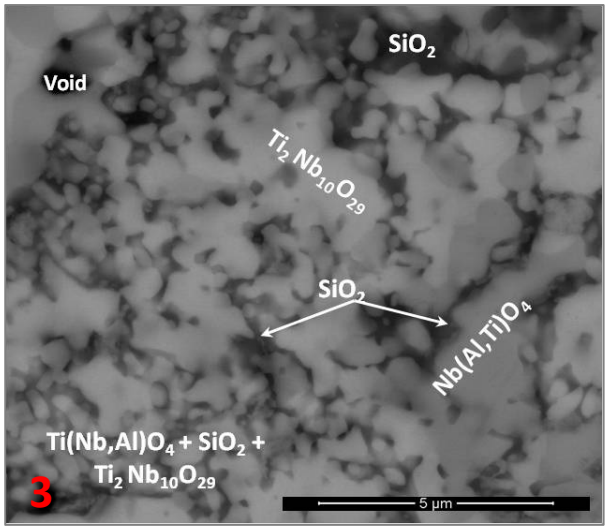
Void
SiO_2
$Ti_2Nb_{10}O_{29}$
SiO_2
$Nb(Al,Ti)O_4$
$Ti(Nb,Al)O_4 + SiO_2 +$
$Ti_2Nb_{10}O_{29}$
3
5 µm

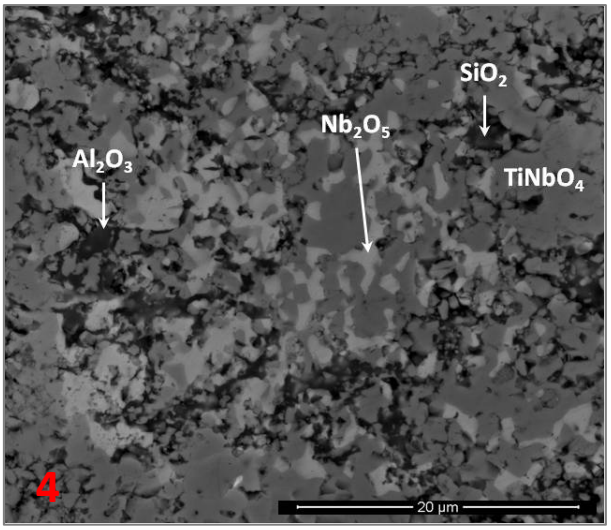
SiO_2
Nb_2O_5
Al_2O_3
$TiNbO_4$
4
20 µm

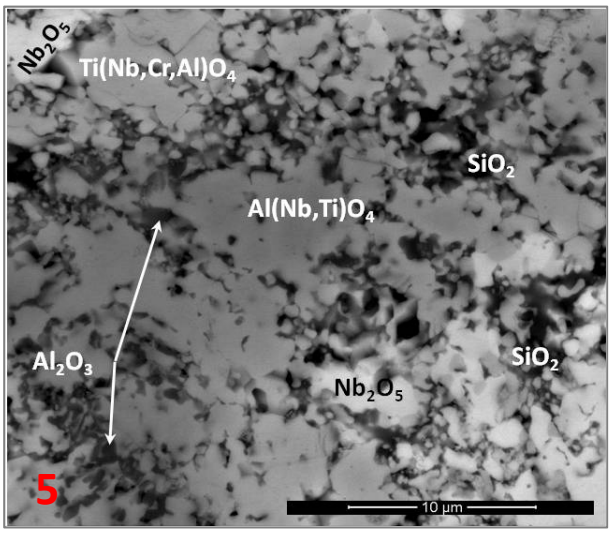
Nb_2O_5
$Ti(Nb,Cr,Al)O_4$
SiO_2
$Al(Nb,Ti)O_4$
Al_2O_3
SiO_2
Nb_2O_5
5
10 µm

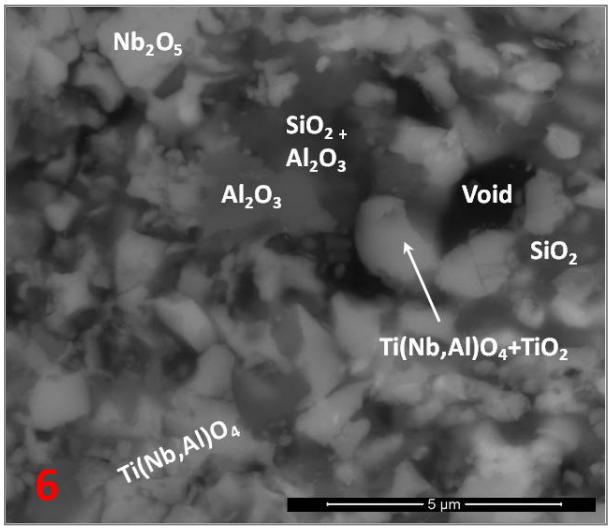
Nb_2O_5
$SiO_2 +$
Al_2O_3
Al_2O_3
Void
SiO_2
$Ti(Nb,Al)O_4+TiO_2$
$Ti(Nb,Al)O_4$
6
5 µm

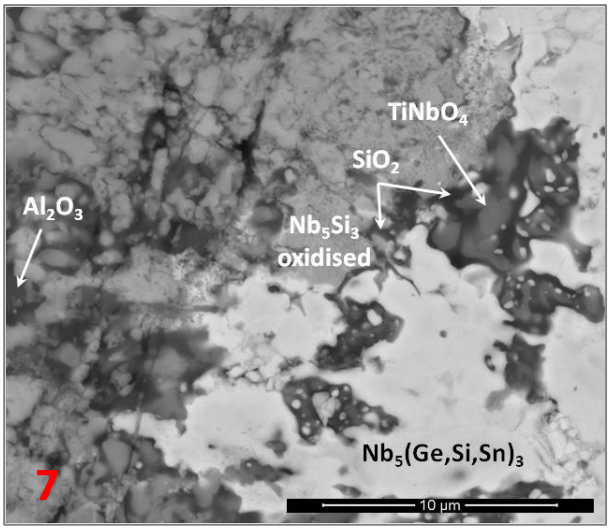
$TiNbO_4$
SiO_2
Al_2O_3
Nb_5Si_3
oxidised
$Nb_5(Ge,Si,Sn)_3$
7
10 µm

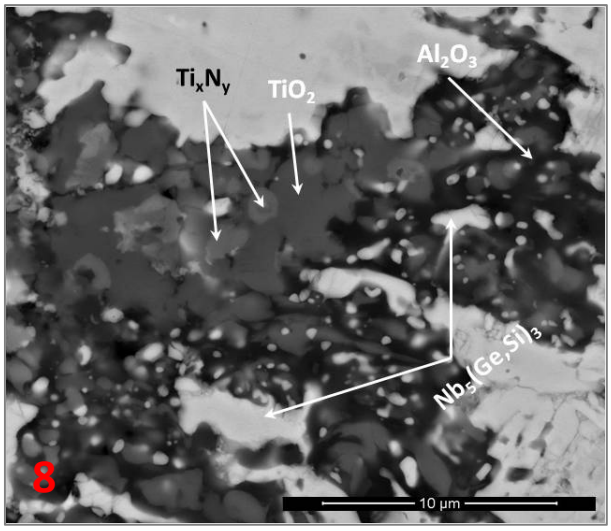
Ti_xN_y
TiO_2
Al_2O_3
$Nb_5(Ge,Si)_3$
8
10 µm

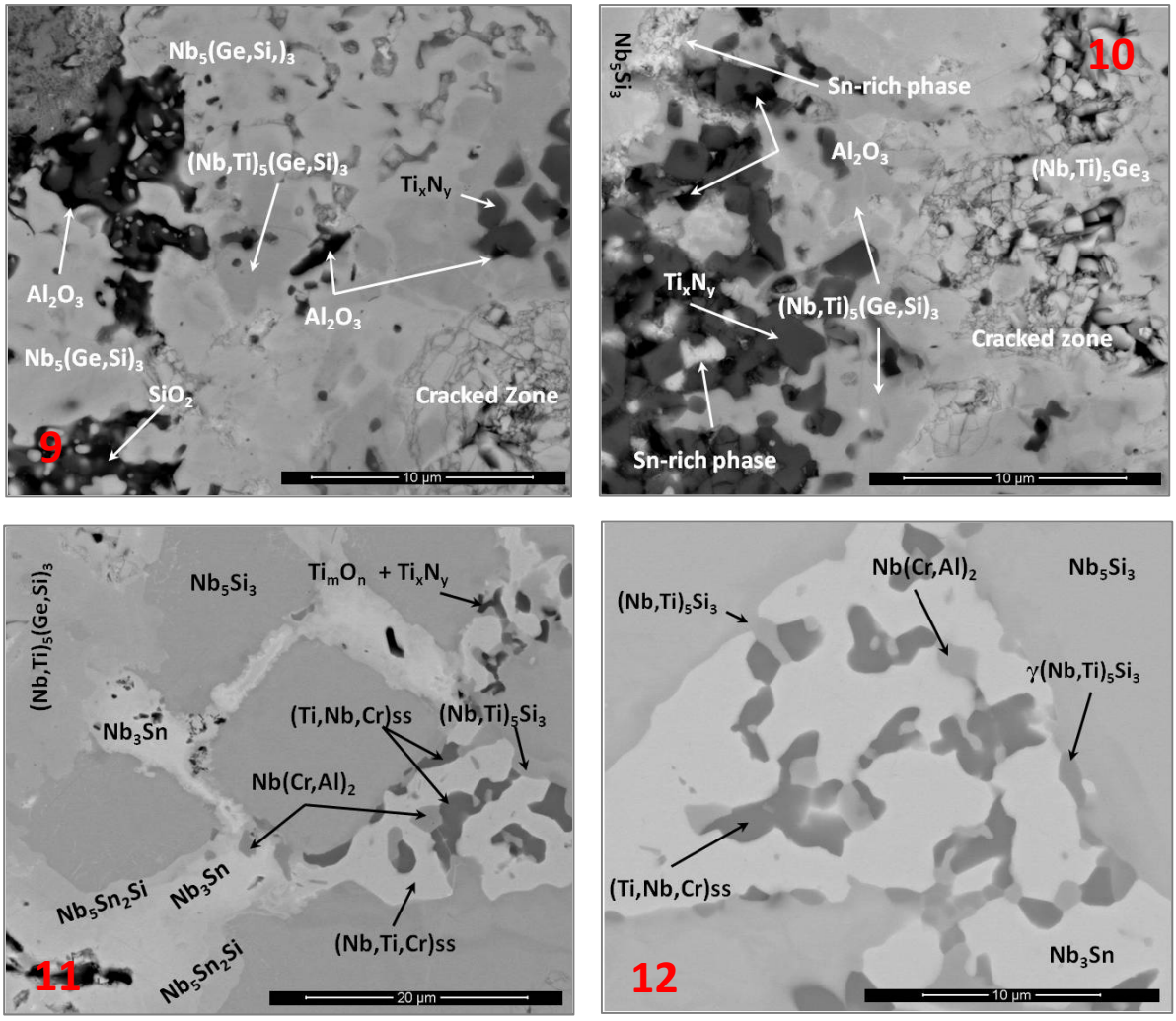

Figure 134. Cross section images of the alloy OHS1 after isothermal oxidation in air at 1200 °C, (a) SE, X500, (b) BSE, X500 the insert red numbers are related to the following BSE images, c) #1 Oxide Scale (OS), X6000, d) #2 OS, X8000 e) #3 OS, X20000, f) #4 OS, X6000, g) #5 OS, X8000, h) #6 OS, X20000, i) #7 Diffusion Zone (DZ), X10000,j) #8 DZ, X10000, k) #9 DZ, X1000, l) #10 DZ, X10000, m) #11 DZ, X5000, n) #12 inside of the alloy after oxidation. For yellow box in (b) see figure 134.

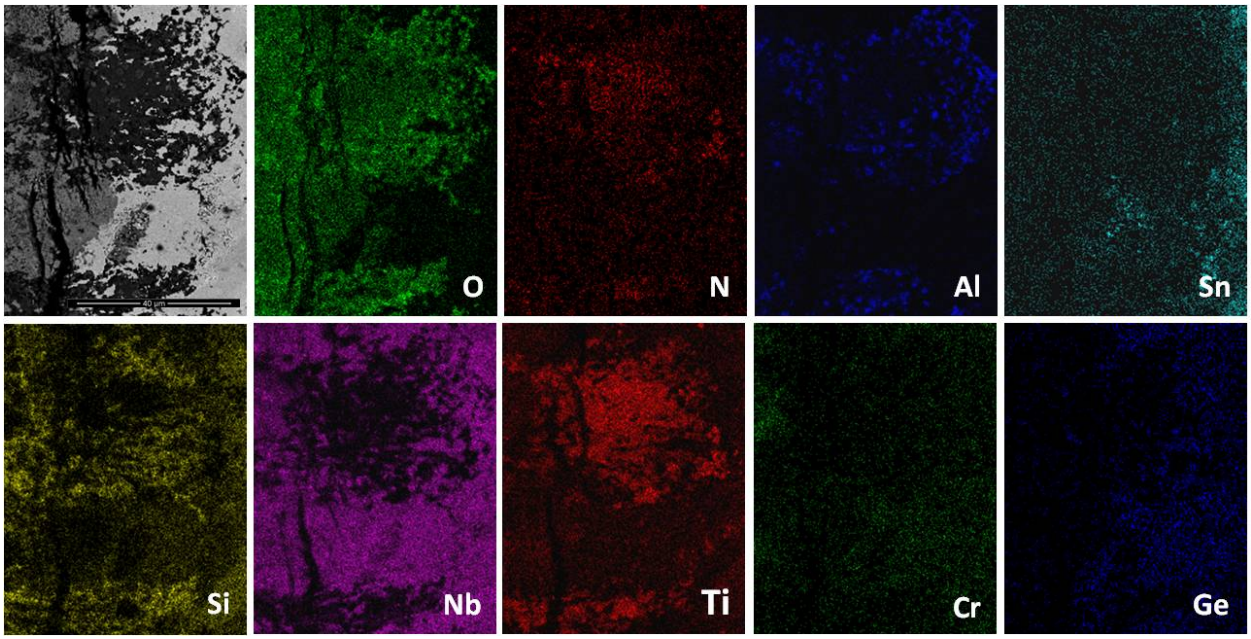

Figure 135. X-ray elemental maps from a cross section of the scale/ metal interface of the alloy OHS1 alloy after isothermal oxidation in air at 1200 °C, X3000. The selected area corresponds to the yellow box in figure 134b.

6.3 Discussion

6.3.1 Microstructure

In the alloy OHS1-AC there was strong macrosegregation of Si and Ti, and weak macrosegregation of Al, Cr and Sn. For Nb-silicide based alloys the "criterion" for macrosegregation of an element i has been defined as $C_{max}^{i} - C_{min}^{i}$, i.e., the difference between the maximum and minimum concentration of element i in the alloy. Macrosegregation of an element is considered to occur when MACS = $C_{max}^{i} - C_{min}^{i} > 2$ at% [Vellios and Tsakiropoulos (2010)].

Tsakiropoulos (2014a) discussed the macrosegregation of elements in cast Nb-silicide based alloys and linked the macrosegregation of Si with the partitioning of other solutes between the key phases in the microstructures of Nb-silicide based alloys, namely the Nb_{ss}, Nb_5Si_3, $NbCr_2$

Laves and the Nb_{ss} + Nb_5Si_3 eutectic. Tin and Ge are two of the alloying additions that have been found to have a strong effect on the macrosegregation of Si [Tsakiropoulos (2014a)].

Tsakiropoulos (2014a) studied the macrosegregation of Si in sixty nine Nb-silicide based alloys with different chemistries and microstructures (meaning not all alloys had the same phases and the same volume fractions of phases) using a number of material parameters in order to find trends for specific parameters. The ranking of alloys in terms of increasing Si macrosegregation indicated that the latter tended to increase in Nb-silicide based alloys when the parameters $\Delta H_m/T_m$ ("alloy entropy of fusion"), T_m^{sp} (melting temperature of sp electronic configuration elements) and $[\Delta H_m/T_m][\Delta H_m^{sd}/\Delta H_m^{sp}]^{-1}$ increased and the ratios $\Delta H_m^{sd}/\Delta H_m^{sp}$ and T_m^{sd}/T_m^{sp} and the parameters ΔH_m ("alloy enthalpy of melting"), T_m (alloy melting temperature) and T_m^{sd} (melting temperature of the sd electronic configuration elements) decreased.

In Table 26 the alloys KZ5, ZF6, OHS1 and ZX8 have been ranked according to their MACS values. The rational for using this data is as follows. The alloys (nominal compositions in at.%) KZ5 (Nb-18Si-24Ti-5Al-5Cr), ZF6 (Nb-18Si-24Ti-5Al-5Cr-5Ge), OHS1 (Nb-18Si-24Ti-5Al-5Cr-5Ge-5Sn) and ZX8 (Nb-18Si-24Ti-5Al-5Cr-5Sn) allow us to consider the effects of Ge and Sn added individually and simultaneously in the "basis" alloy KZ5. The data for the parameters given in the Table 26 was calculated using the actual compositions of the cast alloys from Zelenitsas (KZ5) [Zelenitsas (2005)], Zifu Li (ZF6) [Zifu Li (2012)] and Xu (ZX8) [Xu (2016)]. The data in Table 26 shows no obvious trends between the parameters mentioned in the previous paragraph, when all four alloys are considered. However, if only the data for the alloys KZ5, ZF6 and OHS1 were to be considered, then the "predicted" trends are clear (indicated by arrows) and "obeyed" by the alloys KZ5, ZF6 and OHS1, which means that the trend in MACS values is linked with synergies of alloying elements.

Table 26 Alloy parameters for the macrosegregation of Si in the cast alloys KZ5, ZF6, OHS1 and ZX8

Alloy	**ΔH_m (kJ/mol)**	**T_m (K)**	**$\Delta H_m/T_m$ (J/molK)**	**$\Delta H_m^{sd}/\Delta H_m^{sp}$**	**T_m^{sd} (K)**	**T_m^{sp} (K)**	**T_m^{sd}/T_m^{sp}**	**$[\Delta H_m/T_m] \times [\Delta H_m^{sd}/\Delta H_m^{sp}]^{-1}$**	**MACS (at.%)**
ZX8	26.9	2152	12.48	1.84	1794	358	5	6.78	10
OHS1	27.7 ↓	2090 ↓	13.25 ↑	1.37 ↓	1653 ↓	437 ↑	3.8 ↓	9.67 ↑	6.8
ZF6	27.7 ↓	2151 ↓	12.9 ↑	1.6 ↓	1752 ↓	399 ↑	4.4 ↓	7.56 ↑	4.3
KZ5	27.5 ↓	2239 ↓	12.28 ↑	2.05 ↓	1909 ↓	330 ↑	5.78 ↓	5.99 ↑	1.3

To gain some insight as to how Al and Cr affect the macrosegregation of Si when they are in synergy with Sn or Ge individually and simultaneously the data in the Tables 27 to 29 will be used.

In the Table 27 the alloys (nominal compositions) KZ7 (Nb-18Si-24Ti-5Al), ZF5 (Nb-18Si-24Ti-5Al-5Ge) and ZX6 (Nb-18Si-24Ti-5Al-5Sn) are compared with the alloy OHS1 and allow us to consider what the effects of Ge and Sn are when these are added individually and simultaneously in the "basis" alloy KZ7. The data for the parameters was calculated using the actual compositions of the cast alloys from Zelenitsas (KZ7) [Zelenitsas (2005)], Zifu Li (ZF5) [Zifu Li (2012)] and Xu (ZX6) [Xu (2016)]. The data in Table 27 shows that the aforementioned trends between the parameters are "obeyed", with the exception of the parameter ΔH_m. This would suggest (i) that Al in synergy with Ge and Sn individually increase the macrosegregation of Si, (ii) that Sn has a stronger effect than Ge and (iii) that their combined effect is enhanced when Al, Ge and Sn are present simultaneously in the alloy. What is then the role of Cr? To answer this question we need to consider the Table 28.

Table 27: Alloy parameters for the macrosegregation of Si in the cast alloys KZ7, ZF5, ZX6 and OHS1 considering the Al effect with Ge and Sn individually and simultaneously. Bold red numbers and arrows for strong trends, non-bold red numbers and arrow for weak trend.

Alloy	**ΔH_m (kJ/mol)**	**T_m (K)**	**$\Delta H_m/T_m$ (J/molK)**	**$\Delta H_m^{sd}/\Delta H_m^{sp}$**	**T_m^{sd} (K)**	**T_m^{sp} (K)**	**T_m^{sd}/T_m^{sp}**	**$[\Delta H_m/T_m] \times [\Delta H_m^{sd}/\Delta H_m^{sp}]^{-1}$**	**MACS (at%)**
OHS1	27.7	**2090** ↓	13.25 ↑	**1.37** ↓	**1653** ↓	**437** ↑	**3.8** ↓	**9.67** ↑	6.8
ZX6 (Al)	27.3	**2148** ↓	12.71	**1.69** ↓	**1765** ↓	**383** ↑	**4.61** ↓	**7.52** ↑	5.5
ZF5 (Al)	28	**2202** ↓	12.72	**1.72** ↓	**1820** ↓	**382** ↑	**4.76** ↓	**7.39** ↑	2.9
KZ7 (Al)	27.7	**2272** ↓	12.19	**2.15** ↓	**1948** ↓	**324** ↑	**5.78** ↓	**6** ↑	2.3

In the Table 28 the alloys (nominal compositions) KZ4 (Nb-18Si-24Ti-5Cr), ZF4 (Nb-18Si-24Ti-5Cr-5Ge) and ZX4 (Nb-18Si-24Ti-5Cr-5Sn) are compared with the alloy OHS1 and allow us to consider what the effects of Ge and Sn are when these elements are added individually and simultaneously in the "basis" alloy KZ4. The data for the parameters was calculated using the actual compositions of the cast alloys from Zelenitsas (KZ4) [Zelenitsas (2005)], Zifu Li (ZF4) [Zifu Li (2012] and Xu (ZX4) [Xu (2016)]. The data in Table 28 shows that the aforementioned trends between the parameters are "obeyed" for the alloys in which Ge or Sn are in synergy with Cr

individually (red numbers and arrows in the table). As was the case in the Table 27, the parameter ΔH_m does not follow the "predicted" trend.

The data in the Table 28 shows that the synergy of Cr with Sn has a stronger effect on (increases) the MACS of Si than that of Cr with Ge. Furthermore, when the data for the alloy OHS1 is considered, the values of its parameters are "minimum" or "maximum" in the trends established by the synergy of Cr with Ge or Sn individually in the alloys. Thus, Tables 27 and 28 confirm that, compared with Ge, Sn has a stronger effect on the MACS of Si when it is in synergy with Al or Cr individually and that the strong effect of the synergy of Sn with Cr can be "controlled" having Ge added in the alloy.

Thus, the alloying additions of Al, Cr, Ge and Sn in Nb-silicide based alloys are beneficial not only in terms of oxidation behaviour but also because they tend to reduce the macrosegregation of Si, see also Table 29.

Table 28: Alloy parameters for the macrosegregation of Si in the cast alloys KZ4, ZF4, ZX4 and OHS1 considering the Cr effect with Ge and Sn individually and simultaneously. Bold red numbers and arrows for strong trends excluding Sn + Ge synergy, minima in trend in ***bold italics*** and maxima in trend in non-bold italics.

Alloy	**ΔH_m (kJ/mol)**	**T_m (K)**	**$\Delta H_m/T_m$ (J/molK)**	**$\Delta H_m^{sd}/\Delta H_m^{sp}$**	**T_m^{sd} (K)**	**T_m^{sp} (K)**	**T_m^{sd}/T_m^{sp}**	**$[\Delta H_m/T_m] \times [\Delta H_m^{sd}/\Delta H_m^{sp}]^{-1}$**	**MACS (at%)**
ZX4 (Cr)	27.8	**2205** ↓	**12.63** ↑	**1.85** ↓	**1862** ↓	**342** ↑	**5.44** ↓	**6.85** ↑	7.3
OHS1	27.7	***2090***	*13.25*	***1.37***	***1653***	*437*	3.8	*9.67*	6.8
ZF4 (Cr)	28.4	**2254** ↓	**12.6** ↑	**1.9** ↓	**1917** ↓	**337** ↑	**5.7** ↓	**6.63** ↑	5.3
KZ4 (Cr)	28.2	**2335** ↓	**12.1** ↑	**2.44** ↓	**2060** ↓	**275** ↑	**7.5** ↓	**4.96** ↑	1.9

Table 29 Alloy parameters for the macrosegregation of Si in the cast alloys KZ5, ZX8 and OHS1. Minima in trend in ***bold italics*** and maxima in trend in non-bold italics.

Alloy	**ΔH_m (kJ/mol)**	**T_m (K)**	**$\Delta H_m/T_m$ (J/molK)**	**$\Delta H_m^{sd}/\Delta H_m^{sp}$**	**T_m^{sd} (K)**	**T_m^{sp} (K)**	**T_m^{sd}/T_m^{sp}**	**$[\Delta H_m/T_m] \times [\Delta H_m^{sd}/\Delta H_m^{sp}]^{-1}$**	**MACS (at%)**
ZX8	26.9	2152	12.48	1.84	1794	358	5	6.78	10
OHS1	*27.7*	***2090***	*13.25*	***1.37***	***1653***	*437*	***3.8***	*9.67*	6.8
KZ5	27.5	2239	12.28	2.05	1909	330	5.78	5.99	1.3

Niobium can form the A15 Nb_3Al, Nb_3Ge, Nb_3Sn and Nb_3Si (metastable) phases which have as prototype the Cr_3Si, and thus the above elements would be expected to stabilise the A15

structure. Vellios and Tsakiropoulos (2007a) showed that the Nb_3Sn was stable in cast Nb-silicide based alloys with 5 at.% Sn and this was confirmed by Xu (2016). In the alloys with up to 5 at.% Ge addition studied by Zifu Li (2012) and Tweddle (2014) an A15 phase was not observed.

Papadimitriou et al. (2015) showed that the Nb_5Ge_3 with prototype the W_5Si_3 (i.e., isomorphous with βNb_5Si_3) is stable at all temperatures while the Nb_5Ge_3 with prototype the Cr_5B_3 (i.e., isomoprhous with αNb_5Si_3) is mechanically unstable and thus not a stable phase in the Nb-Ge binary. The Nb_{ss} + βNb_5Si_3 eutectic is metastable in the Nb-Si binary and in binary alloys this eutectic is promoted by solidification at high cooling rates and/or high melt undercoolings (i.e., under RS conditions) while in ternary and higher order alloys it is also promoted by additions that can suppress the Nb_3Si. Sn and Ge are such additions, as is Al but not Cr when added in Nb-24Ti-18Si [Zelenitsas and Tsakiropoulos (2006b)]. Furthermore, when Al and Cr are present simultaneously in Nb-24Ti-18Si based alloy (e.g. alloy KZ5) the Nb_{ss} + βNb_5Si_3 is formed in the cast alloy instead of the Nb_{ss} + Nb_3Si eutectic. In the binary the Si content of the metastable eutectic was suggested to be about 20 at.% (though this value depends on which version of the Nb-Si binary phase diagram is used and could be lower) and in ternary and higher order alloys experimental work in our research group has shown that the Si + other simple element(s) (like Al, Sn, Ge) content of the eutectic is about 21 at.%. What happens when Ge and Sn are present simultaneously in the alloy? To the author's knowledge, the research on the alloy OHS1 presented in this thesis is the first study of Nb-silicide based allloys where Ge and Sn are simultaneously present in the alloy.

The microstructure of OHS1-AC would suggest that the primary phase was the βNb_5Si_3, which is also consistent with the higher melting temperature of this phase compared with the A15-Nb_3Sn, the Nb_{ss} and the C14 $NbCr_2$ Laves phase. As the βNb_5Si_3 formed the surrounding liquid became richer in Ti, Cr, Al and Sn and poor in Si and Ge. In the latter liquid formed the A15-Nb_3Sn, the Nb_{ss} and the C14 $NbCr_2$ Laves phase and the eutectic.

The architecture of the microstructures of the alloys KZ5, ZF6, ZX8 (see discussion above for the nominal compositions of these alloys) and OHS1 was the same in that it consisted of primary

βNb_5Si_3 with the other phases formed in-between the primary silicide grains. In the alloy KZ5 (no Ge and Sn) the other phases were Nb_{ss} halos and Nb_{ss} + βNb_5Si_3 eutectic, in ZF6 (Ge present) the Nb_{ss} and $NbCr_2$ Laves phase and in ZX8 (Sn present) the A15-Nb_3Sn and $NbCr_2$ Laves phase. This would suggest (i) that in OHS1 the solidification path of the interdendritic melt "was defined" by the synergy of Sn with the other alloying elements and (ii) that even though Ge partitioned to the 5-3 silicide it was not able to destabilise the βNb_5Si_3. In OHS1-AC the eutectic was too fine to be characterised, it was rich in Cr and its average Al+Ge+Si+Sn content was ~ 17.9 at. % but ~ 20 at. % when the highest analyses values are considered. On the basis of previous research it is suggested that in the eutectic in OHS1 the phases Nb_{ss} and βNb_5Si_3 participated, but because of its high Cr content and the evidence for the presence of $NbCr_2$ in the eutectic (see insert in figure 121b) it is suggested that the eutectic was a ternary one formed by the Nb_{ss}, βNb_5Si_3 and $NbCr_2$ Laves phase. Thus, it is suggested that the solidification path of OHS1-AC was $L \rightarrow L + \beta Nb_5Si_3 \rightarrow L + \beta Nb_5Si_3 + Nb_3Sn \rightarrow L + \beta Nb_5Si_3 + Nb_3Sn + Nb_{ss} \rightarrow L + \beta Nb_5Si_3 + Nb_3Sn + Nb_{ss} + NbCr_2 \rightarrow \beta Nb_5Si_3 + Nb_3Sn + Nb_{ss} + NbCr_2 + (Nb_{ss} + \beta Nb_5Si_3 + NbCr_2)_{eutectic}$.

The architecture of the microstructures of the heat treated alloys KZ5, ZF6, ZX8 (see discussion above for the nominal compositions of these alloys) and OHS1 was the same in that it consisted of 5-3 silicide grains with the "stable"phase(s) in-between the silicide grains. In the alloys KZ5 and ZF6 the other "stable" phase was the Nb_{ss}, in the ZX8 the A15-Nb_3Sn and the Nb_{ss} and in OHS1-HT the A15-Nb_3Sn and $NbCr_2$ Laves phase. In the heat treated alloys KZ7 (Nb-18Si-24Ti-5Al) and ZX8 the βNb_5Si_3 had transformed to αNb_5Si_3 but in the heat treated KZ5 both silicides were present and in ZF6-HT there was weak evidence (three XRD peaks) for αNb_5Si_3 though most of the XRD peaks corresponded to βNb_5Si_3, while in the Ge containing alloys studied by Tweddle the βNb_5Si_3 was stable after the heat treatment, as was the case for OHS1-HT. This would suggest that the synergy of Ge and Sn with the other elements could stabilise the $NbCr_2$ Laves phase (which is important for oxidation), and that in this the other alloying elements controlled the stability of the βNb_5Si_3, given that the latter did not transform to αNb_5Si_3, which is promoted by Sn.

6.3.2 Oxidation

Oxidation at 800 °C

The oxidation behaviour of Nb-silicide in-situ composites depends on the oxidation of the Nb_{ss} which is dramatically improved by elemental additions. In the alloy OHS1-AC the synergy of Sn and Ge reduced significantly the volume fraction of the Nb_{ss} which was not stable at 1400 °C. The specimen did not pest after oxidation at 800 °C. Additions of 5 at.% Sn are known to eliminate the pest oxidation in Nb-silicide in-situ composites [Geng and Tsakiropoulos (2007b) and (2007c)], and Ge has a similar beneficial effect [Jackson et al. (2005) and Zifu Li and Tsakiropoulos (2012)]. The synergy of Sn and Ge did not have an adverse effect on the oxidation of the alloy in the pest regime. In fact, the alloy followed parabolic oxidation with no partial disintegration but formation of an uneven scale consisting of a compact oxide on top of the Nb_5Si_3 phase, and whiskers and oxide lumps on top of the Ti-rich areas. The oxidation rate constant was $K_p = 2.4 \times 10^{-11}$ ($g^2.cm^{-4}.s^{-1}$) and the weight gained after 100 h was 3.19 mg/cm^2. The latter values were similar of those reported for the hypereutectic alloy Nb-24Ti-18Si-5Cr-5Al-2Mo (JG3-AC) [Geng et al. (2006b) and (2006c)] which contained the Nb_3Si phase, a much higher volume fraction of the Nb_{ss} than the alloy OHS1 and did not pest. Compared with the alloy Nb-24Ti-18Si-5Cr-5Al (KZ5) [Zelenitsas and Tsakiropoulos (2006a)] the additions of Ge and Sn improved the oxidation behaviour of OHS1 significantly.

The oxides of the scale were TiO_2, $TiNbO_4$, $CrNbO_4$, $Nb_2O_5.GeO_2$, SiO_2, $SnGeO_3$, $Ti_2Nb_{10}O_{29}$, Nb_2TiO_7. The XRD data did not confirm GeO_2 +SiO_2 formation. The oxide scale formed on top of the Nb_5Si_3 phase was thin and compact with some oxide buckling in areas of the surface that were above the microstructure between the βNb_5Si_3 grains (Figure 124) where thicker oxide was formed as observed in the cross section (Figure 127) where the Nb_5Si_3 presented microcracking. Scale buckling is produced by the rise of internal stresses in the oxides forming the scale. The growth of voluminous oxide particles could cause scale buckling and cracking of the Nb_5Si_3 near the metal/scale interface. The deeper oxygen penetration was found at the phase boundaries, and would suggest that they played a very important role in the inward transport of oxygen and the outward transport of reactants. The intergranular areas were rich

in Ti and were expected to react with oxygen. Brittle phases unable to cope with the fast rise of stresses induced by the growth of oxide particles crack for relief allowing further oxygen diffusion into the alloy. The high solubility of Ti, Cr, Si, Sn and Al in the Nb_{ss} and oxygen anion diffusion in the alloy would embrittle the solid solution. It was not possible to confirm this using hardness testing because the areas with Nb_{ss} were too small. Furthermore the inherent brittleness of the Laves and Nb_3Sn phases could also have contributed to cracking of the scale and could explain the cracks parallel to the oxide surface observed in some areas near to the metal / scale interface. Oxide transformations also change the growth rate of oxide, the growth of different oxides in some small areas could lead to stresses and crack formation particularly in the Nb_5Si_3 and Nb_3Sn phases. Keeping all the above in mind, it was encouraging to see that there was no oxide spallation or specimen disintegration. The TiO_2 whiskers seen in figure 124 could have formed as a result of the oxidation of the Nb_{ss} which was very rich in Ti [also observed by Menon et al. (2001)]. According to Kofstad and Kjöllesdal (1961) whiskers may form through a plastic flow mechanism caused from the growth of stresses in the oxide scale. Within the Nb_3Sn submicron $(Ti,Sn)O_2$ rutile type oxide particles were observed at the metal/scale interface. These features were also observed by Geng and Tsakiropoulos (2007b) in the alloy Nb-24Ti-18Si-5Cr-5Al-2Mo-5Hf-5Sn (JG6) alloy.

Oxidation at 1200 °C

The alloy OHS1 was not able to form a compact and continuous oxide scale at 1200 °C. The oxide scale did not detach from the specimens even though there was a macrocrack parallel to the metal / scale interface. Mixtures of multiphase oxides with abundant boundaries are permeable to oxygen. The oxide scale thickness was about 300 μm and the IOZ was about 100 μm deep. As discussed by Hurlen (1959) and Kofstad and Kjollesdal (1961), the oxidation resistance of Nb at high temperatures is strongly influenced by its oxygen solubility that could increase above saturation values under particular conditions. The starting microstructure of the oxidised specimen contained a low vol. % of the Nb_{ss} and in the latter the solute additions of Al, Cr, Ge, Sn and Ti were in solution. The oxidation of the Nb_{ss} depends on the concentration of these solutes [Menon et al. (2001)].

The n value was 0.83 which indicates that the oxidation of the alloy was linear. The oxidation behaviour was characterised by two oxidation mechanisms, in the first 3.1h the oxidation was parabolic with K_p= 4.9 x 10^{-10} ($g^2.cm^{-4}.s^{-1}$) and for the rest of the experiment was linear with K_l = 1.1 x 10^{-7}($g.cm^{-2}.s^{-1}$). Both values were slightly better that those reported for the alloy JG6, although Geng and Tsakiropoulos (2007b) and (2007c) reported the same two mechanisms. This indicates that the alloy was not able to sustain the growth of more protective oxides instead voluminous and less protective oxides formed that allowed further oxygen intake. In some areas of the scale surface a coarse and compact oxide with no Ge and Si content and composition 69.6O-14.29Ti-7.34Nb-4.58Cr-2.18Al-1.38Sn was detected. This composition could correspond to Ti(Nb,Cr,Al)O_4. This oxide was not continuous and was surrounded by different Ti niobates and SiO_2. There was Ge and Sn enrichment in the diffusion zone in the metal / scale interface where phases like Nb_5Ge_3 and Nb_5Sn_2Si formed. The latter was unoxidised and also observed by Geng and Tsakiropoulos (2007b) after oxidation at 1200 °C of the alloy JG6. The oxygen solubility in the Nb_5Ge_3 was as high as 15 at. % O and the oxidation products that surrounded this phase were TiO_2 and SiO_2 oxides. The Ge and Sn enrichment at the metal / scale interface had reduced the concentration of Cr and Ti at the metal/ scale interface.

The GAXRD suggested that SiO_2 was an oxide in the scale. According to Mitra et al. (2006), amorphous SiO_2 is the most preferred since it is capable to form modified glasses with inclusions of elements from the substrate alloy or from the environment. Furthermore, amorphous SiO_2 could offer its selfhealing capability at high temperature in case of failure. It is likely that in the alloy OHS1, the SiO_2 formation competed with formation of more thermodynamically stable oxides of other components in the alloy. GeO_2 was not formed in the oxide scale, it was only found in the Nb_5Si_3 and Nb_5Ge_3 in the IOZ.

Although, most of the Cr was found at the surface of the scale in the Ti(Cr,Nb)O_4 oxide, the chemical analysis showed that the Cr content increased towards the surface of the oxide scale. However, no Cr oxide particles were found and no Cr as a solute in the Al_2O_3. Probably Ti and Cr affected the oxygen solubility in Nb and thus the formation of Nb_2O_5 was dramatically reduced

allowing the formation of $Ti(Cr,Nb)O_4$. The metal /scale interface could have been embrittled by the formation of Ti_xN_y compounds (Figure 135).

6.4 Conclusions

The microstructural study of the as cast and heat treated alloy OHS1 allowed the following coclusions tobe made:

The phases in the as cast alloy were the βNb_5Si_3, Nb_3Sn, Nb_{ss}, and the $NbCr_2$ C14 Laves. The eutectic reaction $L \rightarrow Nb_{ss} + \beta Nb_5Si_3 + NbCr_2$ with Al+Ge+Si+Sn of the eutectic in the range 17.9 to 20 at. % had occurred. The βNb_5Si_3 was the primary phase and was retained after heat treatment along with the Nb_3Sn, and the $NbCr_2$ C14 Laves phases while the Nb_{ss} and the eutectic were destabilised.

The synergy of Ge and Sn stabilised the $NbCr_2$ Laves phase and reduced the Nb_{ss} volume fraction in the cast alloy and destabilised the Nb_{ss} after heat treatment.

There was strong macrosegregation of Si and Ti and weak macrosegregation of Al, Cr and Sn.

Al in synergy with Ge and Sn simultaneously increased the macrosegregation of Si than Al in synergy with Ge and Sn individually. Al in synergy with Sn had a stronger effect on the macrosegregation of Si than Al in synergy with Ge.

The synergy of Cr with Sn had a stronger effect on the macrosegregation of Si than that of Cr with Ge.

Sn in synergy with Al and Cr individually has a stronger effect on the macrosegregation of Si than Ge with Al and Cr individually.

The strong effect of the synergy of Sn with Cr on the macrosegregation of Si can be controlled by adding Ge.The additions of Al, Cr, Ge and Sn simultaneously in the Nb-silicide based alloys reduced the macrosegregation of Si.

The thermogravimetric studies at 800 and 1200 °C of the alloy OHS1 led to the following conclusions:

At 800 °C, the alloy did not suffer pest oxidation, partial disintegration or oxide scale spallation. The alloy exhibited a parabolic oxidation behaviour and gained 3.19 mg/cm^2 after 100 h. The oxide scale formed was composed of TiO_2, $TiNbO_4$, $CrNbO_4$, $Nb_2O_5.GeO_2$, SiO_2, $SnGeO_3$, $Ti_2Nb_{10}O_{29}$, Nb_2TiO_7. GeO_2 + SiO_2 was not confirmed. There was internal oxidation with a deeper attack at the phase boundaries which played a very important role in the inward and outward transport of reactants. Microcraks formed in the Nb_5Si_3 at the metal / scale interface close to grain boundaries were associated with the oxidation of the Nb_{ss} since the Nb_5Si_3 in these areas was unoxidised.

The voluminous oxide scale formed at 1200 °C remained on the specimen. The alloy exhibited a linear oxidation behaviour and gained 31.28 mg/cm^2 after 100 h. The oxide scale formed was composed of TiO_2, SiO_2, $Ti_2Nb_{10}O_{29}$, $TiNb_2O_7$, rutile type $TiNbO_4$ and $AlNbO_4$, Nb_2O_5 and Al_2O_3. The alloy presented an internal oxidation zone with some Ti_xN_y compounds in the Ti- rich areas near the metal / scale interface and GeO_2 close to Ge rich areas in the diffusion zone. The diffusion zone was enriched by Ge and Sn due to the formation of the Nb_5Ge_3 and Nb_5Sn_2Si phases which impeded further oxygen penetration.

The synergy of Sn and Ge increased the oxidation resistance of the alloy at both temperatures.

Chapter 7

Summarising remarks, conclusions and suggestions for future work

7.1 Summarising remarks

Niobium silicide based alloys will need a coating system to enable the substrate alloy to operate with surface temperatures $\leq$ 1623 K (1350° C) in the environment of the next generation aero-engines where turbine entry temperatures could be around 2100 K (~ 1830 °C) to meet environmental and noise targets (for example the current flightpath year 2050 goals on year 2000 basis) are reductions of 75%, 90% and 65% respectively of CO_2, NO_x and noise, [Tsakiropoulos (2014b)]. Thus, R&D is considering coating systems consisting of bond coat (BC), TGO and ceramic top coat (CTP). In other words thermal barrier (type) coatings (TBC) are considered for Nb silicide based alloys, see section 1.3.

If we were to assume similar engine architecture in the high pressure turbine in future aero-engines, where Nb silicide based alloys are envisaged to replace Ni based superalloys in aerofoils (blades), the latter will be attached to a disk and should meet (satisfy) property goals (requirements) along the length of the blade with the highest temperatures experienced at the tip of the blade and the highest stresses at its route, near the disc.

The BC most likely will be a multi-layer or functionally graded material (see section 1.3) in which the Nb and Al activities respectively should be decreasing and increasing with distance from (perpendicularly to) the substrate, to have α-Al_2O_3 as the TGO. Given that the substrate will be Si rich and the CMAS (CaO-MgO-Al_2O_3-SiO_2) issues with state of the art coating systems in modern aero-engines using the latest generations of Ni based superalloys, it is envisaged that the activity of Si will also decrease with distance from (perpendicularly to) the substrate. R&D has also been challenged to consider variations of the coating system along the length of the blade from route to tip.

Considering the liquidus temperatures of developmental Nb silicide based alloys that offer a balance of mechanical and environmental properties (i.e., multicomponent alloys from Nb-Ti-Si-Al-Cr-Hf-Mo-Ta-W-Sn-Ge-B systems with 10 < Ti < 25 at%, 16 < Si < 22 at%), the substrate will be operating at high homologous temperatures ($\leq$ 0.75). Equally high homologous temperatures will be experienced by the BC. Thus, inter-diffusion of elements across the BC/substrate interface and within the BC is expected to affect phase stability in the latter (and the substrate) and the ability of the coating system to sustain α-Al_2O_3 as the TGO.

The processing of coating systems that are currently used on Ni based superalloys includes methods such chemical (CVD) and physical (PVD) deposition methods (e.g. EBPVD), and air (APS) or vacuum (VPS) plasma spraying. These methods are envisaged to be used for the application of TBC type coating systems on Nb silicide based alloys. Under the aforementioned non-equilibrium processing, metastable (non-equilibrium) phase equilibria prevails in the "as processed" coating system and thus in service the latter "moves towards equilibrium" driven by diffusion of solutes in the micro and macrostructures (for example the Thorton diagram shows four structure zones in PVD coatings depending on substrate homologous temperature and pressure, Zone I - porous tapered crystallites separated by voids, Zone II – large columnar grains, Zone III - coarse grains and Zone T - densely packed fibrous grains) produced by processing and by the diffusion of interstitial elements, both of which are affected by stress and temperature [Thorton (1975)].

Designing and understanding (predicting) the behaviour of BC alloys as deposited and in service requires accurate phase equilibria for the alloy systems in which the alloys belong. In sections 1.3, 1.4 and 4.1 it was discussed that Si-Cr-Fe, iron modified $(TM)_7Si_6$ (TM = Cr, Fe, Nb, Ti) silicide coatings and $NbSi_2$ based silicide coatings have been (are) considered for Nb silicide based alloys. Available phase equilibria for Cr-Si-Ti, Fe-Si-Cr, Fe-Si-Ti and Fe-Al-Si shows a plethora of phases that can be stable in alloys of these systems, which makes the selection of alloy compositions and the characterisation of their microstructures a challenging task even in equilibrium. Phase equilibria for Nb-Si based systems is equally challenging because of numerous controversies and disagreements, for example for the Nb-Si binary regarding the

(stable and metastable) eutectic compositions, eutectic, peritectic, eutectoid and peritectoid temperatures, and for the Nb-Si-Ti and Nb-Cr-Si ternaries for the liquidus projections.

Controversies about the phase equilibria for the aforementioned systems arise because of inhomogeneities in the experimentally studied alloys, the latter arising from macrosegregation, cooling rate variations and various phenomena interfering with the formation of microstructures in intermetallic alloys “grown” using optical floating zone (OFZ) melting, [McCaughey (2016)] (e.g. in OFZ the surface tension will vary because of gradients in temperature and solute concentration and the liquid will be in motion owing to surface tension gradients, gravity driven (natural) convection and stirring arising from rotation of the solid and crucible).

Given the implications of the aforementioned for phase equilibria and non-equilibrium processing regarding understanding phase stability in the dynamic microstructures of a real coating system, the research described in this thesis considered (i) clean melting in water cooled crucibles instead of CVD, PVD, EBPVD, APS and VPS for alloy making and (ii) alloys that could be used as components of a BC with chemistries chosen to highlight the effect(s) of key elements like Al, Cr, Hf, Si, Ti, Nb (a) on phase stability and (b) on oxidation behaviour. The (i) allowed the study of microstructures and the stability of phases in chemically inhomogeneous (for example, macro-segregated) macro-structures and micro-segregated microstructures that were formed over a range of cooling rates.

The results of the alloy OHC1, which was chosen to study the effects of Ti in the microstructure and oxidation of a (basis) Si rich Si-25Fe-15Cr alloy, showed that the alloying with Ti, even though it did not lead to pest oxidation at 800 °C, (i) stabilised the $L \rightarrow FeSi + FeSi_2Ti$ eutectic at ~ 1300 °C and (ii) contributed to melting of the oxide forming over the (Fe,Cr,Ti)Si silicide during oxidation at 1200 °C via $L \rightarrow FeO + Cr_2O_3 + SiO_2$ at ~ 1155 °C. Therefore, the alloy OHC1 could not be used in a coating system above 1100 °C because, even though it has good oxidation resistance at 800 and 1200 °C and forms a SiO_2 sublayer that could function as an excellent barrier, insipient melting would occur at ~ 1300 °C as well as melting in the oxide scale at ~ 1155 °C and evaporation of CrO_3 from the Cr_2O_3 layer at 1200 °C.

The results for the alloy OHC2, which was chosen to study how the synergy of Ti with Al affects the microstructure and oxidation of an essentially similar Si rich Si-Fe-Cr basis alloy as that of the alloy OHC1 with Al substituting Si and Ti + Nb content equal to that of Ti in OHC1, showed that the alloy did not pest at 800 °C, but liquation at 1200 °C and insipient melting at ~ 975 °C via a eutectic reaction involving the $Fe_3Al_2Si_3$ intermetallic ocurred.

The results for the alloys OHC1 and OHC2 would thus suggest that a Si rich Si-Fe-Cr basis alloy with ~ 22 to 25 at% Fe and 12 to 15 at% Cr could not be used in a BC because alloying with Ti, Al and Nb (where alloying could be due to inter-diffusion with the substrate and/or other BC components) would lead to liquation and insipient melting.

The alloy OHC5 was designed to be $NbSi_2$ based with nominal Si + Al content of 65 at%. In the ingots of this alloy there were very low volume fractions of (Al) and (Si) in the parts that had experience the highest cooling rates. There was melting of the (Al) at T > 660 °C. The solidification path of the alloy OHC5 would thus suggest that under non-equilibrium processing the formation of (Al) and (Si) is highly probable, which means that depending on the volume fractions of the latter solid solution phases liquation could occur upon exposure to high temperature. No solid solution stable at high temperature (up to 1400 °C) was observed in the microstructure of OHC5-HT, which was 100% intermetallic based, meaning that the fracture toughness of the alloy (not measured) should be poor.

At 800 and 1200 °C the alloy OHC5 followed parabolic oxidation with low rate constants and did not pest. The synergy of Cr and Ti was effective in promoting alumina formation in the scale of this very Si rich alloy. At 800 °C the scale consisted of an outer layer of silica and alumina and an inner layer of alumina. At 1200 °C the scale was α-Al_2O_3. Alumina formation depended on the Al concentration in the disilicide being above a critical concentration (~ 3 at. %). At lower than the critical Al concentrations there was evidence of internal oxidation.

Compared with the alloys OHC1 and OHC2, the alloy OHC5 is a candidate worth further consideration regarding alloy development for a BC application owing to its ability to form silica and alumina scales even at such low Al concentration in the alloy. One of the objectives of alloy

development should be to find out the critical Al concentration in $(Nb,Ti)(Si,Al)_2$ in disilicide based Nb-Si-Al-Cr-Ti alloys for avoiding internal oxidation.

The alloy OHC3 was Al rich. Its microstructure was stable to 1500 °C and exhibited melting at about 1520 °C via $L \rightarrow Al_3Nb + NbCr_2$. Its oxidation was parabolic at 800, 1200 and 1300 °C with no pesting and no scale spallation at 800 and 1200 °C. At all three oxidation temperatures the scale consisted of an inner α-Al_2O_3 formed below an out layer of Al and Cr niobates and α-Al_2O_3. At 1300 °C the adherence of the inner α-Al_2O_3 to the substrate was very good and there was partial spallation of the outer scale. There was some internal oxidation along grain boundaries at 800 °C and the $(Nb,Cr,Al)_{ss}$ was not stable above 1000 °C, which has implications for fracture toughness.

Like the alloy OHC5, the alloy OHC3 is a candidate worth further consideration regarding alloy development for a BC application owing to its ability to form well adhering alumina scales, and its stable microstructure up to 1500 °C. The objective of alloy development should be to define window of alloy compositions where internal oxidation does not occur. Stability of the solid solution to temperatures above 1000 °C is also desirable.

Only one substrate alloy was investigated in this research, namely the alloy OHS1. Its composition was based on other research in the group that had shown the benefits of having Ge [Li,(2012)] and Sn [Geng (2006) and Xu (2016)] individually on oxidation resistance at 800 and 1200 °C, with pest oxidation suppressed at the former temperature and oxidation improved at the latter but with scale spallation. To the author's (and the group's) knowledge this was the first study of Nb silicide based alloys with Ge and Sn being simultaneously in synergy with Al, Cr and Ti, i.e., with the other solutes that are known to "control" the oxidation of this new alloy family.

The microstructure of the alloy OHS1 consisted of the βNb_5Si_3, A15-Nb_3X (owing to the presence of Ge and Sn) and $NbCr_2$ Laves with a small volume fraction of Nb_{ss}, the latter not being stable at 1400 °C. The oxidation was parabolic at 800 °C (no pest) and linear at 1200 °C, but with no scale spallation. Niobates of Cr and Ti with mixed oxides of Ge and Sn formed the

scale at 800 °C and there was also evidence of internal oxidation. At 1200 °C the scale was not compact and continuous and consisted of Ti niobates and Nb oxides and had no Ge and Sn in it. The synergy of Ge and Sn in OHS1 did not supress the surface segregation of these two elements and encouraged the formation of Ge and Sn intermetallics, namely Nb_5Ge_3, Nb_6Sn_5 and Nb_5Si_2Sn, below the scale at the substrate/scale interface, which was also observed in alloys with only Sn [Geng (2006d), Vellios (2008), Xu (2016)] or Ge [Bywater (2016) and Tweedle (2014)]. Importantly, even though there was some internal oxidation in the substrate immediately below the scale, the core of the substrate was not contaminated by interstitials.

The alloy OHS1 is not an alloy having balance of mechanical and oxidation properties close to satisfying property goals. Indeed, it was designed with emphasis on oxidation resistance. According to the alloy design methodology developed in our group the calculated creep rate at 1200 °C and 170 MPa is 4.14 10^{-6} s^{-1} (i.e., the alloy OHS1 does not meet the creep goal of creep rate 2.10^{-8} s^{-1} at 1200 °C and 170 MPa) but the measured weight gains at 800 and 1200 °C, respectively 3.2 10^{-3} and 0.0313 g/cm^2, compare very well with the calculated ones using the same alloy design methodology, being respectively 2.1 10^{-3} and 0.0332 g/cm^2 [Tsakiropoulos, (2014b)].

If there were coating processing facilities available to the author of this research and available time and resources, the coating system shown in figure 136a would have been produced for a preliminary study of stability and oxidation of the two-layer BC and the stability of the substrate/BC interface. Given the results of this research, it would be recommended that a similar investigation should be done for the system shown in figure 136b.

The improved alloy OHS1 (to be called OHS1i) should aim to stabilise a slightly higher volume fraction of the Nb_{ss} to meet the fracture toughness goal ($\geq$ 20 MPa$\sqrt{m}$) and move closer to the creep goal without causing significant changes in oxidation behaviour. The research for an improved BC alloy OHC5 (OHC5i) should aim to find out the critical Al concentration that can sustain alumina scale growth without internal oxidation. It should be recognised that $Al_{critical}$ would depend on inter-diffusion with OHS1i and OHC3i and the microstructure of OHC5i "delivered" by the processing method used (e.g. see above for comments about the Thornton

diagram). The research for an improved BC alloy OHC3 (OHC3i) should aim to define "window" of alloy compositions that can sustain alumina scale growth without internal oxidation paying particular attention to how the "window width" is affected by inter-diffusion with OHC5i and solid solution stable above 1000 °C. Particular attention should be paid in optimising the Cr and Nb concentrations in the coating system in the as coated condition (can we sustain alumina scale growth with less Nb and Cr in OHC3i?).

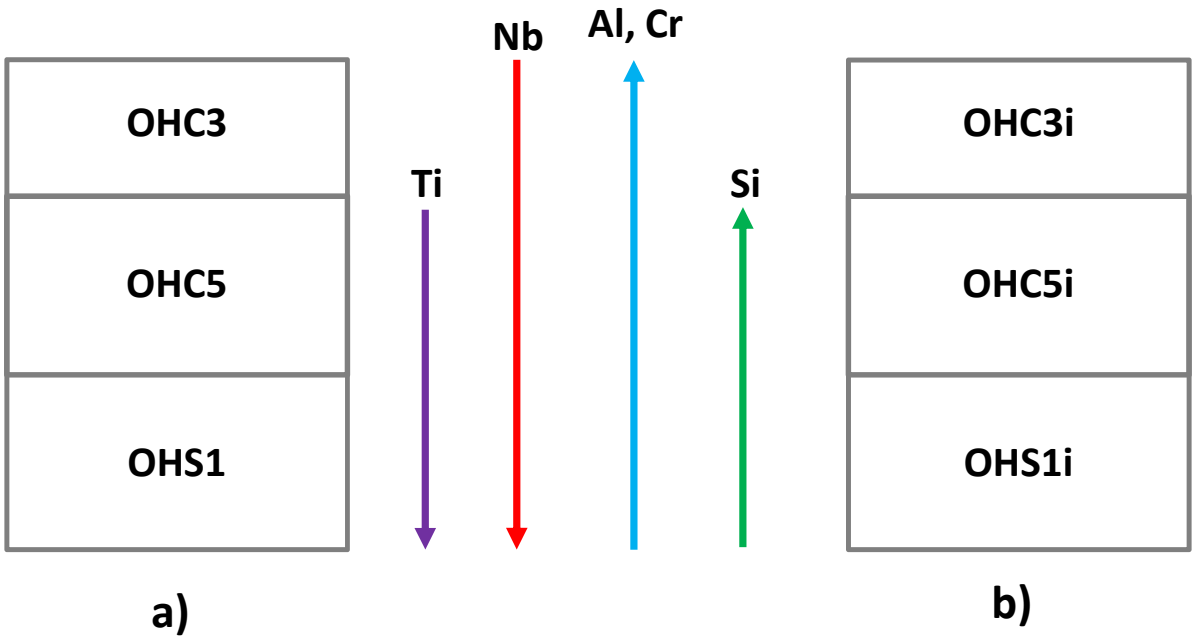

Figure 136. Schematic diagrams showing substrate and two layer BC systems based (a) on the alloys studied in this thesis and (b) on improved versions of the alloys. Purple, red, blue and green arrows indicate respectively trends in increasing Ti, Nb, Al and Cr, and Si in coating system.

7.2 Conclusions

All the objectives of the research described in this thesis which were set out in the introduction, were achieved. At the end of each of the chapters 3, 4, 5 and 6 the results for the alloys OHC1, OHC2 (section 3.4), OHC5 (section 4.4), OHC3 (section 5.4) and OHS1 (section 6.4) were summarised and the suitability or not of the alloys OHC1, OHC2, OHC3 and OHC5 as bond coat alloys was discussed briefly, with a further discussion of the latter in the previous section (7.1).

The research addressed phase selection and stability in the microstructures of all five alloys as well as their oxidation behaviour at 800 and 1200 °C (and 1300 °C for OHC3). The former proved very successful because it identified (i) the alloys where insipient melting and liquation occurred and the reason(s) why this happened, (ii) dependence of some microstructures on non-equilibrium processing and (iii) the highest temperature where the alloy microstructure was stable. The choice of the two oxidation temperatures was informed by previous research in the group and the open literature and allowed comparisons to be made with other research.

The research highlighted that Si rich intermetallic alloys based on the Si-Fe-Cr system like the alloys OHC1 and OHC2 should be considered to be unlikely candidate materials for multi-alloy BC type applications in coating systems for Nb silicide based alloys because even though they can form silica and alumina containing scales they tend to suffer from insipient melting, with Al, the key element for achieving oxidation resistance at high temperatures, significantly affecting their stability at T > 900 °C, as demonstrated by the results for the alloy OHC2. This research also explained the poor performance of Si-TM-Cr (pack cementation) BCs on the MASC type alloy Nb-25Ti-16Si-8Hf-2Al-2Cr (the 1st generation Nb silicide based alloy developed by GE is known as MASC) that were studied (evaluated) in the EU FP6 programme ULTMAT [Tsakiropoulos, (2014b)].

The two most promising alloys for BC type application were the alloys OHC5 and OHC3, with the latter being stable to 1500 °C. The former, though Si rich, was able to sustain alumina scale growth with only 5 at. % Al in its composition, which would suggest that the synergy of Al with Cr and Ti enhanced the activity of Al in the alloy. The latter, though with significant Nb content, was also able to sustain inner (strongly adhering) alumina scale that formed below a layer of mixed alumina and Al niobate oxides. The optimum alloy chemistries of these alloys to avoid pest oxidation, sustain growth of alumina scales with no scale spallation and no internal oxidation were not defined in this work. However, this research identified which the focal points of future alloy development work should be. These points were discussed in the previous section, and are not repeated here to avoid duplication.

7.3 Suggestions for future work

The research on the alloy OHS1 confirmed that the synergy of Ge and Sn is capable of supressing scale spallation. It should be noted that the alloy OHS1 is Hf free. Hafnium is a very important alloying addition in Nb silicide based alloys not only because it scavenges oxygen but also because it provides solid solution strengthening to the Nb_{ss} without having a strong effect on the DBTT of Nb. However, the actual concentration of Hf in the alloy is critical for creep, as discussed in the academic and patent literature with the help of the Nb/(Ti+Hf) ratio. Thus, future research should consider a variant of OHS1 with Hf addition.

This research has confirmed the surface segregation of Ge and Sn in the substrate just below the scale and the participation of both elements in oxides in the scale formed at 800 °C. It is suggested that variants of the alloys OHC5 and OHC3 with small additions of Ge and Sn are studied. Sn partitions to the Nb_{ss} and Ge to the Nb_5Si_3 in Nb silicide based alloys. Given that Ge can substitute Si in the silicide, it is suggested that in the variants of OHC5 and OHC3 the priority should be given to Sn addition before both elements are present simultaneously in the BC type alloy with Sn/Ge > 1.

Other areas of future research could be on variants of the alloys OHC5 and OHC3, for example as discussed for OHC5i and OHC3i in section 7.1.

References

T. Adachi and G. H. Meier. Oxidation of Iron-Silicon Alloys. Oxidation of Metals, 27 (1987) pp.347-366

H.B. Awais, PhD thesis, University of Manchester (1995)

S. Becker, A. Rahmel, M. Schiitze. Oxidation of $TiSi_2$ and $MoSi_2$. Solid State Ionics, 56 (1992) pp. 280-289

B.P. Bewlay, H. A. Lipsitt, M.R. Jackson, W.J. Reeder, J.A. Sutliff. Solidification processing of high temperature intermetallic eutectic-based alloys, Materials Science and Engineering A, 192 (1995a) pp. 534-543

B. P Bewlay, M.R. Jackson, W.J. Reeder, H.A. Lipsitt. Microstructures and properties of DS in-situ composites of Nb-Ti-Si alloys. Materials Research Society Symposium Proceedings, 364 (1995b) pp. 943-948.

B.P. Bewlay, M.R. Jackson, and H.A. Lipsitt. The Balance of Mechanical and Environmental Properties of a Multielement Niobium-Niobium Silicide-Based In Situ Composite. Metallurgical and Materials Transactions A, 27A (1996) pp. 3801-3808

B.P. Bewlay, M.R. Jackson and H.A. Lipsitt. The Nb-Ti-Si Ternary Phase Diagram: Evaluation of Liquid-Solid Phase Equilibria in Nb- and Ti-Rich Alloys. Journal of Phase Equilibria, 18 (1997a) pp. 264-278

B.P. Bewlay, J.J. Lewandowksi, and M.R. Jackson. Refractory Metal-Intermetallic In-Situ Composites for Aircraft Engines. JOM, 49 (8) (1997 b) pp. 44-45,67

B.P. Bewlay, M.R. Jackson, and P.R. Subramanian. Processing High-TemperatureRefractory-Metal Silicide In-Situ Composites. JOM (1999) pp. 32-36

B.P. Bewlay, M.R. Jackson, and M.F.X. Gigliotti. Niobium silicide high temperature in situ composites, chapter 26. Intermetallic compounds: Vol. 3, Principles and practice Edited by H.J. Westbrook and R.L Fleischer. John Wiley & Sons Ltd. (2002) pp. 541-560

B.P. Bewlay, J M.R. Jackson, Creep resistant Nb-Silicide based multiphase composites, United states patent US6 409848B1; 2002

B.P. Bewlay, M.R. Jackson, J.-C. Zhao, and P.R. Subramanian. A Review of Very-High-Temperature Nb-silicide–Based Composites. Metallurgical and Materials Transactions A, 34A (2003) pp. 2043-2052

B.P. Bewlay, M.R. Jackson, J-C. Zhao. Coatings, method of manufacture and the articles derived therefrom, United states patent US 0126613 A1; 2004a

B.P. Bewlay, S.D. Sitzman, L.N. Brewer and M.R. Jackson. Analyses of Eutectoid Phase Transformations in Nb–Silicide In Situ Composites. Microscopy and Microanalysis, 10 (2004b) pp. 470–480

B.P. Bewlay, Y. Yang, Y.A. Chang Solid-state phase equilibria in metal-rich Hf-Ti-Si system at 1350 °C. Intermetallics 16 (2008) pp. 353-359

B.P. Bewlay, Y. Yang, R.L. Casey, M.R. Jackson, Y.A. Chang. Experimental study of the liquid–solid phase equilibria at the metal-rich region of the Nb–Cr–Si system. Intermetallics, 17 (2009) pp. 120–127

N. Birks, G.H.Meier and F.S Pettit. Introduction to the high-temperature oxidation of metals. Chapter 4. Second edition. Cambridge university press, (2006)

F.Bosselet, D.Pontevichi, M. Sacerdote-Peronnet, and J.C. Viala. Measurement of the Isothermal Section at 1000 K of Al-Fe-Si. J. Phys. IV, 122 (2004) pp. 41-46

M.P. Brady and P.F. Tortorelli. Alloy design of intermetallics for protective scale formation and for use as precursors for complex ceramic phase surfaces. Intermetallics, 12 (2004) pp. 779-789

C. Brukl, H. Nowotny und F. Benesovsky. Untersuchungen in den Dreistoffsystemen: V-Al-Si, Nb-Al-Si, Cr-A1-Si, Mo-Al-Si bzw. Cr(Mo)-Al-Si. Monatshefte ür Chemie und verwandte Teile anderer Wissenschaften, 92 (1961) pp. 967-980

M. W. Brumm and H.J. Grabke. The oxidation behaviour of NiAl-I. Phase transformation s in the alumina scale during oxidation of NiAl and NiAl-Cr alloys. Corrosion Science, 33 (1992) pp. 1677-1690

G.Bywater. Research in progress, University of Sheffield (2014)

K.S. Chan and D.L. Davidson. Delineating Brittle-Phase Embrittlement and Ductile-Phase Toughening In Nb-Based In-Situ Composites. Metallurgical and Materials Transactions A, 32A (2001) pp. 2717-2727

G.M. Cai, F. Zheng,D.Q. Yi, H.M. Chen, S.X Zhou, Z.H. Long, Z.P. Jin. Experimental investigation and thermodynamic modeling of Hf-Si-B system. Journal of alloys and compounds, 494 (2010) pp. 148-154

K.S. Chan. Alloying effects on fracture mechanisms in Nb-based intermetallic in-situ composites. Materials Science and Engineering, A329–331 (2002) pp. 513–522

H. Chen, F. Weitzer, J.C. Schuster, Y. Du, H. Xu. The isothermal section of the Al–Cr–Si system at 800 °C and the crystal structure of τ_2 (Cr_3Al_9Si). Journal of Alloys and Compounds, 436 (2007) pp. 313–318

A. D. Chirkin, V. O. Lavrenko and V. M. Talash. High-temperature and electrochemical oxidation of transition metal silicides. Powder metallurgy and metal ceramics, 48 (2009) pp. 330-345

A.M. Da Silva Costa, G. F. de Lima, G. Rodriguez. Evaluation of Ti_3Si phase stability from heat-treated, rapidly solidified Ti-Si alloys. Journal of Phase Equilibria and Difussion, 31 (2010) pp. 22-27

N. David, Y. Cartigny, T. Belmonte, J.M. Fiorani, M. Vilasi. Thermodynamic description of the Cr–Nb–Si isothermal section at 1473 K. Intermetallics, 14 (2006) pp. 464–473

A. Deal, W. Heward, D. Ellis, J. Cournoyer, K. Dovidenko, B.P. Bewlay. Phase Identification in Nb-Cr-Si Alloys. Microscopy and Microanalysis, 13 Suppl 2, (2007) pp. 90-91

D. M. Dimiduk, P.R. Subramanian and M.G. Mendiratta. Exploration of Nb-Based advanced intermetallic materials. Acta metallurgica sinica (English letters), 8 (1995) pp. 519-530

J. Doychak and M. G. Hebsur. Protective Al_2O_3 Scale formation on $NbAl_3$-Base Alloys. Oxidation of Metals, 36 (1991) pp. 113-141

Y. Du and J.C. Schuster**.** Experimental investigation and thermodynamic description of the Cr-Si-Ti system, Scandinavian Journal of Metallurgy, 31 (2002) pp. 25–33

Y. Du, J.C. Schuster, Z.K. Liu, R. Hu, P. Nash, W. Sun, W. Zhang, J. Wang, L. Zhang, C. Tang, Z. Zhu, S. Liu, Y. Ouyang, W. Zhang, N. Krendelsberger. A thermodynamic description of the Al-Fe-Si system over the whole composition and temperature ranges via a hybrid approach of CALPHAD and key experiments. Intermetallics, 16 (2008) pp. 554-570

P.B. Fernandes, G.C. Coelho, F. Ferreira, C.A. Nunes, B. Sundman. Thermodynamic modeling of the Nb–Si system. Intermetallics, 10 (2002) pp. 993–999.

M. C. Garcıa-Alonso, J. L. Gonzalez-Carrasco, M. L. Escudero, and J. Chao. Oxidation Behavior of Fine-Grain MA 956 Superalloy. Oxidation of Metals, 53 (2000) pp. 77-98

J. Geng, G. Shao, P. Tsakiropoulos. Study of three-phase equilibrium in the Nb-rich corner of Nb–Si–Cr system. Intermetallics, 14 (2006a) pp. 832–837

J. Geng, P. Tsakiropoulos, G. Shao. Oxidation of Nb–Si–Cr–Al in situ composites with Mo,Ti and Hf additions. Materials Science and Engineering A, 441 (2006b) pp. 26–38

J. Geng, P. Tsakiropoulos, G. Shao. The effects of Ti and Mo additions on the microstructure of Nb-silicide based in situ composites. Intermetallics, 14 (2006c) pp. 227–235

J.Geng, PhD thesis, University of Surrey (2006c)

J. Geng, P. Tsakiropoulos, G. Shao. A study of the effects of Hf and Sn additions on the microstructure of Nb_{ss}/Nb_5Si_3 based in situ composites. Intermetallics, 15 (2007a) pp. 69-76.

J. Geng, P. Tsakiropoulos, G. Shao. A Thermo-gravimetric and microstructural study of the oxidation of Nb_{ss}/Nb_5Si_3 based in situ composites with Sn addition. Intermetallics, 15 (2007b)b pp. 270-281.

J. Geng, P.Tsakiropoulos. A study of the microstructures and oxidation of Nb-Si-Cr-Al-Mo in situ composites alloyed with Ti, Hf and Sn. Intermetallics, 15 (2007c) pp. 382-395.

J. L. Gonzalez-Carrasco, M. C. Garcıa-Alonso, M. A. Montealegre, M. L. Escudero, and J. Chao, Comparative Study of the Alumina-Scale Integrity on MA 956 and PM 2000 Alloys, Oxidation of Metals, 55 (2001) pp. 209-221

H.J. Grabke, M. Steinhorst, M.Brumm and D. Wiemer. Oxidation and Intergranular Disintegration of the Aluminides NiAl and $NbAl_3$ and Phases in the system Nb-Ni-Al. Oxidation of Metals, 35 (1991) pp. 199-222

I. Grammenos and P. Tsakiropoulos. Study of the role of Al, Cr and Ti additions in the microstructure of Nb-18Si-5Hf base alloys. Intermetallics, 18 (2010) pp. 242-253

S.P. Gupta. Formation of intermetallic compounds in the C-Al-Si ternary system. Materials Characterization, 52 (2004) pp. 255-370

M.G. Hebsur., J.R Stephens, J.L. Smialek, C.A. Barret and D.S. Fox. Influence of alloying elements on the oxidation behavior of $NbAl_3$. Oxidation of high-temperature intermetallics; Proceedings of the Workshop, Minerals, Metals, and Materials Society, Unknown volume (1989) pp. 171-183.

G.A. Henshall, P.R. Subramanian, M.J. Strum and M.G. Mendiratta. Continuum Predictions of Deformation in Composites with two Creeping Phases-II Nb_5Si_3/Nb Composites. Acta Materialia, 45 (1997) pp. 3135 -3142

C.R. Hunt and A. Raman. Alloy Chemistry of σ(βU)-Related Phases. Z. Metallkd., 59 (1968) pp. 701-707.

V. Ivanchenko. Chapter Light Metal Systems. Part 1 Volume 11A1 of the series Landolt - Börnstein - Group IV Physical Chemistry (2004) pp. 360-370

M. R. Jackson, R.G. Rowe, and D.W. Skelly. Oxidation of some intermetallic compounds and intermetallic matrix composites. Materials research society symposium proceedings, 364 (1995) pp. 1339-1344

M.R. Jackson, A.M. Ritter. Oxidation-Resistant Coating for Niobium-Base Alloys, United States Patent 5721061; 1998

M.R. Jackson, B.P. Bewlay, J-C. Zhao. Niobium-Silicide based composites resistant to high temperature oxidation, United states patent US 6913655; 2005

M.R. Jackson, P. Subramanian, J.C. Zhao, B. Bewlay, R. Darolia, R. Schafrik. Turbine Blade For Extreme Temperature Conditions, United States Patent 7189459; 2007

I. S. Kainarskii and E. V. Degtyareva. Chromic Oxide as refractory material. Ukrainian scientific-research institute of refractories. Translation from Ogneupory, 1 (1977) pp. 42-47

S. Kamiya, S. Hirano, And S. Somiya.The Compound Cr_2TiO_5 in the System Cr_2O_3-TiO_2. Journal Of Solid State Chemistry, 28 (1979) pp.21-28

B.L. Kirkwood, E.M.W. Picha. Silica-enriched Protective Coating for Hypersonic Flight Vehicles and Method of Applying same, Including Field Repair. United States Patent 5431961; 1995

S. Knittel, S. Mathieu, L. Portebois, M.Vilasi. Effect of tin addition on Nb-Si based in situ composites. Part II: Oxidation behaviour. Intermetallics, 47 (2014) pp. 43-52

P. Kofstad and H. Kjollesdal. Oxidation of Niobium (columbium) in the temperature range 500 to 1200 °C.Transactions of the metarllurgical society of AIME, 221 (1961) pp.285-294

P. Kofstad. High Temperature Oxidation of Metals. Chapter, Formation of Compact scales at High Temperatures. Corrosion monographs series, Oslo 1966.

P. Kofstad, High-Temperature Oxidation, Elsevier, London (1988), pp. 558.

N. Krendelsberger, F. Weitzer, J.C. Schuster. On the reaction Scheme and liquidus surface in the ternary system Al-Fe-Si. Metall. Mater. Trans. A., 38A (2007) pp. 1681-1691

O. Kubaschweski. Iron-binary phase diagrams.Springer-Verlag, New York Inc., (1982)

O. Kubaschweski. Phase diagrams of binary Iron alloys. H. Okamoto (edit). Materials information society, Ohio, (1993)

K. S. Kumar and C. T. Liu. Precipitation in a Cr-Cr_2Nb Alloy. Acta materialia, 45 (1997) pp. 3671-3686

K. Kurokawa, A. Yamauchi and S. Matsushita. Improvement of Oxidation resistance of $NbSi_2$ by addition of Boron. Materials Science Forum, 502 (2005) p. 243-245

M.H.Li, X.F.Sun, J.G. Li, Z.Y. Zhang, T.Jin, H.R. Guan, Z. Q.Hu. Oxidation behaviour of single-crystal Ni-base superalloy in air. I: At 800 and 900 °C. Oxidation of Metals, 59 (2003) pp.591-605

H. Liang, Y.A. Chang. Thermodynamic modeling of the Nb-Si-Ti ternary system. Intermetallics, 7 (1999) pp. 561-570

M. Lindholm. A thermodynamic description of the Fe-Cr-Si system with emphasis on the equilibria of the sigma (G) phase. Journal of phase equilibria, 18 (1997) pp. 432-440

C.T. Liu, P.F.Tortorelli, J.A. Horton, C.A. Carmichael. Effects of alloy additions on the microstructure and properties of Cr-Cr_2Nb alloys. Materials Science and Engineering A, 214 (1996) pp.23-32

Z.K. Liu, Y.A. Chang. Thermodynamic assessment of the Al-Fe-Si System, Metall. Mater. Trans. A, 30A, (1999) pp. 1081-1095

L.A. Lysenko, V.Y. Markiv, O.V. Tsybukh, E.I. Gladyshevskii. Inorganic Materials, 7 (1971) pp. 157-159

M.C.J. Marker, B. Skolyszewska-Kühberger, H.S. Effenberger, C. Schmetterer, K.W. Richter., Phase equilibria and structural investigations in the system Al-Fe-Si. Intermetallics, 19 (2011) pp. 1919-1929

M.C.J. Marker, L.I. Duarte, C. Leinenbach, K.W. Richter. Characterisation of the Fe-rich corner of Al-Fe-Si-Ti. Intermetallics, 39 (2013) pp.38-49

K. Mahdouk, J.C. Gachon, L. Bouirden. Enthalpies of formation of the Al–Nb intermetallic compounds. Journal of Alloys and Compounds, 268 (1998) pp. 118–121

K. Mahdouk, J.C. Gachon. A thermodynamic study of the Al–Cr–Nb ternary system. Journal of Alloys and Compounds, 321 (2001) pp. 232–236

S. Majumdar, P. Segupta, G.B. Kale, and I.G. Sharma. Development of multilayer oxidation resistant coatings on niobium and tantalum. Surface and Coatings Technology, 200 (2006) pp. 3713-3718

V.Y. Markiv. The crystal structures of the compounds $R(MX)_2$ and RMX_2 in Zr-Ni-Al, Ti-Fe-Si and related systems. Acta crystallogr, 21 (1966) pp.84-85

C. McCaughey, PhD thesis, University of Sheffield (2016)

G.H. Meier. Fundamentals of the oxidation of high temperature intermetallics in T. Grobstein and J. Doychak (eds.), Oxidation of High-Temperature Intermetallics, TMS, Warrendale,PA. (1989) pp. 1-15

G.H. Meier, and F.S. Pettit, The oxidation behavior of intermetallic compounds. Materials Science and engineering A, 153 (1992) pp. 548-560

E.S.K. Menon, M.G. Mendiratta, D.M. Dimiduk, in: K.J. Hemker, D.M. Dimiduk, H. Clemens, R. Darolia, H. Inui, J.M. Larsen, V.K. Sikka, M. Thomas, J.D. Whittenberger (Eds.) High temperature Oxidation Mechanisms in Nb- Silicide Bearing Multicomponent Alloys, Structural Intermetallics, TMS, The Minerals, Metals & Materials Society, (2001) pp. 591–600

R. Mitra. Mechanical Behaviour and Oxidation Resistance of Structural Silicides. International Materials Reviews, 51 (2006) pp. 13-64

D. Munson. A clarification of the phases occurring in Aluminum-rich, Aluminum-Iron-Silicon Alloys with particular reference to the ternary phase α-AlFeSi. J. Inst. Met., 95 (1967) pp. 217-19.

T. Murakami, S. Sasaki, K. Ichikawa, A. Kitahara. Microstructure, mechanical properties and oxidation behavior of Nb–Si–Al and Nb–Si–N powder compacts prepared by spark plasma sintering. Intermetallics, 9 (2001a) pp. 621–627

T. Murakami, S. Sasaki, K. Ichikawa, A. Kitahara. Oxidation resistance of powder compacts of the Nb–Si–Cr system and $Nb_3Si_5Al_2$ matrix compacts prepared by spark plasma sintering. Intermetallics, 9 (2001b) pp.629-635

T. Murakami, S. Sasaki, and K. Ito. Oxidation behavior and thermal stability of Cr-doped $Nb(Si,Al)_2$ and $Nb_3Si_5Al_2$ matrix compacts prepared by spark plasma sintering. Intermetallics, 11 (2003) p. 269-278

T. Nakano, M.Kishimoto, D. Furuta and Y. Umakoshi. Effect of substitutional elements on Plastic deformation behavior of NbSi2-based Silicide single crystal with C40 structure. Acta Materialia, 48 (2000) pp. 3465-3475

T. Nakano, Y. Nakai, S. Maeda and Y. Umakoshi. Microstructure of duplex-phase NbSi2(C40)/MoSi2(C11b) crystals containing a single set of lamellae. Acta Materialia, 50 (2002) pp. 1781-1795

P. Novák, M. Zelinková, J. Serák, A. Michalcová, M. Novák, D. Vojtech. Oxidation resistance of SHS Fe-Al-Si alloys at 800 °C in air, Intermetallics Vol. 19 (2011) pp. 1306-1312

H. Okamoto. Cr-Si (Chromium-Silicon). Journal of Phase Equilibria, 18 (1997) p. 222

H. Okamoto. Cr-Si (Chromium-Silicon). Journal of Phase Equilibria, 22 (2001) p. 593

H. Okamoto. Al-Cr (Aluminium-Chromium). Journal of Phase Equilibria and diffusion, 29 (2008) pp.112-113

I.Papadimitiou, C. Utton, P. Tsakiropoulos. On the Nb-Ge binary system. Metallurgical and Materials transactions A, 46 (2015) pp. 5526-5536

G.B. Olson, D.J. Bryan, A.Misra. Oxidation Resistant Niobium Based Alloys, United States Patent 0172142 A1; 2006

R.A. Perkins, K.T. Chiang, G. H. Meier and R.A. Miller. Efect of alloying, rapid solidification, and surface kinetics on the high temperature environmental resistance of niobium, AFOSR report, LMSC-F195926, 1989

R.A. Perkins and G. H. Meier. The oxidation behaviour and protection of niobium. JOM, 42(1990) pp. 17-21

B.A. Pint. Optimization of Reactive-Element additions to improve oxidation performance of Alumina-Forming alloys. Journal of American Ceramics Society, 86 (2003) pp. 686-695

B.A. Pint, J.R. DiStefano, I.G. Wright. Oxidation resistance: One barrier to moving beyond Ni-base superalloys. Materials Science and Engineering A, 415 (2006) pp. 255–263

S.H.Pitman and P.Tsakiropoulos. Study of the microstructure and oxidation of $NbSi_2$ base alloys. Materials Research Society Symposium Proceedings, 364 (1995) pp. 1321-1326

L. Portebois, S. Mathieu, S. Knittel, L. Aranda, M. Vilasi. Protective Coatings for Niobium Alloys: Manufacture, Characterization and Oxidation Behaviour of $(TiXCr)_7Si_6$ with X= Fe, Co and Ni. Oxidation of Metals, 80 (2013) pp. 243-256

M.I. Pownceby, K.K. Constanti-Carey, and M.J. Fisher-White. Subsolidus phase relationships in the system Fe_2O_3–Al_2O_3–TiO_2 between 1000° and 1300°C. J. American Ceramic Society, 86 (2003) pp. 975-980

R. Prescott and M. J. Graham. The formation of Aluminium Oxide Scales on High-Temperature Alloys. Oxidation of Metals, 38 (1992) pp. 233-254

R. Prescott, D.F. Mitchell, M.J. Graham. A study og the growth of α-Al_2O_3 scales using high resolution imaging secondary ion mass spectrometry. Corrosion Science, 50 (1994) pp. 62-71

O. Prymak, F. Stein. The ternary Cr-Al-Nb phase diagram: Experimental investigations of isothermal sections at 1150, 1300 and 1450 °C. Journal of alloys and Compounds, 513 (2012) pp. 378-386

V. Raghavan. Cr-Fe-Si (Chromium-Iron-Silicon). Journal of phase equilibria and diffusion, 23 (2003) pp. 265-266

V.Raghavan. Cr-Fe-Si (Chromium-Iron-Silicon). Journal of phase equilibria and diffusion, 25 (2004) pp. 545-546

V. Raghavan. Al-Cr-Nb (Aluminum-Chromium-Niobium). Journal of Phase Equilibria and Diffusion, 29 (2008) pp. 173-174

V. Raghavan. Al-Si-Ti (Iron-Silicon-Titanium). Journal of phase equilibria and diffusion, 30 (2009a) pp. 82-83

V. Raghavan. Al-Fe-Si (Aluminium-Iron-Silicon). Journal of phase equilibria and diffusion, 30 (2009b) pp. 184-188

V. Raghavan. Fe-Si-Ti (Iron-Silicon-Titanium). Journal of phase equilibria and diffusion, 30, (2009c) pp. 393-396

G.V. Raynor and V.G. Rivlin. Al-Fe-Si in phase equilibria in Iron ternary alloys. Institute of metals, London, (1988) pp. 122-139

M.E. Schlesinger, H. Okamoto, A.B. Gokhale, R. Abbaschian. The Nb-Si (Niobium-silicon) system. Journal of Phase Equilibria, 14 (1993) pp. 502-509

N. Sekido, Y. Kimura, S. Miura, F.G. Wei, Y. Mishima. Fracture Toughness and High Temperature Strength of Unidirectionally Solidified Nb–Si Binary and Nb–Ti–Si Ternary Alloys. Journal of Alloys and Compounds, 425 (2006) pp. 223–229

G. Shao. Thermodynamic assessment of the Nb–Si–Al system. Intermetallics, 12 (2004) pp. 655–664

G. Shao. Thermodynamic modeling of the Cr-Nb-Si system. Intermetallics, 13 (2005) pp. 69-78

Q. ShiYu, H. YaFang, K. YongWang. Effects of Ti, Al and Hf on niobium silicides formation in the Nb-Si in situ composites. Sci China Ser E-Tech Sci, 52 (2009) pp. 37-40

S.A. Souza, C.T. Rios, A.A. Coelho, P.L. Ferrandini, S. Gama, R. Carama. Growth and morphological characterization of Al–Cr–Nb eutectic alloys. Journal of Alloys and Compounds, 402 (2005) pp. 156–161

S.A. Souza, P.L. Ferrandini, C.A. Nunes, A.A. Coelho, R. Caram. Liquidus projection of the Nb–Cr–Al system near the Al_3(Nb,Cr) + Cr(Al,Nb) eutectic region. Materials Science and Engineering A, 424 (2006) pp. 77–82

S.A. Souza, P.L. Ferrandini, E.A. Souza. On the properties of the eutectic alloy A_{l3}(Nb,Cr) + Cr(Al,Nb). Journal of Alloys and Compounds, 464 (2008) pp. 162–167

F. Stein, C. He, I. Wossack. The liquidus surface of the Cr-Al-Nb system and re-investigation of the Cr-Nb and Al-Cr phase diagrams. Journal of alloys and compounds, 598 (2014) pp. 253-265

F. Stein, M. Palm, G.Sauthoff. Structure an stability of Laves phases part II- structure type variations in binary and ternary systems. Intermetallics 13 (2005) pp. 1056-1074

M. Steinhorst and H.J. Grabke. Oxidation of Niobium Aluminide $NbAl_3$. Materials Science and Engineering A, 120 (1989) pp. 55-59

A. Stergiou, P. Tsakiropoulos and A. Brown, The intermediate and high temperature oxidation behavior of Mo ($Si_{1-x}Al_x$) intermetallic alloys. Intermetallics, 5 (1997a) pp. 69-81

A. Stergiou and P. Tsakiropoulos, The intermediate and high temperature oxidation behavior of (Mo,X)Si_2 (X=W,Ta) intermetallic alloys. Intermetallics, 5 (1997b) pp. 117-126

W. J. Strydom and J. C. Lombaard. Thermal oxidation of the silicides $CoSi_2$, $CrSi_2$, $NiSi_2$, $PtSi_2$,$TiSi_2$, and $ZrSi_2$. Thin solid films, 131 (1985) pp. 215-231

P.R. Subramanian, M.G. Mendiratta, D.M. Dimiduk. High temperature silicides and refractory alloys. Materials research society Symp proccedings, 322 (1994) pp. 491-502

P.R. Subramanian, T.A. Parthasarathy, M.G. Mendiratta, D.M. Dimiduk. Compressive Creep Behaviour of Nb_5Si_3. Scripta Metallurgica et Materialia, 32 (1995) pp. 1227-1232

P.R. Subramanian, M.G. Mendiratta, D.M. Dimiduk, M.A. Stucke. Advanced intermetallic alloys-beyond gamma titanium aluminides. Materials Science and Engineering, A239–240 (1997) pp. 1–13

H.P. Takeda and K. Mutuzaki. The equilibrium diagram of the Iron-Aluminum-Silicon system. Tetsu to Hagane, 26 (1940) pp. 335-361

D.J. Thoma and J.H. Perepezko. An experimental evaluation of the phase relationships and solubilities in the Nb-Cr system. Materials Science and Engineering A, 424 (1992) pp. 97–108

J.A.Thorton. In fluence of substrate temperatureand deposition rate on structure of thick sputtered Cu coatings. Journal of vacuum science and technology, 12 (1975) pp.830-835

V.K. Tolpygo and H. J. Grabke. Mechanism of the intergranular Disintegration (Pest) of the Intermetallic Compound $NbAl_3$. Scripta Metallurgica at Materialia, 28 (1993) pp. 747-752

P.F. Tortorelli, B.A. Pint. Oxidation behaviour of Cr-Cr_2Nb alloys. D. A. Shores and P.Y. Hou eds, Fundamental aspects of high temperature corrosion. The electrochemical society proccedings V, (1996) pp. 74-85

P. Tsakiropoulos. Beyond Nickel based superalloys. Editors, R.Blockley and W. Shyy. Encyclopaedia of aerospace engineering. John Wiley & Sons, Ltd. (2010) pp. 2345-2355

P. Tsakiropoulos. On the macrosegregation of silicon in niobium silicide based alloys. Intermetallics, 55 (2014a) pp. 95-101

P. Tsakiropoulos. Private communication, University of Sheffield (2014b).

M.S.Tsirlin, G.M. Anurova, and A.D.Aliev. Structure and oxidation resistance of a slurry-difussion coating on Nb. Translated form Poroshkovaya Metallurgiya, 11 (1981) pp. 69-73

A. Tweddle, PhD thesis, University of Sheffield (2014)

N.Vellios and P. Tsakiropoulos. The role of Sn and Ti additions in the microstructure of Nb-18Si base alloys. Intermetallics, 15 (2007a) pp. 1518-1528

N.Vellios and P. Tsakiropoulos. The role of Fe and Ti additions in the microstructure of Nb-18Si-5Sn silicide-base alloys. Intermetallics, 15 (2007b) pp. 1529-1537

N. Vellios, PhD thesis, University of Surrey (2008)

N.Vellios and P. Tsakiropoulos. Estudy of the role of Fe and Sn additions in the microstructure of Nb-24Ti-18Si-5Cr silicide based alloys. Intermetallics, 18 (2010) pp. 1729-1736

M. Vilasi, M. Francois, R. Podor, J. Steinmetz. New silicides for niobium protective coatings. Journal of Alloys and compounds, 264 (1998a) pp. 244-251

M. Vilasi, M. Francois, H. Brequel, R. Podor, G. Venturini, J. Steinmetz. Phase equilibria in the Nb-Fe-Cr-Si system. Journal of Alloys and compounds, 269 (1998b) pp. 187-192

C. Wagner. Reacktionstypen bei der oxydation von legeirungen. Z. Elektrochemie, 63 (1959) pp. 772-782

G. Wahl. Coating Composition and the formation of protective oxide layers at high temperature. Thin Solid Films, 107 (1983) pp. 417-426

Y. Wang, J.L. Smialek and M. Suneson. Oxidation behavior of Hf-Modified Al Coatings on Inconel-718 at 1050 °C. Journal of Coating Science and Technology, 1 (2014) pp. 25-45

R.G. Weber, J.Bouvier and G. Slama. Failure Mechanisms of Aluminide and Silicide coatings on Niobium Alloy subjected to thermal cycling in Air. Journal of the Less-common Metals, 23 (1973) pp. 1-20

F. Weitzer, J. C. Schuster, M. Naka, F. Stein, M. Palm. On the reaction scheme and liquidus surface in the ternary system Fe-Si-Ti. Intermetallics, 16 (2008) pp. 273-282

J. P. Wittke. Solubility of iron in TiO2 (Rutile). Journal of The American Ceramic Society, 50 (1967) pp. 586-588

V.T. Witusiewicz, A. A. Bondar, U. Hecht, T. Ya. Velikanova. The Al-B-Nb-Ti system IV. Experimental study and thermodynamic re-evaluation of the binary Al-Nb and ternary Al-Nb-Ti systems. Journal of Alloys and Compounds, 472 (2009) pp.133-161

H. Xu, Y. Du, H. Chen, Y. He, Z. Pan, J.C. Schuster, R. Wang. Isothermal section at 1000 °C of the Nb–Ti–Si system. Journal of Alloys and Compounds, 394 (2005) pp. 235–239

K. Yamamoto, Y. Kimura, Y. Mishima. Phase constitution and microstructure of the Fe–Si–Cr ternary ferritic alloys. Scripta Materialia, 50 (2004) pp. 977–981

Y. Yang, Y.A. Chang, J.C. Zhao, B.P. Bewlay. Thermodynamic modeling of the Nb–Hf–Si ternary system Intermetallics, 11 (2003) pp. 407–415

K. Zelenitsas, PhD thesis, University of Surrey (2005)

K. Zelenitsas, P. Tsakiropoulos. Effect of Al, Cr and Ta additions on the oxidation behaviour of Nb–Ti–Si in situ composites at 800 °C. Materials Science and Engineering A, 416 (2006a) pp. 269–280

K. Zelenitsas, P. Tsakiropoulos. Study of the role of Ta and Cr additions in the microstructure of Nb–Ti–Si–Al in situ composites. Intermetallics, 14 (2006b) pp. 639–659

Y. Zhan, S. Zan, J. Jichao, M. Jianbo, X. Zhang, Z. Yinghong. The 773K isothermal section of the ternary phase diagram of the Nb–Ti–Si system. Journal of Alloys and Compounds, 468 (2009) pp. 150–153

F. Zhang, L.T. Zhang, A.D. Shan, and J.S. Wu. In situ observations of the pest oxidation process of $NbSi_2$ at 1023 K. Scripta Materialia, 53 (2005) pp. 653-656

F. Zhang, L.T. Zhang, A.D. Shan, and J.S. Wu. Microstructural effect on oxidation kinetics of $NbSi_2$ at 1023 K. Journal of Alloys and Compounds, 422 (2006) pp. 308-312

J.C. Zhao, B.P. Bewlay, M.R. Jackson. Determination of Nb–Hf–Si phase equilibria. Intermetallics, 9 (2001) pp. 681–689

J.C. Zhao, L.A. Peluso, M.R. Jackson, L. Tan. Phase diagram of the Nb–Al–Si ternary system. Journal of Alloys and Compounds, 360 (2003a) pp. 183–188

J.C. Zhao, M.R. Jackson, L.A. Peluso. Determination of the Nb–Cr–Si phase diagram using diffusion multiples. Acta Materialia, 51 (2003b) pp. 6395–6405

J.-C. Zhao, M.R. Jackson, L.A. Peluso. Mapping of the Nb–Ti–Si phase diagram using diffusion multiples. Materials Science and Engineering A, 372 (2004a) pp. 21–27

J.C. Zhao. Reliability of the diffusion-multiple approach for phase diagram mapping. Journal of Materials Science, 39 (2004b) pp. 3913 – 3925

J.C. Zhao, M.R. Jackson, L.A. Peluso. Evaluation of phase relations in the Nb-Cr-Al sytem at 1000 °C using diffusion-multiple approach. Journal of phase equilibria and diffusion, 25 (2004c) pp. 152-159

H. Zheng, Z. Lu, S. Lu,Z. Q. Su and F. Quan. Study on scaling of mechanically alloyed and hot pressed $NbCr_2$ Laves phase at 1200° C. International Journal of Refractory Metals & Hard Materials, 26 (2008) pp. 1-4

H. Zheng, Z. Lu, S. Lu, Z. Jianye, L. Guangming. Effect of Al additions on the oxidation behaviour of Laves phase $NbCr_2$ alloys at 1373 K and 1474 K. International Journal of Refractory Metals & Hard Materials, 27 (2009) pp. 659-663

Zheng Xu, PhD thesis, University of Sheffield (2016)

Zifu Li, PhD thesis, University of Sheffield (2012)

W.A. Zinsser Jr. and J.J. Lewandowski. Effects of R-Ratio on the fatigue crack growth of Nb-$(Si)s_s$and Nb-10Si in situ composites. Metallurgical and Materials transactions A, 29A (1998) pp. 1749-1757